

LOAN DOCUMENT

DTIC ACCESSION NUMBER	LEVEL	PHOTOGRAPH THIS SHEET	INVENTORY <div style="border: 1px solid black; border-radius: 50%; width: 40px; height: 40px; margin: 0 auto; display: flex; align-items: center; justify-content: center;">1</div>												
<div style="float: right; margin-right: 50px;">Vol. 1</div> <div style="font-size: 1.2em; margin-bottom: 5px;">Army Science Conf. Proceedings, 17-20 Jun 80 . . .</div> <div style="text-align: center; border-bottom: 1px solid black; margin-bottom: 5px;">DOCUMENT IDENTIFICATION</div>															
<div style="border: 1px solid black; padding: 5px; display: inline-block;"> DISTRIBUTION STATEMENT A Approved for Public Release "DTIC USERS ONLY" Distribution Unlimited </div>															
<div style="border: 1px solid black; padding: 2px;"> <small>ACCESSION FOR</small> <table style="width: 100%; border-collapse: collapse;"> <tr> <td style="width: 50%;"><input type="checkbox"/> NTIS</td> <td style="width: 50%;"><input type="checkbox"/> GRAM</td> </tr> <tr> <td><input type="checkbox"/> DTIC</td> <td><input type="checkbox"/> TRAC</td> </tr> <tr> <td colspan="2"><input type="checkbox"/> UNANNOUNCED</td> </tr> <tr> <td colspan="2"><input type="checkbox"/> JUSTIFICATION</td> </tr> </table> </div> <div style="border: 1px solid black; padding: 2px; margin-top: 5px;">BY</div> <div style="border: 1px solid black; padding: 2px; margin-top: 5px;">DISTRIBUTION/</div> <div style="border: 1px solid black; padding: 2px; margin-top: 5px;">AVAILABILITY CODES</div> <table border="1" style="width: 100%; border-collapse: collapse; margin-top: 5px;"> <tr> <th style="width: 50%;">DISTRIBUTION</th> <th style="width: 50%;">AVAILABILITY AND/OR SPECIAL</th> </tr> <tr> <td style="height: 40px; vertical-align: top;"> <div style="font-size: 1.5em; margin-bottom: 10px;">A-1</div> <div style="font-family: cursive; font-size: 0.8em;">[Signature]</div> </td> <td style="height: 40px;"></td> </tr> </table>		<input type="checkbox"/> NTIS	<input type="checkbox"/> GRAM	<input type="checkbox"/> DTIC	<input type="checkbox"/> TRAC	<input type="checkbox"/> UNANNOUNCED		<input type="checkbox"/> JUSTIFICATION		DISTRIBUTION	AVAILABILITY AND/OR SPECIAL	<div style="font-size: 1.5em; margin-bottom: 10px;">A-1</div> <div style="font-family: cursive; font-size: 0.8em;">[Signature]</div>		<div style="border: 1px solid black; height: 150px; margin-bottom: 10px;"></div> <div style="text-align: center; font-weight: bold; font-size: 0.8em;">DATE ACCESSIONED</div> <div style="border: 1px solid black; height: 100px; margin-bottom: 10px;"></div> <div style="text-align: center; font-weight: bold; font-size: 0.8em;">DATE RETURNED</div> <div style="border: 1px solid black; height: 100px;"></div> <div style="text-align: center; font-weight: bold; font-size: 0.8em;">REGISTERED OR CERTIFIED NUMBER</div>	
<input type="checkbox"/> NTIS	<input type="checkbox"/> GRAM														
<input type="checkbox"/> DTIC	<input type="checkbox"/> TRAC														
<input type="checkbox"/> UNANNOUNCED															
<input type="checkbox"/> JUSTIFICATION															
DISTRIBUTION	AVAILABILITY AND/OR SPECIAL														
<div style="font-size: 1.5em; margin-bottom: 10px;">A-1</div> <div style="font-family: cursive; font-size: 0.8em;">[Signature]</div>															
<div style="border: 1px solid black; padding: 10px; font-size: 1.5em; font-weight: bold;">19990512 088</div>															
DATE RECEIVED IN DTIC															
PHOTOGRAPH THIS SHEET AND RETURN TO DTIC-FDAC															

HANDLE WITH CARE

RIA-80-U924

Vol. I



TECHNICAL
LIBRARY

Army Science Conference Proceedings

17-20 June 1980

Volume I

Principal Authors A thru D

This document has been approved for public
release and sale; its distribution is unlimited.

**Deputy Chief of Staff for Research,
Development & Acquisition
Department of the Army**



DEPARTMENT OF THE ARMY
OFFICE OF THE DEPUTY CHIEF OF STAFF
FOR RESEARCH, DEVELOPMENT, AND ACQUISITION
WASHINGTON, D.C. 20310

REPLY TO
ATTENTION OF
DAMA-ARZ-D

21 July 1980

SUBJECT: Proceedings of the 1980 Army Science Conference

SEE DISTRIBUTION

1. The twelfth in a series of Army Science Conferences was held at the United States Military Academy, 17-20 June 1980. The conference presented a cross section of the many significant scientific and engineering programs carried out by the Department of the Army and provided an opportunity for Department of the Army civilian and military scientists and engineers to present the results of their research and development efforts before a distinguished and critical audience.
2. These Proceedings of the 1980 Army Science Conference are a compilation of all papers presented at the conference and the supplemental papers that were submitted. The Proceedings consist of four volumes, with Volumes I through III unclassified, and Volume IV classified.
3. Our purpose for soliciting these papers was:
 - a. To stimulate the involvement of scientific and engineering talent within the Department of the Army.
 - b. To demonstrate Army competence in research and development.
 - c. To provide a forum wherein Army personnel can demonstrate the full scope and depth of their current projects.
 - d. To promote the interchange of ideas among members of the Army scientific and engineering community.
4. It is hoped that the information contained in these volumes will be of benefit to those who attended the conference and to others interested in Army research and development.

DONALD R. KEITH
Lieutenant General, GS
Deputy Chief of Staff for Research,
Development, and Acquisition

DISTRIBUTION:

Director of Army Research
Office of the Surgeon General
Office, Chief of Engineers, ATTN: DAEN-ZA
Office, Chief of Engineers, ATTN: DAEN-ZC
Office, Chief of Engineers, ATTN: DAEN-RDM
Office, Chief of Engineers, ATTN: DAEN-RDZ-A
Office, Chief of Engineers, ATTN: DAEN-MPR-A
Office, Chief of Engineers, ATTN: DAEN-CWM-R
The Army Library, ATTN: ANRAL-RS

COMMANDERS/DIRECTORS

US Army Ballistic Missile Defense Systems Command
US Army Computer Systems Command
US Army Forces Command
US Army Intelligence and Security Command
US Army Materiel Development and Readiness Command, ATTN: DRCLDC
US Army Armament Materiel Readiness Command
Rock Island Arsenal
Watervliet Arsenal
US Army Armament Research and Development Command
US Army Ballistic Research Laboratory
US Army Chemical Systems Laboratory
Fire Control and Small Caliber Weapons Systems Laboratory
Large Caliber Weapons Systems Laboratory
Benet Weapons Laboratory
US Army Aviation Research and Development Command
US Army Aviation Center
US Army Avionics R&D Activity
US Army Research and Technology Laboratories (USARTL, AVRADCOM)
Aeromechanics Laboratory, NASA-Ames Research Center
Applied Technology Laboratory
Propulsion Laboratory, NASA-Lewis Research Center
Structures Laboratory, NASA-Langley Research Center
US Army Communications and Electronics Materiel Readiness Command
US Army Communications Research and Development Command
US Army Center for Communications
US Army Center for Technical Computer Sciences
US Army Electronics Research and Development Command
US Army Atmospheric Sciences Laboratory
US Army Combat Surveillance and Target Acquisition Laboratory
US Army Electronic Warfare Laboratory
US Army Electronics Technology and Devices Laboratory
US Army Harry Diamond Laboratories
US Army Night-Vision and Electro-Optics Laboratory
US Army Signals Warfare Laboratory
US Army Missile Command
Propulsion Directorate, US Army Missile Laboratory

US Army Mobility Equipment Research and Development Command
 US Army Electrical Power Laboratory
 US Army Natick Research and Development Command
 US Army Tank-Automotive Materiel Readiness Command
 US Army Tank-Automotive Research and Development Command
 US Army Test and Evaluation Command
 US Army Aircraft Development Test Activity
 US Army Aberdeen Proving Ground
 Materiel Testing Directorate
 US Army Cold Regions Test Center
 US Army Dugway Proving Ground
 US Army Electronics Proving Ground
 US Army Tropic Test Center
 US Army White Sands Missile Range
 Instrumentation Directorate
 National Range Operations Directorate
 US Army Yuma Proving Ground
 US Army Troop Support and Aviation Materiel Readiness Command
 US Army Electronics Materiel Readiness Activity
 US Army Foreign Science and Technology Center
 US Army HQ TRADOC Combined Arms Test Activity
 US Army Human Engineering Laboratory
 US Army Logistics Center
 US Army Materials and Mechanics Research Center
 US Army Materiel Systems Analysis Activity
 US Army Research Office
 US Army Research, Development and Standardization Group (Europe)
 US Army Training and Doctrine Command
 US Army Concepts Analysis Agency
 US Army Operational Test and Evaluation Agency
 US Army Japan, Camp Zama
 US Army Inst for Research in Management Info and Computer Sciences
 US Army Reserve Components Personnel and Administration Center
 US Army Soldier Support Center
 Lawrence Livermore National Laboratory, Univ of California, Livemore
 Los Alamos Scientific Laboratory
 US Army Health Services Command
 US Army Institute of Surgical Research
 US Army Medical Research and Development Command
 US Army Medical Research Institute of Infectious Diseases
 US Army Research Institute for the Behavioral and Social Sciences
 US Army Research Institute of Environmental Medicine
 Letterman Army Institute of Research
 Walter Reed Army Institute of Research
 US Army Aeromedical Research Laboratory
 US Army Biomedical Laboratory
 US Army Environmental Hygiene Agency
 US Army Medical Bioengineering Research and Development Laboratory

Brooke Army Medical Center
Dwight D. Eisenhower Medical Center
Fitzsimons Army Medical Center
Madigan Army Medical Center
US Army Tripler Medical Center
Walter Reed Army Medical Center
Armed Forces Institute of Pathology
US Army Institute of Dental Research
US Army Coastal Engineering Research Center
US Army Cold Regions Research and Engineering Laboratory
US Army Construction Engineering Research Laboratory
US Army Engineer Topographic Laboratories
US Army Engineer Waterways Experiment Station
US Army Engineering Division, North Atlantic

PROJECT MANAGERS

Army Tactical Data Systems (ARTADS), Fort Monmouth
Remotely Monitored Battlefield Sensor Systems (REMBASS), Fort Monmouth
Army Tactical Communications Systems (ATACS), Fort Monmouth

COMMANDANTS

National Defense University
National War College
Industrial College of the Armed Forces
Academy of Health Sciences
US Army Field Artillery School
US Army Infantry School
US Army Intelligence Center and School
US Army Military Police Chemical School and Training Center
US Army Signal Center at Fort Gordon
US Army Transportation School

SUPERINTENDENT

US Army Military Academy, ATTN: Technical Library
US Army Military Academy, ATTN: Acquisition Branch

COPIES FURNISHED:

Office, Under Secretary of Defense for Research and Engineering
Office, Deputy Director for Science and Technology, Defense Nuclear Agency
Chairman, Defense Science Board
Defense Advanced Research Projects Agency
Defense Communication Agency
Defense Communication Engineering Center
Defense Documentation Center
Defense Science Board
Institute for Defense Analysis
Deputy Chief of Staff for Logistics, HQDA
Deputy Chief of Staff for Operations and Plans, HQDA
Deputy Chief of Staff for Personnel, HQDA
Assistant Chief of Staff for Automation and Communications, HQDA
Assistant Chief of Staff for Intelligence, HQDA
Office of the Chief of Public Affairs, HQDA

First United States Army
National Academy of Sciences
National Aeronautics and Space Administration (Code L-2)
National Bureau of Standards
National Institute for Occupational Safety and Health, HEW
National Institutes of Health
National Science Foundation
National Security Agency
Office of Personnel Management
US Army Acquisition Information Systems Agency
US Army Scientific Information Center
Air Force Institute of Technology
Air Force Office of Scientific Research
Air Force Systems Command
Naval Air Systems Command
Naval Materiel Command
Naval Research Laboratory
Naval Research Library (Code 2627)
Office of Naval Research (Code 102)
Office of Naval Research (Code 230)
HQ US Marine Corps (Code RD-1)
Science Advisor to the Commandant, US Coast Guard
Battelle Columbus Laboratories
Mathematics Research Center, Univ of Wisconsin, Madison
Southwest Research Institute

PROCEEDINGS

OF THE

1980 ARMY SCIENCE CONFERENCE

UNITED STATES MILITARY ACADEMY

WEST POINT, NEW YORK

17-20 JUNE 1980

V O L U M E I

Principal Authors A through D

All experiments involving live animals that are reported in the Proceedings were performed in accordance with the principles of laboratory animal care as promulgated by the National Society of Medical Research.

TABLE OF CONTENTS

PROCEEDINGS OF THE 1980 ARMY SCIENCE CONFERENCE

<u>Author</u>	<u>Title</u>	<u>Vol</u>	<u>Page</u>
Abramovitz, I. J.	See Berg, N. J.	4	1
Ahn, B. H. Clark, W. W., III	Second Harmonic Generation of Near Millimeter Wave Radiation by Non- Linear Bulk Material	1	1
Aiken, E. W.	The Effects of Control System and Display Variations for an Attack Helicopter Mission Through Piloted Simulation	1	17
Aitken, G. W. Richmond, P. W., III Albert, D. G.	Impact Fuze Performance in Snow	1	31
Albert, D. G.	See Aitken, G. W.	1	31
Albritton, G. E. Balsara, J. P.	Response of Buried Vertically Oriented Cylinders to Dynamic Loading	1	47
Alexander, P. M.	Frequency Diverse Tracking/Guidance Millimeter Radar Adapted to Target Acquisition	1	61
Alley, B. J.	Low Temperature X-Ray Diffraction Investigation of Embrittled Mini- mum Signature Chaparral Propellant	1	77
Alster, J. Slagg, N Dewar, M. J. S. Ritchie, J. P. Wells, C.	A Reaction Mechanism in the Shock Initiation of Detonation. A Theo- retical Study	1	91
Ashman, W. P. Thornton, W. Broome, P. H. King, J. W. Sacco, W. J.	Pattern Recognition Applications in Chemistry and Pharmacology: A 'Pharmacophore Acetylcholino- receptor' Subunit Environment Model	1	105
Atkins, R. M.	See Heberlein, D. C.	4	67

<u>Author</u>	<u>Title</u>	<u>Vol</u>	<u>Page</u>
Aucoin, T. R. Savage, R. O. Wade, M. J. Gualtieri, J. G. Schwartz, A.	Large High Quality Single Crystal Aluminum Phosphate for Acoustic Wave Devices	1	121
Aucoin, T. R.	See Ross, R. L.	3	205
Baladi, G. Y. Rohani, B.	A Terrain-Vehicle Model for Analysis of Steerability of Tracked Vehicles	1	135
Ballato, A. Lukaszek, T.	Combat Hardened Communications: High Precision Frequency Control Using Resonators Immune to Accele- ration and Stress Fields	1	151
Ballato, A. T.	See Iafrate, G. J.	2	295
Balsara, J. P.	See Albritton, G.	1	47
Banderet, L. E. Stokes, J. W. Francesconi, R. Kowal, D.	Simulated, Sustained-Combat Oper- ations in the Field Artillery Fire Direction Center(FDC): A Model for Evaluating Biomedical Indices	1	167
Banister, G. H.	Testing of the Army's Inter- operating Network of Tactical C ³ I Systems	1	183
Beatrice, E. S.	See O'Mara, P. A.	3	31
Beck, R. R.	See Hoogterp, F. B.	2	263
Beisel, W. R.	See Daniels, W. L.	1	429
Berg, N. J. Abramovitz, I. J. Lee, J. N. Casseday, M. W.	Acousto-Optic Time Integrating Correlator for Detection and Characterization of Broad Band LPI Communications	4	1
Berry, P. Keane, W. Hatfield, G. Filler, M.	The Biological Detector and Warning System, XM19/XM2	1	197

<u>Author</u>	<u>Title</u>	<u>Vol</u>	<u>Page</u>
Biggs, S. L.	See Zwick, H.	3	461
Blackman, G. R.	Geometric and Temporal Characterization of Battlefield Smoke and Dust by Multispectral Digital Image Analysis	1	211
Bowden, C. M. Howgate, D. W.	MICOM Program in Optical Bistability	1	225
Brandt, H. E.	See Kehs, R. A.	2	339
Britt, J. R.	Calculation of Ground Shock Motion Produced by Near Surface Airburst Explosions Using Cagniard Elastic Propagation Theory	1	241
Brodman, B. W.	See Devine, M. P.	1	467
Bromborsky, A.	See Kehs, R. A.	2	339
Broome, P. H.	See Ashman, W. P.	1	105
Brown, N. D.	See Doctor, B. P.	1	487
Bruce, C. W.	See Bruce, D.	1	255
Bruce, D. Bruce, C. W. Yee, Y. P. Burket, H.	Experimentally Determined Relationship Between Extinction and Liquid Water Content	1	255
Brynjolfsson, A.	See Wang, C. P.	3	357
Burket, H.	See Bruce, D.	1	255
Buser, R. G.	See Rohde, R. S.	3	195
Bush, C. C.	See Sturek, W. B.	3	281
Bussell, N. E. Miller, R. A. Hawley, C. E.	Preliminary Studies on the Effects of Organophosphate Chemical Warfare Agents on Oral Cavity Physiology	1	265

<u>Author</u>	<u>Title</u>	<u>Vol</u>	<u>Page</u>
Butler, D. K.	Microgravimetry and the Measurement and Application of Gravity Gradients	1	279
Cadwallender, W. K. Kramer, K. Jankowski, P. Z. Kisatsky, P. J.	Full Field Interferometry Applications to Army Problems	1	293
Canonico, P. G. Little, J. S. Jahrling, P. B. Stephen, E. L.	Mechanism of Action of Ribavirin: An Antiviral Drug of Military Importance	1	309
Casseday, M. W.	See Berg, N. J.	4	1
Cassidy, T. W.	See Moulton, J. R.	4	111
Charland, J. J.	Computer Graphics for the Army	1	321
Chen, F.	Materials Deterioration in Tropic Versus Conus Sites	1	337
Chen, P. F. Seemuller, W. W.	Detection of Signal Signatures of Cartographic Features	1	353
Chernick, J. A.	See Scungio, R. C.	3	219
Choi, C. S.	See Prask, H. J.	3	153
Christensen, C. R. Hartman, R. L.	Optical Correlation Seeker	1	369
Chubb, D. W. J. Miller, J. A.	The Design and Implementation of Digital Demodulator for Use Against On-Off Keyed Signals	4	17
Chylek, P.	See Pinnick, R. G.	3	101
Clark, E. J.	See Neely, E. S.	3	1
Clark, W. W., III	See Ahn, B. H.	1	1
Clare, V. R.	See Posey, W. R.	3	137

<u>Author</u>	<u>Title</u>	<u>Vol</u>	<u>Page</u>
Cline, J. H.	See Hammond, C. E.	2	147
Cohen, S. H.	See Walker, J. E., Jr.	3	345
Cole, J. E.	See Fifer, F. A.	2	13
Coleman, A. J.	The Adsorption and Electrooxidation of Simple Hydrocarbons for Direct Oxidation Hydrocarbon-Air Fuel Cells	1	385
Collett, E.	Spatial Coherence and Intensity Properties of Quasihomogeneous Optical Sources	1	399
Comas, J.	See Zavada, J. M.	3	445
Cook, C. F., Jr.	See Iafrate, G. J.	2	295
Corbin, N. D.	See McCauley, J. W.	2	453
Crowson, A.	Powder Metallurgy Steel Forgings for Small Arm Applications	1	413
Cuthbert, B. N.	See Graeber, R. C.	2	73
Cutright, D. E.	See Grower, M. F.	2	105
Cutright, D. E.	See Posey, W. R.	3	137
D'Agostino, J. Lillie, T.	Overhead IR Target Signature Data Base	4	43
Daniels, W. L. Wright, J. E. Knapik, J. J. Vogel, J. A. Friman, G. Beisel, W. R.	The Effect of Experimentally Induced Viral Infection on Physical Performance Capacity	1	429
Daniels, W. L.	See Wright, J. E.	3	381
Daum, G. R.	Broadband Absorption Studies	4	55

<u>Author</u>	<u>Title</u>	<u>Vol</u>	<u>Page</u>
Dean, A. M., Jr.	Evaluation of Ice-Covered Water Crossings	1	443
Dehn, J.	The Particle Dynamics of Penetration	1	455
Devine, M. P. Brodman, B. W.	The Effect of Chemical Interactions on the Small Arms Deterring Process	1	467
Dewar, M. J. S.	See Alster, J.	1	91
Dixon, S. Jacobs, H.	Millimeter-Wave Self Mixing Oscillators	1	473
Doctor, B. P. Brown, N. D. Sleeman, H. K.	The Stability of Benactyzine.HCl Under Simulated Storage and Packing Conditions	1	487
Douglas, C. D. Lewis, R. W.	Advanced Composite Applications to Large Caliber Weapons Systems	1	503
Drabo, M. J.	See Klarich, C. R.	2	365
Embury, J. F.	In Search of Strong Infrared Extinction in Aerosols	2	1
Faden, A. I.	See Holaday, J. W.	2	233
Fifer, R. A. Cole, J. E.	Burning Rate Transitions for HMX Burned as a Binderless Propellant	2	13
Figucia, F.	Energy Absorption of Kelvar [®] Fabrics Under Ballistic Impact	2	29
Fileccia, R. J.	See Vogel, R. S.	3	329
Filler, M.	See Berry, P.	1	197
Francesconi, R.	See Banderet, L. E.	1	167
Frey, R. B.	The Initiation of Explosive Charges by Rapid Shear	2	43

<u>Author</u>	<u>Title</u>	<u>Vol</u>	<u>Page</u>
Frickel, R. H.	See Stuebing, E. W.	3	265
Friman, G.	See Daniels, W. L.	1	429
Gavanis, T. J.	See Zavada, J. M.	3	445
Gilbert, A. L.	See Machuca, R.	2	427
Goldstein, S.	Interior Ballistic Modeling for Blank Ammunition	2	59
Graeber, R. C. Cuthbert, B. N. Sing, H. C. Schneider, R. J. Sessions, G. R.	Rapid Transmeridian Deployment: Cognitive Performance and Chrono- biologic Prophylaxis for Circa- dian Dyschronism	2	73
Gray, J.	Army GPS-Doppler Hybrid Navi- gation System	2	89
Grower, M. F. Cutright, D. E. Russell, E. A., Jr.	Regeneration of Surgically Excised Segments of Dog Esophagus Using Biodegradable Pla Hollow Organ Grafts	2	105
Gualtieri, J. G.	See Aucoin, T. R.	1	121
Hackett, R. M.	Three-Dimensional Finite Element Combustion Instability Analysis	2	119
Hahn, F. E.	Experimental Chemotherapy: A Rapid and Simple Screening Method for Drug Binding to DNA	2	133
Hammond, C. E. Cline, J. H.	On the Use of Active Higher Har- monic Blade Pitch Control for Helicopter Vibration Reduction	2	147
Hansen, F. V. Pena, R. Umstead, R. K.	Deliberate Air Pollution: The Art of Smoke Screening	2	165
Hartman, R. L.	See Christensen, C. R.	1	369

<u>Author</u>	<u>Title</u>	<u>Vol</u>	<u>Page</u>
Harvey, J. F.	Analysis of Multipass Laser Amplifier Systems for Storage Laser Media	2	181
Hatfield, G.	See Berry, P.	1	197
Hawley, C. E.	See Bussell, N. E.	1	265
Heberlein, D. C. Atkins, R. M.	Projection of Vehicle Magnetic Signatures for the Defeat of Magnetic Mine Influence Sensors	4	67
Heaston, R. J.	Redefinition of the Four Fundamental Forces	2	203
Helbert, J. N.	See Iafrate, G. J.	2	295
Henry, M. C. Laible, R. C.	Improvements in CB Protective Clothing	2	219
Holaday, J. W. Faden, A. I.	The Role of Endorphins in the Pathophysiology of Shock and the Therapeutic Benefit of Opiate Antagonists	2	233
Holst, G. C.	Infrared Transmission Measurements Through Screening Smokes: Experimental Considerations	2	247
Hoogterp, F. B. Beck, R. R.	Vehicle Mobility or Firing Stability-a Delicate Balance	2	263
Houghton, W. W.	See Shuford, R. J.	3	235
Houle, M. J. Janroga, S.	The Effect of EA 3834 on Plants	4	81
Howgate, D. W.	See Bowden, C. M.	1	225
Huber, W. A.	Coding and Processing for Reliable Data Transmission	2	279
Huddleston, R. L.	See Klarich, C. R.	2	365
Hunsperger, R. G.	See Zavada, J. M.	3	445

<u>Author</u>	<u>Title</u>	<u>Vol</u>	<u>Page</u>
Iafrate, G. J. Helbert, J. N. Ballato, A. T. Cook, C. F., Jr. McAfee, W. S.	Fundamental Limitations of Electron Beam Lithography for Future Military IC Device Fabrication	2	295
Jacobs, H.	See Dixon, S.	1	473
Jahrling, P. B.	See Canonico, P. G.	1	309
Jankowski, P. Z.	See Cadwallender, W. K.	1	293
Janroga, S.	See Houle, M. J.	4	81
Jenkinson, H. A.	See Zavada, J. M.	3	445
Jennings, S. G.	See Pinnick, R. G.	3	101
Kascak, A. F.	The Response of Turbine Engine Rotors to Interference Rubs	2	309
Kayser, L. D.	See Nietubicz, C. J.	3	17
Keane, W.	See Berry, P.	1	197
Kearney, F.	Nondestructive Testing for Field Welds: Real Time Weld Quality Monitor	2	325
Kehs, R. A. Brandt, H. E. Bromborsky, A. Lasche, G.	The Generation of Gigawatt Power Levels of Microwave Radiation	2	339
Kelso, D. H. Marley, J. J.	Network Traffic Analysis Model	2	351
King, J. W.	See Ashman, W. P.	1	105
Kisatsky, P. J.	See Cadwallender, W. K.	1	293
Klarich, C. R. Huddleston, R. L. Drabo, M. J.	Electron Microscopy Used for Fracture Mode Identification	2	365

<u>Author</u>	<u>Title</u>	<u>Vol</u>	<u>Page</u>
Klose, D. R. Skudera, W. J.	Dual-Channel SAW Compressive Direction-Finding Techniques	4	95
Knapik, J. J.	See Daniels, W. L.	1	429
Knapik, J. J.	See Wright, J. E.	3	381
Kowal, D.	See Banderet, L. E.	1	167
Kramer, K.	See Cadwallender, W. K.	1	293
Kulpa, S. M.	See Weber, B. A.	3	371
Kuzanek, J. F.	Improved Methods for Computing Drag Corrected Missile Impact Predictions in Real Time	2	381
Lahoti, G. Lee, F. M.	Application of Process Modeling to Shell Drawing Operations	2	395
Laible, R. C.	See Henry, M. C.	2	219
Lampo, R. G.	See Vogel, R. S.	3	329
Larson, D. C.	See Zavada, J. M.	3	445
Lasche, G.	See Kehs, R. A.	2	339
Lee, F. M.	See Lahoti, G.	2	395
Lee, J. N.	See Berg, N. J.	4	1
Lewis, R. W.	See Douglas, C. D.	1	503
Lillie, T.	See D'Agostino, J.	4	43
Link, L. E.	Terrain Thermal Modeling for Camouflage and Target Acquisition	2	411
Little, J. S.	See Canonico, P. G.	1	309
Lukaszek, T.	See Ballato, A.	1	151

<u>Author</u>	<u>Title</u>	<u>Vol</u>	<u>Page</u>
Lund, D. J.	See O'Mara, P. A.	3	31
Machuca, R. Gilbert, A. L.	Finding Edges in Noisy Scenes	2	427
Malik, R. J.	See Ross, R. L.	3	205
Marley, J. J.	See Kelso, D. H.	2	351
Martin, L. A.	High Performance Vehicles	2	443
McAfee, W. S.	See Iafrate, G. J.	2	295
McCauley, J. W. Corbin, N. D.	Transparent, Polycrystalline Cubic Aluminum Oxide	2	453
McKnight, C. E.	Disposal of Soluble Salt Waste From Coal Gasification	2	469
Mikucki, W. J.	See Vogel, R. S.	3	329
Miller, J. A.	See Chubb, D. W. J.	4	17
Miller, R. A.	See Bussell, N. E.	1	265
Miller, R. J., Jr.	See Reichard, D. W.	3	169
Moore, R. L.	Non-Linear Least Chi-Square Algorithm-an Improvement on Non- Linear Least Squares	2	483
Moss, G. L.	Armor Design Based on Material Properties	2	499
Moulton, J. R. Cassidy, T. W.	Grafenwoehr II Realistic Battle- field Sensors Trials	4	111
Mylin, D. C.	See Sturek, W. B.	3	281
Neely, E. S. Clark, E. J.	Case Study Use of EDITSPEC, the Corps of Engineers Computer Aided Specification Preparation System	3	1
Nelson, J. F.	See Posey, W. R.	3	137

<u>Author</u>	<u>Title</u>	<u>Vol</u>	<u>Page</u>
Nietubicz, C. J. Kayser, L. D.	A Comparison of Navier-Stokes Computations With Experimental Data for a Projectile Shape at Transonic Velocities	3	17
Nomiyama, N. T.	See Rohde, R. S.	3	195
Obert, L. P. Ratches, J. A.	Realistic European Battlefield Target Acquisition Model	4	127
O'Mara, P. A. Stamper, D. A. Beatrice, E. S. Lund, D. J.	Laboratory Investigations of Biomedical Factors Influencing Laser Designator Operator Performance	3	31
O'Mara, P. A.	See Zwick, H.	3	461
Oscar, K. J.	Effects of Low Power Microwaves on the Local Cerebral Blood Flow of Conscious Rats	3	45
Owens, F. J.	Molecular Level Modeling of the Mechanism of Shock Initiation of Solid Explosives	3	55
Patton, J. F.	See Vogel, J. A.	3	313
Patton, J. F.	See Wright, J. E.	3	381
Pena, R.	See Hansen, F. V.	2	165
Peterson, E. G. Salomon, L. L.	Methodology for Evaluation of Obscuration	3	71
Perkins, J. S.	Laser Interaction with TBR Materials	3	85
Pinnick, R. G. Jennings, S. G. Chylek, P.	Relationships Between Extinction and Mass Content of Atmospheric Fog and Military Smokes	3	101
Pleasants, W. A., III White, G. T., III	Status of Improved Autorotative Landing Capability Research	3	117

<u>Author</u>	<u>Title</u>	<u>Vol</u>	<u>Page</u>
Posey, W. R. Cutright, D. E. Russell, E. A., Jr. Nelson, J. F. Clare, V. R.	The Effects of High Velocity Variable Mass Projectiles on the Maxillofacial Complex	3	137
Prask, H. J. Choi, C. S. Trevino, S. F.	Nondestructive Testing of Arma- ment-System Components by Means of Neutron Diffraction	3	153
Ratches, J. A.	See Obert, L. P.	4	127
Redwinski, R. J.	See Smith, R. C.	4	171
Reichard, D. W. Miller, R. J., Jr.	Chemiluminescence Immunoreactive Assay (CLIA): A Rapid Method for the Detection of Bacterial and Viral Agents - Francisella Tular- ensis, Live Vaccine Strain (LVS) and Venezuelan Equine Encephalo- myelitis Vaccine Strain (VEE TC-83)	3	169
Richmond, P. W., III	See Aitken, G. W.	1	31
Ritchie, J. P.	See Alster, J.	1	91
Rittenbach, O. E.	A New Technique for Doppler Fre- quency Analysis of Radar Signals	3	181
Robbins, F. M.	See Walker, J. E., Jr.	3	345
Rohani, B.	See Baladi, G. Y.	1	135
Rohde, R. S. Buser, R. G. Nomiya, N. T.	Pulse Code Modulation of CO ₂ TEA Laser Pulse	3	195
Ross, R. L. Aucoin, T. R. Savage, R. O. Winter, J. J. Malik, R. J.	Semi-Insulating Gallium Arsenide for Millimeter Wave and High Speed IC Device Applications	3	205
Rubel, G. O.	See Stuebing, E. W.	3	265

<u>Author</u>	<u>Title</u>	<u>Vol</u>	<u>Page</u>
Russell, E. A., Jr.	See Grower, M. F.	2	105
Russell, E. A., Jr.	See Posey, W. R.	3	137
Sacco, W. J.	See Ashman, W. P.	1	105
Salomon, L. L.	See Peterson, E. G.	3	71
Sampson, J. B.	See Wright, J. E.	3	381
Savage, J. J. Shaffer, R. E.	Multispectral Screening Agent Studies	4	143
Savage, R. O.	See Aucoin, T. R.	1	121
Savage, R. O.	See Ross, R. L.	3	205
Schneider, R. J.	See Graeber, R. C.	2	73
Schwartz, A.	See Aucoin, T. R.	1	121
Scungio, R. C. Chernick, J. A.	Performance Evaluation for Direct Fire Systems	3	219
Seemuller, W. W.	See Chen, P. F.	1	353
Sessions, G. R.	See Graeber, R. C.	2	73
Shaffer, R. E.	See Savage, J. J.	4	143
Shank, E. B. Thein, B. K.	MOUT/Assault Weapon Status	4	159
Share, S. Wasilik, J.	Nuclear Radiation Effects in Fiber-Optic Waveguides	3	223
Shuford, R. J. Houghton, W. W.	Acoustic Emission as a NDE Tech- nique for Determining Composite Rotor Blade Reliability	3	235
Sing, H. C.	See Graeber, R. C.	2	353
Skudera, W. J.	See Klose, D. R.	4	95

<u>Author</u>	<u>Title</u>	<u>Vol</u>	<u>Page</u>
Slagg, N.	See Alster, J.	1	91
Sleeman, H. K.	See Doctor, B. P.	1	487
Smith, R. C. Redwinski, R. J.	PATRIOT Survivability Study	4	171
Soicher, H.	Correlation and Prediction of Propagation Time-Delays Along Earth-Space Links	3	251
Stamper, D. A.	See O'Mara, P. A.	3	31
Stephen, E. L.	See Canonico, P. G.	1	309
Stokes, J. W.	See Banderet, L. E.	1	167
Stuebing, E. W. Frickel, R. H. Rubel, G. O.	Recent Research on Phosphorus Smoke	3	265
Sturek, W. B. Mylin, D. C. Bush, C. C.	Computational Parametric Study of the Aerodynamics of Spinning Slender Bodies at Supersonic Speeds	3	281
Tarbell, A. B.	Noise Performance of a New Type of Low Noise FM Detector	3	297
Thein, B. K.	See Shank, E. B.	4	159
Thornton, W.	See Ashman, W. P.	1	105
Trevino, S. F.	See Prask, H. J.	3	153
Umstead, R. K.	See Hansen, F. V.	2	165
Van Sice, C. W.	See Zwick, H.	3	461
Vogel, J. A. Wright, J. E. Patton, J. F.	Development of New Gender-Free Physical Fitness Standards for the Army	3	313
Vogel, J. A.	See Daniels, W. L.	1	429

<u>Author</u>	<u>Title</u>	<u>Vol</u>	<u>Page</u>
Vogel, J. A.	See Wright, J. E.	3	381
Vogel, R. S. Fileccia, R. J. Mikucki, W. J. Lampo, R. G.	Studies in the Identification of Hydrocarbon Products in Wastewater	3	329
Wade, M. J.	See Aucoin, T. R.	1	121
Walker, J. E., Jr. Robbins, F. M. Cohen, S. H.	The Effects of Catheptic Enzymes on Muscle Proteins	3	345
Wang, C. P. Brynjolfsson, A.	Heat Conduction in Finite Cylin- ders and the Computer-Aided Cal- culation of Bacteria Survival in Heat Sterilization	3	357
Wasilik, J.	See Share, S.	3	223
Weber, B. A. Kulpa, S. M.	The Extension of [Hg,Cd] Te Detector Technology to the Near-Milimeter Spectral Region	3	371
Wells, C.	See Alster, J.	1	91
White, G. T., III	See Pleasants, W. A., III	3	117
Winter, J. J.	See Ross, R. L.	3	205
Wright, J. E. Vogel, J. A. Sampson, J. B. Patton, J. F. Daniels, W. L. Knapik, J. J.	Physiological Work Capacity and Performance of Soldiers Follow- ing Transatlantic Deployment	3	381
Wright, J. E.	See Daniels, W. L.	1	429
Wright, J. E.	See Vogel, J. A.	3	313

<u>Author</u>	<u>Title</u>	<u>Vol</u>	<u>Page</u>
Wright, T. W.	Penetration With Long Rods: A Theoretical Framework and Comparison With Instrumented Impacts	3	397
Wu, J. J.	The Initial Boundary Value Problem of Gun Dynamics Solved by Finite Element-Unconstrained Variational Formulations	3	413
Yalamanchili, R.	New Concepts in Recoil Mechanisms	3	425
Yee, Y. P.	See Bruce, D.	1	255
Zavada, J. M. Jenkinson, H. A. Gavanis, T. J. Hunsperger, R. G. Larson, D. C. Comas, J.	Ion Implanted Guided Wave Devices for Army Fire Control	3	445
Zwick, H. Biggs, S. L. O'Mara, P. A. Van Sice, C. W.	A Solid State Dark Adaptometer	3	461

*AHN & CLARK

SECOND HARMONIC GENERATION OF NEAR MILLIMETER
WAVE RADIATION BY NONLINEAR BULK MATERIAL (U)

*BYONG H. AHN, Mr.
WILLIAM W. CLARK, III, PhD
NIGHT VISION & ELECTRO-OPTICS LABORATORY
FORT BELVOIR, VA 22060

I. Introduction.

Bulk crystals have been used frequently to obtain second harmonic generation (SHG) and third harmonic generation (THG) of radiation from the fundamental input frequency, particularly in the optical region.

For example, ammonium dihydrogen phosphate,⁽¹⁾ potassium dihydrogen phosphate,⁽²⁾ semiconductor materials,⁽³⁾ and ferroelectric materials⁽⁴⁾ were used for the SHG of input laser beams.

SHG and THG have also been realized in the microwave region. Boyd, et. al.,⁽⁵⁾ reported on the nonlinear coefficients and other important parameters at 55 GHz. Later, Boyd and Pollack⁽⁶⁾ published a comprehensive paper on the nonlinear coefficients of LiTaO_3 and LiNbO_3 in the microwave region. DiDomenico, Jr., et. al.,⁽⁷⁾ obtained a 9 GHz TH output with an efficiency of 8.5% from a 2200 watt 3 GHz source by use of a 73% BaTiO_3 - 27% SrTiO_3 ceramic in a coaxial cavity configuration.

Impetus for bulk harmonic generation in the microwave region was given by the discovery that some ferroelectric⁽⁵⁾ crystals have very large nonlinear coefficients, large enough to compensate for the lower frequencies of the microwave region in comparison to those of the optical region.

Our interest in SHG and THG in the microwave region started with the need for a radiation source at 220 GHz. Tube type sources

(i.e., klystron and magnetron) and solid state sources (i.e., IMPATT and GUNN diodes) encounter inherent material limitations and fabrication difficulties in terms of the electron and hole mobility and the small geometrical dimensions and high electrical field. These problems make it difficult and/or impossible to obtain 220 GHz radiation from these sources. On the other hand, size and weight of the source are very important system design criteria. A powerful gyrotron is too big and too heavy a system for portable use. Extended Interaction Oscillators (EIO) represent recent source options whose specified output power is 60 W at 220 GHz. Unit cost, lifetime, and ease of fabrication are also important parameters for consideration. At the present time, the lower frequency radiation sources tend to have a longer lifetime and are easier to make, both of which result in lower cost.

After weighing various system parameters, such as the efficiency, weight, size, power output, lifetime, and ease of fabrication, it was decided to investigate the bulk SHG and THG techniques as an option to satisfy the requirement for source development for specific NV&EOL systems applications. The performance specifications of the EIO will be used as the basis for our requirements analysis.

This paper will develop the theoretical conversion efficiency equations for the SHG and THG, illustrate the input power requirements for the known nonlinear materials and the material requirements for the available input power sources, and list the ferroelectric materials which show promise as bulk crystal harmonic generators. The experimental setup and the preliminary results will be described briefly.

II. Theory.

1. SHG. SHG is possible only in acentric crystals, wherein the input radiation produces polarization at the second harmonic given by⁽⁸⁾

$$P_i(2\omega) = \epsilon_0 \sum_{jk} d_{ijk}^m E_j(\omega) E_k(\omega) \quad \text{Eqn. (1)}$$

where $E_k(\omega)$ and $E_j(\omega)$ are the electric fields at the fundamental frequency, ω , ϵ_0 is the free space electric permittivity and d_{ijk}^m is the nonlinear coefficient.

a. Conversion Efficiency. Assuming the conversion efficiency is low and the absorption of the input power by the crystal is negligible, i.e., $E_{inc}^2(\omega)(z=0) \approx E_1^2(\omega)(z=l)$, then by proper adjustment

for d_{ijk}^m , the conversion efficiency can be expressed as⁽⁹⁾

$$\eta = p(2\omega)/p(\omega) = \frac{2\mu_o^{3/2}\epsilon_o^{1/2}\omega^2 (d^m)^2 \ell^2 p(\omega) \sin^2(\pi\ell/2\ell_c)}{n^3 A (\pi\ell/2\ell_c)^2} \quad \text{Eqn. (2)}$$

ℓ = interaction length

A = beam size

ℓ_c = coherence length

n = index of refraction

$p(\omega)$ = input power

d^m = nonlinear coefficient, usually expressed in 10^{-12}m/V

unit.

The unit of d in Reference 9 is obtained by multiplying d^m in this paper by 8.85×10^{-12} . If the conversion efficiency is high, i.e., $E_{\text{inc}}^2(\omega)(z=0) = E_1^2(\omega)(z=\ell) + E_2^2(2\omega)(z=\ell)$, the conversion efficiency is expressed as⁽¹⁰⁾

$$\eta = \tanh^2(\omega d^m E_{\text{inc}} \ell / nc)$$

converting this to more familiar terms

$$\eta = \tanh^2[\sqrt{2} \omega d^m \epsilon_o (\mu_o/\epsilon)^{3/4} \ell \sqrt{p(\omega)/A}] \quad \text{Eqn. (3)}$$

If the absorption is significant, then the second harmonic power is modified by⁽¹¹⁾

$$p'(2\omega) = p(2\omega) \exp(-\alpha_\omega \ell + 1/2 \alpha_{2\omega} \ell)$$

b. Nonlinear Coefficient. The generalized nonlinear coefficient is expressed as⁽¹²⁾

$$d^m(\omega) = \delta_{AB} [(\chi^i)^3 + (\chi^i)^2 (\chi^e)] + \delta_C (\chi^i) (\chi^e)^2 + \delta_D (\chi^e)^3 \quad \text{Eqn. (4)}$$

where χ^i = linear ionic susceptibility

χ^e = linear electronic susceptibility

$d^0 = \delta_D (\chi^e)^3$ nonlinear optical coefficient

the δ_i values in Eqn. (4) are all on the order of 10^{-12}m/V . In the optical region, only the linear electronic susceptibility χ^e contributes, whereas in the microwave region, all the terms contribute. In diatomic materials, such as GaAs and CdTe, χ^i is about the same as χ^e and d^m is about the same as d^0 . In ferroelectric materials, such as LiNbO_3 and BaTiO_3 , $\chi^i \gg \chi^e$ and $d^m \gg d^0$. Furthermore, the linear ionic susceptibility is related to the electrical permittivity as $\chi^i = \epsilon/\epsilon_o - n^2 - 1$ and $\chi^e = n^2 - 1$ (this n is the index of

refraction in the optical region). This indicates that a promising nonlinear material in the microwave region will have a large electrical permittivity, ϵ . In the ferroelectric crystals where $\chi^i \gg \chi^e$, we can assume that $\chi^i \approx \epsilon_\omega / \epsilon_o = n_\omega^2$, where ϵ_ω is the microwave electrical permittivity. The magnitude of the microwave nonlinear coefficient can be approximated as $d^m \approx \delta_{AB}(\chi^i)^3$

$$\approx \delta_{AB}(\epsilon_\omega / \epsilon_o)^3 \quad \text{Eqn. (5)}$$

$$\approx \delta_{AB}(n_\omega)^6$$

In the conversion efficiency, Eqn. (2), we notice that $\eta \propto (d^m)^2 / n^3$. By use of Eqn. (5), the above relationship can be expressed as

$$\eta \propto \delta_{AB}^2 (n_\omega^m)^{12} / (n_\omega^m)^3$$

$$\eta \propto (\delta_{AB})^2 n_\omega^9 \quad \text{Eqn. (6)}$$

The conversion efficiency is thus proportional to the 9th power of the index of the refraction in the microwave region.

The following table gives the summary of important parameters for SHG in bulk crystals.

Table I. Physical Parameters of Bulk Harmonic Generators⁽⁵⁾

MATERIAL	POINT GROUP	n_e	ϵ / ϵ_o	α cm^{-1}	χ^e	χ^i	δ_{AB} 10^{-12}m/V	d_{ijk} 10^{-12}m/V	ijk
BaTiO ₃	4mm	2.29	57	1.7	4.25	52	0.64	97,000	333
LiTaO ₃	3m	2.14	40	1.0	3.58	35.4	0.33	16,000	333
LiNbO ₃	3m	2.16	25.5	0.5	3.66	20.8	0.63	6,700	333
KDP*	$\bar{4}2\text{m}$	1.51	44	0.9	1.24	41.8	0.053	1,850	123
		1.47	21		1.13	18.9			
GaAs	$\bar{4}3\text{m}$	3.27	13.05	0.024	9.71	2.34	+0.12 -1.40	± 51	123

*Upper and lower values are for 1- and 3- axes, respectively.

Pollack and Turner⁽¹³⁾ reported the magnitude of BaTiO₃ in d_{113}^m to be $+3.9 \times 10^7$ in the units of 10^{-12} m/V . This value is greater than d_{333}^m of BaTiO₃ by a factor of 402. This is largely due to the constant strain dielectric constant of BaTiO₃ in the 1-axis, which is 2300.

c. Discussion. The coherence length in Eqn. (2) is the maximum useful length of the crystal for SHG.

In the optical region, the coherence length can be made large by carefully orienting the birefringent crystal such that $n_{2\omega}$ is very nearly equal to n_{ω} in the direction of the respective radiations. No such precaution is used in the microwave region because of the longer wavelength. Letting $n_{2\omega} - n_{\omega} = 0.01$,⁽¹⁴⁾ l_c at $\lambda = 5.45 \text{ mm}$ (55 GHz) is 136 mm.

Other factors which affect the conversion efficiency are the frequency, nonlinear coefficient, index of refraction, and the beam size. The decrease in frequency in going from the optical to the NMMW region is offset by the increase in the nonlinear coefficient, d^m , as can be seen in Table I. However, the increase in conversion efficiency due to the material coefficients is reduced somewhat by the factor of n^3 in the denominator of Eqn. (2). The true material dependence is given by Eqn. (6) which shows that conversion efficiency is roughly proportional to n^9 .

The conversion efficiency is also affected by the decrease in radiation intensity in the NMMW region. Assuming the beam size is limited by diffraction, the intensity is proportional to the inverse square of the wavelength. In going from a wavelength of 1 μm to 1 mm the reduction in conversion efficiency is on the order of 10^6 . The beam size in the NMMW region can be made somewhat smaller by use of waveguide.

2. Third Harmonic Generation (THG). THG is another technique to use for frequency multiplication. Cubic crystals can be used for THG. Terhune, et. al.,⁽¹⁵⁾ obtained THG from calcite using a ruby laser with a peak power of 200 kW. The conversion efficiency obtained was about 4×10^{-6} . Shelton and Shen⁽¹⁶⁾ obtained THG in cholesteric liquid crystals. Puell and Vidal⁽¹⁷⁾ obtained THG from alkalai metal vapors. Akitt and Coleman⁽¹⁸⁾ obtained THG in HCN gas in the microwave region with an efficiency of 1.5×10^{-5} using a 100 kW source. Bloom, et. al.,⁽¹⁹⁾ obtained a high conversion efficiency of 10% in a medium of xenon and rubidium with a mode-locked Nd:YAG laser with a peak power of 3×10^8 watt. Depending upon the available input power, THG can be a viable option to SHG.

The induced third-order polarization is given by

$$p^{(3)}(3\omega) = \epsilon_0 \chi^{(3)} E^3(\omega)$$

and the third harmonic output by (20)

$$p^{(3)}(3\omega) = \frac{9\mu_0^2 \omega^2 \ell^2 (\chi^{(3)})^2 p^3(\omega) \sin^2(\pi \ell / 2\ell_c)}{n A^2 (\pi \ell / 2\ell_c)^2}$$

where $\ell_c = \lambda / 6(n_{3\omega} - n_\omega)$

It can be seen that the third harmonic output is proportional to the third power of the input signal strength. The third harmonic nonlinear coefficients are typically smaller by a factor of 10^5 - 10^8 from their second harmonic counterparts. SrTiO_3 is an example of a material with a high nonlinear third harmonic coefficient in the NMMW region.

3. Temperature Effects. Changing the temperature can affect the SHG or THG in a number of ways. For instance, the phase transition temperature determines the crystal symmetry and thus its harmonic application. Theoretically SHG is possible only in acentric crystals.

Ferroelectric crystals have cubic symmetry in the paraelectric phase, cubic perovskite. In their ferroelectric phase, below the phase transition temperature, they lose the center of inversion. For example, KTaO_3 has a cubic symmetry at room temperature, but was observed to generate SH and TH at 4.2 K, (21) a few degrees above the extrapolated Curie temperature. The conversion efficiency for SHG was 10^{-3} - 10^{-4} and for THG was 10^{-5} - 10^{-6} in the 2-5 GHz range. Another example is SrTiO_3 which goes from cubic to tetragonal (C_{4v}) below 100 K. (22)

The index of refraction and the absorption coefficient also depend upon the temperature as well as the frequency. (14) Both values are smaller at the lower temperature and longer wavelengths. In addition, dielectric constants undergo a dramatic change around the Curie temperature (23) and follow the Curie-Weiss law for ferroelectric crystals.

Kaminov and Harding (24) measured the change in the dielectric constant and the loss tangent as a function of temperature at 9.2 GHz in KDP ($T_c = 123^\circ\text{K}$) and Talyanskij, et. al., (25) found that in general the second harmonic and the nonlinear coefficient changed in the same manner as the dielectric constants. They found that the

SH power at -120°C goes up as much as 7.5 times the room temperature SH power.

4. Applied DC Fields. Symmetric crystals can also be distorted into acentric structures under the influence of electric fields. Calcite, which possesses a center of inversion, was observed to generate SH even without an applied field. (26, 27) The output was observed to increase by a factor of 10 in a dc field of 200 kV/cm. The effective nonlinear coefficient in the optical region was about $3 \times 10^{-4} d_{36}$ (ADP). Maker and Terhune (20) expressed the nonlinear polarization of the electric field induced SHG in calcite by

$$P^{(3)}(3\omega) = 2\epsilon_0 \chi^{(3)} E^2(\omega) E_{dc}$$

They reported that with $E_{dc}=20$ kV/cm, SH power was about 1/500 that of KDP under similar setup using a ruby laser.

In SrTiO_3 the transverse optical frequency (ω_{to}) at 8 K shifts from 10 cm^{-1} to 45 cm^{-1} with an applied field of 12 kV/cm. (9) It is also slightly deformed under the dc field by about .056%. (28) This material can be grown by the flame fusion techniques in large sizes ($1 \times 1 \times 2 \text{ cm}$).

5. Numerical Calculation of the Output Power. Using the conversion efficiency equation, the SH power of LiNbO_3 , LiTaO_3 , and BaTiO_3 is calculated using an input power of .1 W at 55 GHz with a sample length of 1 cm.

LiNbO_3	$P(2\omega) = .049 \times 10^{-9} \text{ W}$
LiTaO_3	$P(2\omega) = .14 \times 10^{-9} \text{ W}$
BaTiO_3	$P(2\omega) = 3.35 \times 10^{-9} \text{ W}$

The above numbers assume that the input beam fills the waveguide, the phase is matched, and the polarization of the beam and the crystal orientation are consistent with the nonlinear coefficients given in Table I. It can be seen that at this input power level (which is typical for a klystron oscillator) a very sensitive detector is necessary to observe the SH output.

6. Performance Criteria for the Harmonic Generation. For high SHG, we must have a crystal with high d^m and/or a high power fundamental source.

An EIO producing 1 kW at 110 GHz and 60 W at 220 GHz is available from Varian of Canada. An equivalent conversion efficiency of 6% is used as the performance baseline.

By use of a BaTiO_3 crystal 1 cm long (d_{333}^m) and an EIO of 1 KW at 110 GHz, a calculated SH output of 4.46 W ($\eta=.446\%$) is obtained. Using the same crystal in the d_{113}^m mode a SH output of 174 W should be obtained.

For THG, SrTiO_3 requires a fundamental input power of 150 megawatts to obtain a 100 W third harmonic output at 210 GHz (assuming a value $\chi^{(3)}=7 \times 10^{-19}$ (mks) from optical data).

7. Crystals with High SHG Possibility. Ferroelectric crystals above and below the phase transition temperature can be useful for THG and SHG respectively in the microwave region. This is mainly due to the large ionic linear susceptibility which is related to the crystal distortion from the cubic structure. The materials with non-cubic structure and high constant-strain dielectric constants are selected for further study.

$\text{K}_6\text{Li}_4\text{NbO}_3$, (29) a crystal symmetry of 4mm, has a Curie temperature of 420°C and was found to be stable under high laser intensity. Its constant-strain dielectric constant is approximately 295 at 100 MHz. This material showed nonlinear properties comparable to LiNbO_3 without double refraction in the optical region. The ratio of K and Li can be changed to obtain different physical parameters.

$\text{Sr}_x\text{Ba}_{1-x}\text{Nb}_2\text{O}_6$, (30) 4mm, is another ferroelectric which shows promise as a SHG material in the NMMW. Depending upon the mix of Sr and Ba, the Curie temperature is found to vary between 60°C to 250°C and the dielectric constant varies from 118 to 3400 (measured at 15 MHz).

$\text{KSr}_2\text{Nb}_5\text{O}_{15}$ (31) has a tetragonal crystal symmetry with a Curie temperature of $+160^\circ\text{C}$ and a dielectric constant of 10^3 at 10^4 Hz. It was grown by the Czochralski technique and, again, its physical parameters can be varied by the K-Sr mix.

III. Experiment.

1. SHG and THG. Figure 1 shows the experimental arrangement for SHG and THG.

*AHN & CLARK

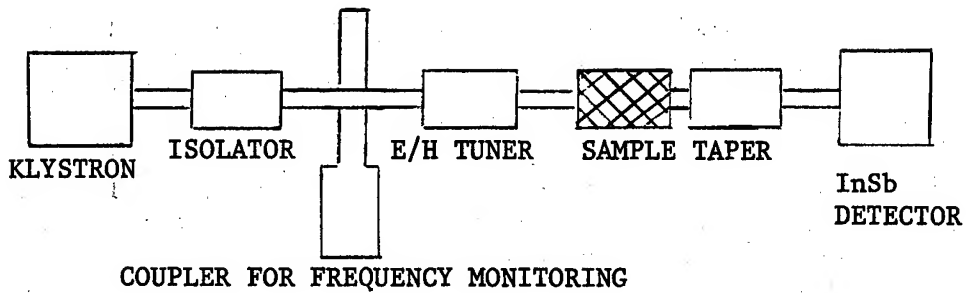


Figure 1. Experimental Setup

Fundamental power from a klystron is sent through various monitoring and tuning devices and then onto the sample which is inserted in fundamental waveguide. For observation of the SH the signal from the sample passes through a waveguide taper section which attenuates the fundamental frequency. The remaining signal is sent into a cooled InSb detector. For observation of the fundamental frequency the taper section is eliminated. For temperature effect measurements E - bend waveguide sections can be placed before and after the sample to enable it to be placed into a cooled bath at various temperatures.

For dc field studies, a slotted waveguide section was used such that the crystal could be inserted directly into the waveguide through the top (broad face). For this experiment, the crystal was coated with conducting paste on the top and bottom, and the high voltage lead could be passed through the slot in the waveguide and soldered to the crystal. The ground lead was connected to the waveguide.

A quasi-optical arrangement can also be used in which the output from the E/H tuner is radiated into the open air with a gain horn. This radiation is focused onto the sample by TPX lenses. The output from the sample is collected by the appropriate gain horn and waveguide system to filter out the fundamental frequency power.

2. d^m Measurement. (3) The nonlinear coefficient is determined by measuring the side-band power and the carrier power when the crystal is modulated by an a-c field above the piezoelectric resonance frequency. The sideband-to-carrier power ratio is approximately (4)

$$\frac{p(\omega_3)}{p(\omega_2)} \approx \frac{\omega_3^2 (d_{\text{eff}}^m)^2 (\ell/b)^2 V(\omega_1)^2}{c^2 \epsilon_3 / \epsilon_0}$$

where b is the width of the waveguide
 $V(\omega_1)$ is the modulating voltage
 ω_2 is the carrier frequency
 ω_3 is the sideband frequency

The experimental apparatus is similar to that used to study the dc effects.

3. Experimental Results and Analysis. The experiment was performed at 55 GHz using an OKI klystron with an output of about 0.1 watt. There was also the klystron generated second harmonic (KGSH) and third harmonic which had to be considered in the measurements. The low power measurements were made by using the manufacturers responsivity specifications of 3910 V/W for the InSb detector.

The results obtained should be considered as preliminary and qualitative. There were uncertainties as to the true temperature of the sample crystal with respect to the temperature of the waveguide which was monitored with a copper-constantin thermocouple and a digital voltmeter. The thermocouple was soldered to the waveguide adjacent to the sample crystal. The temperature of the waveguide and the sample were varied with LN₂ and a heat gun; no attempt was made to keep the sample crystal at a particular temperature other than at LN₂ temperatures and room temperature.

As the crystals were cooled the output fluctuated as much as an order of magnitude. This may be due to resonance behavior of the cavity formed by the crystals in the waveguide where the resonant frequency changes with temperature variations of the crystal index of refraction. In such cases the transmission should show maxima at⁽¹³⁾ $K\ell = I\pi$ and minima at $K\ell = (I+1/2)\pi$ where K is the propagation constant in the crystal and I is an integer.

Measurements on the transmission and fluctuation of the fundamental frequency signal were made to explain the results obtained with the second harmonic frequency signal. For example, the change in the absorption coefficient at the second harmonic between 300 K and 77 K was assumed to be the same as that observed at the fundamental frequency.

a. Fundamental Frequency. Observation of the fundamental frequency signal produced two phenomena:

i) There were variations in the output power which may be due to crystal cavity resonance. Upon cooling a 22mm sample of LiNbO₃ produced the same number of maxima and minima in transmission as

predicted. But in samples of LiTaO_3 there were more maxima and minima than predicted assuming that the index of refraction changes the same as LiNbO_3 ($\Delta n = .2$).⁽¹⁴⁾ The discrepancy was not rectified when thermal expansion was considered, and is still open to discussion.

ii) The absorption coefficient of LiTaO_3 was reduced 0.9 cm^{-1} upon cooling from 300 to 77 K. The absorption coefficient of LiNbO_3 was found to be 2.64 cm^{-1} and did not change appreciably between 300 K and 77 K. This value is 5 times higher than previously reported.

b. Second Harmonic. As mentioned earlier, the klystron was observed to generate a second harmonic signal of its own, as much as $140 \times 10^{-10} \text{ W}$, which was significant compared to the calculated bulk crystal SH as shown in Table II. This 110 GHz input to the crystal had to be accounted for in the total SH output. But this signal was attenuated completely at room temperature by all the samples except a 0.5 cm LiNbO_3 . As the samples were cooled, the amplitude of the 110 GHz signal increased. The magnitudes of the 110 GHz signals at liquid nitrogen temperatures are also shown in Table II.

Table II. Effect of Temperature in the Second Harmonic Signal

MATERIAL	LENGTH	CALCULATED SH SIGNAL (300°K)	EXPERIMENTAL* SH SIGNAL (300°K)	EXPERIMENTAL SH SIGNAL (77°K)
LiNbO_3	2.2cm	2.4×10^{-10} watts	no signal	$5-10 \times 10^{-10}$
	0.5cm	0.1×10^{-10} watts	$\sim 1 \times 10^{-10}$ watts	$2.5-5 \times 10^{-10}$ watts
LiTaO_3	0.775cm	0.8×10^{-10} watts	no signal	3.1×10^{-10} watts
	1.0cm	1.4×10^{-10} watts	no signal	7.3×10^{-10} watts

*Detection limit is of the order of 1×10^{-10} watts.

As can be seen, the SH frequency signal increased in each case upon lowering the temperature. Two explanations are provided:

i) Increase in transmission of the klystron SH. This should not account for more than 2×10^{-10} watts assuming that the absorption coefficient at the SH frequency behaves similarly to the observed absorption coefficient at the fundamental frequency.

ii) Increase in the crystal generated SH due to the increase in the fundamental frequency input caused by the reduction of the absorption. This increases the SH power by the square of the increase in the input power (see Eqn. (2)). This amounts to an increase by a factor of 4. On the other hand, the SH signal is also proportional to the 9th power of the index of refraction. This reduces the bulk generated SH by 25%-30% assuming the index of refraction decreases by 0.2.⁽¹⁴⁾ The net gain in the bulk generated SH is, therefore, a factor of 3. If the calculated SH signals in Table II are multiplied by a factor of 3, they are comparable to the experimental values except in the 0.5cm LiNbO₃.

There was some indication of resonance behavior in LiNbO₃ at 110 GHz but none was seen in LiTaO₃.

SrTiO₃ and proustite were also tested at 110 GHz but no signal or change in the signal amplitude was detected even with cooling. In KDP a signal was observed upon cooling but no absolute measurements were made.

IV. Conclusion.

The review was made on the need, the theory, the techniques, and the materials suitable for the SHG and THG. Further research on materials in forms of the growth technique and the characterization of physical parameters is needed.

Some of the important features of these are:

- i) Large size availability.
- ii) Large linear ionic susceptibility.
- iii) High microwave intensity damage threshold.
- iv) Proper crystal symmetry.

*AHN & CLARK

The materials with high potential are $K_xLi_{1-x}NbO_3$, $Sr_xBa_{1-x}Nb_2O_6$, and $K_xSr_{1-x}Nb_5O_{15}$. The potential payoff is a 220 GHz source which has a longer lifetime, is easy to fabricate, and is readily available.

Preliminary results were also reported and analyzed. It was observed that the cavity resonance behavior makes the crystal length and the possible location of the sample in the waveguide important parameters of experiment. The increased signal strength of the harmonic frequency at lower temperatures cannot be explained by the reduction of the absorption coefficient alone. More efficient transmission of the fundamental input with consequent increase in the bulk generated SH could have contributed to the result. Further experiments will be done to verify the result.

The authors gratefully acknowledge Professor F. DeLucia of Duke University for many valuable technical discussions and for the use of the Duke University Microwave Laboratory equipments and facilities.

*AHN & CLARK

References.

1. N.I. Adams and P.B. Schoefer, Appl. Phys. Lett. 3, 19, (1963).
2. J.A. Giordmaine, Phys. Rev. Lett. 8, 19 (1962).
3. R.C. Miller, Appl. Phys. Lett. 5, 17, (1964).
4. G.D. Boyd, R.C. Miller, K. Nassau, W.L. Bond, and A. Savage, Appl. Phys. Lett. 5, 234 (1964).
5. G.D. Boyd, T.J. Bridges, M.A. Pollack, and E.H. Turner, Phys. Rev. Lett. 26, 387 (1971).
6. G.D. Boyd and M.A. Pollack, Phys. Rev. B 7, 5345 (1973).
7. M. DiDomenico, Jr., D.A. Johnson, and R.H. Pantell, J. Appl. Phys. 33, 1697 (1962).
8. J.G. Bergman and S.K. Kurtz, Mater. Sci. Eng. 5, 235 (1969/70).
9. A. Yariv, Introduction to Optical Electronics, 2nd Ed., Holt, Rinehart and Winston, 1976.
10. R.L. Byer and R.L. Herbst, Nonlinear Infrared Generation, ed Y.R. Shen, P. 87, Springer-Verlag, 1977.
11. S. Singh, Handbook of Lasers, P. 496, The Chemical Rubber Company, Cleveland, OH.
12. C.G.B. Garrett, IEEE J. Quantum Electronics 4, 70 (1968).
13. M.A. Pollack and E.H. Turner, Phys. Rev. B 4, 4578 (1971).
14. D.R. Bosomworth, Appl. Phys. Lett. 9, 330 (1966).
15. R.W. Terhune, P.D. Maker and C.M. Savage, Appl. Phys. Lett. 2, 54 (1963).
16. J.W. Shelton and Y.R. Shen, Phys. Rev. Lett. 25, 23 (1970).
17. H.B. Puell and C.R. Vidal, IEEE J. Quantum Electronics 14, 364 (1978).
18. D.P. Akitt and P.D. Coleman, J. Appl. Phys. 36, 2004 (1965).

*AHN & CLARK

19. D.M. Bloom, G.W. Bekkers, J.F. Young and S.E. Harris, Appl. Phys. Lett. 26, 687 (1975).
20. P.D. Maker and R.W. Terhune, Phys. Rev., V 137, A801 (1965).
21. J.E. Geusic, S.K. Kurtz, T.J. Nelson and S.H. Wemple, Appl. Phys. Lett. 2, 185 (1963).
22. R.C. Casella, Phys. Rev., V 154, 743 (1967).
23. C. Kittel, Introduction to Solid State Physics, 2nd Ed., John Wiley and Sons, Inc. (1956).
24. I.P. Kaminow and G.O. Harding, Phys. Rev., V 129, 1562 (1963).
25. V.I. Talyanskii, A.A. Filimonov and E.G. Yashchin, Sov. Phys. Solid St. 12, 2224 (1971).
26. R.W. Terhune, P.D. Maker and C.M. Savage, Phys. Rev. Lett. 8, 404 (1962).
27. J.E. Bjorkholm and A.E. Siegman, Phys. Rev., V 154, 851 (1967).
28. Lytle, J. Appl. Phys. 35, 2212 (1964).
29. L.G. Van Uitert, S. Singh, H.J. Levinstein, J.E. Geusic and W.A. Bonner, Appl. Phys. Lett. 11, 169 (1967).
30. P.V. Lenzo, E.G. Spenur, A.A. Ballman, Appl. Phys. Lett. 11, 23 (1967).
31. E.A. Giess, G. Burns, D.F. O'Kane and A.W. Smith, Appl. Phys. Lett. 11, 233 (1967).

AIKEN

**THE EFFECTS OF CONTROL SYSTEM AND DISPLAY VARIATIONS FOR AN
ATTACK HELICOPTER MISSION THROUGH PILOTED SIMULATION (U)**

**MR. EDWIN W. AIKEN
AEROMECHANICS LABORATORY
U.S. ARMY RESEARCH AND TECHNOLOGY LABORATORIES (AVRADCOM)
AMES RESEARCH CENTER
MOFFETT FIELD, CALIFORNIA 94035**

Research into methods by which highly maneuverable advanced helicopters can be made to function — with reasonable pilot workload levels — as stable platforms for target designation and/or weapon delivery at night and in adverse weather is a major interest of the U.S. Army Aeromechanics Laboratory. Two candidate techniques under investigation are: (1) helicopter control system modifications that alter the aircraft's response to pilot control inputs and to external inputs such as turbulence and (2) variations in the methods by which critical information is displayed to the pilot in an attempt to reduce the effort required to interpret and respond to a given situation while still maintaining a satisfactory level of system performance. In support of this research, a piloted simulator experiment was designed and conducted to assess the effects on overall system performance and pilot workload of variations in control system characteristics and display format and logic for a nighttime attack helicopter mission. This paper describes the experiment and presents major results and conclusions.

BACKGROUND

The requirement that VTOL aircraft operations be conducted at night and under conditions of limited visibility has given impetus to research that is best understood by reference to the pilot-controlled vehicle-display system depicted in figure 1. This figure defines the elements of the system; when integrated, these elements determine the pilot workload necessary to achieve a given level of system performance.

The pilot's effort comprises three elements: (1) the mental workload required to collect the required information from sources such as motion and visual cues; (2) the decision-making process based on this information; and (3) the physical workload, such as control motions, required to perform the task. The pilot's task in this experiment demands a high level of mental effort because of the requirement to stabilize and control the aircraft in several axes simultaneously with limited visual cues while searching for and acquiring a target under hostile conditions.

In attempts to reduce pilot effort without significantly degrading overall system performance, the system designer must address the characteristics of the controlled vehicle and of the pilot's display. That is, given the characteristics of the unaugmented aircraft and the particulars of its environment,

AIKEN

system performance, as a function of pilot effort, is determined by (1) the stability and control augmentation system (SCAS) and (2) the display format and logic.

Control/display research, both generic and specific in nature, has been applied to particular VTOL aircraft tasks; reference 1 presents a survey of the results of such investigations of the helicopter decelerating instrument approach task; reference 2 describes research into the problem of VTOL aircraft hover and low-speed operations during reduced visibility conditions. The investigation described herein extends the experimental approaches of references 1 and 2 to the Army's requirement for attack and scout helicopter missions conducted at night and in adverse weather.

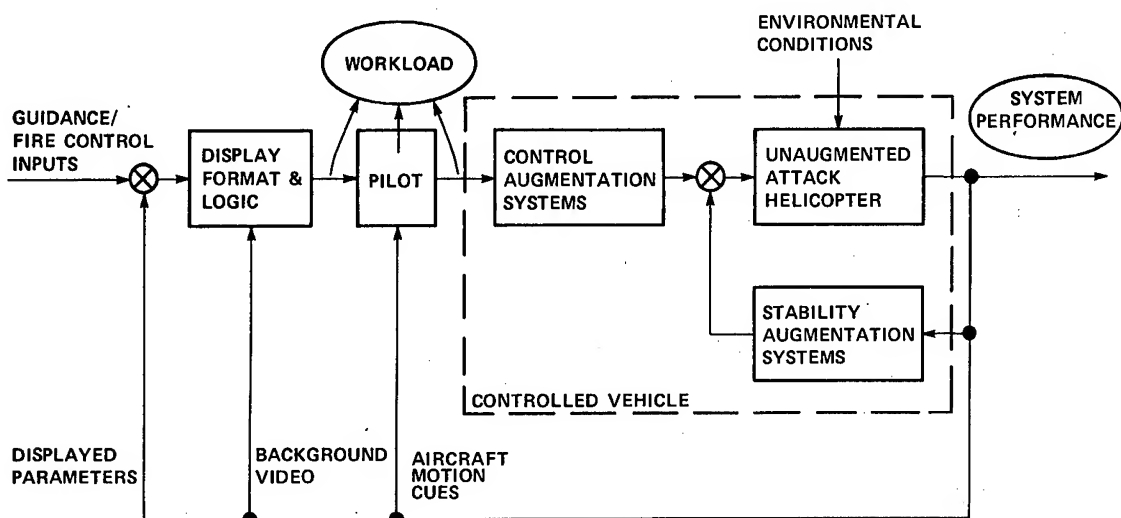


Figure 1.— Control/display system for advanced helicopter.

The design of the present experiment was influenced by previous studies in which the high workload inherent in the low-speed, low-altitude portion of nighttime attack/scout helicopter missions was addressed. One display-oriented concept, evaluated at length in both simulator and flight tests by the Army Avionics Research and Development Activity (AVRADA), consists of the display of flight information superimposed on the video output from a forward-looking infrared (FLIR) sensor; the combined imagery has been presented both on a panel-mounted display with a fixed FLIR sensor and on a helmet-mounted display (HMD) with the FLIR sensor slaved to the motions of the pilot's head (ref. 3). The HMD version of this concept has been adopted as a requirement for the Army's Advanced Attack Helicopter (AAH) Pilot Night Vision System (PNVS) (ref. 4). Preliminary simulations of a system similar to the PNVS conducted by AVRADA revealed that a high workload condition existed during the bob-up maneuver (in which the pilot attempts to maintain a precise hover position over the ground during vertical unmasking and remasking) even though no additional tasks, such as those related to target search and acquisition, were required of the pilot. As a result, it was recommended that the potential benefits of alterations in the dynamics of the hover symbology and/or the implementation of automatic hover augmentation in the aircraft control system be investigated. The design of the experiment described in this paper incorporated those recommendations into a more general investigation of control system and display effects on aircraft handling qualities for an attack helicopter mission that included a weapon delivery task.

EXPERIMENT DESIGN

As a result of a 1969 agreement between NASA and the Army, the Army's Aeromechanics Laboratory, which is collocated with the Ames Research Center (ARC), has access to ARC research facilities for the purpose of conducting investigations of aerodynamics, rotor system and aircraft dynamics, flight controls and displays, guidance and navigation, and acoustics of rotary wing aircraft.

The experiment reported here was conducted on ARC's six-degree-of-freedom moving-base simulator facility, designated S.01. The simulator cab, which was modified to include a typical helicopter instrument panel and controllers (fig. 2), was integrated with other simulation support facilities as indicated in figure 3. A key element of the simulation was the representation of a helmet-mounted display (HMD) image; the image was presented to the pilot on a panel-mounted TV monitor located so that it reproduced the actual HMD field of view characteristics: an arc, subtended at the pilot's eye, of 30° vertically and 40° horizontally (fig. 4). The black and white image consisted of flight control and fire-control symbology superimposed on the video from a simulated forward-looking infrared (FLIR) sensor mounted on the chin of the aircraft. The simulated FLIR imagery was derived from the camera and terrain board visual system; the scaled terrain used for this experiment is a 400:1 model representative of the Army's Ft. Hunter-Liggett facility.

As indicated in figure 1, it was expected that several elements of the pilot-controlled vehicle-display system would interact to determine the workload required of the pilot to attain a given level of performance for the task in question. Accordingly, three sets of experimental variables were selected for investigation in the simulation program:

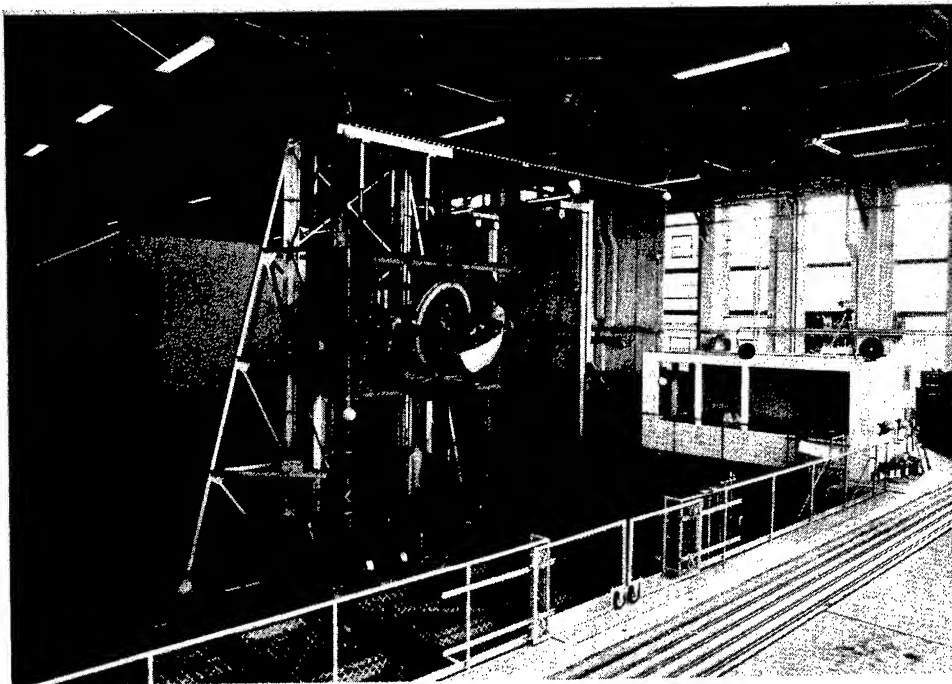


Figure 2.— NASA-ARC S.01 simulator.

AIKEN

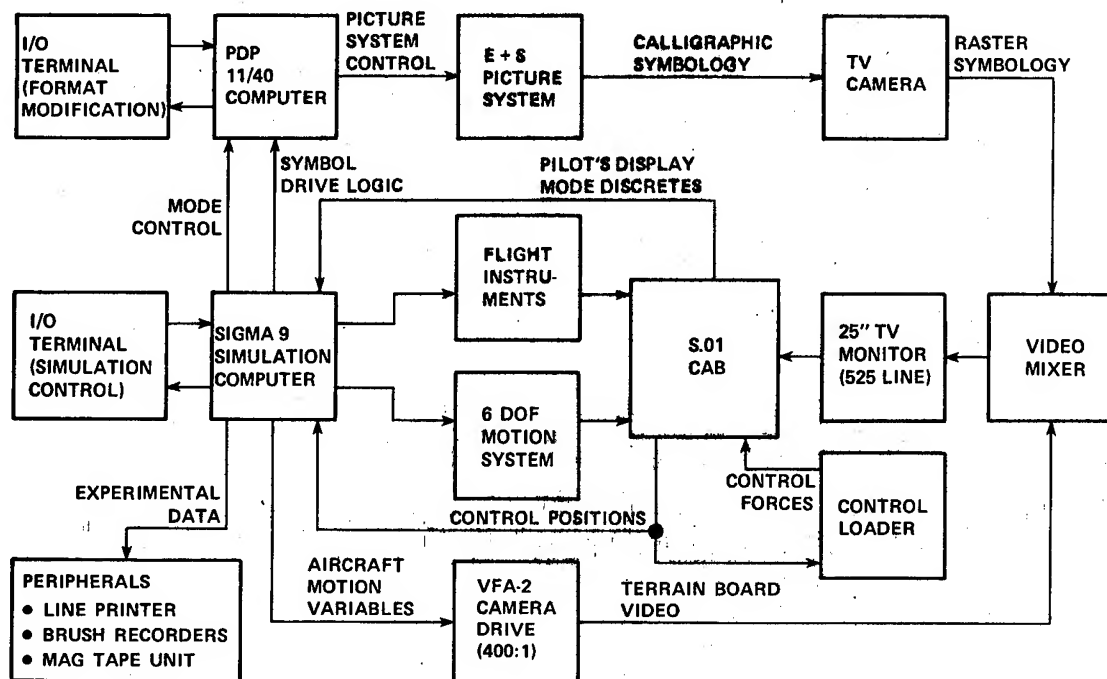


Figure 3.— Simulator systems.

1. Control system — varying degrees of stability and control augmentation, including control system failures.
2. Display — variations in both the format, that is, the location and physical characteristics of the symbols, and in the logic that drives certain key symbols (and thus determines the dynamics of these symbols in response to pilot control and external inputs such as turbulence).
3. Environment — variations in environmental conditions consisting of steady wind, wind shear, and turbulence.

Control Systems

For this experiment, the mathematical model of the unaugmented attack helicopter consisted of six-degree-of-freedom aircraft equations of motion. The equations included a simplified representation of the aerodynamic forces and moments based on both computer-generated and flight-test data for the AAH. No rotor system dynamics were included. The stability and control augmentation systems (SCAS) investigated include two systems specific to the AAH and several hover augmentation system (HAS) concepts designed for the hover and low-speed portion of the mission. Details of the model and the actual implementation of these control systems for the simulation are discussed in reference 5. The resultant generic controlled vehicle characteristics in hover are summarized in table 1.

The control systems presented in table 1 are arranged in an order that is associated with expected reductions in pilot workload for a precision hover task performed under visual meteorological conditions; that is, they are listed in order of increasing ease of hover position control, which is a dominant parameter that determines system performance. Relatively simple SCAS configurations for the AAH

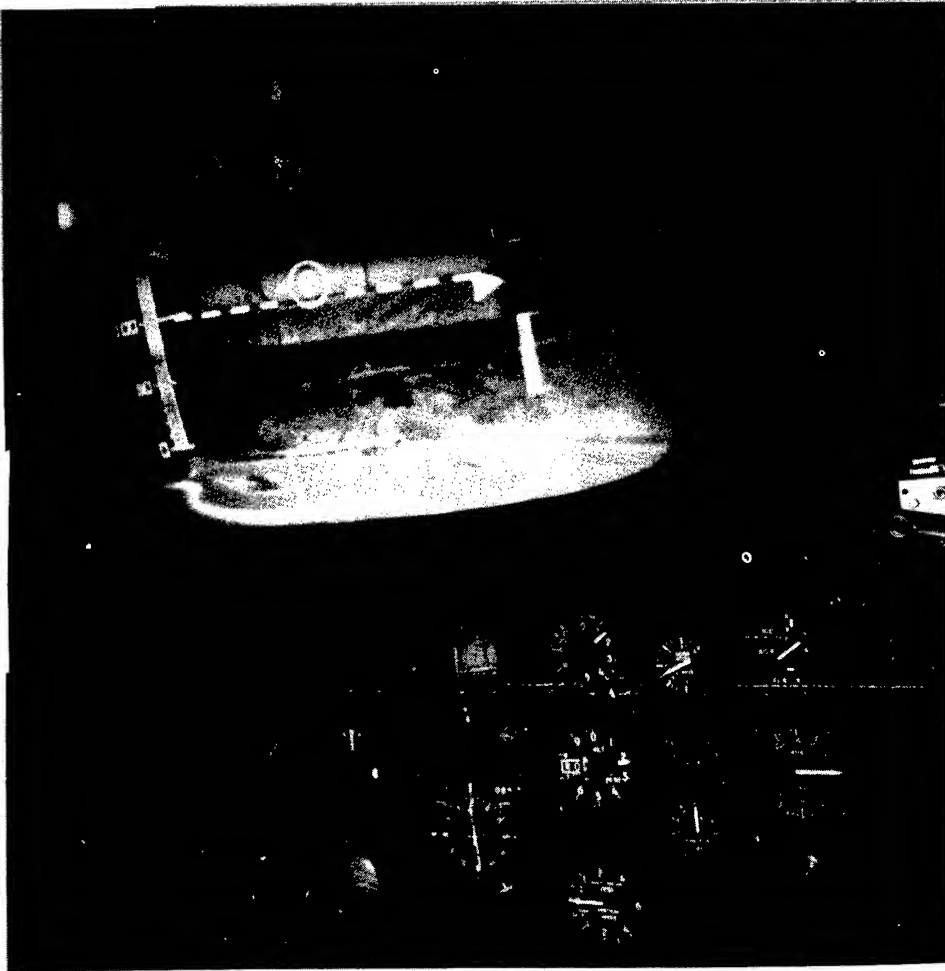


Figure 4.— S.O1 cockpit arrangement.

are listed first; they provide the pilot with short-term pitch and roll-rate command and long-term attitude command through the cyclic stick. For a helicopter in hover, a pitch attitude change corresponds to a short-term change in linear acceleration; therefore, a pitch-rate command system in essence places the pilot three integrations away from the desired change in longitudinal position. In order to achieve a satisfactory level of performance with this system, the pilot must be provided with high quality, easily interpretable information on the results of those integrations, that is, pitch attitude, longitudinal inertial velocity, and longitudinal position. Under visual flight conditions, the real world is the source of the required information, however, at night or under reduced visibility conditions, the required information must be obtained, at least in part, from the cockpit instruments and displays. In contrast, the more sophisticated configurations, such as HAS 3, provide the pilot with a controlled vehicle that responds to a longitudinal cyclic stick input with the commanded longitudinal inertial velocity and holds the resulting longitudinal position when the stick is released. This particular system places the pilot only one integration away from

TABLE 1.—GENERIC CHARACTERISTICS OF CONTROLLED VEHICLE-HOVER

Control system	Controlled axis			
	Pitch	Roll	Yaw	Collective
AAH SCAS	Quickened pitch attitude command	Quickened roll attitude command	Yaw rate damping augmentation with quickened control response	Unaugmented
AAH Attitude Hold	Pitch attitude command	Roll attitude command	Pseudo-heading hold	Unaugmented
HAS 1	Longitudinal inertial acceleration command, velocity hold	Lateral inertial acceleration command, velocity hold	Yaw rate command, heading hold	Unaugmented
HAS 2	Longitudinal inertial velocity command	Lateral inertial velocity command	See HAS 1	Unaugmented
HAS 3	Longitudinal inertial velocity command, position hold	Lateral inertial velocity command, position hold	See HAS 1	Unaugmented
Vertical Augmentation 1	HAS 2 or HAS 3 characteristics			Altitude rate command
Vertical Augmentation 2	HAS 2 or HAS 3 characteristics			Altitude rate command, altitude hold

the desired position change and, as a result, may reduce the mental workload required for satisfactory performance.

The hierarchy of control systems presented in table 1 is in general dependent on the task that the pilot-vehicle system is expected to perform. Specifically, the various hover augmentation systems have been designed to assist the pilot in reaching and maintaining a precision hover. It is important to realize that the ranking of these control systems when applied to other tasks will likely change drastically; for example, the SCAS is designed to enhance aircraft agility and may therefore be preferable for the higher speed maneuvering flight required for some nap-of-the-earth missions.

In addition to an evaluation of the AAH control systems and the various HAS concepts of table 1 for the nighttime mission, the effects of degraded SCAS modes were also investigated. Specifically, total failures of each of the AAH SCAS axes — pitch, roll, and yaw — were simulated. Finally, a full SCAS failure, resulting in a controlled vehicle with the characteristics of the unaugmented attack helicopter, was implemented.

Displays

One function of the pilot's display during the nighttime attack helicopter mission is to compensate for the lack of external visual cues. It has been demonstrated that a helmet-mounted display that consists only of a limited field-of-view FLIR image of the outside world is insufficient for the low-speed, low-altitude portion of the mission and that superimposed flight control symbology can considerably enhance the usefulness of this particular display medium (ref. 3). From the pilot's point of view, three display characteristics determine the suitability of a given set of superimposed symbols for a particular task:

1. Information content — Is the displayed information inadequate, sufficient, or excessive for the task?
2. Format — Do the location and physical characteristics of the individual symbols enhance or degrade the efficiency of information transfer?
3. Logic — Do the symbols accurately reflect aircraft status, and do they respond in an orderly fashion to pilot control inputs and external disturbances?

These sets of display characteristics formed the basis for the display variations considered in this experiment.

The baseline display format that was investigated (ref. 4) consists of four discrete display modes — cruise, transition, hover, and bob-up — selectable by the pilot. Reference 3 describes the operational requirements associated with each display mode as (1) cruise — high-speed level flight enroute to the forward edge of the battle area; (2) transition — low-speed, nap-of-the-earth maneuvers, such as dash, quick stop, and sideward flight; (3) hover — stable hover with minimum drift; and (4) bob-up — unmask and remask maneuvers over a selected ground position. The bob-up mode of the baseline format is depicted in figure 5.

In order to explain more clearly the information content and details of the baseline symbology, the symbols are divided into three categories: central (fig. 6), peripheral (fig. 7), and fire control (fig. 8). The central symbology changes as a result of display mode switching; the characteristics of the four display modes are (1) cruise — velocity vector, cyclic director, and hover position symbols deleted; (2) transition — horizon line and hover position symbols deleted; (3) hover — horizon line deleted and hover position symbol fixed at center, velocity vector sensitivity increased compared to transition mode; and (4) bob-up — horizon line deleted, hover mode velocity vector sensitivity retained.

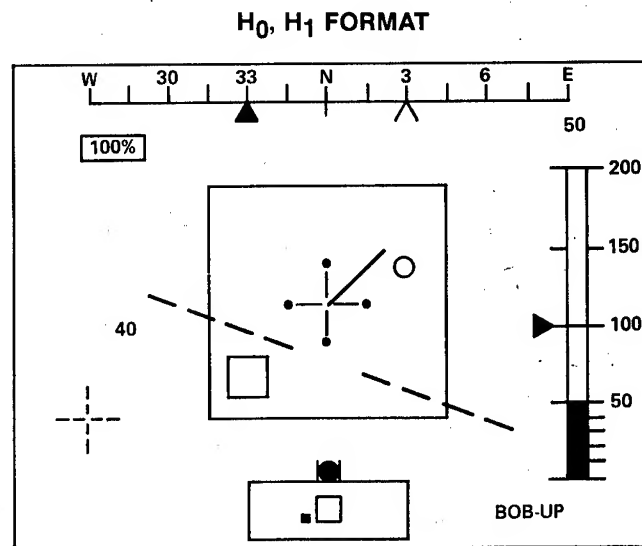
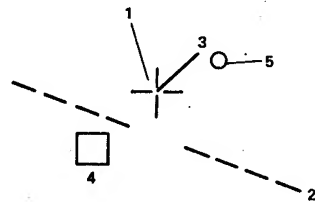
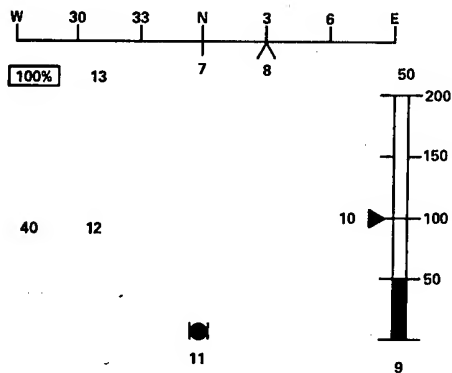


Figure 5.— Baseline display format.



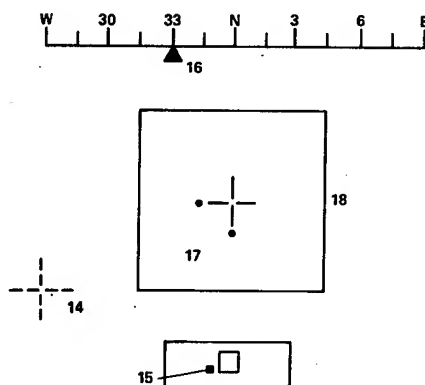
SYMBOL	INFORMATION
1. Aircraft reference	Fixed reference for horizon line, velocity vector, hover position, cyclic director, and fire control symbols
2. Horizon line (cruise mode only)	Pitch and roll attitude with respect to aircraft reference (indicating nose-up pitch and left roll)
3. Velocity vector	Horizontal Doppler velocity components (indicating forward and right drift velocities)
4. Hover position	Designated hover position with respect to aircraft reference symbol (indicating aircraft forward and to right of desired hover position)
5. Cyclic director	Cyclic stick command with respect to hover position symbol (indicating left and aft cyclic stick required to return to designated hover position)

Figure 6.— Central symbology.



SYMBOL	INFORMATION
7. Aircraft heading	Moving tape indication of heading (indicating North)
8. Heading error	Heading at time bob-up made selected (indicating 030)
9. Radar altitude	Height above ground level in both analog and digital form (indicating 50 ft)
10. Rate of climb	Moving pointer with full-scale deflection of $\pm 1,000$ ft/min (indicating 0 ft/min)
11. Lateral acceleration	Inclinometer indication of side force
12. Airspeed	Digital readout in knots
13. Torque	Engine torque in percent

Figure 7.— Peripheral symbology.



SYMBOL	INFORMATION
14. Cued line of sight	Overlays designated target position on background video when target is in display field of view
15. Coarse target location	Designated target position with respect to display field of view (inner rectangle) and sensor limits (outer rectangle)
16. Target bearing	Designated target bearing (indicating 330° or 30° to left of current heading)
17. Target location dots	Illumination of two adjacent dots indicates display quadrant in which designated target is located
18. Missile launch constraints	Limits with respect to aircraft reference for successful weapon lock-on to designated target

Figure 8.— Fire-control symbology.

Effects of variations in displayed information content, format, and logic were investigated by alterations to the hover and bob-up modes of this baseline format.

Variations in information content were mechanized in the form of the following display failures: FLIR failure — loss of background video; loss of velocity vector symbol; loss of cyclic director symbol; loss of velocity vector and cyclic director symbols; and loss of all hover symbols — velocity vector, cyclic director, and hover position symbols inactive.

To explore the effects of variations in the display format, an alternative format, consisting of potential improvements to the baseline format, was implemented (fig. 9). The separation of the horizontal status and command information (fig. 6) from the vertical status information located on the right side of the display (fig. 7) was judged to be a possible deficiency in the baseline format. Concentration on the central symbols could result in degraded altitude tracking performance because of (1) the lack of vertical-horizontal information integration, (2) the incompatibility of the location of the vertical information with the location of the pilot's primary vertical controller (the collective pitch control) located on the pilot's left side, and (3) the lack of vertical command information. The first of these possible deficiencies was not addressed for this experiment. As a potential solution to the latter two deficiencies, the alternative format includes the radar altitude information on the left-hand side and, in lieu of a rate-of-climb indicator, a collective control director driven by blended altitude and altitude rate information; when positioned on the desired value of displayed altitude by the pilot's collective control inputs, the collective control director causes the aircraft to reach and maintain that altitude. This format also includes a horizon line — which remains on the display in all four modes to provide a compelling display of aircraft attitude in hover — and an analog display of low-range airspeed.

Possible display deficiencies associated with the logic driving the central hover symbols were also identified. In reference 3, a relatively noise-free estimate of the horizontal inertial velocity components is derived for use in driving the velocity vector symbol of the baseline display (fig. 6). This estimate involves the complementary filtering of low-frequency Doppler velocity with high-frequency estimates of inertial velocity based solely on aircraft attitude. Improvements in the accuracy of this estimated velocity were obtained by changing filter characteristics and by including linear accelerometer data in the high-frequency velocity estimate. In addition, the sensitivities of the baseline hover symbology — velocity vector, cyclic director, and hover position — documented in reference 3 were altered, using classical manual control theory, to be compatible with the controlled

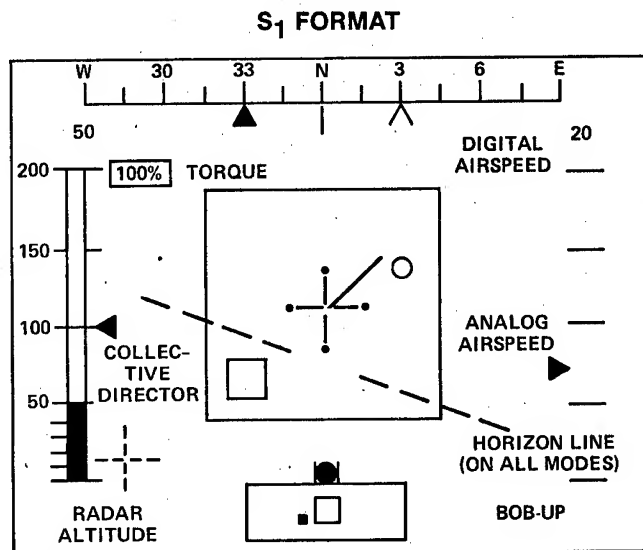


Figure 9.— Alternative display format.

AIKEN

vehicle characteristics. As a result, the sensitivity of the cyclic director symbol varied, in general, with the control system characteristics (table 1).

The investigation of these three display areas of interest resulted in the following three basic display variations:

1. H_0 — baseline display format (figs. 5–8); reference 3 hover symbology logic
2. H_1 — baseline display format; revised inertial velocity estimate; sensitivity of hover symbology based on classical manual control theory; five display failure modes
3. S_1 — alternative display format (fig. 9); H_1 display logic

Environment

To provide a more realistic environment for the simulation and to assess the effects of external disturbances, a model of low-altitude wind and turbulence was implemented for the simulation (ref. 5). Two levels of disturbances were investigated: (1) calm — no wind or turbulence, and (2) moderate — a 10-knot steady wind at the nominal altitude, a moderate wind shear with altitude, and 3.4 ft/sec rms vertical and 6.8 ft/sec rms horizontal gusts.

EXPERIMENT

Three pilots served as evaluation pilots for the experiment: Pilot A, an Army experimental test pilot with 3,165 flight hours, 2,450 of which are in rotary wing aircraft (~90 evaluations); Pilot B, an experimental test pilot with 4,800 flight hours, 2,700 of which are in rotary wing aircraft (~12 evaluations); and Pilot C, a NASA aerospace engineer and pilot with 7,700 flight hours, 1,160 of which are in rotary wing aircraft (~30 evaluations).

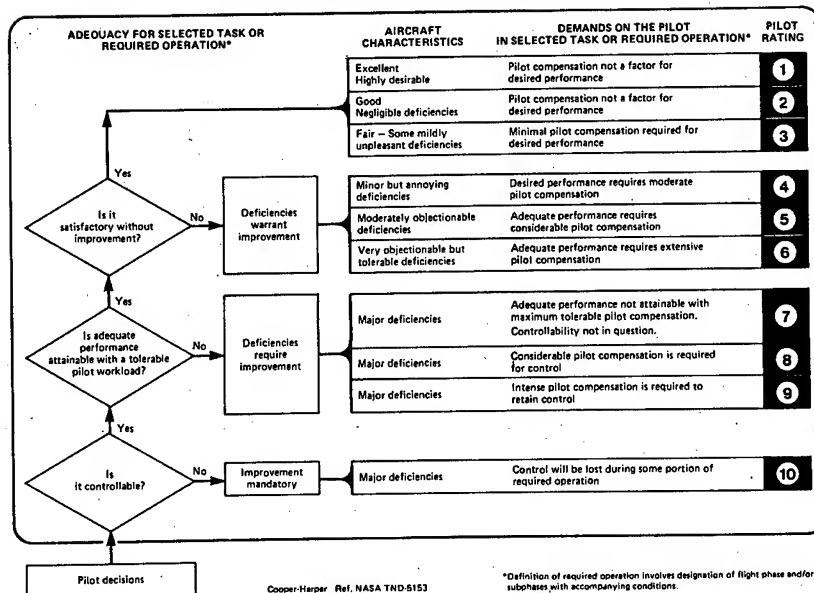
The evaluation task for this investigation consisted of several segments of the primary attack helicopter mission. These segments and the corresponding display modes follow:

1. Cruise: accelerate to an airspeed (V) of 40 knots at 100 ft above ground level (AGL).
2. Transition: descend to 50 ft AGL and decelerate to a hover near a designated point on the terrain.
3. Hover: hover between 0–50 ft AGL.
4. Bob-up: bob-up to 100 ft AGL over designated hover position.
5. Bob-up: conduct target search in azimuth; when target designated, bring target within the missile launch constraints and simulate missile launch.
6. Bob-up: descend to original hover position.
7. Transition-hover: accelerate to $V = 40$ knots and depart the area.

Most of the evaluations were performed for an abbreviated task that comprised segments 3–6 above. Each evaluation consisted of two runs of either the full mission or the hover and bob-up task. For each run, system performance data, such as hover position accuracy and attitude and velocity excursions, and pilot physical workload data, in the form of control activities, were collected. At the end of each evaluation the pilot was asked to assign a numerical Cooper-Harper pilot rating (ref. 6) for the task from the scale of figure 10 and to provide commentary, based on a pilot commentary guide, to assist the experimenter in identifying the areas that most heavily influenced the rating.

The Cooper-Harper pilot rating (PR) is commonly used in aircraft handling qualities research and is the basis for the handling qualities "Levels" used in specifications for military aircraft (e.g., ref. 7). The rating scale of figure 10 emphasizes the interdependence of system performance and pilot workload in the dichotomous decisions required of the evaluation pilot for the selection of a numerical rating.

HANDLING QUALITIES RATING SCALE



Cooper-Harper Ref. NASA TND-5153

DEFINITIONS FROM TN-D-5153

COMPENSATION

The measure of additional pilot effort and attention required to maintain a given level of performance in the face of deficient vehicle characteristics.

HANDLING QUALITIES

Those qualities or characteristics of an aircraft that govern the ease and precision with which a pilot is able to perform the tasks required in support of an aircraft role.

MISSION

The composite of pilot-vehicle functions that must be performed to fulfill operational requirements. May be specified for a role, complete flight, flight phase, or flight subphase.

WORKLOAD

The integrated physical and mental effort required to perform a specified piloting task.

PERFORMANCE

The precision of control with respect to aircraft movement that a pilot is able to achieve in performing a task. (Pilot-vehicle performance is a measure of handling performance. Pilot performance is a measure of the manner or efficiency with which a pilot moves the principal controls in performing a task.)

ROLE

The function or purpose that defines the primary use of an aircraft.

TASK

The actual work assigned a pilot to be performed in completion of or as representative of a designated flight segment.

Figure 10.— Cooper-Harper pilot rating scale.

Specifically, a "controllable" control/display combination may be assigned a numerical rating that places it in one of the three primary performance-workload categories, or handling qualities "Levels" (ref. 6):

1. Level 1 ($1 \leq PR \leq 3$): Desired, or at least clearly adequate, performance for the task is attainable with a satisfactory level of pilot workload.

2. Level 2 ($4 \leq PR \leq 6$): Desired performance is not necessarily obtained; however, adequate performance is attainable with pilot compensation, that is, increased workload, up to the maximum tolerable level.

3. Level 3 ($7 \leq PR \leq 9$): Adequate performance is not attainable with maximum tolerable pilot workload; an excessive workload level would be required for adequate performance.

Thus, the pilot evaluation data — the ratings and commentary — gathered for this experiment are an important source of information regarding the interdependence and necessary tradeoffs of system performance and pilot workload.

The analysis of the pilot evaluation data is complete, and a summary is presented below. An analysis of the quantitative performance and workload data is in progress.

RESULTS

Figure 11 shows the pilot rating results from pilot A for the primary experimental matrix. It demonstrates that, for the hover and bob-up task with moderate wind and turbulence, the baseline control-display configuration (SCAS/ H_0) is rated as being unsatisfactory without improvement and approaches Level 3 handling qualities.

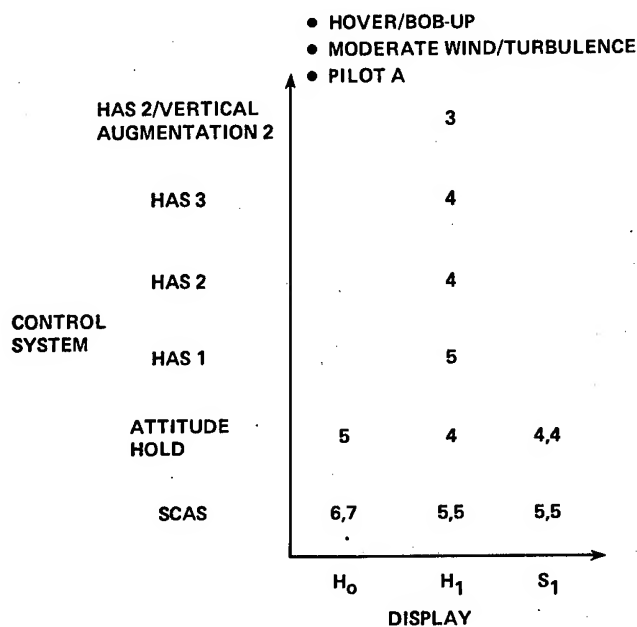


Figure 11.— Pilot rating data — primary configuration matrix.

Improvements in the pilot's ratings are obtained both by control system modifications (e.g., Attitude Hold/ H_0) and by the alterations to the velocity vector logic and hover symbology scaling (SCAS/ H_1). However, no further improvements occur as a result of the display format modifications (SCAS/ S_1). The H_1 display with either the Attitude Hold feature or the two velocity command control systems (HAS 2 and 3) provides adequate but still unsatisfactory (Level 2) systems for the task. Vertical augmentation together with a horizontal velocity command system is required for a satisfactory pilot rating (Level 1).

Figure 12 demonstrates a general degradation of pilot rating with control system and display failures. The improvement in pilot rating for the FLIR failure is attributed, according to pilot commentary, to the improvement of the quality of the symbology

with the resultant uniform video background. The hover/vertical augmentation system improved the pilot rating for each of the display failures investigated, never allowing the handling qualities to fall below

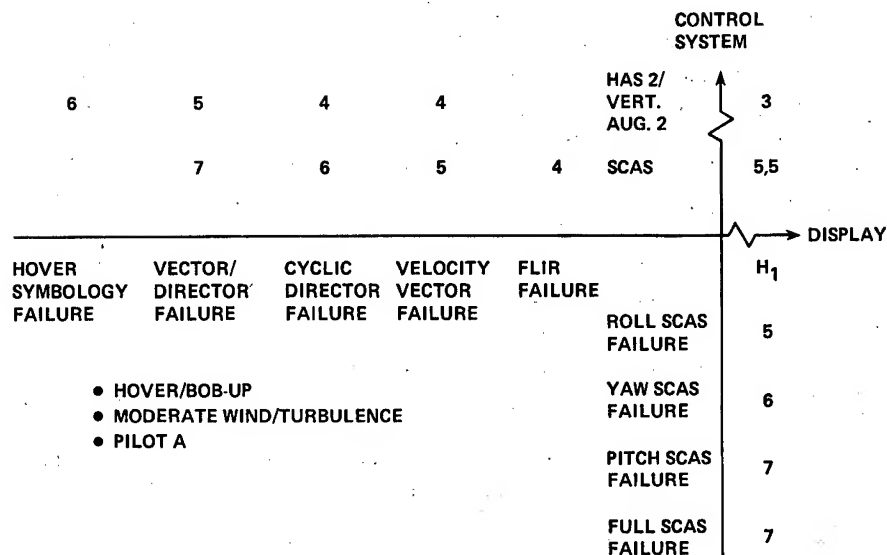


Figure 12.— Pilot rating data — failure effects.

Level 2. The pitch SCAS and full SCAS failures result in Level 3 handling qualities as does the loss of the velocity vector and cyclic director with the SCAS fully functional.

No system was found to have Level 1 handling qualities for the full mission; the need for maneuverability during the higher speed flight segments degraded the ratings assigned to the more heavily-augmented control systems. The lack of turbulence generally improved pilot ratings for the less-heavily augmented control systems — the SCAS/H₁ and SCAS/S₁ combinations received pilot ratings of 3 for the hover/bob-up task. Finally, inter-pilot variations were only significant for the two AAH control systems and the control system failures; for example, pilot C rated the SCAS/H₁ combination as a 7 for the hover and bob-up task in turbulence, that is, Level 3 handling qualities; pilot B rated the same configuration as a 4.

For most of the evaluations, especially those conducted in turbulence, the pilot commentary indicates that the division of attention among horizontal position control, altitude control, and target acquisition during the hover and bob-up was crucial to their ratings.

CONCLUSIONS

The following conclusions are based on the handling qualities results obtained from the piloted simulator evaluations:

1. The baseline control-display system is unsatisfactory for the task evaluated and requires improvement.
2. Improvements to the baseline system may be achieved by modifying either the control system or display.
3. The display modifications that most significantly improve pilot ratings are the increased accuracy of the velocity vector symbol drive logic and the rescaling of the hover symbology based on the

AIKEN

characteristics of the controlled vehicle; the variations in display format investigated provided no significant improvements. The information content of the baseline display format is satisfactory for the task.

4. A horizontal velocity command system and artificial augmentation of the collective axis are required for satisfactory handling qualities during hover and bob-up in moderate turbulence.

5. A failure of the baseline pitch SCAS, even with the improved hover symbology dynamics, makes the system inadequate for the task. With the baseline SCAS, a failure of the hover symbols also results in an inadequate system; a hover and vertical augmentation system with the same display failure results in a system that is adequate but still unsatisfactory for the task.

In general, the single-mode SCAS represented by the baseline system is unsatisfactory for the entire nighttime attack helicopter mission; the requirements for the hover, bob-up, and weapon delivery tasks are sufficiently different from those for the higher speed flight tasks that widely different controlled vehicle characteristics are necessary for these mission segments for a satisfactory system overall. Finally, the dynamics of the central hover symbols of the pilot's display must be designed to be compatible with the dynamic characteristics of the controlled vehicle to ensure pilot acceptability.

REFERENCES

1. Lebacqz, J. V.: Survey of Helicopter Control/Display Investigations for Instrument Decelerating Approach. NASA TM-78565, 1979.
2. Hoh, R. H.; and Ashkenas, I. L.: Handling Quality and Display Requirements for Low Speed and Hover in Reduced Flight Visibility. AHS Preprint 79-29, 35th Annual National Forum of the American Helicopter Society, Washington, D.C., May 1979.
3. Keane, W. P.; Shupe, N. K.; Sun, P. B.; Robbins, T.; and Campagna, R. W.: A Versatile Display for NOE Operations. AHS Preprint 77.33-24, 33rd Annual National Forum of the American Helicopter Society, Washington, D.C., May 1977.
4. Tsoubanos, C. M.; and Kelley, M. B.: Pilot Night Vision System (PNVS) for Advanced Attack Helicopter (AAH). AHS Preprint 78-16, 34th Annual National Forum of the American Helicopter Society, Washington, D.C., May 1978.
5. Aiken, E. W.: A Mathematical Representation of an Advanced Helicopter for Piloted Simulator Investigations of Control System and Display Variations. USAAVRADCOM TM 80-A-2, Feb. 1980.
6. Cooper, G. W.; and Harper, R. P., Jr.: The Use of Pilot Rating in the Evaluation of Aircraft Handling Qualities. NASA TN D-5153, 1969.
7. Military Specification, Flying Qualities of Piloted Airplanes. MIL-F-8785B (ASG), 7 Aug. 1969.

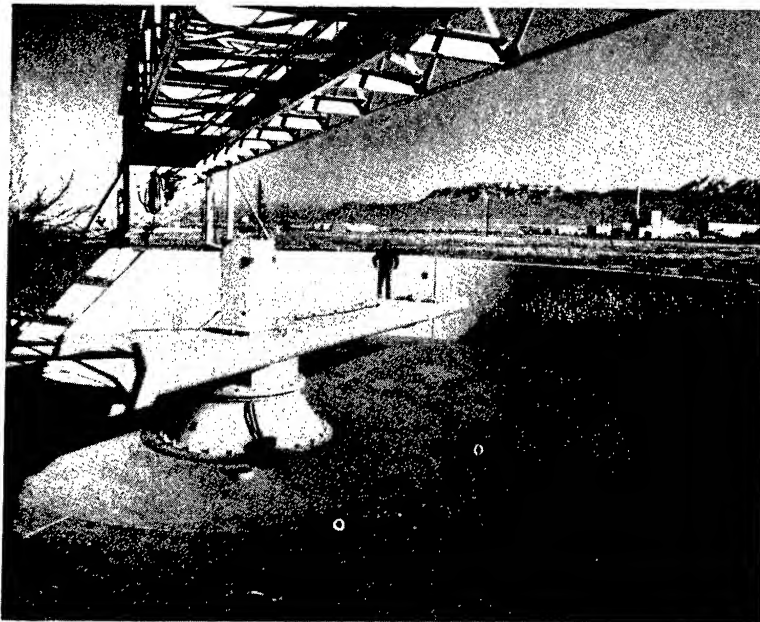
IMPACT FUZE PERFORMANCE IN SNOW (U)
(Initial Evaluation of a New Test Technique)

GEORGE W. AITKEN, P.W. RICHMOND III and D.G. ALBERT
U.S. Army Cold Regions Research and Engineering Laboratory
Hanover, N.H. 03755

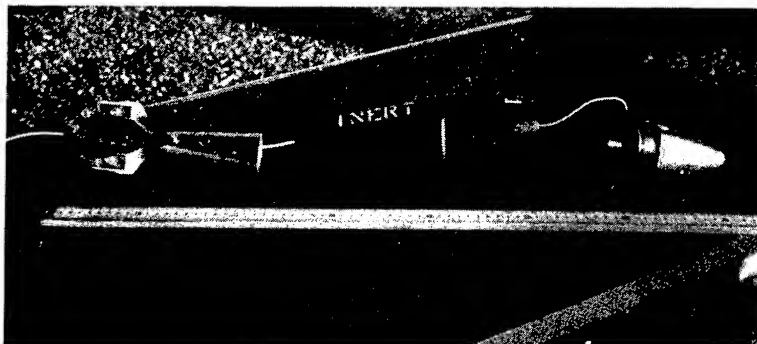
Introduction: Snow greatly reduces the effectiveness of impact-fuzed projectiles. In order to obtain maximum effectiveness in a winter battlefield environment, design of new fuzes and evaluation of current equipment requires detailed knowledge of the snow penetration event. Fuze performance data under various impact conditions can be obtained by both direct and reverse ballistic test procedures (1). In the direct test the fuzed projectile is subjected to realistic launch accelerations, but the test presents problems in accurately locating the point of impact and requires telemetry to obtain data from on-board transducers. The reverse ballistic technique, where the target is fired into a stationary projectile, has the advantage of allowing instrumentation in the projectile to be directly wired to recording equipment. However, this technique is difficult to utilize with snow since this material cannot sustain the high acceleration loads involved.

The centrifugal launch method that was used to conduct the tests discussed here is unique in that it provides advantages normally found in both techniques, i.e. sensors in the projectile can be directly wired to recording equipment, and the target is not subjected to the acceleration loads experienced in the reverse ballistic technique. The point of impact can also be closely controlled using the centrifugal launch technique.

The information obtained from these tests consisted of measurements of the deceleration of a projectile when it impacts against a snow target. The deceleration data were smoothed using a low pass digital filter and integrated to obtain depth of penetration. This



1. View of the 10.7-m centrifuge located at Sandia Laboratories, Albuquerque, N.M.



2. Close-up view of instrumented M524 fuze and M374 81-mm projectile.

information was then compared with a modified hydrodynamic drag equation (2) that has been used to describe fuze impact into both snow and mud. Kovacs (3) and Davis (4) also used similar equations to analyze fuze performance.

Test Procedure: The centrifuge facility utilized for these tests (Fig. 1) is located at the Sandia Laboratories in Albuquerque,

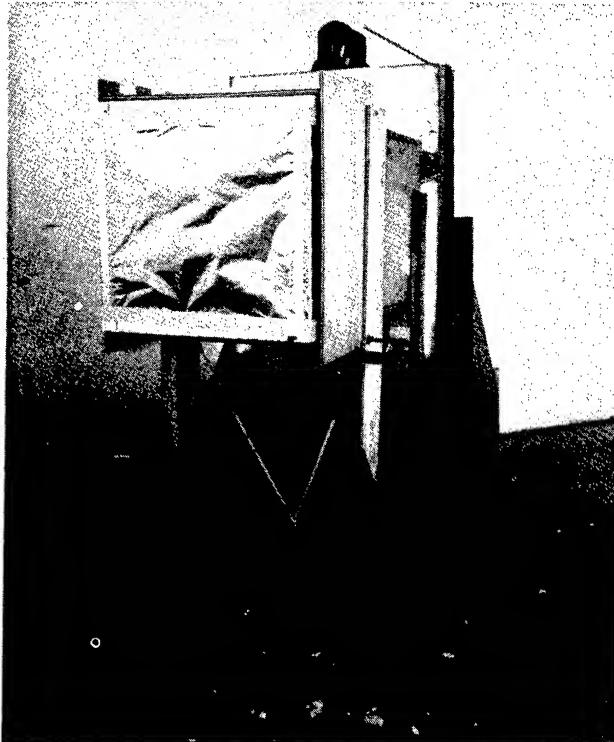


3. Preparation of the snow target.

N.M. Otts (5) presented a description of the centrifuge and an example of its use as an impact testing machine. It has a 10.7-m radius and is capable of subjecting a test item to tangential velocities up to 164 m/s.

An inert M374 81-mm projectile with an M524 fuze was used in these tests. The fuze was instrumented by replacing the striker and explosive train with a piezoresistive accelerometer mounted on an aluminum plug (Fig. 2). The instrumentation lead was run through the projectile body and out the tail section.

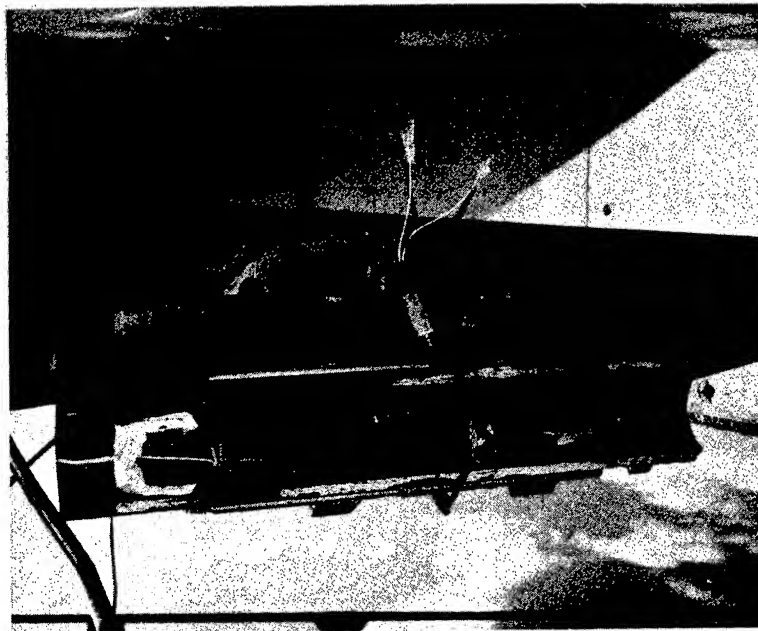
Targets made from both snow and nylon shavings (a candidate material to simulate snow) were used in these tests. The snow targets were prepared by sifting snow through a 6-mm-mesh screen into 610-mm-square by 150-mm-deep boxes constructed of 50-mm-thick Styrofoam (Fig. 3). These targets were then aged at least 24 hours to allow the snow to sinter. Snow densities of about 0.4 Mg/m^3 were obtained. The nylon targets were prepared by pouring 10-mm-long nylon shavings into the 150-mm-deep Styrofoam boxes. A piece of cheesecloth was placed over the surface of the shavings to keep them in place when the box was turned on its side for the test.



4. Snow target, with aluminum foil wind screen in place, positioned in stand prior to test event.

The target boxes were placed in a rigid stand located on a tangent to the arc made by the centrifuge arm and positioned to insure a near normal impact (Fig. 4). An aluminum foil wind screen was placed 150 mm in front of the snow targets to protect the snow surface from wind damage. Alternating layers of Styrofoam and plywood were placed behind the targets to stop the projectile.

The instrumented projectile was mounted on the centrifuge as shown in Fig. 5. When the centrifuge achieved the desired velocity, the projectile was released so that it impacted the target. The accelerometer output was amplified and recorded on an analog tape recorder. The frequency response of this system was flat to 5 kHz. Data were obtained for impact velocities ranging from 15 m/s (50 ft/s) to 91 m/s (300 ft/s).

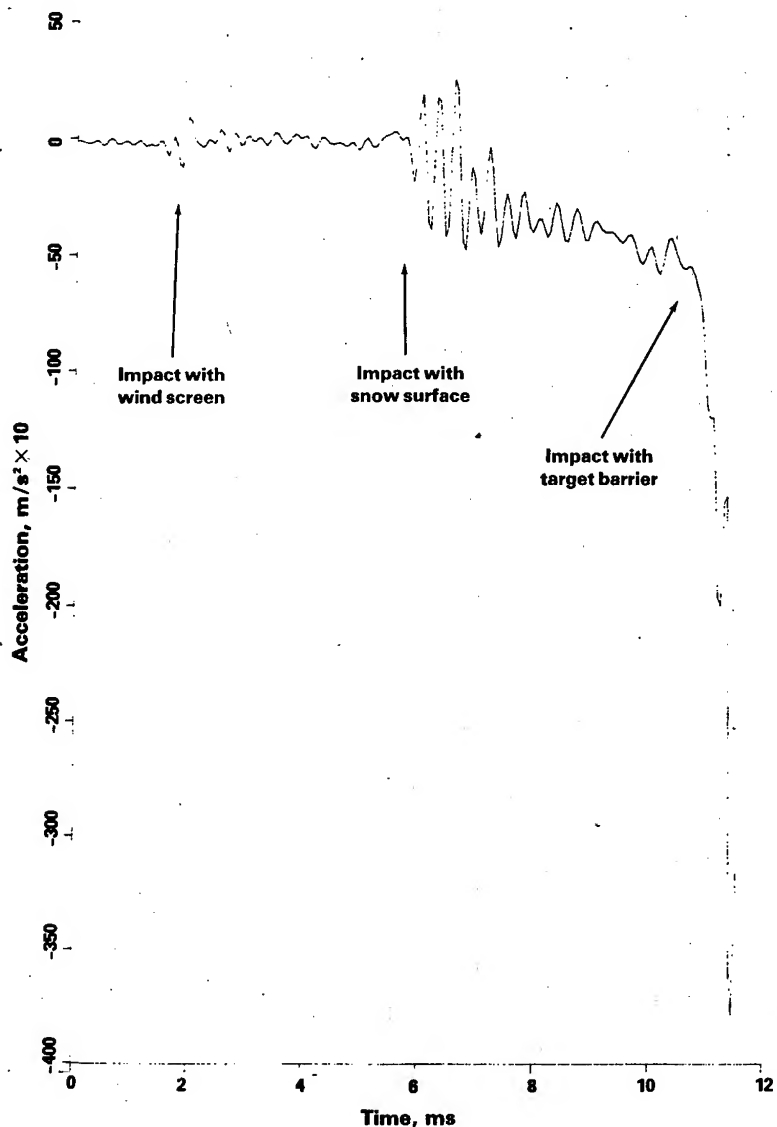


5. Close-up view of test projectile mounted on centrifuge arm. Note steel cable holding projectile to arm and explosive cable cutter used for projectile release.

Data Reduction: The test data were digitized for computer analysis using a sampling rate of 20 kHz which was high enough to avoid aliasing problems.* Input signals of known acceleration values were used to calibrate the system.

A typical acceleration vs. time signal for a snow impact at 30 m/s is shown in Fig. 6. Projectile impacts with the wind screen, the snow surface, and the barrier behind the snow target are identified in the figure. The travel times between these impacts were used to verify the impact identifications given in the figure.

*Aliasing, defined as the disguising of high frequency components of a signal as low frequencies, occurs when a sampling rate which is too low is used in the digitizing procedure (6, 7).



6. Acceleration vs. time data for 30-m/s impact of projectile into 0.39-Mg/m^3 density snow target.

This signal has been passed through a zero phase low pass digital filter with a cutoff frequency of 5 kHz, corresponding to the bandwidth of the analog recording equipment. The filter removes any high frequency noise produced by the digitizing process (7) without introducing any time shifts to the signal. This latter property of the filter is quite important. Computer

programs to apply digital Butterworth filters to signals are readily available (8). However, these filters will introduce a frequency-dependent phase shift, which causes the output signal to be delayed in time by an amount proportional to the frequency of each component. To remove the phase shift, the filter was first applied to the signal, obtaining a phase-shifted, filtered output. The filter output was then reversed and the signal passed through the filter again. This procedure has two effects: a) the final output will not be phase (or time) shifted, since the phase shift caused by the second pass will be the negative of the phase shift caused by the first pass; and b) the final amplitude response of the filter will be the square of the amplitude response of a single filter operation. After filtering, however, some high frequency noise superimposed on the snow impact signal is still visible. This noise cannot be attributed to the digitizing process and therefore must have some other physical cause.

A possible source of this high frequency noise is resonant vibration of the projectile. A test was conducted to ascertain whether or not the resonant frequency of the projectile was of the same order as the high frequency noise on the data traces by suspending the projectile from a string attached to its tail and then tapping it with a hammer. The output from the accelerometer was digitized and is shown in Fig. 7. The amplitude vs. frequency plot obtained from the Fourier transform of this signal is shown in Fig. 8. The peak amplitude is around 1.5 kHz, with significant amounts of power located at frequencies up to about 3.5 kHz, suggesting that resonant vibration of the projectile could be the cause of the noise on the data traces. In most cases, it was found that a low pass filter with a cutoff frequency of around 1.5 kHz was sufficient to remove this high frequency noise. For the higher impact velocities, however, the low pass filtering procedure did not give usable results even if a lower cutoff frequency was used.

The poorer quality of the data at higher impact velocities is due to two factors. First, as the impact velocity increases, the amplitude of the resonant vibrations increases, thereby decreasing the signal to noise ratio. This effect is analogous to increasing the force of the hammer blow in the experiment discussed above. Second, the data are degraded because the impacting time interval decreases significantly. For a given impact velocity, V_0 , the number of significant data points N obtained during an impact with a target of thickness d is limited

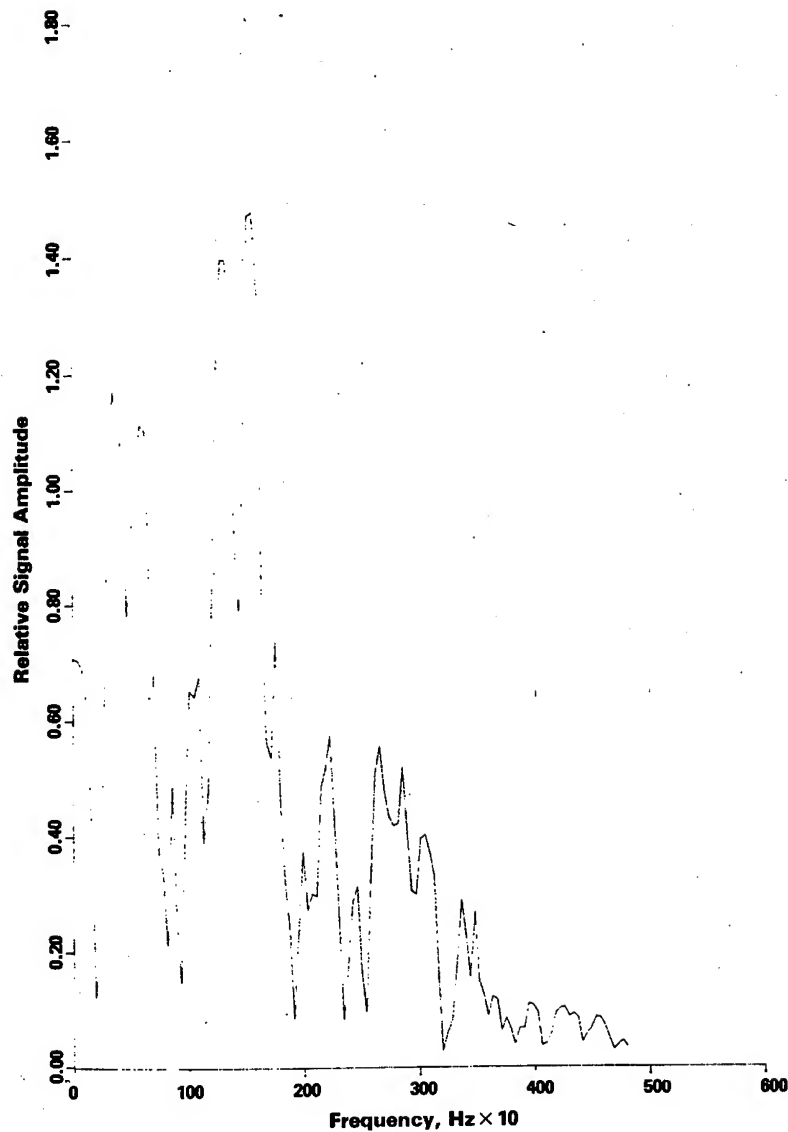


7. Acceleration vs. time response of test projectile supported by a string after hammer impact.

by the bandwidth of the recording instrument B and is given by

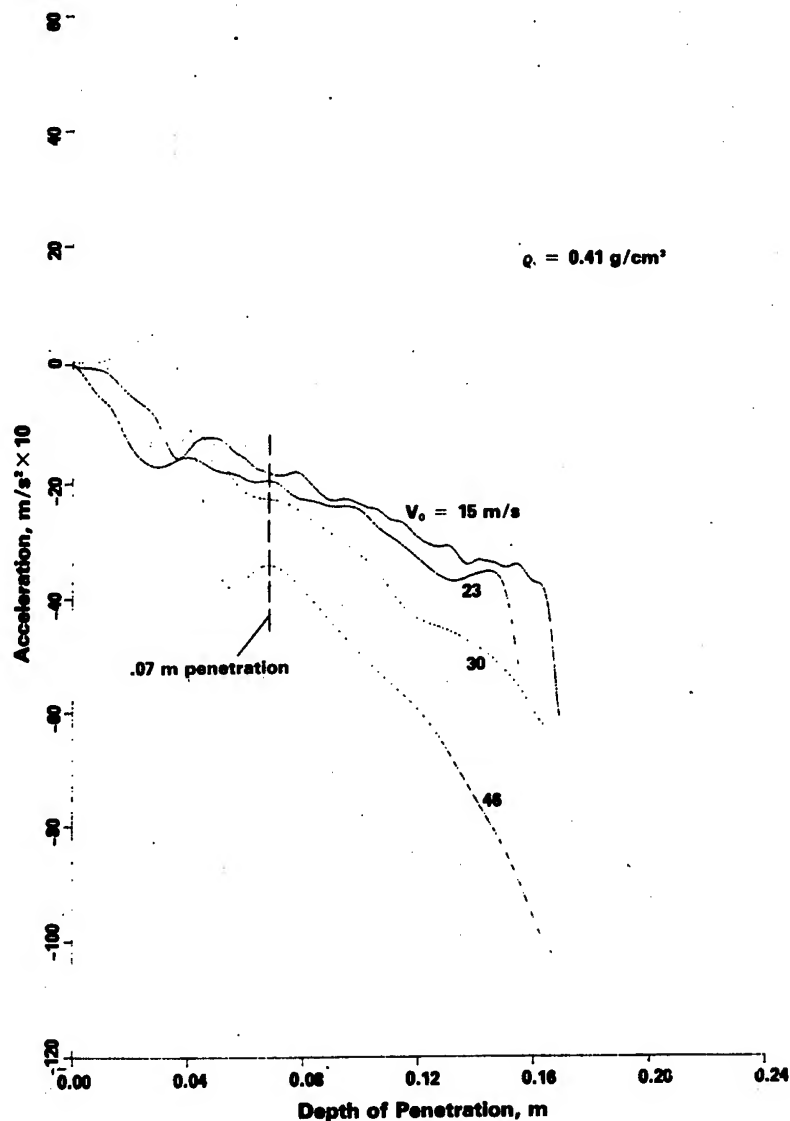
$$N = \frac{d}{V_0} B. \quad (1)$$

For this experiment $B = 5$ kHz and $d = 0.15$ m. For a relatively



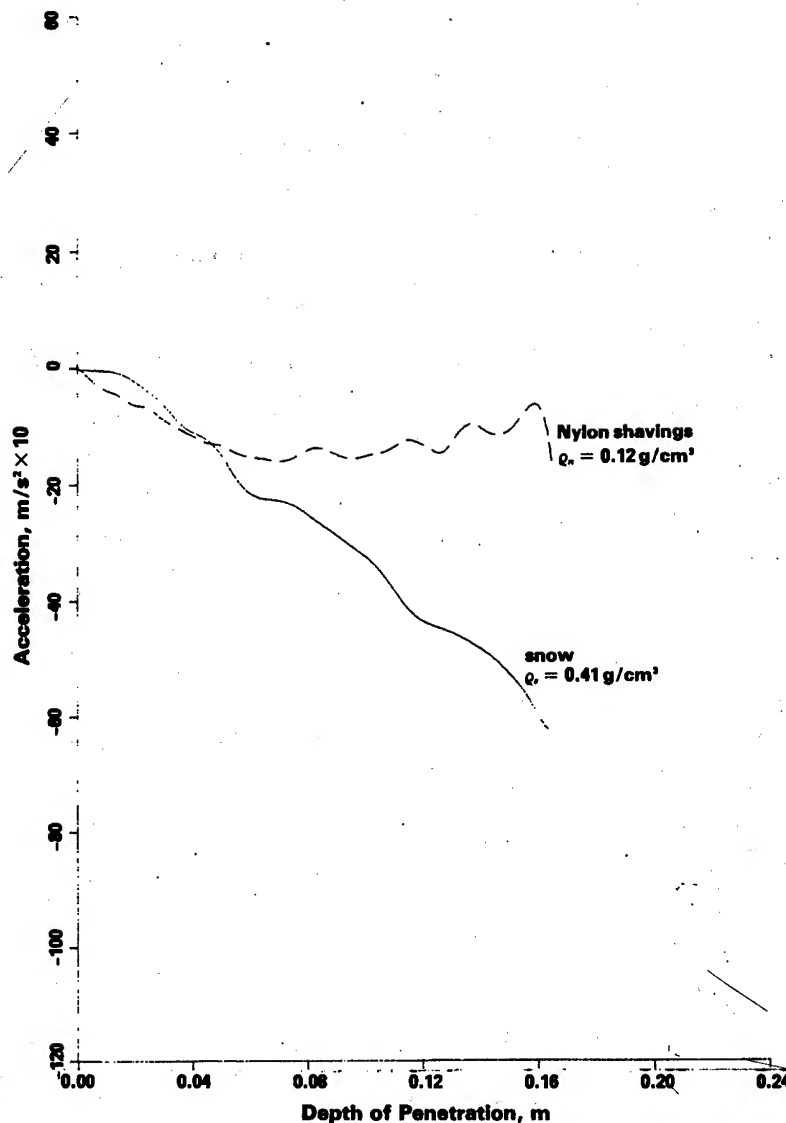
8. Amplitude vs. frequency curve obtained using hammer input data in Fig. 7

low impact velocity of 30 m/s, N is 25, but for a high velocity of 90 m/s the number of data points is reduced to only 8. It is difficult to accurately define the deceleration of the projectile with only 8 data points available for the event. With noise superimposed on the signal, accurate measurement of the deceleration with this limited number of data points becomes impossible.



9. Acceleration vs. depth-of-penetration curves for snow at various impact velocities.

After filtering to remove the noise, the deceleration data were integrated to obtain curves of depth of penetration as a function of time. The penetration vs. time data and the original deceleration vs. time data were then used to construct deceleration vs. penetration curves at velocities from 19 to 46 m/s (Fig. 9).



10. Projectile impacts into snow and nylon shaving targets at 30 m/s (solid line: snow; dashed line: nylon shavings).

Analysis of Results: As shown in Fig. 9 approximately the first 0.07 m of the deceleration vs. penetration curves was influenced by the resonant vibration of the projectile. The vibration level was relatively high during that part of the penetration event and was not adequately reduced by the filtering technique. After the

0.07-m point, the data appear reasonable and show a linear increase in deceleration with increasing penetration. There also seems to be a linear trend to the increase with impact velocity.

Data from representative impacts into targets constructed from nylon shavings are compared with snow data in Fig. 10. The nylon material, which had a density of 0.12 Mg/m^3 , has been used by the USAF to simulate snow for missile nose cone impact tests. Projectile penetration into the nylon sample is characterized by an initial increase in deceleration (which might possibly be attributed to the projectile resonance) followed by a period with roughly constant deceleration. As shown, this is different from the characteristic shape of the deceleration vs. penetration curve for snow. However, there is also a considerable difference in density between these two targets.

A hydrodynamic drag force equation,

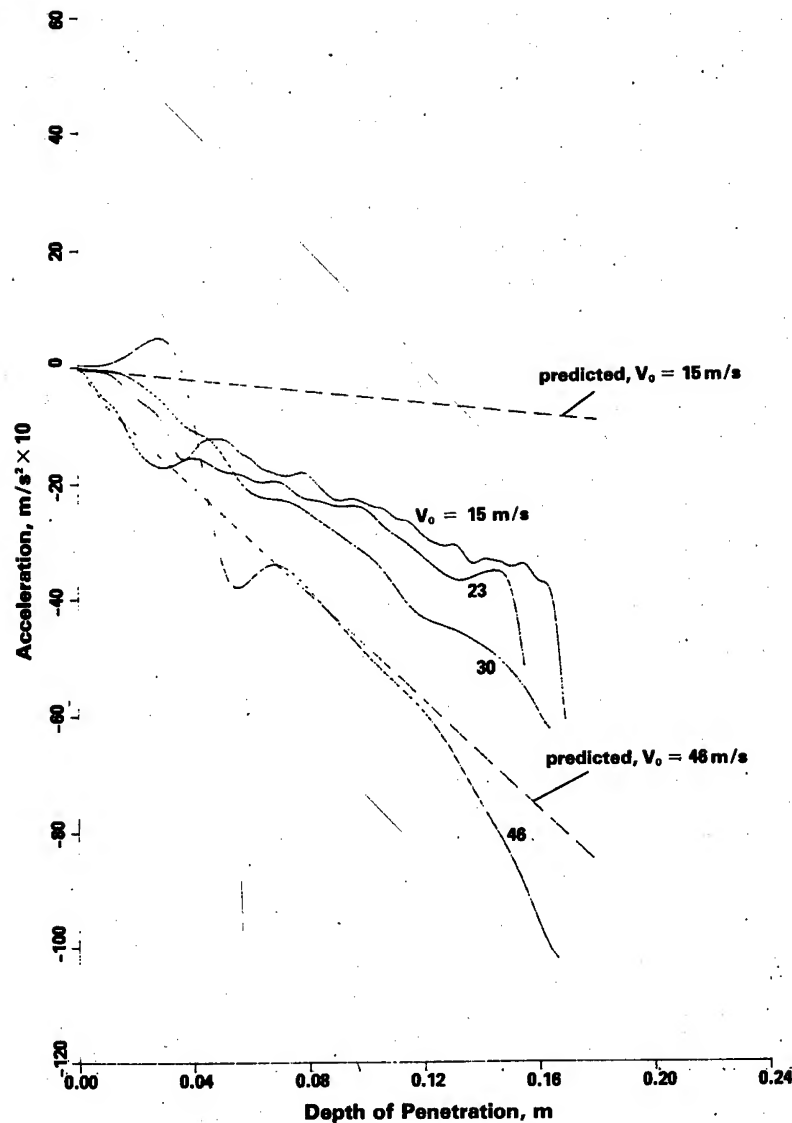
$$F = \frac{1}{2} C_D \rho V_o^2 A, \quad (2)$$

where

- F = drag force on projectile,
- C_D = drag coefficient,
- ρ = target density,
- V_o = projectile velocity, and
- A = projectile area,

has been used by several investigators as a basis for determining fuze performance against water, snow, or mud targets. Kornhauser (2) reported that eq. 2 produces conservative estimates of fuze performance, i.e. the calculated force is lower than the actual force. However, he did not have access to any test data against snow targets to verify his hypothesis. Kornhauser also stated that when calculating forces on point detonating devices the drag coefficient C_D should be 1. Equation 2 then reduces to the equation for the stagnation pressure for a body traveling in a fluid medium:

$$F/A = \frac{1}{2} \rho V_o^2. \quad (3)$$



11. Comparison of predicted vs. measured snow impact data (solid line: measured values; dashed line: predicted values).

Data from impacts into snow are compared with predictions made using eq. 3 in Fig. 11. For low velocities (15-30 m/s), this equation predicts a lower value for deceleration than was measured. At 46 m/s, there is close agreement between the theoretical and the measured deceleration values. The experimental data above this velocity are severely degraded by noise but were

used to estimate deceleration values. These estimated values are less than predicted by eq. 3.

Conclusions: The centrifuge technique is an acceptable method of launching instrumented projectiles and has the capability of providing data without the use of telemetry.

For snow, the data presented show that the forces on a projectile increase as projectile impact velocity increases, and that this relationship is approximately linear.

Projectiles launched into targets prepared from nylon shavings undergo much less deceleration than those launched into snow targets.

Hydrodynamic theory appears to agree with snow test results at an impact velocity of 46 m/s but deviates from measured decelerations at other velocities.

Recommendations: A technique (such as deconvolution) should be developed to eliminate the resonant noise from the data signals so that tests can be conducted over a much greater velocity range.

Future tests should be conducted with higher bandwidth instrumentation to provide sufficient data for analysis at the higher impact velocities. It is estimated that a bandwidth of 40 kHz would be adequate for impact velocities up to 240 m/s.

Future testing should also include deeper targets so that a steady-state penetration condition could be achieved. This condition would also be facilitated by a simpler projectile shape (i.e., cylindrical) than that of the M374 projectile used here.

Acknowledgments: This study was conducted under the Corps of Engineers military RDT&E program at the U.S. Army Cold Regions Research and Engineering Laboratory, Hanover, N.H. The authors acknowledge the assistance of Glenn Durell, Dennis Farrell and Gregor Fellers of CRREL and the many personnel at Sandia Laboratories who made this study possible.

Literature Cited

1. F.R. Lascher, R. Parisse and B.L. Schulman, 1975, Terminal Ballistic Technology Overview Paper, Proceedings of the

AITKEN, RICHMOND & ALBERT

Fuze/Munitions Environment Characterization Symposium, Vol 2.

2. M. Kornhauser, 1969, Prediction of Firing Depths of Impact Fuzes, DEP Methodology and Evaluation Working Group Report No. 4, AD856947.
3. J.E. Kovacs, 1971, Experimental and Predicted Firing Depths of Point Initiating Impact Fuzes Impacting Sand, Mud, Water, and Snow (Confidential Report), Picatinny Arsenal, PA-TR-4095.
4. H.J. Davis, 1975, Impact Sensors for Use with Electronic Fuzes, Harry Diamond Laboratories, HDL-TR-1728.
5. J.V. Otts, 1973, Impact Testing with the 35-Foot Centrifuge, Shock and Vibration Bulletin, Vol 44(3).
6. R.B. Blackman and J.W. Tukey, 1958, The Measurement of Power Spectra, Dover Publications, Inc., N.Y.
7. R.K. Otnes and L. Enochson, 1978, Applied Time Series Analysis, John Wiley and Sons, N.Y.
8. S.D. Stearns, 1975, Digital Signal Analysis, Hayden Book Co., Rochelle Park, N.J.

RESPONSE OF BURIED VERTICALLY ORIENTED CYLINDERS
TO DYNAMIC LOADING

GAYLE E. ALBRITTON, MR.* AND JIMMY P. BALSARA, DR.
U. S. Army Engineer Waterways Experiment Station
Vicksburg, Mississippi 39180

INTRODUCTION

One of the primary concepts proposed for basing advanced ballistic missile systems is to emplace the missile in a buried vertical cylindrical shelter. Since little data were available on the response of vertically oriented cylinders that could be used to assess the hardness of missile silos, a field test program was conducted by the Structures Laboratory of the U. S. Army Engineer Waterways Experiment Station (WES) to determine the response to failure of generic vertical shelters having different wall construction designs and subjected to the effects of simulated nuclear surface overpressure loadings. Results obtained from the simulation program were to provide information to support selection and design of prototype vertical shelters.

The specific objective of the field test program was to obtain information whereby cylinder wall construction designs could be ranked as to their survivability/vulnerability. Thus, with such information, the cost performance of the various designs could be determined with structural hardness a major consideration.

This paper summarizes the results of three dynamic tests conducted on vertical cylinders in a dry sand with wall designs consisting of plain concrete with an inner liner, plain concrete with shear studs and an inner liner, and reinforced concrete without an inner liner. Using the experimental results in which three different wall thicknesses were tested for each design and considering relative costs, a candidate wall design for the vertical shelters is presented.

TEST PROCEDURES

To accomplish the objective of the investigation, three field tests utilizing the FOAM High-Explosive Simulation Technique (FOAM HEST) test environment were conducted at the Fort Polk Military Reservation in Louisiana, site of previous field tests conducted by WES. The three tests were identified as Dynamic End on Tests (DEOT) in which three cylinders were included in each test (Figure 1), i.e. the DEOT 1 cylinders were constructed of plain concrete with steel inner liners, the DEOT 2 cylinders were constructed of plain concrete with shear studs and steel inner liners, and the DEOT 3 cylinders were constructed of reinforced concrete without inner liners. The scale-model cylindrical structures had a 0.61-metre (2-foot) inside diameter and an overall length of 1.83 metres (6 feet). The only construction variable for the cylinders in a specific test was the wall thickness which was 4.32, 7.11, and 10.16 cm (1.7, 2.8, and 4.0 inches). The end caps for the cylinders consisted of a steel shell filled with high-strength concrete; however, the end caps were not designed to be test articles. The average concrete compressive strength of the cylinders on test day was 44.0 MPa (6,380 psi).

The three DEOT test beds were excavated to 3.05 metres (10 feet) deep, the structures placed, and then backfilled with clean, dry sand. After a test bed was excavated, circular foundation blocks with hold down rods were placed in the bottom of the bed on preleveled surfaces. The vertical cylinders were then placed on their foundations (Figure 2) and instrumentation connections made. The dry sand was placed in 15.2-cm (6-inch) lifts with each lift receiving three vibration passes (Figure 3) to obtain the desired density of 1681 kg/m³ (105 pcf).

During the tests, electronic measurements were made to obtain the airblast surface overpressure, vertical soil stress, relative vertical deformation of certain cylinders, and strain in the concrete of the cylinder walls. The strain gages were mounted either vertically or radially at locations of 0.61 metres (2 feet) and 1.22 metres (4 feet) from the top of the cylinders.

The test environment was generated by uniform FOAM HEST's over the test bed areas, as generally shown in Figure 1. An 11.4 cm (4.5 inch) charge cavity was filled with polystyrene and evenly distributed strands of 2.86-cm (1-1/8-inch) diameter Iremite explosive. A sand overburden of 0.81 metres (32 inches) was placed over the explosive to control the duration of the pressure pulse.

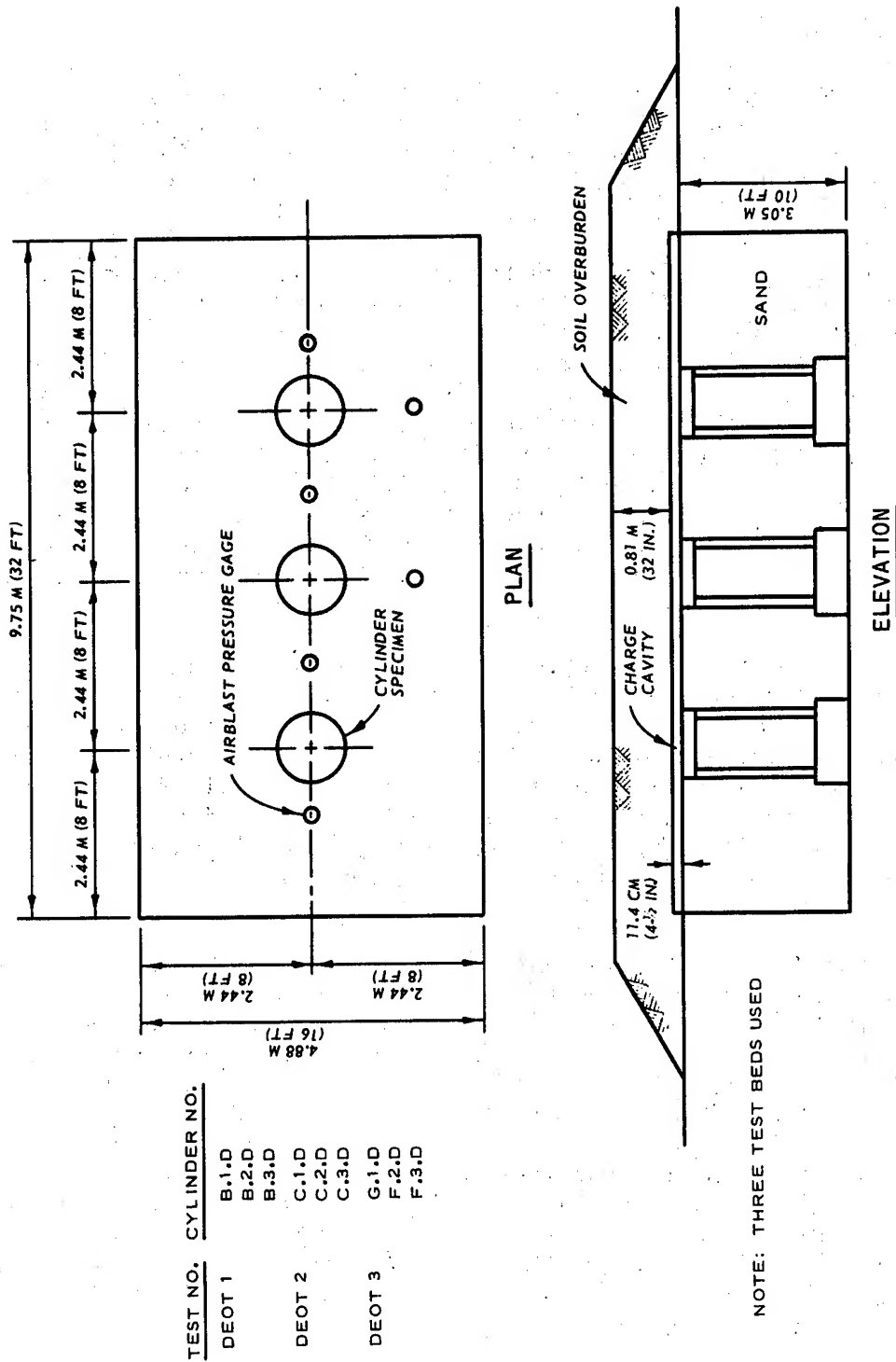


Figure 1. DEOT test bed layout and FOAM HEST configuration

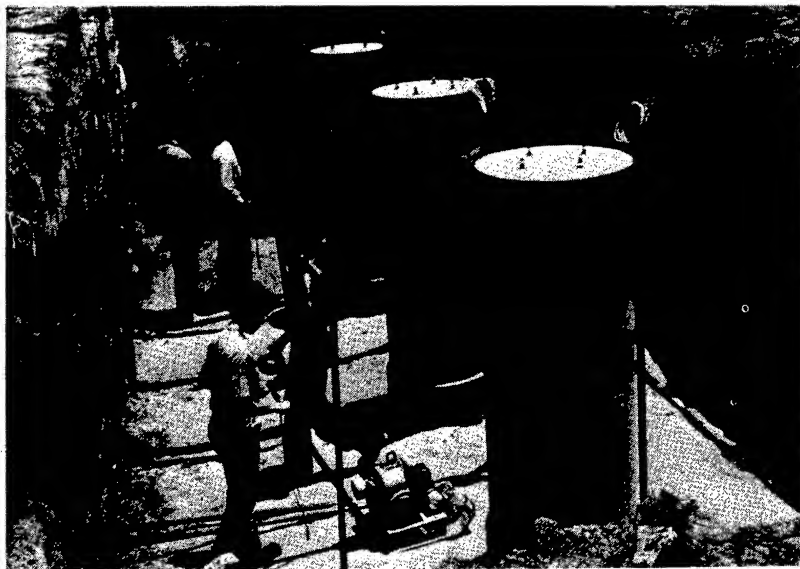


Figure 2. Cylinders placed on foundations

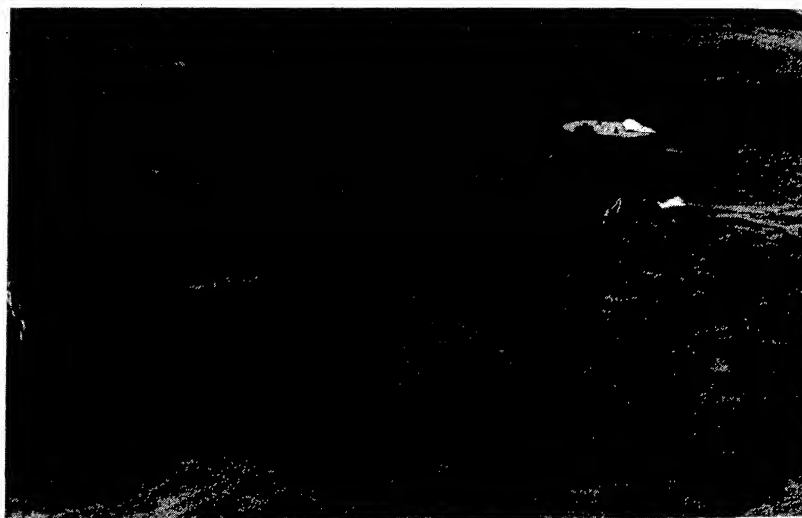


Figure 3. Backfill around cylinders

RESULTS AND DISCUSSION

The primary results obtained during this test series include the measured airblast pressure, strain in the cylinder walls, and posttest structural damage. Discussion herein will consider these parameters in an attempt to rank the construction designs as to their survivability/vulnerability.

Test Environment

The planned pressure levels for the tests were 17.2 MPa (2500 psi) for DEOT 1 and 27.6 MPa (4000 psi) for DEOT 2 and 3. It was determined that the average peak pressure for the DEOT 1 test was close to the planned pressure and was 16.1 MPa (2339 psi); the weapon simulation was for an average yield of 13.24 TJ (5.52 kt). For DEOT 2, the average peak pressure was 34.1 MPa (4942 psi) and with a nuclear weapon simulation yield of 56.16 TJ (13.37 kt). The DEOT 3 average peak pressure was somewhat greater than DEOT 2 and was 42.5 MPa (6209 psi); the average weapon simulation yield was 23.66 TJ (3.02 kt). Typical blast pressure curves for the three tests are shown in Figure 4. Although the average peak pressure for DEOT 3 was approximately 26 percent greater than the average for DEOT 2, the average impulse at 10 msec for DEOT 3 indicated an increase of only 12 percent greater than the DEOT 2 average impulse at this same time.

Structural Response

Vertical strain plots from each of the nine cylinders in the three DEOT tests are shown in Figure 5. These strains are for the vertical gage located in the upper portion of the cylinders and oriented toward the detonation side of the test beds. As shown in Figure 5 for the DEOT 1 test (plain concrete with liner) the thinnest wall cylinder B.1.D had appreciably more compressive strain (2000 $\mu\text{in/in}$) than the other two thicker wall cylinders (1000 $\mu\text{in/in}$). The two cylinders with wall thicknesses of 7.11 and 10.16 cm (2.8 and 4.0 inches) had approximately the same magnitude of compressive strain. For the pressure obtained, this response infers that there was increased resistance by increasing the wall thickness from 4.32 cm (1.7 inches) to 7.11 cm (2.8 inches) but there appeared to be little additional resistance obtained by increasing the wall thickness to 10.16 cm (4.0 inches).

During the DEOT 2 test on similar constructed cylinders as DEOT 1, but with shear studs, the compressive strains for all three cylinders were approximately 1600 $\mu\text{in/in}$. The peak pressure for this

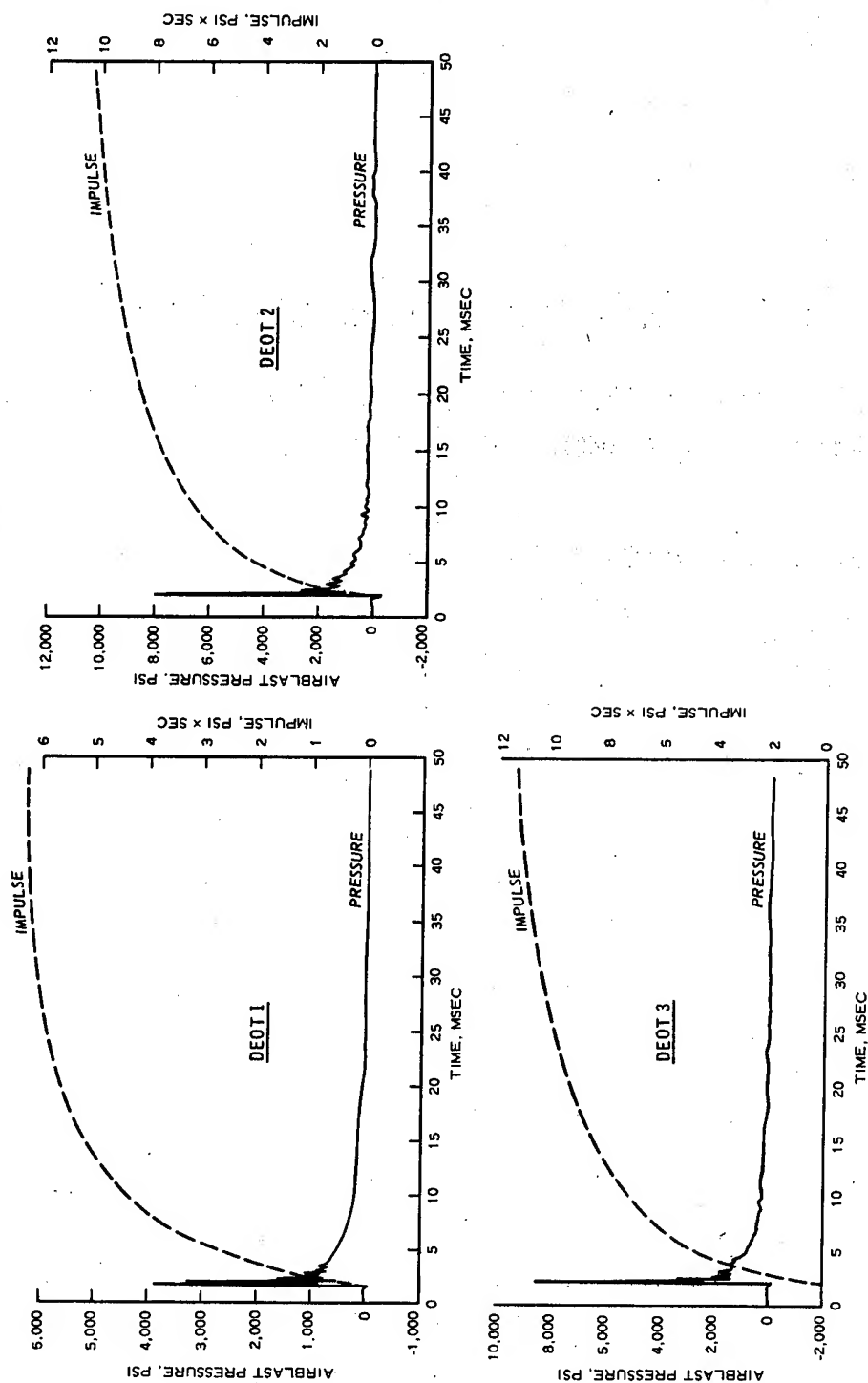
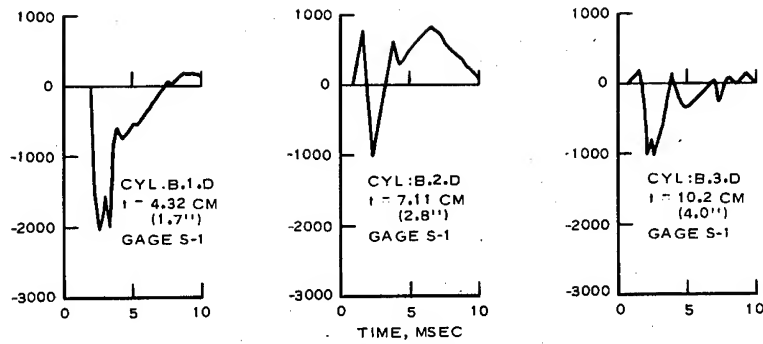
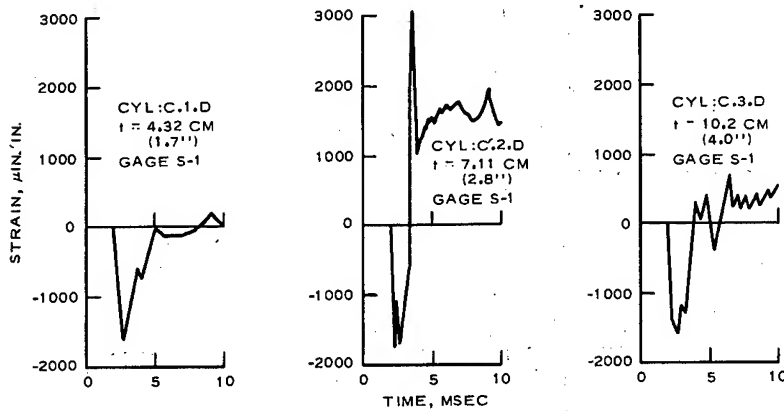


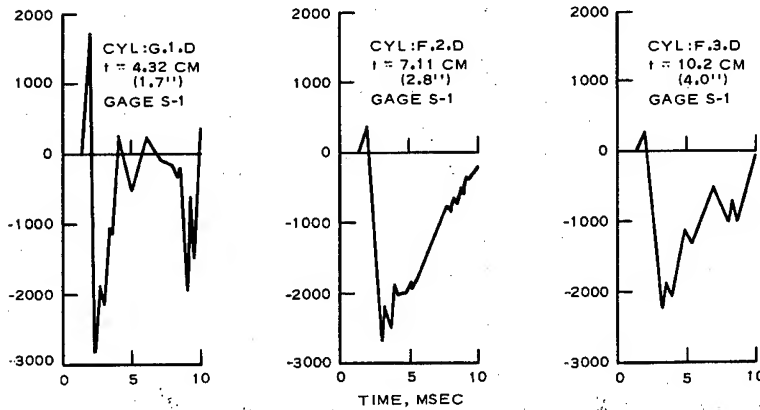
Figure 4. Typical airblast pressure and impulse curves for DEOT tests



DEOT 1: PLAIN CONCRETE WITH LINER



DEOT 2: PLAIN CONCRETE WITH SHEAR STUDS AND LINER



DEOT 3: REINFORCED CONCRETE WITHOUT LINER

Figure 5. Vertical strain comparison for DEOT cylinders

ALBRITTON* AND BALSARA

test was approximately 2.1 times as great as that for DEOT 1. The fact that all three cylinders of DEOT 2 registered approximately the same strain is believed to be due to the liner, acting along with the shear studs, carrying most of the load. Cylinder C.2.D (middle cylinder) does register more tensile strain than the other two cylinders in the test and this was due to a buckle in the liner occurring at approximately the same location as the strain gage.

For the reinforced concrete cylinders of DEOT 3, the peak pressure was approximately 2.7 times as great as that for DEOT 1. During this test, the peak strains were approximately 2800 $\mu\text{in/in}$, 2600 $\mu\text{in/in}$, and 2200 $\mu\text{in/in}$, respectively, for the thin, middle, and thick cylinders. Thus, there did not appear to be any substantial decrease in the cylinder wall strain level by increasing the wall thickness by factors of 1.6 and 2.4.

It is interesting to compare cylinders with the same wall thickness for the DEOT tests. The comparison will be for the three thinnest cylinders as they incurred various levels of damage. The peak strain levels for the cylinders are:

<u>Test No.</u>	<u>Cylinder No.</u>	<u>Peak Pressure</u>	<u>Pressure Ratio</u>	<u>Peak Strain</u>
DEOT 1	B.1.D	2339 psi	1.0	2000 $\mu\text{in/in}$
DEOT 2	C.1.D	4942 psi	2.1	1600 $\mu\text{in/in}$
DEOT 3	G.1.D	6209 psi	2.7	2800 $\mu\text{in/in}$

These results show that with an increase in peak pressure by a factor of 2.1 for DEOT 2 with respect to DEOT 1 there was a decrease in peak strain from 2000 $\mu\text{in/in}$ to 1600 $\mu\text{in/in}$. For DEOT 3, the peak pressure increased by a factor of 2.7 over DEOT 1 and there was an increase in peak strain from 2000 $\mu\text{in/in}$ to 2800 $\mu\text{in/in}$. Thus, based on the strain behavior of these three cylinders with different wall designs, it appears that the cylinder constructed of plain concrete with shear studs and an inner liner was more resistant to dynamic loading than cylinders with other wall design features.

Structural Damage

After the DEOT 1 test, the sand on top of the cylinders end caps was removed and this permitted measuring the displacement of the cylinders relative to the nuts on the hold down rods. The thinnest cylinder B.1.D appeared to have been displaced downward approximately 1.91 cm (3/4-inch). The other two cylinders did not appear to have

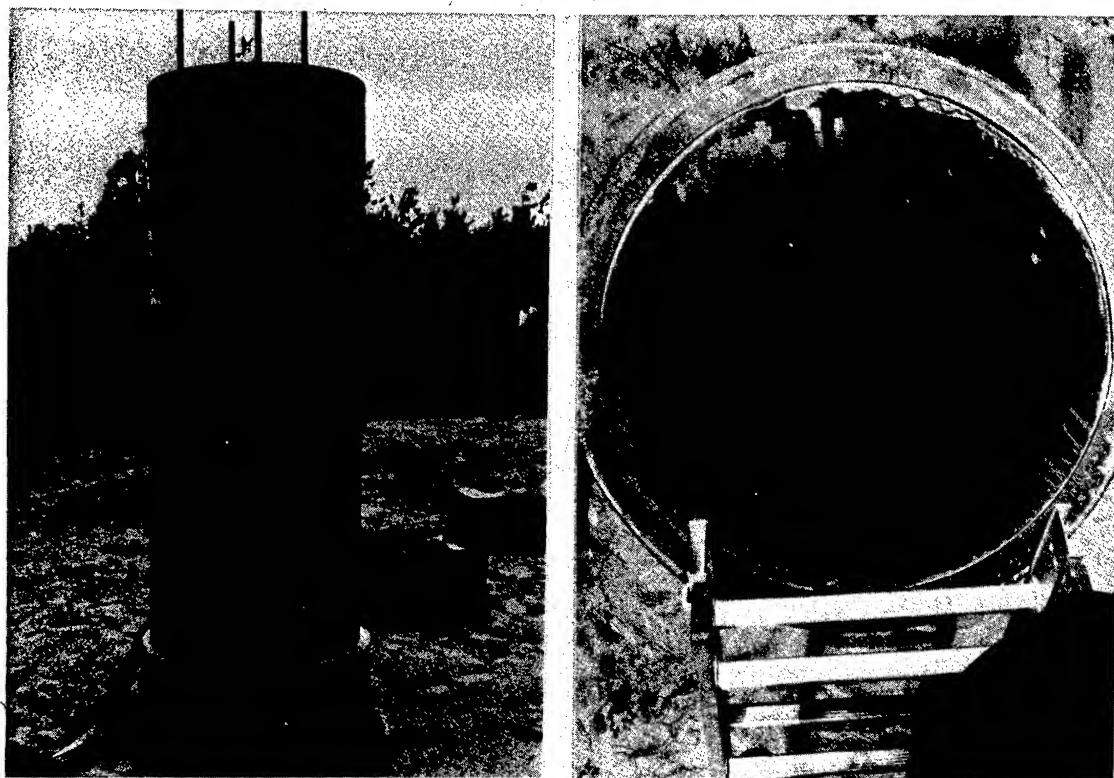
moved relative to the nuts, although the nuts were loose. The sand backfill was excavated from around the cylinders in order to conduct a posttest examination of any damage. Posttest check of the cylinders length indicated only that the thinnest cylinder had shortened 1.91 cm (3/4-inch). Posttest views of damage to cylinder B.1.D are shown in Figure 6 after removing the cylinder from the test bed. Damage had occurred completely around the outside of this cylinder and the liner inside was also damaged and showed ripples at approximately the same location at which the concrete was crushed. Both of the thicker cylinders in the DEOT 1 test incurred negligible damage.

Posttest check of the length change of each cylinder in the DEOT 2 test indicated that the thinnest cylinder had been displaced 5.08 cm (2 inches), the middle cylinder had been displaced 0.32-cm (1/8-inch), and there was no apparent displacement of the thickest cylinder. The thinnest cylinder, C.1.D, was found to have circumferential cracks near the top on the exterior. The other two cylinders had negligible cracks on the exterior. However, the inner liner and concrete of the thinnest cylinder was displaced at the cylinder top (Figure 7). The middle cylinder, C.2.D, appeared to have a slight ripple of the liner at approximately one-fourth of the height from the top on the detonation side. There did not appear to be any damage to the interior of the thickest cylinder, C.3.D.

Posttest check of the DEOT 3 cylinders indicated a length change of 9.53, 2.54, and 0.64 cm (3-3/4, 1, and 1/4 inch), respectively, for the thinnest, middle, and thickest cylinder. The thinnest cylinder, G.1.D, had a vertical crack on the exterior which was wide and open completely through the cylinder. The middle cylinder, F.2.D, showed some exterior crushing below the top and some circumferential spalling at approximately midheight. There was also some cracking below the top exterior for the thickest cylinder, F.3.D. Posttest views of damage to the interior of each cylinder are shown in Figures 8 through 10. Damage to these cylinders was more drastic on the inside with considerable crushing and spalling at the cylinder top portion. The overall damage to the DEOT 3 reinforced concrete cylinders was much greater than that observed for the DEOT 1 and 2 cylinders with inner liners.

Relative Cost Comparison

In addition to structural response and damage, it is interesting to compare the relative material and construction costs of the three different designs for prototype cylinders similar to those tested in this program. Actual dollar amounts for the costs will not



a. Damage to exterior

b. Damage to inner liner

Figure 6. Damage to cylinder B.1.D ($t = 1.7$ in.) during DEOT 1 test

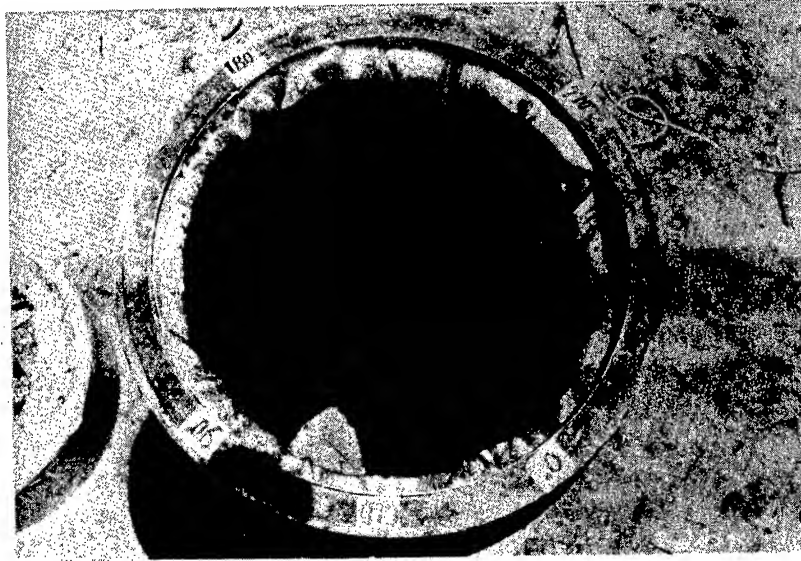


Figure 7. Damage to interior of cylinder C.1.D ($t = 1.7$ in.) during DEOT 2 test

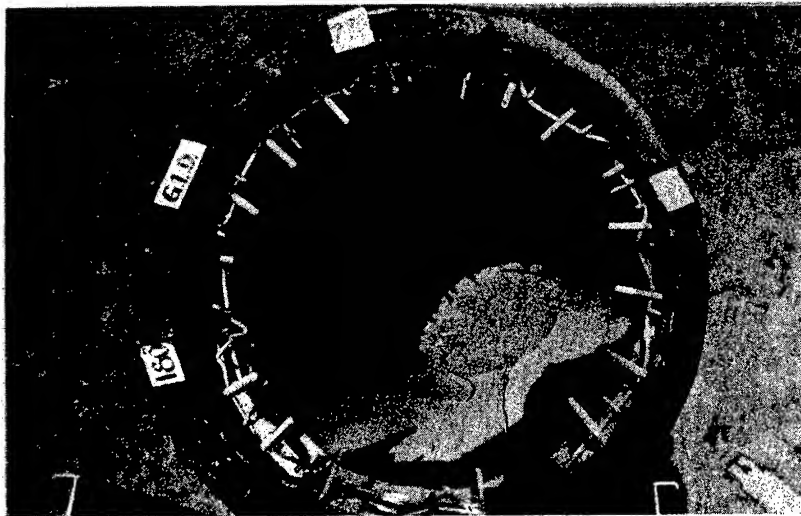


Figure 8. Damage to interior of cylinder G.1.D ($t = 1.7$ in.) during DEOT 3 test

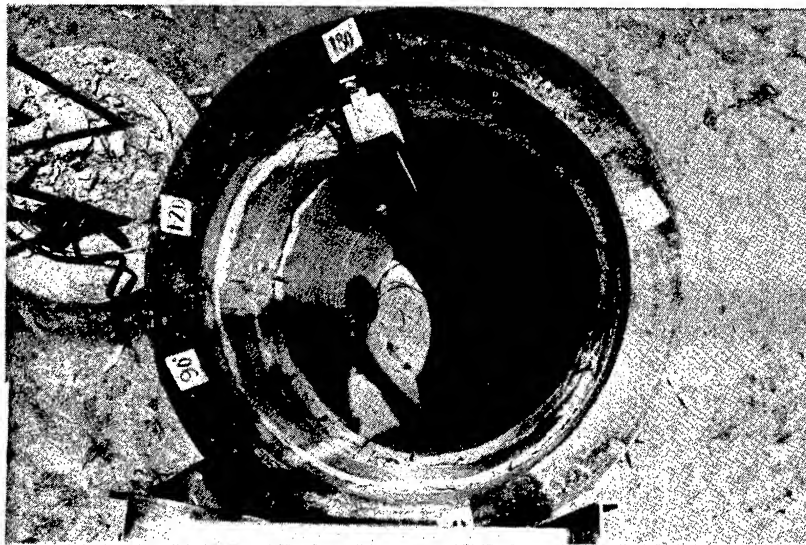


Figure 9. Damage to interior of cylinder F.2.D ($t = 2.8$ in.) during DEOT 3 test



Figure 10. Damage to interior of cylinder F.3.D ($t = 4.0$ in.) during DEOT 3 test

be presented; however, a cost index will be used whereby the cost of each design is normalized by the least cost of the three. The cost index was prepared for the middle cylinder thickness (baseline design). The estimated cost index for prototype cylinder materials and construction including necessary interior and exterior construction forms is given as follows:

<u>Wall Design</u>	<u>Estimated Cost Index</u>
Reinforced concrete without steel liner	1.00
Plain concrete with steel liner	1.37
Plain concrete with steel liner and shear studs	1.42

As shown in the cost index, the reinforced concrete construction without a steel liner is the least cost method. Construction cost with a steel liner is approximately 1/3 more than the reinforced case, and it should be noted that the addition of shear studs does not appreciably change the cost index.

CONCLUSIONS

1. The middle cylinders (baseline design) appeared to have less structural damage than the thinner cylinders and there did not appear to be any significant increase in structural resistance by increasing the wall thickness over the baseline thickness for the overpressure ranges of these tests.
2. Damage to the lined cylinders did not appear to be as severe as the unlined cylinders, i.e. internal spalling of concrete was almost negligible.
3. The results indicate that plain concrete cylinders with inner steel liners and shear studs were more resistant to dynamic loading than reinforced concrete cylinders without internal liners.
4. Although the cost of material and construction for the concrete cylinder with steel liners and studs was approximately 40 percent greater than that for reinforced concrete cylinders, the lined cylinder with studs was proportionately more resistant to dynamic loads.
5. The results of this field test program have shown that the FOAM HEST test environment procedure provides an acceptable simulation technique and was relatively inexpensive to conduct.

ALEXANDER

FREQUENCY DIVERSE TRACKING/GUIDANCE MILLIMETER
RADAR ADAPTED TO TARGET ACQUISITION

P. MARTIN ALEXANDER, PhD
US ARMY MISSILE COMMAND
REDSTONE ARSENAL, ALABAMA 35809

I. INTRODUCTION

Millimeter wave radar fire control for ground-to-ground tactical weapons provides a compromise between the resolution offered by electro-optical and infrared systems and the adverse environment (fog, battle-field smokes) penetrability which is characteristic of microwave systems. The effectiveness of millimeter sensors would be greatly enhanced if they could also be used to classify radar returns resulting from clutter, tanks, personnel carriers, etc., and particularly from stationary targets.

Missile fire control requires accurate target location, and, as a result, the use of frequency diversity has been investigated as a method of angle noise (glint) reduction to improve centroid tracking (1), (2), (3). Frequency diversity has more recently been examined as a tool for target acquisition (i.e., detection and classification) (4), (5), (6), (7), (8).

The detection/classification technique is based on: (1) the fact that, in general, targets and clutter consist of separate, individual reflectors distributed in range; and (2) the fact that the radar returns from any pair of reflectors will constructively or destructively interfere, depending on their separation in radar range and on the transmitted frequency. Thus, the basic measurement used in the acquisition technique is the radar response as a function of transmitted frequency.

It is hypothesized that the spacing in range for natural objects is more random than for manmade objects and, further, that manmade

ALEXANDER

objects have unique range spacings allowing discrimination of object classes. With this hypothesis, an analysis of frequency diverse radar returns is developed. The analysis is constrained by practical radar design parameters for a state-of-the-art, coherent, 142 GHz experimental radar, so that the analytical results can be experimentally tested. The analysis is also constrained to stationary targets and clutter.

Computer simulations are presented for a two-reflector target model and a three-reflector target model, and the analysis is extended to complications resulting from a chirped waveform. The applicability of the technique to real targets and clutter is considered. The parameters used for the analysis are: (1) a 3.0 microsecond pulse; (2) a 640 MHz frequency diverse bandwidth beginning at 142 GHz; (3) thirty-two frequency steps of 20 MHz for data acquisition; and (4) a linear frequency modulated chirp of 20 MHz for each pulse.

II. TWO-REFLECTOR TARGET MODEL

In the monostatic radar scenario depicted in Figure 1, the vertical, linearly polarized electric field incident on the i^{th} reflector can be written

$$\begin{aligned} E_i^t &= E_0 \cos [2\pi f(t-t_i/2)] \\ t_i/2 \leq t \leq t_i/2 + T \end{aligned} \quad (1)$$

where: f = radar frequency,

t_i = round trip echo time = $2R_i/c$, and

T = transmitted pulse length.

The echo, the electric field returned from the i^{th} reflector, at the receiver is given approximately by

$$E_i^r = \frac{\sqrt{\sigma_i}}{4\pi R_i^2} E_0 \cos [2\pi f(t-t_i)] \quad t_i \leq t \leq t_i + T \quad (2)$$

where σ_i is the radar cross section (RCS) of the reflector for vertical transmit and receive. Implicit in Equation (2) are the assumptions that the target is stationary, that the target reflectors are in the far-field of the radar, and that the radar is in the far-field of the reflectors. For antenna aperture D and characteristic reflector dimension a , the far-field region (Fraunhofer region) is given by

$$R_i > 2D^2/\lambda \quad R_i > 2a^2/\lambda \quad (\text{for all } R_i) \quad (3)$$

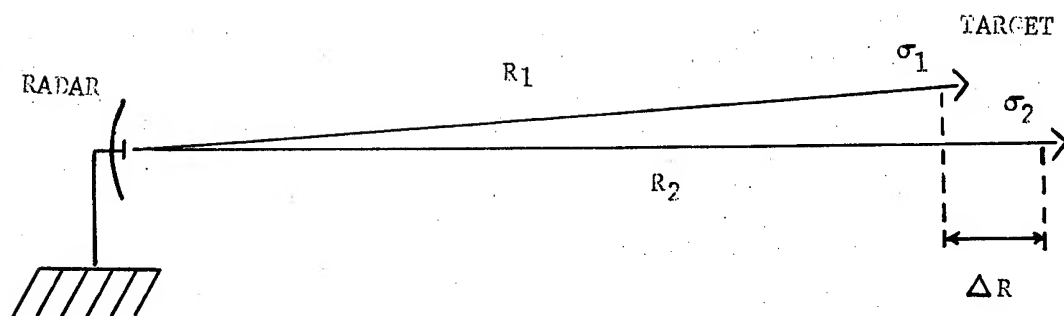


Figure 1. Radar/Target Scenario.

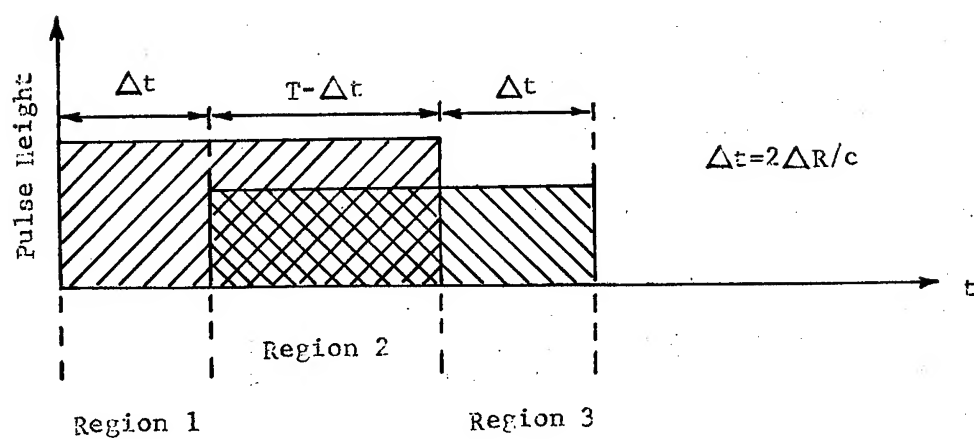


Figure 2. Arrival of Pulses from Two Reflectors ($\sigma_1 > \sigma_2$).

ALEXANDER

where λ is the transmitted wavelength.

It shall also be assumed for this analysis that $2\pi a \gg \lambda$ (optical region), and that the RCS of the reflectors vary as f^2 , as for flat plates and corner reflectors.

For two reflecting centers on a target, the electric field strength at the antenna is

$$E^r = E_1^r + E_2^r \quad (4)$$

Figure 2 characterizes the arrival of the pulses at the antenna. In Region 2, the pulses overlap, resulting in constructive or destructive interference, depending on the relative phase. The electric field amplitude is given approximately by

$$E_m^r = \frac{E_0}{4\pi R^2} \left[\sigma_1 + \sigma_2 + 2\sqrt{\sigma_1\sigma_2} \cos\left(\frac{4\pi}{c} f \Delta R\right) \right]^{\frac{1}{2}} \quad (5)$$

$$R = \frac{1}{2}(R_1 + R_2) \quad \Delta R \ll R$$

After square-law detection, the output signal voltage can be written

$$V_s = A \left[\sigma_1 + \sigma_2 + 2\sqrt{\sigma_1\sigma_2} \cos\left(\frac{4\pi}{c} f \Delta R\right) \right] \quad (6)$$

where A is a constant. It is variation in this voltage due to changes in f that is the intended target signature. The dependence of RCS on frequency is taken to be insignificant. For a frequency diverse bandwidth of 1%, RCS will monotonically increase by 2% over the bandwidth. The signal of interest, however, is the sinusoidal variation due to the cosine factor.

The video signal can be processed by either detecting the peak voltage or by integrating over the combined pulses; the signal dynamic range will depend on which method is used. Considering Figure 2, and assuming $\sigma_1 \geq \sigma_2$, it is seen that, for detecting the peak voltage,

$$A\sigma_1 \leq V \leq A(\sigma_1 + \sigma_2 + 2\sqrt{\sigma_1\sigma_2}) \quad (7)$$

If the dynamic range, DR, is defined as the ratio of the maximum value to the minimum value, then

$$DR = (1 + \sqrt{\sigma_2/\sigma_1})^2, \quad (8)$$

this ratio being independent of the amount of pulse overlap.

The dynamic range for the integrated pulse case does, however, depend on the overlap:

$$DR = \frac{\sigma_1 + \sigma_2 + 2\sqrt{\sigma_1\sigma_2}(1 - \Delta t/T)}{\sigma_1 + \sigma_2 - 2\sqrt{\sigma_1\sigma_2}(1 - \Delta t/T)} \quad (9)$$

For complete overlap,

$$DR = \left[\frac{1 + \sqrt{\sigma_2/\sigma_1}}{1 - \sqrt{\sigma_2/\sigma_1}} \right]^2 \quad (10)$$

which is larger than DR given in Equation (8). For $\sigma_1 = \sigma_2$, when $\Delta t > 2T/5$, sampling the peak voltage gives a larger dynamic range; for $\Delta t < 2T/5$, integration is better. In this analysis it is assumed that the pulse overlap is always large enough to make pulse integration advantageous, i.e., $\Delta t = 2\Delta R/c \ll T$.

The integrated signal voltage is then

$$V = A \left[(\sigma_1 + \sigma_2)T + 2\sqrt{\sigma_1\sigma_2}(T - 2\Delta R/c) \cos\left(\frac{4\pi f \Delta R}{c}\right) \right] \quad (11)$$

Equation (11) was used in a computer simulation in which the frequency was stepped in thirty-two 20 MHz increments over a 640 MHz bandwidth beginning at 142 GHz. These numbers were chosen to assess the value of adding automatic frequency diversity to a 142 GHz coherent radar currently being tested by the US Army Missile Laboratory. The radar pulse is linearly chirped (20 MHz bandwidth), so a 20 MHz increment was chosen for this analysis to assure no frequency overlap. The voltage was normalized by dividing by the largest possible value.

The simulation for the two-reflector case was designed to show: (1) how large σ_1/σ_2 may be before the effect is unmeasurable; and (2) how large or small ΔR may be before the effect is ambiguous or unmeasurable.

Figure 3 provides a reference amplitude-frequency pattern in which $\sigma_1 = \sigma_2$ and $\Delta R = 1.0$ meter. A little over four complete oscillations can be observed, with every other peak being clipped due to the relatively few number of samples taken. Voltage variations are $\pm 100\%$ of the average.

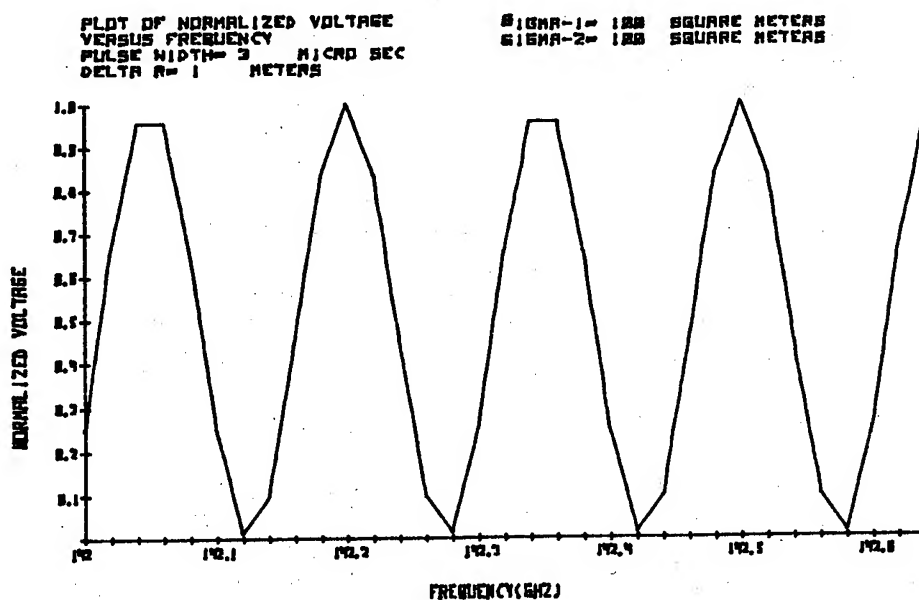


Figure 3. $\sigma_1/\sigma_2=1$, Range Separation = 1.0 meter.

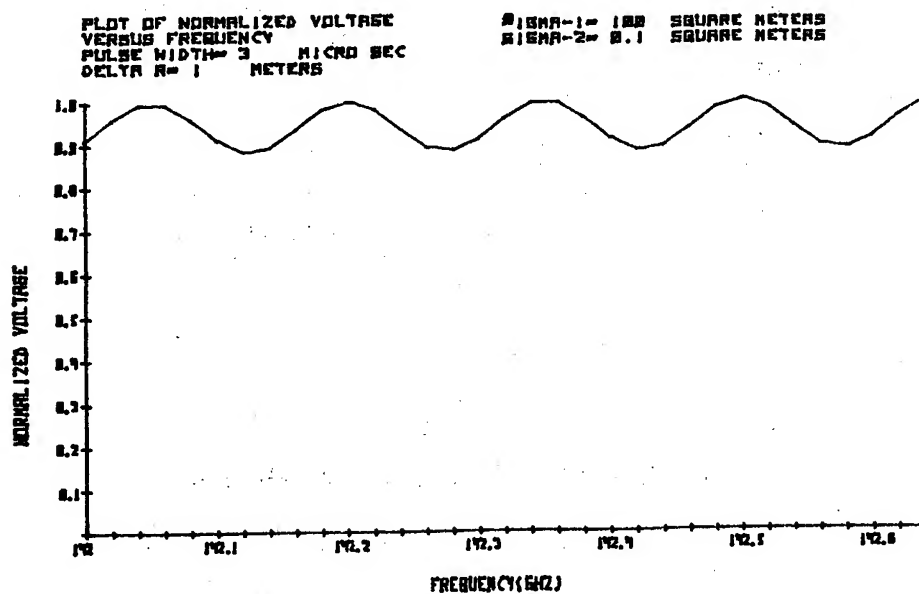


Figure 4. $\sigma_1/\sigma_2=1,000$, Range Separation = 1.0 meter.

ALEXANDER

In Figure 4, the simulation shows a significant voltage variation for one reflector RCS being 1,000 times larger than the other. Ratios of 10, 100, and 1,000 give voltage variations of $\pm 57\%$ (5.7 dB), $\pm 20\%$ (1.8 dB), and $\pm 6.3\%$ (0.5 dB) respectively. Clearly, the detectability of a weak reflector in the presence of a large one is limited by radar system fluctuations, multipath, atmospheric effects, etc. Note especially that multipath may cause severe problems.

Considering different range separations, in the limit of small ΔR , the voltage variation goes to zero. If it is established, for example, that at least one-half cycle must be observable over the bandwidth, then the minimum reflector separation which provides a usable signal is about 0.1 meter. This case is shown in Figure 5.

The maximum ΔR giving an unambiguous signal is determined by the number of sampled points over the (fixed) bandwidth. At large ΔR , there are so many cycles over the bandwidth that the frequency step size does not provide enough resolution. Applying the Nyquist sampling theorem for the case of 20 MHz frequency steps, one obtains a maximum allowable ΔR of 3.75 meters. This maximum is not unreasonable for vehicle reflector separations, but if two separate targets, or perhaps one target and strong clutter, are illuminated by the radar beam, then ambiguities may occur. Figure 6 shows that the pattern for a range separation of 6.5 meters is the same as for 1.0 meter, due to the aliasing effect.

III. THREE-REFLECTOR TARGET MODEL

If a similar analysis is applied to a three-reflector target, again integrating the total received pulse, the signal voltage is found to be

$$\begin{aligned} V = A & \left[(\sigma_1 + \sigma_2 + \sigma_3) T \right. \\ & + 2 \sqrt{\sigma_1 \sigma_2} (T - 2\Delta R_{12}/c) \cos\left(\frac{4\pi}{c} f \Delta R_{12}\right) \\ & + 2 \sqrt{\sigma_1 \sigma_3} (T - 2\Delta R_{13}/c) \cos\left(\frac{4\pi}{c} f \Delta R_{13}\right) \\ & \left. + 2 \sqrt{\sigma_2 \sigma_3} (T - 2\Delta R_{23}/c) \cos\left(\frac{4\pi}{c} f \Delta R_{23}\right) \right] \end{aligned} \quad (12)$$

where $\Delta R_{ij} = |R_j - R_i|$.

The extension to many reflectors is

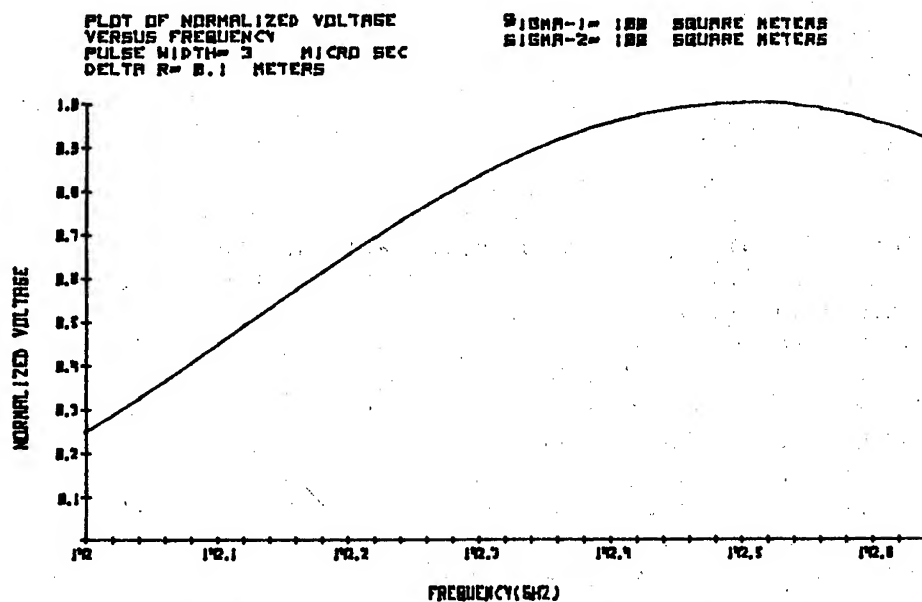


Figure 5. $\sigma_1/\sigma_2=1$, Range Separation = 0.1 meter.

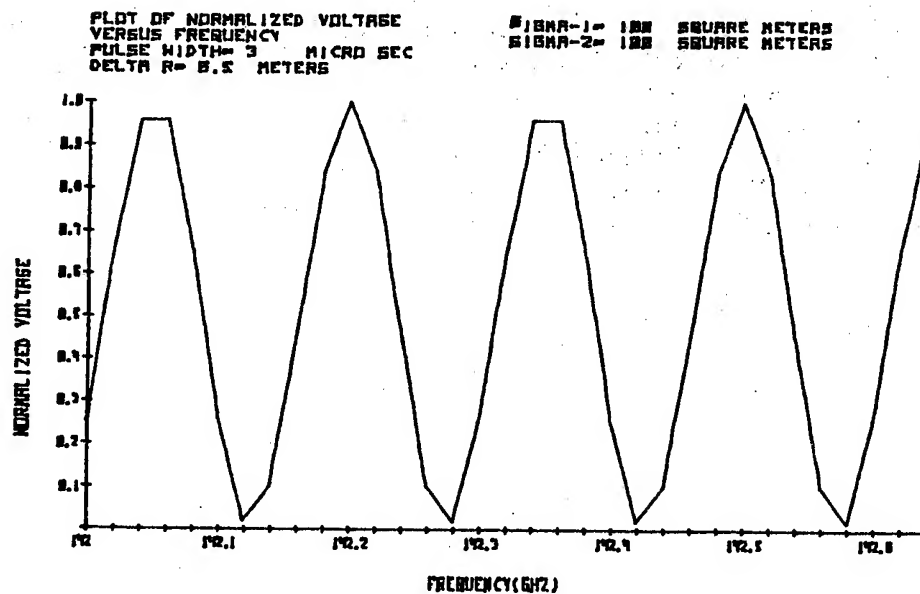


Figure 6. $\sigma_1/\sigma_2=1$, Range Separation = 6.5 meters.

clear; there will be a sinusoidal variation for each pair of reflectors on the target.

In Figures 7 and 8, the parameters have been chosen to demonstrate the complex signatures resulting from three reflectors. Possible discrimination algorithms involve using such parameters as number of peaks, peak height ratios, etc. However, the total signature information content is contained in the "spectral content" of the voltage versus frequency plot. It would seem appropriate to obtain the finite (discrete) Fourier transform of the data; then, being wary of possible aliasing, apply classification algorithms to this spectrum.

IV. THE EFFECT OF CHIRP

The analysis of Section II (two-reflectors) is now complicated by the inclusion of a linear FM chirp of 20 MHz applied to each pulse. The instantaneous frequency, f_I , of a given pulse is described by

$$f_I = f + \frac{B}{T} t \quad 0 \leq t \leq T, \quad (13)$$

where f is the nominal frequency for a given frequency step, and B is the chirp bandwidth (20 MHz). The phase of the electric field intensity is then

$$\theta = 2\pi f t + \pi \frac{B}{T} t^2 + \theta_0 \quad (14)$$

For simplicity of analysis, the $t=0$ point is chosen to be when the pulse returned by the nearest reflector reaches the receiver:

$$E_1^r = \frac{\sqrt{\sigma_1} E_0 \cos(2\pi f t + \pi \frac{B}{T} t^2)}{4\pi R_1^2} \quad 0 \leq t \leq T \quad (15)$$

$$E_2^r = \frac{\sqrt{\sigma_2} E_0 \cos[2\pi f(t - \Delta t) + \pi \frac{B}{T} (t - \Delta t)^2]}{4\pi R_2^2} \quad \Delta t \leq t \leq T + \Delta t \quad (16)$$

The amplitude of the square law detected voltage during pulse overlap is

$$V_s = A [\sigma_1 + \sigma_2 \quad (17)$$

$$+ 2 \sqrt{\sigma_1 \sigma_2} \cos \left(\frac{4\pi f \Delta R}{c} - 4\pi B(\Delta R)^2 / c^2 T + \frac{4\pi B}{c} \frac{\Delta R t}{T} \right)].$$

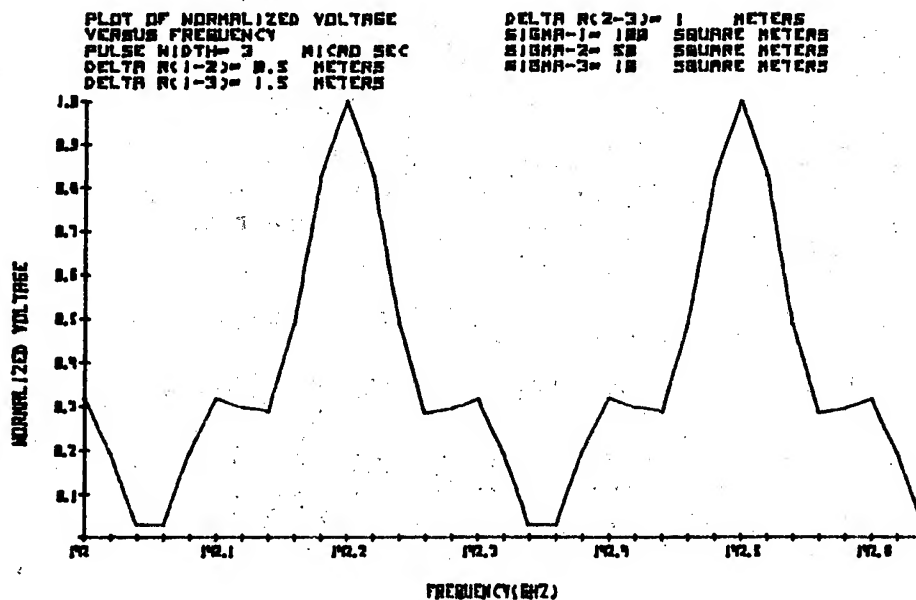


Figure 7. Three Reflector Simulation

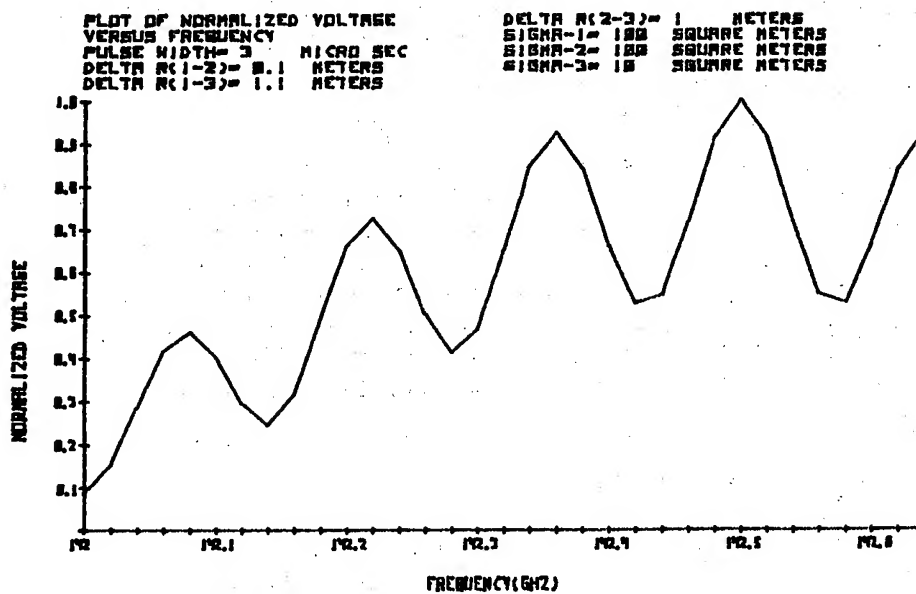


Figure 8. Three Reflector Simulation

ALEXANDER

Examining the phase of the cosine, it is seen that: the first term is the same frequency dependent factor as in Equation (6); the second term is a constant independent of frequency and time; and the third term is a time dependent phase factor which is not a function of frequency.

Using the radar parameters and $\Delta R=5$ meters, the second term gives a phase shift of 0.02 or $(0.004(2\pi))$ radians, which is negligible. Dropping this term and integrating with respect to time over the total pulse gives

$$V = A \left[(\sigma_1 + \sigma_2)T + C 2 \sqrt{\sigma_1 \sigma_2} (T - 2\Delta R/c) \cos\left(\frac{4\pi f \Delta R}{c} + \theta\right) \right] \quad (18)$$

$$C = \left\{ 2 - 2 \cos\left[\frac{4\pi}{c} B \Delta R (1 - 2\Delta R/cT)\right] \right\}^{1/2} / \frac{4\pi}{c} B \Delta R (1 - 2\Delta R/cT) \quad (19)$$

$$\tan \theta = \frac{\cos\left(\frac{4\pi}{c} B \Delta R\right) - \cos\left[8\pi B (\Delta R)^2 / c^2 T\right]}{\sin\left(\frac{4\pi}{c} B \Delta R\right) - \sin\left[8\pi B (\Delta R)^2 / c^2 T\right]} \quad (20)$$

Comparing Equation (18) to Equation (11), one sees that the only differences are the additional phase angle θ and the amplitude factor C , both of which are independent of the nominal frequency. The effect of θ is to merely shift the amplitude versus frequency pattern. The amplitude factor C , however, can be small, resulting in insufficient sinusoidal variations. The amplitude factor is of the form

$$C = \sqrt{2 - 2 \cos x} / x, \quad (21)$$

and the general characteristics of this function are shown in Figure 9. For the radar parameters chosen for this analysis, at $\Delta R=1$ meter, $C=.97$. For $\Delta R=3$ meters, $C=.76$, which results in about a 1dB loss in the sinusoidal variation. The net effect of the chirp is a small reduction in signal variation for large separations between reflectors. Incidentally, the analysis shows that, for typical IMPATT diode characteristics ($B=500$ MHz, assumed linear, $T=50$ ns), the effects of glint due to interference are reduced to less than 25% for reflector separations larger than about 0.3 meter.

V. APPLICABILITY TO REAL TARGETS AND CLUTTER

While this paper is intended primarily to assess the feasibility of preliminary testing with simple targets, it is imperative that the technique be evaluated for real targets and clutter. In the model presented here, manmade targets are characterized by six and eight major reflectors, representing a tank and an armored personnel

ALEXANDER

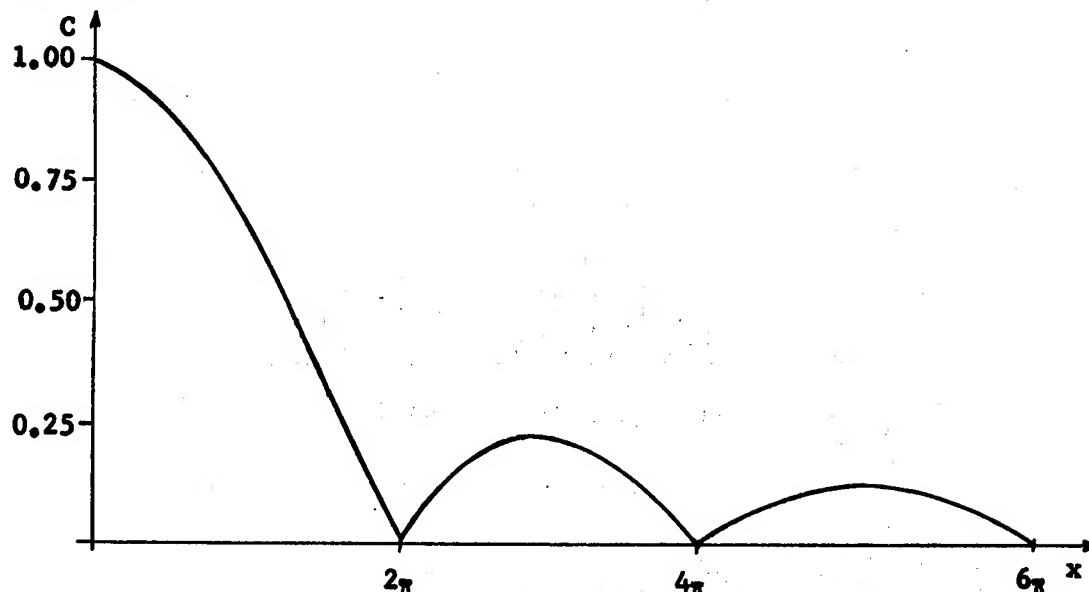


Figure 9. Amplitude Factor for a Chirped Waveform.

carrier respectively. A clutter patch of ten major reflectors representing a tree line is chosen for comparison.

From Equation (12), it is seen that each pair of reflectors provides a contribution to the Fourier transform of the data given by

$$F_{ij} = 2 A \sqrt{\sigma_i \sigma_j} (T - 2\Delta R_{ij}/c) \cos [2\pi (2\Delta R_{ij}/c) f] \quad (22)$$

Thus, assuming infinite resolution in the Fourier transform or "frequency" domain, each pair of reflectors creates a spike of amplitude

$$A_{ij} = 2A \sqrt{\sigma_i \sigma_j} (T - 2\Delta R_{ij}/c) \quad (23)$$

at a "frequency" of

$$f_0 = 2 \Delta R_{ij}/c \quad (24)$$

The number of contributions to the Fourier transform domain increases in an arithmetic series with the number of reflectors, although pairs with equal range separation contribute to the same spike. For n reflectors, there are $\frac{1}{2} n(n-1)$ contributing pairs.

Figure 10 shows the simulated Fourier transform spectra for models of a clutter patch, a tank, and an armored personnel carrier (APC). A 128 sample Fourier transform was used, allowing range

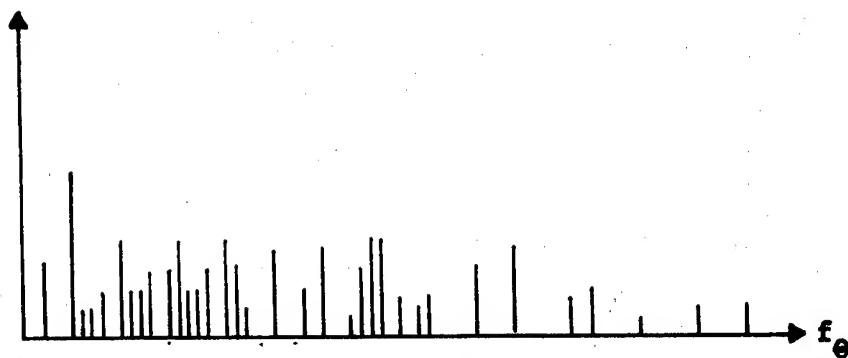


Figure 10a. Clutter Model

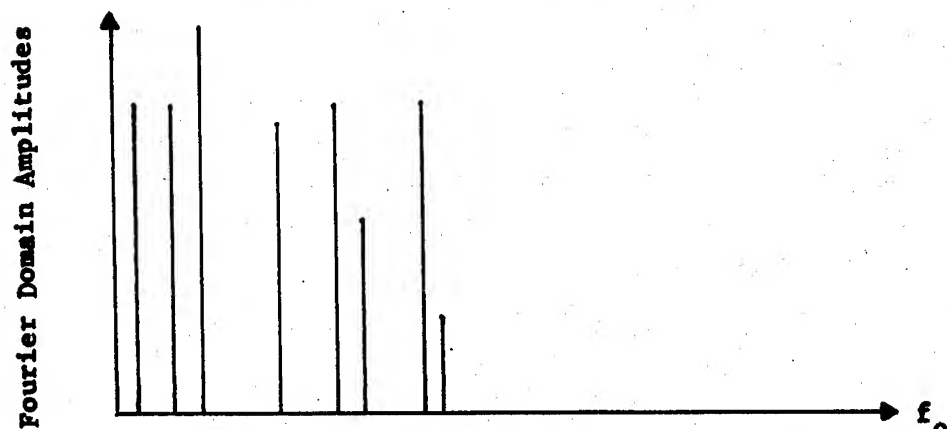


Figure 10b. Tank Model

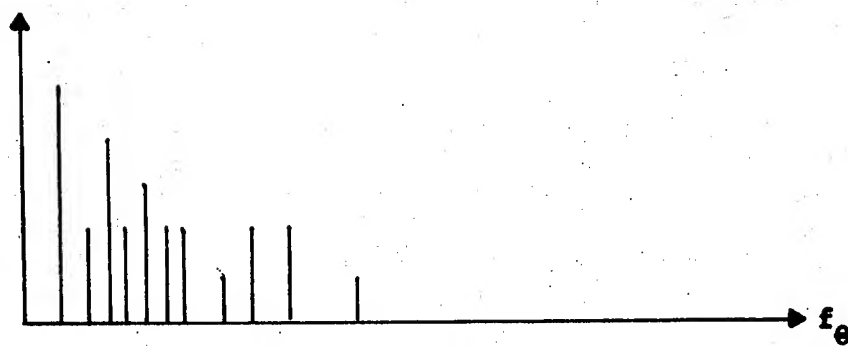


Figure 10c. APC Model

Figure 10. Fourier Domain Simulation.

ALEXANDER

separations up to 15m without aliasing.

For the clutter, the model consisted of a patch of ten trees randomly distributed over a 10 meter deep cell and having radar cross sections of 2, 5, and 10sm. For the tank model, five equally spaced road wheels (10sm) and a turret reflector (100sm) were used. The APC model consisted of six equally spaced road wheels (5sm) and two drive sprockets (2sm, 10sm).

The conclusion drawn from the simulation is that the symmetry and periodicity inherent in manmade targets distinguishes them from random natural clutter and from each other. Clearly, spikes of the same amplitude, spikes whose amplitudes are multiples of others, and uniform spacing between spikes are telltale signs of manmade targets.

VI. CONCLUSIONS

The analysis shows that the frequency diversity (frequency stepping) introduced into radar systems to reduce glint has a potential application to target/clutter discrimination and target classification for stationary targets. At a simplistic level of implementation, an experienced operator looking at the amplitude-frequency pattern could estimate the approximate size of a target. A sophisticated implementation would include microprocessor memory storage of Fourier transforms of target returns at various aspect angles to be automatically compared with the transform of an unknown response. The practical problems of implementation are the choice of diversity bandwidth (within limits) and the choice of frequency step size which will result in statistically significant Fourier components for reasonably large target or target-in-clutter data sets.

With respect to sampling, the analysis shows the desirability of increasing the number of frequency steps to 64 or 128. Using powers of two simplifies the frequency control circuit and allows data processing via the fast Fourier transform. Increasing the number of sampling points improves resolution in the transform "frequency domain" and increases the maximum allowable reflector separation. The smaller beamwidth of the millimeter radar also tends to reduce aliasing possibilities and clutter problems. Results from the three-reflector target model indicate that the most expedient data processing involves taking the discrete Fourier transforms of the amplitude-frequency patterns. Classification algorithms would then be applied to these transform spectra.

ALEXANDER

The result of using a moderately chirped waveform was found to be some signal degradation, particularly at larger reflector separations. This result is not altogether disadvantageous, since ambiguous aliased signals tend to be reduced. However, an increase in frequency steps implies a decrease in step size (fixed diversity bandwidth), and a chirp bandwidth larger than the frequency step will degrade signal resolution. It is recommended that the chirp not be used and that coherent integration of pulses be used to enhance interference effects over other fluctuations which are frequency independent.

As a final note, it should be pointed out that the complications inherent in classifying a moving target using this technique have not been considered. One might suspect, assuming that each reflector has the same radial velocity, that only a constant phase shift in the amplitude-frequency pattern would result. However, the complexities in signal amplitude variations due to target aspect angle changes and due to conical scan or monopulse tracking must also be considered.

REFERENCES:

1. N. Backmark, J. E. V. Krim, and F. Sellberg, "Frequency-agile Radar," Philips Technical Review, Vol. 28, pp. 323-328, 1967.
2. G. Lind, "Reduction of Radar Tracking Errors with Frequency Agility," IEEE Transactions on Aerospace and Electronic Systems, Vol. AES-4, pp. 410-416, May 1968.
3. R. J. Sims and E. R. Graf, "The Reduction of Radar Glint by Diversity Techniques," IEEE Transactions on Antennas and Propagation, Vol. AP-19, pp. 462-468, July 1971.
4. E. K. Reedy, J. L. Eaves, S. O. Piper, W. K. Parks, S. P. Brookshire, R. D. Wetherington, and R. N. Trebits, "Stationary Target Detection and Classification Studies (U)," Georgia Institute of Technology, Report ECOM-76-0961-2, 1978, CONFIDENTIAL.
5. P. M. Alexander and J. L. Brown, "A Preliminary Assessment of Target Classification using Noncoherent Radar Waveforms," US Army Missile Command, Technical Report T-79-80, 1979.
6. L. M. Novak, "Stationary Target Acquisition: Modeling, Prediction and Experimental Results (U)," presented at the 25th Annual Tri-Service Radar Symposium, Monterey, CA, Sept 18-20 1979, CONFIDENTIAL.
7. ———, "ARPA/TTO Program HOWLS (U)", Massachusetts Institute of Technology, Lincoln Laboratory, ESD-TR-79-218, 1979, CONFIDENTIAL.
8. L. M. Novak, "Millimeter Seeker Radar Target Acquisition Studies (U)," Proceedings of the Eighth DARPA/Tri-Service Millimeter Wave Conference, 1979, pp. 469-487, CONFIDENTIAL.

ALLEY

**LOW TEMPERATURE X-RAY DIFFRACTION
INVESTIGATION OF EMBRITTLED MINIMUM SIGNATURE
CHAPARRAL PROPELLANT**

BERNARD J. ALLEY, MR.
PROPULSION DIRECTORATE
US ARMY MISSILE COMMAND
REDSTONE ARSENAL, ALABAMA 35809

The Army has been developing a minimum signature propellant motor for an improved CHAPARRAL air defense weapon system since 1975. As part of validation and qualification, the motor was subjected to a diurnal temperature cycling test during FY78 to simulate field temperature storage conditions. The special cycling test consisted of 30 cycles of 24 hours each from 283°K (50°F) to 347°K (165°F) followed by 30 cycles of 24 hours each from 283°K to 219°K (-65°F). Inspection of smokeless CHAPARRAL motors after 30 cold cycles revealed severe propellant grain cracking that, because of the increased burning surface, could result in catastrophic motor failure upon firing. This type of grain failure, with randomly located cracks, had not previously been found in other minimum signature propellants under development or in conventional double-base propellants used in Army tactical missiles.

Because of the uniqueness and seriousness of the problem, and its potential impact on production of the CHAPARRAL minimum signature propellant motor, an intensive program was initiated jointly by the Army Propulsion Directorate [1] and the propulsion contractor, Hercules Incorporated [2], to determine the cause of the grain failure and solve the problem. A number of possible failure mechanisms were proposed and investigated. The CHAPARRAL propellant involved in the grain failure is comprised of glycerol trinitrate (nitroglycerine) plasticizer; a crosslinked binder of polyglycoladipate, nitrocellulose, and polycaprolactone; a solid oxidizer; and inorganic additives. A primary failure hypothesis was that the nitroglycerine plasticizer or the crosslinked propellant binder was crystallizing during cold temperature cycling, resulting in propellant embrittlement and subsequent grain cracking. The grain, in either event, would inevitably crack because it would not have sufficient strain capability to withstand thermal cycling.

Low temperature x-ray diffraction research on crystallization phenomena in nitrate ester plasticized smokeless propellants and gumstocks was conducted by the Army Propulsion Directorate in support of the CHAPARRAL Project Office. The Propulsion Directorate had previous x-ray diffraction analysis experience with binder crystallization phenomena in other types of propellants that facilitated the CHAPARRAL propellant research. The objective was to determine the possible roles of both nitrate ester, particularly nitroglycerine, and binder low temperature crystallization in CHAPARRAL propellant embrittlement. A number of variables such as moisture content, propellant surface contamination, conditioning temperature, and energetic plasticizer mixtures were investigated for their influence on nitroglycerine crystallization in propellants and gumstocks. The details of the investigation are described in this paper.

The results of the low temperature x-ray diffraction research showed unequivocally that low temperature CHAPARRAL propellant embrittlement is caused by nitroglycerine crystallization. Having established the cause of embrittlement, an alternative propellant, containing a mixed plasticizer of nitroglycerine and 1,2,4-butanetriol trinitrate was developed by Hercules, Incorporated in cooperation with the Army Propulsion Directorate. This alternative minimum signature formulation has undergone extensive low temperature thermal cycling without embrittling, and is expected to replace the original minimum signature propellant formulation in future CHAPARRAL XM121 smokeless motor production.

EXPERIMENTAL

Instrumentation

An x-ray diffractometer marketed by Philips Electronic Instruments was used. Copper $K\alpha$ radiation was produced by a high intensity copper target x-ray tube operated at 35 kV constant potential and 30 mA. The copper $K\beta$ component of the x-ray tube output was reduced with a lithium fluoride monochromator. The copper $K\alpha$ radiation was collimated with a 1° divergence slit. Voltage to the x-ray generator was stabilized with a 5 kVA line voltage stabilizer. The recorder was a Sargent-Welch Model SR. The diffracted copper $K\alpha$ x-ray intensity was measured with a scintillation detector. The associated electronic circuit panel (type 12206/0) has a linear/log rate meter, a decade scaler with an electronic timer, and a pulse height analyzer.

To permit periodic low temperature x-ray diffraction analyses of samples over an extended period of time, a temperature controlled attachment, constructed earlier for binder crystallization studies,

ALLEY

was modified slightly for this application. The design, which is described in detail elsewhere [4], is based on that of Sakurai and Suzuki [5]. Commercially available attachments are not suitable for this application, because they are not designed for the effective transfer of samples at low temperatures. The attachment was insulated with Styrofoam. The copper K α radiation passed through a 180° opening in the attachment chamber that was sealed with two layers of Mylar film separated by an air space. Frost was prevented from collecting on the outer Mylar window by blowing air over its surface. The attachment was connected by means of an insulated tube to a 12-liter Dewar flask containing liquid nitrogen. The temperature within the attachment was capable of being cooled to well below the required 219°K in a short period of time by passing cold nitrogen gas around the sample. The nitrogen gas was generated by applying voltage to a resistor suspended in the liquid nitrogen, by means of a variable transformer. The temperature in the attachment was controlled by manual adjustment of the transformer and read with a digital thermometer. The most important feature of the attachment is that it can be easily disassembled and reassembled at low temperatures for the insertion and removal of samples.

Procedure

All propellant and cured gumstock samples were cut into slices measuring 2.54 cm x 3.81 cm with thicknesses varying from 1.5 - 3 mm. The cured gumstock was composed of all of the propellant ingredients except the solids. Various samples were preconditioned at equilibrium relative humidities of <1%, 20%, 44%, 58%, and 81% for the evaluation of moisture effects on low temperature embrittlement. The equilibrium relative humidity of <1% was achieved by drying with 4A molecular sieve, and the others were achieved by equilibration of the samples in sealed vessels containing appropriate salt solutions. Each sample was placed against an aluminum plate having the same dimensions and the sample and plate were tightly wrapped with aluminum foil. The other wrapped sample surface was then placed against a second aluminum plate. A clamp was placed on each end of the sample so that it was tightly sandwiched between the plates, thus preventing contamination from the sample storage environment. Some samples were thermally cycled from 283°K to 219°K whereas others were stored at constant temperatures of 255°K (0°F), 233°K (-40°F), and 219°K.

Samples were periodically removed from the conditioning boxes and transferred to the x-ray diffractometer on dry ice. The low temperature attachment was precooled to 219°K and then rapidly disassembled and reassembled for sample insertion and analysis. During sample insertion in the attachment, the sample surface collected

a thin film of frost, and the internal temperature of the attachment warmed to approximately 273°K. Upon reassembly, the sample temperature was rapidly cooled to the 219°K test temperature so that no possible nitroglycerine or binder crystallites melted. The thin film of frost on the sample surface rapidly sublimed in the dry nitrogen environment. The mounted sample at 219°K was continuously scanned at 2° per minute, generally over the range of 10-40° 2 θ with a rate meter time constant of 1 or 2 seconds and a full scale recorder sensitivity of 1000-2000 counts/second.

RESULTS AND DISCUSSION

Temperature and Moisture Effects

Propellant and gumstock samples were temperature cycled daily from 283°K to 219°K to duplicate the condition under which minimum signature propellant in CHAPARRAL motors embrittled. The samples were also equilibrated to different moisture levels because previous surveillance data indicated a possible dependence of propellant embrittlement on moisture content. The primary purpose of constant temperature storage at 219°K, 233°K, and 255°K was to insure that any binder crystallization that might occur would be detected. Thermal cycling to 283°K would likely melt binder crystallites, based on previous experience [3]. Also, different constant storage temperatures would provide valuable information on nitroglycerine crystallization initiation and propagation rates. The crystallization of nitroglycerine is a two step process involving initiation (nucleation) and propagation (crystal growth). If either step is prevented, the propellant will not embrittle. Initiation can occur homogeneously within the nitroglycerine itself or heterogeneously by external nucleating materials. Both types of nucleation were considered.

The baseline x-ray diffraction pattern of amorphous CHAPARRAL propellant gumstock at 219°K is shown in Figure 1. Only weak diffraction peaks from ice on the sample surface are evident for crystalline material. In contrast to the amorphous gumstock diffraction pattern, the pattern for crystallized nitroglycerine in gumstock is shown in Figure 2. The two largest peaks were recorded off-scale to bring out the weaker peaks in the pattern. The interplanar d-spacing in angstroms of each peak is noted by the peak. The intensities of the second and third largest peaks relative to the most intense peak (I/I_1) are also noted on the pattern. This particular sample had been cycled between 283°K and 219°K for 36 days. Typically, the average induction time for the initiation of nitroglycerine crystallization during this temperature cycle was found to be about 30 days, but the actual time varied substantially.

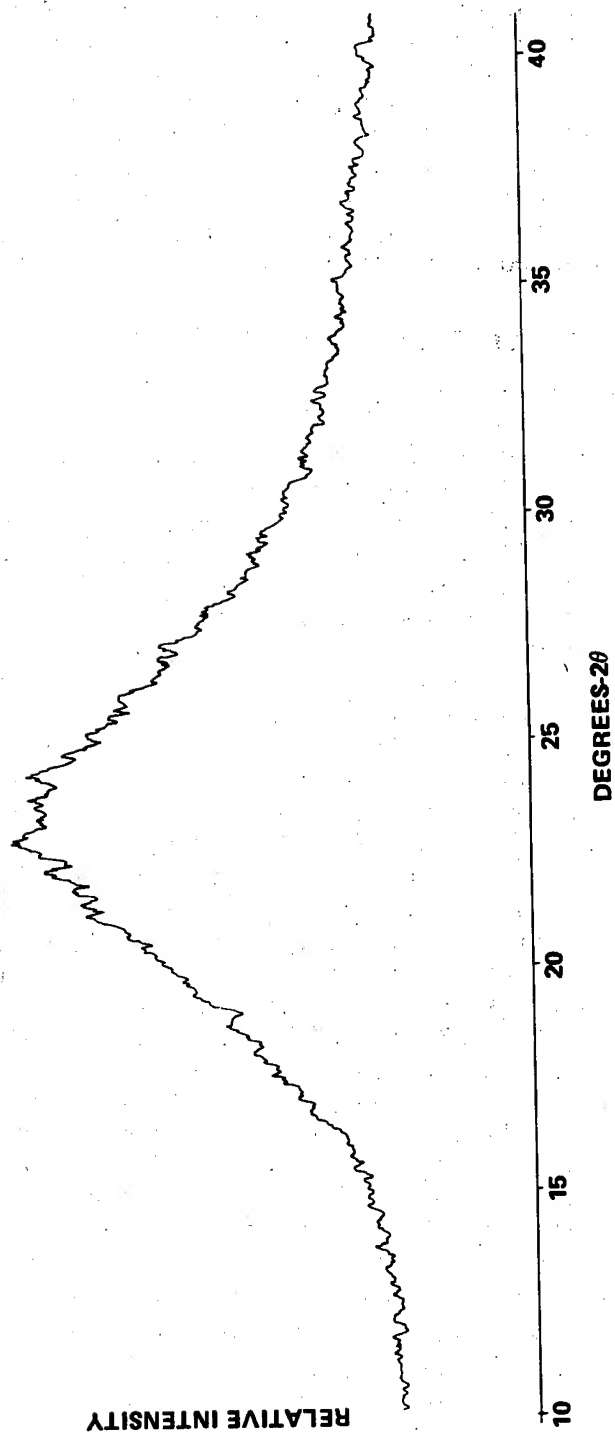


Figure 1. X-ray diffraction pattern of amorphous CHAPARRAL propellant gumstock at 219°K (-65°F).

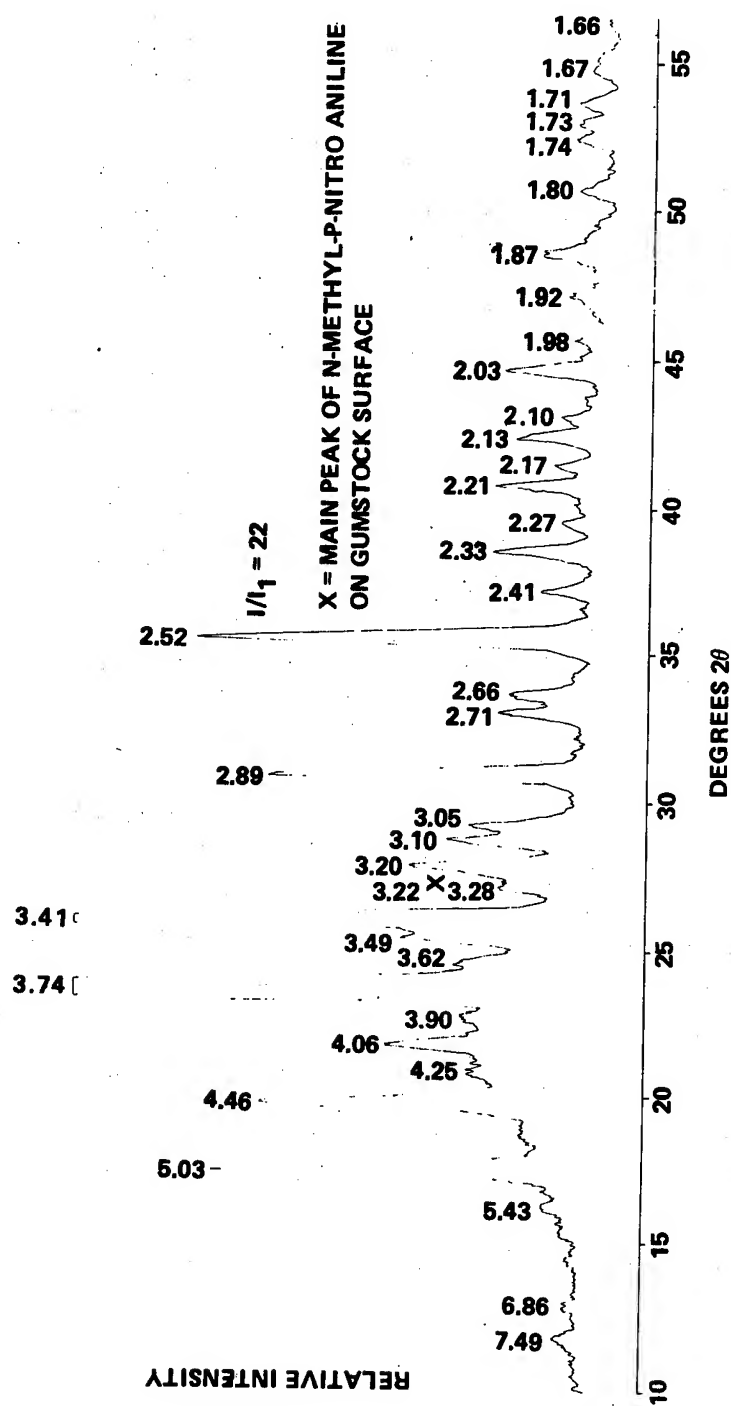


Figure 2. X-ray diffraction pattern of crystallized nitroglycerine (stable form) in embrittled CHAPARRAL propellant gumstock.

When the diffraction pattern shown in Figure 2 was first observed, it was clear that a large amount of crystalline material had formed and that it was most likely nitroglycerine. An immediate identification from the pattern could not be made, however, because x-ray diffraction data on crystallized nitroglycerine is not available in the literature. Consequently, a neat sample of the nitroglycerine was crystallized at 244°K (-20°F), by seeding with a portion of the embrittled gumstock, and analyzed. Except for unavoidable preferred orientation of crystallites in the neat nitroglycerine, the pattern agreed with that in Figure 2 and thus confirmed that the nitroglycerine in the gumstock had crystallized. That the embrittled gumstock seeded the neat nitroglycerine crystallization is evidence itself that the nitroglycerine had crystallized in the gumstock during thermal cycling.

Neat nitroglycerine when cooled is viscous and readily supercools, and therefore is very difficult to crystallize without seeding. This might account at least partially for the long induction period for nitroglycerine nucleation. Once nucleation occurs, however, crystal growth is rapid during thermal cycling. The optimum temperature regions for both nucleation (219°K-233°K) and crystal growth rates (244°K-250°K) were included in each temperature cycle.

The x-ray diffraction pattern in Figure 2 is that for the stable form of nitroglycerine that melts at about 286°K. The x-ray diffraction pattern of embrittled CHAPARRAL propellant that was also cycled between 219°K and 283°K for 36 days is shown in Figure 3. The peaks of crystallized nitroglycerine are superimposed on those of the propellant crystalline solids, but are clearly discernible. This data showed conclusively that CHAPARRAL propellant embrittlement is due primarily to nitroglycerine crystallization at low temperature.

The effect of propellant and gumstock moisture content on the time required for nitroglycerine to crystallize during temperature cycling from 219°K to 283°K is given in Table 1. The time for crystallization or the induction period definitely increases as the moisture content decreases. In fact, samples that were predried over molecular sieve 4A (< 1%) did not embrittle when stored for the maximum test time of 8.1 months. This suggests that the propellant embrittlement problem might be solved by insuring that propellant in CHAPARRAL motors is initially dry and maintained dry during storage. This is not considered a practical solution because of the low moisture levels required, and the fact that heterogeneous nucleation could still possibly occur from extraneous material such as dust. The sample in this investigation was protected from the environment. If nucleation occurs, then crystal growth will proceed rapidly. A better solution would be to assume that nucleation will occur and to significantly reduce subsequent growth by kinetic means. This is the approach

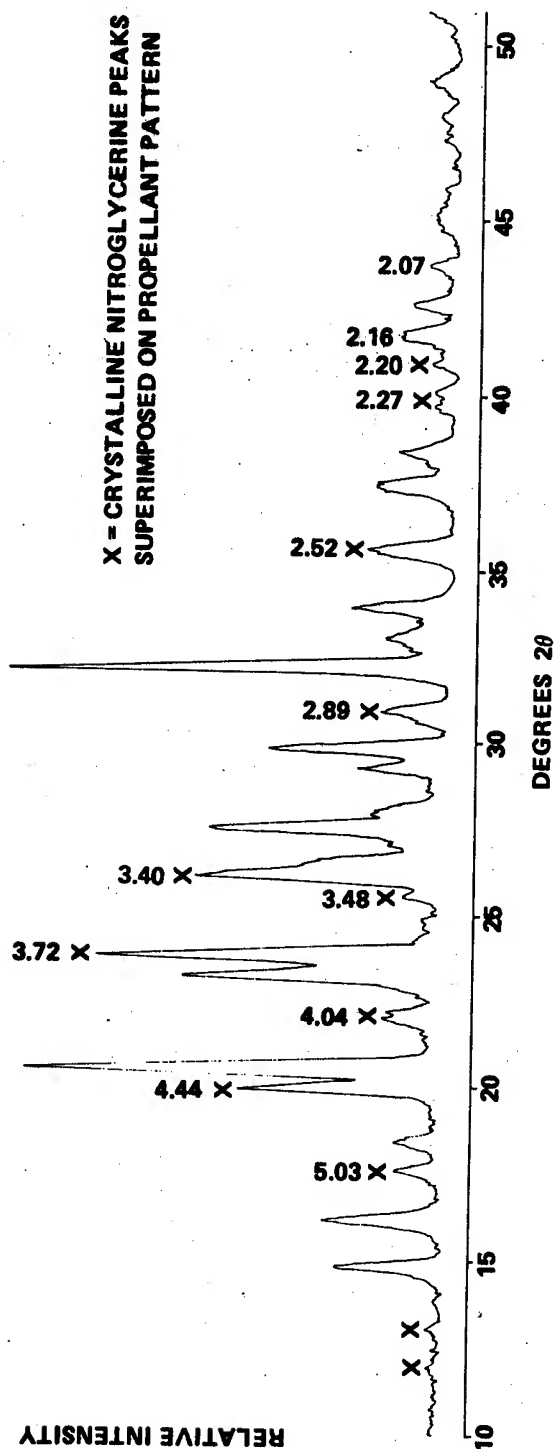


Figure 3. X-ray diffraction pattern of embrittled CHAPARRAL propellant showing crystalline nitroglycerine peaks.

TABLE 1. EFFECT OF MOISTURE ON CHAPARRAL PROPELLANT AND GUMSTOCK NITROGLYCERINE CRYSTALLIZATION (TEMPERATURE CYCLED DAILY FROM 283°K TO 219°K)

Sample Equilibrium Relative Humidity, %	Moisture Content, Wt %		Months for Nitroglycerine Crystallization	
	Gumstock	Propellant	Gumstock	Propellant
* <1	<0.005	<0.002	>8.1	>8.1
20	0.120	0.049	4.2	3.3
44	0.265	0.108	3.1	2.7
58	0.350	0.143	3.3	2.3
81	0.488	0.199	1.5	1.5

* Samples dried over 4A molecular sieve desiccant.

usually used [2] to solve the crystallization problem. Nevertheless, as a result of these and other data, stricter moisture controls were instituted during propellant and motor manufacture and motor storage.

The role of moisture in CHAPARRAL propellant embrittlement was not clearly established, but it appears that ice crystals forming within the propellant might act as sites for heterogeneous nitroglycerine nucleation. The induction period for the formation of internal ice crystals, which was readily detected by the x-ray diffraction analysis, generally preceded nitroglycerine crystallization by a short period of time.

The effect of constant temperature storage on the time for nitroglycerine crystallization to occur in propellants and gumstocks is shown in Table 2. At 219°K no crystallization occurred up to the maximum test period of 4.2 months. As expected, the times for crystallization at 233°K and 255°K were longer than for samples of the same moisture content that were temperature cycled. The stable form of nitroglycerine was formed at 255°K (see Figure 2) whereas what is believed to be the labile form was initially observed at 233°K. The labile form slowly converted to the stable form after 1 to 2 months

ALLEY

storage. The x-ray diffraction pattern of a propellant lacquer sample seeded with a portion of gumstock sample embrittled at 233°K (see Figure 4) illustrates the labile nitroglycerine form. Only the 4.17A peak is easily discernible in embrittled propellant. Lacquer is similar to gumstock, but is not crosslinked.

TABLE 2. EFFECT OF CONSTANT TEMPERATURE STORAGE ON NITROGLYCERINE CRYSTALLIZATION IN CHAPARRAL PROPELLANT AND GUMSTOCK

Storage Temperature, °K	Equilibrium Relative Humidity, %	Months for Nitroglycerine Crystallization	
		Propellant	Gumstock
255 (0°F)	81	---	3.6
233 (-40°F)	81	2.4	2.9
233 (-40°F)	44	>3.2	---
219 (-65°F)	81	>4.2	>4.2

Special Investigations

A number of special investigations were conducted to further elucidate the mechanism of nitroglycerine crystallization and subsequent propellant embrittlement. A summary of propellant and gumstock samples with various plasticizer and polymer combinations is given in Table 3. Polyglycoladipate polymeric binder, which is used in CHAPARRAL propellant, was not found to crystallize during either temperature cycling or constant temperature storage. A candidate polyethyleneglycol binder, however, did crystallize to a large extent in gumstock, but no evidence of crystallization could be found in propellants.

During previous thermal cycling, N-methyl-p-nitroaniline (MNA), a propellant ingredient, was observed to form on gumstock surfaces. The rate of formation and the amount formed was proportional to the sample moisture content. The MNA did not form on samples stored at constant temperature. It was suspected that MNA might initiate nitroglycerine crystallization on the sample surface. Three types of samples were analyzed for the influence of MNA: a) normal gumstock samples, b) gumstock samples with MNA omitted from the formulation, and c) gumstock samples with additional MNA added to the

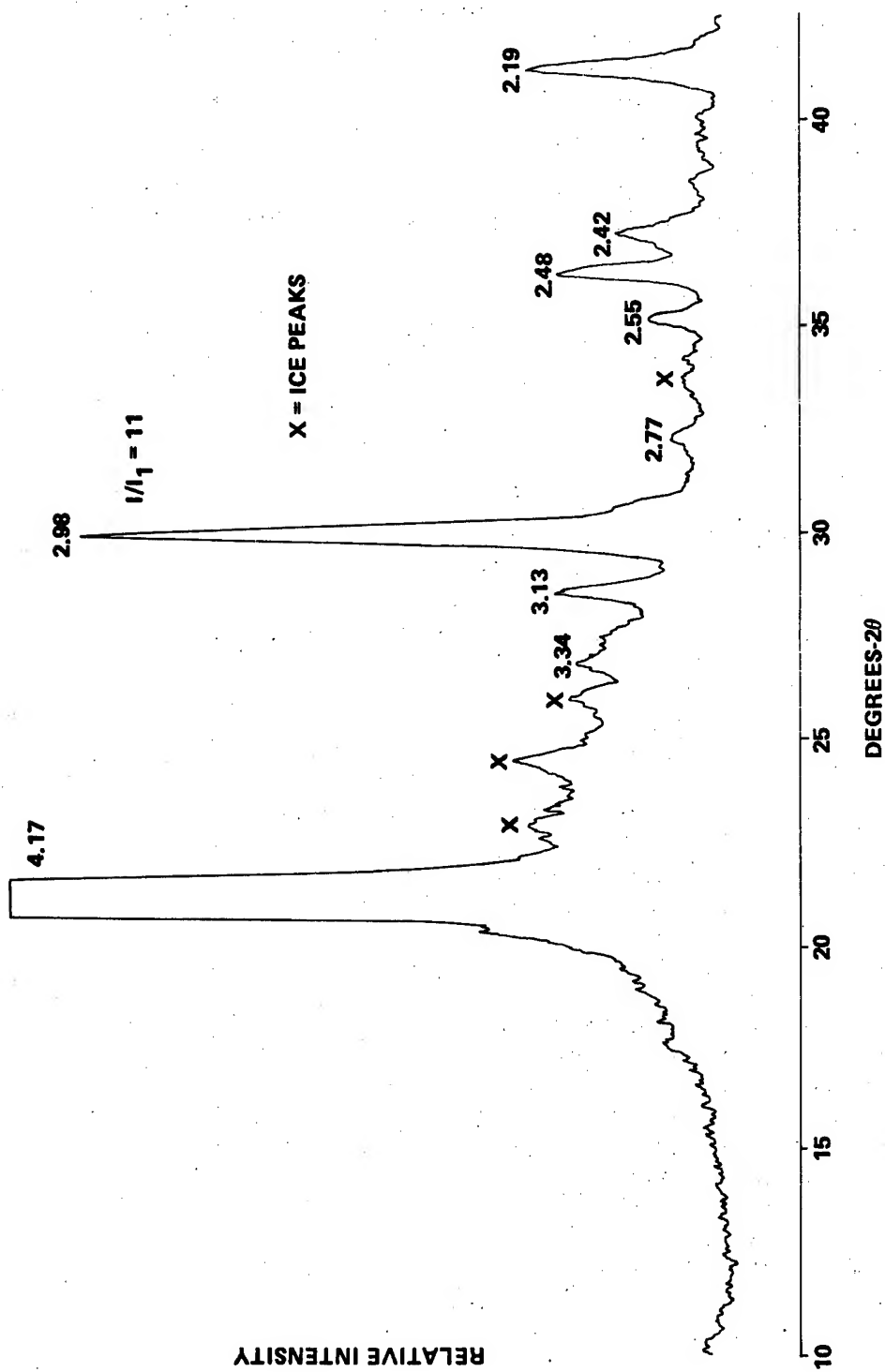


Figure 4. X-ray diffraction pattern of crystallized nitroglycerine (labile form) in CHAPARRAL propellant lacquer.

ALLEY

TABLE 3. PLASTICIZER/POLYMER COMBINATIONS INVESTIGATED IN CHAPARRAL CANDIDATE PROPELLANT AND GUMSTOCK FORMULATIONS

<u>Polymer</u>	<u>^aPlasticizer</u>	<u>Type Sample</u>	<u>Low Temperature Crystallization</u>	
			<u>Plasticizer</u>	<u>Polymer</u>
Polyglycol-adipate	NG	Propellant	Yes	No
	NG	Gumstock	Yes	No
	None	Gumstock	Yes	No
	NG	Gumstock (No PCP)	Yes	No
	NG	Gumstock (No MNA)	Yes	No
	NG	Gumstock (MNA added to Surface)	Yes	No
	NG + BTTN	Gumstock	No	No
Polyethylene-Glycol	TMETN	Propellant	Yes	No
	TMETN + DEGDN	Propellant	No	No
	TMETN + DEGDN	Gumstock	No	Yes
	TMETN + BTTN	Propellant	No	No
	BTTN + TMETN + DEGDN	Propellant	No	No

^aPlasticizer mixtures were equal weight proportions

NG = Nitroglycerine
PCP = Polycaprolactone
MNA = N-methyl-p-nitroaniline
BTTN = 1,2,4-Butanetriol Trinitrate
TMETN = Trimethylolethane Trinitrate
DEGDN = Diethylene Glycol Dinitrate

surface. These samples were investigated as a function of moisture content during temperature cycling from 219°K to 283°K. The results showed that MNA in the presence of moisture significantly reduced the induction time for nitroglycerine crystallization over that for moisture alone, but it was not a primary causative factor for propellant embrittlement.

Nitroglycerine crystallization can be initiated both homogeneously and heterogeneously by extraneous materials, and the subsequent crystal growth rate is rapid. Consequently, the only

practical solution to the embrittlement problem was to change the plasticizer composition to one that either could not be crystallized thermodynamically, or to one that upon initiation would have a negligible crystal growth rate. The latter approach, using a plasticizer mixture of nitroglycerine and 1,2,4-butanetriol trinitrate in a 1:1 weight ratio, was chosen. The thermodynamic solution was not possible, because the freezing points of acceptable pure plasticizers and plasticizer mixtures are above the lower temperature limit for the CHAPARRAL motor. The six plasticizer mixtures shown in Table 3 were evaluated for their crystallization properties during 219°K to 283°K cycling and constant storage at 233°K. No plasticizer crystallization was found in these mixtures after extensive temperature conditioning even when the samples contained a high percentage of moisture.

CONCLUSIONS

The x-ray diffraction research demonstrated unequivocally that low temperature embrittlement of the original minimum signature CHAPARRAL propellant was caused by crystallization of the nitroglycerine plasticizer. The exact mechanism of nitroglycerine crystallization was not established, but several parameters that influence the rate of initiation or nucleation of nitroglycerine were identified. Propellant moisture in particular increases the rate of initiation in proportion to the moisture content. A propellant component, N-methyl-p-nitroaniline, which forms on the propellant surface, further decreases the time to initiation in the presence of moisture. The propellant binder, which was initially suspect, shows no evidence of crystallization at low temperature.

Low temperature x-ray diffraction analyses of plasticizer mixtures that did not crystallize upon extended low temperature storage demonstrated the feasibility of this approach for solving the embrittlement problem. A modified minimum signature CHAPARRAL propellant, containing a mixed plasticizer of nitroglycerine and 1,2,4-butanetriol trinitrate, is undergoing requalification and has successfully withstood extensive low temperature cycling without embrittlement.

The x-ray diffraction research is significant because it established the cause of the embrittlement problem and evaluated selected approaches for solution of the problem, thus enabling a confident, rapid solution without seriously impacting CHAPARRAL XM121 motor production. Furthermore, fundamental data on low temperature propellant crystallization phenomena were obtained that will enhance future minimum signature propellant development programs.

ALLEY

REFERENCES

1. Palm, E. J., "CHAPARRAL Smokeless Motor Special Investigation," 1979 JANNAF Propulsion Meeting, CPA publication No. 300, Vol. IV, August 1979, p. 413.
2. Comfort, T. F. and Herriott, G. E., "Development of Propellant for the Smokeless CHAPARRAL Rocket Motor," 1980 JANNAF Propulsion Meeting (in press).
3. Alley, B. J. and Higgins J. H., "X-Ray Diffraction Investigation of Propellant Gumstocks at Low Temperatures," US Army Missile Command, Report No. RK-TR-63-5, February 1963.
4. Alley, B. J., "X-Ray Diffraction Studies of Crystallinity in Propellant Gumstocks," Quarterly Progress Report 1 July to 30 September 1961, Propulsion Laboratory, ARGMA Report No. TR-2L1R-9, September 1961, pp. 14-20.
5. Sakurai, T. and Suzuki, T., "A Low Temperature Attachment for the Norelco X-Ray Diffractometer, Norelco Reporter, Vol. VI, No. 6, Nov-Dec 1959, pp. 122-128.

*Alster, Slagg, Dewar, Ritchie, & Wells

A REACTION MECHANISM IN THE SHOCK INITIATION OF
DETONATION. A THEORETICAL STUDY. (U)

*JACK ALSTER, DR., NORMAN SLAGG, DR.
ARRADCOM, DOVER, NJ 07801

MICHAEL J.S. DEWAR, DR., JAMES P. RITCHIE, MR.
UNIVERSITY OF TEXAS, AUSTIN, TEXAS 78712

CHARLES WELLS, DR.
JUDSON COLLEGE, MARION, ALABAMA 36756

INTRODUCTION: In a chain explosion, the initial chemical reaction follows one or more modes of reaction (1,2). The ensuing highly reactive transient species, commonly believed to be radicals, react with intact explosive molecules to produce more radicals which ultimately recombine and release energy sufficient to support a detonation wave. To achieve better control over the detonation process it is important to know the rate of the relatively slow, primary reaction step and the nature of the transient species produced in this step. When, in particular, a condensed explosive experiences the high dynamic pressure of a strong, initiating shock wave, it may initially decompose via a bimolecular rather than a more commonly accepted unimolecular process. The present study was undertaken to examine this question in relation to the primary reaction step in liquid methyl nitrate undergoing shock initiation of detonation. In particular, the physical and chemical effects of the incident shock on the molecules are viewed in terms of the following three plausible modes of reaction:

1. Compression of a single molecule along its weakest bond, followed by scission of this bond as the molecule relaxes,
2. curling of fuel and oxidizer ends of the molecule towards each other followed by an intramolecular abstraction reaction, and
3. squeezing together of a pair of neighboring molecules such that the fuel end of one molecule reacts with the oxidizer end of the other.

*Alster, Slagg, Dewar, Ritchie, & Wells

Methyl nitrate was chosen as the first of a series of explosives since the $\text{H}_3\text{CO} - \text{NO}_2$ bond is considerably weaker than the other bonds in the molecule. Hence, a theoretical treatment should yield more dramatic effects for this molecule than for a molecule which has a narrower distribution of bond energies. Moreover, methyl nitrate is a simple prototype of alkyl nitrate explosives such as nitroglycerine and pentaerythritol tetranitrate.

THEORETICAL PROCEDURES: The quantum chemical Modified Intermediate Neglect of Differential Overlap (MINDO/3) method (3) was employed. As a semi-empirical, self-consistent field molecular orbital treatment, it was parametrized by Dewar to yield equilibrium geometries and heats of formation for a wide variety of closed shell systems, including CHNO-molecules, giving good agreement with experiment (4). The parametrization apparently simulates the actual electric fields due to electrons and nuclei in stable, closed shell molecules. Thus, Dewar and coworkers predicted heats of formation with a mean absolute error of 5 kcal/mole. Equilibrium geometries are also satisfactory as bond lengths, bond angles and dihedral angles are given with mean absolute errors of .02Å, 6°, and 6° respectively. Although MINDO/3 was parametrized for just these equilibrium properties, it also predicts the activation energy for a variety of reactions involving complex organic molecules with a mean absolute error of 5 kcal/mole (5,6). It is, therefore, more than just a curve fitting technique as is also demonstrated by its ability to predict a variety of other molecular properties (5) that depend on the valence shell electron distribution.

MINDO/3 is used to calculate first the equilibrium geometry of the methyl nitrate molecule and then three minimum energy reaction paths (MERPs) (5,6) corresponding to the aforementioned three modes of reaction. Finally, values of the volume-, entropy-, and energy-of activation derived from the MERP are inserted into the absolute rate theory equation to yield the specific rate constant for a given reaction path at a given temperature and pressure. Of course, the most likely path to be followed under the given conditions will be the one with the highest rate constant.

GEOMETRY OF THE ISOLATED MOLECULE: Since the starting point for a chemical reaction is the equilibrium conformation of the molecule, its geometry is calculated first. A complete optimization of all bond distances, bond- and dihedral-angles was carried out. Figure 1 gives the overall shape of the molecule. The heavy atoms and one hydrogen atom H_1 are in the plane of the paper whereas the hydrogens H_a and H_b are above and below the plane, respectively. The staggered arrangement of the hydrogen atoms is correctly predicted.

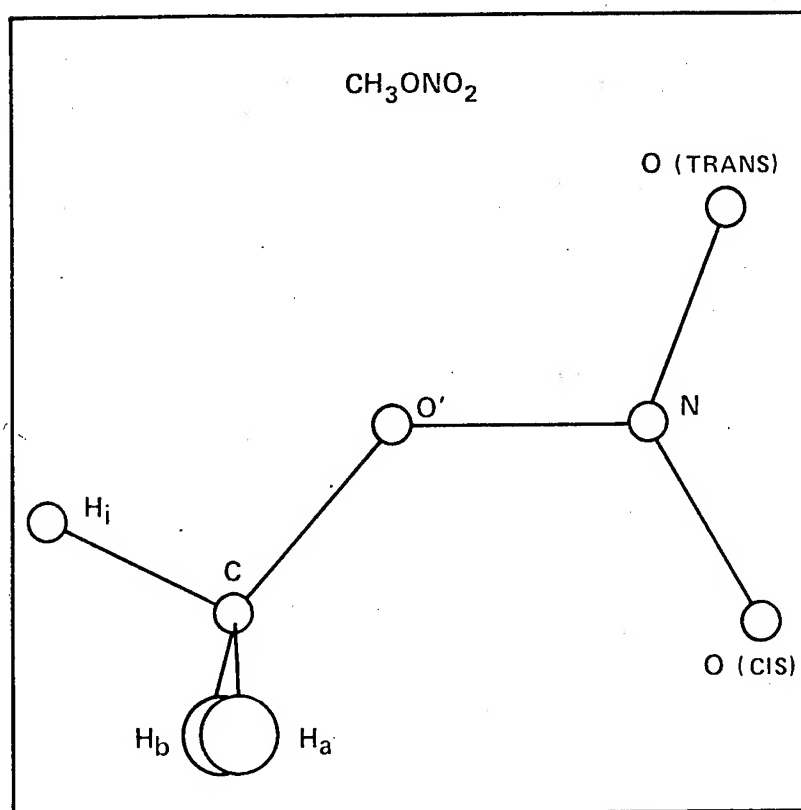


Figure 1. Calculated Shape of Methyl Nitrate Molecule

*Alster, Slagg, Dewar, Ritchie, & Wells

Moreover, calculated values for six bond distances and six bond angles agree with experimental values (obtained by microwave spectral measurements (7)) within mean absolute errors of 0.03Å and 5°, respectively. The heat of formation calculated for the equilibrium structure is -28.3 kcal/mole which also agrees well with the experimental value of -29.1 kcal/mole (8).

PROCEDURE FOR CALCULATING MERPS: In the course of generating the MERP beginning with the equilibrium geometry of the stable molecule, one encounters an uphill curve of total energy versus reaction variable. Here, we take for the variable either an interatomic distance or a bond angle. (For each chosen value of the reaction variable, the remaining molecular parameters are optimized to yield the lowest energy for that value of the reaction variable.) Eventually, a maximum is attained which, when compared to the initial energy, yields the activation energy for the assumed process.

The distorted molecular system corresponding to the energy maximum is known as the transition state or activated complex. Since the maximum is a saddle point, all energy gradients with respect to the molecular variables must vanish (9). This criterion is used to find the exact location of the transition state. Moreover, from the gradients at the extremum, second derivatives are calculated which represent the theoretical force constants. Since the transition state is stable to deformations along all coordinates other than the reaction coordinate, it has one and only one negative force constant. Thus, one can establish that the extremum corresponds to a transition state rather than a stable intermediate in which case all force constants are positive. In addition, a normal coordinate analysis is carried out on the transition state using the theoretical force constants as input. From the resulting set of normal modes of vibration, the vibration along the transition vector is selected for examination. In particular, it is determined whether the transition state indeed corresponds to the assumed reaction path and thus leads to the formation of the intended reaction products. Finally, after the transition state is located and characterized, all molecular parameters are optimized to yield final geometries and heats of formation of the reaction products.

UNIMOLECULAR REACTION PATHS

Scission of the Weakest Bond: Since $\text{H}_3\text{CO} - \text{NO}_2$ is the weakest bond in the molecule, a MERP corresponding to stretching this bond has been calculated. Table 1 gives heats of formation, H_f , of the equilibrium and transition states of the molecule and the activation energy, ΔE^\ddagger , derived from the difference in H_f values.

Table 1. Properties of three plausible reaction paths of methyl nitrate

Species	Reaction type, R	H _F (kcal/mole)	ΔE [‡] (kcal/mole)	ΔH _R (kcal/mole)
		<u>calc</u> <u>obs.</u>	<u>calc</u> <u>obs.</u>	<u>calc</u> <u>obs.</u>
Menitr*				
[H ₃ CO -- NO ₂] [‡]		-28. -29.		
		6.		
	Bond scission:		34. 40	34. 40.
Menitr		-28. -29.		
<div>$\left[\begin{array}{c} \text{H} \\ \diagup \\ \text{O} \text{---} \text{N} \text{=O} \\ \quad \\ \text{H}_2\text{C} \text{---} \text{O} \end{array} \right]^{\#}$</div>		28.		
H ₂ CO		-26. -26.		
HONO		-14. -19.		
	Intramol. H-Abstr:		56.	-11. -16.
Menitr . Menitr		-57.		
[Menitr . Menitr] [‡]		-24.		
CH ₃ ONO		-14. -15.		
(OH)H ₂ CO NO ₂		-73. -71.**		
	Bimol. O-Insert:		33.	-31.
**				
Menitr ≡ methyl nitrate Obtained via additivity rules.				

The latter agrees reasonably well with the observed quantity. Figure 2 is a graphical representation of the MERP describing stretching of this bond to the point of scission. Finally, Figure 3 describes the geometry of the transition state and the transition vector, the arrows representing the amplitudes and directions of motion of the atoms in the normal coordinate corresponding to reaction. The methoxy oxygen-nitrogen bond ($O'-N$) is stretched by $\sim 0.5\text{\AA}$ from its original bond distance value of 1.4\AA whereas all the other molecular parameters remain essentially unchanged.

Intramolecular Hydrogen Abstraction Reaction: The molecule is imagined to curl up, bringing a hydrogen atom into the vicinity of a terminal oxygen atom. The geometry of the transition state and the transition vector are depicted in Figure 4. The transition state is fully planar except for the non-ring hydrogens. Major changes in geometry which have occurred relative to the initial equilibrium conformation of Figure 1 are: $C-H_1$ and $O'-N$ bond distances have stretched by .25 and .2 \AA , respectively, the $O_{cis} - H$ distance has shrunk by $\sim 1.5\text{\AA}$ and the $CO'N$ and $O'NO$ bond angles have collapsed by $\sim 27^\circ$ and 10° , respectively. The directions and magnitudes of the arrows in Figure 4 help visualize the manner in which planar H_2CO and trans-HONO are formed. The energetics of this reaction process are given in Table 1. The heats of formation of reactant and product molecules and the resulting exothermic heat of reaction ΔH_p are predicted with reasonable accuracy. Moreover, ΔE^\ddagger is ~ 20 kcal/mole higher than that of the unimolecular bond scission process.

BIMOLECULAR REACTION PATH: In this reaction path two molecules of methyl nitrate are brought together in such a way that the methyl group of one molecule interacts with the nitrate group of the other, as shown in Figure 5. In fact, the figure represents the transition state in which reaction is imminent. The arrows on the atoms in the reaction site suggest insertion of an oxygen atom into the $C-H_1$ bond in the plane of the heavy atoms. Thus, methyl nitrite and hydroxymethyl nitrate are predicted as products. Although the latter molecule is not known, it appears to have some thermodynamic stability as is illustrated by its very negative heat of formation. According to Table 1, the reaction requires an activation energy of 32 kcal/mole which is comparable to that of the unimolecular bond scission process. Moreover, the reaction is exothermic by ~ 31 kcal/mole. Hence, the molecules could act as energy carriers in a reaction sequence leading to detonation.

CALCULATION OF REACTION RATES: Assuming that thermal equilibrium exists between the transition state and the stable

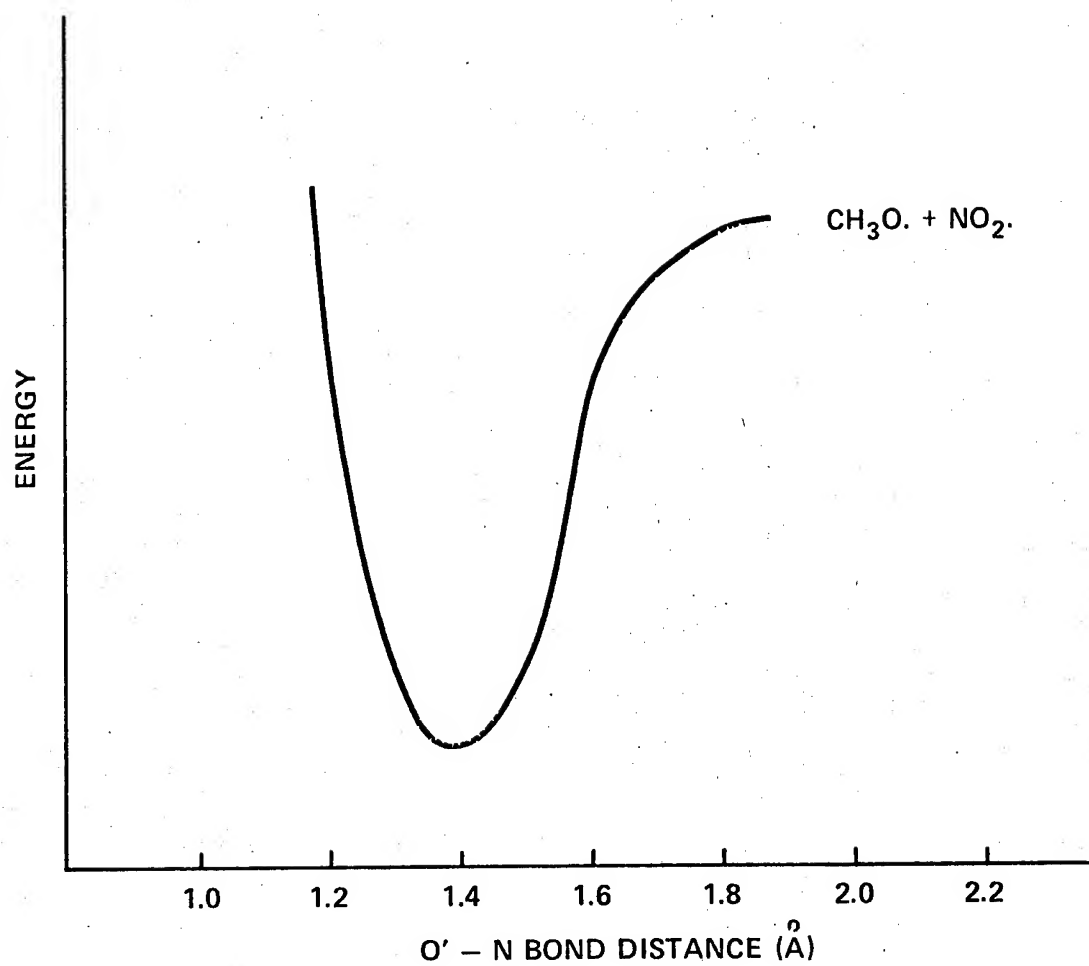


Figure 2. MERP of the Bond Scission Reaction in Methyl Nitrate

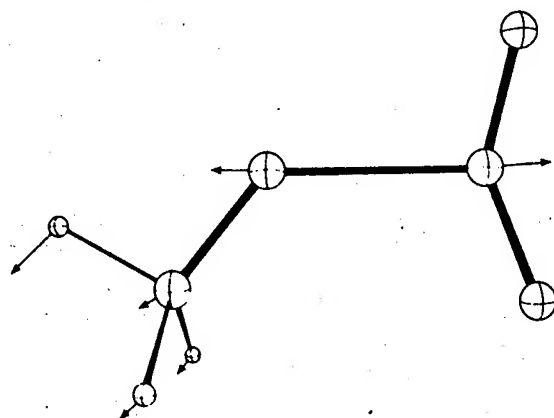


Figure 3. Shape and Transition Vector of the Bond Scission Transition State of Methyl Nitrate

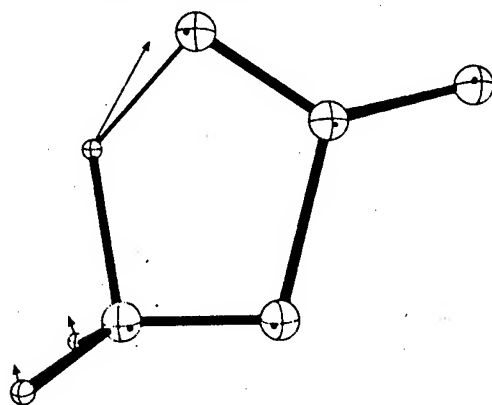


Figure 4. Shape and Transition Vector of the Cyclic Transition State of Methyl Nitrate

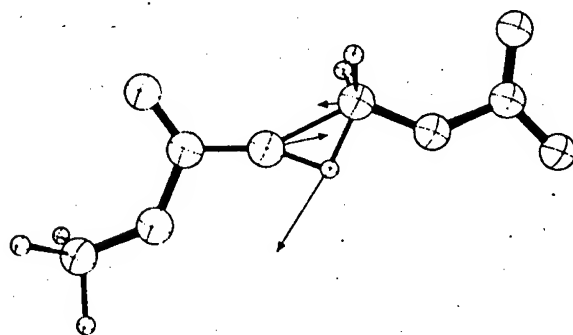


Figure 5. Shape and Transition Vector of the Bimolecular Transition State of Methyl Nitrate

*Alster, Slagg, Dewar, Ritchie, & Wells

molecule, the specific reaction rate constant is given by the following thermodynamic formulation of transition state theory:

$$k = \frac{KT}{h} \cdot \exp\left(\frac{-P\Delta V^\ddagger}{RT}\right) \cdot \exp\left(\frac{\Delta S^\ddagger}{R}\right) \cdot \exp\left(\frac{-\Delta E^\ddagger}{RT}\right) \quad (1)$$

where ΔS^\ddagger , ΔV^\ddagger , and ΔE^\ddagger are entropies-, volumes-, and energies-of-activation, respectively. In order to assess the relative importance of different reaction paths, we must evaluate or, at least, estimate these quantities for each path. The MERPs have been analyzed, in fact, to provide values for these quantities. In particular, ΔV^\ddagger and the rotational contribution to ΔS^\ddagger are obtained from the calculated geometries of the stable methyl nitrate molecule and the different transition states. Moreover, the vibrational contribution to ΔS^\ddagger is derived from the vibrational frequencies generated by a normal coordinate analysis. Finally, ΔS^\ddagger is obtained as the sum of these contributions and that of translation, the latter being readily calculated from the molecular weights of the reactant and transition state species (10). This procedure gives good agreement between calculated values of the volume and entropy of the stable methyl nitrate molecule at 298K and 1 atm viz. 115\AA^3 and 74.5 eu, respectively and the corresponding values derived from experiment viz. 106\AA^3 and 75.9 eu (11,12).

Since Equation 1 interrelates a vast body of chemical kinetic information on reactions in both gas- and condensed-phases (13), we apply it to the case at hand which is shock initiation of liquid methyl nitrate. Low- and high- velocity detonations have been measured in liquid methyl nitrate (14). However, the pressure and temperature conditions associated with the initiating shock were not determined. We, therefore, estimated a typical set of values for liquid methyl nitrate based on (1) a measurement by Campbell et al. (15) of the pressure and associated temperature of an initiating shock wave in liquid nitromethane and (2) measurements by Shaw (16) on pressures and corresponding reaction times for initiating shocks in nitromethane and methyl nitrite liquids. The values thus estimated for liquid methyl nitrate are 60 kbars and 800K.

To make proper use of Equation 1, values of the activation parameters ΔV^\ddagger , ΔS^\ddagger , and ΔE^\ddagger should correspond to the elevated temperature and pressure associated with the initiating shock wave. Therefore, ΔS^\ddagger and ΔE^\ddagger were calculated for 800K via the use of statistical thermodynamic relations involving partition functions but ΔV^\ddagger which had been calculated for 298K is assumed to be constant over the temperature range 298-800K. As for the pressure dependence

of these properties experimental evidence in the literature (17,18) indicates that for several unimolecular and bimolecular reactions carried out in the pressure range .001-60 kbars, their combined effect on specific rate constants is no greater than two orders of magnitude. As shown in Table 2, the rate constants at 60 kbars and 800K differ by many more orders of magnitude. Clearly, the first exponential term in Equation 1 overshadows the pressure dependence of the activation parameters.

DISCUSSION OF RESULTS

Table 2 shows that at 60 kbars and 800K the specific rate constant for bond scission is four orders of magnitude larger than that of the intramolecular hydrogen abstraction reaction. Of greater interest is the finding that the specific rate constant for the bimolecular reaction is nine orders of magnitude greater than the faster of the two unimolecular reaction processes. It is apparent from Table 2, that this is entirely due to the highly compressed form of the bimolecular transition state, viz. $\Delta V^\ddagger = -32.2$ cc/mole. This, in turn, results from the formation of C-O and O-H bonds at the expense of rupture of an N-O bond during the oxygen insertion reaction. This is, in fact, the first time that theory suggests a reaction in which a bound $-\text{NO}_2$ group directly donates its oxygen to another molecule. Traditionally, it has been assumed that oxidation occurs only after the formation of the NO_2 molecule. Since MINDO/3 was originally parametrized for equilibrium properties and its reliability for predicting activation parameters of insertion reactions has not yet been established, it is planned to put these conclusions to an experimental test.

Nevertheless, the results are consistent with thermo-hydrodynamic predictions and observed detonation phenomena. In particular, a finding from Figure 6 that the bimolecular methyl nitrate system compresses by $\sim 23\%$ on reaching the transition state accords with thermo-hydrodynamic predictions of a maximum compression of condensed explosives by strong shock waves of 25-37.5% (15,19). Similarly, a 5% compression of a single methyl nitrate molecule along the repulsive portion of the curve in Figure 2 to a state isoenergetic with the transition state for bond scission is also consistent with thermohydrodynamics. It is clear that most of the compression by shock is due to intermolecular rather than intramolecular processes. With respect to detonation phenomena, Kusakabe and Fujiwara (14) observed that liquid methyl nitrate propagates at a stable, low velocity detonation (LVD) of ~ 2500 m/s when the initiating shock pressure is low and high velocity detonation (HVD) of ~ 6700 m/s when

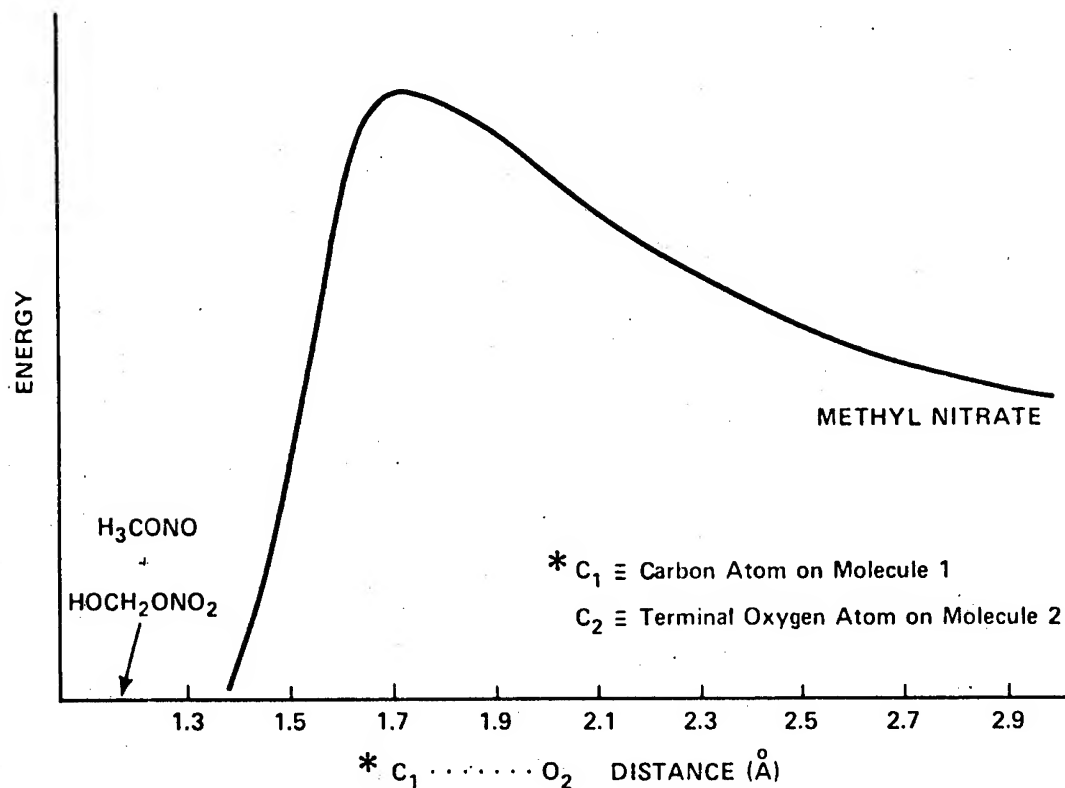


Figure 6. MERP of the Bimolecular Reaction in Methyl Nitrate

Table 2. Transition State Parameters and Relative Rates of Reaction, $k_x/k_{\text{bond sciss.}}$ at 800K and 60 kbars.

	ΔV^\ddagger (cc/mole)	ΔS^\ddagger (cal/mole-deg)	ΔE^\ddagger (kcal/mole)	$k_x/k_{\text{bond sciss.}}$
Bond Scission:	5.4	-1.4	34.0	1.0
Intramolecular H-Abstraction:	-2.1	-4.2	56.5	10^{-4}
Bimolecular O-Insertion:	-32.2	-32.3	32.3	10^9

the pressure is high. In view of the importance of the $\exp(-P\Delta V^\ddagger/RT)$ term in the rate expression, our calculations show that the HVD phenomenon is explainable in terms of the fast bimolecular process and LVD in terms of the much slower unimolecular bond scission process. The exothermicity of the bimolecular reaction path as opposed to the endothermicity of the unimolecular bond scission path provides yet another reason for relating these processes with HVD and LVD, respectively. Thus, energy to support the HVD front could become available to it immediately from the bimolecular reaction step whereas energy for the LVD front would be forthcoming from radical recombination reaction steps which occur much later and many reaction steps after the primary bond scission step (2).

SUMMARY AND CONCLUSIONS

A theoretical approach is described which permits one to calculate rates of reaction from the structural formula of an explosive molecule. The theoretical tools are the MINDO/3 semi-empirical quantum chemical procedure of Dewar and the transition theory rate equation. The applicability of this approach to the study of shock initiation of detonation is illustrated by way of the liquid explosive, methyl nitrate. The relative rates of three plausible reaction paths are calculated. They are the unimolecular bond scission reaction which yields $\text{CH}_3\text{O}.$ and $\text{NO}_2.$, the intramolecular hydrogen abstraction reaction which yields HONO and H_2CO and the bimolecular oxygen insertion reaction which yields CH_3ONO and $\text{HOCH}_2\text{ONO}_2.$ Surprisingly, it was found that at conditions believed to be typical for shock initiation of high velocity detonation in liquid methyl nitrate viz. 60 kbars and 800K, the bimolecular reaction proceeds nine orders of magnitude faster than the commonly accepted bond scission reaction whereas the intramolecular reaction is four orders of magnitude slower than bond scission. Moreover, the bimolecular reaction is exothermic by ~ 30 kcal/mole. If experimentally confirmed, this finding would represent the first instance of a reaction in which a bound NO_2 group directly inserts oxygen into the bond of another molecule. The results are consistent with thermohydrodynamic predictions for shock compression of condensed explosives and with observations of stable high velocity and low velocity detonation in liquid methyl nitrate.

The approach taken here has yielded a new view of processes in the detonation regime. It is recognized that future experimental observations are needed to confirm the above conclusions. Moreover, it is felt that, in addition to the use of a semi-empirical quantum chemical procedure, a combination of a state-of-the-art ab initio

*Alster, Slagg, Dewar, Ritchie, & Wells

method and new experimental techniques for monitoring transient chemical species can provide new insights into detonation phenomena.

REFERENCES

1. N.N. Semenov, "Some Problems of Chemical Kinetics and Reactivity", Volume 1, translated by J.E.S. Bradley, Pergamon Press, NY, NY, 1958.
2. J. Alster, and N. Slagg, "Proceedings of the Conference on Mechanisms of Explosions and Blast Waves, sponsored by JTCG/ALNNO, US ARRADCOM, Dover, NJ (November 1973) p. XV.
3. R.C. Bingham, M.J.S. Dewar, and D.H. Lo, J. Am. Chem. Soc. 97, 1285 (1975).
4. Ibid, 1302.
5. M.J.S. Dewar, Science, 187, 1037 (1975).
6. M.J.S. Dewar, Faraday Discussions of the Chem. Soc. 62, 197 (1977).
7. A.P. Cox and S. Waring, Trans. Faraday Soc. 76 , 3441 (1971).
8. J.D. Cox and G. Pilcher, "Thermochemistry of Organic and Organometallic Compounds," Academic Press, NY, NY, 1970.
9. J.W. McIver and A. Komornicki, Chem. Phys. Lett. 10, 303 (1971).
10. G. Herzberg, "Molecular Spectra and Molecular Structure, II. Infrared and Raman Spectra of Polyatomic Molecules," Chapter V, D. Van Nostrand Co., Inc., NY, NY, 1945.
11. J.A. Dean, Lange's Handbook of Chemistry, 11th Edition, McGraw Hill Book Co., NY, NY, 1973.
12. J.C.D. Brand and T.M. Cawthon, J. Am. Chem. Soc. 77, 319 (1955).
13. I. Amdur and G.G. Hammes, "Chemical Kinetics, Principles and Selected Topics," McGraw-Hill Book Co., NY, NY, 1966, p. 44.
14. M. Kusakabe and S. Fujiwara, Fifth Symposium of Detonation, sponsored by US Naval Surface Weapons Center, White Oak, MD and Office of Naval Research, Washington, DC (1970).

*Alster, Slagg, Dewar, Ritchie, & Wells

15. A.W. Campbell, W.C. Davis, and J.R. Travis, *Physics of Fluids* 4, 498 (1961).
16. R. Shaw, *Combustion and Flame* 21 127 (1973).
17. R.S. Bradley, "High Pressure Physics and Chemistry," Volume 2, Chapter 8, "Chemical Kinetics" by S.D. Hamman, Academic Press, NY, NY, 1963.
18. R.S. Bradley, *Ibid*, Chapter 9, Table II, p. 227.
19. J. Taylor, "Detonation in Condensed Explosives," Oxford University Press, London, 1952.

*ASHMAN, THORNTON, BROOME, KING, & SACCO

PATTERN RECOGNITION APPLICATIONS IN CHEMISTRY AND PHARMACOLOGY:
A 'PHARMACOPHORE ACETYLCHOLINORECEPTOR' SUBUNIT ENVIRONMENT MODEL (U)

*WILLIAM P. ASHMAN, Mr.

WILLIAM THORNTON, Mr.

PAUL H. BROOME, Mr.

JAMES W. KING, PhD

WILLIAM J. SACCO, PhD

CHEMICAL SYSTEMS LABORATORY, USAARRADCOM

ABERDEEN PROVING GROUND, MD 21010

In the analysis of a compound's structure for the prediction of its resultant pharmacological activity, the ultimate goal of the researcher is the explanation of the physiological mechanisms and compound interactions involved from the moment the drug is administered until the time it completes its effect. Having this knowledge, the researcher can then design compounds producing the efficaciousness desired. With this objective, investigators at the Research Division, Chemical Systems Laboratory, APG, MD have conducted chemical structure-biological activity relationship (SAR) studies (1) on various classes of compounds whose pharmacological actions 'in vivo' are directly related to the cholinergic system. The studies have included toxicity, cholinolytic and cholinomimetic activity, and the medical prophylactic and/or therapeutic efficacy of compounds or mixtures of compounds against anticholinesterase poisoning.

Of the possible receptors in this system, three types have been described (2) that are specific for interaction with acetylcholine (ACh). These are the nicotinic acetylcholine receptor (NACHR), the muscarinic acetylcholine receptor (MAChR), and the acetylcholinesterase enzyme (AChE). In this report, the general term 'acetylcholinoreceptor' (AChRE) refers to all three. Extensive research has been conducted on the pharmacological receptors and the biological mechanisms of action associated with the neurotransmitter acetylcholine (3-5) and many receptor configuration and biochemical mechanistic models have been proposed and modified as experimentation

*ASHMAN, THORNTON, BROOME, KING, & SACCO

has added new information (6-23). However, the precise environment of each acetylcholine receptor (AChR) type has not been defined.

This report defines a generalized pharmacophore acetylcholinoreceptor environment (AChRE) model. It is a 3-dimensional description of a composite acetylcholine receptor and of the relative geometric positions of specific compound functional group-receptor interaction regions. The relationship of this 'generalized AChRE' model to the AChE-acetylcholine receptor-ionophore complex and its potential application in the above research as a compound-receptor interaction reference template are discussed.

METHODOLOGY.

A. Chemical Structures.

A search was made for studies of ligand binding on muscarinic receptor, nicotinic receptor, and acetylcholinesterase and for relevant physiological studies. Structures of the compounds were obtained from the articles (6-30) or from various drug description indexes (31-33). Structures of chemical compounds from our SAR studies were also used. The 3-dimensional configuration of each compound was constructed using Dreiding Stereomodels. If X-ray diffraction analyses or crystal structure data were available, this information (14, 24-30) was employed to define the most likely configuration; if not, basic stereochemical principles were followed in construction of the molecules. Table 1 gives examples of the types of compounds found and used in the model formulation. The compounds are of both rigid and flexible structure types.

B. Compound-Cholinergic Activity 'Feature' Selection.

The identification of the compound features to be evaluated involved consultation with experts, literature searches and analyses of both drug-cholinergic receptor interaction models of the receptor types (NAChR, MAChR, AChE) being investigated, and data from 'in vitro' and 'in vivo' biochemical and physiological research related to the cholinergic system. The features included 3-dimensional geometric interatomic distances, specific compound functional groups, physicochemical and electronic properties.

Pattern recognition and clustering techniques are used to identify, rank, and quantify these features as to their relevance to cholinergic activity and to proposed compound-receptor interaction models. Of the 3-dimensional conformational receptor (AChR and AChE) models analyzed for significant features, the concepts and models of

*ASHMAN, THORNTON, BROOME, KING, & SACCO

Sommer (18), Golikov (8), Khromov-Borisov and Michelson (10), Kabachnick (16), and Pauling and Petcher (14) have the qualitatively 'best fit' compound-receptor feature interface.

C. Design of the 'Acetylcholinoreceptor' Model.

The 3-dimensional receptor model of Pauling and Petcher (14) was used as an elementary template amenable to modification and incorporation of features based upon requirements evolving from our SAR studies.

The overall development and refinement of our model took place in three phases:

1. (a) The 3-dimensional structures of the rigid neuromuscular blocking agents that Pauling and Petcher studied, were built using Dreiding Stereochemical models. (b) Using these compounds, their drug-receptor interaction template model was reconstructed to a Dreiding model scale for a definition of the relative positions of each proposed binding area and location of lipophilic, hydrophilic, or other potential compound-receptor interaction regions.

2. Using the Dreiding models, each compound noted in section A was constructed and superimposed on the basic template, with specific atoms and physicochemical binding regions of the compounds oriented for a 'best' possible fit. Common 3-dimensional structural features of these compounds and their potential receptor binding regions were defined.

3. Features identified in section B were incorporated and the results were then applied to modify the basic template. In this manner specific chemical compound bonding areas were eliminated and other interaction regions and physicochemical and macromolecular features were added until the proposed 'pharmacophore acetylcholinoreceptor' model was developed.

RESULTS. - 'Pharmacophore Acetylcholinoreceptor' Environment Model.

A. 3-Dimensional Geometric and Structural Components.

Figures 1 and 2 show the general AChRE model and its important interaction regions as conceptualized within a folded and partially closed or restricted area of a continuous membrane, the lower and upper surfaces of which are designated as A and B, respectively, and whose inner surfaces are at most 4.8 Å apart. Specific reaction sites and locations on the receptor are suggested

by the nature of the chemical, electronic, or physicochemical binding potentials and characteristics present in the analyzed compounds. It is important to note that the model does not necessarily represent a single receptor that might actually be found in vivo, but is a composite of the several receptor models previously noted and the modifications and inclusions resulting from our structural studies. The membrane surfaces serve as a reference framework to assist in visualizing and defining the placement, extent, and limitations of various compound interaction regions. For clarity, the convention used to define the electronic (cation, anion) interaction sites of the receptor should be noted. In this report, these sites are defined in reference to the electronic charge of the compound interacting at these areas. By definition, the cationic site of the receptor refers to a negative area (labeled \ominus in the figures) to which a positively charged region (cation) of a compound may interact. The anionic site of the receptor refers to a positive area (labeled \oplus) to which a negatively charged (anion) region of a compound may interact.

The basic structural features (Figures 1,2,3,4,5) of the model are:

1. A hydrophobic or van der Waals interaction ridge shown as a 3-dimensional cloud between and surrounding the cationic sites. Eight methylene groups can be accommodated along this ridge between the cationic regions. This is in agreement with the Pauling and Petcher model (14).
2. Two cationic sites, designated 1 and 2, separated by a distance of 11 Å along the van der Waals ridge and located 1.3 Å above Surface A (Figure 4). These sites provide binding areas for a compound's positively charged atom or functional group.
3. Three anionic sites, designated 1, 2, and 3, one of which is located on or slightly dimpled into Surface A, while the others are located on Surface B (Figure 5), optimally, at 2.2 Å (Site 2) and 2.3 Å (Site 3) above Surface A. These are sites of binding for an oxygen atom or oxygen isosteres.
4. Two planar lipophilic (hydrophobic) or π - π charge transfer binding regions, one of which is located on Surface A and is about the size of the planar tricyclic anthracene ring system. The second area of this type is smaller, about the size of a benzene ring, and is located on the inner side of Surface B, optimally at 2.6 Å above the plane of Surface A. These sites provide areas for planar group interaction with the receptor.

5. Methyl or methylene group affinity regions are defined around both cationic sites (Figure 3).

6. Conformational allosteric flexibility of the receptor template, i.e., the proposed receptor can change its conformation causing displacement of its bonding areas and thus is capable of undergoing "allosteric" changes.

Figure 3 is a view from above the receptor model. This view necessarily superimposes portions of some features but shows the interaction regions in their optimal relative positions for acetylcholine interaction. All referenced distances are in angstrom units (Å). In this view the receptor is divided into 4 quadrants differentiated by X and Y axes which are orthogonal. The geometric positions can be calculated from Figure 3 and specific chemical atom and structural types which may preferentially interact with the general regions are referenced.

Figures 4 and 5 show the receptor features associated with Surfaces A and B. The cationic sites, van der Waals ridge, and methyl or methylene group affinity regions are considered as common to both surfaces. The 3-dimensional perspectives of Figures 1 and 2 illustrate this concept. Cationic site 2 is located in an environment that is more lipophilic or hydrophobic than cationic site 1. The anionic site 1 located on Surface A prefers hydroxyl -OH type interaction. Anionic site 2 on Surface B prefers esteratic oxygen -O- or sulfur -S- type interaction while anionic site 3 prefers carboxyl, phosphoryl, or hydroxyl type bonds. Also on Surface A, there is an additional methyl type interaction region (C-9) located adjacent to the 8 carbon methylene bridge separating the two cationic areas. In combination with methylene binding sites C-5 and C-6 on the van der Waals ridge, this site forms a hydrophobic pocket for a compound (Neostigmine) so structured as to require an affinity for this region.

Surface B can undergo greater allosteric changes than Surface A. These changes result in alterations of the positions of the methylene and oxygen binding regions (anionic sites 2 and 3). Surface B is loosely bound to Surface A so that it can easily be opened along the hydrophobic ridge and 'flap' like a page in a book (Figures 1 and 2). The degree to which it can undergo conformational change is limited. The maximum possible separation of the inner faces of Surfaces A and B appears to be 4.8 Å (14) based on compounds thus far studied.

B. Compound-Receptor Model Interactions.

In nerve or neuro-muscular cholinergic synaptic systems, the actual 'in vivo' position of true acetylcholine receptors in relation to the post-synaptic membrane and the synaptic cleft has not been definitively established. Our model can be positioned to encompass a receptor located on a membrane surface, embedded in a membrane, or combinations of these two, with the possibility of partial extension of the receptor from the membrane into the synaptic cleft. In Figure 2, all dimensions and positions of the interaction regions are referenced to the lower plane (Surface A). In this model, compounds interacting with Surface A are not hindered by possible 'receptor' structural components located on the Surface A parallel to the van der Waals ridge and where there is no overlap by Surface B. The limitations on a compound binding to Surface A are due to the compound's inherent lipophilic or π - π characteristics and to its degree of geometric planarity.

It is proposed that compounds interacting with the receptor approach the cleft formed by Surface A and the van der Waals ridge area. In order to attach to Surface B, a compound must bind to the receptor either along the ridge and to binding areas adjacent to the ridge, or in some manner create an opening between the two surfaces, thereby allowing the molecule to attach to the π - π regions and/or the anionic binding regions of Surface B that are otherwise masked by the unknown membrane structural components above and to the right of the inner face of surface B (see Figures 1 and 2). As is indicated in the figures, and symbolized by the slit in the right end membrane enclosing the subunit model, it may be possible to enlarge this area.

C. Compound-Receptor Stoichiometry.

The stoichiometry of a compound interacting with the receptor depends on its geometrical size, the positions of its potential interaction groups relative to each other and to the receptor binding regions, and its degree of lipophilicity or hydrophilicity. Accordingly, the model is a 3-dimensional template or puzzle diagram into which the 3-dimensional structural components of the compound are to be fitted. One or two molecules of a compound may bind to this pharmacophore model, or a compound may not bind at all. This pharmacophore receptor model can accommodate two acetylcholine molecules. As shown in Figure 6, the molecules are bound to the common cationic areas, to the hydrophobic ridge, and to corresponding anionic regions of Surface B.

DISCUSSION AND RECOMMENDATIONS.

A. SAR Studies.

The proposed composite model contains parameters identified 'qualitatively' as similar to those suggested for the various types of acetylcholine receptors (NACHR, MACHR, AChE); it should not be construed as one specific receptor type. The important aspect of this model is that it can be used in biochemical ligand binding studies and SAR cholinergic activity studies as a basic 'pharmacophore' template for compounds or mixtures of compounds interacting with the cholinergic system, both for better definition of the individual receptor environments and for improvement of the design of drugs having a desired pharmacological or physiological effect. The model can be used to locate compound substituent groups in relation to potential interaction areas on the receptor template; and thereby, one can use more efficiently the SAR methods of Hansch (34) or others (35,36) in the analysis of congeneric series of compounds.

Activities that can be investigated include toxicity, anticholinergic activity, cholinomimetic activity, anticonvulsant activity, acetylcholinesterase inhibition, and reactivation of inhibited enzymes by oximes.

It is suggested that investigators reconstruct the proposed model (at least the 2-dimensional level of Figure 3) to the scale of stereomodels (Dreiding) and then use the model to position to scale stereomodels of the compounds of interest for their 'best fit' on it. It is recommended that the model be constructed in two sections, as defined previously, and the sections overlapped with the edge of Surface B positioned above Surface A along the axis formed by the van der Waals ridge and the two cationic areas. Surface A should be placed so that it is stationary and all its binding groups remain on its plane. Surface B should be flexible to allow for conformational change of the position of its binding groups due to interaction of the compounds on the receptor.

In SAR analyses, it is suggested that the following features be included:

1. Compound-Receptor Interface. - A compound must penetrate between Surfaces A and B in order to attach to the binding areas on Surface B. It cannot penetrate from the right of the hydrophobic ridge as viewed in Figures 1 and 2.

2. Stoichiometry. - Stoichiometry is important in studying the cholinomimetic activity of a compound. Various biochemical studies (9,12) indicate that two cholinergic binding sites may be involved in the mechanism of the resultant nervous transmission. It also has been proposed (12) that there are two sites on the AChR having different affinities for acetylcholine molecules. The hypothesis is that one molecule-site interaction modifies the receptor conformation to allow for interaction of the second molecule of acetylcholine at a second site, or in some manner, the first interaction modulates the activity. The resultant pharmacological activity of a compound, therefore, may be correlated with the number of molecules that can bind.

3. Position of the Compound on the Model. - It is suggested that the model be divided into 4 regions labeled J, K, L, M as in Figure 7. Compounds believed to bind to region J are suggested primarily as antagonists of cholinergic activity. In general, this receptor region may be considered a regulatory area of either the AChR or AChE.

Region K contains the hydroxyl (OH) oxygen binding area (anionic site 1); most compounds binding here are anticholinergics.

Regions L and M contain interaction areas related to those of compounds having agonistic cholinomimetic activity. Generally, compounds that can fit one molecule in these regions without having part of its structure extended into region K display cholinomimetic activity. Also, regions L and M can be related to the active site of acetylcholinesterase.

Examples of compounds positioned to the receptor and their pharmacological actions are as follows:

a. Benactyzine can be positioned in regions K, L, and M. Its activity is anticholinergic.

b. Diazepam fits in region J. It is an anticonvulsant.

c. Phencyclidine could fit all 4 regions. Two of its molecules can be positioned without sterically hindering each other; one molecule positioned in regions J and K and one in regions L and M. Depending on dosage, its action can be inhibition of AChE, or interaction on the AChR-ionophore complex (37).

d. The oxime, 2 Pam Chloride fits all 4 regions. The regions (L,M) are assumed to be similar to the active site on AChE

*ASHMAN, THORNTON, BROOME, KING, & SACCO

and we believe these regions are oxime reactivation activity regions. The possibility also exists that regions (J,K) may be regulatory (22, 38) areas for actions occurring at regions (L,M). Certain oximes may also interact with the AChR.

e. Waksman (39) used a series of fluorescent acyl-cholines that displayed agonist and antagonist activity on an isolated nicotinic AChR. We propose that these compounds can be positioned on the model and their resultant fit could qualitatively define their activity. The agonist compounds fit the receptor in a position similar to that of one decamethonium molecule or 2 acetylcholine molecules.

4. Separation of Surfaces A and B. - It is suggested that a measurement be taken of the inner surface separation made when the compound is positioned between Surfaces A and B. The degree of separation may indicate antagonistic cholinergic action possibly by interfering with the ionophore mechanism (8,19). This mechanism occurs in all 4 regions.

B. Drug Design Studies.

The model can be used in drug design studies as follows:

1. The structural and physicochemical feature characterization of compounds for isolation of efficacious parameters related to cholinergic and AChE activity.

2. Recommendation of new compounds to test, incorporating structural and physicochemical features suggested by the model.

3. Indication of possible new directions (new lead series of compounds or new combinations of compounds to test) that may increase efficacy or improve a proposed model.

4. As an aid in the development of mechanistic and structural models of the 'in vivo' AChR-AChE-ionophore complex.

An example of a drug design study where the AChRE model has effectively been used is in the development of improved medical treatment of organophosphate poisoning. The organophosphate compound Soman (Table 1) is an anticholinesterase agent. Bullock (40) has reported that Soman can attack not only AChE irreversibly, but at high concentrations may also bind to the nicotinic AChR. Our composite receptor model predicts this possibility and allows for

*ASHMAN, THORNTON, BROOME, KING, & SACCO

analyses of interactions with both receptors. Also, two molecules of Soman can bind to the model. In essence, a compound acting not only at different regions of the individual cholinergic receptors, but also at more than one receptor-type poses a greater toxicity hazard. This situation would probably require a more intense medical prophylactic and therapeutic regimen.

Classical treatment of organophosphate poisoning involves the use of an oxime for reactivation of the inhibited AChE and the use of atropine to counteract the muscarinic effects of excess acetylcholine. Kepner and Wolthuis (41) reported on the therapeutic efficaciousness of the oxime HI-6 and atropine against Soman poisoning in mice and rats. Using this mixture, via intramuscular route of administration in mice, a protective ratio of 17 LD₅₀ (42) against Soman poisoning was obtained. Our objective was to increase this protective ratio by the inclusion of a third compound into the mixture. Using the model as a guide, compounds with the following characteristics were recommended for syntheses or to be obtained: (a) stoichiometry of two, (b) oxygen or its isostere positioned in relation to anionic sites 2 and 3, (c) nitrogen at cationic site 1, (d) planar π - π structure positioned as on Surface B; (e) rigid ring structure along hydrophobic ridge (separation of Surface A from Surface B).

The compound 2-ethylamino-2(2-thienyl)cyclohexanone has the recommended features and its functional groups can be positioned geometrically to fit the model. In combination with HI-6 and atropine, it had a protective ratio of 29 (42) against Soman poisoning when tested as above.

REFERENCES.

1. Sacco, W.J., et al. ARCSL-TR-77058 (1977).
2. Heilbronn, E. Cholinergic Mechanisms, ed. Waser, Raven Press, NY, 343-365 (1975).
3. Cohen, J.B. and Changeux, J.P. An. Rev. Pharm., 15, 83-103 (1975).
4. Karlin, A. Life Sciences 14, 1348-1415 (1975).
5. Magazanick, L.G. An. Rev. Pharm. Tox., 16, 161-175 (1976).
6. Loomis, Ted. A. NTIS, AD 782 491, March 1974.
7. DeRobertis, Eduardo. Science 171, 963-971 (1971).
8. Golikov, S.N. and Kuznetsov, S.G. Vestnik Academic Meditsinskikh Nauk SSSR 25(2), 67-85 (1970).
9. Gibson, Raymond E. Biochemistry 15(17), 3890-3901 (1976).
10. Khromov-Borisov, S.N. and Michelson, M.J. Pharm. Rev., 18(3), 1051-1090 (1966).
11. Krupka, R.M. and Laidler, K.J. J.A.C.S., 83, 1445-1460 (1961).

*ASHMAN, THORNTON, BROOM, KING, & SACCO

12. Eldefrawi, M.E. and Eldefrawi, A.T. *Bioch. Pharm.*, 22, 3145-3150 (1973).
13. Weigand, U., et al. *Biochm. Pharm.*, 25, 1719-1726 (1976).
14. Pauling, P. and Petcher, T.J. *Chem. Bio. Inter.*, 6, 351-365 (1973).
15. Symthies, J.R. *Eur. J. Pharm.*, 14, 268-279 (1971).
16. Kabachnick, M.I., et al. *Pharm. Rev.*, 22(3), 355-388 (1970).
17. Belleau, B. *J. Medicinal Chem.*, 7, 776-784 (1964).
18. Sommer, Harold Z., Personnel Communication.
19. Karlin, A. J. *Gen. Physiology* 54, 245-264 (1969).
20. Changeux, J.P., et al. *J. Gen. Phys.*, 54, 225-245 (1969).
21. Roufogalis, B. and Wickson, V.M. *Mol. Pharm.*, 11, 352-360 (1975).
22. Wombacher, H. and Wolf, H.U. *Mol. Pharm.*, 7, 554-566 (1971).
23. Maayani, S., et al. *Biochm. Pharm.*, 23, 1263-1281 (1974).
24. Baker, R. W., et al. *Nature* 230, 439-444 (1971).
25. Sundaralingam, M. *Nature* 217, 35-37 (1968).
26. Argos, Patrick, et al. *Acta. Crystal.*, B26, Part 1, Jan 1970.
27. Clothia, C., et al. *J. Mol. Biol.*, 105, 517-526 (1976).
28. Lutteringhaus, U.A. and Hagedorn, I. *Arzneim-Forsch.*, 14, 1-5 (1964).
29. Scheiber, P. and Nador, K. *Arneim-Forsch.*, 25(3), 375-378 (1975).
30. Camerman, A. and Camerman, N. *J.A.C.S.*, 94(1), 268-272 (1972).
31. Merck Index, 8th ed, Merck & Co., Rahway, NJ, USA, 1968.
32. Russian Drug Index, U.S. Dept of Health, Education, and Welfare, Public Health Service, Washington, DC, 1961.
33. Drill's Pharmacology in Medicine, 3rd ed, McGraw-Hill Book Co., New York, 1965.
34. Leo, A., et al. *Chem. Rev.*, 71(6), 525-616 (1971).
35. Cammarata, A. and Menon, G.K. *J. Med. Chem.*, 19(6), 739-748 (1975).
36. Redl, G., et al. *Chem. Soc. Rev.*, 3, 273-292 (1974).
37. Tsai, M.C., et al. *Fed. Proc.*, 38(3), 274 (1979).
38. Kuhnen, H. *Bio. Pharm.*, 21, 1187-1196 (1972).
39. Waksman, G., et al. *FEBS Letters* 67(3), 335-343 (1976).
40. Bullock, J.O., et al. *Bioch. Pharm.*, 26, 337-343 (1977).
41. Kepner, L.A. and Wolthuis, O.L. *Eur. J. Pharm.*, 18, 377-382 (1978).
42. W. J. Lennox, Personnel Communication.

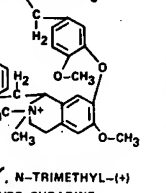
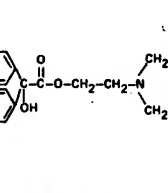
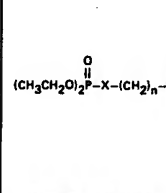
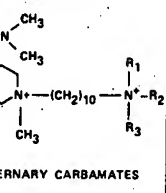
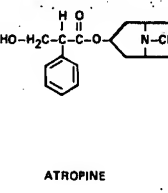
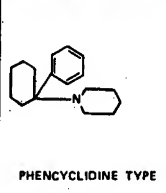
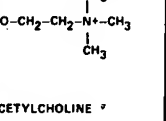
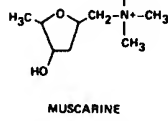
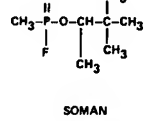
NICOTINIC RECEPTOR	MUSCARINIC RECEPTOR	ACETYLCHOLINESTERASE
 <p>O,O', N-TRIMETHYL-(+) TUBO CURARINE</p>	 <p>BENACTYZINE</p>	 <p>ORGANOPHOSPHATES</p>
 <p>BISQUATERNARY CARBAMATES</p>	 <p>ATROPINE</p>	 <p>PHENCYCLIDINE TYPE</p>
 <p>ACETYLCHOLINE</p>	 <p>MUSCARINE</p>	 <p>SOMAN</p>

TABLE 1. EXAMPLES OF CHEMICAL COMPOUND CONFIGURATIONS

ACETYLCHOLINORECEPTOR MODEL

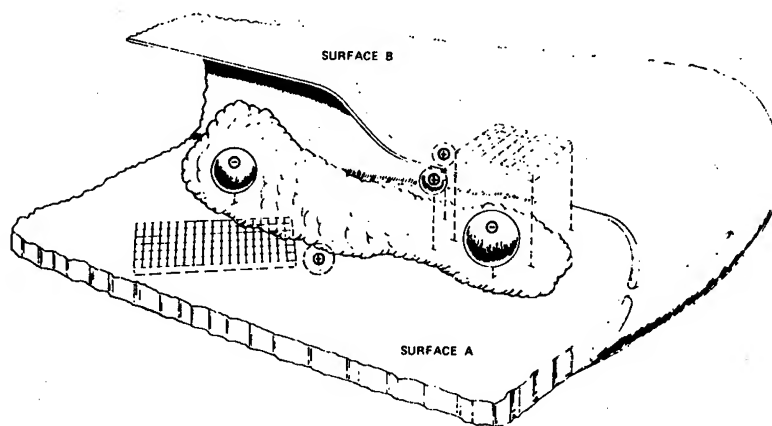


FIGURE 1. THE "PHARMACOPHORE ACETYLCHOLINORECEPTOR" SUBUNIT ENVIRONMENT MODEL. SURFACES A AND B ARE CONTIGUOUS; CROSSHATCHING IDENTIFIES AREAS OF POSSIBLE INTERACTION OF PLANAR AROMATIC MOIETIES WITH THE RECEPTOR. THE ANIONIC AND CATIONIC AREAS ARE SHOWN AS SPHERES WITH THEIR CHARGE NATURE INDICATED; THE CLOUD REPRESENTS A POTENTIAL VAN DER WAALS INTERACTION SPACE.

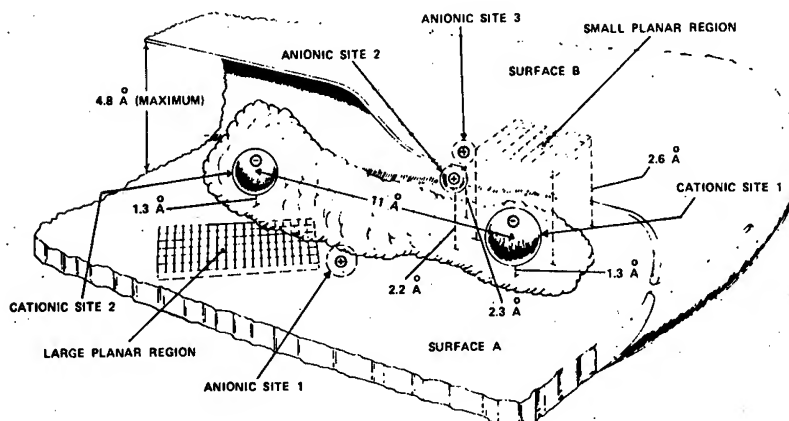


FIGURE 2. DIMENSIONS OF THE "PHARMACOPHORE ACETYLCHOLINORECEPTOR" SUBUNIT ENVIRONMENT MODEL. AS IN FIGURE 1, THE CLOUD REPRESENTS A POTENTIAL VAN DER WAALS INTERACTION SPACE THAT ENCOMPASSES BOTH CATIONIC SITES AND IS VERTICALLY BOUNDED BY SURFACES A AND B.

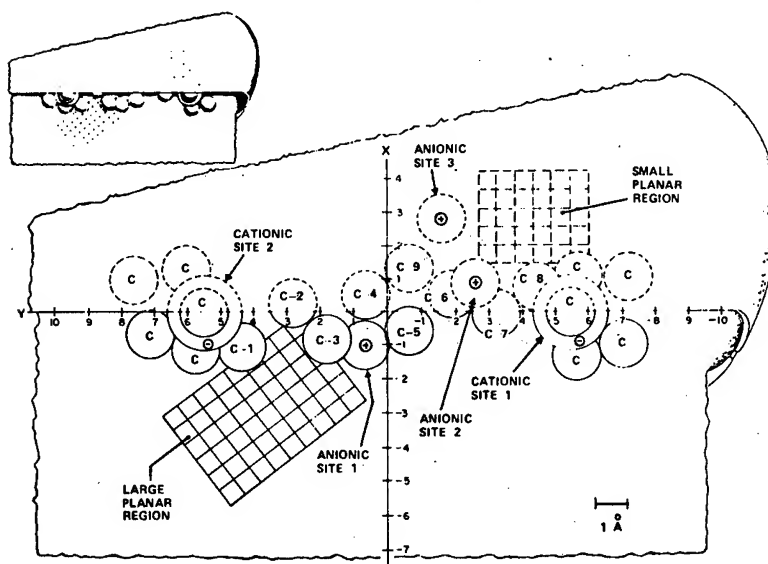


FIGURE 3. TOP VIEW OF THE RECEPTOR MODEL. C_1 - C_9 REPRESENT POTENTIAL METHYLENE CHAIN BINDING SITES EXTENDING ALONG THE VAN DER WAALS RIDGE BETWEEN THE CATIONIC SITES; THE LATTER PROVIDE POSITIVELY CHARGED CATION BINDING AREAS. C_9 AND THE UNSCRIPTED C_1 AROUND EACH CATIONIC SITE REPRESENT METHYL OR METHYLENE GROUP AFFINITY REGIONS. CARBONYL, ETHER, OR HYDROXYL OXYGEN ATOMS AND ISOTERES OF OXYGEN, S OR S_{H_2} , WOULD BE EXPECTED TO BIND AT THE ANIONIC SITES WHILE THE PLANAR REGIONS PROVIDE SITES FOR AROMATIC π - π OR LIPOPHILIC INTERACTIONS.

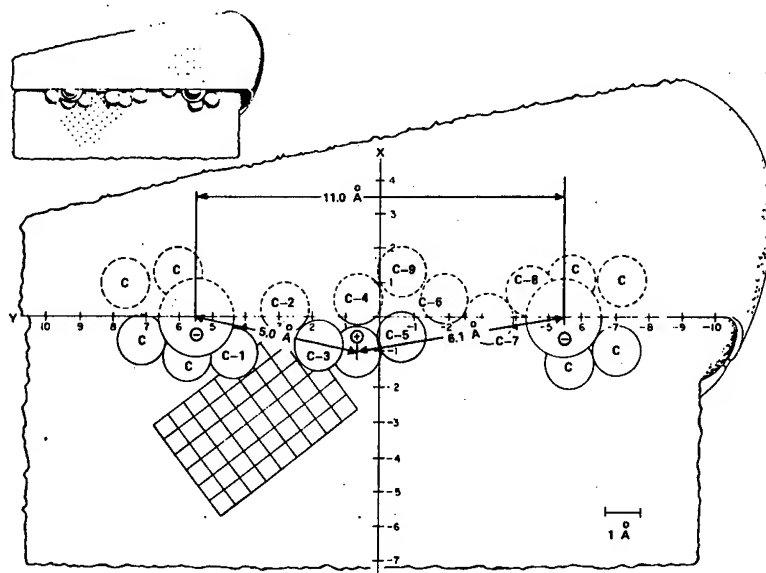


FIGURE 4. TOP VIEW OF THE RECEPTOR FEATURES ASSOCIATED WITH SURFACE A (SEE FIGURES 1 AND 2). THE CATIONIC AREAS, VAN DER WAALS RIDGE AND METHYLENE AFFINITY REGIONS ARE COMMON TO BOTH SURFACE A AND B, AND ARE SHOWN FOR CLARITY AND ORIENTATION WITH REFERENCE TO FIGURE 3.

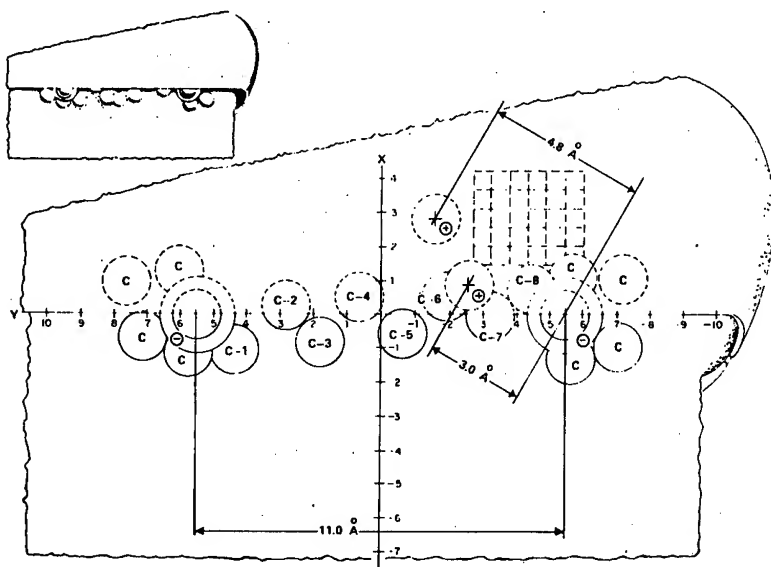


FIGURE 5. TOP VIEW OF THE RECEPTOR FEATURES ASSOCIATED WITH SURFACE B. THE CATIONIC AREAS, VAN DER WAALS RIDGE AND METHYL OR METHYLENE AFFINITY REGIONS ARE COMMON TO BOTH SURFACE A AND B (REFER TO FIGURES 1-3).

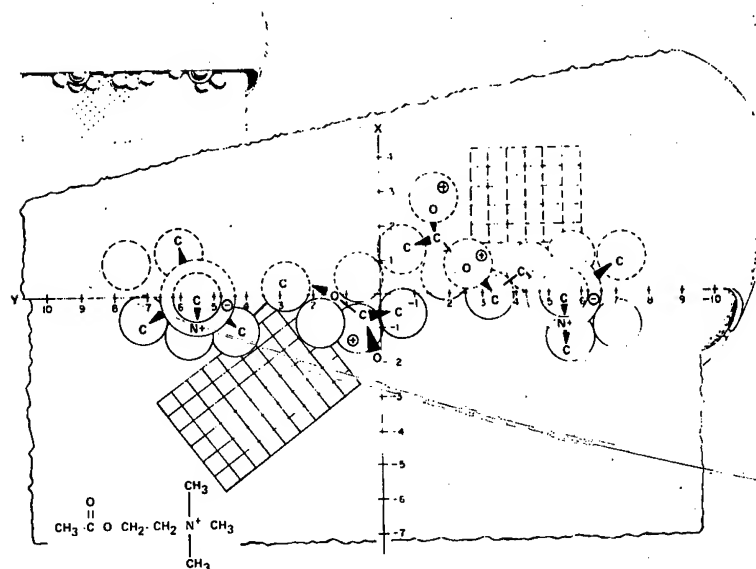


FIGURE 6. POSSIBLE ACETYLCHOLINE RECEPTOR INTERACTION, WITH A STOICHIOMETRY OF 2.

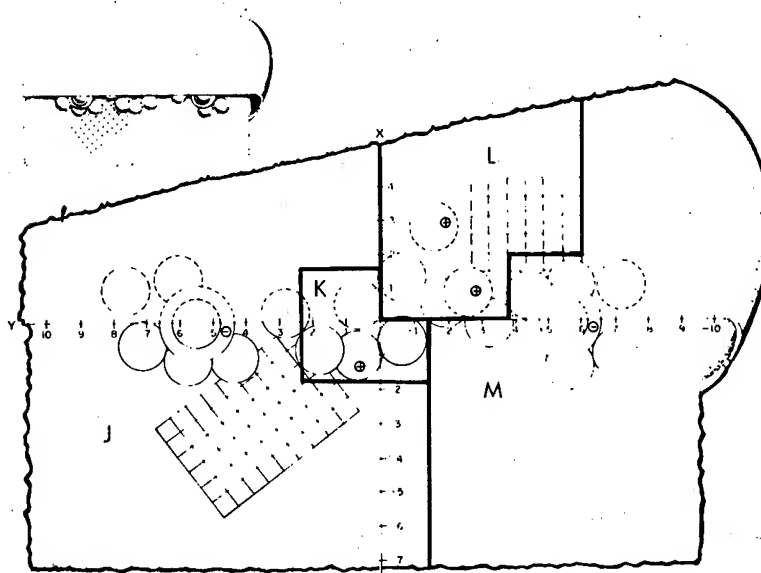


FIGURE 7. DIVISIONAL QUADRANTS OF THE PHARMACOPHORE MODEL

CHOLINERGIC RECEPTOR - ANALYSIS QUADRANTS

J - REGULATORY AREA (ANTAGONIST, NON COMPETITIVE)

K - AREA CONTAINING OH BINDING SITE

L - *AGONIST BINDING AREA (ESTERATIC AND ANIONIC REGIONS)

M - *AGONIST BINDING AREA (CATIONIC REGION)

*DEPENDENT ON STRUCTURE OF COMPOUND - COMPOUNDS BINDING TO THESE AREAS MAY BE ANTAGONISTS.

AUCOIN, *SAVAGE, WADE,
GUALTIERI and SCHWARTZ

LARGE HIGH QUALITY SINGLE CRYSTAL ALUMINUM PHOSPHATE
FOR ACOUSTIC WAVE DEVICES

THOMAS R. AUCOIN, MR., *ROBERT O. SAVAGE, MR., MELVIN J. WADE, MR.,
JOHN G. GUALTIERI, MR., and ABRAHAM SCHWARTZ, MR.†
USA ELECTRONICS TECHNOLOGY AND DEVICES LABORATORY (ERADCOM)
FORT MONMOUTH, NEW JERSEY 07703
†195 WOODCREST ROAD, OAKHURST, NEW JERSEY 07755

INTRODUCTION

Advanced military electronic warfare, secure communication, and surveillance/target acquisition systems such as mini-RPV's, REMBASS, and mortar and artillery locator radars, utilize a variety of acoustic wave devices. Typical are crystal oscillators, convolvers correlators, bulk and surface wave filters, resonators, delay lines, encoders, and decoders. High piezoelectric coupling, low acoustic loss (high Q), and temperature stability are critical requirements for materials to be used in the fabrication of next generation, high performance devices. Of the two crystals commonly used today, quartz exhibits temperature stability and low acoustic loss, while lithium niobate has relatively low loss and high coupling. α -AlPO₄ offers the highly desirable combination of all three.

Aluminum phosphate (α -AlPO₄), also known as the mineral Berlinite, recently emerged as a promising piezoelectric material for acoustic wave devices, offering one the unique combination of high electro-mechanical coupling with requisite temperature stability. Results of Chang and Barsch (1), O'Connell and Carr (2), and Ballato (3,4) show α -AlPO₄ to be an outstanding candidate for military signal processing applications.

AlPO₄ is in the same crystal class as quartz (Class 32) and similar geometric and physical properties are expected. Computed piezoelectric coupling factors based on the measurements of Chang and Barsch (1) translate into a large coupling advantage for α -AlPO₄

AUCOIN, *SAVAGE, WADE,
GUALTIERI and SCHWARTZ

over α -quartz; up to 250% for bulk resonators and 400% for surface acoustic wave (SAW) devices as shown in Figures 1 and 2 for rotated y- cuts. This coupling factor advantage over quartz would be of little practical value, if it were not for the fact that AlPO_4 can be cut to have essentially zero temperature coefficients.

In projecting the use of a higher-coupling temperature stable material such as α - AlPO_4 in acoustic wave device applications, several advantages over existing materials are apparent. AlPO_4 devices would have lower insertion losses and eliminate the need for ovens to stabilize temperature when compared to quartz and lithium niobate components, respectively. One could then expect improved device performance and system reliability, as well as decreased acquisition cost and power consumption. However, the evaluation and testing of α - AlPO_4 in prototype components has been precluded by the poor quality and general unavailability of single crystals.

Alpha-aluminum phosphate generally crystallizes in a pseudo-hexagonal bipyramidal habit (Figure 3a) possessing no planes or center of symmetry but only axes of symmetry. The major and minor rhombohedra, r $\{10\bar{1}1\}$ and z $\{01\bar{1}1\}$, are predominant forms on α - AlPO_4 crystals. The major rhombohedron r is somewhat larger in size than the minor rhombohedron z. Prismatic m $\{10\bar{1}0\}$ faces are rarely encountered as contrasted to quartz (Figure 3b), and usually are not well developed.

α - AlPO_4 is isoelectronic and isostructural with α -quartz undergoing a phase transformation at approximately 584°C . Because of the severe strain, cracking, etc., which is created when cooling a crystal through a first order phase change, a low temperature growth technique is required. Standard hydrothermal growth techniques using saturated solutions of AlPO_4 in diluted phosphoric acid (H_3PO_4) have been used by several investigators (5-8) in Morey (9) type autoclaves at temperatures ranging from 150°C to 400°C . McBride and Hills (10) grew crystals from saturated solutions in sealed pyrex ampoules heated in a drying oven. In all articles published to date, actual crystal growth was obscured from the experimenter. However, the technique reported here (11) allows one to visually observe real time nucleation and growth kinetics. This feature has allowed, for the first time, precise determination of nucleation temperatures and optimum temperature-ramp rates for seeded solution growth. Using x-, y-, z-, and major (r) and minor (z) rhombohedral cuts for seed plates, large, high-optical-quality single crystals have been grown using this method.

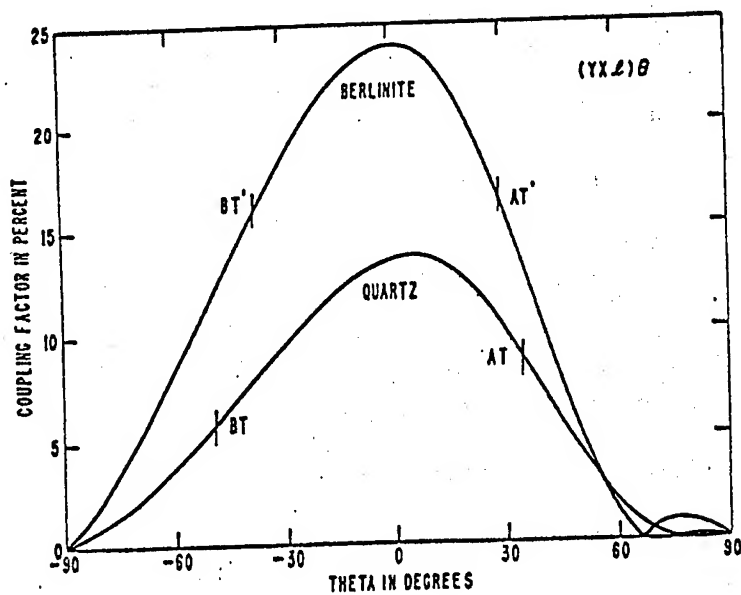


Figure 1. Coupling factor for α -quartz and α -AlPO₄.

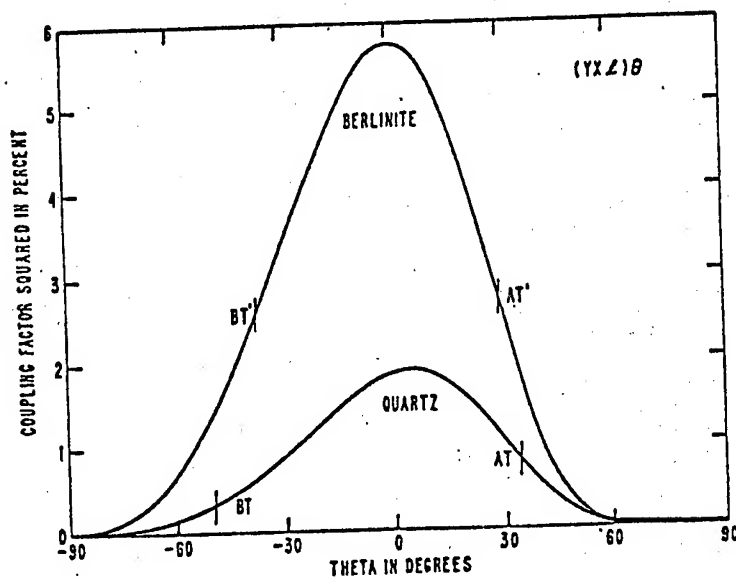


Figure 2. Coupling factor squared for α -quartz and α -AlPO₄.

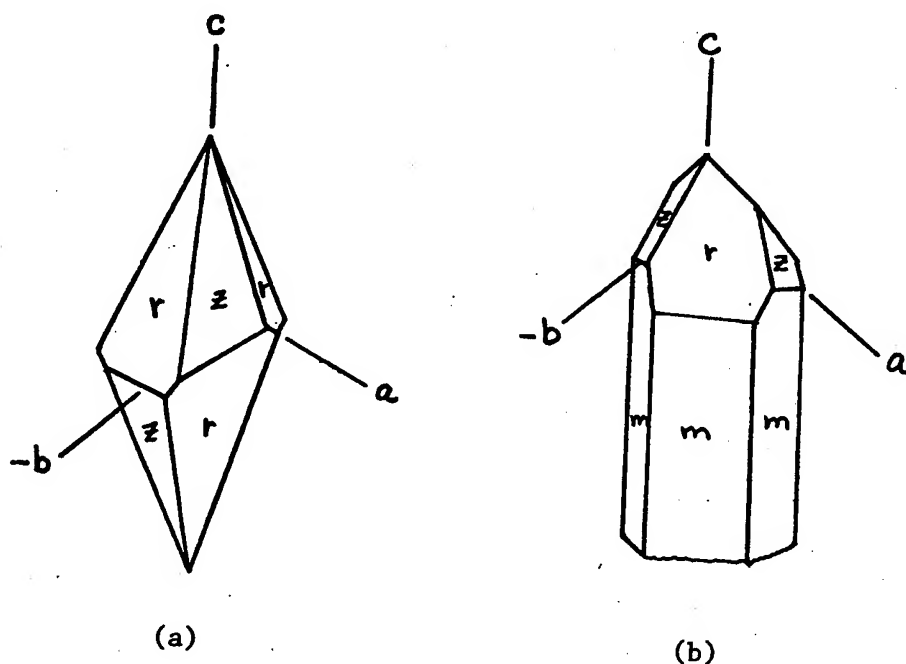


Figure 3. Frequently observed morphological habits of berlinite(a) and quartz(b).

EXPERIMENTAL

The solubility of α - AlPO_4 in phosphoric acid decreases with increasing temperature as shown in Figure 4 from data by Stanley (5). Because of this retrograde solubility, two seeded methods are generally used to grow α - AlPO_4 : slowly increasing the temperature of a saturated solution; and mass transport from a nutrient feed in a reverse temperature gradient. The solubility of AlPO_4 in diluted phosphoric acid is greatly dependent on the acid concentration, increasing as the concentration increases. For example, at 175°C , 0.6 mole and 1.7 moles of AlPO_4 are soluble in one liter of 5.0 molar and 9.5 molar H_3PO_4 , respectively.

In attempting to obtain bulk crystals of high perfection, trial and error growth runs conducted in conventional hydrothermal autoclaves were found to be very time consuming. Little or no information was obtained relating to the origin of the growth defects observed in α - AlPO_4 crystals, e.g., channeling, twinning, veiling, cracking, inclusions, etc. A hydrothermal growth system was designed and constructed (Figure 5) which allowed the direct observation of crystal formation during free nucleated and seeded growth. Growth processes

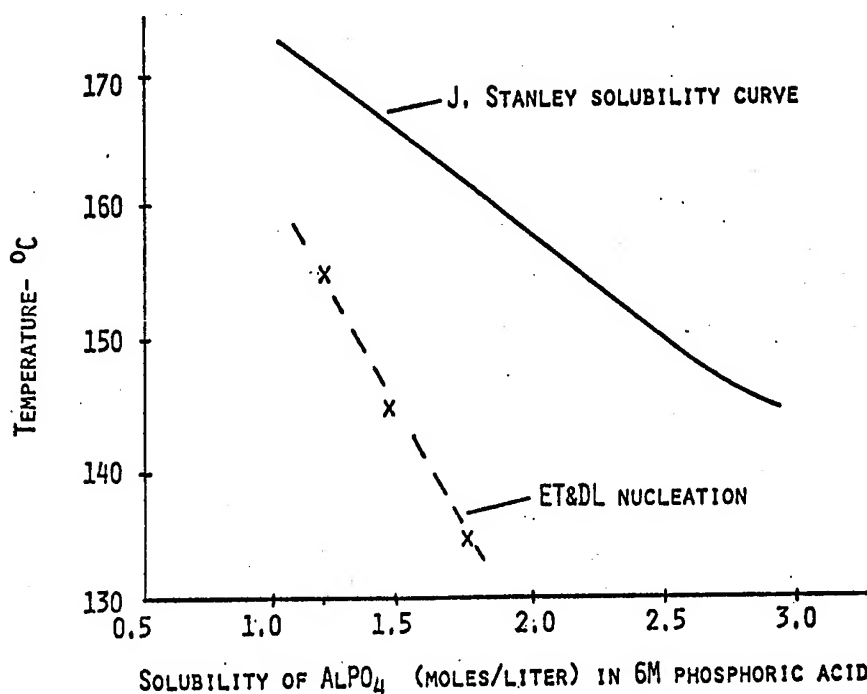


Figure 4. Solubility/nucleation of $\alpha\text{-AlPO}_4$ in 6M phosphoric acid.

such as etch-back, nucleation, veiling, cracking and surface roughening are all easily observable.

A Braun precision circulator, capable of maintaining temperatures at $\pm 0.004^\circ\text{C}$ to 250°C , was used to control the temperature of a silicone oil bath contained in a ten liter pyrex jar. This jar was placed in a larger pyrex container and the annular space filled with silicone oil for thermal insulation. Heavy wall quartz ampoules up to 3mm thick were selected for containment of growth solutions for several reasons: they are transparent; withstand vapor pressures to 200 psi or more; can be rapidly quenched without danger of explosion (runs must be quickly cooled and crystals removed due to the retrograde solubility of $\alpha\text{-AlPO}_4$ in H_3PO_4 as noted above); and can be hermetically sealed. The temperature of the growth solution was precisely programmed by increasing or decreasing the total resistance of the thermostat in the circulator. Ramp rates varying from 0.05°C to 3.5°C per day could be obtained by this technique.

Since high purity sources of AlPO_4 are not generally available, several approaches to obtaining satisfactory starting materials were explored. Our early growth runs were made from saturated solutions

AUCOIN, *SAVAGE, WADE,
GUALTIERI and SCHWARTZ

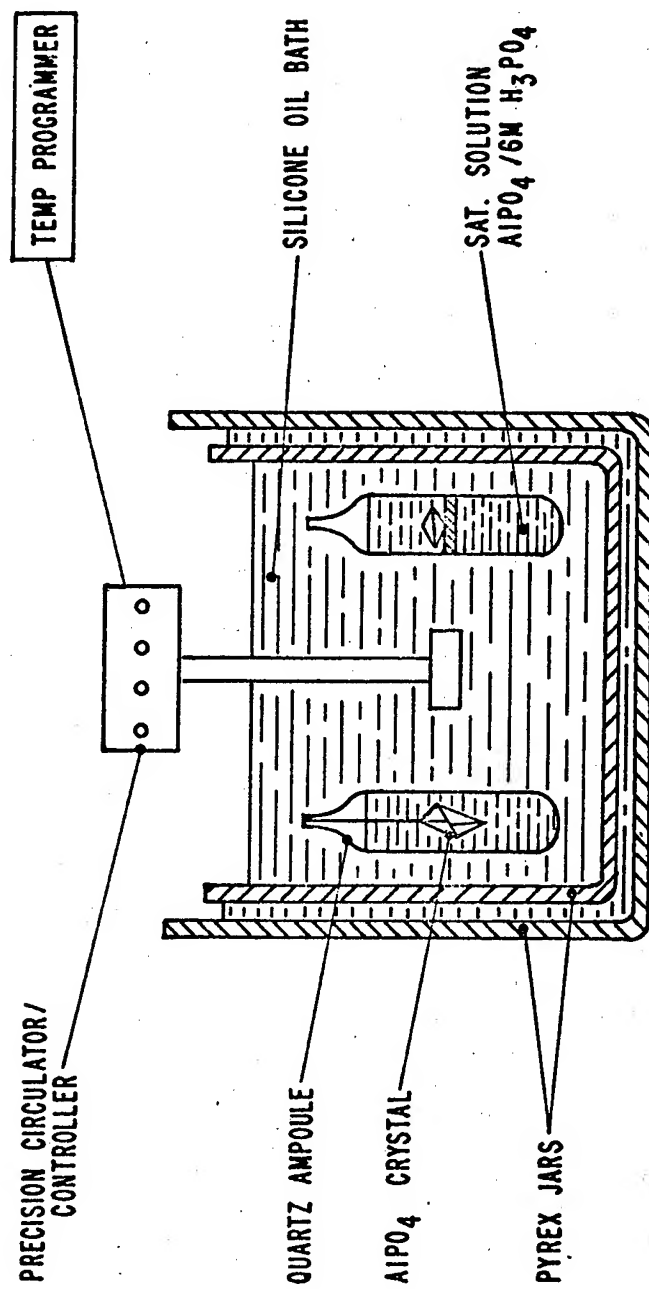


Figure 5. Modified hydrothermal system for direct observation of α - AlPO_4 crystal growth.

AUCOIN, *SAVAGE, WADE,
GUALTIERI and SCHWARTZ

of twenty five year old Fisher purified AlPO_4 used by Stanley (5). Upon heating this material to $1,000^\circ \text{C}$ in air for one hour, a weight loss corresponding to two waters of hydration was observed. X-ray powder diffraction patterns taken before and after firing confirmed the Fisher material to be $\text{AlPO}_4 \cdot 2\text{H}_2\text{O}$. Reagent ACS grade H_3PO_4 was diluted with DI water to 6 molar strength and used to dissolve the AlPO_4 powder. As seen in Table I, atomic absorption analysis indicated that transition metal impurity levels were very low in these solutions.

In order to synthesize our own supply of high purity starting materials, the following approach was successfully used. De-ionized water was very slowly added to high purity phosphorus pentoxide (P_2O_5), having less than 3 ppm iron, to form H_3PO_4 . This reaction was very exothermic, requiring a water cooled refluxer to prevent vaporization losses. High purity aluminum (99.9999%) was then reacted with the acid to form an $\text{AlPO}_4/\text{H}_3\text{PO}_4$ solution. The amount of water, P_2O_5 , and aluminum was carefully calculated to yield a solution of the correct composition for crystal growth, e.g., 20 gms AlPO_4 per 100 ml of 6M H_3PO_4 . Solutions prepared by this technique contained approximately one-half the amount of iron and up to seventy times less chromium than the amounts found in the Fisher based solutions. See Table I.

The concentration of AlPO_4 in H_3PO_4 investigated during this study varied from 15 gms per 100 ml to 22.5 gms per 100 ml of acid. The onset of crystal growth (nucleation) was determined for each AlPO_4 concentration by carefully monitoring etch-back and growth initiation on oriented seed plates. The seeds were generally used as cut by a wire saw. In some cases, additional seed preparation such as alumina polishing or ammonium bifluoride etching was performed. The nucleation temperatures obtained for AlPO_4 concentrations of 15.0, 20.0, and 22.5 gms per 100 ml (1.23, 1.64, and 1.85 moles/liter respectively) of 6M H_3PO_4 are shown in Figure 4. Having established the nucleation temperature for several concentrations, the effect of varying temperature ramp rates from 0.1°C to 2.0°C per day on crystal perfection was investigated. The quality of the growing crystals could be directly observed as a function of the rate of temperature rise.

The quartz ampoules used for growth were filled to 80% of their volume with the desired solution and sealed with or without seed crystals. Up to eight ampoules could be placed in the previously described growth apparatus (Figure 5) at one time. Conventional hydrothermal systems would require eight separate pressure vessels for the same number of runs. Ampoules up to 5cm in diameter and 150 ml in volume were used with seed plates consisting of x, y, z, and major

AUCOIN, *SAVAGE, WADE,
GUALTIERI and SCHWARTZ

Atomic Absorption Analysis AlPO ₄ /6M H ₃ PO ₄ solutions				Emission Spec. Analysis α-AlPO ₄ crystals			
Element	Fisher AlPO-30	ET&DL HPALPO-1	ET&DL HPALPO-2	Fisher AlPO-30	Stanley -	ET&DL HPALPO-1	ET&DL HPALPO-2
Fe	10.3	5.3	6.0	10	50	10	10
Ti	0.4	0.6	0.4				
Cr	2.8	0.04	0.04				
Mn	0.37	0.15	0.14				
Ni	1.90	0.08	0.09	ND	ND	ND	ND
Cu	0.30	0.44	0.36				
Zn	1.90	0.57	1.17				
Co	0.02	0.03	0.02				
Si	-	-	-	50	50	50	100
Mg	-	-	-	1	1	1	5

ND - Not Detected

TABLE I. Atomic absorption and emission spectroscopic analysis of AlPO₄ solutions
and α-AlPO₄ crystals. (ppm by weight/Eagle-Picher)

AUCOIN, *SAVAGE, WADE,
GUALTIERI and SCHWARTZ

rhombohedral faces. The temperature of the system was raised from room temperature to a point several degrees below the nucleation temperature to effect a slight etch back of the seed plate prior to growth. The temperature was then slowly raised until the seed underwent a slightly opaque to transparent transition, indicating nucleation had occurred.

RESULTS/DISCUSSION

The key factor to our successful growth of high-optical-quality single crystals of α - AlPO_4 was the development of a visual, hydro-thermal growth system. The ability to observe real time seed etch-back, nucleation, and veil formation at the seed/crystal interface and in the bulk crystal, allowed us in a minimum number of runs to ascertain optimum growth conditions. Figure 6 shows two examples of α - AlPO_4 single crystals which were grown on free nucleated seed crystals suspended by 3 mil gold wires. A saturated solution consisting of 20 gms per 100 ml of 6M H_3PO_4 and an increasing temperature rate of 2°C per day was used. These conditions resulted in growth rates of approximately 15 mils per day along the c- axis. Upon inspection, one observes severe etching and precipitate formation on the as-grown faces. Inspection of interior of the crystals after polishing or immersion generally revealed scattering centers and some cracks.

Figure 7 shows three crystals grown from the same concentration solution as those in Figure 6 except the rate of temperature rise has been decreased to 0.25°C per day. High-optical-quality (scatter-free) single crystals can be routinely grown on x, y, z, and major and minor rhombohedral faces using these conditions. It is possible by careful initiation of growth to completely eliminate veil formation at the seed crystal interface. Growth rates along the c- axis on basal-cut seeds was approximately 7 mils per day. The resulting crystals had excellent optical and mechanical properties and could be cut in any crystallographic direction using a wire saw. Crystal plates could also be lapped and polished without evidence of cleavage and fracture.

Transition metal ions and in particular iron, are expected to be a source of acoustic loss in α - AlPO_4 . Chemical analysis of the ET&DL starting solutions (Table I) indicate both a low iron content ($\sim 10\text{ppm}$) and a very low level of other transition metal ions. Emission spectroscopic analysis of crystals grown from these solutions show the levels of iron to be $\sim 10 \text{ ppm}$, while silicon is on the order of 50 ppm except for HPA1PO-2 (100 ppm). The reason for the higher amount of silicon in HPA1PO-2 may be that this run was approximately twice as long as the others and leaching of the quartz ampoule has occurred.

AUCOIN, *SAVAGE, WADE,
GUALTIERI and SCHWARTZ



Figure 6. α -AlPO₄ crystals grown from 6M H₃PO₄ at 2° C/day temperature ramp rate.

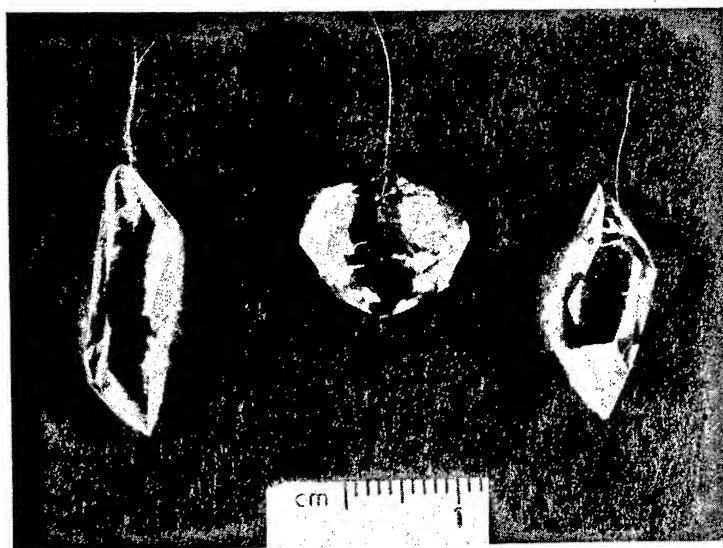


Figure 7. α -AlPO₄ crystals grown from 6M H₃PO₄ at 0.25° C/day temperature ramp rate.

AUCOIN, *SAVAGE, WADE,
GUALTIERI and SCHWARTZ

Experiments are planned to investigate the effect of using teflon lined ampoules on silicon impurity level, now that the growth parameters have been established in our visual system.

Brazil or optical twinning is very common in α - AlPO_4 while Dauphiné or electrical twinning is encountered infrequently. Brazil twinning shows straight regular boundaries perpendicular to the y-axis, which are best detected by etching in saturated ammonium bifluoride solutions at room temperature, (Figure 8). In a Brazil twinned region the polarity of the x-axis is reversed. A consequence of extensive Brazil twinning in rotated y-cuts is a reduced or even zero piezoelectric coupling (12). The twinning behavior of α - AlPO_4 is similar to that of the amethyst variety of quartz. Amethyst almost always displays Brazil twinning and only rarely Dauphiné twinning. Since the Brazil twinning in amethyst is usually related to the iron content, it is possible that such twinning in α - AlPO_4 may also be impurity induced.

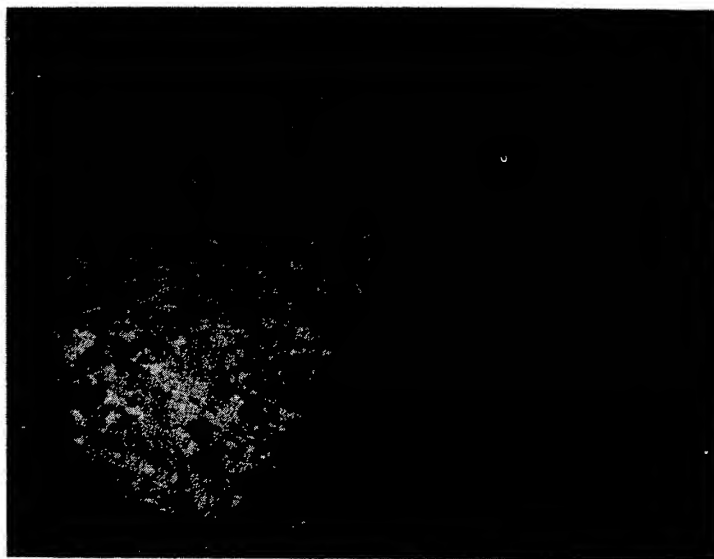


Figure 8. Reflection microphotograph of a Brazil twinned basal cut. The sample was etched in saturated ammonium bifluoride for 14 minutes at room temperature.

SUMMARY

Recently there has been considerable interest in the potential for using single crystal α -AlPO₄ in a variety of acoustic wave applications. This interest was prompted by the possibility of obtaining simultaneously in one material, the properties of temperature stability, low acoustic loss, and high piezoelectric coupling. The poor quality and general lack of large α -AlPO₄ single crystals has precluded the evaluation and testing of this material in the desired prototype devices. This situation has motivated our developing a novel synthesis technique for attaining such crystals. We have described a unique modification (patent pending) of the conventional hydrothermal growth method which yields large (>3cm), high-optical-quality single crystals. The method permits continuous visual observation of the pressurized crystal growth process thus permitting close control of real-time nucleation and growth kinetics. The optimum conditions for attaining high quality crystals such as temperature-ramp rates, reagent concentration and purity, system design, and ampoule configuration have been presented. These preliminary, very encouraging results have led to a definition of the barrier to attaining low loss crystals as being related to impurity content of the starting growth solutions and crystals, and Brazil type twinning. Approaches to overcoming these problems have been delineated and are now being implemented.

ACKNOWLEDGEMENTS

We would like to thank Dr. Arthur D. Ballato for computational analysis, Mr. Roger J. Malik for his assistance in design and construction of the temperature programmers, Mr. Donald W. Eckart for x-ray analysis, and Dr. Frederick Rothwarf for his helpful discussions.

AUCOIN, *SAVAGE, WADE,
GUALTIERI and SCHWARTZ

REFERENCES

1. Z.-P. Chang and G.R. Barsch, IEEE Trans., Sonics Ultrason. SU-23 127-135 (1976).
2. R.M. O'Connell and P.H. Carr, Proc. of 32nd Frequency Control Symposium, Atlantic City, 182 (1978).
3. A.D. Ballato, Physical Acoustics: Principles and Methods, 13 Academic Press, New York, 115-181 (1977).
4. A.D. Ballato and G.J. Iafrate, Proc. 30th Frequency Control Symposium, Atlantic City, 141-156 (1971).
5. J.M. Stanley, Indust. Eng. Chem. 46 1684-1689 (1954).
6. E.D. Kolb and R.A. Laudise, J. Crystal Growth 43 313-319 (1978).
7. J. Detaint, M. Feldmann, J. Henaff, H. Poignant, and Y. Tondic, Proc. of 33rd Frequency Control Symposium (1979).
8. E.J. Ozimek and B.H.T. Chai, Proc. of 33rd Frequency Control Symposium (1979).
9. G.W. Morey and P. Niggli, J. Am. Chem. Soc. 35 1086 (1913).
10. W.R. McBride and M.E. Hills, ICCG-5, Boston, Mass., Abst #65 (1977).
11. T.R. AuCoin, A. Schwartz, M.J. Wade, and R.J. Malik, Method of Growing Single Crystal Berlinite, US Patent Application No. 046,916, 8 June 1979.
12. A.D. Ballato, private communication.

*BALADI & ROHANI

A TERRAIN-VEHICLE MODEL FOR ANALYSIS OF
STEERABILITY OF TRACKED VEHICLES (U)

*GEORGE Y. BALADI, PH.D.

BEHZAD ROHANI, PH.D.

U.S. ARMY ENGINEER WATERWAYS EXPERIMENT STATION
VICKSBURG, MISSISSIPPI 39180

INTRODUCTION

Development of high-mobility/agility tracked combat vehicles has received considerable attention recently because of the possibilities they offer for increased battlefield survivability through the avoidance, by high-speed and violent maneuver, of hits by high-velocity projectiles and missiles. In order to design and develop such vehicles rationally, it is necessary to have a quantitative understanding of the interrelationship between the terrain factors (such as soil type, soil shear strength and compressibility, etc.) and the vehicle's characteristics (weight, track length and width, location of center of gravity, velocity, etc.) during steering. To study such an interrelationship, it is necessary to construct idealized mathematical models of the terrain-vehicle interaction. The accuracy and range of application of such models must, of course, be determined from actual mobility experiments and obviously must depend on the degree of relevance of the idealized model as an approximation to the real behavior.

The basic concepts of the theory of terrain-vehicle interaction were developed by Bekker during the 1950's (1). By assuming various load distributions along the tracks, Bekker was able to develop several mathematical expressions relating the characteristics of the vehicle and the tractive effort of the terrain during steering. By considering the lateral and longitudinal coefficients of friction between the track and the ground, Hayashi (2) developed simple equations for practical analysis of steering of tracked vehicles. Hayashi's work, however, did not include the effect of the centrifugal forces on steering performance of the vehicle. Kitano and Jyozaki (3)

developed a more comprehensive model for uniform turning motion including the effects of centrifugal forces. This model, however, is based on the assumption that ground pressure is concentrated under each road wheel and the terrain-track interaction is simulated by Coulomb-type friction. The model given in Kitano and Jyozaki was extended by Kitano and Kuma (4) to include nonuniform (transient) motion, but the basic elements of the terrain-track interaction part of the model were retained. Baladi and Rohani (5) developed a model for uniform turning motion parallel to the development reported in Reference 3 insofar as the kinematics of the vehicle are concerned. In contrast to Reference 3, however, this model is based on a more comprehensive soil model. In the present paper, the terrain-vehicle model reported in Reference 5 is extended to include nonuniform (transient) motion. In addition, the soil model is modified to include a nonlinear failure envelope describing the shearing strength of the terrain material.

To demonstrate the application of the model, the steering performance of an armored personnel carrier has been predicted and correlated with full-scale test results.

SOIL MODEL

Strength Components

One of the most important properties of soil affecting trafficability is the in situ shear strength of the soil. The shear strength of earth materials varies greatly for different types of soil and is dependent on the confining pressure and time rate of loading (shearing). This dependence, however, is not the same for all soils and varies with respect to two fundamental strength properties of soil: the cohesive and the frictional properties. It has been found experimentally that the shear strength of purely cohesive soils (soils without frictional strength) is independent of the confining stress and is strongly affected by the time rate of shearing. On the other hand, in the case of purely frictional soil (soils without cohesive strength), the shear strength is found to be independent of time rate of loading and is strongly dependent on the confining pressure. In nature, most soils exhibit shearing resistance due to both the frictional and cohesive components. The cohesive and frictional components of strength are usually added together in order to obtain the total shear strength of the material, i.e.,

$$\tau_M = A - M \exp(-N\sigma) \quad (1)$$

where τ_M is the maximum shearing strength of the material,

$C = A - M$ is the cohesive strength of the material corresponding to static loading (very slow rate of deformation), σ is normal stress, and N is a material constant. Equation 1 is shown graphically in Figure 1.

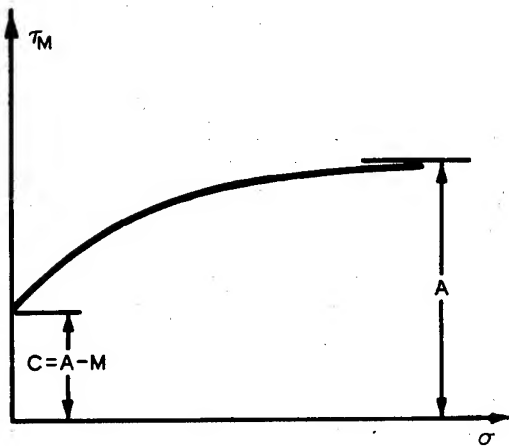


Figure 1. Proposed failure relation for soil.

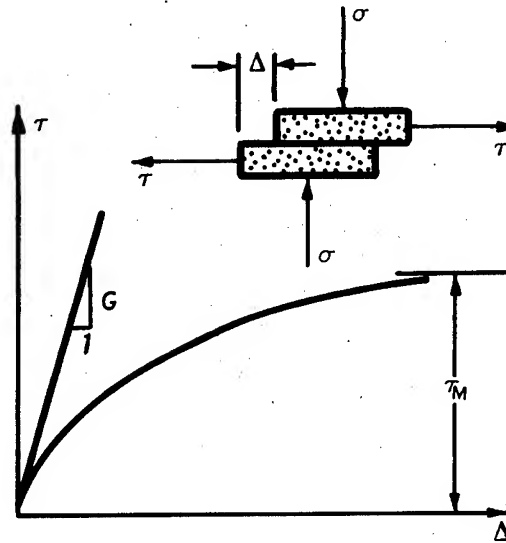


Figure 2. Proposed soil-stress/deformation relation during shearing process.

Effect of Rate of Deformation

As was pointed out previously, the cohesive strength of the material is dependent on the time rate of loading (shearing); i.e., the cohesive component of strength increases with increasing rate of loading. For the range of loading rates associated with the motion of tracked vehicles, the contribution to cohesive strength due to dynamic loading can be expressed as $C_d[1 - \exp(-\Lambda\dot{\Delta})]$, where C_d and Λ are material constants, and $\dot{\Delta}$ is time rate of shearing deformation. In view of the above expression and Equation 1, the dynamic failure criterion takes the following form:

$$\tau_M = A + C_d[1 - \exp(-\Lambda\dot{\Delta})] - M \exp(-N\sigma) \quad (2)$$

Shear Stress-Shear Deformation Relation

Prior to failure, the shear stress-shear deformation characteristics of a variety of soils can be expressed by the following mathematical expression (6):

$$\tau = \frac{G \tau_M \Delta}{\tau_M + G|\Delta|} \quad (3)$$

The behavior of Equation 3 is shown graphically in Figure 2. In Figure 2, τ denotes shearing stress, Δ is shearing deformation, and G is the initial shear stiffness coefficient. In view of Equation 2, the shear stress-shear deformation relation for soil (Equation 3) becomes

$$\tau = \frac{G[A + C_d - C_d \exp(-\Lambda \dot{\Delta}) - M \exp(-N\sigma)] \Delta}{G|\Delta| + A + C_d - C_d \exp(-\Lambda \dot{\Delta}) - M \exp(-N\sigma)} \quad (4)$$

For purely cohesive soils, $N = 0$ and τ is only a function of Δ and $\dot{\Delta}$. For granular material, $M = A$ and C_d is zero, and τ is a function of Δ and σ . For mixed soils exhibiting shearing resistance due to both frictional and cohesive components, τ is dependent on Δ , $\dot{\Delta}$, and σ . In the following section, the equations of motions for a track-laying vehicle during steering are developed using the proposed soil model (Equation 4) in conjunction with track slippage, centrifugal forces, and vehicle characteristics.

DERIVATION OF TERRAIN-VEHICLE MODEL

Boundary Conditions

The geometry of the vehicle and the boundary conditions of the proposed model are shown schematically in Figure 3. The XYZ coordinates are the local coordinate system of which X is always the longitudinal axis of the vehicle and Y is a transverse axis parallel to the ground. These axes intersect at the center of geometry of the vehicle O . The Z axis is a vertical axis passing through the origin O . The center of gravity of the vehicle (CG) lies on the X axis and is displaced by a distance C_X from the origin. The numerical value of C_X is assumed to be positive if CG is displaced forward from the center of geometry of the vehicle. The XY coordinates of the instantaneous center of rotation ICR are $P + C_X$ and R , respectively, where P is the offset. The center of rotation and the radius of the trajectory of the CG are, respectively, CR and R_0 . The height of the center of gravity measured from ground surface is denoted by H . The length of the track-ground contact, the track width, and the tread of the tracks are L , D , and B , respectively. As shown in Figure 3, the components of the inertial forces F_C in X and Y directions are, respectively, F_{CX} and F_{CY} . The weight of the vehicle is W .

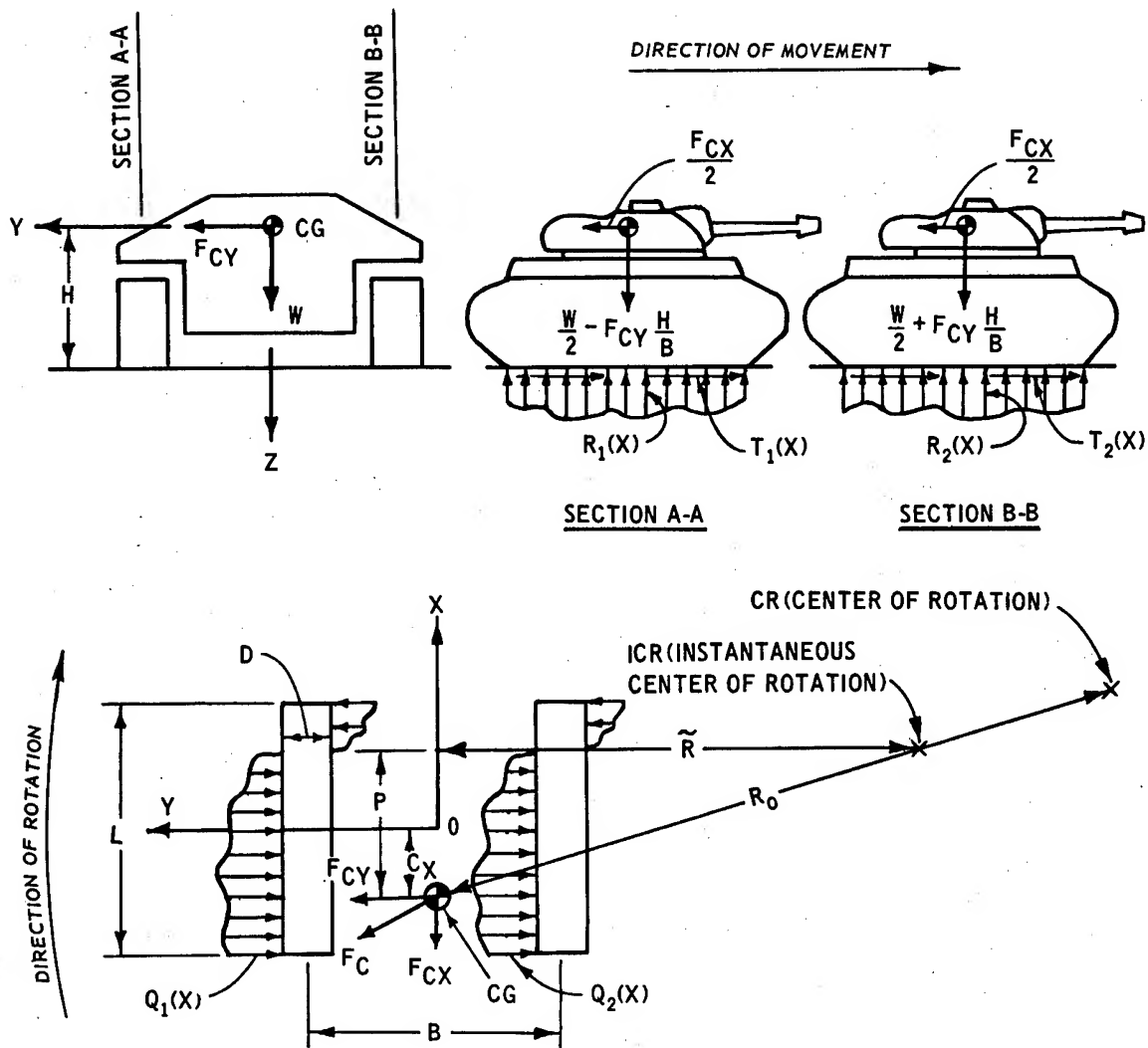


Figure 3. Geometry and boundary conditions of the terrain-vehicle model.

Stress Distribution Along the Tracks

Two types of stress, i.e., normal and shear stresses, exist along the track. As indicated in Figure 3, the normal stresses under the outer and inner tracks are denoted by $R_1(X)$ and $R_2(X)$, respectively. The components of the shear stress in X and Y directions are respectively, $T_1(X)$ and $Q_1(X)$ for the outer track, and $T_2(X)$ and $Q_2(X)$ for the inner track. These stresses are dependent

on the terrain type, vehicle configuration, and speed and turning radius of the vehicle.

The magnitude of normal stresses $R_1(X)$ and $R_2(X)$ can be determined in terms of the components of the inertial force, the track tensions, and the characteristics of the vehicle by considering the balance of vertical stresses and their moments in Figure 3.* Thus:

$$R_1(x) = \frac{W}{dL^2} \left[\frac{1}{2} + 6xc_X - \frac{h}{b} \frac{F_{CY}}{W} - 6hx \frac{F_{CX}}{W} \right] \quad (5)$$

$$R_2(x) = \frac{W}{dL^2} \left[\frac{1}{2} + 6xc_X + \frac{h}{b} \frac{F_{CY}}{W} - 6hx \frac{F_{CX}}{W} \right] \quad (6)$$

where $h = H/L$, $b = B/L$, $d = D/L$, $c_X = C_X/L$, $x = X/L$, $y = Y/L$, and $z = Z/L$.

The components of the shear stress in the X and Y directions along both the outer and inner tracks can be obtained by combining Equations 4, 5, and 6. Thus (it is noted that R_1 and R_2 replace the normal stress σ in Equation 4)

$$T_i(x) = \frac{W}{L^2} \mu \delta_i \left\{ \frac{da + dc_d - dc_d \exp(-\lambda \delta_i) - m \exp[-nr_i(x)]}{\mu \delta_i [d + da + dc_d - dc_d \exp(-\lambda \delta_i) - m \exp[-nr_i(x)]]} \right\} \cos \gamma_i \quad (7)$$

$$Q_i(x) = \frac{W}{L^2} \mu \delta_i \left\{ \frac{da + dc_d - dc_d \exp(-\lambda \delta_i) - m \exp[-nr_i(x)]}{\mu \delta_i [d + da + dc_d - dc_d \exp(-\lambda \delta_i) - m \exp[-nr_i(x)]]} \right\} \sin \gamma_i \quad (8)$$

where $i = 1, 2$; $r_i(x) = dL^2 R_i(x)/W$; $\delta_i = \Delta_i/L$; $\dot{\delta}_i = \dot{\Delta}_i/L$; $\mu = GL^3/W$; $\lambda = \Lambda L$; $a = AL^2/W$; $m = ML^2/W$; $n = NW/L^2$; and $c_d = C_d L^2/W$. The variables γ_1 and γ_2 , in Equations 7 and 8, are the slip angles and can be written as

$$\left. \begin{aligned} \gamma_1 &= \tan^{-1} \frac{X - P - C_X}{C_1} = \tan^{-1} \frac{x - p - c_X}{\xi_1} \\ \gamma_2 &= \tan^{-1} \frac{X - P - C_X}{C_2} = \tan^{-1} \frac{x - p - c_X}{\xi_2} \end{aligned} \right\} \quad (9)$$

* For sake of brevity, the effect of track tension is not included in this paper. The reader is referred to Reference 7 for a complete analysis of track tension and its effect on steering performance of tracked vehicles.

where $\xi_1 = C_1/L$, $\xi_2 = C_2/L$, and $p = P/L$. The parameter C_1 is the distance between the instantaneous center of rotation of the outer track and its axis of symmetry, and C_2 is the distance between the instantaneous center of rotation of the inner track and its axis of symmetry.

In order to use Equations 7-9, the track slip velocities and displacements (i.e., Δ_1 , Δ_2 , and Δ_3), and the inertial forces F_{CX} and F_{CY} , have to be determined.

Kinematics of the Vehicle

A tracked vehicle in transient motion is shown schematically in Figure 4. The XYZ coordinates are the local coordinate systems that are fixed with respect to the moving vehicle (also see Figure 3). The origin 0 of this coordinate system stays, for all time, at a distance C_X from the center of gravity of the vehicle. The $\Psi\Phi$ coordinate system is fixed on level ground, and its origin coincides with the center of gravity at time zero. The vehicle can maneuver on the $\Psi\Phi$ plane and the displacements of the center of gravity of the vehicle from this reference frame are $\Psi(t)$ and $\Phi(t)$.

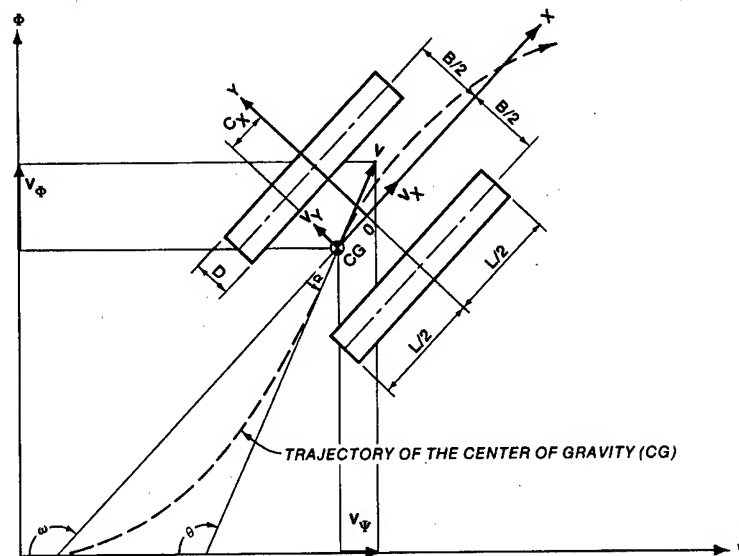


Figure 4. Tracked vehicle in transient motion.

The velocities v_X and v_Y (relative to the origin of the $\Psi\Phi$ coordinate system) as well as the velocities v_Ψ and v_Φ are related to the instantaneous velocity v of the CG by

$$v = \sqrt{v_X^2 + v_Y^2} = \sqrt{v_\Psi^2 + v_\Phi^2} \quad (10)$$

The side-slip angle α , which is the angle between the velocity vector v and the longitudinal X axis of the vehicle, is related to the velocities v_X and v_Y as

$$\alpha = \tan^{-1} \frac{v_Y}{v_X}, \quad \frac{d\alpha}{dt} = \left(v_X \frac{dv_Y}{dt} - v_Y \frac{dv_X}{dt} \right) / v^2 \quad (11)$$

The yaw angle ω and the directional angle θ are related to α as

$$\theta = \omega - \alpha, \quad \frac{d\theta}{dt} = \frac{d\omega}{dt} - \frac{d\alpha}{dt} \quad (12)$$

Substitution of Equation 11 into Equation 12 leads to

$$\frac{d\theta}{dt} = \frac{d\omega}{dt} - \left(v_X \frac{dv_Y}{dt} - v_Y \frac{dv_X}{dt} \right) / v^2 \quad (13)$$

The radius of curvature of the trajectory of the center of gravity (i.e., the distance between CR and CG, Figure 3) is

$$R_o = v \frac{d\theta}{dt} = \frac{v^3}{v^2 \frac{d\omega}{dt} - v_X \frac{dv_Y}{dt} + v_Y \frac{dv_X}{dt}} \quad (14)$$

The coordinates of the trajectory of the center of gravity of the vehicle can be written as

$$\left. \begin{aligned} \Psi(t) &= -\int_0^t v \cos \theta \, dt \\ \Phi(t) &= \int_0^t v \sin \theta \, dt \end{aligned} \right\} \quad (15)$$

The coordinates of the instantaneous center of rotation (ICR) of the hull in the XY systems (X_I , Y_I) and the instantaneous radius of curvature are (Figure 3)

$$\left. \begin{aligned} X_I &= P + C_X = v_Y / \frac{d\omega}{dt} + C_X \\ Y_I &= \tilde{R} = v_X \frac{d\omega}{dt} \\ R_I &= \sqrt{\tilde{R}^2 + P^2} \end{aligned} \right\} \quad (16)$$

and

Track Slip Velocity and Displacement

Assume that v_{s1} ($v_{s1} = \dot{\Delta}_1$) and v_{s2} ($v_{s2} = \dot{\Delta}_2$) are the slip velocities of geometrically similar points of the outer track and the inner track, respectively. The X and Y components of these velocities can be shown to be

$$\left. \begin{aligned} v_{sX1} &= C_1 \frac{d\omega}{dt} = \xi_1 L \frac{d\omega}{dt} \\ v_{sY1} &= (X - P - C_X) \frac{d\omega}{dt} = L(x - c_X) \frac{d\omega}{dt} - v_Y \end{aligned} \right\} \text{For the outer track} \quad (17)$$

$$\left. \begin{aligned} v_{sX2} &= C_2 \frac{d\omega}{dt} = \xi_2 L \frac{d\omega}{dt} \\ v_{sY2} &= v_{sY1} \end{aligned} \right\} \text{For the inner track} \quad (18)$$

The angular velocity $d\omega/dt$ and \tilde{R} can be written as

$$\left. \begin{aligned} \frac{d\omega}{dt} &= \frac{1}{bL} (v_{X1} - v_{sX1} - v_{X2} + v_{sX2}) \\ \tilde{R} &= \frac{1}{2 \frac{d\omega}{dt}} (v_{X1} - v_{sX1} + v_{X2} - v_{sX2}) \end{aligned} \right\} \quad (19)$$

where v_{X1} = the velocity of the outer track in X direction
 v_{X2} = the velocity of the inner track in X direction

The ratio of v_{X1} and v_{X2} is defined as the steering ratio ϵ .
 Thus,

$$\epsilon = v_{X1}/v_{X2} \quad (20)$$

Substitution of Equations 16 and 20 into Equation 19 leads to

$$v_{sX1} = \epsilon v_{X2} - \left(v_X + \frac{bL}{2} \frac{d\omega}{dt} \right) \text{For the outer track} \quad (21)$$

$$v_{sX2} = v_{X2} - \left(v_X - \frac{bL}{2} \frac{d\omega}{dt} \right) \text{For the inner track} \quad (22)$$

Comparison between Equations 21 and 22 and Equations 17 and 18 results in

$$\xi_1 = (\epsilon v_{X2} - v_X) / \left(L \frac{d\omega}{dt} \right) - \frac{b}{2} \quad (23)$$

$$\xi_2 = (v_{X2} - v_X) / \left(L \frac{d\omega}{dt} \right) + \frac{b}{2} \quad (24)$$

The slip velocities and displacements of the outer and inner tracks can be obtained from Equations 17, 18, 21, and 22. Thus,

$$\frac{v_{s1}}{\sqrt{Lg}} = \sqrt{\frac{L}{g}} \frac{d\omega}{dt} \sqrt{\xi_1^2 + \left[(x - c_X) - \frac{v_Y}{L} \frac{d\omega}{dt} \right]^2} \quad (25)$$

$$\frac{v_{s2}}{\sqrt{Lg}} = \sqrt{\frac{L}{g}} \frac{d\omega}{dt} \sqrt{\xi_2^2 + \left[(x - c_X) - \frac{v_Y}{L} \frac{d\omega}{dt} \right]^2} \quad (26)$$

$$\frac{\Delta_1}{L} = \int_0^{t_1} \frac{v_{s1}}{L} dt + \frac{\Delta_{I1}}{L}, \quad \frac{\Delta_2}{L} = \int_0^{t_2} \frac{v_{s2}}{L} dt + \frac{\Delta_{I2}}{L} \quad (27)$$

where $t_1 = (L/2 - X)/v_{X1}$

$t_2 = (L/2 - X)/v_{X2}$

Δ_{I1} = initial displacement of the outer track

Δ_{I2} = initial displacement of the inner track

The balance of forces and moments dictates that these initial displacements be numerically equal to $L\delta$ (δ is the coefficient of rolling resistance which must be measured experimentally for each soil type and each vehicle).

Inertial Forces

The X and Y components of the inertial force can be shown to be (7).

$$F_{CX} = \frac{W}{g} a_x = \frac{W}{g} \left(\frac{dv_X}{dt} + v_Y \frac{d\omega}{dt} \right), \quad F_{CY} = \frac{W}{g} \left(\frac{dv_Y}{dt} - v_X \frac{d\omega}{dt} \right) \quad (28)$$

The Rolling Resistance

The rolling resistance is a function of terrain type, vehicle speed, track condition, etc. Therefore, rolling resistance should be measured for every specific condition. In this formulation, however, the rolling resistance is assumed to be proportional to normal load. Thus,

$$R_s = \frac{W}{dL^2} \oint \int_{-\frac{1}{2}}^{\frac{1}{2}} [r_1(x) + r_2(x)] dx \quad (29)$$

Equations of Motion

Steerability and stability of tracked vehicles depend on the dynamic balance between all forces and moments applied on the vehicle. According to Figure 4, the following three equations govern the motion of the vehicle:

$$\int_{-\frac{1}{2}}^{\frac{1}{2}} [t_1(x) + t_2(x)] dx - \oint \int_{-\frac{1}{2}}^{\frac{1}{2}} [r_1(x) + r_2(x)] dx = f_{CX} \quad (30)$$

$$\int_{-\frac{1}{2}}^{\frac{1}{2}} [q_1(x) + q_2(x)] dx = f_{CY} \quad (31)$$

$$\begin{aligned} \int_{-\frac{1}{2}}^{\frac{1}{2}} [q_1(x) + q_2(x)] (x - c_X) dx + \frac{b}{2} \int_{-\frac{1}{2}}^{\frac{1}{2}} [t_1(x) - t_2(x)] dx \\ + \frac{b}{2} \oint \int_{-\frac{1}{2}}^{\frac{1}{2}} [r_2(x) - r_1(x)] dx = \frac{I_z}{LW} \frac{d^2 \omega}{dt^2} \end{aligned} \quad (32)$$

where $t_1(x) = dL^2 T_1(x)/W$, $t_2(x) = dL^2 T_2(x)/W$, $q_1(x) = dL^2 Q_1(x)/W$, $q_2(x) = dL^2 Q_2(x)/W$, $f_{CX} = F_{CX}/W$, and $f_{CY} = F_{CY}/W$

and I_z = mass moment of inertia about an axis passing through the center^z of gravity of the vehicle and parallel to the Z axis (Figure 3). Equations 30 through 32 with the aid of Equations 7 through 29 constitute three equations that involve three unknowns. The three unknowns are either v_X , v_Y , and $d\omega/dt$ or ξ_1 , ξ_2 , and p . In order to obtain a complete solution for either of the two sets of unknowns, one of the following driving conditions must be specified:

(a) time history of the steering ratio $\epsilon(t)$ and the initial speed of the vehicle, (b) time history of the velocity of the individual tracks $v_{x1}(t)$ and $v_{x2}(t)$ and the initial speed of the vehicle, (c) time history of the velocity of the vehicle $v(t)$ and the trajectory of motion, (d) time history of the velocity of the vehicle and a constant value of steering ratio ϵ , or (e) the trajectory of motion and a determination of the maximum velocity time history at which the vehicle can traverse the specified trajectory. A computer program called AGIL was developed to solve Equations 30 through 32 using Newton's iteration technique. In addition, this computer program has the capability of calculating the power requirements at the sprockets (7).

Correlation with Test Results

In order to determine the accuracy and range of application of the terrain-vehicle model, a series of steering tests was conducted on several different terrains with various soil strengths in the vicinity of Vicksburg, Mississippi. The tracked vehicle used for these experiments is an armored personnel vehicle with characteristics: $W = 18,000$ lb, $L = 105$ in., $H_2 = 35.7$ in., $D = 15$ in., $B = 90$ in., $I_z = 92,000$ lb-in.-sec² and $C_x = 0$. Each experiment involved steering the vehicle in a circular path, by first accelerating the vehicle to a maximum speed (controlled by either the available power or the stability conditions of the vehicle) and then continue turning with a more or less constant speed. Data collected during each test consisted of time histories of (a) the inner and outer track velocities, (b) the speed of the vehicle, (c) the turning radius, and (d) the power requirement. In addition, for each terrain several in situ direct shear tests were conducted to characterize the soil and to determine the parameters of the soil model. The results of these steering tests are presently being analyzed for correlation and comparison with the terrain-vehicle model predictions. The result of one of the tests which was recently analyzed and correlated with model prediction is presented in this paper. This particular test was conducted on a soft clay soil with characteristics: $G = 200$ psi/in., $A = 5$ psi, $M = 4.06$ psi, $N = 0.22$ 1/psi, $C_d = 0.61$ psi, and $\Lambda = 3.68$ sec/in. The coefficient of rolling resistance for the vehicle was measured experimentally and has a value $\phi = 0.2$.

To correlate the test data with model predictions, the measured time histories of the inner and outer track velocities were used to drive the model. For these specified driving conditions, the time histories of the vehicle speed and power requirements were then predicted and compared with the corresponding field measurements. Figures 5a and 5b depict the time histories of the inner and outer track

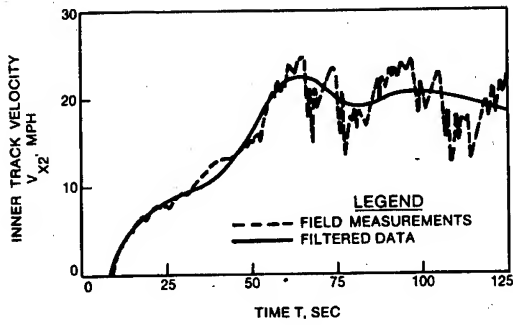


Figure 5a. Inner track velocity-time history.

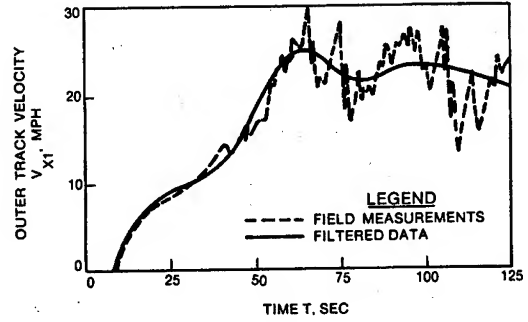


Figure 5b. Outer track velocity-time history.

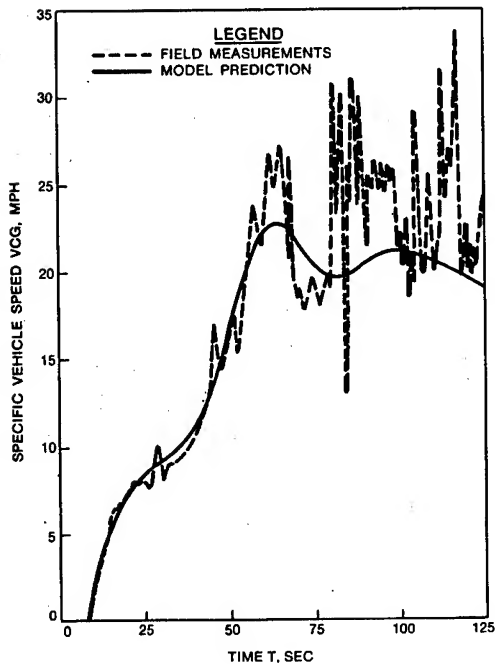


Figure 5c. Vehicle velocity-time history, field measurement versus model prediction.

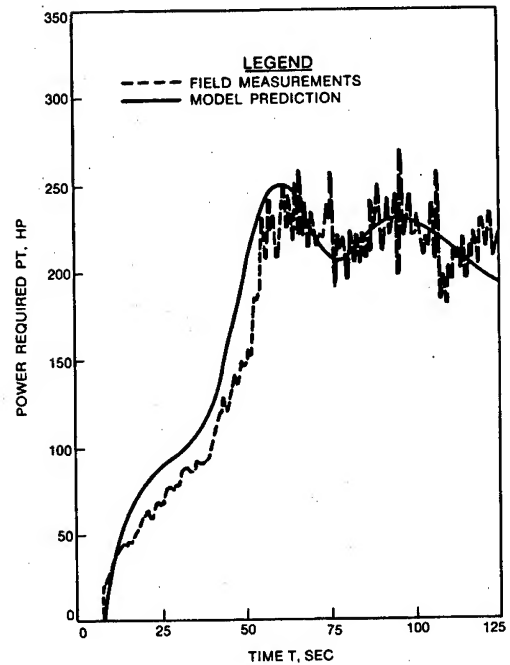


Figure 5d. Total power-time history, field measurement versus model prediction.

velocities, respectively. As observed from these figures, the actual field measurements are quite noisy during the steady state portion of the steering (i.e., for times greater than approximately 60 sec). These high frequency oscillations are believed to be mostly due to instrumentation and must be filtered out. The filtered records are also shown in Figures 5a and 5b and are simply "best" fit curves to the field measurements satisfying the condition that the total area under both curves should be equal. These filtered track velocity-time histories were used as input to drive the terrain-vehicle model.

Comparisons of the predicted time histories of the vehicle speed and power requirements during steering with the corresponding field measurements are shown in Figures 5c and 5d. Similar to Figures 5a and 5b, the field measurements are quite noisy during the steady state steering. The predicted results, of course, do not manifest these oscillations because of the filtering of the input data. The degree of correlation of the predicted and measured results, however, is quite good, indicating that the modeling of the overall interaction between the soil and the track is physically reasonable.

ACKNOWLEDGEMENT

The work reported herein was conducted at the U.S. Army Engineer Waterways Experiment Station under the sponsorship of the Office, Chief of Engineers, Department of the Army, as part of Project 4A161102AT24, "Effect of Terrain and Climate on Army Material."

The authors are grateful to Mr. Clifford J. Nuttall, Jr., for providing valuable insight during the course of this study, and acknowledge the efforts of Mr. Donald E. Barnes for assisting in the numerical calculations.

REFERENCES

1. Bekker, M. B. 1963. The Theory of Land Locomotion, The University of Michigan Press, Ann Arbor, Mich.
2. Hayashi, I. 1975. "Practical Analysis of Tracked Vehicle Steering Depending on Longitudinal Track Slippage," Proceedings, The International Society for Terrain Vehicle Systems Conference, Vol 2, p 493.
3. Kitano, M. and Jyozaki, H. 1976. "A Theoretical Analysis of Steerability of Tracked Vehicles," Journal of Terramechanics, The International Society for Terrain Vehicle Systems, Vol 13, No. 4, pp 241-258.

*BALADI & ROHANI

4. Kitano, M. and Kuma, M. 1977. "An Analysis of Horizontal Plane Motion of Tracked Vehicles," Journal of Terramechanics, The International Society for Terrain Vehicle Systems, Vol 14, No. 4, pp 221-225.
5. Baladi, G. Y. and Rohani, B. 1978. "A Mathematical Model of Terrain-Vehicle Interaction for Predicting the Steering Performance of Track-Laying Vehicles," Proceedings of the 6th International Conference of the International Society for Terrain-Vehicle Systems, Vienna, Austria.
6. Kondner, R. L. "Hyperbolic Stress-Strain Response: Cohesive Soils," Journal, Soil Mechanics and Foundations Division, American Society of Civil Engineers, Vol 89, No. SM1, Feb 1963, pp 115-143.
7. Baladi, G. Y. and Rohani, B. 1979. "A Terrain-Vehicle Interaction Model for Analysis of Steering Performance of Track-Laying Vehicles," Technical Report GL-79-6, U.S. Army Engineer Waterways Experiment Station, CE, Vicksburg, Miss.

*BALLATO & LUKASZEK

COMBAT HARDENED COMMUNICATIONS: HIGH PRECISION FREQUENCY CONTROL
USING RESONATORS IMMUNE TO ACCELERATION AND STRESS FIELDS (U)

*ARTHUR BALLATO, PhD
THEODORE LUKASZEK, Mr.

USA Electronics Technology & Devices Laboratory, ERADCOM
Fort Monmouth, NJ 07703

INTRODUCTION

Exceedingly stringent frequency control requirements follow from the performance specifications of the latest generations of command, control, communications, & intelligence (C³I) systems, and systems for navigation and position location. Unfortunately, the crystal resonators, which are the stabilizing elements in the reference oscillators required in such systems, are frequency sensitive to acceleration fields produced by the dynamic environments surrounding land- and air- mobile use. These resonators are also susceptible to frequency shifts due to transient temperature variations and static stresses transmitted by their electrode and mounting systems. The acceleration effects lead to degradation of the short-term frequency stability, while the stress component contributes primarily to long-term aging and to distortions of the frequency-temperature behavior of the oscillator.

This paper describes quartz resonators that provide simultaneous compensation against both dynamic and static conditions, and that are compensated, moreover, against rapid temperature transients encountered in fast-warmup oscillators for manpack use.

The acceleration problem is minimized by utilizing a novel monolithic compound vibrator having a racemic structure to nullify the frequency shifts. Static compensation is achieved by means of unique lateral mounting contours, located so that nonlinear elastic constants cancel. Compensation of thermal transients comes about by use of a special, doubly rotated orientation of cut. We show that all

three features may be realized at one time to yield a highly stable quartz resonator immune to accelerations in any direction, and to boundary stresses and thermal transients. No additional electronics are required, nor are increases in size, weight, and power requirements necessary.

The resulting units are applicable to a wide variety of high precision frequency control uses, such as oscillators in shock/vibration environments (tanks, helicopters), sensors, position location (GPS), and collision avoidance systems. An examination of these various systems uses, or derivations of the frequency control requirements from performance specifications in any detail are not permitted due to space limitations.

The stringency of the frequency control requirements imposed by time-ordered secure operation in combat environments is such that they could not be met by conventional crystal resonators. The effects of vibration alone on conventional resonators would degrade their performance to the point where the unthinkable would be necessary: tanks and helicopters would have to turn off their motors in order to communicate!

Fortunately, recent breakthroughs, mentioned briefly above, are available to permit the requirements to be met. These developments are consistent with the chronology of progress in timekeeping accuracy shown in Figure 1 (1). The entry marked "quartz crystal" is representative of a laboratory standard of conventional design, using an AT cut crystal, and protected to the greatest possible extent from environmental disturbances. Its fractional frequency stability is about 5 parts in 10^9 . Contrast this with a requirement of the Global Positioning System (GPS) calling for 100 meter range accuracy. To hold this accuracy for one day requires a stability of $100\text{m}/(3 \times 10^8 \text{ m/s} \times 86,400\text{s}) \approx 4 \times 10^{-12}$, or about a factor of one thousand and better than the conventional laboratory standard of some years ago.

A parallel to GPS, as well as a contrast, is furnished by another entry on Figure 1: the marine chronometer built by John Harrison in 1759 (2). Its purpose was to determine longitude at sea by accurately keeping London time for comparison with local time determined on board ship from measurements of the sun or stars. Pendula-controlled escapements (Huygens, 1660) had proved useless at sea except in a dead calm. Harrison improvised new techniques to reduce the influences of ship motion and other environmental effects, and won the £20,000 prize offered in 1714 for a device that would determine the longitude within 30 minutes of arc ($\sim 56 \text{ km}$). The 56 km of

Harrison's time has shrunk to 100 meters in the GPS program (10 meters in the secure mode), but the environmental factors that must be overcome now are much the same as those he had to contend with: primarily temperature and motional effects.

We have mentioned GPS because of the obvious and interesting comparison with work more than two centuries old; it must be emphasized, however, that the environmental hardening features to be addressed below apply with equal cogency to other systems such as JTIDS, NIS, SINGARS, SEEK TALK, etc.

In Figure 2 is shown an idealized frequency-time plot of a conventional quartz oscillator subjected to disturbances of various kinds. At time t_1 an abrupt temperature change produces a sharp frequency transient, followed by an asymptotic approach to a new frequency characteristic of the new temperature. A similar effect occurs between t_5 and t_6 where power shut-off followed by oscillator restart leads to mis-frequency operation that is of concern for fast-warmup manpack use. Between t_2 and t_3 , at t_4 and again at t_7 , are shown the effects of vibration, shock, and tip-over (reversal of crystal attitude with respect to the gravity field), respectively. These three effects are due to acceleration forces, and are not further distinguished in the sequel. Superimposed upon the collection of disturbances seen in Figure 2 is the long-term aging slope. The principal contributors to this are the slow change in electrode stress due to relaxation of the metal films deposited on the resonator plate surfaces and the relaxation of the mounting and support system; these will be discussed further below, as will be the fine-structure of the frequency-time curve labeled "short-term instability".

STATIC AND DYNAMIC TEMPERATURE EFFECTS

The standard frequency control element commonly used is the AT cut quartz resonator, a singly rotated plate, shown in Figure 3, with $\theta \sim 35^\circ$. Its traditional popularity is due to ease of manufacture coupled with a zero temperature coefficient (ZTC) of frequency at room temperature. A family of doubly rotated cuts of quartz possesses a ZTC; these are more difficult to manufacture because of the second angle ϕ . The locus of ZTC as function of θ and ϕ is shown for quasi-static temperature changes in Figure 3 (3). The cut marked "SC" on the locus at $\phi \sim 22^\circ$, $\theta \sim 34^\circ$ denotes the newly developed "stress compensated" resonator (4,5,6). Because the double rotation leads to manufacturing problems, growth of cultured quartz bars incorporating the first (ϕ) rotation has been undertaken (7) with the resulting bar shown schematically in Figure 4; SC cuts may be produced from these bars with a single cutting operation.

Figure 5 gives the frequency versus temperature (f-T) behavior for cuts located near the SC value when the temperature change is made very slowly. The inflection temperature is 96°C, and for small temperature departures about this value the frequency changes expected are small. The conventional AT cut has a similar cubic f-T shape, but with inflection temperature of 26°C. Operation of an AT cut in an oven with millikelvin stability leads to the conclusion, based on the static f-T curve, that frequency stabilities in the 10^{-15} range are possible, where, in fact, the observed stabilities are orders of magnitude worse. Figure 6 gives an example, showing the elliptical orbits that result from sinusoidal temperature variations having periods of 8 & 16 hours, and 1 week, superimposed on the static f-T curve (8). For the SC cut, this dynamic thermal stress effect is absent; it arises from nonlinear elastic constants which cancel at the SC orientation. The implications for fast-warmup operation are demonstrated in Figure 7 where AT and SC responses to oven warmup are shown. Note the logarithmic ordinate scale. The SC is on frequency in a time dictated solely by the oven; the AT transient effect persists much longer. Use of doubly rotated SC cuts effectively eliminates the transients that occur at times t_1 and t_5 - t_6 in Figure 2.

STATIC FORCE EFFECTS

Static and quasi-static edge forces occur due to relaxation of the mounting and support structure holding the resonator and because of differential thermal expansion coefficients between the quartz and mount. These forces produce frequency shifts and distort the shape of the f-T curves of Figure 5. For diametric force pairs, shown on the right-hand illustration in Figure 8, the effect is quantified by a coefficient K_f that is directly proportional to the observed frequency shift $\Delta f/f$ and inversely proportional to the applied force F (9,10). K_f is a function of the plate azimuth ψ . Altitude contours of $K_f(\psi)$ are plotted in Figure 9 for doubly rotated plates having orientations along the upper ZTC locus in Figure 3. It is seen that for each cut (value of ϕ), azimuths (ψ) exist such that $K_f(\psi)$ becomes zero. At these angles of ψ edge forces do not produce frequency shifts. Mounting resonator plates at these points, however, produces large edge stresses with consequent susceptibility to breakage, especially in high shock applications such as REMBASS.

We have shown experimentally (11) that collinear forces acting upon chords trimmed from the circular resonator plate normal to the $K_f=0$ locations also produce no frequency shift. The case for the AT cut is seen in Figure 10. Forces acting at paired locations (1).. ..(6), for example, do not produce deviations in vibrator resonance

frequency. Superposition has also been shown to hold for multiple force-pairs, with the result that the entire chordal edge may be used for mounting, and the stress levels appreciably reduced without affecting frequency stability. As shown in Figure 11, which is again for the AT cut, the remaining circular boundaries may be trimmed to produce a rhomboid shape. The $K_f=0$ angles of ψ vary with the cut of quartz used, as shown in Figure 9; the rhomboidal outline required will also change. The outline for the $\phi=10^\circ$ cut is given in Figure 12. Also shown on this figure are the four mounting edges, the "key-hole" electrode pattern normally used, and the offset of the electrode tabs from the crystallographic axis for the purpose of reducing undesired resonance modes. The asymmetrical rhomboid shape is characteristic of doubly rotated cuts; the AT cut of Figure 11 is symmetrical because X_1 is a two-fold axis of symmetry in quartz. For the SC cut ($\phi=21.9^\circ$), the rhomboid shape, by fortunate coincidence, degenerates to a square (or rectangular) outline, as shown in Figure 13. All four edges are used for mounting, which may be extremely rigid. The plate itself must be cut with respect to the crystallographic axes at an angle of 36.8° as shown, in order to possess the static force insensitivity property. SC cuts with square outline are self-aligning when placed in ceramic flatpack holders, a feature that leads to reduced cost of manufacture.

DYNAMIC FORCE EFFECTS

The dynamic force effects illustrated in Figure 2 at times t_2 - t_3 , t_4 and t_7 are subsumed under the phrase "acceleration effects". They may range from the shocks of cannon launching (20,000 g's) to vibrations due to microseisms of a few micro-g's. The typical level of sensitivity of AT cut resonators is 10^{-9} per g - seemingly a small number for many applications (the average shock level for trucks is a few g's), until contrasted with the typical value given in the introduction for GPS, or indeed with the accuracies that are quoted for any of the modern C³I systems.

Experimental data provided by Valdois (12) for AT cut quartz is shown in Figure 14. It is seen that the frequency shift depends upon the direction of the acceleration field, and, more importantly, is a linear function of the acceleration G , changing sign with reversal of G . This observation is the key to producing acceleration-immune resonators, for if two resonators can be paired so that their respective crystallographic axes are antiparallel, then the frequency shifts induced by an acceleration field in any arbitrary direction will be opposite in the two resonators and thus cancel in the combination (13). The required antiparallelism can be produced by using

enantiomorphous pairs of resonators (right- and left-handed crystals), a feature that very fortunately exists in quartz. In Figure 15 are shown stacked crystal plate resonator combinations configured for parallel (left drawing) and series electrical connection. Each stack consists of a left-handed and a right-handed, singly rotated (e.g. AT) cut, identical except for the handedness, bonded together to form a composite resonator requiring no increase in size, weight and power for its operation over a single resonator of thickness equal to twice that of either racemic half of the stack. The plates are drawn with rectangular outline for clarity; in practice they would be of rhomboid contour as discussed above.

Modeling of the physics of these structures is best accomplished by means of equivalent electrical networks. These have never taken into account the handedness of the crystal, so we have developed the network of Figure 16 to accomplish this. The transmission line represents the acoustic waves in the thickness mode plate; the mechanical ports CD and EF account for the mechanical boundary conditions (traction free surface = short circuit); the electrical port AB is connected to the oscillator; the mechanism of piezoelectric transduction is represented by the transformers located at the plate surfaces to produce tractions. Placement of the transformer polarity dots characterizes the crystal handedness for the purposes required for simulations. The effect of acceleration is simply incorporated into the transmission line parameters. Using two networks of different handedness, the structures of Figure 15 may be accurately modeled.

Doubly rotated (e.g. SC cut) plates represent an additional degree of difficulty when considering stacked resonators - or seemingly so. These resonators exhibit the same type of behavior as seen in Figure 14, but whereas the symmetry of AT-cut quartz leads to simple vibratory motion (thickness-shear with motion along the X axis), doubly rotated plates such as the SC cut have particle motion inclined to the crystal axes. It at first appears that stacking two plates would produce mode interference, but this is not so. In Figure 17 is shown on the left a left-handed plate with motion taken to be along the major diagonal OA; the center illustration is the situation that obtains with the mirror-image right-hand mate. The right-handed plate has motion along OB. When the right-handed plate is properly rotated as shown in the right-most illustration, the particle motion during vibration is seen to be parallel to that of OA in the left-most illustration, so that stacking can take place with respective crystallographic axes antiparallel, as is necessary for acceleration compensation.

It should be emphasized that the compensation holds for any direction of the acceleration field, and no preferred orientation of the composite stack is necessary.

Networks for left- and right-handed plates are shown joined in Figure 18 to represent a composite resonator. The electrical terminals are connected either in parallel or series to achieve the structures of Figure 15. Inductors represent electrode mass loading on the crystal surfaces, and the 1:-1 mechanical transformer models the reversal of crystal axes to form the acceleration-immune stack.

COMPENSATION FOR ADDITIONAL EFFECTS

It was mentioned earlier that the long-term aging slope seen in Figure 2 arose largely from electrode stress relief. In Figure 19 is shown the graphs of the static force coefficient $K_f(\psi)$ versus ψ for the three thickness modes in the SC cut. For the "c mode" (the slower shear mode having the thermal transient compensation property described above), it may be shown (14) that the area under the curve of $K_f(\psi)$ vs ψ is zero. Because superposition holds for point force-pairs, one may show the direct proportionality between the film stress coefficient K as portrayed on the left of Figure 8, and calculated in Figure 20, and the angle-average coefficient $\langle K_f \rangle$; this relation is also given in Figure 20. Calculating $\langle K_f \rangle$ for the cuts on the upper ZTC locus of Figure 3 and comparing with experiment gives the results of Figure 21, where it is seen that the film stress effect produces no frequency change, and consequent aging, for the SC cut.

Cancellation of the nonlinear elastic constants responsible for thermal and mechanical effects in quartz resonators at the SC orientation is additionally responsible for lessening the phase noise contribution to the short-term instability seen in Figure 2.

CONCLUSION

We have made available quartz resonator configurations frequency compensated for acceleration, static forces, thermal transients and other effects encountered in combat, and more benign environments. These units are comprised of:

- doubly rotated, SC-cut orientations
- rhomboidal contours for mounting
- stacked enantiomorphous pairs

combined in a rugged unit of exceptional stability requiring no increases in size, weight or power consumption. Anticipated oscillator

*BALLATO & LUKASZEK

stabilities with these resonators for the 1985-1990 time-frame are:

stability	1 sec	10^{-14}
	24 hours	10^{-13}
	5 years	10^{-10}
acceleration sensitivity < $10^{-12}/g$.		

REFERENCES

1. J.A. Barnes, "Basic Concepts of Precise Time and Frequency", in Time and Frequency: Theory and Fundamentals, (B.E. Blair, ed.), NBS Monograph 140, May 1974. U.S. Government Printing Office, Washington, DC 20402, pp. 1-40.
2. L.A. Brown, "The Longitude", in The World of Mathematics, (J.R. Newman, ed.). Simon and Schuster, New York, 1956. Volume 2, pp. 780-819.
3. R. Bechmann, A. Ballato, and T.J. Lukaszek, "Higher-Order Temperature Coefficients of the Elastic Stiffnesses and Compliances of Alpha-Quartz", Proc. IRE, Vol. 50, August 1962, pp. 1812-1822.
4. E.P. EerNisse, "Calculations on the Stress Compensated (SC-cut) Quartz Resonator", Proc. 30th Annual Frequency Control Symposium, US Army Electronics Command, Fort Monmouth, NJ 07703, June 1976, pp. 8-11.
5. J.A. Kusters, "Transient Thermal Compensation for Quartz Resonators", IEEE Trans. Sonics Ultrason., Vol. SU-23, July 1976, pp. 273-276.
6. A. Ballato, "Doubly Rotated Thickness Mode Plate Vibrators", in Physical Acoustics: Principles and Methods (W.P. Mason and R.N. Thurston, eds.) Vol. 13, Chap. 5. Academic Press, New York. 1977, pp. 115-181.
7. Sawyer Research Products Inc., Eastlake, OH 44094; Motorola Inc., Carlisle, PA 17013.
8. A. Ballato, "Static and Dynamic Behavior of Quartz Resonators", IEEE Trans. Sonics Ultrason., Vol. SU-26, July 1979, pp. 299-306.
9. A. Ballato, "Force-Frequency Compensation Applied to Four-Point Mounting of AT-Cut Resonators", IEEE Trans. Sonics Ultrason., Vol. SU-25, July 1978, pp. 223-226.

*BALLATO & LUKASZEK

10. E.P. EerNisse, T. Lukaszek, and A. Ballato, "Variational Calculation of Force-Frequency Constants of Doubly Rotated Quartz Resonators", IEEE Trans. Sonics Ultrason., Vol. SU-25, May 1978, pp. 132-138.
11. T.J. Lukaszek and A. Ballato, "Resonators for Severe Environments", Proc. 33rd Annual Frequency Control Symposium, US Army Electronics Command, Fort Monmouth, NJ 07703, May-June 1979, pp. 311-321.
12. M. Valdois, "Étude de l'Influence d'Accélérations sur les Propriétés des Résonateurs à Quartz", Thèse, Université de Besançon, June 1974, 73 pp.
13. A. Ballato, "Resonators Compensated for Acceleration Fields", Proc. 33rd Annual Frequency Control Symposium, US Army Electronics Command, Fort Monmouth, NJ 07703, May-June 1979, pp. 322-336.
14. A. Ballato, E.P. EerNisse, and T.J. Lukaszek, "Experimental Verification of Stress Compensation in the SC Cut", Proc. IEEE Ultrason. Symposium, September 1978, pp. 144-147.

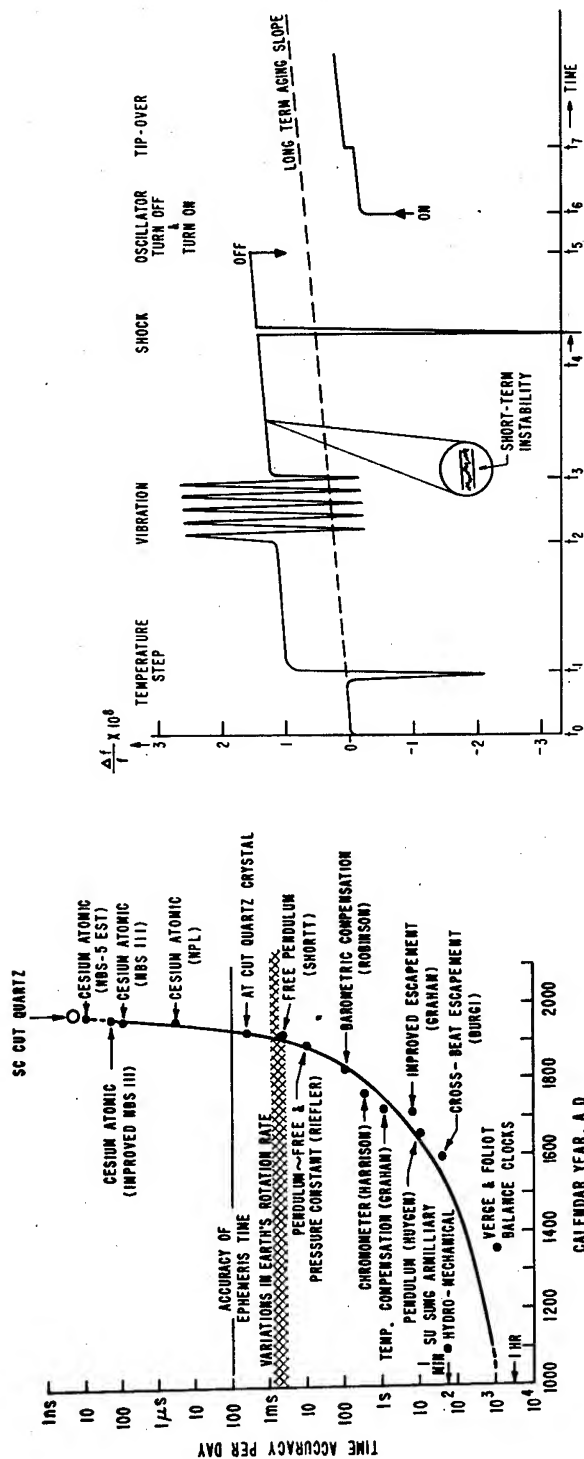


Fig. 1 - Progress in Timekeeping Accuracy

Fig. 2 - Idealized Frequency-Time Behavior of a Quartz Oscillator

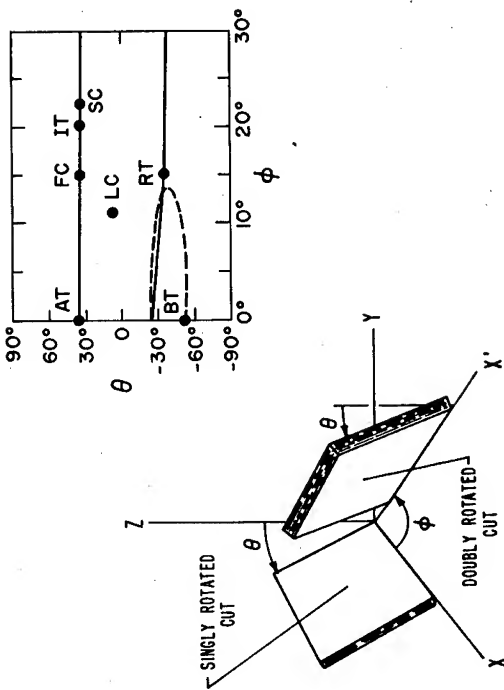


Fig. 3 - Rotated Quartz Cuts and Temperature Coefficients

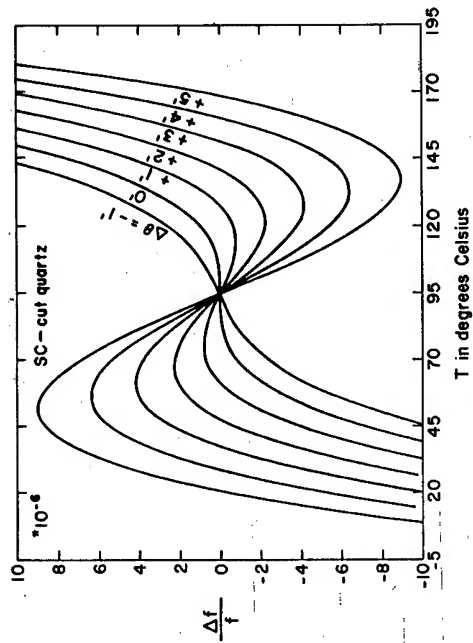


Fig. 5 - Static Frequency-Temperature-Angle Plots

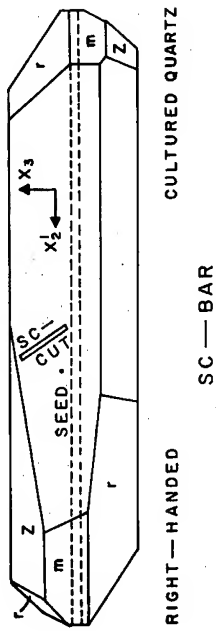


Fig. 4 - Quartz Bar Showing SC Cut

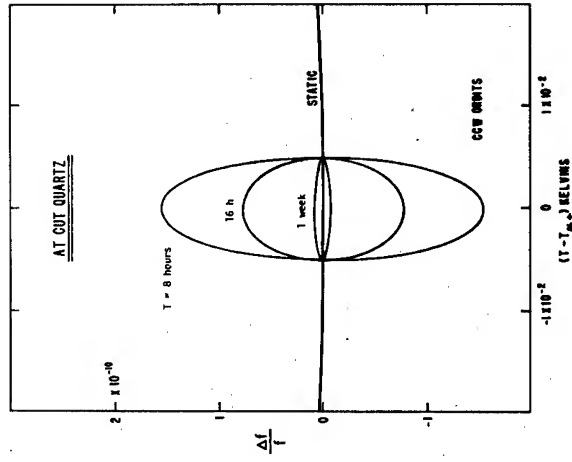


Fig. 6 - Dynamic Frequency-Temperature Behavior

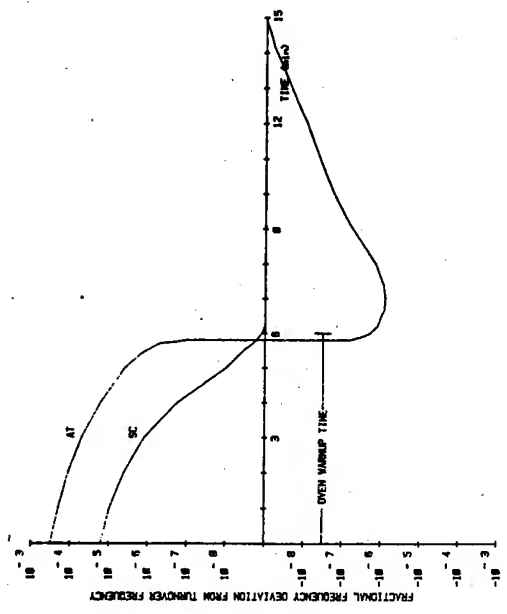


Fig. 7 - Warmup Characteristics of AT and SC Resonators

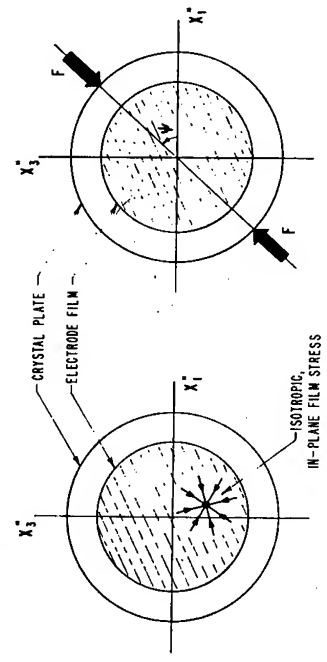


Fig. 8 - Schematics of In-plane Film Stress and Static Edge Force

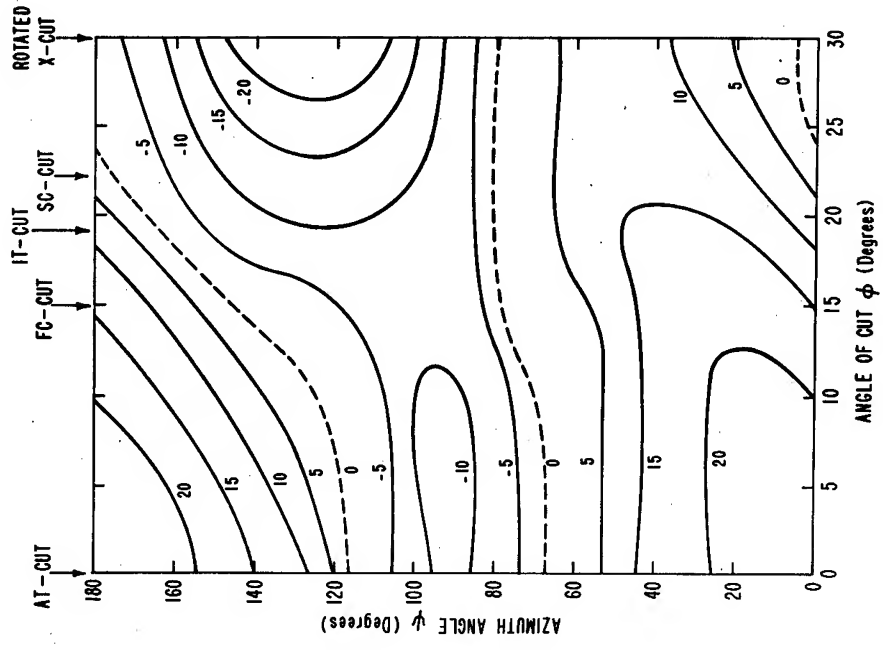


Fig. 9 - Contours of Force Coefficient K_f : Mode a (10^{-15} m . s / N)

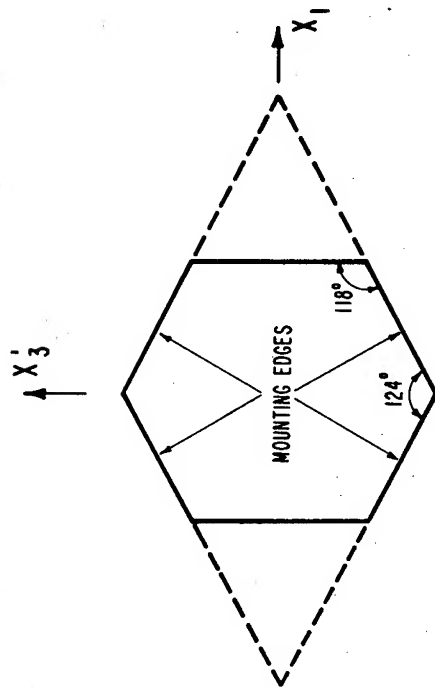


Fig. 11 - AT Cut Polygon for Minimum Force-Frequency Effect

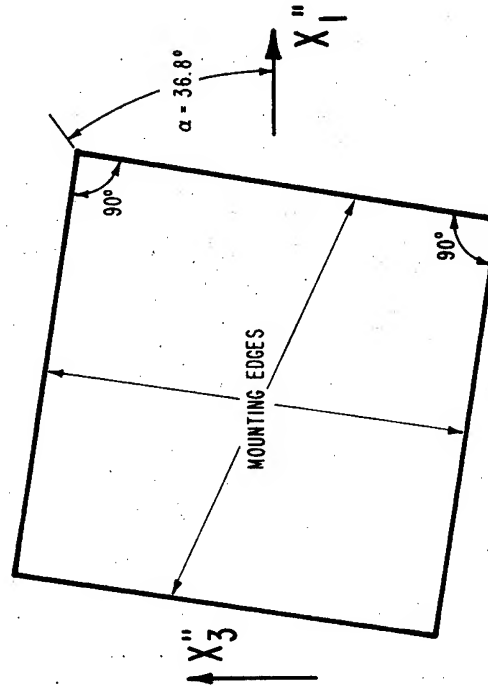


Fig. 13 - SC Cut Polygon for Minimum Force-Frequency Effect

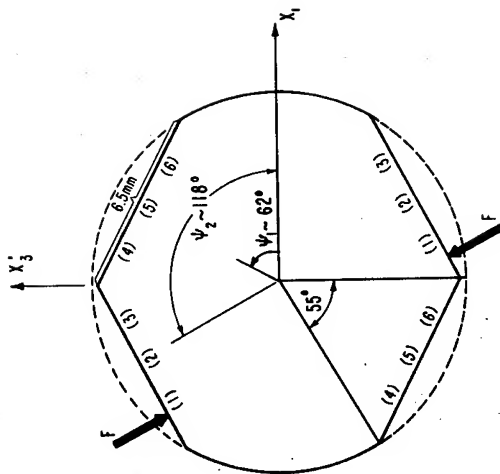


Fig. 10 - Rhomboid Configuration Construction

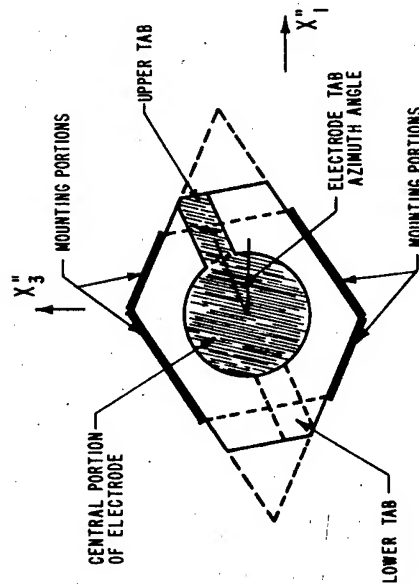


Fig. 12 - Polygonal Resonator with Electrode/Mounting Tabs

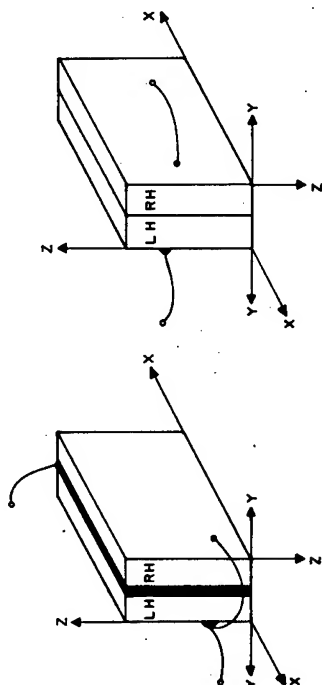


Fig. 15 - Stacked-Crystal Enantiomorphs for Parallel and Series Connections

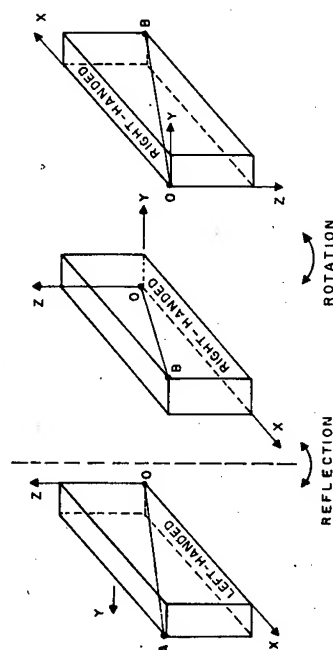


Fig. 17 - Doubly Rotated Enantiomorphs for Stacking

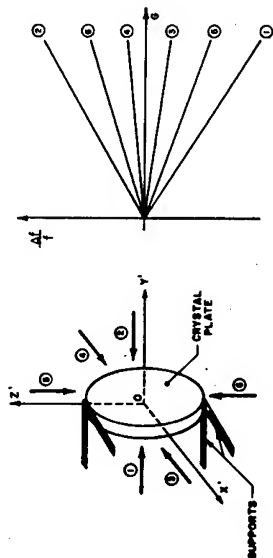


Fig. 14 - Experimental Acceleration-Frequency Behavior

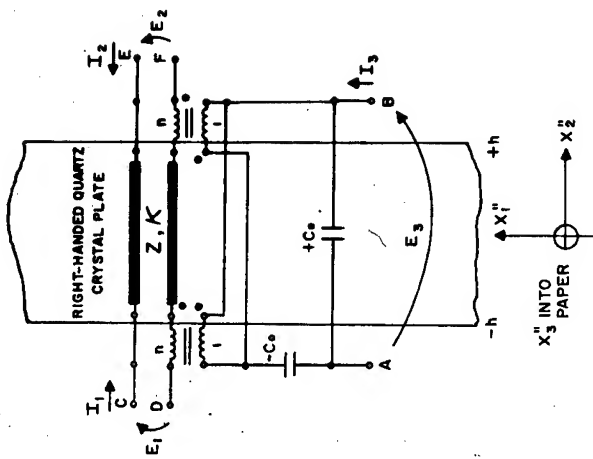


Fig. 16 - Single Resonator Transmission Line Network

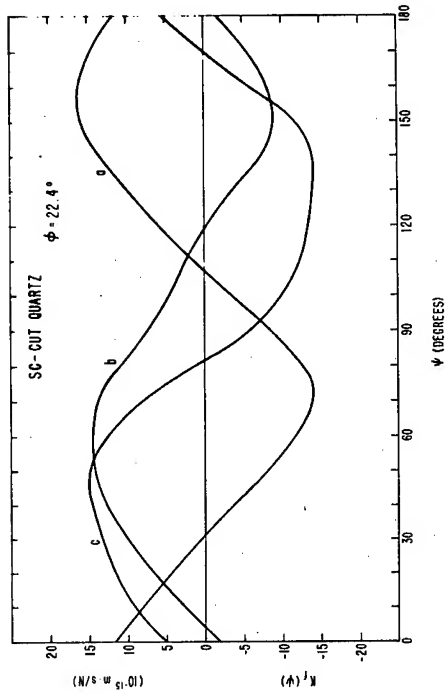


Fig. 19 - SC Cut Force Coefficients: a, b, & c Modes

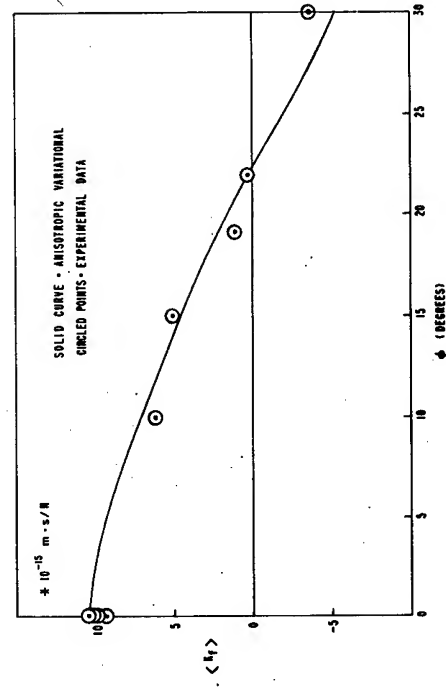


Fig. 21 - Average Edge Force Coefficients vs Angle of Cut

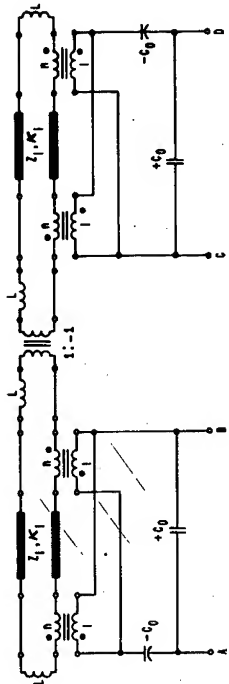


Fig. 18 - Stacked-Crystal Transmission Line Equivalent Network

FILM STRESS: $K = \frac{\Delta F}{F} / \bar{T}_0$

$\bar{T}_0 = \frac{2}{\pi} \cdot (F/2H \cdot D)$

EDGE FORCE: $K_F(\psi) = \frac{(2H \cdot D/F)}{H_0} \cdot \frac{\Delta F(\psi)}{F}$

$\langle K_F \rangle = \frac{1}{\pi} \int_0^\pi K_F(\psi) d\psi$

$$\langle K_F \rangle = \frac{2}{\pi} \cdot \frac{K}{N_0}$$

Fig. 20 - Relation between Film Stress and Average Edge Force Coefficients

*BANDERET, STOKES, FRANCESCONI, KOWAL

SIMULATED, SUSTAINED-COMBAT OPERATIONS IN THE FIELD ARTILLERY
FIRE DIRECTION CENTER(FDC): A MODEL FOR EVALUATING
BIOMEDICAL INDICES (U)

*LOUIS E. BANDERET, Ph.D.

JAMES W. STOKES, LTC, MC.

RALPH FRANCESCONI, Ph.D.

DENNIS KOWAL, CPT, MSC.

US ARMY RESEARCH INSTITUTE OF ENVIRONMENTAL MEDICINE
NATICK, MA 01760

When military biomedical research addresses practical problems, the scientist must evaluate if biological and behavioral phenomena have real-world consequences for military planners and users. The military scientist must scale and translate his findings into a suitable framework so military planners can anticipate how such consequences will degrade (or sustain) the operational effectiveness of military personnel. In evaluating conditions which affect human performance, the scientific literature (1-5) indicates the importance of task, personnel, and organizational variables. These include: task complexity, feedback, pacing, level of training, intrinsic task interest, experience, motivation, and social factors. Such variables are considered critical determinants of performance capability under a variety of conditions. Furthermore, in both modern industrial society and in the Armed Forces tasks are increasingly organized around teams rather than individuals. In the military community, concerns are often expressed as to the generality and predictive validity of past studies which have not included variables inherent in many military tasks.

To address these issues and provide a framework for communicating research results to the military community, the Field Artillery fire direction center (FDC) was selected by the US Army Research Institute of Environmental Medicine (USARIEM) as a "model" team for study. It was postulated that these issues could be addressed in a laboratory simulation which would use actual Army teams performing their normal functions. This would permit control and replication of environmental and situational conditions and measurement and correlation of mission effectiveness, behavior and biological processes (3,4). This approach capitalized on pre-existing training, professional pride, social support and military task organization. Such factors are critical in the study of group task performance, the contribution of individual performance to system (team) output (3,4) and physiological and psychological responses to stress (5).

*BANDERET, STOKES, FRANCESCONI, KOWAL

The FDC team seemed well-suited for scientific study and laboratory simulation since 1) FDCs are common and critical to successful ground combat operations, 2) FDC teams are located immediately behind the FEBA and are exposed to most extent stresses, 3) FDCs include tasks common to other command/control and communication elements, 4) Detailed scenarios can be developed to provide calibrated performance demands, 5) FDC tasks provide quantifiable measures of both individual and team performance, 6) The compactness of FDCs allows collection of a wide range of biomedical and psychosocial data, 7) Many variables which influence performance are inherent in FDCs, and 8) FDCs provide a performance paradigm with operational criteria, recognized by the military community, with which various data arrays can be correlated.

FDC TASKS & ORGANIZATION

In the Field Artillery, the FDC is a service center which receives requests from various groups who require artillery shells to hit target areas. These targets are typically kilometers away and out of view of the guns. In the US Army (Artillery battery level) a team of 5 to 7 individuals process these requests. Non-computerized FDCs have existed since World War I and have evolved to insure that performance is robust to adverse conditions. Roles, tasks, communication sequences and content, error detection and resolution capabilities, information readback procedures, etc. are well specified and practiced. To understand variations in system output, individual task contributions and interactions can be analyzed (6,7). Many FDC tasks are similar to classical performance tests. Sometimes FDC tasks are embedded in contexts which limit interpretation, but they can be compared with the scientific literature.

METHODS

STANDARDIZATION OF TASK DEMANDS

Much precision of conventional laboratory paradigms was applied to the complex mission demands of the Field Artillery to document FDC performance and to reduce extraneous variance. This methodology was incorporated into a detailed script ("scenario") of radio messages which provided the task demands, as well as the supporting documents, e.g. map overlays and unit SOP. The scenario represented a tactical battle played on 1:50,000 scale maps and followed current doctrine for the light infantry with armored cavalry opposing a well-equipped screening force. Tasks demands were communicated to the FDC over three simulated radio nets; other roleplayers provided the telephone communications of the nearby gun crews and controlled the guns' sound effects.

To permit performance assessment with time the scenario was organized into equivalent 6 h epochs of mission demands. In each 6 h, events of differing importance, complexity, and urgency, requiring different individual and team responses, recurred frequently to permit event pooling for analysis of

*BANDERET, STOKES, FRANCESCONI, KOWAL

performance data. Some mission demands included: 1) Unplanned Missions -- Calls for Artillery fires on a target which were often followed by several subsequent adjustments, i.e., repetitions with small variations. 2) Preplanning -- These tasks were initiated by the receipt of encoded preplanned target messages. All team members were involved, but for most delayed responses were required. 3) Prioritizing -- At any time, 2 of 16 preplanned targets were designated as having priority to emphasize that an especially rapid and accurate response might be required on these targets. 4) On-call Missions -- These demands were calls for Artillery fires on preplanned targets. Typically, they occurred at least 15 min after receipt of encoded preplanned target messages. 5) Revising -- These initial 12 preplanned targets were encountered at the beginning of each 6 h epoch. Task demands differed somewhat from those of preplanning. The targets were preplotted on the chart sheets so the chart operators did not have to plot them nor did the radio operator have to decode them. 6) Updating -- Updating should have occurred about 150 min into each epoch. It was to improve ballistic correction factors on 12 preplanned targets. 7) Multiple Mission Sequences -- Periods of intense fire mission activity included: unplanned missions, on-call missions, non-standard missions, adjusts and shifts. 8) Lulls -- These were two 10-12 min intervals in which no new mission demands were sent to the FDC although irrelevant radio traffic continued. These events created a standardized setting, embedded among other demands, where social interactions might be more likely to occur. Such intervals could also be used to complete prior preplanning activities.

EXPERIMENTAL DESIGNS

Two designs were utilized. They differed in number of sustained challenges and their durations. Design I had a single 86 h operational challenge; whereas, Design II had two 38 h challenges separated by a 34 h rest interval. Both designs had identical, pre-challenge familiarization and training trials. Design I was essentially an "open ended" challenge since 86 h was judged to be beyond the limits for sleep deprived subjects to perform such cognitive tasks. Design II was to evaluate the FDC model in a repeated-measures design.

SUBJECTS & SIMULATION FACILITIES

The 5-man, FDC teams were males aged 18-24 and fully informed volunteers from two battalions of the 82nd Airborne Division. These teams used manual fire direction procedures exclusively, without the assistance of digital computers. Manual FDC equipment was assembled in a tent inside a 6.1 x 2.7 x 2.4 m climate-controlled chamber at USARIEM. Temperature was maintained 20-24°C, relative humidity 35-50%, and lighting was superior to field FDCs for continuous videotaping. Each subject wore a microphone and transmitter for individual voice reproduction, a physiological cassette recorder, wrist- activity sensor, ECG electrodes and, in some instances, EEG electrodes. Speech from each field radio, the FDC-gun telephone line, and from each FDC team member, as well as a time code, were recorded on separate channels of an audio recorder for post-study analyses.

SIMULATION PROCEDURES

All teams received a 5 h orientation followed by 3 days of simulation training (8 h/day) at the scenario work load used subsequently. Teams 1 and 4 then underwent a single challenge which they were told could run 86 h. Teams 2 and 3 underwent two 38 h challenges separated by a 34 h rest; they were told each challenge would run 36 to 42 h. All subjects were instructed not to set shifts or withdraw to sleep. Teams 1 and 4 received no instructions about job rotations; whereas, Teams 2 and 3 were instructed not to rotate jobs. In the simulation, each team was challenged by the scenario demands described previously. Performance-contingent, positive and negative feedback for accuracy and timeliness were given to the FDC from simulation roleplayers. During the simulations, FDC teams did not physically move the FDC, erect camouflage, or dig emplacements. All operational challenges began at 7 a.m. Every 6 h during a simulated tactical move, approximately 48 min were spent in non-operational, administrative activities. Self-report questionnaires were administered, urine and sometimes blood samples were collected, electrodes and instrumentation were maintained by "field medics" and meals were eaten.

PERFORMANCE ASSESSMENT

Performance indices were derived for system (team) performance. Post-study, accuracy and timeliness data were scored from audio recordings. Accuracy deviations, i.e. errors, were defined as the algebraic difference (in mils) between each FDC team's firing data and the correct solution as computed manually by the Department of Gunnery, USAFAS. Timeliness was the latency between mission input and the team's output.

INTERACTION ANALYSES

Interaction Process Analysis (IPA) by R.F. Bales assesses the quality of interactions occurring in a group (8). The FDC studies provided a unique opportunity to evaluate this non-invasive technique in small Army teams during acute exposure to situational stress and fatigue and to relate IPA trends to operational changes. In IPA, all verbal utterances are divided into communication units (CU). A CU is a group of sounds, words, gestures, etc. that conveys a single thought or action. Each CU is assigned to 1 of 12 categories based on the predominant quality of the interaction.

The FDC teams differed from many of the groups studied by Bales. Since the FDC's highly specified tasks, roles, and task organization generated many task communications which were standard in content and their time sequencing, an additional category, i.e., Task SOP, was specified for the FDC analyses. This category was for those CUs which were formal communications in the standard, sequential process of computing and transmitting ballistic data. Task SOP CUs only included standard communications about task or mission.

In the analyses, each team member's vocalizations during the two 12-minute lulls were transcribed from audio records and arrayed in parallel against a common time line. All verbal utterances were divided into CUs and all Task

*BANDERET, STOKES, FRANCESCONI, KOWAL

SOP CUs were identified. All remaining CUs, i.e. All Other CUs, were identified and classified into one of Bales's categories. The sender and receiver for each CU were also specified. All information was formatted and encoded for automatic data processing. Video records were viewed prior to scoring each lull.

In the data reduction, group functions were computed for Teams 1, 2 & 4 (Team 3 is in progress). Each function represented the contributions of all 5 members. All CUs were categorized as Task SOP or All Others. To show the relative proportion of each a ratio was calculated:

$$\text{Task-Oriented Ratio} = \frac{\text{No. Task SOP CUs}}{\text{No. All Others CUs}}$$

RESULTS & DISCUSSION

OVERVIEW

Other investigators collaborated in the design and conduct of the study, but only selected data obtained by USARIEM investigators will be presented. The teams differed substantially in organizational style, social history, prior experience, and mastery of the simulated mission demands. Generally, Teams 1 and 4 showed less initial mastery and greater performance changes over time (Design I). All teams responded to the competitive challenges and became quite involved with the simulation (6,9).

Team 1 withdrew from the study at 7 a.m. after 48 h. A chart operator appeared especially sleepy after 42 h, choose to terminate, and the officer decided that the team should leave together. Team 4 withdrew voluntarily at 4 a.m. after 45 h. The younger enlisted personnel had little field experience and were very fatigued. The officer was also fatigued from his continuous supervision but persevered until his sergeant prompted him for the decision to stop. Both teams made several errors which "endangered" friendly troops; they had also become deficient in their preplanning and prioritizing. Team 2 showed some deterioration in the second challenge; three team members had slept very poorly the previous evening. Team 3 completed both 38 h trials with little performance deterioration. After 6 h of the second trial, a chart operator terminated; the remaining four continued. They had slept well in the interim.

SYSTEM OUTPUT: ACCURACY

For all teams, accuracy of firing data for unplanned missions was generally maintained even until termination. In contrast, accuracy of firing data for pre-planned targets fired upon during on-call missions was less for all teams. Accuracy deteriorated with time in Teams 1 and 4; they showed increased 7-14 mil errors. These usually involved omissions of correction factors in speed-accuracy tradeoffs. Generating preplanned target data required increased processing compared to unplanned missions. In addition, negative feedback criteria for on-call missions were more demanding, e.g.

*BANDERET, STOKES, FRANCESCONI, KOWAL

20- 60 vs 60-180 sec. Teams 2 and 3 showed some variability in on-call mission accuracy; no progressive deterioration was evident.

SYSTEM OUTPUT: TIMELINESS

Although accuracy for unplanned missions was generally maintained, timeliness suffered in all but one team. Latencies for the subsequent adjustments increased more than 35% from initial values (approximately 30 sec) during sustained operations for Teams 1, 2, and 4. The within- team differences between initial and final 6-h performance latencies were statistically significant ($p < 0.05$ for Teams 1 and 2; $p < 0.01$ for Team 4). Video review confirmed that speed was sometimes sacrificed for accuracy through increased individual latencies and double-check procedures. Such increased latencies have tactical significance since they would result in reduced effectiveness of Artillery fires on battlefield targets. This would increase FDC and battery vulnerability.

Timeliness, as well as accuracy, for on-call missions against preplanned targets suffered in Teams 1 and 4. Initial median latencies, e.g. 8-10 sec, increased $>400\%$ after 42 h in Team 1 and 50-400% after 30 h in Team 4 ($p < 0.01$). Teams 2 and 3 responses to on-call missions were less varied; Team 2's responses increased 30-60% from 18 to 30 h of the second challenge ($p < 0.05$).

In responding to on-call missions against preplanned targets during the multiple mission sequences, Teams 2 and 3 showed some increased variability and latencies. In contrast, the quick responses to be achieved by preplanning deteriorated markedly in Teams 1 and 4 in those very situations where responsiveness was tactically most crucial. For Team 4, the 300-700% increases began after 24 h but recovered slightly after 36 h. In Team 1, increased latencies (40-300%) occurred from 6-30 h. After approximately 45 h, (0215 and 0400 a.m.), latencies increased 10-12 times from initial values. It is evident a median response >300 sec to deliver what Artillery doctrine requires in <20 sec was a marked change in operational efficiency. Such delays would have serious consequences in combat where rapid delivery of preplanned Artillery fires is essential to suppress hostile, wire-guided weapons.

Preplanning is intended to generate firing data for a preplanned target and send it to the guns before an on-call mission occurs. If preplanning was achieved, response latencies were minimal. If not, data computation was required "on the spot", increased latencies resulted, and teams were more likely to make errors in haste (or through deliberate omissions) as they attempted to respond quickly.

SYSTEMS OUTPUT: PREPLANNING & PRIORITIZING LATENCIES

Examining the efficiency of preplanned target processing activities, (i.e. preplanning, prioritizing, revising, and updating) suggests how the observed differences in team effectiveness in responding to on-call mission events occurred. It has the advantage of assessing risk of serious mission failure for the total population of preplanned targets. Operationally, preplanning required processing target messages and sending the firing data for each target to the

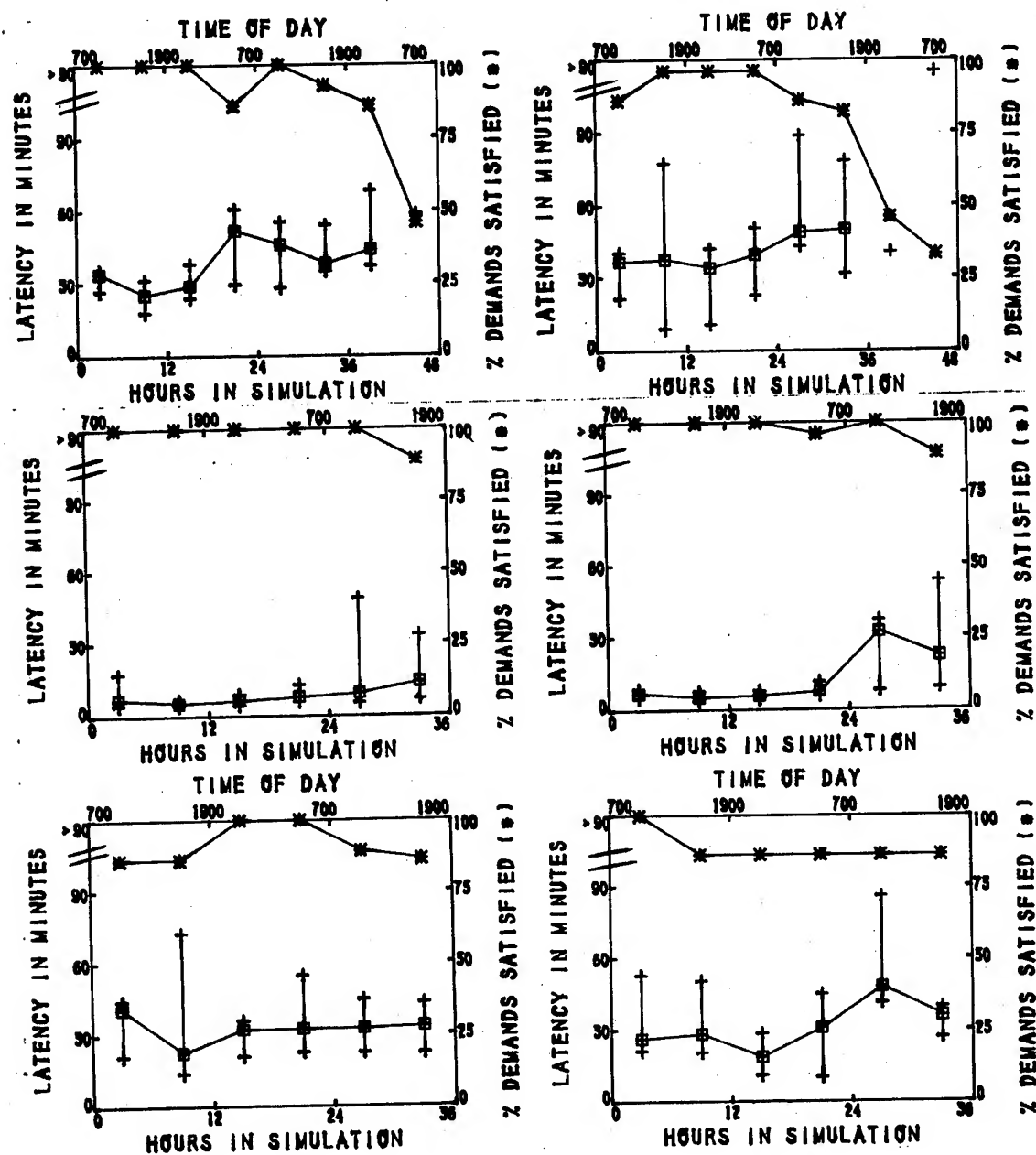


Figure 1. Preplanning latencies for Teams 1 (top left), 4 (top right), 2 (middle) and 3 (bottom) are shown as a function of h in the simulation. The squares, with lower and upper points, indicate the 50, 25, and 75th percentiles, respectively. Values plotted above the break on each left ordinate were >90 min. Also shown are the percent preplanning demands satisfied for each 6 h.

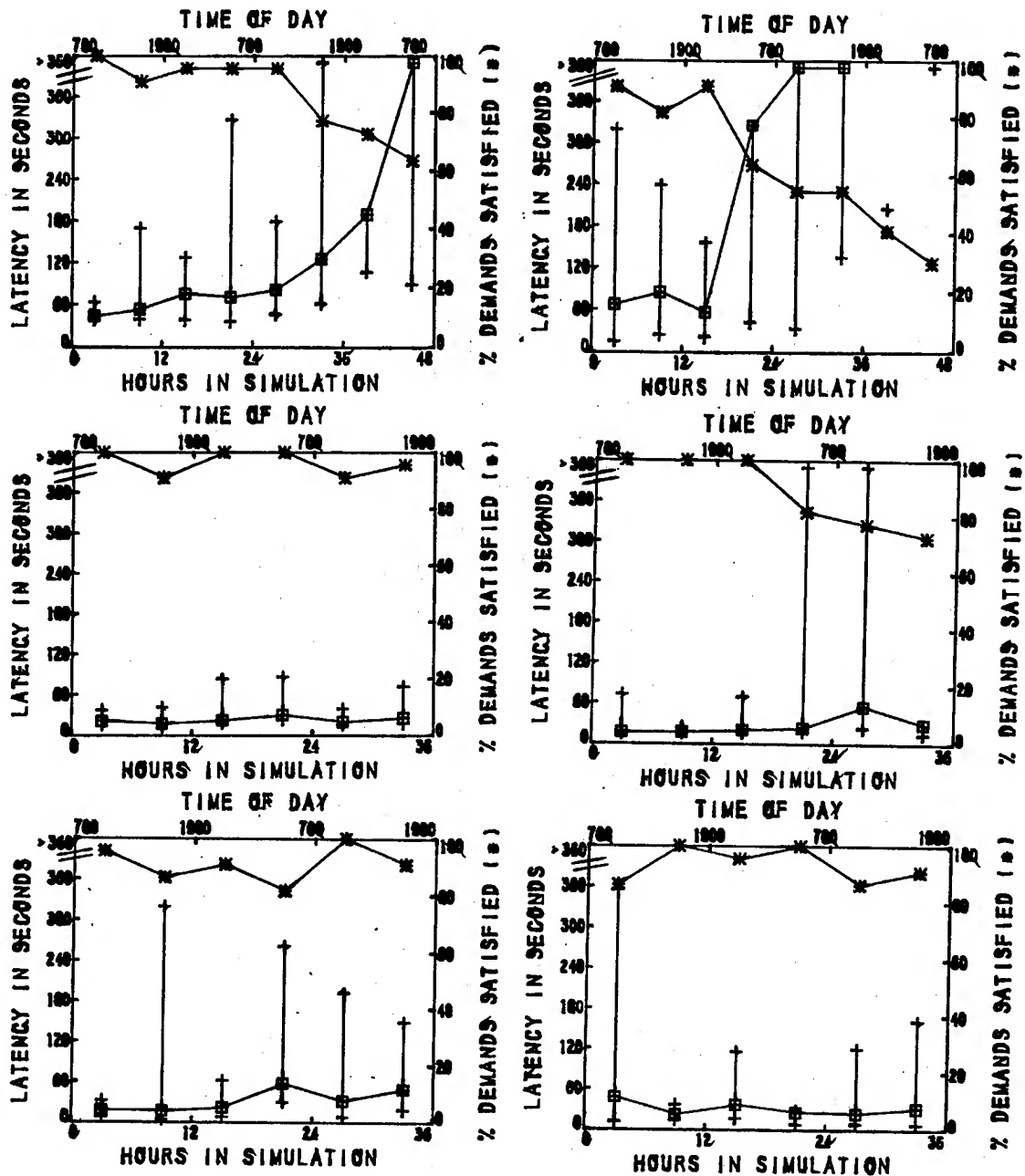


Figure 2. Prioritizing latencies for Teams 1 (top left), 4 (top right), 2 (middle) and 3 (bottom) are shown as a function of h in the simulation. The squares, with lower and upper points, indicate the 50, 25, and 75th percentiles, respectively. Values plotted above the break on each left ordinate were >360 sec. Also shown are the percent of prioritizing demands satisfied each 6 h.

guns as soon as possible. Preplanning involved all members; each had to complete his work on a target before another could proceed (serial processing). Hence, individual tasks were delayed. Team members had to schedule time to complete these tasks amidst "breaks" and other demands. Unless completed quickly, other scenario events would inevitably interrupt processing.

Preplanning latencies for the four teams are shown in Figure 1. Teams 1 and 4 showed increased latencies after 18-24 h; these increases were 30-70% greater than initial values. After 36 h performance was characterized predominantly by a failure to process several preplanned targets. Team 2 was very proficient; their latencies were approximately 25% those of other teams. Latencies of teams 2 and 3 did not change during the first 38 h challenge, although processing for team 2 was more varied after 24 h. During the second challenge of Teams 2 and 3 processing times increased after 24 h. Hence, the observed loss of effectiveness in responding to on-call missions (single and multiple missions sequences) in Teams 1 and 4 resulted from failure to preprocess data. Decreased accuracy resulted largely from speed-accuracy trade-offs or from lapses due to haste.

Figure 2 shows the prioritizing aspect of preplanned target processing. This task involved specifying to the guns which preplanned target was of greatest importance to the forward observer and calling ballistic data to the guns, if not communicated previously. Prioritizing emphasized some preplanned targets as being more important than others. Teams 1 and 4 showed increased latencies for prioritizing. Changes, 200 to 600% greater than initial values, were evident after 18 h in both teams. Teams 2 and 3 were more proficient and stable in their prioritizing, although some periods were characterized by increased variability. Consistent with the preplanning trend, Team 2's prioritizing was also impaired after 24 h in the second challenge.

The percent of demand satisfied decreased with time in Teams 1,2 (second challenge), and 4. This occurred even though preplanned data were usually at the guns when a target was specified as priority by the role player. Specifically, for Teams 1, 2, 3, and 4 data were already at the guns 87, 94, 96, and 67% of the times when each sergeant failed to specify a target as priority. Although in these circumstances each sergeant only needed to announce the priority target number to the guns, all but one increasingly failed to do so. We suspect attention to detail and involvement increased markedly with time as teams attempted to keep current on their preplanning. Such demands made it more likely that responsible members did not hear the information when it came over the radio or they subsequently forgot it. Additional analyses will document why this critical performance was not maintained.

SYSTEM OUTPUT: UNPROCESSED PREPLANNED TARGET DEMANDS

The quantity of work never done may be more useful as an index of team capacity and performance efficiency than increased errors or latencies. Table I highlights differences between the 4 teams on preplanned target activities. Entries show the percentage of various preplanned target activities,

*BANDERET, STOKES, FRANCESCONI, KOWAL

as well as percentage of total target processing never completed. Several trends are evident. Total target processing was less adequate at 36 h for Teams 1 and 4 (Design I) than for Teams 2 and 3 (Design II); revising and updating contributed predominately to this trend. Although one cannot rule out level of training, experience, and organizational variables these data suggest the uncertainties, expectancies, and demands of an 86 h challenge took an earlier and greater toll on Teams 1 and 4. This observation is further supported by trends in the biochemical data (6). Secondly, Team 4, the least proficient and experienced team, was the team which demonstrated the least adequate total target processing. Lastly, updating was the preplanning target activity most frequently not completed by all four teams. It is interesting that updating was the only preplanned target activity done by a single team member.

Table I. Percentages of various uncompleted, preplanned target tasks. Values are shown for the 4 Teams studied for the initial 36 h in the simulation. Second challenge, 36 h comparisons are also shown for Teams 2 & 3. For Teams 1 & 4, 48 h comparisons are also indicated. Team 4's values for 45-48 h (interval after Team 4's termination) were extrapolated.

TEAM	PREPLANNING	PRIORITIZING	REVISING	UPDATING	% TOTAL TARGET PROCESSING NEVER COMPLETED
INITIAL 36 HOUR COMPARISON (CHALLENGE 1)					
1	4	8	4	100	29
2	2	5	0	12	5
3	9	10	0	36	14
4	9	27	28	86	38
SECOND 36 HOUR COMPARISON (CHALLENGE 2)					
2	2	11	0	11	6
3	12	7	0	19	10
INITIAL 48 HOUR COMPARISON					
1	11	14	14	95	34
4	19	34	49	88	48

INTERACTION ANALYSES

Figure 3 shows total CUs, i.e. all team members' CUs during the two lulls, each 6 h for Teams 1, 2, and 4. Task SOP and All Other CUs totals are also shown. Total communications declined with increasing h in all three teams. Maximal values ranged from 850-1200 CUs for the two 12 min lulls analyzed. Minimum values for each team were approximately 50% of maximum.

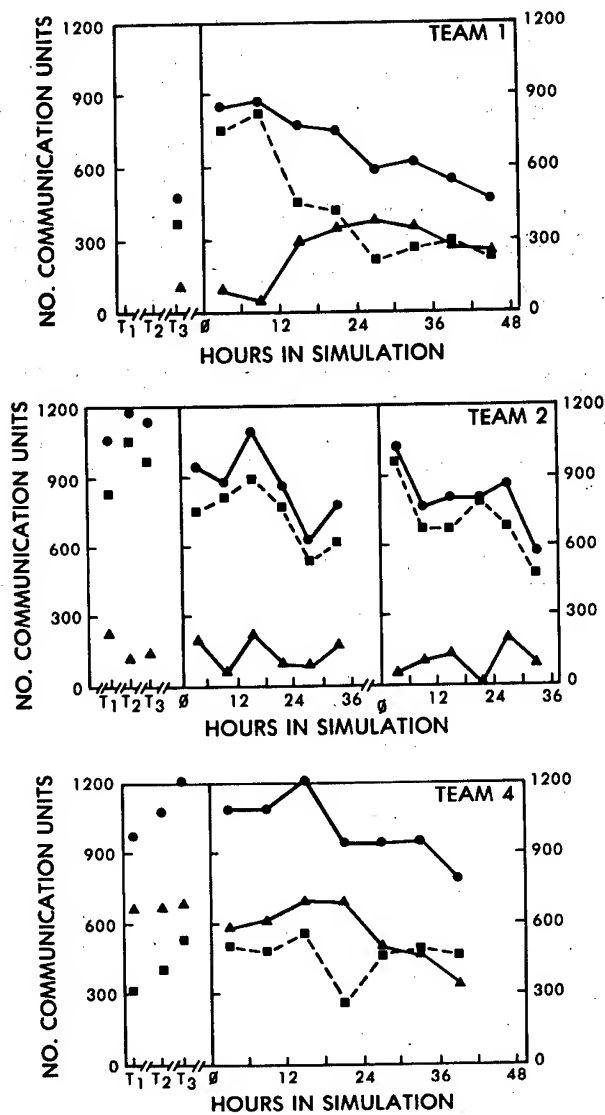


Figure 3. Group communication units (CU) for two, 12-min lulls are shown as a function of increased h in the simulation. Total CUs (solid circles), Task SOP CUs (solid squares), and All Other CUs (solid triangles) are shown.

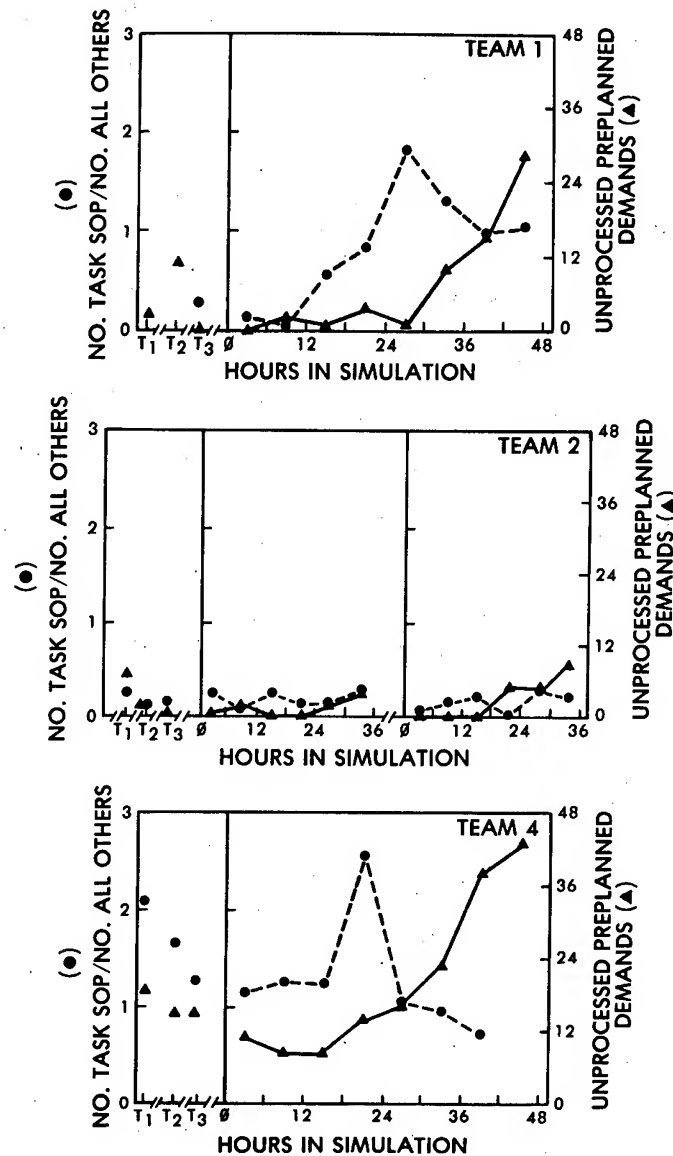


Figure 4. Task-related ratios (solid circles) and number of unprocessed preplanned demands (solid triangles) are shown for Teams 1,2 and 4 as a function of h in the simulation. Unprocessed preplanned demands are the sum of any revising, preplanning, and prioritizing targets which were not completed by each team. Increased task-related ratios indicate a greater preponderance of Task SOP CUs to All Other CUs.

*BANDERET, STOKES, FRANCESCONI, KOWAL

Shown in Figure 4 are unprocessed preplanned demands and task-oriented ratio functions for each team with h in the simulation. The former measure is the total number of targets not completed from the preplanning, prioritizing, and revising tasks; the latter indicates the relative preponderance of Task SOP CUs to All Other CUs. Larger ratios generally occurred when a team had preplanning activities to perform during the lulls.

The teams differed markedly in how "lulls" were used. Teams 1 and 4 are similar but unlike Team 2. Team 2 used the lulls to rest and to interact with each other. In contrast, Teams 1 (after 12 h) and 4 engaged heavily in Task SOP CUs. This is shown dramatically by the fact that Team 2's ratios were typically <0.3 ; whereas, after 12 h, Team 1's ratios were always ≥ 1.0 , except in the final hours prior to termination. In Teams 1 and 4, increased unprocessed demands were evident after 30 and 18 h; however, increases in the task-oriented ratio preceded these performance changes. With increasing unprocessed preplanned demands, communications became more task-oriented for Teams 1 and 4 up to some limit. Thereafter, the ratios decreased although both teams had increased amounts of unprocessed demands. Hence, after 24-30 h Task SOP CUs decreased in spite of increasing backlogs which eventually resulted in dramatic operational failures. The decreases in task-related communications reflected the fact that fewer and fewer task communications followed SOP and individuals began to discuss other topics. Although teams often remained concerned with task requirements, their behaviors became much less goal directed and their nonstandard communications reflected this. Such deviations sometimes resulted in confusion; increased effort and attention were required for task demands.

Team 2's data are in marked contrast to these data just described. At 36 h (second challenge) unprocessed demands were comparable to those for Team 1, yet changes in the task-oriented ratio were not observed. It was previously cited the single 86 h challenge took an earlier and greater toll on Teams 1 and 4 and that Team 2 was more proficient at preplanning. It appears that Team 2 had more reserve capacity and were able to maintain their preplanning without using the lulls. At no time was their ratio >0.3 . Other interaction data for Team 2 (not shown) indicate that 18-30 h in the second challenge CU's showing negative affect (feelings) increased almost 200%, a level even greater than that observed after 36 h in the first challenge. Positive affect CU's dropped to an unprecedented low after 24 h. In fact, after appraising their multiple mission sequence performance at 27 h, Team 2 members expressed doubts to each other about their ability to finish the challenge. This was a remarkable display of self-and team-doubt since they completed the first challenge and knew the second was the same duration! These trends contrast with those from Team 2's first challenge and correlate nicely with the observed deteriorations in preplanning and prioritizing noted previously for Team 2.

Increased Task SOP CUs are a likely compensatory reaction to reduced individual and team efficiency and the recognition that more and more demands remain to be completed. In Teams 1 and 4, increased task-related ratios were

*BANDERET, STOKES, FRANCESCONI, KOWAL

evident 0-30 and 0-18 h, before unprocessed demands began to increment substantially. Later, when the compensation was no longer adequate to oppose the increasing amounts of unsatisfied demands, compensatory behavior was reduced. This occurred perhaps to conserve, knowing that only 24-30 h of the simulation were completed, or perhaps these demands have physiologic or neuroendocrine costs which cannot be ignored and must be repaid. Biochemical and physical fitness data for Teams 1 and 2 (6) documented different patterns of response for each team; analogous data were not collected for Team 4.

These interaction data suggest that teams and their predominant activities can be characterized by communications occurring during lull periods. Furthermore, number and type of communications bear some relationship to operational and performance capabilities at that time. In the future, the contributions of various individuals to each group's communications will be explored. Ultimately, other biomedical indices will be arrayed with the operational performance data to gain insights as to how selected physiological, biochemical, and social variables influence operational capabilities in small Army teams.

CONCLUSIONS

1. Teams 1 and 4 ended their participation in the simulation at times corresponding to their physiological lows. Instruction, experience, leadership and social support can attenuate the impact of these physiological effects.
2. The 86 h single sustained operations challenge (Design I) was more demanding at equivalent points in time than the two, 38 h repeated challenges separated by 34 h of rest (Design II). Performance deteriorations occurred earlier and were greater. The implied mission demands, self- and team-doubts, and uncertainties associated with the anticipated 86 h challenge were likely contributing factors.
3. Performance deterioration appeared in most teams after 30-36 h in the simulation. Adverse environments, real-world situational uncertainties, and combat conditions would likely have additional disruptive influences.
4. Analyses of communications during lulls appear to provide useful correlates (predictors) of changes in team performance. Compensation and conservation reactions were also inferred.
5. This project methodology is adaptable to field research and training situations. The program suggests training, supervision, task, and biomedical issues for reducing the impact of sustained operations upon military personnel.

REFERENCES

1. Johnson, L. C., and P. Naitoh. 1974. The operational consequences of sleep deprivation and sleep deficit. AGARD-AG-193.
2. Woodward, D. P. and P. A. Nelson. 1974. A user-oriented review of the literature on the effects of sleep loss, work-rest schedules, and recovery on performance. Office of Naval Research, ACR.
3. Davis, R. H., and Behan, R. A. 1962. Evaluating system performance in simulated environments. In R. M. Gagne (Ed), Psychological Principles in System Development. Holt, Rinehart, & Winston, New York, 476-515.

*BANDERET, STOKES, FRANCESCONI, KOWAL

4. Glanzer, M. Experimental study of team training and team functioning. In R. Glaser (Ed), Training Research and Education. J. Wiley & Sons, New York, 379-407.
5. Bourne, P. G. The Psychology and Physiology of Stress (Vietnam). Academic Press, New York.
6. Banderet, L. E., J. W. Stokes, R. Francesconi, D. M. Kowal, and P. Naitoh, 1981. Artillery Teams in Simulated, Sustained Combat: Performance and Other Measures. In L. C. Johnson, D. I. Tepas, W. P. Colquhoun, & M. J. Colligan (Eds.). The 24-Hour Workday. A Symposium on Variations in Work-Sleep Schedules. National Institute for Occupational Safety and Health, Washington, D.C., (in press).
7. Stokes, J. W., L. E. Banderet, R. P. Francesconi, A. Cymerman, and J. B. Sampson. 1975. The Field Artillery Fire Direction Center as a laboratory and field stress-performance model: I Position paper; II Progress towards an experimental model. In The Role of The Clinical Laboratory in Aerospace Medicine, AGARD Publication AGARD-CP-180, A10-1 to A10-10.
8. Bales, R. F. 1970. Personality and Interpersonal Behavior. Holt, Rinehart & Winston, Inc, New York.
9. Stokes, J. W., and L. E. Banderet. 1978. A War for Science. Field Artillery Journal, 43-44.

ADDENDA

Human subjects participated in the studies after giving their free and informed voluntary consent. Investigators adhered to AR 70-25 and USAMRDC Regulation 70-25 on Use of Volunteers in Research.

The views, opinions, and/or findings contained in this report are those of the author(s) & should not be construed as an official Department of the Army position, policy, or decision, unless so designated by other official documentation.

The studies reported were conducted jointly by USARIEM, the Walter Reed Army Institute of Research (WRAIR), and the Naval Health Research Center (NHRC) in 1977. The administrative, technical, and professional contributions of numerous individuals are acknowledged and greatly appreciated.

*BANISTER

TESTING OF THE ARMY'S INTEROPERATING
NETWORK OF TACTICAL C³I SYSTEMS

*GRADY H. BANISTER, MR.
US ARMY ELECTRONIC PROVING GROUND
FORT HUACHUCA, ARIZONA 85613

INTRODUCTION

The Army has embarked upon a coordinated program to develop and field a collection of automated command control, communications, and intelligence (C³I) systems to provide the effective battle management that is required if we are to overcome the numerical superiority of the Soviet Block. The Army Battlefield Interface Concept 1979 (1) describes the basic architecture for integrating these systems into a functional and interoperating network. The purpose of this paper is to discuss some of the voids in current information science technology as it relates to the testing of individual systems and the network to insure that each system and the network will properly perform their functions under the stress of combat. To fully appreciate the technical nature of the problems anticipated in testing this network, let us examine three major aspects of the situation.

- (1) The nature and size of the network
- (2) The environment in which the network must function
- (3) The purpose of and information required from the test.

THE NETWORK

The network will be composed of numerous automated systems and subsystems which can be grouped into five basic functional areas: (1) Administrative and Logistics, (2) Intelligence and Electronic Warfare, (3) Field Artillery, (4) Air Defense, and (5) Command and Control.

There is, in fact, a sixth area required to complete the

*BANISTER

network -- the communications system. Each of these areas may be composed of various systems and subsystems (see Fig. 1). For example, the field artillery area consists of TACFIRE (Tactical Fire Direction System), BCS (Battery Computer System), FAMAS (Field Artillery Meteorological Acquisition System), RPV (Remotely Piloted Vehicle,) FIRE-FINDER (Artillery and Mortar Locating Radar), plus other support systems. These systems, in some cases, are a subnetwork; for example, TACFIRE consists of processing centers or nodes at Corps, Division, and Battalion level, with terminals at various locations from the forward observers to the Corps Headquarters.

The Army tactical C³I network must also interconnect and interoperate with the other services as well as our allies. Thus, there is a super network even before we consider the theater or national level interfaces. To assist in visualizing the size of the Army tactical C³I network, a Corps with four Divisions may have in excess of 200 processing nodes, and this does not include communications nodes. The communications support to this network will consist of various data transmission media, from dedicated point-to-point wideband circuits provided by multichannel systems, to dial-up voice grade data circuits, to combat net radios (shared with voice traffic), to time division multiple access systems.

A very significant aspect of this network is that it is evolving with time. Each system or subsystem is being developed and tested on its own schedule and may or may not be available at a specific time so that its interface with another system can be tested. For example, TACFIRE is in production now but its interfaces with other field artillery systems could not be tested prior to the production decision because the other systems were not available and some will not be available for at least another three or four years. In addition, the communications system which the processing systems will depend on for communications is also changing during the same time frame that these systems are being introduced.

THE ENVIRONMENT

The Army tactical C³I network must survive and provide the capability to continue to function in spite of the environment of the battlefield. Three aspects of the environment must be considered: (1) physical, (2) communications/traffic stability, and (3) radio electronic combat.

The physical environment includes shock and vibration and the physical damage, destruction, or capture of portions of the network by enemy action in addition to the disruption and reconfiguration of the network due to the movement and relocation of nodes. The

*BANISTER

BATTLEFIELD AUTOMATED SYSTEM CATEGORIZATION

BATTLEFIELD FUNCTIONAL SYSTEM LIFE CYCLE STATUS	ADMIN AND LOG	INTEL AND EW	FA	ADA	C ²	COMMO	ENGR
CATEGORY I CONCEPT/ DEFINITION	(MEDMIS) MEDREG* PAR* MEDLOG* WHOLE BLOOD MGMT* JACS*	ELOCARS HAALS RAWS ASAS ATRNL AMS* REMBASS	U/E ECM	APPS II FANAS BSTAR	CTOS	PACKET RADIO JTIDS MSE ADDS SDA(OLDED) CEOI PROD FACILITY ATFES	ARTINS*
CATEGORY II VALIDATION/ DEVELOPMENT	(CS3) TUFMIS	AGTELIS SOTAS TACELIS ENHANCED GUARDRAIL TEP	MULTENS-A QUICK FIX TACJAM CAS ECM	TPQ-36 TPQ-37 APPS-PIP (PHOTO- LOCATOR) PADS BCS RPV	DTOS NBDS	TTC-39 TYC-39 TCCF PLRS GPS TENLY/ SEELY	
CATEGORY III APPROVED PRODUCTION/ INSTALLATION	STANFINS** (CS3) SIDPERS	MAGLIC QUICKLOOK II TRAILBLAZER COMFAC GUARDRAIL V INTERIM SLAR DATA LINK	TACFIRE	TSQ-73			

*SOFTWARE ONLY - NO HARDWARE IDENTIFIED
 **OPERATES IN CORPS (EUROPE) DURING PEACETIME ONLY
 ***EAC - BAND WILL TRACK DEVELOPMENT

Figure 1

*BANISTER

communication/traffic stability aspects of the environment include the effects of the physical environment on the data flow between nodes that may cause rerouting of messages, reallocation of circuits, and create dynamically varying workloads at the processing nodes. The effects of enemy radio electronic combat may reduce the quality of existing circuits, deny us the use of circuits, and introduce confusion by injecting false messages into our communications system. In addition, the network must be secure so that information being exchanged is not available to the enemy and he cannot exploit the network even with captured equipment.

THE TEST

The testing of automated C³I systems must be designed to completely exercise all functions of the item under test, stress the system in accordance with the environment, determine the system's ability to protect itself and the network from hostile activities, and insure that it will continue to function in an error prone communications environment. With the introduction of each new or modified system, the test must also determine what is the impact on the network and the other processing nodes. While doing all of the above, the testing procedure must provide a high degree of repeatability as to the content (including error cases) and timing of the stimuli presented to the system under test to aid the developer in the diagnosis of failures and the validation of corrections. The tests must also be designed so that all of the network is not required to test a single node. It may not be possible to collect and operate the entire network except during major exercises and actual combat.

AN APPROACH

USAEPG has developed a concept for testing automated C³I systems which has the potential to solve a large part of the test community's problems. This concept is embodied in a program to provide USAEPG with an advanced test capability covering all phases of USAEPG's test mission. Emphasis is on the application of automation and simulation technology to meet the challenge of complete systems performance and interoperability testing of automated C³I systems. This overall program is called MAINSITE which is the acronym for Modular Automated Integrated Systems/Interoperability Test and Evaluation (Fig. 2). The MAINSITE concept has evolved from earlier efforts by the Army Security Agency Test and Evaluation Center and Program Manager, Army Tactical Data Systems, to solve portions of the overall testing problem. USAEPG has combined and extended these earlier concepts and now is in the process of implementing them.



MAINSITE ARCHITECTURE

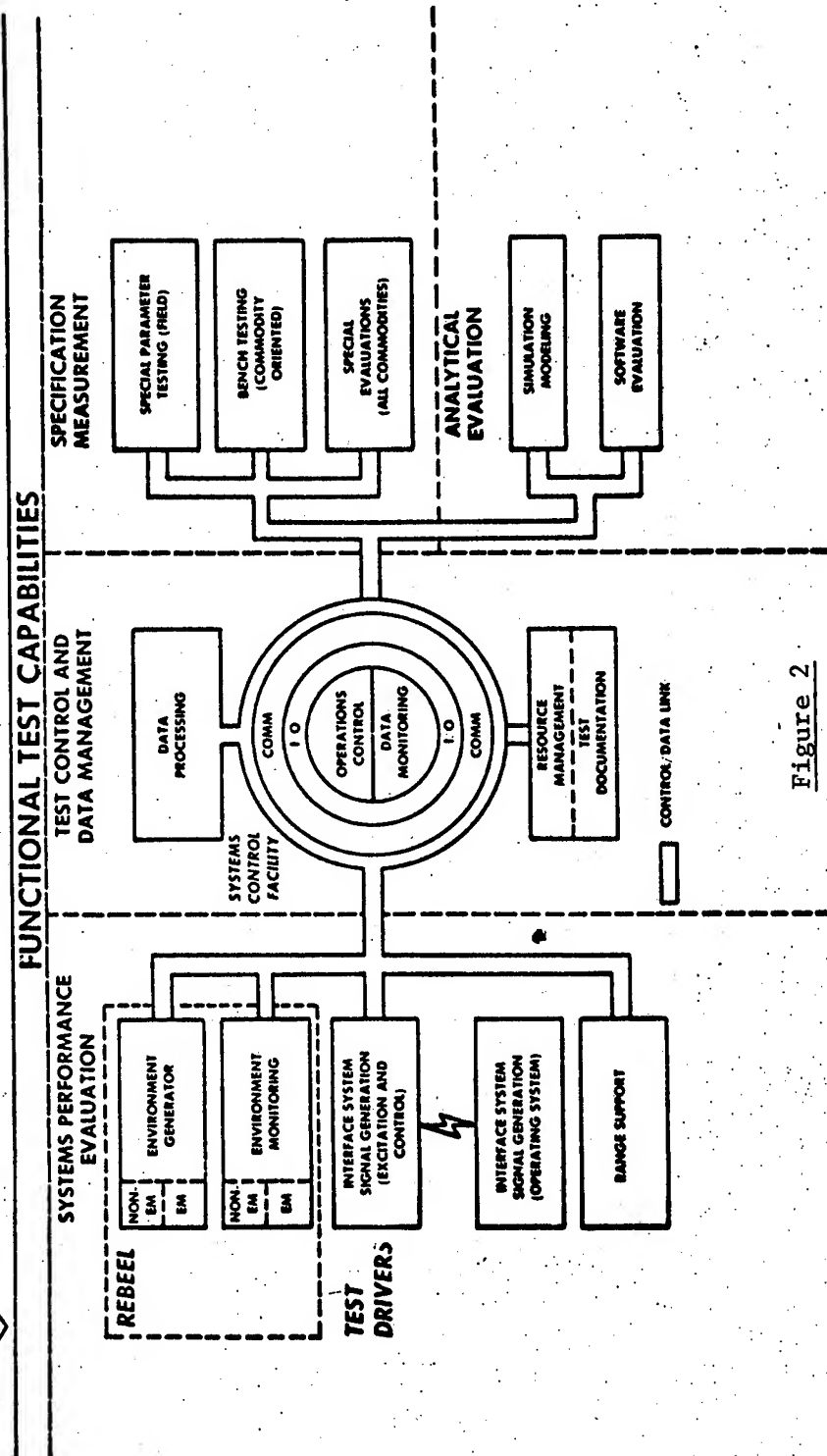


Figure 2

*BANISTER

The key elements of the USAEPG approach are:

- (1) Automated presentation of stimuli (messages) to the system under test.
- (2) Automated control of the electromagnetic environment around the system.
- (3) A flexible, modular design approach applicable to the testing of all C³I systems.
- (4) Transportability of the basic elements to permit use at other locations as required.
- (5) Central control to extend the capability when required.

THE CONCEPT OF TEST

The Concept of Test which has established the capability requirements for the MAINSITE program is based on subjecting the system to three progressively more difficult phases of testing. These phases are:

- (1) Test the System Logic
 - (a) Single Thread -- Each function is tested independently of other functions to provide control of the relationships of responses to stimuli to include error conditions (Step 1).
 - (b) Multithread -- All functions are tested in combination to the maximum practical extent to expose negative effects of synergism and interaction (Step 2).
- (2) Test the System Capacity
 - (a) Required Load -- Loading of the system up to the stated requirements to determine performance versus requirement (Step 3).
 - (b) Saturation Load -- Multithread load is increased to systematically saturate system resources so that throughput, response time, and degradation effects may be determined (Step 4).

*BANISTER

(3) Test the System in a Realistic Communications Environment

(a) Without Radio Electronic Combat -- Communications by automated systems over less than optimal communications channels requires additional processing and the retransmission of digital messages, both of which adversely affect system timing (Step 5).

(b) With Radio Electronic Combat -- Step 5 is repeated but in the degrading EM environment produced by threat radio electronic combat to insure that the system and network are capable of surviving despite disrupted communications (Step 6).

It should be noted that phases 1 and 2 are conducted with error free communications and therefore provide a baseline for evaluating the effect of the real world communications on system performance.

The System Control Facility, the Realistic Battlefield Environment-Electronic, and the Test Driver portions of the MAINSITE program are essential to this concept of test.

THE SYSTEM CONTROL FACILITY (SCF)

The SCF is the USAEPG real time test control and data management facility consisting of a large central computation center, test operations control centers, and communications to the mobile remote test facilities. In addition to providing real time control to multiple test facilities, the SCF will be capable of simulating on a real time dynamic basis the responses of other systems not physically present for a test.

THE REALISTIC BATTLEFIELD ENVIRONMENT - ELECTRONIC (REBEEL)

The REBEEL is a collection of mobile simulators, replicas, and actual emitters which create a controlled electronic environment to represent the radio electronic combat threat, targets for our electronic sensor systems and the electronic environment representing friendly emitters. The REBEEL will be automatically controllable from the SCF permitting rapid, repeatable execution of complex test conditions. Wherever possible the emitter simulators will be designed to permit preprogrammed sequences of operations to be executed without dependence on the SCF for use at locations other than Fort Huachuca.

THE TEST DRIVER

Each Test Driver (Fig. 3) will consist of a rugged mini-computer with sufficient storage for messages (stimuli) to be trans-

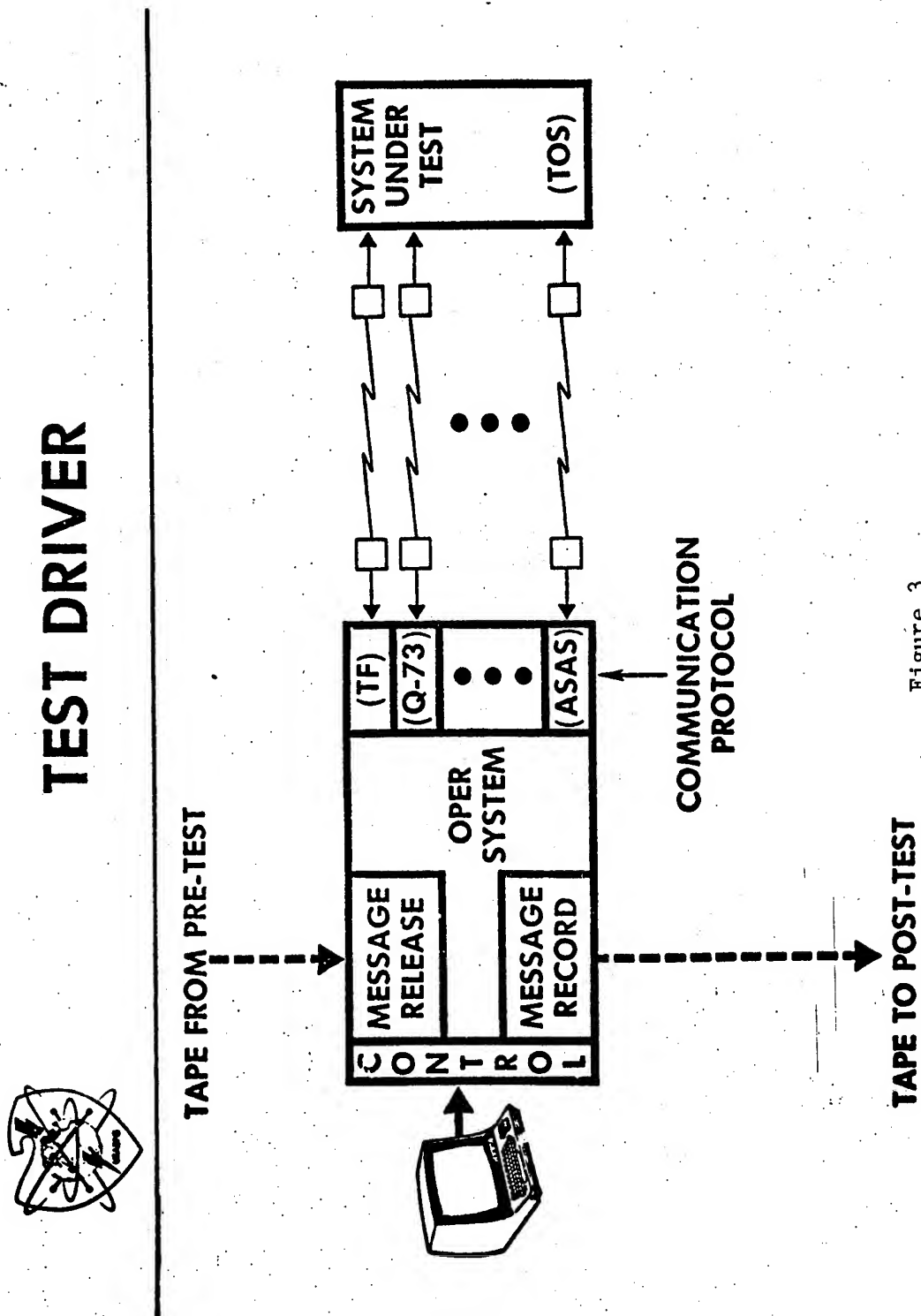


Figure 3

*BANISTER

mitted and the recording of all traffic across the interface. Facilities for both remote and local test monitoring and control as well as a communications interface with the SCF will be included.

The Test Driver will automatically transmit digital messages over the communications channels to the system under test, receive messages transmitted by the system under test, and record all exchanges over the communications system. It will utilize prepared tapes of messages representing the stimuli to the system under test from those elements of the network which interface with the system under test but are not physically present. It will utilize the same communications channels, protocol, and encryption devices as the missing systems to provide as realistic a communication interface as possible. A single Test Driver may have to represent a number of missing systems (Fig. 4); therefore, it must be capable of handling multiple communications channels, various data rates and protocols. The Test Drivers will be capable of being controlled from the SCF or of operating in a stand-alone mode. Multiple Test Drivers, controlled by the SCF, will be utilized when the test requirements exceed the capacity of a single Test Driver. The Test Drivers will be transportable to provide realistic communication distances and to facilitate their use at other locations.

THE TECHNICAL PROBLEMS

The planning for the MAINSITE test capability described above has drawn heavily on experience gained during the testing of individual real time systems. This approach provides assurance that the lessons learned in solving prior testing problems will be applied to the development of future capability, but it does not guarantee adequate solutions to problems yet to be encountered. Thus the motive for this paper -- to attempt to identify any new testing problems which can be anticipated and to generate interest in the information science community on developing effective solutions.

UNANTICIPATED DATA CONDITIONS

The vast majority of the literature on testing of automated systems concentrates on proving that the system correctly processes the expected inputs. There are even automated techniques to trace the execution of computer problems to help identify all portions of the logic exercised by the test cases. (2) A good specification will identify some of the potential error conditions and state what the program should do when these errors occur. However, there has been little, if any, effort in identifying the potential sources of errors in data inputs, determining the types of errors, and developing the



TEST CONCEPT

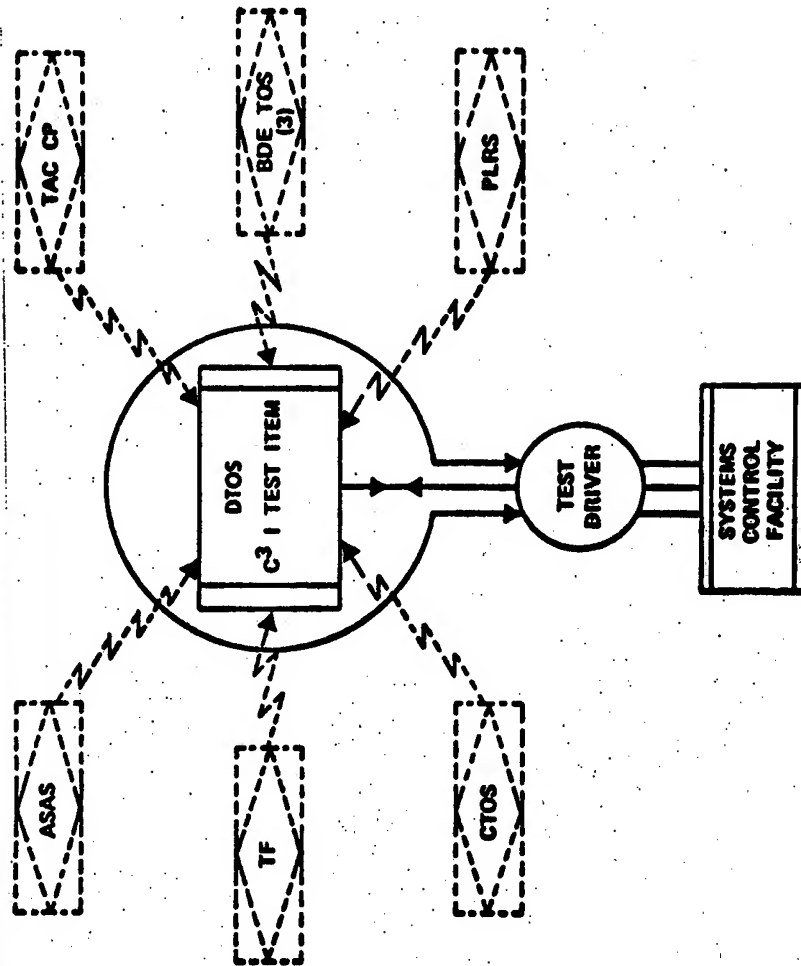


Figure 4

*BANISTER

methodology required to generate and present an adequate set of input errors to the system under test.

It is very difficult, if not impractical, to construct a complete set of expected valid inputs for testing large programs but they are at least a finite set. The error conditions represent the remainder of the universe of possible data inputs and are for all practical purposes an infinite set. In the large network environment the original source of an error may be far removed from the system that detects it; for example, an operator at a terminal connected to system "A" (see Fig. 5) may compose a message containing an error in a specific data element (field). System "A" may process the message and generate a new message for system "C" which is relayed through system "B" containing the erroneous data element. The error may not be detected until system "C" attempts to utilize the erroneous data element.

Techniques need to be developed to provide methods to identify all sources of possible errors, determine the characteristics of the errors, quantify the probability of occurrence, and generate test cases which will realistically test the network and its individual systems. An effort to analyze the error sources in a small portion of the network shown in Fig. 5 has been initiated at USAEPG to gain an insight into the complexity and magnitude of the problem.

NETWORK DYNAMICS

Unfortunately the Army's C³I systems are evolving into an integrated network rather than having a network designed and specified into which each system must fit. It is only natural for the developer of a specific system to consider his system as the center of the universe and when confronted with the task of testing a system, the tester also considers the system under test as the center of his universe. This introspective perception of the testing task leads to a false sense of security since testing is easier if you bound the scope of the test even though major errors of omission may be committed. The real world situation is that the effect of the network on the system under test, as well as the effect of the system under test on the network, must both be tested. This interdependency is much more complex than most designers and testers realize. Let me describe a few examples of the types of network versus system relationships which must function correctly for both the system and the network to perform properly.

It is generally accepted that there must be a well defined set of messages, to include format and data elements, for information

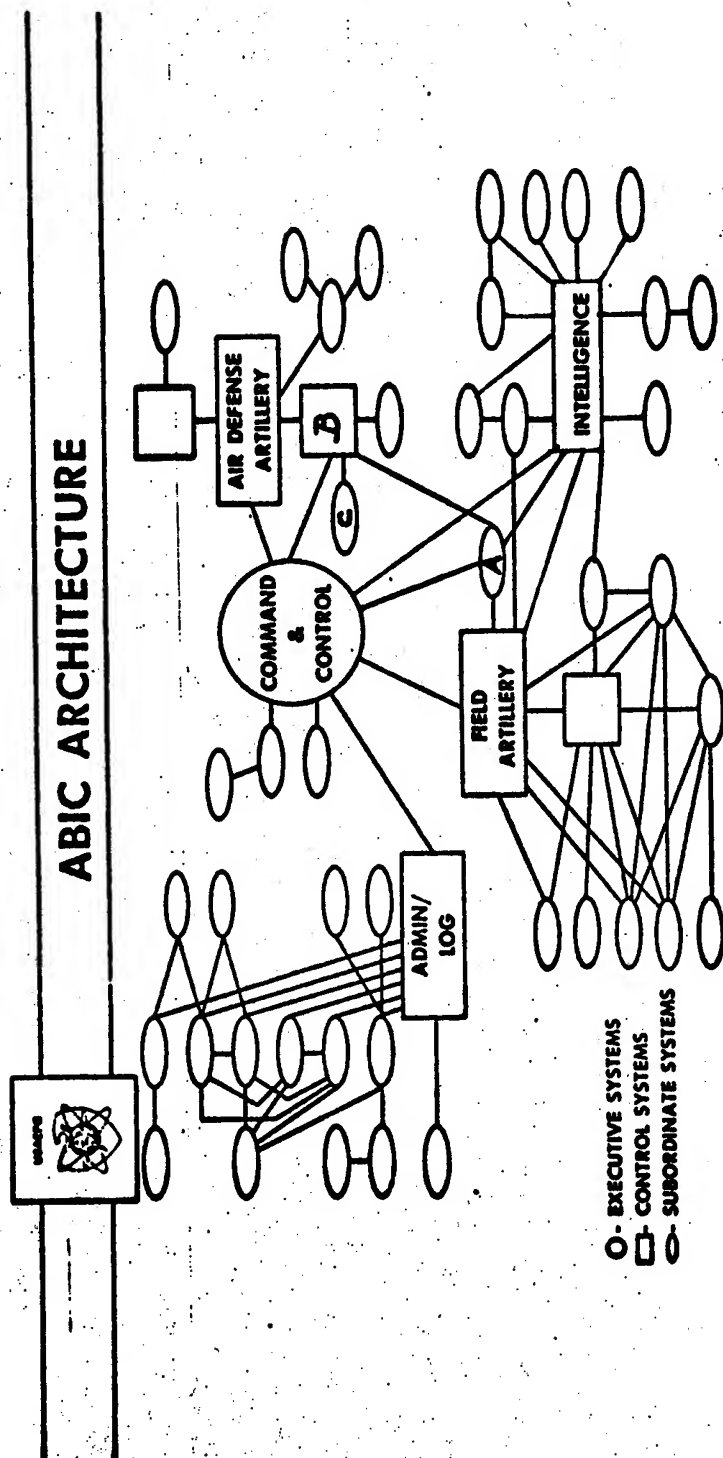


Figure 5

*BANISTER

exchange between interoperating members of a network. However, many of the benefits of automating the Army C³I functions are dependent on rapid allocation of resources to solve problems. Examples are messages which task or command an air defense fire unit to engage a hostile aircraft, command a jammer to jam a specific frequency, command an artillery unit to fire a specific mission, or command a unit to execute a specific action. Thus the network is a military process control system which requires that each of the subsystems which control a part of the process provide feedback as to the status of their part of the process. A well understood principle in the design and testing of on-line process control systems is that the timing and nature of the feedback must be such that oscillations or "hunting" does not occur and that the network converges to a steady state condition. This requires that the processing of the messages which command a system to perform a task must produce the results and/or feedback (messages) which are well defined and utilized by the network to control the overall process. This aspect of the Army's C³I network has not been defined much less tested. The use of the Test Driver with appropriate messages will permit testing of a system to determine if it responds correctly to such messages and performs the required actions to include providing the correct feedback. However, this will not necessarily prove that the processing of the feedback by the rest of the network and the time constraints involved are correct and will prevent oscillations.

In addition, there are very complex dynamic problems associated with the control of the network and its communications which also need to be tested. The Army C³I network creates some unique network control problems. The overall network is constantly evolving by the addition of new processing nodes, the modification of existing nodes, and the changing of the type of communications between nodes. The network will not be maintained in an operational status for long periods of time except during combat. During periods of combat, the network will be changing on a very dynamic basis due to movement of forces, combat losses of communications and nodes, and the functions of individual processing nodes will change to accommodate the essential functions of inoperative nodes. All of the above presents a real challenge to both the designer of a system and the tester.

How do you generate the data and communications environment around the system under test to measure its ability to respond correctly to such a changing environment, and how do you determine the effect on the network of the systems responses when the network is physically not available? I do not have the answer to these questions today. I do anticipate that by utilizing the processing facilities

*BANISTER

of the SCF to simulate the network control logic, when it is defined, we will be able to at least quantify individual systems response times and predict network stability under this type of dynamic stress.

CONCLUSION

There are many problems in the design and testing of large scale distributed processing networks which are not well understood today. The purpose of performing the tests discussed is twofold; first, to find and eliminate as many errors in the system and network design as possible and, second, to assist the designers in developing the most robust, adaptive, distributed C³I system design possible. The implementation of MAINSITE will provide a powerful tool which, if used properly, should provide significant advances in our ability to implement the Army C³I network.

REFERENCES

1. (U) "Army Battlefield Interface Concept 1979" (U) CONFIDENTIAL Department of the Army, ACN 47635.
2. MYERS, G. J., Software Reliability, New York, John Wiley & Sons, 1976.

*BERRY, KEANE, HATFIELD, and FILLER

THE BIOLOGICAL DETECTOR AND WARNING SYSTEM, XM19/XM2 (U)

*PATRICK BERRY, MR., WILLIAM KEANE, MR., GAIL HATFIELD, MR.,
and MELVIN FILLER, MR.

CHEMICAL SYSTEMS LABORATORY, USARRADCOM
ABERDEEN PROVING GROUND, MD 21010

INTRODUCTION

In response to an approved Army requirement Chemical Systems Laboratory is presently engaged in the engineering development of a Biological Detector and Warning System (BDWS) with the capability to detect the presence of biological aerosols and to collect samples of these aerosols for subsequent analysis. This system, when fielded in 1984, will provide the United States with a significant improvement in its defense against biological agents disseminated from airborne delivery systems. The current development program was initiated in 1975 by contract with the Environmental and Process Instruments Division of the Bendix Corporation [1].

Biological agents are primarily candidate weapons systems for large area application. Their release as a respirable aerosol from a single aircraft can easily present a hazard to unprotected humans in an area as large as many hundreds of square kilometers. The size of the area affected is dependent upon the type of agent, the release pattern, and the prevailing meteorological conditions. These weapons are ill suited for use against relatively small targets when accuracy in delivery is important. However, they have great strategic importance, because the resources required to manufacture a biological agent and to deliver an attack against a large target area are modest, and the casualties resulting from a single attack can be very high.

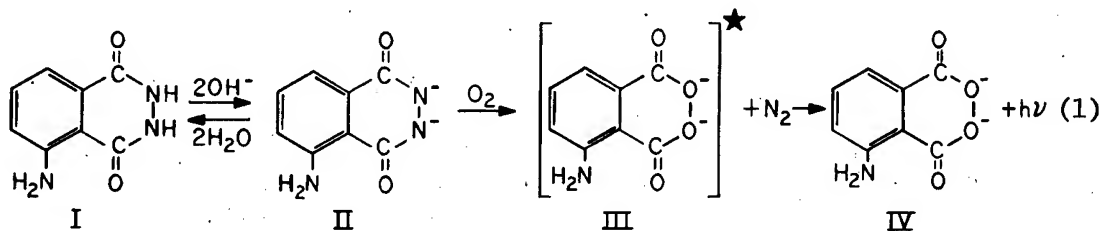
Biological agent munitions systems employ a variety of pathogenic organisms which include bacteria, rickettsiae, and viruses. The

*BERRY, KEANE, HATFIELD, and FILLER

munition fill also contains impurities resulting from the processing of the biologicals and stabilizers added to improve the viability of the organisms during storage. All biological agents contain porphyrin compounds such as hematin or cytochrome. Porphyrins are essential to the metabolism of bacteria and rickettsiae, and while not present in viruses, they are contained in the residual cellular material resulting from cultivation of viral pathogens which becomes part of the munition fill. The detection system under development is sensitive to atmospheric aerosols containing porphyrin-type compounds and is designed to provide an automatic alarm signal upon detection.

Proteinaceous material containing porphyrins can be routinely found in the ambient atmosphere. These natural aerosols are usually composed of spores, pollens, and other products resulting from the life cycle processes of various flora [2], but they often contain a wide variety of other materials due to attrition of surface soils [3]. These aerosols can also contain products of industrial processes, grain handling, fertilizer manufacture, and general agriculture. The temporal concentrations of natural aerosols usually differ from those associated with the release of biologicals as a weapon system. Therefore, the detection of biological agents requires consideration of the dynamic properties, in addition to the concentration, of aerosols containing porphyrins.

The detection principle employed in the BDWS is the chemiluminescence resulting from the oxidation of luminol (5-amino-2,3-dihydro-1,4-phthalazinedione) in alkaline solution. The general chemistry of luminol oxidation in nonacidic solvents, as determined by White [4,5], is shown in equation 1.

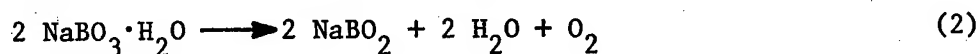


The mononegative ion of luminol does not react with oxygen at an appreciable rate; therefore, two moles of base must be added to form the dinegative ion (II) which is the critical intermediate in the reaction scheme. Due to the equilibrium between luminol (I) and its dianion, the chemiluminescence is highly dependent on the pH of the reaction solution. The dianion reacts with dissolved oxygen through several

*BERRY, KEANE, HATFIELD, and FILLER

intermediate steps to form an excited singlet state of the aminophthalate ion (III) with the liberation of molecular nitrogen. The singlet rapidly decays to the ground state (IV) by emission of a photon. The details of the oxidation process are not precisely understood, but it appears that free radicals are involved.

Oxygen is supplied to the reaction by catalytic decomposition of peroxide. The oxidant used in this detection system is sodium perborate monohydrate ($\text{NaBO}_3 \cdot \text{H}_2\text{O}$) which is a true peroxy derivative rather than a hydrated salt. Porphyrins, as well as other transition metal complexes or ions, catalyze the decomposition of the perborate to produce oxygen and water as shown in equation 2.



Since all reactants are present in excess, the total light emission from the luminol oxidation is directly proportional to the concentration of catalyst or porphyrin-containing material.

The luminol reaction produces a relatively broad spectrum of light extending from 3500 to 6000 Å [5]. Using a photomultiplier tube as the photodetector, an iron-porphyrin (hematin) concentration of 10^{-4} µg/ml can be detected. When this value is translated to an equivalent number of bacterial cells, the minimum sensitivity becomes 10^4 to 10^5 cells/ml, dependent upon the particular organism. Although materials other than porphyrins will catalyze this reaction, it has been found that the light emission rates are significantly slower for porphyrins than for metallic ions or complexes with a non-biological origin. Therefore, it is possible to utilize the reaction kinetics to improve the specificity of the detection scheme.

DESCRIPTION OF SYSTEM

The two principal components of the BDWS are the XM19 Alarm and the XM2 Sampler as illustrated in figure 1. The XM19 performs the detection function of the system by continuously monitoring the ambient air and automatically sounding an alarm if biological agents are detected. The XM2 fulfills the sampling requirement of the system by collecting a sample of the suspected biological aerosol upon command from the XM19 when an alarm is declared.

*BERRY, KEANE, HATFIELD, and FILLER



Figure 1. Operational view of the BDWS showing the XM19 Alarm (left) and the XM2 Sampler (right).

The XM19 Alarm is formally identified as the Alarm, Biological Agent, Automatic: Chemiluminescence, XM19. It is being developed for Army field use in all environments except the Arctic. The XM19 consists of three sequential processes which are shown in figure 2. The air, liquid, and electronic subsystems have each been designed to enhance both the sensitivity and the specificity of the detector. The overall function of the combined detection system is to continuously transfer aerosol particles having properties characteristic of biological agents from the atmosphere into a minimum volume of liquid. Periodically, the liquid sample is reacted with luminol and the resulting light emission analyzed to determine whether or not a biological attack has occurred.

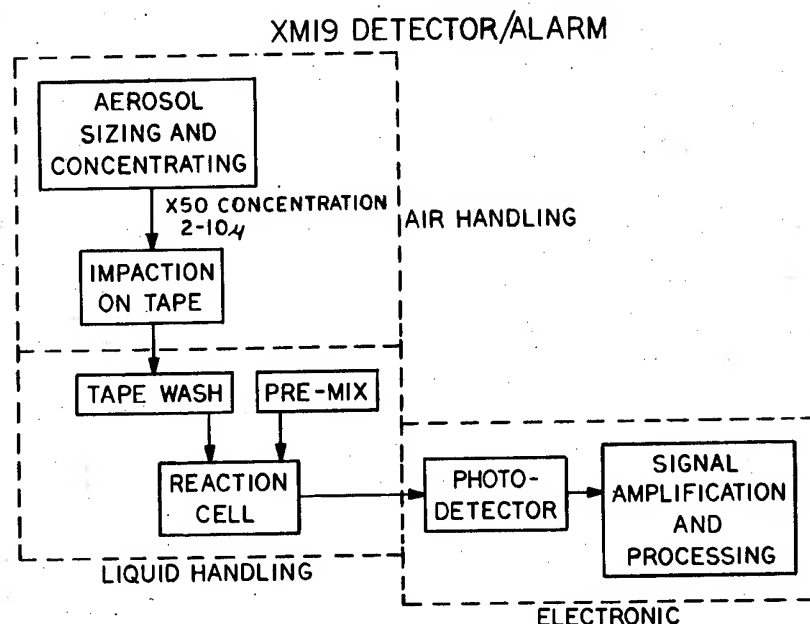


Figure 2. Block diagram of the XM19 functional configuration.

The air handling subsystem samples ambient air at a rate of 1000 ℓ /min. The air enters through a screen-covered annulus, which prevents the ingestion of very large objects such as insects, followed by two stages of dichotomous, or virtual impaction. This device, identified as the collector-concentrator, was developed by the Environmental Research Corporation [6] for this specific application. The first impaction stage utilizes eighteen circular jets arranged in two concentric circles. Each nozzle is designed for a 50% cut-off diameter (d_{50}) of 2.5 micrometers (μ m) based on a specific gravity of 1.0. These larger aerosol particles are concentrated into 15% of the total volume of sampled air and directed through a single rectangular slit having the same cut-off characteristics as the first stage. In this second stage the larger particles are again concentrated into 10% of the volume of incoming air. The remaining air is combined with the unused fraction from the first stage and exhausted through a secondary port. Through the use of two stages of separation, particles having an aerodynamic diameter greater than 2.5 μ m are concentrated from a sampled airstream of 1000 ℓ /min into 15 ℓ /min. Efficiency measurements have shown that over 70% of the sampled particles in the size range from 3 to 8 μ m are transferred to the output of the concentrator.

*BERRY, KEANE, HATFIELD, and FILLER

This enriched aerosol is employed for detection, and the remaining sampled air is used for heat exchange and then exhausted from the unit. The enriched air sample is directed onto the surface of a continuously moving adhesive-coated tape through a rectangular slit impactor. The collection tape was especially developed for this application by Southern Research Institute [7].

The impacted material is transported by the tape to an adjacent device which provides an interface between the air and liquid subsystems. This component, identified as the wash station, permits physical contact of the wash fluid (sterile water) with the impaction surface across a meniscus defined by the geometry of the wash station. The washing of the tape causes agglomerates such as biological particles to separate, releasing individual cells into the water. Discrete, homogeneous particles are not easily removed by the washing operation and tend to remain attached to the tape. As a result, some differentiation between biologicals and non-biologicals is obtained by the overall tape impaction/washing process. The collection tape development optimized the tape coating to provide the greatest degree of differentiation possible between simulant biological aerosols and dusts generated from a representative group of soil samples.

The wash water is transferred by an injection pump from the wash station to a reaction cell. The pump is a dual assembly which simultaneously injects equal volumes of the wash water and the premixed reagent solution into the reaction cell every ten seconds. The reagent or "premix" is an alkaline solution of luminol, sodium perborate, and ethylenediaminetetraacetic acid (EDTA). The composition of the premix has been optimized to accentuate the differences in reaction rates between porphyrins and other metallic complexes or ions [7,8]. The reaction cell consists of a double spiral of transparent tubing mounted on a thermoelectric module which maintains the reaction temperature at 25°C. The cell is closely coupled to an end-window photomultiplier tube (EMI Type 9524B).

The photomultiplier converts the rate of light emission from the reaction cell to a voltage analog which is processed by the electronic subsystem. All signal processing is performed by a dedicated microcomputer utilizing the 8080A as the central processing unit. The signal from the photomultiplier is sampled and digitized at 0.1 second intervals during the first eight seconds of each injection cycle. The resulting 80 data points describe a reaction, or light emission, rate profile which is further reduced to two descriptive parameters designated as A and B. A is the arithmetic average of data points 2 through 5, and B is the average of points 6 through 80. The A and B

*BERRY, KEANE, HATFIELD, and FILLER

values are computed by the microcomputer during the last two seconds of the injection cycle. Both of the parameters are then corrected for background aerosol "noise" by subtracting average background signals to produce net values denoted by ΔA and ΔB . These background levels are approximated by exponential moving averages of the parameters which are computed using a first-order time constant of ten minutes (60 injection cycles). When the unit is not in alarm, these averages are updated at the end of each injection cycle for use in calculating corrected values during the next cycle.

Figure 3 shows two XM19 reaction profiles which illustrate the difference in light emission kinetics between porphyrin compounds and transition metal ions. The A and B parameters act as weighting factors with A representing the contribution of non-biologicals and B representing the contribution of biologicals to the reaction. Therefore, the ratio of $\Delta B:\Delta A$ indicates whether the material is predominately biological or non-biological in nature. For the examples in figure 3, the $\Delta B:\Delta A$ ratio is 0.4 for the ionic and 1.1 for the biological reaction.

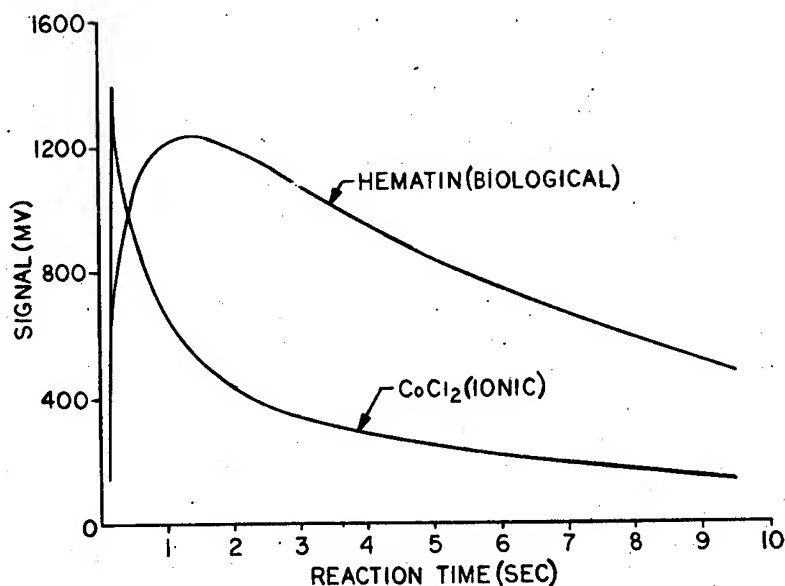


Figure 3. XM19 reaction rate profiles for hematin and cobalt chloride.

*BERRY, KEANE, HATFIELD, and FILLER

The ΔA and ΔB parameters are evaluated by a logic algorithm within the microcomputer program to determine the alarm status of the unit at the end of each injection cycle. An alarm condition (potential alarm) exists when ΔB is both greater than a fixed threshold value and greater than 90% of ΔA . An alarm is declared after six consecutive alarm conditions if the ΔB values increase monotonically. When this restriction on the dynamics of the response is not satisfied, the alarm sounds after the seventh consecutive alarm condition provided that the current value of ΔB is at least two-thirds of the maximum value of ΔB during the first five alarm conditions. If this second dynamic restriction is also violated, the alarm condition counter is reset to zero. The value of the alarm threshold is consistent with the calibration of the unit and the military requirements. The critical ratio of $\Delta B:\Delta A$ has been optimized to give maximum discrimination between biological and non-biological materials without compromising detection. This algorithm also exploits the unique dynamic properties of biological agent aerosols within the limitations imposed by response time constraints.

The XM19 operates from 120 V, 60 Hz electrical power. Control of the operational functions is maintained by the microcomputer. In addition to providing an alarm signal upon detection of a biological aerosol, it performs a variety of self checks to insure correct air pressures, liquid flows and temperatures. Detection of any improper condition generates a malfunction signal to alert the operator of the need for corrective action.

Servicing the XM19 consists of replacing two reagent containers (one containing the premixed reagent solution and the other sterile water) and the collection tape. The tape is provided in an easily replaceable cassette-type housing. The XM19 can operate unattended up to twenty-four hours before reservicing is required. The expendables required for servicing are provided to the operator as a refill kit.

The development of the XM19 refill kit placed great emphasis upon the need to minimize manipulations by the operator. Important design constraints were the requirement of minimal skills and training of military personnel for satisfactory operation and recognition of the need to perform servicing under difficult circumstances. As a result, the refill kit was designed to provide prepackaged reagents for servicing the XM19. The kit contains expendables for 7 days of operation. The water required to wash the tape is contained in sealed, clear containers which are sterilized by gamma irradiation at the time of manufacture. The reagent solution is provided in a yellow container for easy identification. To ready this solution for use, the

*BERRY, KEANE, HATFIELD, and FILLER

operator adds a tablet of sodium perborate which is provided in a sealed tear packet. The container is then shaken to dissolve the tablet, and the premix is ready for use. It was found necessary to separately package the sodium perborate in order to avoid rapid decomposition of the reagent during storage. This packaging scheme for the refill kit is expected to provide a shelf life in excess of two years.

For routine performance checks of the XM19, a simulant is provided in the refill kit. A small dispenser containing microencapsulated cobalt chloride and a propellant aerosolizes metered amounts of the simulant. By switching to a special test algorithm, the ionic reaction produced by the cobalt is properly interpreted by the microcomputer so that an alarm signal is generated if the XM19 is functioning correctly. The simulant and dispenser were developed under contract by Southern Research Institute [1].

In the development of the XM19, considerable attention was given to the design of key components and the materials of construction. The performance requirements are such that a rapid response to biological aerosols is essential. Therefore, it was necessary to develop components which require small volumes of fluids and which do not contaminate or influence the reactive properties of sampled organisms. Silicone tubing is employed for liquid transfer. Gas-tight syringes with fluorocarbon tips are used in the injection pump assembly. The wash station proved to have a number of unique design problems and required more development effort than any other single component. The current design has demonstrated excellent reproducibility in its transfer characteristics and can be manufactured inexpensively by injection molding.

The XM19 has been tested in authorized Government laboratory facilities against a variety of pathogenic organisms, including bacteria, rickettsiae, and viruses, that are representative of possible biological agents. The performance meets the stated Army requirements. Although the reaction kinetics vary with each material, the calibration of the unit has been established on the characteristics of candidate agents which have the lowest reactivity to luminol. Thus, the detection requirements are satisfied for a wide range of pathogenic materials.

*BERRY, KEANE, HATFIELD, and FILLER

The other principal component of the BDWS is the Sampler, Biological Agent: XM2. When activated by a co-located XM19, it automatically samples the atmosphere, collects aerosol particles, and retains the sample in an environment which will maintain the viability of biological organisms. The XM2 is composed of three functional subsystems, as shown in figure 4, which parallel those of the XM19. The air handling subsystem performs the same sampling and aerosol concentration function as in the XM19 by utilizing an identical collector-concentrator.

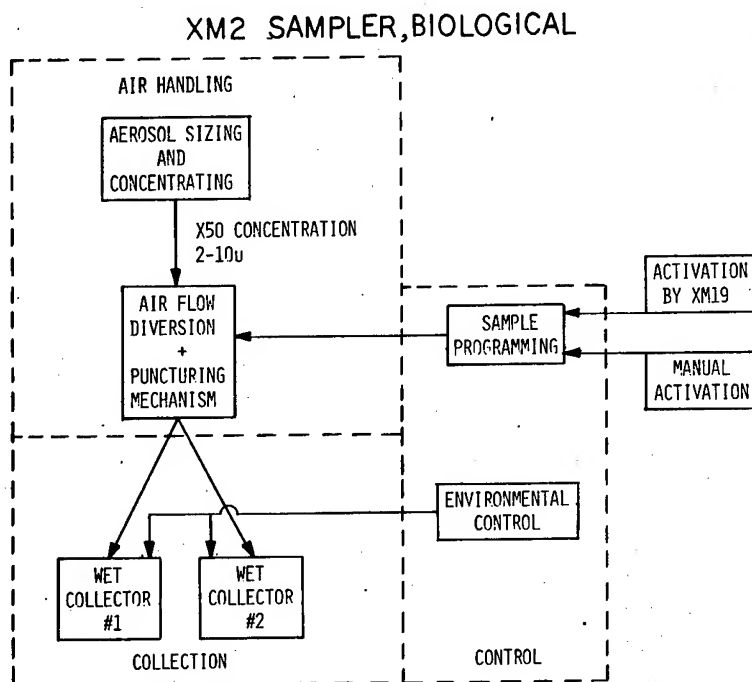


Figure 4. Block diagram of the XM2 functional configuration.

The enriched aerosol from the concentrator is directed into one of two sample containers which compose the collection subsystem. These devices, referred to as wet collectors, are components of the XM2 refill kit. The wet collectors are molded from LexanTM and contain 40 ml of physiological saline with 0.67 M phosphate buffer (pH 7.2) and 0.05% Tween 80TM. Details of the wet collector design [9] are shown in figure 5.

*BERRY, KEANE, HATFIELD, and FILLER

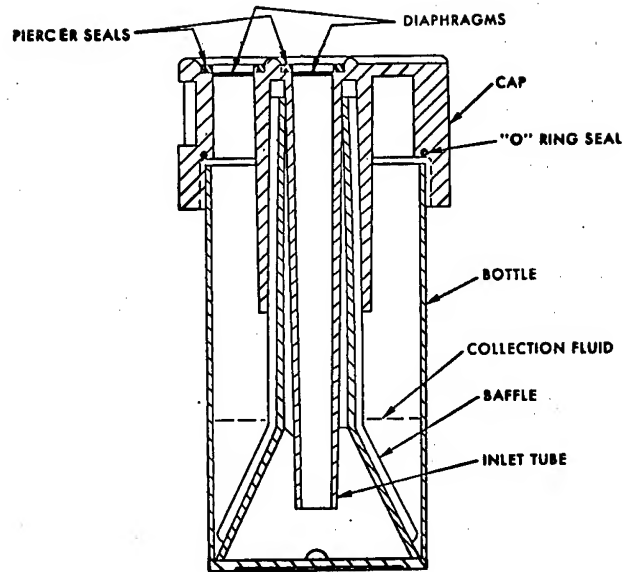


Figure 5. Cross-sectional view of the XM2 wet collector.

The two sample ports are sealed by plastic membranes, and the finished devices are sterilized by gamma irradiation. Activation of the XM2 causes the unit to pierce the seals of one collector and sample for 45 minutes. In the event that the XM19 still indicates an alarm at the end of that interval, the XM2 automatically sequences to the remaining collector and continues to sample for an additional 45 minute period. The collectors are housed in an environmentally controlled chamber which is maintained at 5 to 10°C in all use environments. The collectors can be easily removed from the XM2 and sealed with a threaded cap to ready them for transport.

The electronic subsystem controls the functional operation of the XM2. Air pressures and environmental temperatures are monitored during sampling to insure proper functioning. Malfunction indicators on the control panel alert the operator to possible problems. The power requirements are the same as those for the XM19. The XM2 can be triggered either manually from the control panel or automatically from an XM19 via an interconnecting cable.

*BERRY, KEANE, HATFIELD, and FILLER

The XM2 wet collectors have been tested in authorized Government laboratory facilities against a variety of pathogenic organisms [10], including bacteria, rickettsiae, and viruses, that are representative of possible biological agents. The performance to date meets the stated Army requirements.

SUMMARY

The fielding of the Biological Detector and Warning System in 1984 will provide a unique early detection and warning capability against biological attack which will materially improve the defensive posture of U. S. forces. While the design of the BDWS addresses military needs, the equipment may find other applications. The XM2 offers a unique capability to collect concentrated samples of particulates, and it could prove useful in atmospheric pollution studies. The XM19 provides a means of detecting the presence of various reactive particulates with approximately real time resolution. All operating data from XM19 prototypes are being stored on magnetic tape to create a library of ambient aerosol reaction rate profiles. Further study of these data may suggest additional non-military applications for this equipment.

REFERENCES

1. Lenton, F., and Hoffman, R. The Bendix Corporation. Phase II Report in press. Contract DAAA15-77-C-0009. Engineering Development of the Biological Detector and Warning System. UNCLASSIFIED Report.
2. Putscher, R., and McCrone, W. Walter C. McCrone Associates, Inc. Final Report. Contract DAAA15-72-C-0356. Characterization of Air Particles Giving False Responses with Biological Detectors. July 1975. UNCLASSIFIED Report.
3. Lapple, C., Sancier, K., and Witham, C. SRI International. Final Report. Contract DAAA15-76-C-0141. Separation Techniques for Biological Aerosols and Dusts. April 1978. UNCLASSIFIED Report.
4. White, E. H., Zafirou, O., Kagi, H. H., and Hill, J. H. M. Chemiluminescence of Luminol: The Chemical Reaction. J. Am. Chem. Soc. 86, 940 (1964).

*BERRY, KEANE, HATFIELD, and FILLER

5. White, E. H., and Bursey, M. M. Chemiluminescence of Luminol and Related Hydrazides: The Light Emission Step. J. Am. Chem. Soc. 86, 941 (1964).

6. Graf, L. Environmental Research Corporation. Final Report. Contract DAAA15-77-C-0007. Systematic Investigation of the Design Parameters of a Slit Aerosol Concentrator. November 1978. UNCLASSIFIED Report.

7. Barrett, W., Miller, H., and Boyd, K. Southern Research Institute. Final Report. Contract DAAA15-74-C-0206. Investigation of Luminol and Collection Tape Components and the Effects of Airborne Interferents on the XM19 Detector. December 1976. UNCLASSIFIED Report.

8. Moyer, R. H., and Sibbett, D. J. Geomet, Inc. Final Report. Contract DAAA15-75-C-0233. Suppression of Background on the XM19 Detection Device. April 1977. UNCLASSIFIED Report.

9. Filler, M., Tribble, H., and Saxon, R. Chemical Systems Laboratory Technical Report in preparation. Report of Developmental Tests of the XM2 Automatic Sampler and its Components (1977-1979) II.

10. Filler, M., and Tribble, H. Chemical Systems Laboratory Technical Report in preparation. Report of Developmental Tests of the XM2 Automatic Sampler and its Components (1979-1980) III.

*BLACKMAN

GEOMETRIC AND TEMPORAL CHARACTERIZATION OF
BATTLEFIELD SMOKE AND DUST BY
MULTISPECTRAL DIGITAL IMAGE ANALYSIS (U)

GEORGE R. BLACKMAN, MR.
ATMOSPHERIC SCIENCES LABORATORY
WHITE SANDS MISSILE RANGE, NEW MEXICO 88002

1. INTRODUCTION

The objective of this research is to design and demonstrate an automated technique for: the identification of smoke and dust types observed in simulated battlefield environments; the derivation of the geometry and external dynamics of these features; and prediction of the trajectory, expansion, and dispersion rates with time. The premise is that the use of currently operational passive multispectral image collection systems - with output that is functional in a digital processing mode - will reveal information that either cannot be obtained from data acquired by conventional analog techniques such as photography or at least not as quickly and conveniently for the purpose of effectiveness. An extension of this effort will be to correlate this information with particulate and transmissivity measurements in order to accurately quantify the cloud surface into values that are feasible as input to transport and diffusion modeling.

2. DATA DESCRIPTION AND ACQUISITION

The imaged data input to the techniques development are analog tape recorded raster-scan pictures of the smoke/dust scenes. These records result from observations of the field scenes with optical-vidicon sensors that frame record at rates of 60 per second and are capable of measurement in numerous wavelength bandpasses. The records are digitized to 9-track computer compatible tapes in arrays of 250 x 300 8-bit data

*BLACKMAN

samples. The basic field data acquisition configuration for previous field tests has consisted of a bank of four boresighted sensors recording simultaneously in wavelengths of $0.5\mu - 0.7\mu$, $1.06\mu \pm 0.2\mu$, $3.0\mu - 5.0\mu$, and $8.0\mu - 14.0\mu$. In the field tests to date, data was recorded from two stations positioned approximately 70 degrees apart in perspective of the smoke/dust ignition location and provided eight simultaneous image data sets. Over 100 smoke/dust events have been observed and recorded during participation in the following field experiments:

Dirt I. White Sands Missile Range, September 1978, sponsored by the US Army Atmospheric Sciences Laboratory, 32 events, HE.

Smoke Week II. Eglin AFB, October 1978, sponsored by the PM Smoke Office, 30 events, smokes of all types.

Dirt II. White Sands Missile Range, August 1979, sponsored by the US Army Atmospheric Sciences Laboratory, 40 events, HE - 105mm, 155mm, and C-4.

Dirt III. Fort Polk, Louisiana, April and May 1980, cosponsored by the US Army Atmospheric Sciences Laboratory and the US Army Corps of Engineers, 70 events, HE - 155mm, 105mm, and C-4.

Additional data will be acquired from the Smoke Week III experiment to be conducted at Eglin AFB in early August 1980 sponsored by the PM Smoke Office.

The time incrementation selected for digitization of the analog image records of the earlier field experiments varied due to the uncertainty of what selection would adequately and efficiently describe the growth history of the feature. Prior to the Dirt-II field test, it was established that an incrementation of 0.1 second for the first second of the event and 0.5 second from 1.0 to 10.0 seconds would achieve a comprehensive observation of the effects of the initial blast phase of the event. The externally apparent physical changes that occurred during the buoyant and transport phases were in most cases suitably described with a 2.0-second incrementation - from 10.0 seconds into the event until dissipation. All analog tapes have been retained should the need arise to study selected events in finer detail.

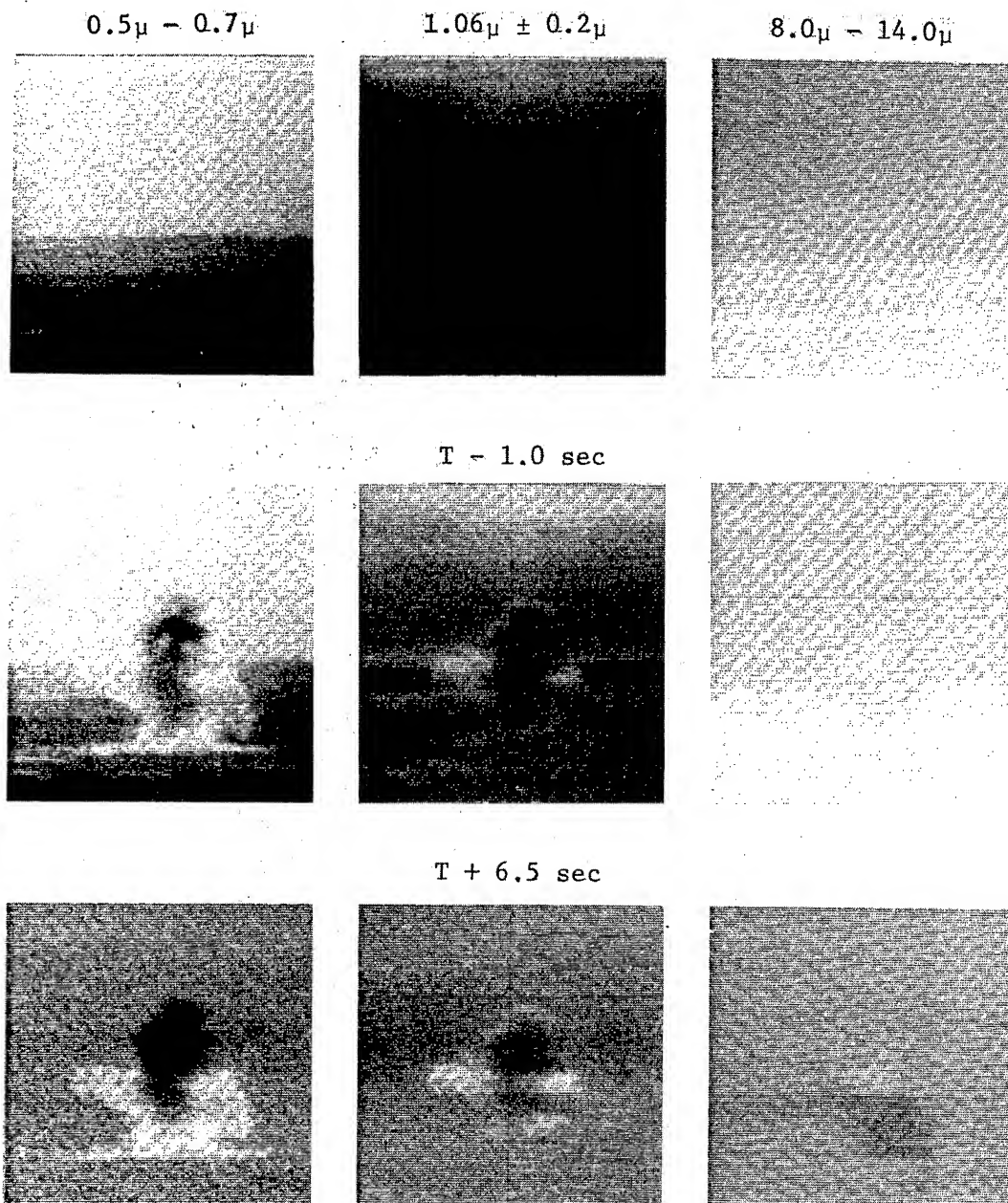
3. TECHNIQUE DEVELOPMENT FOR EXTRACTION OF CLOUD DIMENSIONS

The initial issue undertaken upon availability of the first digitized image data sets of the Dirt-I events was the design of a scheme for isolation of the dust feature from the remainder of the scene. A variety of feature-isolation algorithms was constructed and applied to the least difficult condition - sequential scenes acquired from one sensor station and in one bandpass. The procedure fundamental to the solution was to subtract the gray level values of the array of picture elements of a scene recorded immediately prior to ignition from those corresponding elements in scenes that followed and contained the dust feature. A refinement of this approach was developed later; the gray level slope gradient was computed for the adjacent picture elements in each of the scenes prior to the subtraction. This step tends to subdue the effects of both the high frequency noise and picture wide, average gray level value differences between scenes (figure 1).

Now that the picture elements which comprise the feature have been isolated and consequently, the perimeter well defined, the matter of calculating the geometry is relatively simple. The area of the feature is the product of the number of picture elements and the spatial dimension per picture element as a function of the sensor resolution. The height and width of the feature are the maximum spatial separations in the vertical and horizontal, respectively, and again the number of picture elements times resolution. For the purpose of temporal tracking of the feature and for statistical correlation of growth with time, it was determined that the most efficient and accurate means would be to fit an ellipse to the picture elements that comprise the feature perimeter. The centroid of this ellipse would then be the best estimate of the apparent center of mass; therefore, distance and height relationships as a function of time could be derived by counting picture element separations. Typical computational output are these kinds of values: major axis, minor axis, inclination of the major axis, and the height and lateral offset of the centroid from the location of ignition (figures 2 and 3).

An additional operation is the relative quantization of the cloud surface reflectance. This is being treated by one of two methods: by contouring the raw intensity array, or by contouring the slope gradient array that results from the subtraction procedure. In either case, the contour interval is selected to portray a reasonable representation of the luminance distribution

*BLACKMAN

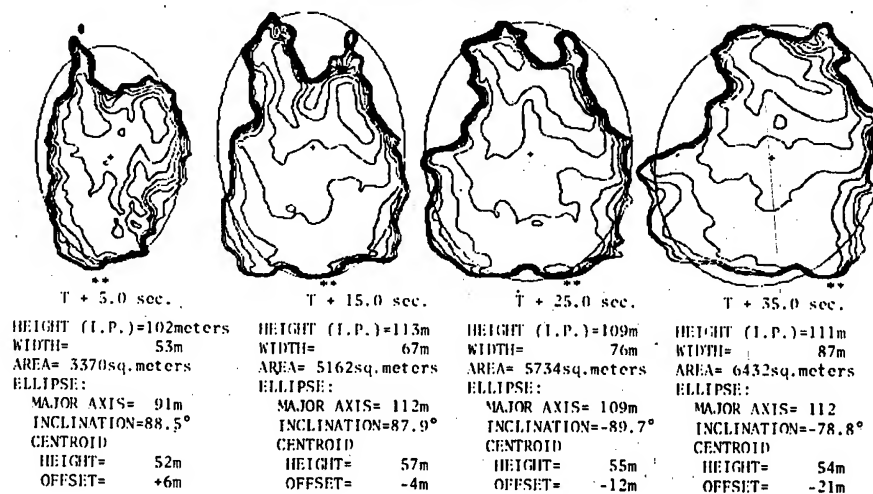
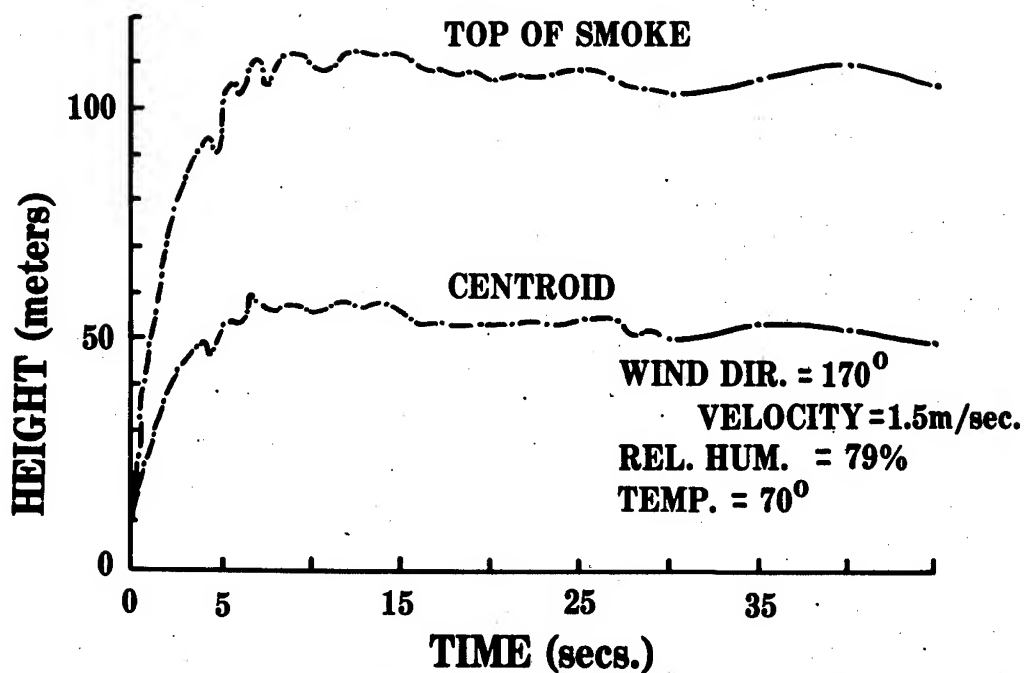


DIRT-II, WSMR - Aug 79

EVENT B-19, 155mm Static

Figure 1. Computer array subtraction.

*BLACKMAN

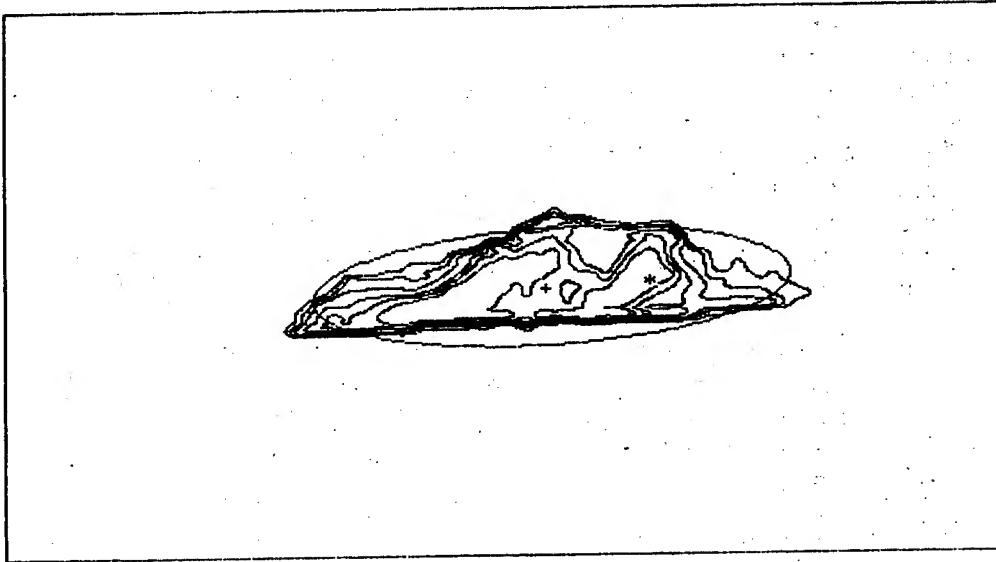


TRIAL #18
 RPW - 155mm XM803

Figure 2. Smoke Week II, Eglin AFB, example of geometry measurements.

*BLACKMAN

DIRT II EVENT # AB7
1857 Z 07-18-79 STATION # 1 SENSOR= 0.5-0.7 MICRON
 T+ 36.0



HEIGHT(ABOVE DETONATION PT.) =	18.0M	HEIGHT OF CENTROID=	9. M
WIDTH(MAX. HORIZONTAL EXTENT)=	57.0M	LATERAL OFFSET	=123. M
VERTICAL EXTENT	= 15.0M	AXES	= 57., 16. M
AREA	= 471.350M	INCLINATION	= -3.7 DEG

CENTROID OF BUOYANT PORTION OF CLOUD: HEIGHT= 10. M OFFSET=134. M
HORIZONTAL EXTENT AT 7 METERS ABOVE SURFACE= 53. M
HOR. EXTENT OF LINE CONTAINING PT. OF MAX. OFFSET OF LEADING EDGE= 46. M
SHEAR(HOR. DISTANCE BETWEEN PT. OF MAX. OFFSET AND PT. AT 7 METERS)= -3. M

** = DETONATION POINT
+ = CENTROID OF PRIMARY ELLIPSE
* = CENTROID OF BUOYANT PORTION OF CLOUD

ATMOSPHERIC SCIENCES LABORATORY
WHITE SANDS MISSILE RANGE, N.M.

Figure 3. DIRT-II, White Sands Missile Range, New Mexico,
example of geometry measurements.

*BLACKMAN

of the surface. In the future, an effort will be made to calibrate selected levels with transmissivity. The spatial integrity of the array is such that if the picture element location is known where an absolute measurement has been obtained, then extrapolation is feasible throughout the scene array.

In the majority of cases, the use of data from one bandpass, particularly that from the 1.06μ sensors, has proven satisfactory for extracting two-dimensional feature geometry. Occasionally, when the scene contrast range is compressed, as evidenced with the minimal lighting conditions found in very early morning or early evening, some difficulty may occur in the separation of feature from background. Therefore, the next logical progression in techniques development was to treat multiple bandpasses in search of compensating strengths.

The prerequisite of multiband analysis is accurate spatial registration and common scaling of the digital arrays. Every picture element in the array of one band must match the corresponding picture elements in the other arrays - both positionally in the image plane and in scale. The design and utilization of tailored interpolation algorithms achieved the necessary relative scaling and magnification or reduction of the arrays.

Two different approaches have been tested with pairs of time coincident data arrays (recorded from the 0.5μ to 0.7μ and 1.06μ spectral regions). One method, initially similar to the single bandpass technique discussed above, performs array subtraction on each of the two spectral scenes from their respective scenes prior to ignition. Those picture element locations from one spectral array that indicate presence of the dust feature are summed with the residual from the other bandpass. The resultant array produces a "window" (a discrimination of the feature from all other characteristics of the scene). This window, or negative mask, can either be used directly as a definition of boundary for computation of the dimensional parameters of the feature, or superimposed upon the raw data array for either of the two bandpasses, thereby permitting relative contouring of the selected wavelength.

The second approach, called a multiband training-field classification technique, is one commonly applied in other disciplines (forestry, crop identification, etc.). It interprets the

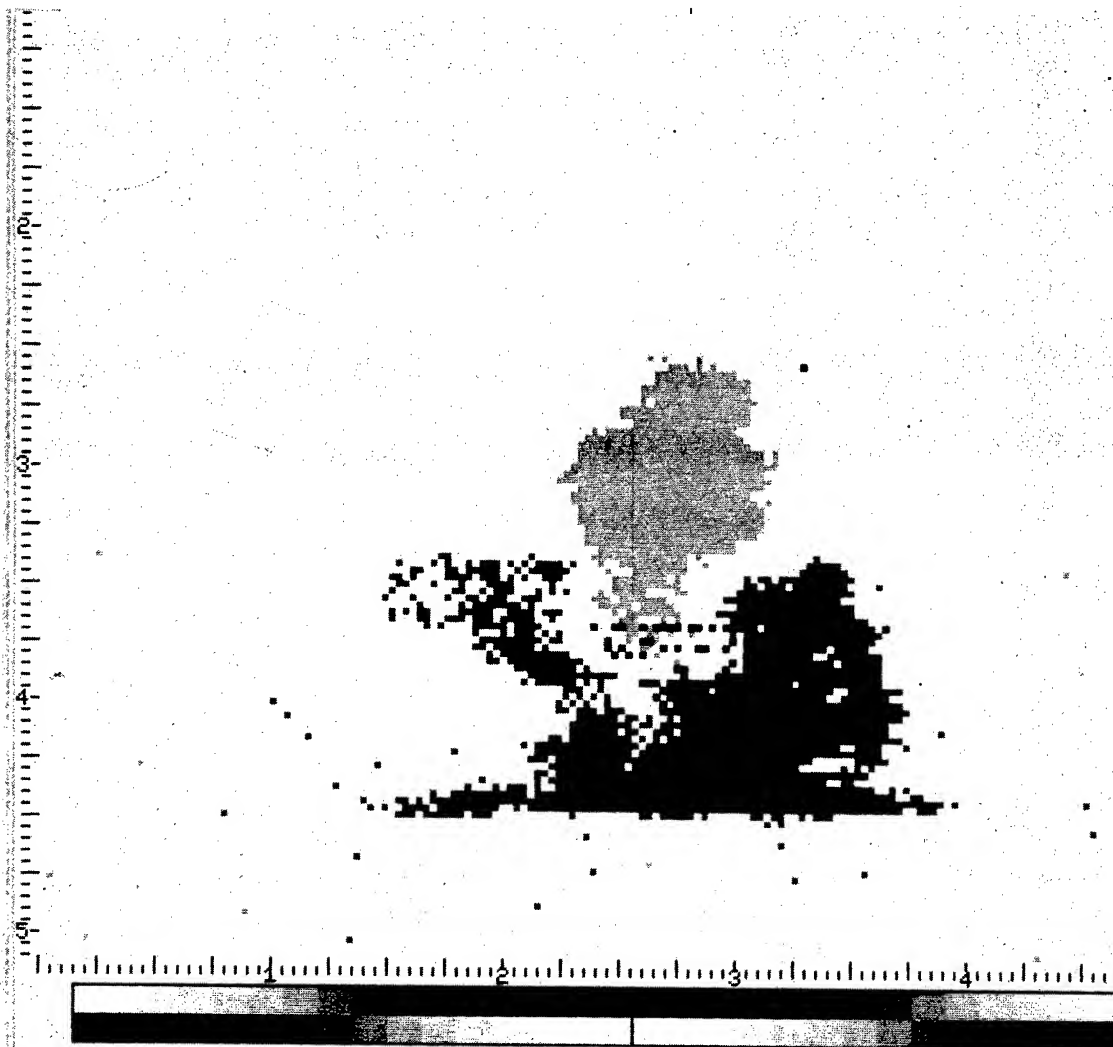
*BLACKMAN

interrelationship of two (or more) bandpasses at each picture element location. This relationship is first established by observing or evaluating the respective gray level ranges found within subarrays dimensioned in the preignition scene where the object features are known (sky, terrain, etc.). Now, every feature is classified and the "signature" pairs of spectral gray level ranges are saved for comparison with each picture-element-pair of a new scene. This comparison, on a picture element position basis, will flag any anomaly or the presence of an object foreign to the "training" scheme and note the location of that picture element. The accumulation of these positions will define the portion of the scene that is dust/smoke (figure 2). In turn, an automatic evaluation of the "anomalous" gray-level ranges will establish a new feature signature that will be used in the classification of subsequent scenes.

The 8.0μ to 14.0μ data has been treated strictly with the single-band extraction technique for definition of boundary and the results registered with the geometry calculations derived by one of the techniques discussed above (figure 4). The predictable fact that the perimeter of the 8.0μ to 14.0μ bandpass is seldom found coincidental with feature perimeters calculated from the other bands was learned very early in this research. In most cases, especially with high explosives and white phosphorous, the temperature band is greater in extent and area during the initial phase of the event and then subsides rather rapidly back to within the particulate perimeter. There appears to be a distinctive correlation of this dissipation rate to the type of smoke, and in the case of the high explosive, to the size of the charge.

Only preliminary results have been achieved in recently instituted attempts to correlate data acquired simultaneously from two widely separated sensor perspectives. Perfection of a method is one of the primary goals of this research, realizing that the results will provide a means of accurately calculating the volume and drift direction of the feature. The reasonable assumption is that the ellipse is the best generalized estimate of the shape of the feature and that the centroid is the best estimate of the apparent center of mass. The approach is to project each of the two ellipses from their respective two dimension domains into three dimension space and to translate the respective centroids to a common point space position, thereby establishing the origin for the three dimensional coordinate system. The angular relationships and dimensions of the two pairs of axes will fix

*BLACKMAN



ASLO10 DIRT II SET 14 MAP-V/N+E EXP3

DIRT-II, WSMR - Aug 79 EVENT B-19, 155mm Static
T+6.5sec.

Smoke Predominates	=	light gray
Dust Predominates	=	dark gray
Temperature Hotter Than Ambient	=	black

Figure 4. Multiband analysis technique
(0.5μ - 0.7μ , $1.06\mu \pm 0.2\mu$, 8.0μ - 14.0μ).

*BLACKMAN

points in the coordinate system at the surface of an ellipsoid. The ellipsoid mass, orientation, and unit translation with time would itself be the best estimate of the three dimensional character of the smoke or dust feature. Other techniques will be tried: photogrammetric mapping of the actual surface and statistical extrapolation of all or some of the dimensions calculated by the techniques discussed earlier, etc.

4. STATISTICAL ANALYSIS

Trends in the parameters resulting from dimensional analysis of the Dirt and Smoke Week field experiments are being evaluated for the purpose of designing statistical schemes for identifying the type and size of the source of the feature and prediction of the growth dimensions and transport distance with time (figure 5).

The events of the three Dirt tests were numerous detonations of C-4, and static and tube-delivered 155mm and 105mm HE rounds. The static rounds were used to simulate a variety of impact orientations by positioning a single round/event either at the surface or at a known subsurface depth and in various angular configurations in respect to the surface. The resultant dust/smoke clouds were observed to effect fairly characteristic dimensions, shapes, sizes, and temperature extinction rates. The amplitudes of these measurements were controlled by the soil and vegetation characteristics of the locality but, interestingly, the meteorology did not distort the source-related dynamics of the feature until at least 8 or 10 seconds into the event. In this short time frame, certain of the dimensional parameters associated with given sets of source conditions have behaved with measurable consistency, hence, the provision of a means for type classification.

The algorithm is a decision comparison of the ratios of combinations of the computed slopes for segments of curves derived from a time sequence of each of the dimension measurements extracted by one of the techniques described earlier in the paper. The comparison is made with ratio values known to correspond to a given set of source conditions. The parameters found most useful so far are these:

a_s/b_s = ratio of the slopes of the major and minor axes

Graph showing the height of the ellipse centroid above the detection point, the offset of the ellipse centroid, the height of the cloud above the detection point, and the width of the cloud over time.

Y-axis: METERS (0.0 to 275.0)

X-axis: TIME (SECS) (0.0 to 110.0)

Legend:

- HEIGHT OF ELLIPSE CENTROID ABOVE DET. PT.
- OFFSET OF ELLIPSE CENTROID
- **** HEIGHT OF CLOUD ABOVE DET. PT.
- ++++ WIDTH OF CLOUD

The graph displays four data series over a 70-second period. The 'HEIGHT OF CLOUD ABOVE DET. PT.' (****) starts at approximately 15 meters and increases linearly to about 215 meters. The 'WIDTH OF CLOUD' (++++), represented by a dotted line, starts at 0 and increases to about 25 meters. The 'HEIGHT OF ELLIPSE CENTROID ABOVE DET. PT.' (-----) starts at 0 and increases to about 15 meters. The 'OFFSET OF ELLIPSE CENTROID' (.....) starts at 0 and increases to about 35 meters.

TIME (SECS)	HEIGHT OF ELLIPSE CENTROID ABOVE DET. PT. (METERS)	OFFSET OF ELLIPSE CENTROID (METERS)	HEIGHT OF CLOUD ABOVE DET. PT. (METERS)	WIDTH OF CLOUD (METERS)
0	0	0	15	0
10	2	5	25	2
20	4	10	35	4
30	6	15	45	6
40	8	20	55	8
50	10	25	65	10
60	12	30	75	12
70	15	35	85	15

105MM. TUBE DELIVERED

221

*BLACKMAN

Y_s/x_s = ratio of the slopes of the height of the centroid above a horizontal plane containing the ignition location and the transport (offset) distance from the ignition point

I_s/x_s = ratio of slopes of the inclination of the major axis and the transport distance.

Experimentation is under way to use numerous combinations of these slope parameters in a multidimensional space coordinate system, whereby defined "cluster" classification separations may enhance the decision accuracy.

The establishment of a procedure for prediction of feature growth and trajectory track with time has been approached in three ways: direct extrapolation of a quadratic fit to the first few seconds accumulation of computed dimension data and the extrapolation of the slopes from short-time segments of least-square curves representative of the earlier dimensions. Either of these approaches works satisfactorily for predictions up to 15 to 20 seconds subsequent to the time of the calculation (data acquisition time) but can become erratic for greater time spans. The most promising approach currently being investigated is the application of a stochastic predictor/corrector interpreter of the early data. The one being tested is the "Kalman filter" and preliminary results indicate the possibility of extrapolation at least as far in advance as 2 minutes from the calculation.

5. SUMMARY OF PROJECT STATUS AND PROBLEMS

As with most research projects, the predominate problems are an insufficient base of controlled test data and the quality of the data itself. The data base has begun to expand both in volume and variety due to increasing interest in the technique and the results and, consequently, invitations for participation in many field tests. As for data quality, the acquisition and the computer handling procedures have improved progressively and the availability of sensors with improved resolution and signal-to-noise ratios is under review. The signal-to-noise related problems have required the development of special data enhancement algorithms that would be unnecessary if the sensor output was of a better quality.

*BLACKMAN

The battlefield environment modeling researchers have set a requirement for computation of the geometry for all events from all field tests in which we participate. The information being furnished reflects the status of our techniques research and computer program engineering - the more recent the information, the more accurate and comprehensive.

At this stage, the technique for computing the cloud geometry, derived from data acquired from one perspective and two bandpasses, is functional with only computer data handling efficiency still in work. The registration scheme for matching the feature perimeter of the thermal bandpass with the geometry is operational. The technique for extracting three dimensional information from two or more perspectives is yet in the preliminary stages of development; early testing with a few data sets have proven the feasibility. The feature identification scheme functions for nearly all test data on hand, but at this stage, with a high degree of interactivity with the computer. Adaption of an automatic procedure is in a very early level of development. The method for predicting feature growth and transport is in a similar state of design.

There are many important subinvestigations of this research that are in planning. A fundamental need is the capability to transform the output of the techniques discussed here to match the output of specific surveillance and designator systems currently in battlefield inventory. Although the data used in this project are acquired in wavelength ranges of the spectrum common to most fielded systems, a refinement of accuracy could be achieved if the total systems response could be mathematically duplicated. How this can be approached has been discussed with many experts in the field of optical/spectral calibration and a preliminary course of action is in design.

Another logical progression will be to assist in updating the current smoke munitions expenditure procedures as required to "smoke" a given area under given conditions of meteorology and tactical perspective.

One more investigation of many that are envisioned would be in support of artillery by providing a means to measure and, as a result, correct for the wind effects in the vicinity of the target. A quick evaluation of the "local" wind profile could be achieved by the expenditure of a single HE round.

*BLACKMAN

6. CONCLUSIONS

Among the many questions presented to a field commander regarding the atmospheric environment of the battlefield are these: What is the type of contaminant? Who does it belong to? How long will it be there? What area will it affect during transport? How much area will it obscure? Which of my electro-optical systems will it incapacitate? Which of the enemy's?

The purpose of this project is to assist in answering these questions - either by empirical input to current efforts in modeling design or as a means of validation of these designs. Another possibility might be the design of a compact field system that could provide answers directly (passive multiband sensors, a special purpose microprocessor and software, and a small graphics display).

MICOM PROGRAM IN OPTICAL BISTABILITY (U)

CHARLES M. BOWDEN, Dr. and DAVID W. HOWGATE, Dr.*
US ARMY MISSILE COMMAND
REDSTONE ARSENAL, ALABAMA 35809

I. INTRODUCTION

Some years ago, a number of people (1-4) independently suggested the use of a saturable absorber to induce optical bistability (hereafter referred to as OB). The phenomenon was demonstrated and studied recently by Gibbs, McCall and Venkatesan (5) who used a cw dye laser to excite atoms of sodium vapor in a cell between the plates of a Fabry Perot interferometer. Under certain experimental and material conditions, they observed a nonlinear dependency of the transmitted field as a function of the dye-laser input which exhibited hysteresis, differential gain, and bistable behavior.

Interest in OB from the practical applications standpoint stems from obvious device applications as the optical analog of the transistor, optical clipper or limiter and digital optical memory element. The recent demonstration of the phenomenon (5) has generated considerable interest from the fundamental point of view as a clear example of spontaneous ordering in an open, stationary system of matter interacting with light. This has led to a surge of recent theoretical activity.

The first model for OB was proposed by McCall (6), who introduced a nonlinear susceptibility into the Maxwell-Bloch representation in the full propagation treatment. His results are necessarily calculational rather than analytical. Bonifacio and Lugiato (7) were the first to obtain the main features of OB from implementation of the Maxwell-Bloch model, which they solved analytically in closed form. They later extended their model (8) to a quantum-statistical representation of a stationary system far removed from thermodynamic equilibrium, but with the same essential assumptions, the most crucial being

the "mean field" approximation which amounts to requiring that the field be sufficiently uniform over the volume of active atoms. Others, such as Walls et al. (9) have considered similar models which are, on the whole, in agreement with the results of Bonifacio and Lugiato.

All of these models have one essential common characteristic, namely, they consider OB within the framework of individual or independent atom response to the electromagnetic field. These are therefore necessarily absorptive models which describe OB as a transition from a state of coherent response of individual atoms to the externally-applied driving field and high absorption (low transmission) to a state of saturation or bleaching of the material (high transmission). The experimental results on sodium vapor (5) exhibited a large dispersive contribution, and these models do not appear to describe the dispersive aspects even qualitatively, although the absorptive characteristics appear to be adequately qualitatively described.

It seemed to us that OB should stem, at least under certain conditions, from the same kind of fundamental interaction that gives rise to the dynamical cooperative process known as superfluorescence (10, 11). This prompted us to take a fresh approach to the interpretation of OB in terms of a model which emphasizes the contribution from interatomic cooperative processes in matter interacting with light. Our model (12) differs from other previous models in that it includes the possibility for atom-atom interaction and correlation via the mutual internal electromagnetic field (virtual photon exchange) as well as the individual atom coupling to the electromagnetic field.

The results of our model (12) and other models (7-9) predict identical behavior for "absorptive" OB (perfect cavity, laser and atomic tuning). However, our results fit the dispersive characteristics reported for the sodium experiment (5) qualitatively quite well. In addition, we predict new results in reversible hysteresis and bistability in the variation of inverse effective temperature T_g with the output field for fixed input above a certain threshold value. This new result (13) has a wide range of potential applications, including a sensitive IR, FIR or millimeter wavelength detector with frequency upconversion.

In addition, our results provide an interpretation of OB as a true first-order phase transition, from atomic order to disorder due to virtual photon exchange between atoms, far from thermodynamic equilibrium. In the absence of an applied field, our results show the existence of a second-order phase transition (12,14) below a critical temperature determined by material parameters and cavity detuning.

Another unique characteristic of our results is that the model constitutes the optical analog of the Meisner effect (15) in superconductivity. Due to the collective atomic behavior (optical Meisner effect), our results predict for the first time the existence of OB in a small volume without mirrors. This could have far-reaching applications in the use of arrays of micron size elements for optical digital information storage and retrieval as well as optical digital image formation.

Finally, it should be pointed out that this work is a direct outgrowth of our program in swept-gain superradiance (16-18). Furthermore, MICOM will co-host, with ARO-D, an International Conference and Workshop on Optical Bistability, in Asheville, North Carolina, 3-5 June 1980. This conference is expected to significantly advance the field and to provide a timely record of the state-of-the-art in this rapidly-developing and potentially extremely useful field. The conference and its impact are anticipated to be similar and of much the same significance as the conference hosted by MICOM on Superradiance (19).

II. THEORETICAL MODEL AND INTERPRETATION OF PHENOMENON

We consider a collection of N identical two-level atoms with energy level separation ϵ interacting with the electromagnetic field in the dipole approximation. The electromagnetic field which interacts with the atoms is comprised of an internal field and, in addition, an applied cw field assumed to be in a coherent state (20), with field amplitude α and carrier frequency ω_0 . The atoms of the material are considered to be confined to a volume V_g which is much smaller than the resonance wavelength λ_r associated with the atomic bare-state separation. This assumption does not critically affect our results and tends to allow emphasis upon the nature of collective atomic aspects in the results in an unencumbered fashion.

The Hamiltonian H which represents this model is written in the form

$$H = H_0 + H' \quad (\text{II-1})$$

where, in units such that $\hbar = c = 1$,

$$H_0 = \sum_{k=0}^{\infty} \omega_k a_k^\dagger a_k + \frac{1}{2}\epsilon \sum_{j=1}^N \sigma_j^z \quad (\text{II-2a})$$

$$H' = \left(\sum_{j=1}^N \sum_{k=0}^{\infty} g_k a_k^+ \bar{\sigma}_j + h \cdot c \right) + \left(\alpha^* e^{i\omega_0 t} \sum_{j=1}^N \sigma_j^- + h \cdot c \right), \quad (\text{II-2b})$$

where $h \cdot c$ means hermetian conjugate, and we have used the rotating wave approximation.

The first and second terms in (II-2a) represent the free field and atomic system, respectively, whereas the first two terms of (II-2b) describe the interaction of the atoms with the internal field and the last two terms describe their interaction with the externally-applied coherent field. The factor α is the complex externally-applied field amplitude. The field photon creation and annihilation operators conform to the Bose commutation relations (12), and the atomic operators are the usual Pauli operators, and

$$g_k = -i(\omega_k/2V)^{1/2} \underline{\epsilon}_k \cdot \underline{d} \quad (\text{II-3})$$

where V is the quantization volume and $\underline{\epsilon}_k$ and \underline{d} are the polarization vector and the matrix element for the transition dipole moment for the atoms (21).

We are interested in determining the steady state properties of the system described by (II-2a, II-2b). In order to retain the essential many-body aspects of the system, it is convenient to treat the system in an ensemble representation. This means taking ensemble averages of relevant dynamical operators such as population difference and dipole moment operators. To facilitate this, we perform the following operations: (i) Canonically transform to a perpendicularly doubly rotating frame, rotating at the laser frequency ω_0 , so the Hamiltonian (II-2) becomes explicitly time-independent (12). The electromagnetic field then appears as a d.c. field in the transformed frame. (ii) Introduce an effective temperature T_s in the transformed representation which is the exact analog of a "spin temperature" (12,22). This is equivalent to a definite statement of the form of the density operator ρ , in the transformed representation.

Although the system is an open system far removed from thermodynamic equilibrium, we can analyze the macroscopic properties of the system in the transformed representation in terms of the free energy F , given by

$$e^{-\beta_s F} = \text{tr } e^{-\beta_s H_T}, \quad (\text{II-4})$$

where $\beta_s = 1/kT_s$ and k is Boltzmann's constant.

Making use of the transformation to the doubly rotating frame (2-4) of reference (12) and adiabatically eliminating the internal field variables, the transformed Hamiltonian H_T , through second order in the atom-field interaction, was shown by Bowden and Sung (12) to be

$$H_T = H_{OT} + H'_T \quad (\text{II-5})$$

where

$$H_{OT} = \Omega a^\dagger a + \frac{1}{2} \Omega_a \sum_{j=1}^N \sigma_j^z, \quad (\text{II-6a})$$

$$H'_T = -\bar{g}/N \sum_{\substack{j, \ell=1 \\ j \neq \ell}}^N \sigma_j^+ \sigma_\ell^- + \alpha \sum_{j=1}^N \sigma_j^- + \alpha^* \sum_{j=1}^N \sigma_j^+. \quad (\text{II-6b})$$

Here,

$$\Omega = \omega - \omega_0, \quad \Omega_a = \epsilon - \omega_0. \quad (\text{II-7})$$

For simplicity, we have considered only a single radiation field mode of frequency ω interacting with the atomic transition. If the atomic medium is in a cavity, then ω is the cavity mode frequency. If there is no cavity, then $\omega = \epsilon$. The first term in (II-6b) is interpreted as atomic interaction via the electromagnetic field, where the effective atom-atom coupling, \bar{g} , is field-dependent (12),

$$\bar{g} = g_0^2 \frac{(\omega - \omega_0 - \lambda)}{[(\omega - \omega_0 - \lambda)^2 + \gamma^2]} \quad (\text{II-8})$$

where

$$g_0^2 = \frac{(4\pi)^2 d^2}{\omega} k \bar{\rho}. \quad (\text{II-9})$$

In the above, λ is the Stark shifted atomic level separation (12),

$$\lambda = +\sqrt{\Omega_a^2 + |\Delta|^2} \quad (\text{II-10})$$

where $|\Delta|$ is the Stark shift which is dependent upon the value for the internal field intensity. Since the latter is to be determined in the result, $|\Delta|$ must be determined self-consistently later on in the results of the calculation. It is crucial to retain the Stark shift in (II-10) (usually neglected in second-order calculations) in order to obtain the first-order phase transition which leads to OB. The damping term γ appearing in (II-8) is just the cavity width (12) or, if no cavity is present, it is just the photon escape rate from the atomic volume. In (II-9), d is the matrix element of the

transition dipole moment, k is the density of field modes in the neighborhood of the principal mode of frequency ω , and $\bar{\rho}$ is the total number of atoms N in a cubic wavelength at atomic resonance λ_r .

The equation (II-6) is our working Hamiltonian. The atom-radiation field interaction (II-2b) has now been recast in terms of an effective interatomic pair interaction via the internal field (II-6b). The pair correlation is depicted by the first term in (II-6b) and may lead to cooperative atomic effects by virtual photon exchange. This term is identical to the interaction which leads to cooperative atomic behavior in superfluorescence, (10,23). The inclusion of the Stark shift correction in \bar{g} , (II-8), (II-10) gives negligible contributions to the results for superfluorescence, but is absolutely essential to arrive at OB in the steady state for this model. This causes the effective interatomic coupling to be internal field intensity dependent, and thus leads to feedback between the atoms and their mutual radiation field. The atomic pair correlation term in the interaction is also identical to that for Cooper pairs in the BCS theory of superconductivity (12,15).

We proceed now to calculate the free energy F from (II-4). To perform the trace on the right-hand side of (II-4), it is necessary to linearize the Hamiltonian (II-6) and to obtain a thermodynamically equivalent linearized Hamiltonian (25,26). The method of references (25) and (26) is used to obtain

$$H'_T = N \bar{g} |\nu|^2 - N \Delta^* \sigma^+ - N \Delta \sigma^- , \quad (\text{II-11})$$

where

$$\Delta \equiv \bar{g} \nu^* - \alpha^* . \quad (\text{II-12})$$

Here, ν is a variational parameter used in the linearization, to be determined by minimization of the free energy F , (25,26).

In the above expressions, we have used the assumption that all the atoms are identical to drop the subscripts, j , and to replace the sums by N and the double sums by $N(N-1)$.

The thermodynamically equivalent Hamiltonian (II-11), i.e., the linearized Hamiltonian which yields the same free energy F in the limit of large N as the original Hamiltonian (II-6b) has an immediate physical interpretation. The interaction expressed in (II-6b) is thermodynamically equivalent to a single atom, mean field interaction expressed in (II-11). The factor Δ , (II-12), is the mean field, i.e., the total field acting on a single atom due to the combined atomic reaction fields of all the other atoms (first term in (II-12)) and the local value of the externally-applied field (second term in (II-12)). The expression for the total local field at an atomic site, (II-12),

is just Maxwell's equation (all electromagnetic fields appear as d.c. fields in the transformed frame rotating at the laser frequency ω_0).

The free energy F is now easily evaluated from (II-4) using (II-11) to give,

$$F = N \bar{g} |v|^2 - \frac{N}{\beta_s} \log \left[2 \cosh \frac{\beta_s}{2} \lambda \right] + \frac{1}{\beta_s} \log (1 - e^{-\beta_s \Omega}) . \quad (\text{II-13})$$

The variational parameter v is evaluated from the normal equation, (25,26),

$$\partial F / \partial v = 0 . \quad (\text{II-14})$$

If we let

$$x = \Delta^* , \quad y = -\alpha \quad (\text{II-15})$$

equation (II-14) yields

$$\frac{\partial F}{\partial v} = N \bar{g} v^* - 2 \bar{g} x^* \frac{\tanh \frac{\beta_s}{2} \lambda}{\lambda} = 0 . \quad (\text{II-16})$$

From (II-16),

$$v = 2 x \frac{\tanh \frac{\beta_s}{2} \lambda}{\lambda} , \quad (\text{II-17})$$

which is easily shown to be the ensemble average for the macroscopic atomic polarization (12). It is furthermore easily shown that the above condition obtained from (II-14) corresponds to an absolute minimum, i.e.,

$$\partial^2 F / \partial v^2 > 0 . \quad (\text{II-18})$$

It is to be noted that the Stark shift Δ is now determined self-consistently from (II-12) and (II-17).

If we use the definitions (II-15) in (II-12) and use (II-12) to eliminate v from (II-17), then after multiplying both sides of (II-17) by \bar{g} , the following equation of state for the applied field y as a function of the internal field x is obtained,

$$x - y = 2 \bar{g} x \frac{\tanh \frac{\beta_s}{2} \lambda}{\lambda} . \quad (\text{II-19})$$

This is the main result of this paper and leads to bistability, reversible hysteresis and differential gain between the three quantities, x , y , and β . These characteristics will be discussed in the next section.

III. INTERPRETATION OF RESULTS

A. Optical Bistability as a First-order Phase Transition

The main result of our model, (II-19), has the form typical of a first-order phase transition. For absolute zero of effective temperature and for perfect laser and cavity tuning, i.e., for $T_g \rightarrow 0$, $\omega = \epsilon = \omega_0$, (II-19) reduces to exactly the form for the equation of state obtained earlier from the single-atom, coupled Maxwell-Bloch models (8), (9), i.e.,

$$y = x + 2c \frac{x}{(1+x)^2}, \quad (\text{III-1})$$

where

$$c = g_0^2 / \gamma^2, \quad (\text{III-2})$$

and we have written x and y in units of γ . Here, however, the physics is quite different as will be discussed later.

Equation (II-19) is shown plotted in Figure 1, input field amplitude y vs. output field amplitude x for various values of equal cavity and laser offtuning. It is readily established that the minimal condition for OB to occur is that $c > 4$, (8,12).

It is easily shown (27) that all points on the curves in Figure 1 are stable steady-state conditions except those for which $dx/dy < 0$. Thus, the points on the curves between the turning points having negative slope are unstable. Increasing the applied field y from zero, the output follows a nearly linear response until the first turning point is reached along the curve for the equation of state. In this regime, the material responds mainly by atom-atom coupling via virtual photon exchange, i.e., \bar{g} , (II-8) is large due to the relatively small Stark shift (II-10). The reaction field due to the collective response of the atoms (first term on the right-hand side of (II-12)) opposes the applied field (second term on the right-hand side of (II-12)) to produce a small output field (II-12, (II-15)). This phenomenon, due to collective response to an external field, is somewhat analogous to the Meissner effect (28) in the theory of superconductivity. In this regime the macroscopic transverse dipole moment, v , (II-17) is small, again due to the relatively small Stark shift.

Once the first turning point is reached (point A of curve a), by increasing y , there are no steady state values available for the system if y is further increased, unless the system jumps to a higher value of the output (point B of curve a). This jump

corresponds to a sudden decrease in \bar{g} , the atom-atom coupling, and a sudden increase in the macroscopic polarization, v . Further increase in y produces a nearly linear, empty cavity response in x . That is, the material is nearly transparent to the input y , i.e., $x \approx y$. In this regime, the atom-atom pair correlation is destroyed and each individual atom's dipole moment follows the driving field y , coherently with definite phase. This could be called the regime of "cw self-induced transparency".

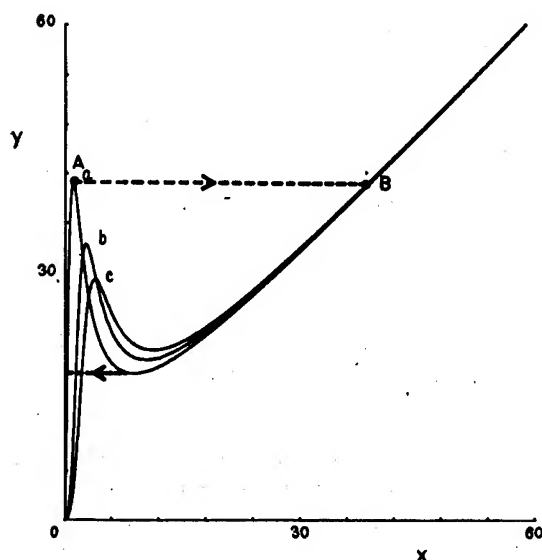


Fig. 1. Effect of cavity and laser detuning on optical bistability. Input field y vs. internal field x from (II-19).

Curve a: $c = 40$, $\delta = v = 0$;
 curve b: $c = 40$, $\delta = v = 2$;
 curve c: $c = 40$, $\delta = v = 4$.
 $\delta = (\omega - \omega_0)/\gamma$; $v = (\epsilon - \epsilon_0)/\gamma$;
 $T_s = 0$.

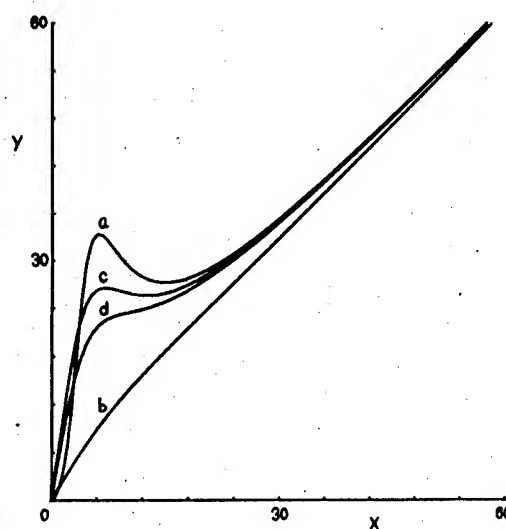


Fig. 2. Asymmetric effect of cavity detuning on optical bistability. Input field y vs. internal field x from (II-19).

Curve a: $c = 60$, $\delta = v = 10$; curve b: same parameters as for curve a, except $\delta = -9$; curve c: same parameters as for curve a, except $\delta = 9$; curve d: same parameters as for curve a, except $\delta = 8$; $T_s = 0$.

The asymmetric effects of cavity off-tuning for fixed laser frequency is shown in Figure 2. These results exhibit large dispersive contributions for cavity off-tuning and are in good qualitative agreement with the experimental results for sodium vapor (5).

The effective temperature dependence of the hysteresis cycle and OB threshold is shown in Figure 3 for input y vs. output x from (II-19) in units of γ . For convenience, we have taken perfect tuning, so (II-19) becomes, in units of γ ,

$$y = x + 2c \frac{x}{(1+x)^2} \tanh \frac{1}{2} \Gamma x, \quad (\text{III-3})$$

where

$$\Gamma = \gamma \beta_s = \gamma / kT_s. \quad (\text{III-4})$$

B. Effective Temperature-induced Bistability and Hysteresis and the Optical Meisner Effect

It is interesting to consider the inversion of (III-3) to obtain Γ in terms of the input y and output x , (29),

$$\Gamma = \frac{1}{x} \ln \left\{ \frac{2cx + (y-x)(x^2+1)}{2cx - (y-x)(x^2+1)} \right\}. \quad (\text{III-5})$$

Equation (III-5) is plotted in Figure 4 for the inverse temperature, Γ vs. output field x for fixed y in units of γ . Each curve corresponds to a different value for the fixed input $y = y_c$. It is seen that bistability and hysteresis occur in the output field x by varying the inverse temperature Γ when the input y is fixed at a value above a certain threshold.

Consider the curve in Figure 4 showing the largest hysteresis area, corresponding to the appropriate fixed input field $y = y_c$. As the effective temperature T_s is increased (Γ decreased) from some small value to larger values, the output x increases slightly as the reaction field $\bar{g}v$ in (II-12), due to the collective atomic pair interaction which opposes the applied field α , is diminished as the temperature T_s is increased, (II-17). This is due to simultaneous reduction of the macroscopic dipole moment (II-17) because of the increase in effective temperature T_s , and to the decrease in \bar{g} (II-8) as a consequence of the increase in the field-induced Stark shift, (II-10), (II-15).

As Γ is decreased to the value corresponding to point A in Figure 4, any further decrease in Γ will necessarily correspond to a stationary state on the upper part of the curve, point B. The system undergoes an abrupt increase in the output x as a consequence of the catastrophic breakdown of the atomic pair correlation and, hence, the reaction field $\bar{g}v$ (II-12). In other words, along the path AB, Figure 4, the macroscopic transverse polarization v (II-17) increases abruptly due to the increased Stark shift caused by the transition to

larger total local field. In the same process, however, the atomic pair correlation \bar{g} undergoes a catastrophic reduction in the transition from A to B. As Γ is further decreased, the macroscopic polarization diminishes due to the increase in T_s and the system approaches the state of atomic saturation (bleaching) at high absolute temperature. The reverse process takes place as Γ is increased (T_s decreased).

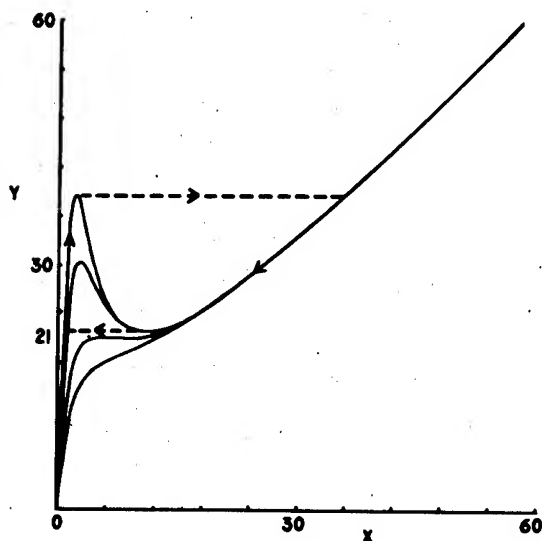


Fig. 3. Normalized externally-applied field y vs. normalized internal field x according to Eq. (III-3) with $c = 60$. Each curve corresponds to a different value for Γ , and in order of decreasing values for the threshold value for y , $\Gamma = 1.00, 0.65, 0.35, 0.25$. The threshold value of Γ for bistability in this case is $\Gamma = 0.35$. The dotted lines and arrows indicate a particular hysteresis cycle.

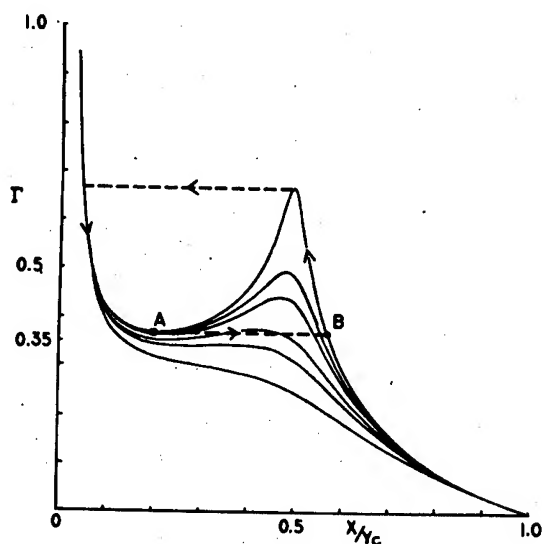


Fig. 4. Γ vs. x/y_c according to Eq. (III-5) for $c = 60$ and various values for the fixed externally-applied field y_c . In order of decreasing values for the threshold for Γ , $y_c = 21.8, 21.7, 21.6, 21.3, 21.0, 20.0$. The threshold value of y_c for bistability is $y_c = 21.0$ which is seen to be consistent with the threshold value of Γ for bistability in Fig. 3. The dotted lines and arrows indicate a particular hysteresis cycle.

The reduction of the internal field x due to atomic pair correlation (11-12), and the abrupt reduction of the reaction field at a critical temperature, T_s , with consequent increase in the total internal field x , for fixed input y_c shown in Figure 4 is quite analogous to the Meisner effect in the theory of superconductivity (15,28). We are tempted to label this effect, the "optical Meisner effect".

C. Second-order Phase Transition in the Absence of Applied Field

In the absence of applied field, i.e., for $y = 0$, (II-19) predicts the existence of a second-order phase transition, provided that the following gap equation is satisfied (12),

$$\tanh \frac{1}{2}\beta_c \epsilon = \frac{\epsilon}{2g_o} \frac{(\omega - \epsilon)^2 + \gamma^2}{\omega - \epsilon}, \quad (\text{III-6})$$

where T_c is here the actual temperature of the heat bath.

If this equation can be satisfied, it defines a critical temperature T_c below which the system exhibits a macroscopic polarization (ordered phase) and above which there is no macroscopic polarization (disordered phase). It is readily seen that (III-6) cannot be satisfied without off-tuning provided by cavity mirrors. Furthermore, it is readily determined that for conditions where OB is observed in the optical regime, i.e., $c > 4$, (III-2), (III-6) will never be satisfied (12). However, it can be satisfied for microwave frequencies. This explains why this effect has not yet been observed in OB experiments.

IV. SUMMARY AND CONCLUSIONS

The effort at MICOM in quantum optics has produced results which for the first time predict OB which is caused by cooperative atom-atom interaction via their mutual radiation fields (12). The mechanism for the atomic pair correlation can be interpreted as due to virtual photon exchange interaction in analogy with the interaction between Cooper pairs via the phonon field in the BCS theory of superconductivity (30). The measure of the strength of the atomic pair correlation is \bar{g} (II-8). The main result of our theoretical model is the equation of state (II-19) relating the input field y to the output field x as a function of the inverse of the effective temperature β_s .

The same mechanism is well known to be responsible for the cooperative atomic interaction which results in the dynamical process of superfluorescence (23,31). Our model also connects for the first

time OB, superfluorescence of the superradiant phase transition in thermodynamic equilibrium in the absence of applied field (32).

A completely new and heretofore unpredicted phenomenon (29) is shown in Figure 4. Here, we have depicted the variation of the output field amplitude x as a function of the inverse temperature Γ for various input fields y_c from (III-5). These curves show bistability and reversible hysteresis in the output field x with variation of the inverse temperature Γ for fixed input field, y_c for the latter greater than a well-defined threshold value. These results could have important applications as a sensitive FIR, IR or millimeter wavelength detector with frequency upconversion. That is, an FIR or IR active material could be introduced as a buffer with the optically nonlinear material in a cavity. The FIR or IR energy absorbed by the buffer can be kinetically transferred to the optically nonlinear material via rotational-vibrational, translational energy transfer to alter Γ . Switching times in the hysteresis cycle could be on the order of the thermal fluctuation times for the system.

We also predict for the first time OB in a small volume without mirrors. For the case without mirrors, the mode frequency $\omega = \epsilon$ and $\gamma = c/2L$ where L is the length of a cylindrical volume of the active material. The conditions for a cavity are that the mode frequency ω is the cavity frequency and need not equal the atomic frequency ϵ , and the photon escape rate $\gamma = c/2L\tau$ where τ is the transmission coefficient for the cavity mirrors. Optical bistability in a small volume without mirrors could have important applications for micron size OB elements imbedded in a neutral binder to constitute a two-dimensional optical digital memory bank or optical digital imaging surface. This certainly would alleviate the problem of having to produce highly uniform reflective surfaces on miniaturized OB elements. It may be also possible to constitute a three-dimensional optical digital memory bank of relatively compact dimensions.

Further work is in progress (27,33) to calculate the relevant switching rates in terms of material parameters and to determine the effects of atomic line shape on cooperative OB. We are also investigating the effects of multimode coupling to the Stark shifted atomic line shape. It is anticipated that this may lead to the establishment of regenerative oscillations which may have applications as passive high intensity laser cw to pulse conversion. We feel that our further work will undoubtedly lead to even further progress and new ideas.

REFERENCES

1. H. Seidel, US Patent No. 3,610,731 (1971).
2. A. Szöke, V. Danen, J. Goldbar and N. A. Kurnit, Appl. Phys. Lett. 15, 376 (1969).
3. J. W. Austin and L. G. DeShazer, J. Opt. Soc. Am. 61, 650 (1971).
4. E. Spiller, J. Opt. Soc. Am. 61, 699 (1971).
5. H. M. Gibbs, S. L. McCall and T. N. C. Venkatesan, Phys. Rev. Lett. 36, 1135 (1976).
6. S. L. McCall, Phys. Rev. A9, 1515 (1974).
7. R. Bonifacio and L. A. Lugiato, Opt. Comm. 19, 172 (1976).
8. R. Bonifacio and L. A. Lugiato, Phys. Rev. A18, 1129 (1978).
9. H. J. Carmichael and D. F. Walls, J. Phys. B10, L685 (1977).
10. R. Bonifacio and L. A. Lugiato, Phys. Rev. A11, 1507 (1975); 12, 587 (1975).
11. C. M. Bowden and C. C. Sung, Phys. Rev. A18, 1558 (1978); 20, 2033 (1979).
12. C. M. Bowden and C. C. Sung, Phys. Rev. A19, 2392 (1979).
13. C. M. Bowden and C. C. Sung, to be published.
14. C. C. Sung and C. M. Bowden, J. Phys. A12, 2273 (1979).
15. A. L. Fetter and J. D. Walecka, "Quantum Theory of Many-Particle Systems", McGraw-Hill (New York, 1971), Section 48.
16. J. J. Ehrlich, C. M. Bowden, D. W. Howgate, S. H. Lehnigk, A. T. Rosenberger and T. A. DeTemple, "Swept-gain Superradiance in CO₂-pumped CH₃F", in Coherence and Quantum Optics IV, edited by L. Mandel and E. Wolf, (Plenum, New York, 1978), p. 923.
17. C. M. Bowden and C. C. Sung, Phys. Rev. A20, 2033 (1979).
18. D. W. Howgate, C. M. Bowden and J. J. Ehrlich, "MIRADCOM Program in Swept-Gain Superradiance", US Army Science Conference Proceedings, June 1978.
19. Cooperative Effects in Matter and Radiation, edited by C. M. Bowden, D. W. Howgate and H. R. Robl, (Plenum, New York, 1977).
20. R. J. Glauber, Phys. Rev. 130, 2529 (1963); 131, 2766 (1963).
21. R. Loudon, The Quantum Theory of Light, (Oxford, Clarendon, 1973).

22. A. Abragam, The Principles of Nuclear Magnetism, (Oxford University, London, 1961), Chapter V, XIIB.
23. L. M. Narducci and C. M. Bowden, J. Phys. A₉, L75 (1976).
24. L. N. Cooper, Phys. Rev. 104, 1189 (1956); J. Bardeen, L. N. Cooper and J. R. Schrieffer, *ibid.* 106, 162 (1957); 108, 1175 (1957).
25. R. Gilmore and C. M. Bowden, Phys. Rev. A₁₃, 1898 (1976).
26. R. Gilmore and C. M. Bowden, J. Math. Phys. 17, 1617 (1976).
27. C. M. Bowden and C. C. Sung, to be published.
28. L. D. Landau and E. M. Lifshitz, Electrodynamics of Continuous Media, (Pergamon Press, NY, 1960), Chapter VI.
29. C. M. Bowden and C. C. Sung, "Effective Temperature-induced Bistability and Hysteresis in Cooperative Optical Bistability", submitted for publication.
30. L. P. Gorkov, Sov. Phys. JETP 34, 505 (1958).
31. G. Banfi and R. Bonifacio, Phys. Rev. A₁₂, 2068 (1975).
32. Reference 14; and references therein. See also R. Gilmore and C. M. Bowden, "Classical and Semiclassical Treatment of the Phase Transition in Dicke Models", in Cooperative Effects in Matter and Radiation, edited by C. M. Bowden, D. W. Howgate and H. R. Robl, (Plenum, New York, 1977), p. 335.
33. D. W. Howgate, to be published.

BRITT

CALCULATION OF GROUND SHOCK MOTION PRODUCED BY
NEAR SURFACE AIRBURST EXPLOSIONS USING
CAGNIARD ELASTIC PROPAGATION THEORY

JAMES R. BRITT, MR.
U.S. Army Engineer Waterways Experiment Station
Vicksburg, Mississippi 39180

1. INTRODUCTION

This paper describes a study which used elastic wave propagation theory to predict and analyze ground motions produced by near surface airburst explosions; the air-earth environment was modeled as three homogeneous elastic layers - air, soil and rock - separated by plane parallel boundaries as illustrated in Figure 1. The explosive source is located on the axis of symmetry. The air is treated as an elastic fluid, while the soil and rock are treated as elastic solids. Elastic material parameters that characterize the wave propagation are the compressional wave (P wave) speeds C_{pi} , the shear wave (S wave) speeds C_{si} , and the densities ρ_i where $i = 1, 2$, and 3 for the air, soil, and rock, respectively.

The exact closed form integral solutions of Cagniard (1) for the reflection and refraction of spherical waves in elastic solids were adapted and extended to model the ground shock propagation in a layered earth. In this formulation the particle motion is obtained as a sum of components propagated along rays or paths (such as shown in Figure 1) associated with distinct P and S wave arrivals. Calculations using the Cagniard procedure were used previously successfully by the author to predict the reflection of underwater explosion shock waves from the ocean bottom. (See References (2)-(5).) The theoretical analysis and computer code development for the ground shock calculations were extensions of the bottom reflection study. The details of the theoretical model and the computer code used in the elastic ground motion calculation are not presented but will be given in a forthcoming report (6). In addition, References (2)-(5) and (7)-(9)

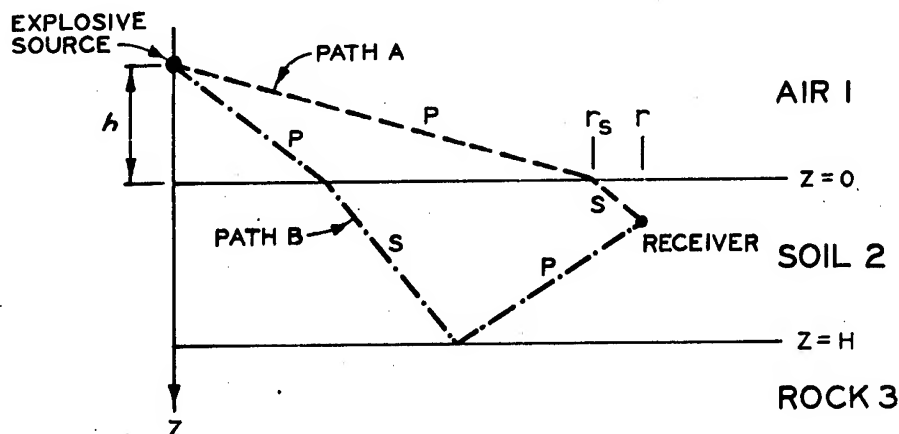


Figure 1. Model for airburst explosions over layered earth media.

provide background information and some other recent applications of the Cagniard elastic propagation theory.

2. MODELING THE AIRBLAST

The airblast pressure produced by an explosion attenuates with radial distance R from the source more like $1/R^2$ for pressure levels 10 to 100 psi than the spherical elastic $1/R$ decay rate. The blast propagation rate decreases with range instead of the constant speed C_{p1} . In addition, the pressure-time waveform changes in shape with range. Thus, the airblast cannot be directly modeled elastically but must be approximated by either (a) linearizing around a particular range related to the time of dominant motion or (b) by simulating the pressure amplitude and arrival time by a distribution of sources. The simpler linearization approach was used in this study. Several procedures were investigated, but linearization around the directly transmitted shear wave (path A of Figure 1) produced the best agreement with measured waveforms for materials ranging from weak soils to hard rocks.

BRITT

The airblast was approximated as follows. The directly transmitted shear wave path A of Figure 1 was determined by iterating for the range r_s at which the ray enters the soil. An empirical formula was used to calculate the airblast arrival time t_a for an initial value of r_s . An average P wave speed C_{p1} was computed from

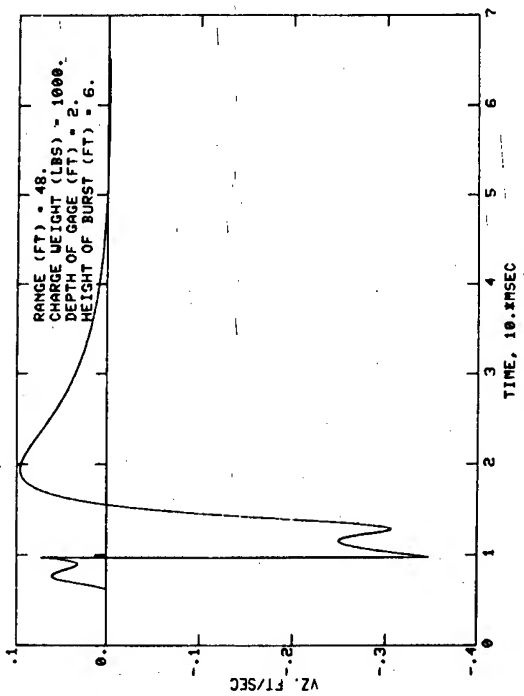
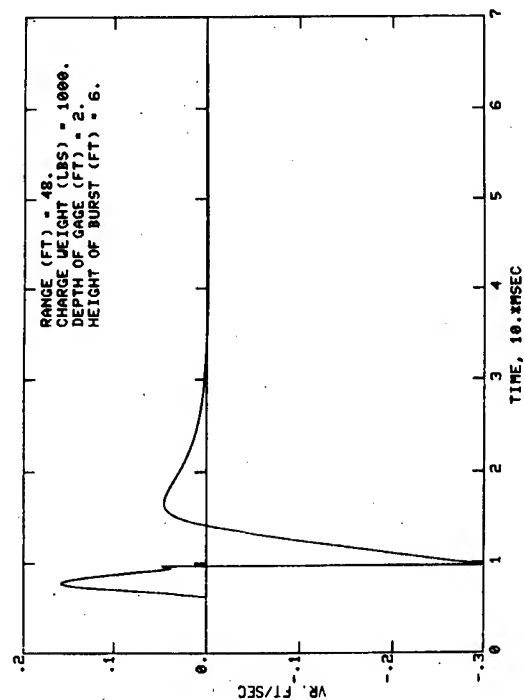
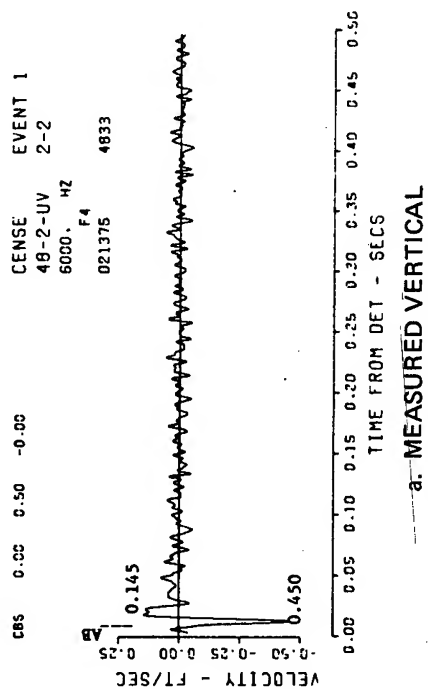
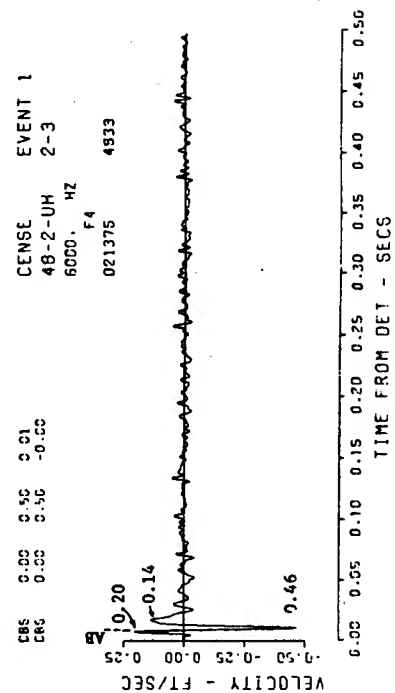
$$C_{p1} = (h^2 + r_s^2)/t_a$$

Then C_{p1} was substituted into the equation for Snell's Law of acoustics to obtain a new estimate for r_s . This process continued until the initial and final values of r_s were within an acceptable tolerance. The point source amplitude and pulse shape were then chosen using empirical formulae so that the airblast pressure was matched at the point $(r_s, 0)$.

3. COMPARISON OF CALCULATED AND MEASURED PARTICLE VELOCITY WAVEFORMS

Calculations were performed for the three CENSE (Coupling Efficiency of Near Surface Explosions) explosive field test series. (See References (10) and (11).) These tests were chosen because they provide a variety of site characteristics which were relatively well controlled. The test beds were either effectively homogeneous or had layering suitable for the two-layer model. In addition, each of the series had near surface airburst explosions for which particle velocity or acceleration was measured in the upper layer for a variety of ranges from the explosions.

CENSE 1 consisted of a series of 1000-lb spheres of nitromethane detonated over a massive Kayenta sandstone formation. These events provide data for checking the calculations for motion in a strong, homogeneous material which behaves elastically for stress levels of hundreds of psi. The surface rock was thick enough that three layers were not needed for the computations. Figure 2 compares the theoretical and measured vertical and radial velocity components. Vertical velocity is positive for upward motion and radial velocity is positive for outward motion. Note that the experimental and theoretical curves are plotted on different scales and that the calculation represents only part of the measured curve. The material properties used for this calculation were $\rho_1 = 0.0012 \text{ gm/cm}^3$, $C_{p2} = 9 \text{ ft/msec}$, $C_{s2} = 4 \text{ ft/msec}$, and $\rho_2 = 2.4 \text{ gm/cm}^3$. Event 1, shown in the figure, was detonated with its charge center 6 ft above the rock. Measurements were made with velocity gages (having a nominal 600-Hz frequency response) placed 2 ft below the rock surface. The airblast peak



d. THEORETICAL RADIAL

c. THEORETICAL VERTICAL

Figure 2. Comparison of particle velocity calculations with CENSE 1 measurements at 48-ft range.

BRITT

pressure above the gages was measured at 51 psi at the 48-ft range. Other calculations not shown here demonstrated equally good agreement at pressure levels from 10 to 120 psi.

The data of CENSE 2 provided information to check the elastic calculations for a two-layered clayey-silt soil site. The explosives used were 300-lb spherical TNT charges. In the calculations shown in Figures 3 and 4, the soil was modeled in two layers: a surface layer 20 ft thick with $C_{p2} = 1.1$ ft/msec, $C_{s2} = 0.6$ ft/msec, and $\rho_2 = 1.7$ gm/cm³, and a lower half-space with $C_{p3} = 1.6$ ft/msec, $C_{s3} = 0.7$ ft/msec, and $\rho = 1.75$ gm/cm³. The measurements were made with velocity gages located 1.5 ft below the surface. Event 2 was detonated with charge center 7.2 ft above the soil surface. Excellent agreement was obtained in Figure 3 at the 67-ft (13-psi) range. There was also similarly good agreement at the 57-ft (16-psi) range. Figure 4 at the 43-ft (34-psi) range shows slightly poorer agreement but still within typical scatter of field measurements. At a range of 32 ft (60 psi) the linear calculations begin to fail to reproduce the major characteristics of the measured motion. The linear theory does not predict the large initial downward and outward displacements seen in the experiments. These differences are probably a result of the nonlinear material properties of the soil becoming important and a result of the close-in source conditions not being adequately modeled by the localized airblast input used in the calculations.

CENSE 3 provided measurements for comparison with theory for a weak soil layer over a hard rock site. This series consisted of seven explosions of 200 lb (226 lb TNT equivalent) of nitromethane. The test bed consisted of compacted backfill of "alluvium" soil placed over a Kayenta sandstone deposit similar to that of CENSE 1. The thickness of the soil was varied from 0 to 6 ft. Measurements of vertical and radial acceleration were made at middepth in the soil layers and in the rock. Velocity histories were obtained by integrating the acceleration records. Events 2 and 4 were surface tangent bursts, that is, the explosive charge was resting on the soil surface. The soil layer thickness in Figure 5 was 6 ft. In Figure 6 the thickness was 3 ft. The material properties used in the calculations were $C_{p2} = 0.9$ ft/msec, $C_{s2} = 0.3$ ft/msec, and $\rho_2 = 1.6$ gm/cm³ for the soil and $C_{p3} = 8$ ft/msec, $C_{s3} = 3$ ft/msec, and $\rho_3 = 2.4$ gm/cm³ for the sandstone.

At the 56-ft (12-psi) range of Figure 5 the calculations are in good agreement with the experimental curves up to a time of about 45 msec if the high frequency spikes are neglected. These spikes result from using an airblast pulse with zero rise time. High frequency

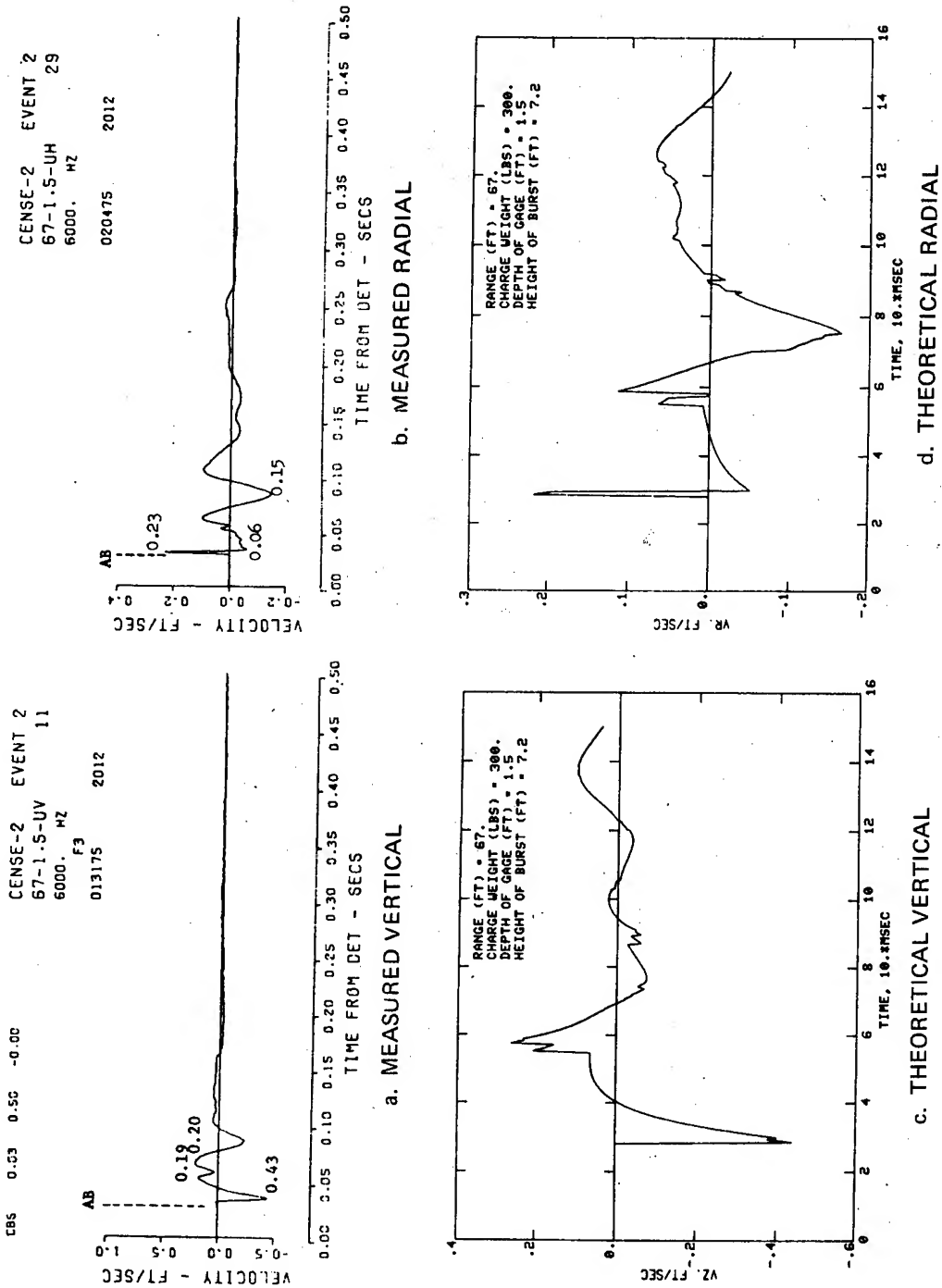
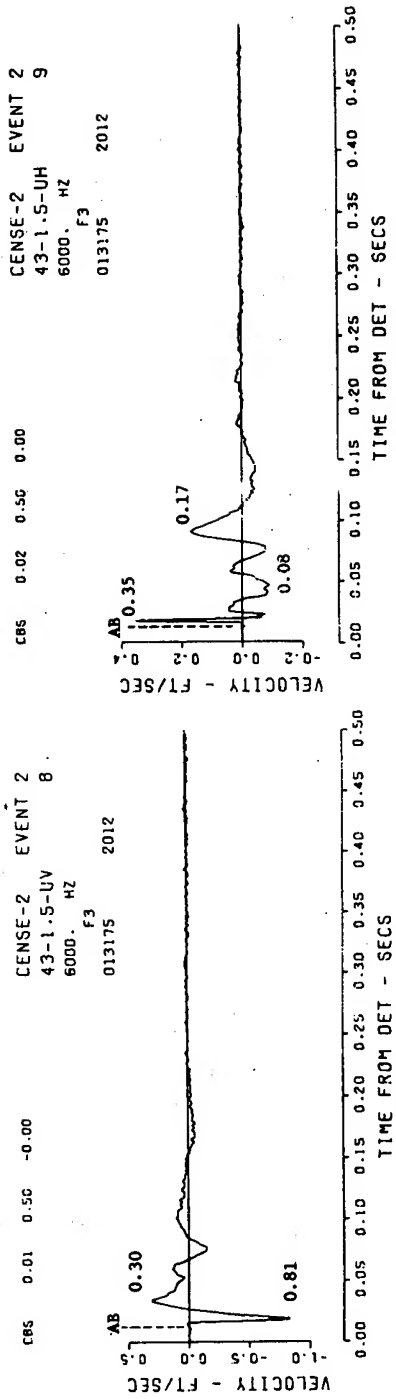
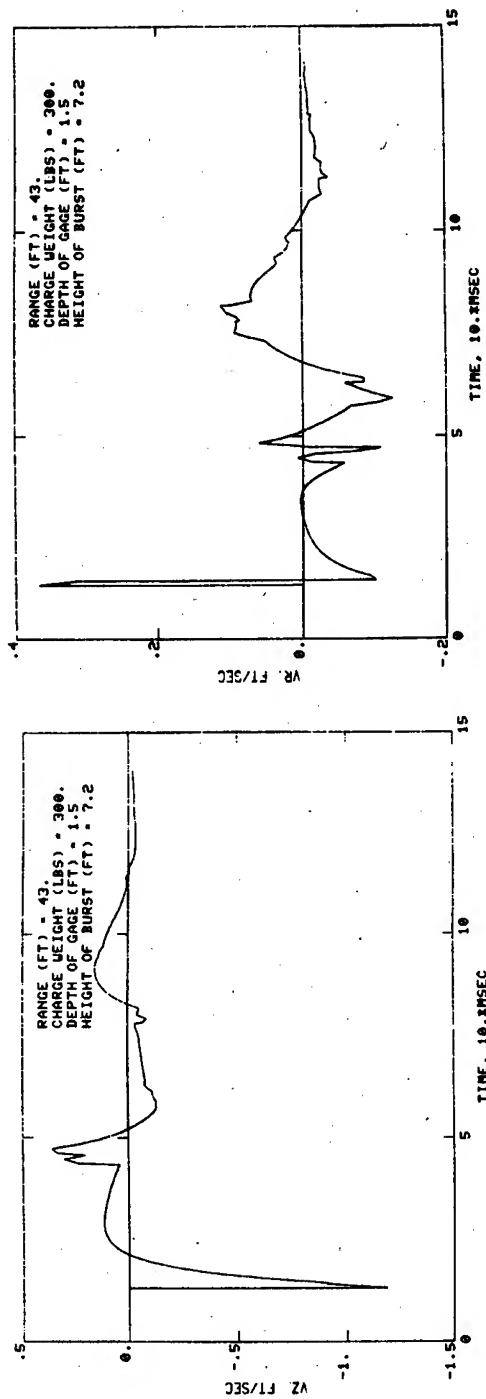


Figure 3. Comparison of particle velocity calculations with CENSE 2 measurements at 67-ft range.



a. MEASURED VERTICAL

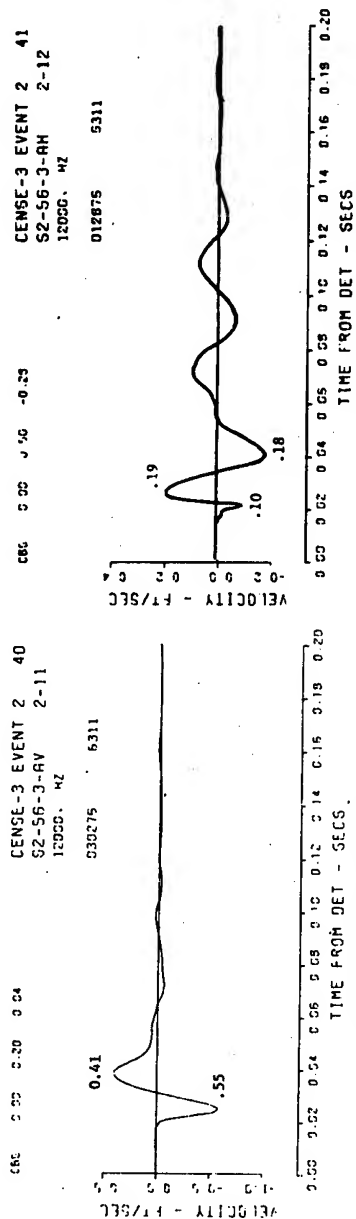
b. MEASURED RADIAL



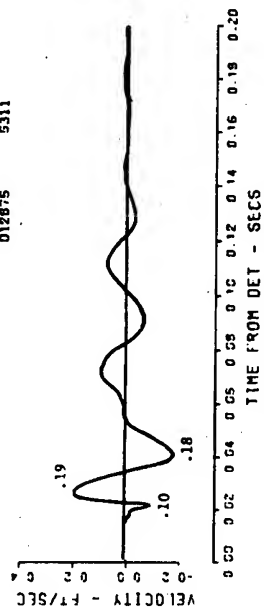
c. THEORETICAL VERTICAL

d. THEORETICAL RADIAL

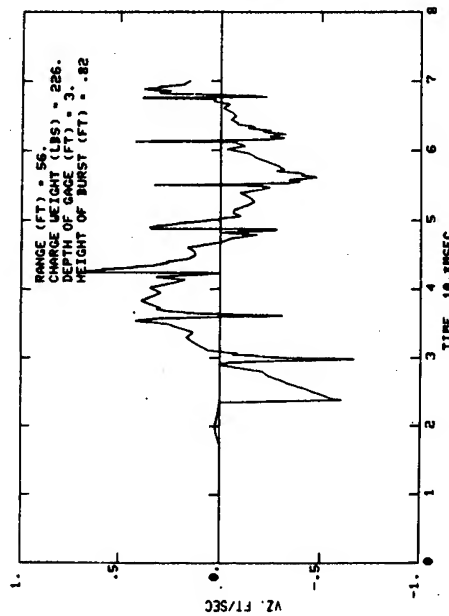
Figure 4. Comparison of particle velocity calculations with CENSE 2 measurements at 43-ft range.



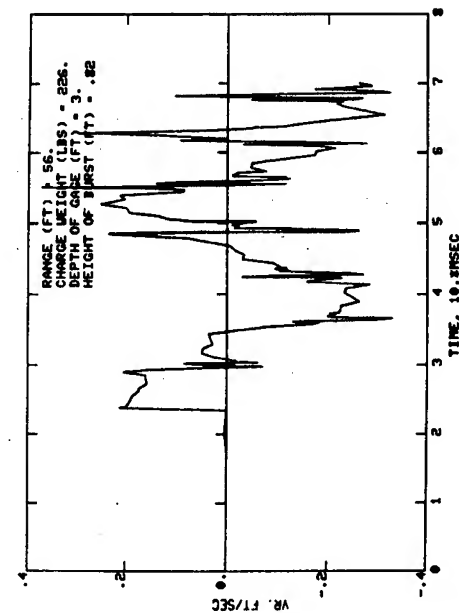
a. MEASURED VERTICAL



b. MEASURED RADIAL

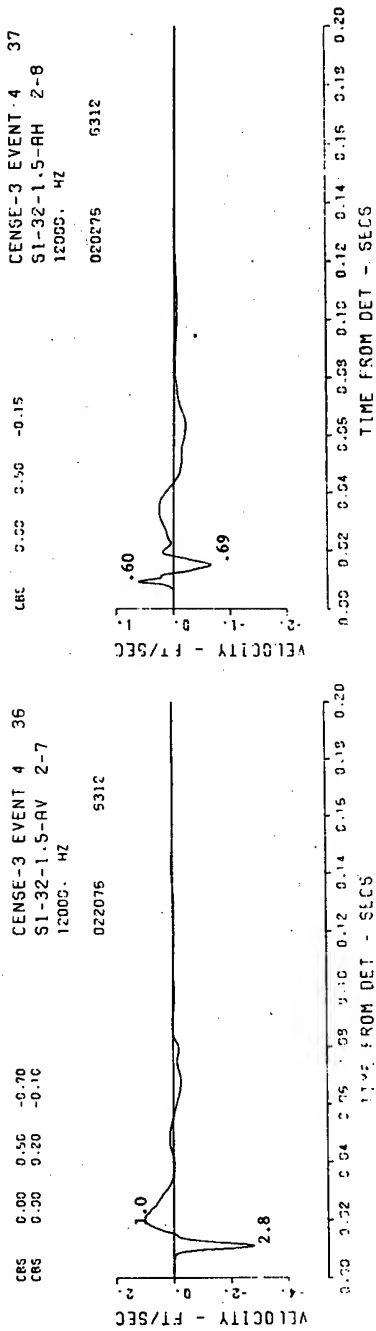


c. THEORETICAL VERTICAL



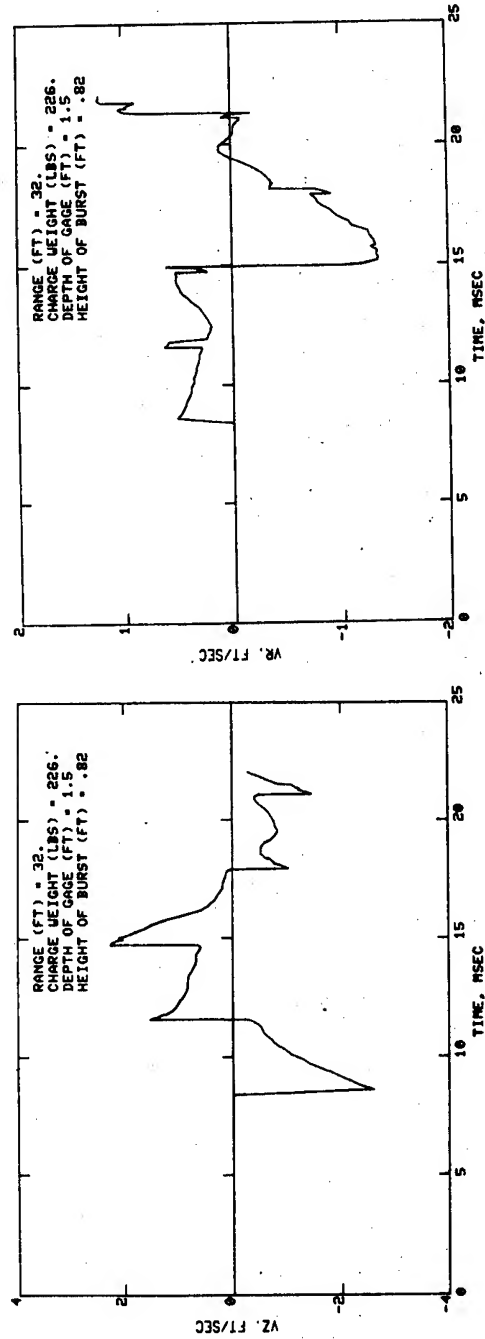
d. THEORETICAL RADIAL

Figure 5. Comparison of particle velocity calculations with CENSE 3 measurements at 56-ft range.



a. MEASURED VERTICAL

b. MEASURED RADIAL



c. THEORETICAL VERTICAL

d. THEORETICAL RADIAL

Figure 6. Comparison of particle velocity calculations with CENSE 3 measurements at 32-ft range.

BRITT

motion of this type is filtered out of the measurements because of the nonlinear effects of the soil and finite frequency response of the gages and recording system. At the 32-ft (52-psi) range of Figure 6, agreement is poorer but the initial velocity amplitudes are still close to the measured values. At a range of 24 ft (110 psi) the calculated initial peaks are nearly a factor or two higher than the experimental.

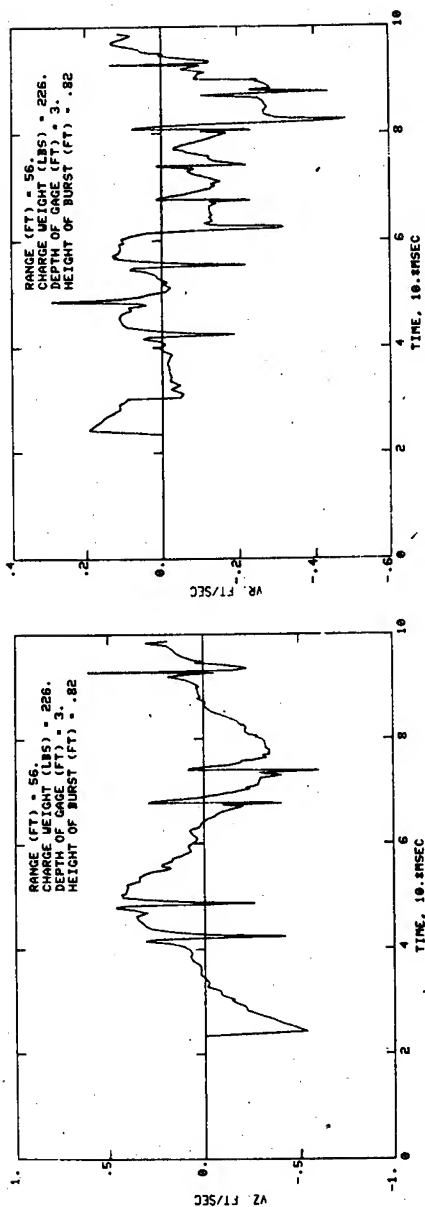
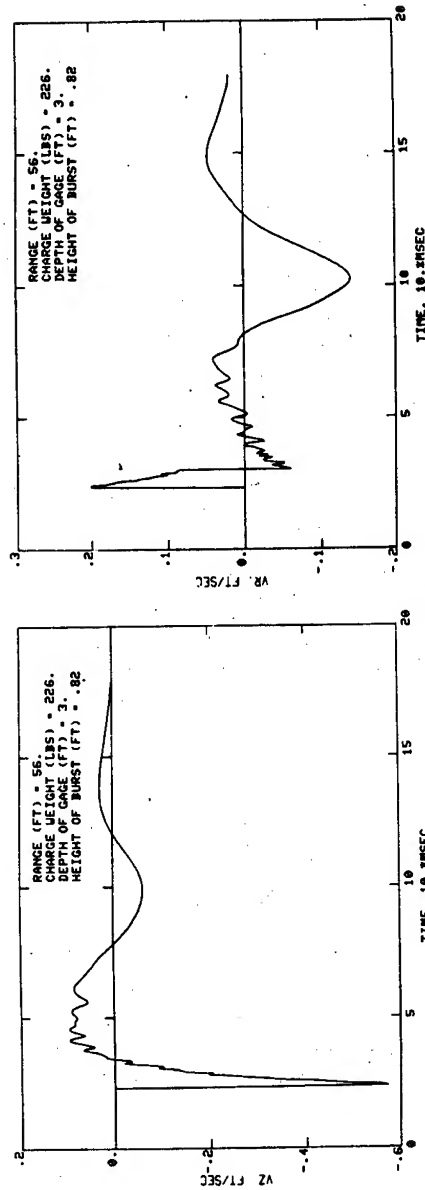
Figure 7 is presented for comparison with Figure 6 to illustrate the effect of increasing the soil layer thickness at the CENSE 3 site. The initial portions of the records are produced by the directly transmitted P and S waves and are not dependent on the soil thickness. The later motion is a complicated interaction of reflected waves for moderate layer thickness. In going from a layer thickness of 3 ft as in Figure 5 to the 6-ft layer in Figure 6, the change in frequency of the motion is roughly proportional to the layer thickness change, but the waveforms at 12-ft thickness do not follow this pattern.

From the few waveforms presented here, one cannot draw general conclusions on factors affecting the period and amplitude of the low frequency motion. A detailed parameter study and analysis will be necessary to determine how the motion changes in going from very thin to very thick layers. It appears that simple rules of thumb based on S or P wave layer transit times will be valid in only very restricted ranges of thickness and elastic parameters.

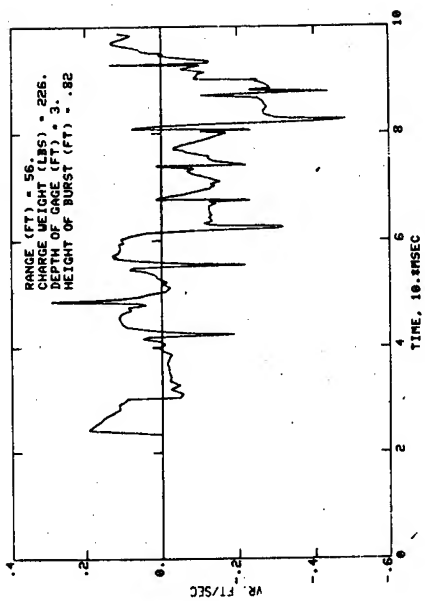
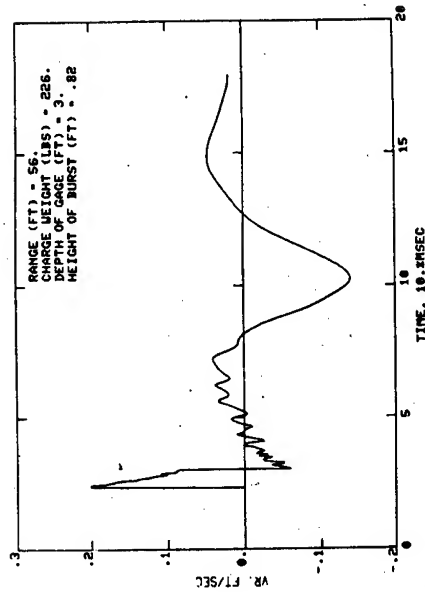
4. CONCLUSIONS

Prediction of velocity waveforms using the Cagniard formulation of the elastic theory and the localized airblast source model can be expected to be accurate within the scatter of explosive tests measurements for times up to about one cycle of the low frequency motion and for airblast overpressure levels at the gage range up to about 40 psi for explosions over weak soils and over 100 psi for strong rocks. At pressure levels in the range of 40 to 100 psi for explosions over soil, the elastic theory still predicts the general character of the motion but overestimates the peak velocities and underestimates the large initial downward and outward displacements.

Introduction of a finite rise time in the airblast source pulse is desirable to eliminate high frequency spikes in the calculations. The simple localized airblast source model linearized around the directly transmitted shear wave may be a major contribution to failure of the calculations at higher pressures and at late time on waveforms.

a. VERTICAL, $H = 12$ FT

c. VERTICAL, THICK LAYER

b. RADIAL, $H = 12$ FT

d. RADIAL, THICK LAYER

Figure 7. Particle velocity calculations for 12-ft and infinitely thick soil layers.

BRITT

The linear wave propagation model can produce motion waveforms for homogeneous sites such as the CENSE 1 sandstone at very small computer cost, but because of the rapidly increasing effort required to calculate the late time portion of waveform for layered media, routine calculations to times greater than about three shear wave transit times of the layer appear to be more expensive than linear finite difference methods or normal modes techniques. Calculations with the Cagniard theory for more than two soil layers appear to be quite expensive except for early time motion or special cases where reflections in one layer can be neglected. The primary applications for computing motion waveforms in layered media appear to be early time motions up to about two shear transit times at a relatively low computing cost and minimal effort to change code input parameters. Since the theory follows rays, the composite waveforms can be dissected to study the contributions of individual arrivals. This property of the method makes it ideal for studying the basic characteristics and effects of the controlling parameters of wave propagations in layered media.

REFERENCES

1. Cagniard, L., Flinn, E. A., and Dix, C. H., Reflection and Refraction of Progressive Seismic Waves, McGraw-Hill, New York, 1962.
2. Britt, J. R., Linear Theory of Bottom Reflections, NOLTR 69-44, Naval Ordnance Laboratory, Silver Spring, MD, 1969.
3. Britt, J. R., A Solution of the System of Partial Differential Equations Which Describe the Propagation of Acoustic Pulses in Layered Fluid Media, NOLTR 70-234, Naval Ordnance Laboratory, Silver Spring, MD, 1970.
4. Britt, J. R., and Snay, H. G., Bottom Reflection of Underwater Explosion Shock Waves, Computer Program, NOLTR 71-110, Naval Ordnance Laboratory, Silver Spring, MD, 1971.
5. Snay, H. G., and Britt, J. R., Response of a Surface Ship to a Shock Wave Reflected from the Bottom of the Sea, Proceedings of the First Ship Structures Workshop, NSRDC Report 3-3806, Vol II, Naval Ship Research and Development Center, Maryland, 1973.
6. Britt, J. R., "Air Burst Ground Shock Predictions Using Cagniard Elastic Propagation Theory, Miscellaneous Paper, U.S. Army Engineer Waterways Experiment Station, Vicksburg, MS, (in preparation).

BRITT

7. Abramovici, F., and Gal-Ezer, J., Numerical Seismograms for a Vertical Point-Force in a Layered Solid, Bulletin of the Seismological Society of America, Vol 68, No. 1, pp 81-101, 1978.
8. Spencer, T. W., The Method of Generalized Reflection and Transmission Coefficients, Geophysics, Vol 25, pp 625, 641, 1960.
9. Pao, Y., Gajewski, R. R., Thau, S. A., Analysis of Ground Wave Propagation in Layered Media, DASA 2697, Defense Nuclear Agency, Washington, 1971.
10. Ingram, J. K., CENSE Explosion Test Program, Report 1, CENSE 1, Explosions in Sandstone, Report 2, CENSE 2, Explosions in Soil, TR N-77-6, Army Engineer Waterways Experiment Station, Vicksburg, MS, 1977.
11. Ingram, J. K., CENSE Explosion Test Program, Report 3, CENSE 3, Explosions in Soil Over Sandstone, Technical Report, Army Engineer Waterways Experiment Station, Vicksburg, MS, (in preparation).

BRUCE, BRUCE, YEE, AND BURKET

EXPERIMENTALLY DETERMINED RELATIONSHIP BETWEEN
EXTINCTION AND LIQUID WATER CONTENT (U)

DOROTHY BRUCE, DR.*
Instrumentation Directorate
White Sands Missile Range, New Mexico 88002

CHARLES W. BRUCE, DR.
YOUNG PAUL YEE, MR.
US Army Atmospheric Sciences Laboratory
White Sands Missile Range, New Mexico 88002

HANS BURKET, MR.
Physical Science Laboratory
New Mexico State University, Las Cruces, New Mexico 88002

INTRODUCTION

To develop effective electro-optical weapon systems, it is necessary to have a clear understanding of the importance of and correlations between various atmospheric parameters in the wavelength regions of interest. A careful measurement program is essential to the development of this understanding and it provides the basis for accurate simulation of electro-optical system performance.

Measurement systems should be chosen to give as direct results as possible. This choice minimizes assumptions which effect the validity of the results. It also reduces the data analysis needed for the interpretation of results, thereby making results available in real time.

This paper reports the results of environmental chamber measurements of extinction coefficients at CO₂ laser wavelengths and of liquid water content (LWC) of a variety of droplet size distributions. The liquid water content measurements were made with two

recently developed systems which are described in detail in Bruce et al. [1] The results are in general agreement with calculated results of Pinnick et al. [2] based on measured fog droplet size distributions and give further verification to Chylek's [3] prediction of a unique linear relation between extinction at approximately $11\mu\text{m}$ and liquid water content of fogs for all size distributions with maximum particle radii less than or approximately equal to $14\mu\text{m}$.

EXPERIMENTAL APPROACH

The measurements of this paper were made in an environmental chamber having a volume of approximately 1 cubic meter. Water droplets were generated within the chamber, and minimum stirring was used to ensure uniform spatial distribution of the particles.

Figure 1 is a diagram of the optical system used in the measurements. The (half power) diameter of the laser beam is approximately 1 cm in the measurement region. Early measurements made with a larger diameter ($\times 3$) beam did not significantly improve the steadiness of the output signal. The laser path through the chamber is in the vertical direction. Warm dry air in the form of a thin sheet is blown across the (exterior) mirrors at the top and

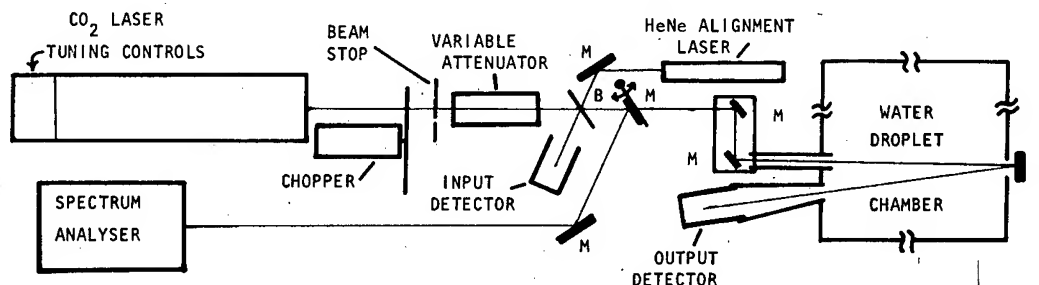


Figure 1. Optical system. M-represent mirrors, B-represents beam splitter. One mirror is rotatable to permit laser line identification. The CO_2 laser incorporates automatic line scanning and stabilization. An optical beam chopper is retained so that an aerosol spectrophone (measures absorption coefficient) and alternate detectors for other lasers may be used. An adjustable aperture for the CO_2 laser beam, window flush for the in- and out-put mirrors, liquid water content measurement systems and particle counter are omitted in this diagram.

bottom of the chamber to prevent accumulation of water droplets on their surfaces. A sample of the input beam is monitored by a reference power meter. Both calculations and parametric measurements have been used to determine the attenuation necessary to prevent significant heating and evaporation of the water droplets. A mirror is rotated into the beam path to direct the beam to a spectrum analyzer during tuning of the laser.

Sampling throats for the liquid water content measuring systems are located approximately in the lower center of the chamber. Sampling is at a rate of 10 to 15 liters per min. The sampling throat of a commercial light scattering counter extends through one side of the chamber to a point close to the extinction path and the liquid water content sampling throats. This instrument is used to monitor the droplet size distributions and, through these, the contributions of different size particles to the extinction coefficient (differential extinction coefficient).

PRELIMINARY EXPERIMENTS

Although the measurement systems used in this study are relatively direct, several extensive preliminary investigations were conducted to ensure the existence of appropriate experimental operating conditions.

The first of these involved the commercial instrument used to monitor the particle size distributions--Particle Measuring Systems (PMS) classical scattering aerosol spectrometer. This instrument is sensitive to water droplets with radii from $0.23\mu\text{m}$ to $16\mu\text{m}$.

This instrument counts particles of different sizes by doing pulse height analysis of laser light ($0.63\mu\text{m}$) scattered by single particles into a particular solid angle. Determination of particle size is indirect because the scattering depends on particle refractive index and on the geometry of the optical system.

The instrument used in this study was checked to be sure that particles were counted in the correct size range channels. This was done by using single-size nearly transparent beads for channels counting particles with radii up to about $4\mu\text{m}$ and with calibrated bead mixtures for channels counting particles with radii between $4\mu\text{m}$ and $16\mu\text{m}$. No measurement was made of particle counting efficiency. The results from the studies with mixed bead sizes indicate that counting efficiency was relatively constant for all channels since the curves obtained with calibrated bead mixtures had approximately the correct shapes for the size mixtures used.

Care must be exercised to limit the density of aerosol sampled by the counter since counting is based on the assumption of single scattering by individual particles and distortion of results may occur at high count rates. A variety of dilution techniques were tried in which droplet-free air was mixed with the droplet sample stream from the chamber in the inlet throat of the PMS counter. Care was taken to minimize disturbance of the flow character. The results obtained indicate that use of these techniques extended the number density range of the instrument by a factor of about 3, but that further dilution of these water droplet distributions caused definite distortion of the differential extinction curves. The differential extinction curves were used only in a relative sense, i.e., the shape of the curve and the particle radius, r_p , at which peak extinction occurred were used as characteristic parameters of the chamber droplet distributions, since an absolute calibration was not available to relate a measured size distribution to actual extinction coefficient and liquid water content.

The second of these preliminary studies was an investigation of the conditions for generation of droplet size distributions and differential extinction profiles within the ranges found in naturally occurring light to heavy fogs. The differential extinction profiles show the contribution to extinction of particles with radii in relatively small size ranges. Peak extinction for fogs normally occurs in the particle radius range of $2\mu\text{m}$ to $10\mu\text{m}$. No attempt was made to specifically tailor size distributions to be representative of any particular type of fog but rather to provide a span of fog droplet sizes.

Commercially available "cool mist vaporizers" were used to generate droplet distributions which had monomodal differential extinction curves. The radius of peak extinction, r_p , could be varied from about $8\mu\text{m}$ to $16\mu\text{m}$ by using a variety of throttling and impaction techniques. A stable mode of operation with peak extinction at particle radii of $10\mu\text{m} \pm 1\mu\text{m}$ was finally used. Condensation droplet distributions were produced by introducing cold gaseous nitrogen into the saturated vapor of the chamber. These distributions are characterized by relatively narrow, monomodal differential extinction curves with peak extinction for droplet radii of $4\mu\text{m} \pm 1\mu\text{m}$. Both types of droplet distributions were generated with densities ranging from about 0.01 to 4.0 gm/m^3 . The shape and peak position of the differential extinction curves were not particularly sensitive to variation of the droplet number density. Typical differential extinction curves are shown in figure 2.

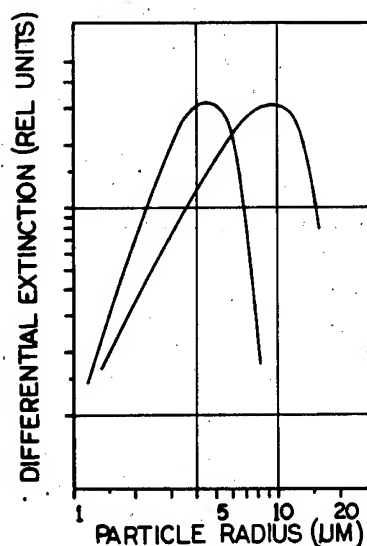


Figure 2. Typical differential extinction curves for condensation droplet (left peak) and mechanically generated (right peak) size distributions.

A study of the spatial uniformity of the droplet distributions was made by varying the location of the droplet generators and using several stirring mechanisms. Most of the mixing results from the circulation caused by the droplet generators. A small fan with specially tailored blades provides the small additional circulation (in the form of a donut within the chamber) required to obtain spatially uniform distributions.

The last of the preliminary studies involved characterization of two new sensing systems which give real-time measurements of liquid water content. These instruments and their characterization will be reported in detail elsewhere [1]. Only a summary will be given here.

One system involves a mass accumulation technique in which droplets are collected on a three-dimensional filter consisting of layers of flannel on a screen base. If the accumulated mass is measured and divided by the sampling time and the volume flow rate through the filter, an absolute measurement of LWC is obtained in units of mass density. The three-dimensional filter is critical to successful measurements since water droplets would clog a two-dimensional filter and lead to inaccurate sampling. Sampling times between 15 s and 4 min were used for both light and heavy mass density droplet distributions and have yielded reproducible results.

Caution is necessary in this measurement to apply a time-dependent correction factor which results from quite rapid initial absorption of water by the dry filter fibers. This effect actually represents equilibration of the flannel to the relative humidity of the chamber. Since this effect is rapid and reproducible, the necessary correction is straightforward. Mass collection was studied to determine an adequate number of layers of flannel.

For the environmental chamber measurements, filters are preweighed in sealed containers, inserted into a sampling throat with O-rings seals, and are replaced in their original container for post sampling weighing. They are then dried with a stream of ambient air for later use. A similar but real-time system incorporated into a top loading electronic balance is also used.

The second LWC measurement system uses a differential sampling technique and phase-sensitive detection. The system has two sampling throats. One throat is vertical and unobstructed and the flow through it contains both vapor and water droplets; the other throat contains a series of flannel filters with offset openings which create free-flow conditions through a tortuous path so that the resulting sample contains only vapor. A rotating half disc alternately selects samples from the two throats and permits them to flow through a heated woven wire grid which evaporates the droplets. The wire diameter was chosen to be much larger than the water droplets to provide a good capture efficiency. Evaporation of water from the grid causes cooling and a change in the grid resistance; This results in an approximately linear change in the voltage applied across the grid by a constant current power supply. A reference signal for a lock-in amplifier is obtained from the throat selecting half disc and the synchronous voltage change across the grid is measured. The resulting signal has been shown to be proportional to the total mass density measured with the filter system in a series of measurements over a wide range of environmental chamber conditions. Single and multiple layer grids have been used and no significant difference in results was found.

EXPERIMENTAL PROCEDURES

The extinction coefficient measurements in this study were made with the laser tuned to the $10\mu\text{m}$ R-16 CO_2 transition line at a wavelength of $10.27\mu\text{m}$. The laser beam power was monitored continuously--both prior to the input mirror for the fog chamber (sampled by a beamsplitter) and after it left the chamber. The length of the path within the chamber was 1.79 m.

Optical alignment and laser line stability were periodically checked and no problems were encountered. The power meters and the differential LWC system were stabilized and baselines were established.

The droplet generators were then turned on and the chamber was brought to a droplet equilibrium condition which was characterized by constant values for both laser output power and LWC. After recording these values, the droplet generators were turned off and the chamber was again allowed to reach an equilibrium with only vapor present. This establishes a procedure for the measurement of changes in transmission of laser power due to droplets only.

The droplet generators were again turned on and, after equilibrium conditions were reached, a set of three filter measurements of liquid water content was made. PMS counter measurements were then made and the droplet generators were turned off. After a settling time to return to vapor-only conditions, the same measurement process was repeated with a different power supplied (by use of a Variac) to the droplet generators. Variac settings between 60 and 100 percent were used to provide a variety of droplet number densities. Size distributions and the shape and position ($r_p = 10\mu\text{m} + 1\mu\text{m}$) of the differential extinction coefficient curves remained almost constant for all similar sets of experiments.

Different droplet size distributions were obtained by following the above procedure for establishing vapor saturation as well as equilibrium droplet conditions and then introducing cold nitrogen gas into the center of the chamber. After an initial mixing period of about 1 min, chamber conditions became essentially uniform. Following this, both the laser output power and differential LWC signals decayed (over a period of 6 to 10 min) back to those representative of ambient temperature conditions.

For some of these condensation droplet measurements, the droplet generators were turned off before the cold nitrogen was introduced. Under these conditions, the position of r_p for the differential extinction coefficient curves was at about $4\mu\text{m} + 1\mu\text{m}$.

When the droplet generators continued operation, the position of r_p either occurred at an intermediate position or the size distribution was bimodal with a variety of shapes and the two-peak extinction positions within the range of $4\mu\text{m}$ to $10\mu\text{m}$.

Since chamber conditions varied with time for these condensation experiments, the LWC filter measurements were made only under the original equilibrium conditions to establish a calibration value for the differential LWC measurement.

The PMS counter measurements also required a special procedure. Since the counter significantly depleted the chamber's contents, size distributions were measured on alternate measurement sets for repeated conditions. There was an equilibration period when the counter was first turned on. The data for this period (about 3 s) were discarded. Then, several valid 2 s sampling sets of data were obtained.

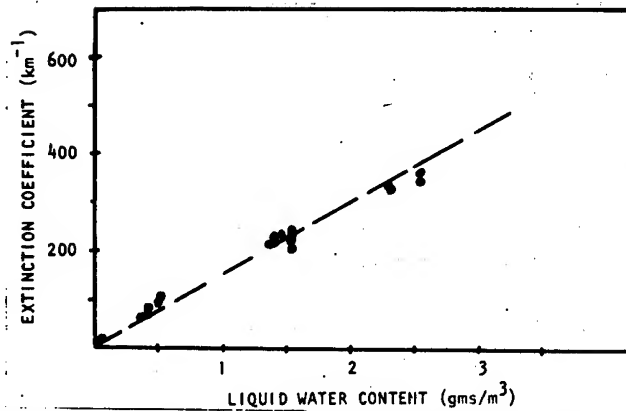
RESULTS

The measured relationship between the extinction coefficient at $10.27\mu\text{m}$ and the liquid water content of environmental chamber droplet distributions are shown in figures 3a through 3c.

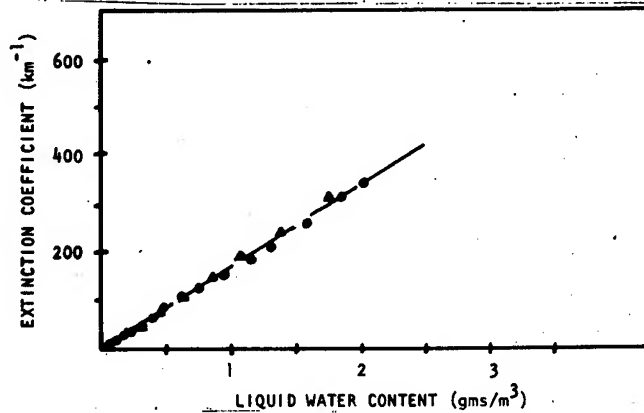
Each of the size distributions clearly show a linear relation between the measured quantities. The ratio between them shows some variation as a function of the droplet distribution generation mechanism: the slope for mechanically generated distribution (figure 3a) is $152\text{ km}^{-1}/(\text{gm}/\text{m}^3)$, for condensation droplet distributions (figure 3b) $168\text{ km}^{-1}/(\text{gm}/\text{m}^3)$, and for the combination of distributions (figure 3c) is $158\text{ km}^{-1}/(\text{gm}/\text{m}^3)$, although it could presumably vary anywhere between the other two values.

However, the data for all of the distributions may be combined to yield a linear relation with a slope of $159\text{ km}^{-1}/(\text{gm}/\text{m}^3)$ with an estimated combined experimental error of $12\text{ km}^{-1}/(\text{gm}/\text{m}^3)$ or 8 percent.

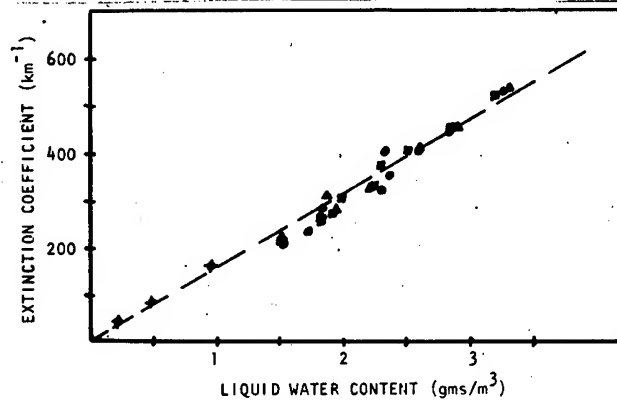
The PMS counter measurements of the size distributions were used in a Mie scattering program calculation of extinction coefficient (using a previously measured value for the complex index of refraction for water at this wavelength by Hale et al. [4] and liquid water content. This data is assumed to give relative results only, because the absolute calibration of the instrument is not known, but the ratio of the calculated quantities of $166 \pm 12\text{ km}^{-1}/(\text{gm}/\text{m}^3)$ is in reasonable agreement with that of the measured slopes. The calculated extinction and liquid water content values themselves were close to the measured values for one counter used but were very different for another, supposedly similar unit.



(a) Mechanically generated droplet size distributions.



(b) Condensation droplet size distributions.



(c) Droplet distributions generated by combinations of the mechanical and condensation techniques.

Figure 3. Extinction coefficients as functions of liquid water content for mechanically generated, condensation, and combination droplet size distributions.

CONCLUSIONS

Measurements have been made of the extinction coefficient at $10.27\mu\text{m}$ and independently, of the liquid water content of a large number of environmental chamber droplet size distributions with radii spanning those of a variety of fogs. A linear relation has been found which is approximately independent of the size distribution. The measured ratio of extinction coefficient to liquid water content is $159\text{ km}^{-1}/(\text{gm}/\text{m}^3)$.

These results are in good agreement with the linear relation predicted by Chylek [3] and calculated by Pinnick et al. [2] at $11\mu\text{m}$ based on PMS counter size distribution measurements of fogs and hazes.

These results involve complex measurements that are very sensitive to the environment. Nevertheless, they do support the thesis that liquid water content can be used at $10\mu\text{m}$ wavelengths as a measure of extinction--a most important quantity in the application of military systems (e.g., to European environments).

Systems for the measurement of liquid water content under field conditions are being developed from those used in this study. They will be used in European and other field environments beginning in 1980.

REFERENCES

1. Bruce, C. W., R. J. Brewer, and H. Burket, 1980, "A System for Measurement of Liquid Water Content," submitted as an ERADCOM report
2. Pinnick, R. G., S. G. Jennings, Petr Chylek, and J. H. Auvermann, 1979a, "Verification of a Linear Relation Between IR Extinction, Absorption and Liquid Water Content of Fogs," J Atmos Sci, 37:1577-1586.
3. Chylek, P., 1978, "Extinction and Liquid Water Content of Fogs," J Atmos Sci, 35:296-300.
4. Hale, G. M., and M. R. Querry, 1973, "Optical Constants of Water in the 200-nm to $20\mu\text{m}$ Wavelength Region," Appl Opt, 12:555-563.

*BUSSELL, MILLER & HAWLEY

PRELIMINARY STUDIES ON THE EFFECTS OF ORGANOPHOSPHATE
CHEMICAL WARFARE AGENTS ON ORAL CAVITY PHYSIOLOGY (U)

*NORMAN E. BUSSELL, MAJ., DC

ROBERT A. MILLER

CHARLES E. HAWLEY, COL., DC

U.S. ARMY INSTITUTE OF DENTAL RESEARCH, WRAMC
WASHINGTON, D.C. 20012

In modern warfare concept, one of the greatest threats to the success of military operations has been the tactical use of chemical warfare (CW) agents by the enemy. Chemical weapons can vary from incapacitants, such as mustards, to lethal agents, such as nerve gas. Both the U.S. and the Soviet Union have large stockpiles of chemical weapons (1). Nerve gas agents such as Sarin (GB) and Soman (GD) are generally difficult to detect in the field, and they exert a rapid, eventually irreversible, paralytic effect upon exposed military personnel. Sarin and Soman are chemically related to methyl phosphonic acid (2) and as such, are classified under the general term, organophosphates. These agents can be produced as aerosols for their immediate potentially lethal effects, but they can also be produced in a thickened form which can be spread upon strategic terrain in order to deny access to opposing forces. Protective clothing has been developed by the military. However, because it cannot be tolerated physiologically over extended periods of time, the protective wear is not normally worn by troops in the field. Consequently, soldiers may become exposed to CW agents before preventive measures may be employed.

Although many lives will be lost to CW weaponry, there will be a considerable number of soldiers that will survive with the rapid initiation of the correct medical therapy. It is these potential survivors, critical to the combat effort, that will require specific diagnostic and supportive care. Critical steps in providing necessary aid to the soldier exposed to CW agents will be the early determination of [1] exposure, [2] the degree of exposure, [3] the nature of the specific agent employed by the enemy and [4] to determine if an antidote has been utilized. Diagnosis may be complicated

by the indiscriminate use of antidote cartridges which have their own potentially serious incapacitating complications.

Presently, the diagnosis of CW exposure in the field is based upon clinical signs displayed by the victim. These signs in the field environment are unreliable. More sophisticated chemical diagnostic tests are available, but they require elaborate laboratory equipment. Therefore, these tests are not applicable in the field. Because saliva can be readily obtained in the field by noninvasive techniques, and since saliva contains its own unique chemical constituents, it was decided to explore the use of saliva for developing a rapid diagnostic test for CW exposure.

Two different approaches can be used for the development of a diagnostic screening test using saliva for organophosphate poisoning. The first could be a direct method in which the test would detect the presence of the agent itself or the inactivation of the specific target of the organophosphates, acetylcholine esterase. The second approach, or indirect method, would be to determine alterations in salivary constituents produced by the agents and/or their antidotes. The indirect method was chosen in this experiment for the following reasons: first, the active agent would probably be undetectable in saliva since it would be readily bound to acetylcholine esterase and, therefore, unavailable for testing in its free biologically active state. In addition, a determination of acetylcholine esterase activity would also be inappropriate since the enzyme is normally present in low concentrations in saliva. It has been estimated that large volume saliva samples would be required for even the most sensitive of assays (3). It was, therefore, decided that the indirect approach offered the best chance for success in the development of a rapid test for organophosphate exposure.

Initially there were important technical considerations in designing experiments. It would first be necessary to establish an animal model system which was comparable to humans, and then to determine the extent to which animal salivary gland physiology data could be directly compared with the human salivary system. Another consideration was to compare animal salivary gland responses to the nerve agents with the glandular responses to other cholinergic drugs, since cholinergic agents might ultimately replace the CW agents in the process of developing our diagnostic tests.

This study reports the results of a preliminary investigation on the effects of nerve agents upon saliva and corresponding changes in glandular physiology which might be potentially useful as diagnostic tests in the future.

MATERIALS AND METHODS:

A. Sample Collection

Fifteen cynomolgus monkeys (*Macaca fascicularis*), including five male monkeys, average weight 13 pounds; and 10 female monkeys, average weight 7 pounds; were tested under the following regimen. Each monkey was sedated with sernalin and placed in a prone position on a monkey restraint board. A baseline whole saliva sample was collected by drooling for 30 minutes and the total volume was measured. One milligram of a cholinergic drug (pilocarpine, neostigmine, or physostigmine) was administered subcutaneously. After 5 minutes, a second sample was collected for 15 minutes, and the volume was measured. Atropine sulfate (0.1 mg) was administered subcutaneously. After 5 minutes more, a third sample was collected for 15 minutes, and the volume was measured. The samples were centrifuged to remove particulate and cellular matter and frozen at -40°C until analyzed.

After baseline and cholinergic drug testing, the monkeys were again sedated with sernalin and placed on a monkey restraint board. A baseline whole saliva sample was collected by drooling for 15 minutes. One estimated LD_{50} dose ($\approx 15 \text{ ug/kg}$) of GB was administered intravenously, and a second 5 minute saliva sample was collected immediately. At the end of the 5 minute collection, 0.15 ml of the nerve agent antidote, TAB (20 mg/ml TMB-4, 2.1 mg/ml Benactyzine HCl, 0.52 mg/ml atropine sulfate) was administered intramuscularly, and a third salivary sample was collected for 5 minutes. This was followed immediately by a 10 minute collection of a fourth saliva sample. The saliva samples were centrifuged to remove particulate and cellular matter and then frozen at -40°C until analyzed.

B. Analysis of Saliva

1. Flow rate was determined by dividing the total volume of each collection by the collection time.

2. Total protein of the saliva samples was determined on a 1:40 dilution of saliva by the method of Lowry (4). All protein determinations were performed in triplicate using bovine serum albumin as a standard.

3. Isoelectrofocusing of saliva samples was performed by applying the saliva on lcm^2 filter paper strips to a pH 3.5-9.5 ampholine thin layer polyacrylamide gel plates (LKB). The plates were fixed and stained with coomassie blue R-250 (5). The shape of the pH gradient was determined by an LKB surface electrode.

4. Salivary amylase activity was determined by a modification of Caraway's method (6). Enzyme activity was determined by using a 1:250 dilution of saliva. If the sample produced a light absorption reading of less than 0.100, then a 1:2 dilution was made

on the 1:250 dilution and reanalyzed. All enzyme activities were determined in duplicate and averaged.

5. Electrolyte determinations: Saliva samples were diluted 1:50 using a 0.1% lanthium chloride solution and standards were also prepared in 0.1% lanthium chloride. Calcium and magnesium levels were determined by standard flame atomic absorption spectrophotometry (7). Potassium concentrations were determined on the above diluted saliva samples using 1 ml of the 1:50 dilution, to which was added 1 ml sodium (1 mg/ml) solution and 3 ml of distilled H₂O. Sodium was determined on the above diluted saliva samples using 0.5 ml of 1:50 dilution to which was added 1 ml potassium, 1 mg/ml, and 2.5 ml of H₂O. Flame emission spectrophotometry using 766.5 nm and 589.6 nm was employed for determination of potassium and sodium concentration respectively.

6. Hemagglutination inhibition titers were determined with modified microtiter methods using whole Fusobacterium polymorphum (ATCC 10953) organisms (8).

7. Student t-tests of data were run to determine if statistically significant changes at the 95% confidence level had occurred during administration of the various drugs (9).

RESULTS AND DISCUSSION:

Excessive salivation is one of the major clinical findings reported with organophosphate intoxication (10, 11, 12). The results of testing pilocarpine, neostigmine and physostigmine show that these cholinergic drugs produced marked increases in salivary flow rates which were 5 to 10 times greater than baseline (Tables 1, 2, 3). This is in agreement with other published reports (13, 14, 15). In this study, pilocarpine produced an increased salivary flow rate which was greater than that of neostigmine, which, in turn, was greater than that produced by physostigmine. The differences in flow rate stimulation between pilocarpine and neostigmine and between pilocarpine and physostigmine were statistically significant. Neostigmine produced a slightly greater increase in salivary flow than physostigmine, however, this difference was not statistically significant.

In contrast, administration of Sarin (GB) did not stimulate increased flow rate (Table 4) even though the clinical signs of Sarin intoxication were evident within 30 seconds after its administration. It was evident in these monkeys that Sarin did not produce the increase in salivation which had previously been ascribed to other forms of organophosphate intoxication and cholinergic stimulation. An explanation for the disagreement may be the specific mode of action and compartmental distribution of the CW agent. All of the

*BUSSELL, MILLER & HAWLEY

Table 1
Mean Salivary Flow Rate and Concentrations of Salivary Constituents
Given Cholinergic Drugs
(Mean Values \pm Standard Deviation)

Constituent	Baseline	Pilocarpine	Atropine
Flow Rate ml/min	0.09 \pm 0.10	1.34 \pm 0.44	0.18 \pm 0.22
Protein mg/ml	5.33 \pm 3.69	6.25 \pm 2.04	4.52 \pm 1.51
Sodium mg/ml	1.0 \pm 0.6	2.7 \pm 0.5	2.9 \pm 0.5
Potassium mg/ml	2.4 \pm 0.6	1.4 \pm 0.4	1.0 \pm 0.2
Calcium μ g/ml	17.3 \pm 11.6	35.4 \pm 24.1	34.1 \pm 24.8
Magnesium μ g/ml	5.1 \pm 4.3	3.5 \pm 1.5	7.7 \pm 3.9
Amylase*	121 \pm 140	415 \pm 692	340 \pm 504

Table 2
Mean Salivary Flow Rate and Concentrations of Salivary Constituents
Given Cholinergic Drugs
(Mean Values \pm Standard Deviation)

Constituent	Baseline	Neostigmine	Atropine
Flow Rate ml/min	0.17 \pm 0.33	1.00 \pm 0.46	0.43 \pm 0.37
Protein mg/ml	6.40 \pm 3.10	7.30 \pm 2.47	5.99 \pm 3.09
Sodium mg/ml	0.8 \pm 0.5	2.0 \pm 0.8	2.7 \pm 0.7
Potassium mg/ml	2.8 \pm 0.7	2.2 \pm 0.8	1.5 \pm 0.7
Calcium μ g/ml	20.3 \pm 9.4	46.5 \pm 16.3	82.4 \pm 54.5
Magnesium μ g/ml	3.8 \pm 2.6	5.2 \pm 2.9	9.4 \pm 4.0
Amylase*	190 \pm 236	290 \pm 225	260 \pm 272

Table 3

Mean Salivary Flow Rate and Concentrations of Salivary Constituents
Given Cholinergic Drugs
(Mean Values \pm Standard Deviation)

Constituent	Baseline	Physostigmine	Atropine
Flow Rate	0.23 \pm 0.37	0.85 \pm 0.45	0.18 \pm 0.12
Protein	4.11 \pm 0.90	7.93 \pm 2.88	6.78 \pm 2.17
Sodium	0.6 \pm 0.4	1.8 \pm 0.7	2.0 \pm 0.5
Potassium	3.2 \pm 1.2	2.8 \pm 1.1	1.9 \pm 0.9
Calcium	16.5 \pm 7.4	31.9 \pm 20.0	32.7 \pm 19.8
Magnesium	2.4 \pm 1.2	2.3 \pm 1.0	9.2 \pm 4.7
Amylase*	137 \pm 245	184 \pm 196	260 \pm 272

Table 4

Mean Salivary Flow Rate and Concentrations of Salivary Constituents
Of Monkeys Exposed to GB
(Mean Values \pm Standard Deviation)

Constituents	Baseline	GB	GB/TAB	TAB
Flow Rate ml/min	0.19 \pm 0.38	0.27 \pm 0.21	0.15 \pm 0.11	0.07 \pm 0.09
Protein	7.12 \pm 3.42	9.95 \pm 3.94	8.90 \pm 4.65	10.37 \pm 4.53
Sodium	2.2 \pm 1.0	2.0 \pm 0.8	2.7 \pm 0.5	2.7 \pm 0.2
Potassium	3.0 \pm 0.6	3.0 \pm 0.4	2.5 \pm 0.3	2.3 \pm 0.4
Calcium	13.9 \pm 6.4	12.8 \pm 4.2	11.6 \pm 4.9	13.4 \pm 4.3
Magnesium	4.0 \pm 1.7	3.3 \pm 1.3	3.6 \pm 1.4	4.4 \pm 3.4
Amylase*	141 \pm 92	118 \pm 107	114 \pm 95	76 \pm 87

*Amylase Units/100 ml $\times 10^3$

drugs used in this study, including Sarin, are classified as cholinergic agents, and each has parasympathomimetic action. Pilocarpine functions as an analogue of acetylcholine (16). Neostigmine and physostigmine are acetylcholine esterase inhibitors but, unlike Sarin, are reversible inhibitors (17). These drugs may also be characterized by their compartmental distribution in the central nervous system (CNS) or peripheral nervous system (PNS). Some agents, e.g., physostigmine and Sarin, demonstrate both CNS and PNS actions while neostigmine and pilocarpine are primarily PNS in action (16). Examination of our flow rate data suggests that Sarin is closer to physostigmine than to either pilocarpine or neostigmine in its physiological effects. But the measureable difference between Sarin and physostigmine could be due to an even greater central nervous system action of Sarin.

The antidote used to block the actions of the cholinergic drugs is atropine (17). Atropine is also used as an antidote for nerve agents and is a part of the combo pen (T.A.B.) antidote for nerve agents (12). The administration of atropine to the monkeys after stimulation effectively returned the salivary flow rate to baseline values. There was no statistical difference between baseline and atropine flow rates in any of the cholinergic drugs used. The antidote TAB produced a decrease in the flow rate when compared to GB stimulation. This difference was statistically significant.

One way of evaluating the function of the salivary glands is an evaluation of the protein concentration in saliva. Protein in saliva is derived from two sources. One part of the protein in saliva takes its origin from plasma, and is derived by transudation into the ductal lumen from the acinar cells. The major portion of salivary proteins are those directly synthesized by the serous and ductal cells. Stimulation by cholinergic drugs produced a slight increase in protein concentration, and administration of atropine reduced the protein concentration to, or slightly below, baseline (Tables 1, 2, 3). These results are in agreement with previously reported results. Administration of GB produced the same increase in total protein as did the cholinergic drugs, but, upon administration of the TAB, the protein remained elevated (Table 4).

More than 20 different proteins have been identified in saliva by isoelectrofocusing which is one of the most powerful techniques used in the separation of proteins. Separation of proteins in different baseline and cholinergic drug stimulated samples showed consistent variation in one protein band (Fig. 1). This band, identified as amylase via various zymogen techniques, had an isoelectric point of 6.4. This band increased in staining intensity upon administration of the cholinergic drugs, and the increased staining intensity remained after the administration of the atropine.

ISOELECTROFOCUSING OF CYNOMOLGUS MONKEY SALIVA

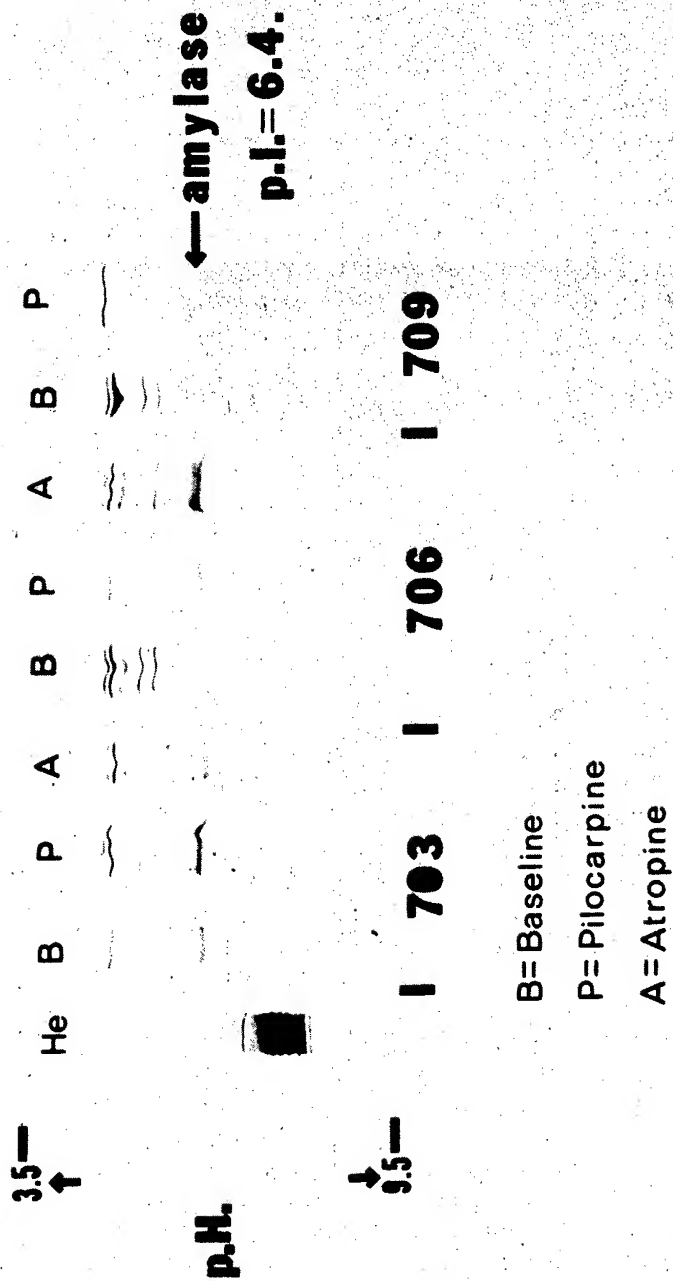


FIGURE 1

The administration of GB did not produce the same increase in staining in this band, but instead produced an apparent decrease in the amylase band (Fig 2).

Salivary amylase is the major enzyme present in saliva (18). Total salivary amylase activity was determined on saliva samples, and the results are shown in Tables 1, 2 and 3. Total salivary amylase activity shows a marked increase with the administration of the different cholinergic drugs. Pilocarpine produced the largest increase in amylase with neostigmine producing the next largest increase. Administration of atropine decreased the amylase activity slightly. Salivary amylase is produced specifically by the serous acinar cells (19), which indicates that the increased acetylcholine caused by the different cholinergic agents stimulates the synthesis of amylase by the serous cells and that atropine only partially blocks this synthesis.

Sarin did not produce the same effect on salivary amylase as did the other cholinergic drugs, but instead, it produced a slight decrease in salivary amylase activity, which is in agreement with the isoelectrofocusing patterns. The antidote TAB produced a further decrease in the concentration of amylase activity. These results correlate with the findings of the salivary flow rate changes produced by the Sarin.

In the interpretation of data developed from an animal model system, care must be taken in extrapolation of that data to the human system. Consequently, in order to test the possible validity of such an extrapolation, saliva from various animal models and humans were run on isoelectrofocusing plates to compare the protein fingerprinting pattern. The findings indicate that no direct comparison could be made between the fingerprint patterns in monkeys and humans since the major protein banding did not overlap (20). This observed disparity could be explained on the basis of phylogenetic amino acid differences in the proteins, even though similar proteins have been identified in both monkey and human salivas.

Another means of examining salivary functions is to evaluate changes in electrolyte concentrations. Salivary fluid in the intercalated duct lumen is iso-osmotic with respect to plasma. Through secretion and reabsorption of various ions, saliva becomes hypo-osmotic. By measuring changes in salivary ion concentration, insight can be gained regarding the influence of various drugs upon salivary gland function. In these studies, sodium, the major extracellular cation showed a marked increase in concentration upon administration of the cholinergic agents, and after administration of atropine, the sodium concentration remained approximately equal to its stimulated value (Table 4). Sarin also produced an increase

ISOELECTROFOCUSING OF CYNOMOLGUS MONKEY SALIVA

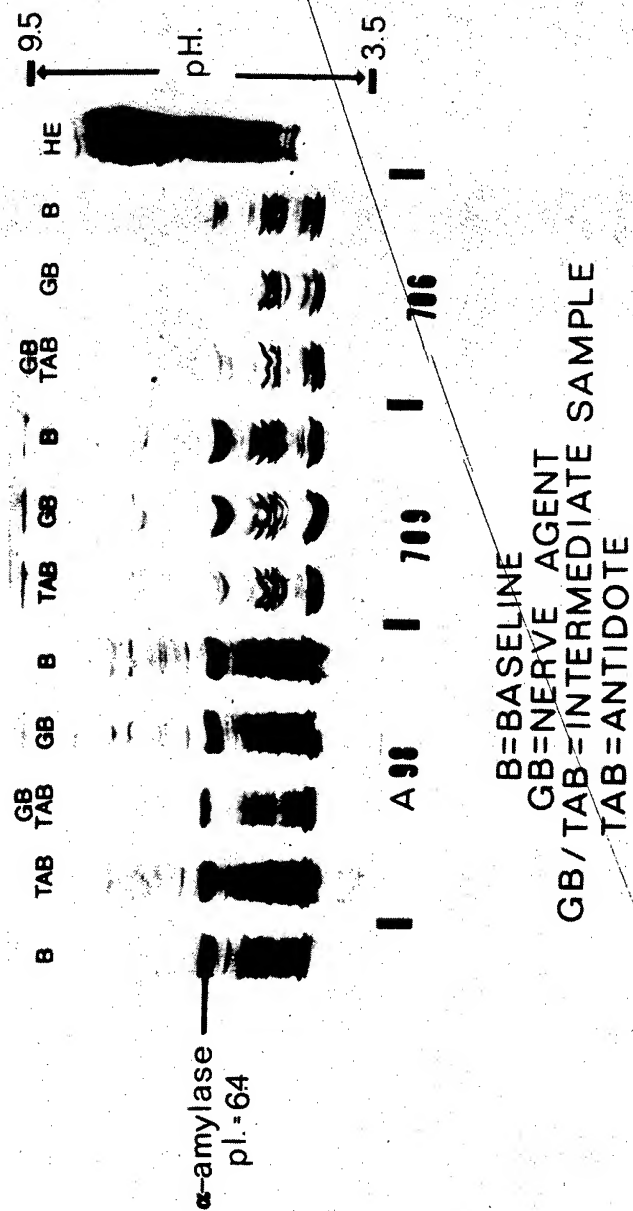


FIGURE 2

in sodium concentration, however, the elevation was masked by an unexplained elevated baseline sodium level. The antidote TAB showed no measureable effects on the increased sodium concentration (Table 4). The data suggest that the excess acetylcholine produced by the cholinergic drugs acts to increase the secretion of sodium.

Potassium, which is usually inversely related to sodium concentration, showed an expected decrease in concentration upon administration of the cholinergic drugs. Physostigmine did not produce as marked a decrease as neostigmine and pilocarpine. Atropine produced a further decrease in potassium concentration which was dependent upon the initial depression produced by the cholinergic agents. Sarin exposure did not produce any change in potassium levels initially, and the TAB produced only a slight decrease in the potassium values. These data suggest that there is a difference in the salivary gland response to the various cholinergic agents. This probably depends upon the previously suggested compartmental distribution of the CNS vs peripheral effects of each drug.

The three cholinergic drugs produced an increase in the concentration of the major intercellular divalent cation, calcium. Atropine maintained the calcium concentration at stimulation levels. The pattern of changes in calcium concentrations was similar to that shown by sodium. Sarin and TAB did not produce changes in calcium concentration.

Magnesium, the major intracellular divalent cation, showed either a consistent increase (physostigmine) or decrease (pilocarpine) in salivary concentration. Neither Sarin nor TAB produced any changes in salivary magnesium concentration.

As discussed earlier, when comparing data collected in an animal model system, care must be taken in extrapolation of the data to humans. However, with respect to changes in salivary electrolytes, the responses in cynomolgus and Rhesus monkeys were found to be comparable. Since the salivary electrolyte concentration in Rhesus monkeys has been reported (21) to be identical to those in humans, the electrolyte information in this study should be a good indicator of how human salivary electrolytes will respond to chemical warfare agents.

Oral cavity physiology and alterations in it may play a major role in the host defense mechanisms of both the oral cavity and the upper respiratory tract. If the defense mechanism against bacterial invasions is compromised, then additional medical supportive measures must be initiated to prevent further loss of manpower during treatment and convalescence. The micro-hemagglutination inhibition test indicated that baseline saliva contained high titers of an inhibitor to bacterial hemagglutination. This assay has been used as an indicator of bacterial colonization mechanisms (4). Salivas

*BUSSELL, MILLER & HAWLEY

collected after stimulation with pilocarpine and Sarin showed a several-fold decrease or absence of titratable colonization inhibitor (Table 5).

Table 5

<u>Salivary Inhibition of Bacterial Hemagglutination</u>				
<u>Monkey</u>	<u>Baseline</u>	<u>Sarin</u>	<u>Pilocarpine</u>	<u>Antidote</u>
B702	1:512*	1:8	- -	ND
B703	1:128	1:32	- -	ND
7B55	1:512	- -	Undiluted	1:128
7B62	1:512	- -	1:128	1:128
7B59	1:128	- -	1:2	1:128

*Two-fold serial dilutions of saliva in phosphate-buffered saline pH 7.4.

One explanation could be a dilution effect upon the inhibitor. However, since there was no linear correlation with increased flow rate and the loss of the salivary inhibitor, the data indicate that both pilocarpine and Sarin had, in this case, two independent specific effects: (1) an increased flow rate and (2) depression of inhibitor activity. Administration of atropine and TAB partially restored the baseline inhibitor titers.

SUMMARY AND CONCLUSIONS:

It is evident from these data presented that Sarin, under these conditions, did not produce the same effect as other cholinergic drugs on salivary gland function. The data clearly shows that Sarin did not increase the salivation rate and this finding is in direct disagreement with the previously reported characteristic signs of organophosphate intoxication.

Normally, increases of acetylcholine in the salivary glands would produce an increase of total protein, amylase activity, sodium and calcium concentrations, and a concomitant decrease in potassium concentration. Sarin produced only increases in protein and sodium, but it did not provide the parallel increases in calcium concentration and amylase activity or the decrease in potassium concentration.

Sarin actually produced a slight decrease in salivary amylase activity. From the data, it is apparent that one of the major considerations of any agent is the central effect of the drug versus its potential peripheral effect. Sarin, under the conditions of this study, apparently displayed a primary CNS effect while the other cholinergic drugs were primarily peripheral in their effect. Sarin closely resembles Soman (GD) in structure, and Soman, like Sarin, produces no salivary stimulation (22). On the other hand, VX does not readily cross biological membranes and therefore would be expected to have an entirely peripheral action which should produce activity parallel to the other cholinergic drugs tested here. If so, this fact may act to differentiate between the effects of the nerve agents GB or GD type from the effects of VX types.

More research is needed on other agents and on their response patterns before any conclusive recommendations can be made. Currently from the data, a hypothetical salivary dipstick could be designed to detect CW agent exposure. The dipstick would contain a set of three spots which would react with the following chemicals: one spot for salivary amylase which would indicate if a soldier has been exposed to a nerve agent, the second spot would be sensitive to magnesium which would indicate if the soldier had been given atropine or TAB, the third spot would act as a cross check on the first two spots by being sensitive to potassium which would indicate administration of both the CW agent and atropine.

Finally, the changes found in the oral cavity immunological defense mechanisms require further study. The findings suggest that exposure to CW agents may compromise the natural defense mechanism. If a soldier were to survive exposure to nerve agents, he would yet ultimately be lost. With a compromised immunological defense mechanism as such, he could be more susceptible to rampant infectious processes.

The authors wish to acknowledge the work of Major Stan Liebenberg in care and dosing of the animals, Captain John McDonough, MSC and Mr. Dave Stecher for their aid in dosing the monkeys and to the other individuals of the Biomedical Laboratory CSL, Aberdeen Proving Ground, MD 21010 without whose help this project could not have been successfully completed.

References

1. Lepkowski, W., Chemical and Engineering News, Jan. 16, 1978.

2. Verweij, A., H.L. Boter, and C.E.A.M. Degenhardt, Science, 204, pp. 616-618 (1979).
3. Ueda, K. and K. Yamaguchi, Bull. Tokyo Dent. Coll., 17, pp. 231-241 (1976).
4. Lowry, O.H., N.J. Rosebrough, A.L. Farr, and R.J. Randall, J. Biol. Chem., 193, pp. 265-275 (1951).
5. Winter, A., K. Ek, and U. Andersson, Application Note #250 Methodological, LKB (1977).
6. Caraway, W., Am. J. Clin. Path., 32, pp. 97-99 (1959).
7. Analytical Methods For Atomic Absorption Spectrophotometry, Perkin-Elmer Corp. (1973), pg. BC-1R.
8. Falkler, W.A., C.E. Hawley, and J.R. Mongiello, J. Periodontal Res. 13, pp. 425-432 (1978).
9. Spiegel, M.R., Statistics, Shaums College Outline, McGraw-Hill, San Francisco, Calif. (1961).
10. Bogoslav, V.V., M.P. Milosevic, and M.R. Terzic, J. Dent. Res., 57, pp. 748-751 (1978).
11. Wills, J.H., Pharmacological Antagonists of the Anticholinesterase Agents, in Cholinesterases and Anticholinesterase Agents. Kolle, G.B. (ed) Springer Berlin (1963).
12. TM 8-285.
13. Nash, L. and L.F. Morrison, Ann. Otol. Rhen. Laryng, 58:976 (1949).
14. Best, C.H., and N.B. Taylor, The Physiological Bases of Medical Practice, 5th ed., Baltimore, Williams & Wilkins Co., (1950).
15. Afonsky, D., Saliva and The Relation to Oral Health. University of Alabama Press, Montgomery, Alabama (1961).
16. Meyers, F.H., E. Jawetz, and A. Goldfien, "Review of Medical Pharmacology, 2nd ed. Long, San Francisco, Calif., 1970, A. Goldfien.
17. Goth, A., Medical Pharmacology, 5th edition, C.V. Mosby Co., St. Louis, Mo. (1970).
18. Shannon, O.L. and R.P. Suddick, "Saliva" in Dental Biochemistry. second edition, E.P. Lazzari (ed), Lea & Febiger, Philadelphia, Pa. (1976).
19. Kraus, F.W., and J. Mestecky, Archs. Oral. Biol., 16, pp. 781-789 (1971).
20. Setterstrom, J.A., N.E. Bussell, R.S. Stanko, and A. Gross, J. Dent. Research, 58:A, 1203, 1979.
21. Bruckman, J.E. and J.A. Mangos, Proc. Soc. Exper. Biol. & Med., 134:606-609 (1970).
22. Personal communication.

BUTLER

MICROGRAVIMETRY AND THE MEASUREMENT AND
APPLICATION OF GRAVITY GRADIENTS

DWAIN K. BUTLER
U. S. ARMY ENGINEER WATERWAYS EXPERIMENT STATION
VICKSBURG, MISS. 39180

INTRODUCTION

Gravimetry is the science which studies the earth's gravitational field in all its aspects. Applied gravimetry involves measurements of the vertical component of the gravitational field g_z and the attempt to deduce geologic structure from the data. Any inversion of the gravity data to yield a possible causative mass (or density) distribution will be nonunique (as with inversions of all potential field data); however, by coupling geological constraints and other available geophysical data, the range of feasible solutions can be narrowly bracketed. Commonly, the objective of gravimetric exploration is the location of structural or stratigraphic environments typical of oil and gas or ore deposits. A perhaps less obvious application of gravimetry is to geotechnical problems, where the objective is shallow structural mapping to detect anomalous conditions such as subsurface cavities, fracture zones, faults, variation in depth to top of rock, buried river channels, etc. These high-resolution applications of gravimetry involve not only a significant scaling down in size and depth of the structures of interest and corresponding decrease in required profile and grid spacings, but also relative measurements of the acceleration of gravity in the μgal range ($1 \mu\text{gal} = 10^{-6} \text{ gal} = 10^{-6} \text{ cm/s}^2 \approx 10^{-9}$ times the normal gravitational acceleration). High-resolution gravimetry is properly referred to as microgravimetry (1-3). Application of microgravimetry, particularly to geotechnical problems, has enjoyed only limited success due to poor gravimeter sensitivity and accuracy and lack of appreciation for proper field procedures. However, the development of

a true "microgal" gravity meter* in the late 1960's has made microgravimetry a viable geotechnical field method.

Recognizing the potential value of microgravimetry for geotechnical applications, the U. S. Army Engineer Waterways Experiment Station (WES) began a research effort in 1978 to assess the benefits to the Corps of Engineers and WES of developing complete in-house capability for application of microgravimetric techniques. One of the most promising areas of application is the detection and delineation of subsurface cavity systems in areas with solution-susceptible bedrock. Microgravimetry has successfully been applied at a field test site in Florida to map a cavity system. Another area of interest and the subject of this paper is the use of microgravimetric techniques to determine the first vertical and horizontal derivatives (gradients) of g_z . The gravity gradients are of fundamental importance and offer three advantages over measurement of just g_z alone: (a) increased detectability limits and resolution of anomalies due to shallow structures; (b) gradient profiles have diagnostic properties which, in many cases, may make subsurface structure identification more straightforward; and (c) the gradients should selectively filter out anomalies from deeper structures and thus enhance the detection of anomalies due to shallow structures. The results of a controlled field study to evaluate techniques for determining gravity gradients and the use of these data for structural interpretations are presented in this paper.

GRAVITY GRADIENTS

Considering a Cartesian coordinate system (x,y,z) , with the z -axis vertically downward, the derivatives of interest are $\partial g_z / \partial z$, $\partial g_z / \partial x$, and $\partial g_z / \partial y$. It is a natural approach to study a function such as g_z by examining its derivatives or gradients in specified directions. Since $g_z = \partial U / \partial z$, where U is the gravitational potential, we are interested in defining various components of the second derivative matrix $U_{,ij}$, where the comma indicates partial differentiation (with respect to the subsequent indices) and i and $j = 1, 2, 3$ corresponding to x, y, z , respectively. For U due to a purely two-dimensional structure, $U_{,ij}$ is a second-order tensor. In particular, we are interested in $U_{,xz}$, $U_{,yz}$, and $U_{,zz}$. Since $\nabla^2 U = 0$ in source-free space, we know that $U_{,zz} = -(U_{,xx} + U_{,yy})$. Also since $\nabla^2 g_z = 0$, we have $g_{z,zz} = -(g_{z,xx} + g_{z,yy})$, which suggests a way in which $g_{z,zz}$ and $g_{z,z}$ (by integrating) could be obtained by numerical methods from gridded g_z data.

* LaCoste and Romberg, Inc., Model-D "Microgal" Gravimeter.

BUTLER

Indeed, numerous techniques for calculating $\partial g_z / \partial z$ ($g_{z,z}$) have been proposed; however, all suffer from all the inaccuracies and deficiencies of the original g_z data and from fictitious anomalies introduced by the numerical process (4). Clearly, the problems associated with calculating $g_{z,x}$ or $g_{z,y}$ from gridded g_z data should be much less difficult. However, the basic problem remains that, for standard survey techniques, the grid data are too widely spaced for the gradient values to have any real significance for delineating structures.

It is highly desirable that field techniques be developed for directly determining the gravity gradients. Since gravity gradiometers do not exist (5), the determinations will be finite difference approximations to the partial derivatives, i.e.

$$\lim_{\Delta z \rightarrow 0} \Delta g_z / \Delta z \rightarrow \partial g_z / \partial z ; \quad \lim_{\Delta x \rightarrow 0} \Delta g_z / \Delta x \rightarrow \partial g_z / \partial x ; \quad \text{etc.}$$

Vertical gradient

For the vertical gradient, the procedure simply involves measuring g_z on the surface and at one or more positions vertically above the surface station. Measurements in tall buildings on a floor-by-floor basis have been utilized (a) for the determination of the free-air vertical gradients and (b) to accurately calibrate gravimeters (6,7). Portable tower structures must be utilized in applications of the vertical gradient data (c) to correct field gravity data and (d) as an exploration method to locate anomalous masses and structures. Attempts to make practical field vertical gravity gradient measurements have met with considerable difficulty. The problem reduces to a trade-off between practical field implementation (manageable tower height), greater tower height (distance between measurement stations) to decrease the probable error in the determination, and the need to approximate the true gradient.

Horizontal gradient

For the determination of horizontal gradients, the situation is much simpler since virtually any horizontal separation between measuring stations is logistically feasible. The main consideration now becomes one of keeping the spacing small enough to adequately define the anomaly. Another consideration is the need to define the direction of the maximum horizontal gradient. This can be accomplished by double track profiling or by measuring at three locations at the corners of say a right triangle (13) for each gradient determination. For geotechnical applications, horizontal separations of the range of

5 to 10 m will be required, and this data will conveniently be available routinely in microgravimetric surveys.

Relation between gradients for two-dimensional anomalous structures

While two-dimensional structures do not exist in nature, in many cases the approximation to two-dimensional conditions is very close. Thus, analytical consideration of two-dimensional structures (constant cross section and long in say the y-direction) is not only convenient but useful for a large number of real geologic conditions. For a two-dimensional anomalous structure, the vertical gradient $g_{z,z}(x,0)$ and horizontal gradient $g_{z,x}(x,0)$ on the surface are related by a Hilbert transform (14)

$$g_{z,z}(x,0) = \frac{1}{\pi} \int_{-\infty}^{\infty} \frac{g_{z,x}(\xi,0)}{\xi - x} d\xi$$

where x is the profile point and the integral is interpreted in the sense of its Cauchy principal value. This relation is of great value, since, if it proves impractical to determine either of the gradients in the field, one of the gradients can be calculated from the other. A computer program has been written to perform the Hilbert transform for discrete data.

RESULTS OF A FIELD STUDY OF GRAVITY GRADIENT TECHNIQUES

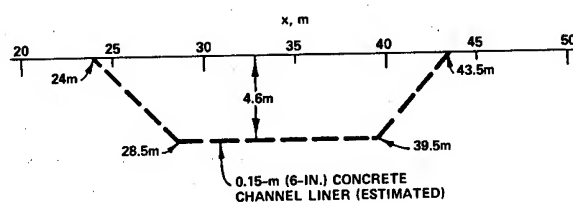
There has been much speculation on the feasibility and utility of gravity gradient determinations. However, no definitive study has been reported. The study reported here is a preliminary attempt at a definitive evaluation of gravity gradient techniques. Three criteria guided the selection of the test case: (a) the anomalous structure should be precisely defined; (b) the anomaly both in g_z and the gradients should be large (in a "microgravimetric sense") and should have a relatively short wavelength; and (c) the structure should approximate two-dimensional conditions. These criteria seemed most easily satisfied by a shallow man-made structure. The structure chosen was the concrete-lined drainage channel shown in Figure 1. Since the structure is at the surface, the gravity anomaly is large and has a short wavelength. Also, since the channel extends to either side of the bridge for at least 100 m with no significant change in cross section, the structure is approximately two-dimensional. The bridge itself is the only major non-two-dimensional



Figure 1. Drainage channel structure chosen for microgravity and gravity gradient field tests

aspect of the site. Pertinent dimensions are given in the diagram in Figure 2, which will also be the basis for two-dimensional model calculations.*

Figure 2. Location of drainage channel along profile line and dimensions of two-dimensional model. Profile line direction is N22°E

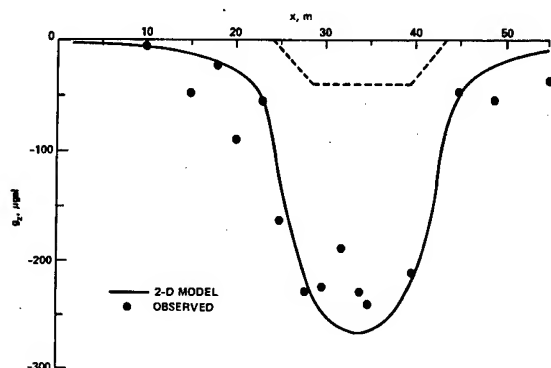


The survey over the drainage channel consisted of 16 stations over a 55-m line perpendicular to the channel, with the approximate center of the channel at the 34-m position. At each station g_z measurements were made at the ground surface and at a nominal elevation of 1.3 m vertically above the ground station. No elevation

* Two-dimensional model calculations were accomplished using a computer program TALGRAD which utilizes the algorithm of Talwani (15) to compute g_z profiles due to an arbitrary number of polygonal cross-sectional structures. The program also allows for the computation of $\Delta g_z / \Delta z$ and $\Delta g_z / \Delta x$ along the profile for arbitrarily specified Δz and Δx .

or Bouguer corrections were necessary for the data (no elevation change). The data were corrected for latitude change in station location in the usual manner (16). Linear drift corrections were applied to the data utilizing base station reoccupations, and the drift curves were compared to theoretical earth tide curves calculated for the site to verify consistent gravimeter performance.

Results of the two-dimensional model calculations and the observed gravity data are compared in Figure 3. The model profile results agree closely in anomaly amplitude and width with the observed data, with the major deviation being the approximately 70- μ gal positive anomaly (relative to the model profile) between 30 and 36 m.



However, this is precisely where the non-two-dimensional aspects of the structure, i.e., the bridge pillars and beams, should make a positive contribution to the observed gravity profile. The maximum positive contribution due to the pillar beneath the profile line should be about 30 μ gal, with the remainder of the 70- μ gal anomaly accounted for by the other pillar and the bridge beams.

Figure 3. Gravity profiles across the drainage channel

the profile were computed for the two-dimensional model and from the observed field data. Figures 4 and 5 present the horizontal and vertical gradient profiles, respectively, for the two-dimensional model. For the horizontal gradient (Figure 4), profile values were computed for $\Delta x = 3$ m and $\Delta x = 10$ m. The finite difference approximation $\Delta g_z / \Delta x$ to $\partial g_z / \partial x$ should become better as Δx decreases; and clearly the horizontal gradient profile for $\Delta x = 3$ m is sharper and has greater amplitude than the profile for $\Delta x = 10$ m, as expected. The vertical gradient profile (Figure 5) was computed for $\Delta z = 1.3$ m, corresponding to the nominal value used for the field measurements. Note that the four corners of the structure are fairly well defined in Figure 5 by the vertical gradient profile.

Horizontal and vertical gradient profiles determined from the field data are shown in Figures 6 and 7. The horizontal gradient

Figure 4. Analytical horizontal gradient profile for two-dimensional model of drainage channel (see Figure 2)

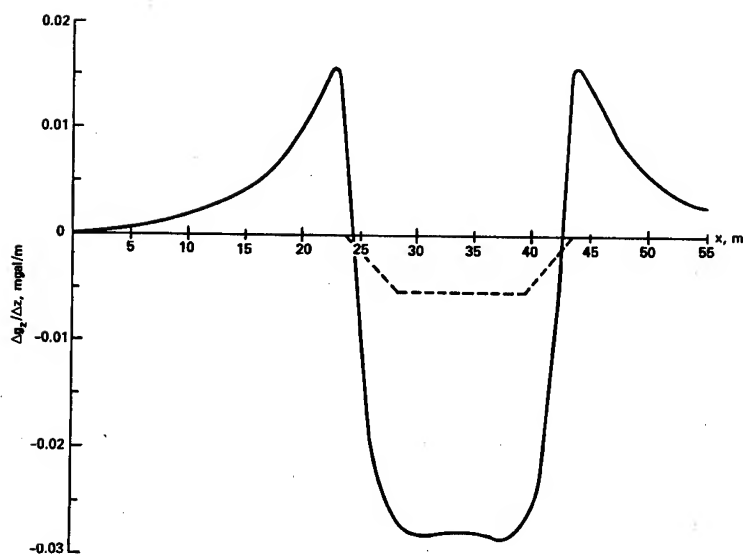
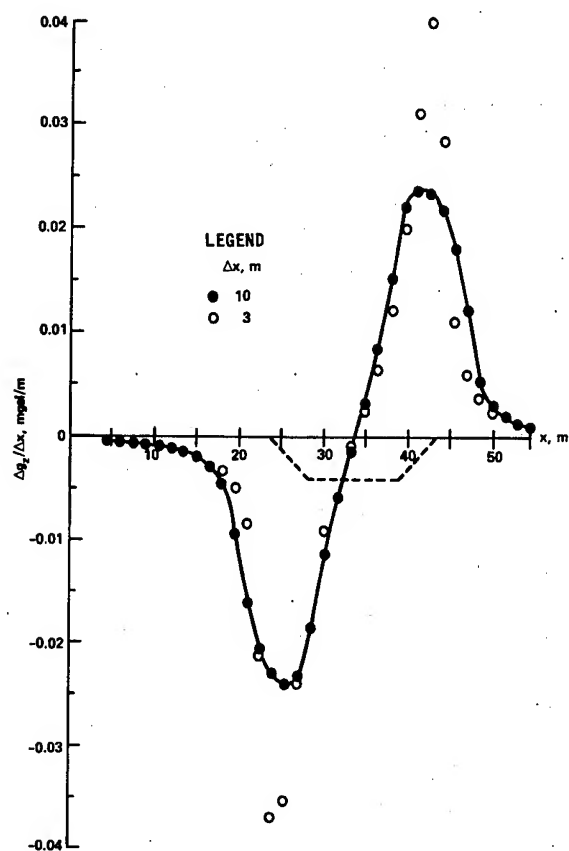


Figure 5. Analytical vertical gradient profile for two-dimensional model of drainage channel determined for $\Delta z = 1.3 \text{ m}$

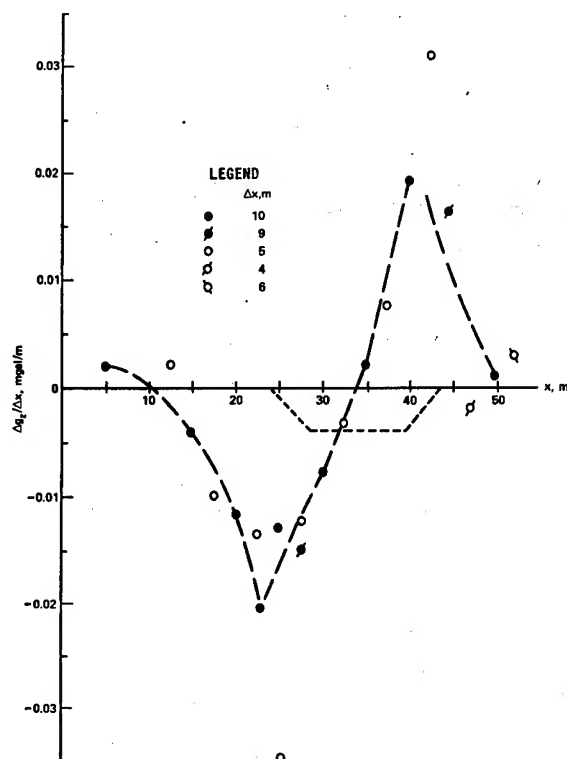


Figure 6. Horizontal gradient profile deduced from the gravity profile over the drainage channel (see Figure 3)

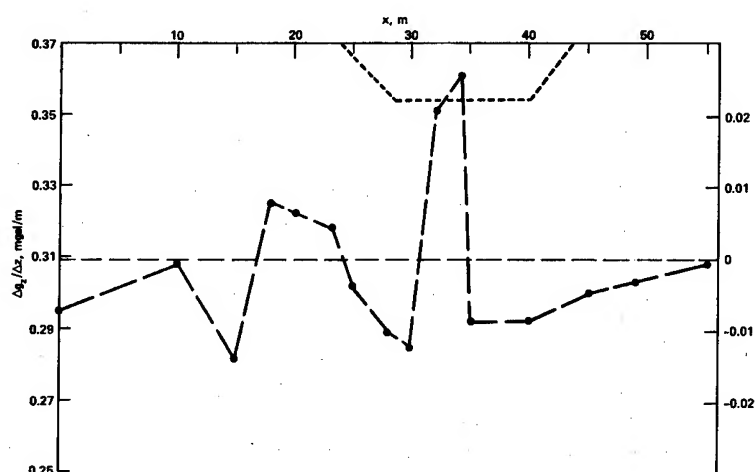


Figure 7. Vertical gradient profile deduced from portable-tower gravity survey over the drainage channel with $\Delta z \approx 1.3 \text{ m}$

BUTLER

values are shown for various values of Δx (corresponding to various possible combinations of stations); however, the dashed line connects points for $\Delta x = 10$ m. The comparison between Figures 4 and 6 is quite good for the curves for $\Delta x = 10$ m, both in general shape and in anomaly amplitude and width. Also, the general trend of increasing anomaly amplitude and sharpness with decreasing Δx is seen in the observed data in Figure 6. The vertical gradient data (Figure 7) are very erratic and only with a great amount of smoothing and imagination do the results resemble the model results of Figure 5. There are several possible reasons for the erratic nature of the vertical gradient data:

a. The value $\Delta z \approx 1.3$ m is too small for the vertical separation between measuring stations due to the probable error in the measurements, i.e., a larger Δz would result in a larger Δg_z and hence decrease the significance of the probable error.

b. The vertical gradient determination is more strongly affected by the non-two-dimensional aspects of the structure than the horizontal gradient determination.

c. The vertical gradient is known to be strongly influenced by very shallow density fluctuations, so a preferable procedure might be to make the lower g_z measurement some small distance, say 0.2 m or so, above the ground surface.

It is probable that the two large positive values of vertical gradient between 30 and 35 m are due to the bridge pillars and beams.

Calculation of vertical gradient profile from the horizontal gradient profile

Utilizing the horizontal gradient profile for the two-dimensional model (Figure 4), the vertical gradient profile shown in Figure 8 was computed using the Hilbert transform relation and computer program discussed earlier. Except for the sign reversal (caused by assuming the z-axis vertically downward for the two-dimensional model results), the vertical gradient profiles in Figures 5 and 8 agree qualitatively very well. The lower amplitudes and frequency content of the profile computed by the Hilbert transform are not unexpected; however, the comparison would improve if the profile itself were longer and/or a smaller Δx were used for the horizontal gradient profile.

Similarly, a vertical gradient profile (Figure 9) was

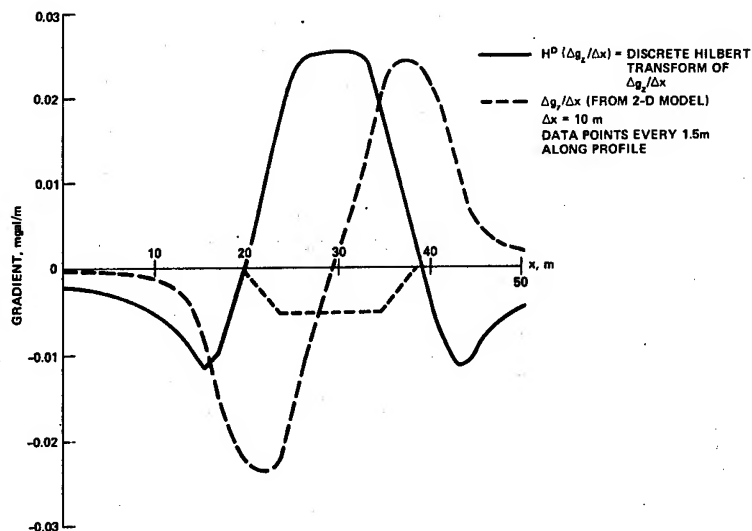


Figure 8. Vertical gradient profile calculated from horizontal gradient profile for the two-dimensional model by the Hilbert transform

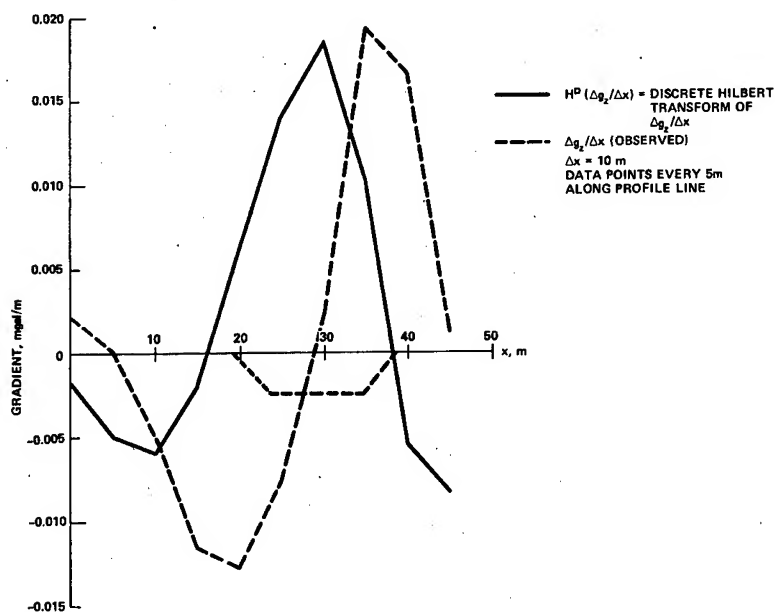


Figure 9. Vertical gradient profile calculated from the observed horizontal gradient profile over the drainage channel by the Hilbert transform ($x = 0$ is at 5 m of actual survey line)

computed from the horizontal gradient profile of the observed data (Figure 6) over the structure using the Hilbert transform. Again, only with extreme smoothing is there even qualitative similarity between the observed and calculated vertical gradient profiles (Figures 7 and 9, respectively). However, the profile in Figure 9 compares qualitatively quite well with the vertical gradient profiles in Figures 4 and 6. Thus, the procedure of determining the horizontal gradient profile from field measurements and then calculating the vertical gradient profile via the Hilbert transform appears very promising.

Utilization of gravity gradients

The motivations for determining gravity gradients have been discussed previously. A complete discussion of the possibilities for utilization of gradient data for subsurface structural delineation is beyond the scope of this paper and also premature. Thus, the concepts under consideration will only be briefly covered.

A very promising technique for displaying the gradient data is a gradient space plot, i.e., $g_{z,z}$ versus $g_{z,x}$. In such a space, each point will correspond to a given profile position or value of x . As an example, the gradient profile data for the two-dimensional model (Figures 4 and 5) result in the gradient space plot in Figure 10. Corresponding points along the profile and the plot are indicated, and the manner in which the geometry of the structure

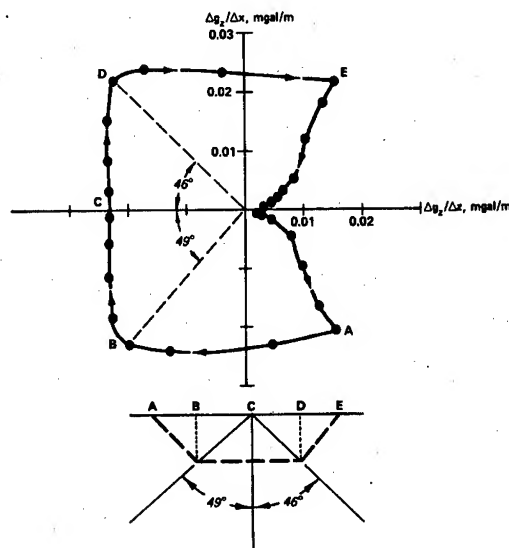


Figure 10. Gradient space plot for two-dimensional model of drainage channel

BUTLER

might be deduced is indicated.

Another promising technique involves the concept of the analytic signal along the profile, defined by $A(x) = g_{z,x}(x) - ig_{z,z}(x)$. Note that the gradient space plot is just a complex plane plot of the components of $A(x)$. The amplitude of $A(x)$ is defined in the usual manner, $a(x) = |A(x)| = (g_{z,x}^2 + g_{z,z}^2)^{1/2}$. Above a two-dimensional structure with corners, the $a(x)$ will be the superposition of symmetrical, bell-shaped curves, one for each of the corners. The properties of the bell-shaped curves determine the profile position and depth of the structural corner causing the signal. Thus, the decomposition of the $a(x)$ signal into bell-shaped curves represents in principle the solution of the structural problem.

SUMMARY AND CONCLUSIONS

Microgravimetry has been successfully applied both to a natural cavity site in Florida and to a man-made structure to delineate small-scale, shallow subsurface features. The horizontal gravity gradient profile has been adequately determined from a microgravimetric survey and successfully compared with the results of a two-dimensional model study. Measurement of the vertical gradient profile with a relatively short tower structure ($\Delta z = 1.3$ m) was not as successful. However, utilization of the Hilbert transform allows the vertical gradient profile to be calculated from the horizontal gradient profile. For cases in which the assumption of a two-dimensional, polygonal cross-sectional geometry is approximately valid, use of the gradient profiles permits a unique structural interpretation.

Future work in this research effort will concentrate on: (a) improved field procedures for microgravimetric surveys; (b) continued attempts to determine vertical gradient profiles across known structures using larger values of Δz than in the past; (c) further study of the application of the discrete Hilbert transform; and (d) in-depth studies of interpretative methods using the gradient data.

REFERENCES

1. Cabrera, D. H., 1973, Methods of relief correction in micro-gravity corrections: Optional Thesis, Ecole des Mines de Paris.
2. Boubakar, K., 1973, Rapid method of quantitative interpretation in micro-gravity measurement: 3rd Cycle Doctorate Diploma, University of Paris, VI.

3. Neumann, R., 1972, High precision gravimetry--recent developments: Report to Paris Commission of E.A.E.G., Compagnie Generale de Geophysique, Massy, France.
4. Fajklewicz, Z. J., 1965, Fictitious anomalies of higher vertical derivatives of gravity: *Geophysics*, V. 30, p. 1094-1107.
5. Jordan, S. K., 1978, Moving-base gravity gradiometer surveys and interpretation: *Geophysics*, V. 43, p. 94-101.
6. Hammer, S., 1938, Investigations of the vertical gradient of gravity: *Transactions, A.G.U.*, 19th Annual Meeting.
7. Kuo, J. T., Ottoviani, M., Singh, S. K., 1969, Variation of vertical gravity gradient in New York City and Alpine, New Jersey: *Geophysics*, V. 34, p. 235-248.
8. Thyssen-Bornemisza, S., Stackler, W. F., 1956, Observation of the vertical gradient of gravity in the field: *Geophysics*, V. 21, p. 771-779.
9. Thyssen-Bornemisza, S., Groten, E., Bazhaw, W., 1972, Correction of accurate gravity surveys by carefully observed vertical gradients of gravity: *Geophysical Prospecting*, V. 20, p. 17-27.
10. Janle, P., Makris, J., Menzel, H., Experimental investigations of the vertical gradient of gravity: *Boll. Geof. Teor. ed. Appl.*, V. 13, p. 254-263.
11. Neumann, R., 1973, Microgravimetry-experimentation on vertical gradient: *Compagnie Generale de Geophysique*, Massy, France.
12. Fajklewicz, Z. J., 1976, Gravity vertical gradient measurements for the detection of small geologic and anthropomorphic forms: *Geophysics*, V. 41, p. 1016-1030.
13. Hammer, S., Anzoleaga, R., 1975, Exploring for stratigraphic traps with gravity gradients: *Geophysics*, V. 40, p. 256-268.
14. Sneddon, I. H., 1972, The use of integral transforms: *McGraw-Hill*, New York.
15. Talwani, M., Worzel, J. L., Landisman, M., 1959, Rapid gravity computations for two-dimensional bodies with application to the Mendocino submarine fracture zones: *Jour. Geophys. Res.*, V. 64, p. 49-59.
16. Telford, W. F., Geldart, L. P., Sheriff, R. E., Keys, D. A., 1976, *Applied geophysics*: Cambridge University Press, New York.

* CADWALLENDER, KRAMER, JANKOWSKI and
KISATSKY

FULL FIELD INTERFEROMETRY APPLICATIONS
TO ARMY PROBLEMS (U)

WILLIAM K. CADWALLENDER
KIMBALL KRAMER
PAUL Z. JANKOWSKI
PAUL J. KISATSKY
US ARMY, ARRADCOM, APPLIED SCIENCES DIVISION
DOVER, NJ 07801

INTRODUCTION: A problem of considerable interest to the Army is the integrity of artillery projectile bodies. The Production Base Modernization Program for ammunition production calls for 100% testing of projectile bodies at high speeds. Traditional methods such as dye penetrant and magnetic particle inspection, and newer techniques such as ultrasonics and flux leakage methods are used to inspect items for cracks and flaws. All these methods have limitations and disadvantages such as long scan times, liquid immersion, and identification of non-structural surface defects.

Optical holography and the various forms of speckle interferometry, being sensitive to surface displacement or strain, tend to show only defects that adversely affect the strength of the shell wall, while not showing "cosmetic" defects. With appropriate configuration, the entire surface of a shell (360°) can be viewed and an easily interpretable "picture" readout of the defects can be provided.

We have, in the past, used standard double exposure holographic interferometry to inspect M393 projectiles and M483 projectiles (1). There are several alternative methods to conventional holography based on the phenomenon of laser speckle. Each offers advantages such as reduced vibration sensitivity and simplified fringe patterns, but have the disadvantage of reduced sensitivity (2,3). Among the most promising of these methods for implementation as a means of inspecting projectile metal parts is the speckle shearing method of Hung and Hovanesian (4,5). This method reveals fringes which are proportional to surface strains, not whole body motion. The method has seen limited employment in the testing of tires. We report here on its application to the testing of M483A1 projectile bodies.

CADWALLENDER, KRAMER, JANKOWSKI and
KISATSKY

SPECKLE: When an object is illuminated by a beam of coherent light such as a laser beam, the surface of the illuminated object takes on a grainy appearance which is termed speckle. This is true whether the illuminated beam is collimated or divergent and whether it originates directly from the laser or has been reflected from a specular surface or scattered from a diffusing surface. The grainy appearance is due to the fact that most surfaces are very rough when considered on the scale of optical wavelengths. When an area of the surface is viewed by the eye or any other optical system (camera, vidicon, etc.) the amplitude (and its square, the intensity) at a given point is a combination of the light coming from different elementary areas of the viewing surface. Because of the roughness of the viewing surface the light waves coming from different areas will have traveled slightly different distances, i.e., their optical paths will differ by a small number of wavelengths. If the light is coherent, there will be both constructive and destructive interference at the image plane (i.e., in the eye or camera) and a collection of random lighter and darker areas will manifest itself. This is speckle.

When an object being viewed is displaced laterally (in its own plane), the speckle pattern on the image plane is also displaced laterally. When the object is displaced axially (i.e., moved closer to or further from the imaging device), the speckles are shifted radially and magnified, and also gradually suffer a decorrelation. These movements of speckle patterns may be utilized to determine small displacements, deformations and strains in an object being viewed (6).

Speckle was first used to measure strain by Leendertz (2). The speckle strain techniques have several advantages over conventional double exposure holography: (a) Coherence demands are less stringent and thus the illuminating laser can often be run with multi-mode output, facilitating an increase in illumination levels and a decrease in necessary exposure time. (b) A modified conventional camera is used with its rather small lens aperture in contrast to conventional holography where an aperture at least the size of the plate to be exposed is needed. This makes it easier to use a narrow band transmission filter to block wavelengths other than that of the laser and thereby operate in ambient light rather than darkroom conditions. (c) By varying the camera aperture the speckle size can be varied as a function of the required resolution, and this can lead to the adoption of vidicon viewing and real-time applications.

The specific technique used in the studies discussed below uses a speckle interferometric camera developed by Hung & Liang (7). It has additional advantages: (d) The reference beam is split off at the recording device (camera) -- a so-called local reference beam -- and this reduces the vibration isolation demands of the system to the point where some work can be done on a standard laboratory table as opposed

to the vibration isolation tables necessary for conventional holography. (e) The technique gives derivatives of surface displacements directly, rather than displacements themselves, and these derivatives, being closely related to strain, reduce computation time and errors if strain is the parameter of interest. In this technique a local reference beam is created by using a wedge, i.e. a small angle prism, in front of half of the camera aperture. This results in a sheared image. Two sheared exposures are made, one before and one after the test object is stressed.

DESCRIPTION OF THE EXPERIMENTAL APPARATUS: The apparatus consists of a laser-illuminated object of interest, and a camera modified to have a thin glass wedge (i.e., a small angle prism) covering one-half of the lens aperture. The wedge angle is a parameter in the sensitivity of the technique and normally is in the 1 to 3 degree range.

We will define the z-axis to be the optical axis and choose the x-axis such that the laser lies in the x-z plane. We may visualize this as the camera, object and laser all lying in a horizontal plane with the object and camera defining the z-axis and the x-axis perpendicular to this. The y axis is thus vertical. The wedge is placed so that the wedge angle is in the x-z plane. Figure 1 is a schematic showing the arrangement looking down from above (along the y-axis).

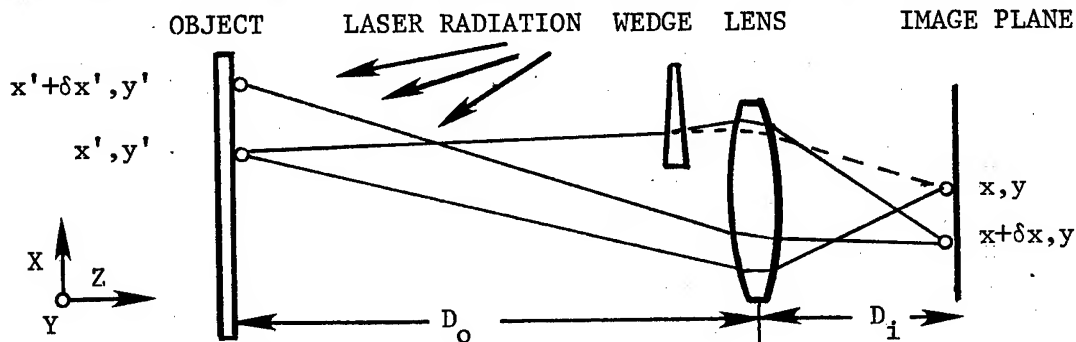


FIGURE 1

Those rays passing from the object to the image plane of the camera which do not pass thru the wedge will, of course, produce an image of the object. Those rays passing thru the wedge will produce an identical image of the object but displaced slightly ("sheared") in the x-direction. A developed image (single exposure) would look like a double exposure with the object moved slightly in the x direction between exposures. However in reality, the doubled image is made at one time by the shearing action of the wedge, and thus there is optical interference between the two parts of the sheared image. Note that this effect does not depend on collimation of the beam.

CADWALLENDER, KRAMER, JANKOWSKI and
KISATSKY

FRINGE FORMATION: We have assumed that the wedge angle is in the x-z plane and thus the two laterally sheared coherent images in the film plane correspond to an apparent shift of the object by δx . (The following analysis would hold, however, if the wedge were rotated by 90° and δy were substituted for δx .)

Let us consider two points on the object at x' , y' and at $x' + \delta x'$, y' . These are separated by the amount $\delta x'$ on the object and are therefore imaged, in the absence of a wedge, on the film at x , y and $x + \delta x$, y , with the relationship between δx and $\delta x'$ determined by the magnification factor M :

$$M = \delta x' / \delta x = D_i / D_o$$

where D_i is the image-lens distance and D_o is the object-lens distance. Let the wavefront of the unsheared image on the film plane corresponding to the object point x' , y' , be:

$$U_{1A}(x,y) = A_{x,y} \exp(i \theta_{x,y})$$

and that corresponding to the object point $x' + \delta x'$, y' , be:

$$U_{1B}(x + \delta x, y) = A_{x + \delta x, y} \exp(i \theta_{x + \delta x, y})$$

Here A is the amplitude and θ is the phase of the wave.

We insert a small angle wedge or prism close to the lens with wedge angle α and index of refraction μ such that the image of the point $x' + \delta x'$, y' is also imaged at x, y on the image (film) plane. Since the two waves are coherent and will interfere, the wavefront at the point x, y on the image plane is now the sum of $U_{1A}(x, y)$, above, and:

$$U_{1B}(x, y) = A_{x + \delta x, y} \exp\{i(\theta_{x + \delta x, y} + 2\pi\gamma x / \lambda)\}$$

where $\gamma = \alpha(\mu - 1)$ is the angle of light deviation due to the prism (for small prism angles) (8). The factor $2\pi\gamma x / \lambda$ enters because the wave U_{1B} is refracted by the prism thru the angle γ and is thus inclined with respect to U_{1A} .

We will assume that the amplitude A is independent of x and y for simplicity and to make clear the phase relationships. We then have the total wavefront (1st exposure only):

$$\begin{aligned} U_1(x, y) &= U_{1A}(x, y) + U_{1B}(x, y) \\ &= A \{ \exp\{i \theta_{x, y}\} + \exp\{i(\theta_{x + \delta x, y} + 2\pi\gamma x / \lambda)\} \} \end{aligned}$$

CADWALLENDER, KRAMER, JANKOWSKI and
KISATSKY

Thus the intensity on the film due to the first exposure is:

$$I_1 = U_1 U_1^* = 2A^2 \{ 1 + \cos(\Delta\theta + 2\pi\gamma x/\lambda) \}$$

where $\Delta\theta \approx \theta_{x+\delta x, y} - \theta_{x, y}$

Between the first and second exposures the object is deformed. We will again assume equal amplitudes at the second exposure. There is again interference, and we find almost the same intensity after deformation except for a small change due to the change of relative displacements between the points. This causes an additional small phase change ϵ , and the intensity due to the second exposure is:

$$I_2 = 2A^2 \{ 1 + \cos(\Delta\theta + 2\pi\gamma x/\lambda + \epsilon) \}$$

The two exposures are made at different times and there can be no interference between the wavefronts which produce I_1 and I_2 . Thus the total intensity at the point on the film (image plane) that we are considering is just the sum of the intensities due to the two exposures:

$$\begin{aligned} I &= I_1 + I_2 = 2A^2 \{ 2 + \cos(\Delta\theta + 2\pi\gamma x/\lambda) + \cos(\Delta\theta + 2\pi\gamma x/\lambda + \epsilon) \} \\ &= 4A^2 \{ 1 + \cos(\Delta\theta + 2\pi\gamma x/\lambda + \epsilon/2) \cdot \cos(\epsilon/2) \}. \end{aligned}$$

(This last equality is merely a trigonometric identity.) Note that if there is no deformation ($\epsilon = 0$), $I = 2I_1$.

FRINGE VISIBILITY: The appearance of these intensity fringes depends on the relative magnitudes of the arguments of the cosine terms in the preceeding equations. The factor describes a rapidly varying, randomly varying component which accounts for the observed speckle. This term will be neglected in the discussion which follows, which is designed to illustrate the types of fringes encountered and will not discuss the character of the superimposed speckle which is present in all cases. We will consider only the other two factors, $2\pi\gamma x/\lambda$ and ϵ . If the arguments in the upper equation are approximately the same, i.e., $2\pi\gamma x/\lambda \gg \epsilon$, the fringe intensity varies as indicated in figure 2a. If the arguments in the upper equation are very different, i.e., $2\pi\gamma x/\lambda \ll \epsilon$, the fringe intensity varies as indicated in figure 2b. In either case, if the eye can resolve the small fringes, we see rapid spatial variation of intensity with superimposed more slowly varying variations. However, if the resolution of the eye is not enough to resolve the small fringes, we see only a local average of the intensity, as plotted for the two cases in figures 2c and 2d.

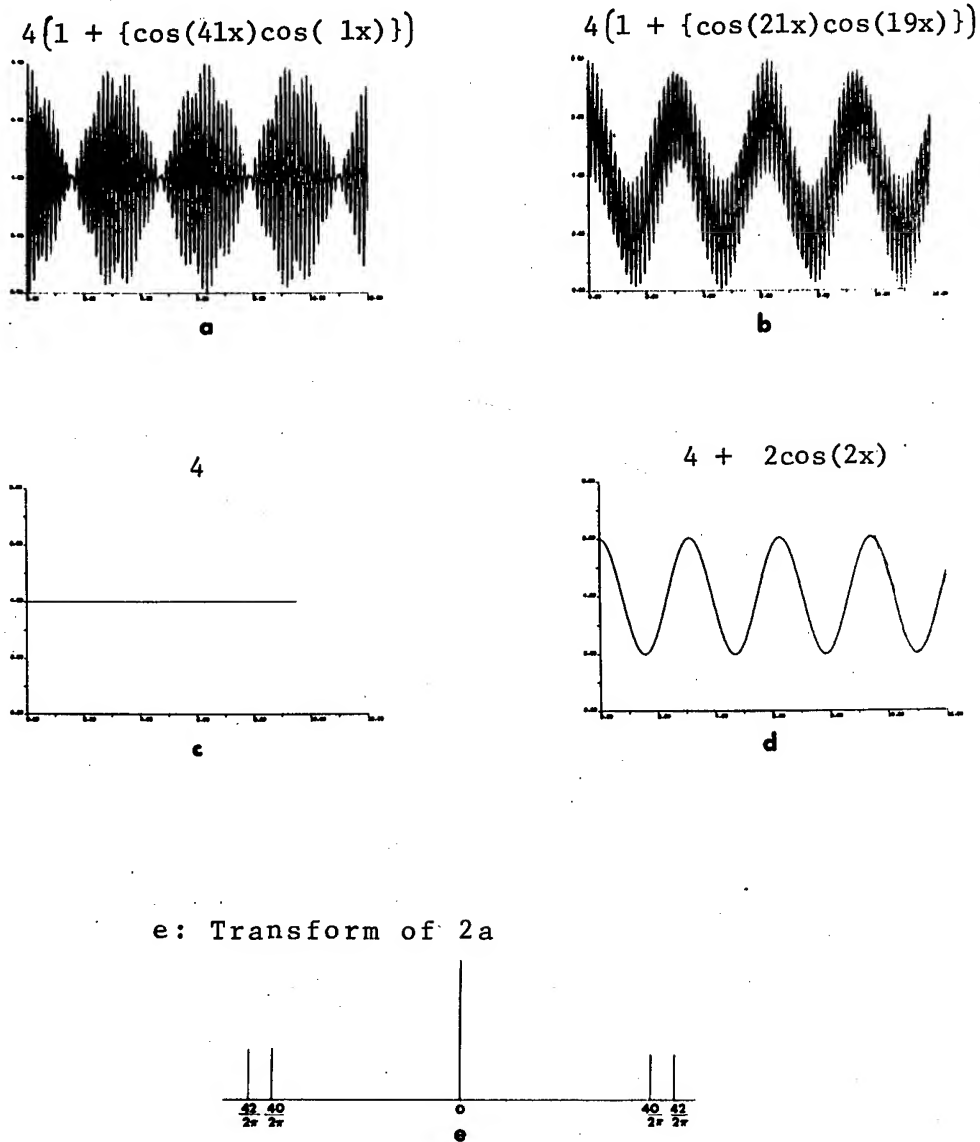


Figure 2

CADWALLENDER, KRAMER, JANKOWSKI and
KISATSKY

Unfortunately, it is the representation in figure 2a which corresponds to the results obtained with the speckle shearing technique. These fringes may be thought of as a high frequency carrier term modulated by a low frequency amplitude modulation. Alternatively we may think of the slowly varying envelope as moiré fringes resulting from superposition of two finer sets of fringes, one created by each exposure. By referring to the second equation describing the intensity variation, we can see that the slowly varying amplitude modulation is due to the cosine ($\epsilon/2$) term and this must be made accessible to analyze the deformation which leads to the phase change ϵ .

The necessary demodulation to render the low frequency spatial variation of intensity visible to the eye (or vidicon) may be accomplished by an optical Fourier transform and filtering technique.

The apparatus consists of: (a) a lens to perform the Fourier transform from the spatial domain to the frequency domain; (b) an opaque stencil for filtering; and (c) a second lens to re-transform the image back from the frequency domain to the spatial domain. To make the process clear, we will consider the demodulation of the light intensity distribution of figure 2a.

Figure 2e is the sum of the transforms of two cosine terms and a constant term. It shows the Fourier transform of the spatial light intensity distribution of figure and is thus the light intensity distribution at the focal plane. If we put an opaque stencil at this plane which (1) blocks out the center peak (this corresponds to a low frequency filter), and which (2) blocks out the two left side peaks, we are left with only the two right side peaks. When we retransform with the second lens, we operate only on the intensity distribution consisting of these two peaks and we have effectively shifted the origin to the point midway between them. The second lens thus performs the transform of the intensity distribution: $1/2 \{ \delta(f - 1/2\pi) + \delta(f + 1/2\pi) \}$ which is $\cos x$. This is the modulation function separated from the term representing the carrier frequency in the original intensity distribution:

$$I = 4 \{ 1 + \cos(41x) \cdot (\cos x) \}.$$

When this retransformed image is viewed by the eye or a vidicon, the fringes due to the phase changes caused by the relative displacements between points, ϵ , are visible. It remains to relate these to the strain.

RELATION OF FRINGES TO STRAIN: Following the analysis given in Ref. 7, we consider two points on an object to be investigated: $P(x, y, z)$ which is displaced under strain to $P'(x+u, y+v, z+w)$, and $P(x+\delta x, y, z)$ which is displaced under strain to $P'(x+\delta x+u+\delta u, y+v+\delta v, z+w+\delta w)$. We assume a laser source located at $S(x_s, y_s, z_s)$ and an image point in the camera located at $O(x_o, y_o, z_o)$ (figure 3):

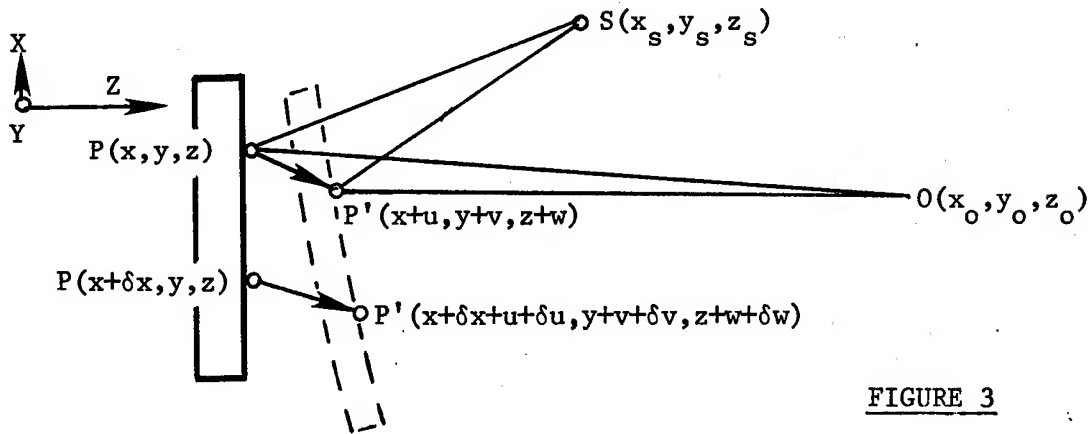


FIGURE 3

Let us consider the first of the two adjacent points. A light ray travels from S to P to O before deformation and from S to P' to O after deformation. The change in path length:

$$\delta l = (SP' + P'O) - (SP + PO)$$

can be shown to be (to first order):

$$\delta l = Au + Bv + Cw$$

$$\text{where } A = \frac{x - x_o}{R_o} + \frac{x - x_s}{R_s}$$

$$B = \frac{y - y_o}{R_o} + \frac{y - y_s}{R_s}$$

$$C = \frac{z - z_o}{R_o} + \frac{z - z_s}{R_s}$$

$$R_o^2 = x_o^2 + y_o^2 + z_o^2$$

$$R_s^2 = x_s^2 + y_s^2 + z_s^2$$

CADWALLENDER, KRAMER, JANKOWSKI and
KISATSKY

Similarly the change in path length for a light ray which travels from the laser to the neighboring point to the camera is:

$$\delta l' = A(u + \delta u) + B(v + \delta v) + C(w + \delta w)$$

and the relative path change between the two points is:

$$r = A \delta u + B \delta v + C \delta w = \left(A \frac{\delta u}{\delta x} + B \frac{\delta v}{\delta x} + C \frac{\delta w}{\delta x} \right) \delta x.$$

The relative phase change is then: $\epsilon = 2\pi r/\lambda$

If δx , the amount of shearing, is small, we may approximately treat these small shifts as partial derivatives and rewrite the equation for the relative phase change:

$$\epsilon = \frac{2\pi}{\lambda} \left(A \frac{\partial u}{\partial x} + B \frac{\partial v}{\partial x} + C \frac{\partial w}{\partial x} \right) \delta x$$

The modulated intensity variations seen on the reconstructed image are due to variations of ϵ . We see here that ϵ is a function of the derivatives of the displacements in the shearing direction.

This expression for ϵ is valid for the most general placement of the experimental apparatus. In practice, simplifying assumptions can be made. If the laser source and the camera lie in the x-z plane and the camera is on the z-axis, we have $x_o = y_o = y_s = 0$. If, in addition, the assumption that the object size is small compared with z_o and R_s is made, we have:

$$A \approx -\frac{x_s}{R_s} = -\sin \phi$$

$$B \approx 0$$

$$C \approx -\left(1 + \frac{z_s}{R_s}\right) = -(1 + \cos \phi)$$

Here the angle ϕ is the angle between the incident and scattered laser beam, angle SPO.

With suitable reconstruction then, we see fringes due to the strain deformation of the form:

$$\epsilon = -\frac{2\pi}{\lambda} \left\{ (1 + \cos \phi) \frac{\partial w}{\partial x} + (\sin \phi) \frac{\partial u}{\partial x} \right\} \delta x$$

Similarly, if the incident laser beam is in the y-z plane with the shear remaining in the x direction, we see fringes:

$$\epsilon = -\frac{2\pi}{\lambda} \left\{ (1 + \cos \phi) \frac{\partial w}{\partial x} + (\sin \phi) \frac{\partial v}{\partial x} \right\} \delta x$$

Finally, by analogy, the reconstructed fringes with the wedge rotated 90° to show displacement derivatives in the y direction are of the forms:

$$\epsilon_x = -\frac{2\pi}{\lambda} \left\{ (1 + \cos\phi) \frac{\partial w}{\partial y} + (\sin\phi) \frac{\partial u}{\partial y} \right\} \delta y \quad \text{and}$$

$$\epsilon_y = -\frac{2\pi}{\lambda} \left\{ (1 + \cos\phi) \frac{\partial w}{\partial y} + (\sin\phi) \frac{\partial v}{\partial y} \right\} \delta y$$

The strains of interest are conventionally:

$$\epsilon_x = \frac{\partial u}{\partial x}$$

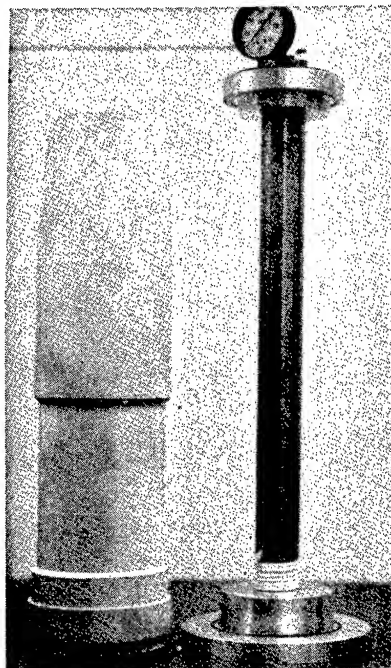
$$\epsilon_y = \frac{\partial v}{\partial y}$$

$$\gamma = \frac{\partial u}{\partial y} + \frac{\partial v}{\partial x}$$

The relations between these and the displacement derivatives measured by the speckle shearing technique are readily apparent. If the in-plane strains themselves are needed, they may be deduced by using two different angles of laser illumination, ϕ_1 , and ϕ_2 , and solving the linear equation for the strain component needed. Out-of-plane strains may be easily obtained by using normal illumination ($\phi = 0$), which gives $\partial w / \partial x$ and $\partial w / \partial y$ directly depending on the orientation of the shearing wedge.

EXPERIMENTAL: The shell body is placed in a fixture (figure 4) which seals the open ends of the body to permit stressing by pressure and also provides an axial load by means of a nut on the central post. An exposure is then made by the method outlined in the theory section, with the shell at atmospheric pressure. The shell is then stressed by pressurization with nitrogen (50-300 psi), and a second exposure made on the same plate. The plate is then developed and fixed in the normal manner and viewed in the image processor described above.

The direction of image shear can be at any angle to the axis of the shell, giving a set of fringes which are a map of strains in the direction of shear. We produced interferograms of all shells both with the shear along the axis of the shell (axial shear), and at right angles



to the axis (transverse shear). We show here only the axially sheared interferograms as these show the defects most clearly. Interferograms of both directions of shear were made for three views of each shell (120° apart) and at both 200 and 300 psi.

Severe problems can arise due to specular reflection. In particular exposure times are increased since most of the illumination is reflected specularly rather than scattered. Most of the shell bodies shown here were painted white to decrease exposure times but this is not necessary if care is taken with the experimental set-up.

We studied sixteen M483 projectile bodies. Four of these have artificial defects induced by electrical discharge machining. The remainder of the shells have apparent natural defects as determined by Magnaflux texting.

Figure 5a shows an interferogram of a good shell body at 300 psi. This is for reference and it can be seen that the fringes are relatively few and smooth. Figure 5b is an interferogram of an M483 with the keyway machined in. The interferogram shows that the keyway weakens the wall considerably, and a prominent and very confusing signature is generated. Finding defects in this area has proven virtually impossible.

The speckle shearing interferograms of four of the test shells with artificially machined defects of known depth are shown in Figures 6a to 6d. The locations are pointed out. For the most part the defect signatures were quite dramatic with the exception of the .080" internal defect in the nose of one test shell (figure 6d) which could not be seen at all, even at 300 psi.

Figures 7a to 7c show results from a selection of the shells with apparent natural defects. Figure 7a shows a shell with a split. Although the split is barely visible to the eye, it shows as a definite series of discontinuities in the fringe patterns. A continuation of this split appears in the base. Figure 7b shows a shell with a crack in the nose and Figure 7c a shell with a crack in the base. The "V's" in these signatures clearly point to the cracks.

SUMMARY AND CONCLUSIONS: A total of sixteen M483A1 projectile bodies were inspected using speckle shearing interferometry. Four had machined defects of known dimensions and the balance were Magnaflux rejects. Six shells were determined to have defects detectable by speckle shearing interferometry, and the remaining six had keyway defects. All machined defects were located, with the sole exception of the .080" internal defects in the nose of one test shell which could not be seen even at 300 psi.

All other defects in the sample could be seen with pressures of no more than 200 psi. Problems encountered included specular reflections which could be minimized by careful arrangement, and the problem

*CADWALLENDER, KRAMER,
JANKOWSKI & KISATSKY



a- no defects



b.- keyway

Figure 5

*CADWALLENDER, KRAMER, JANKOWSKI &
KISATSKY

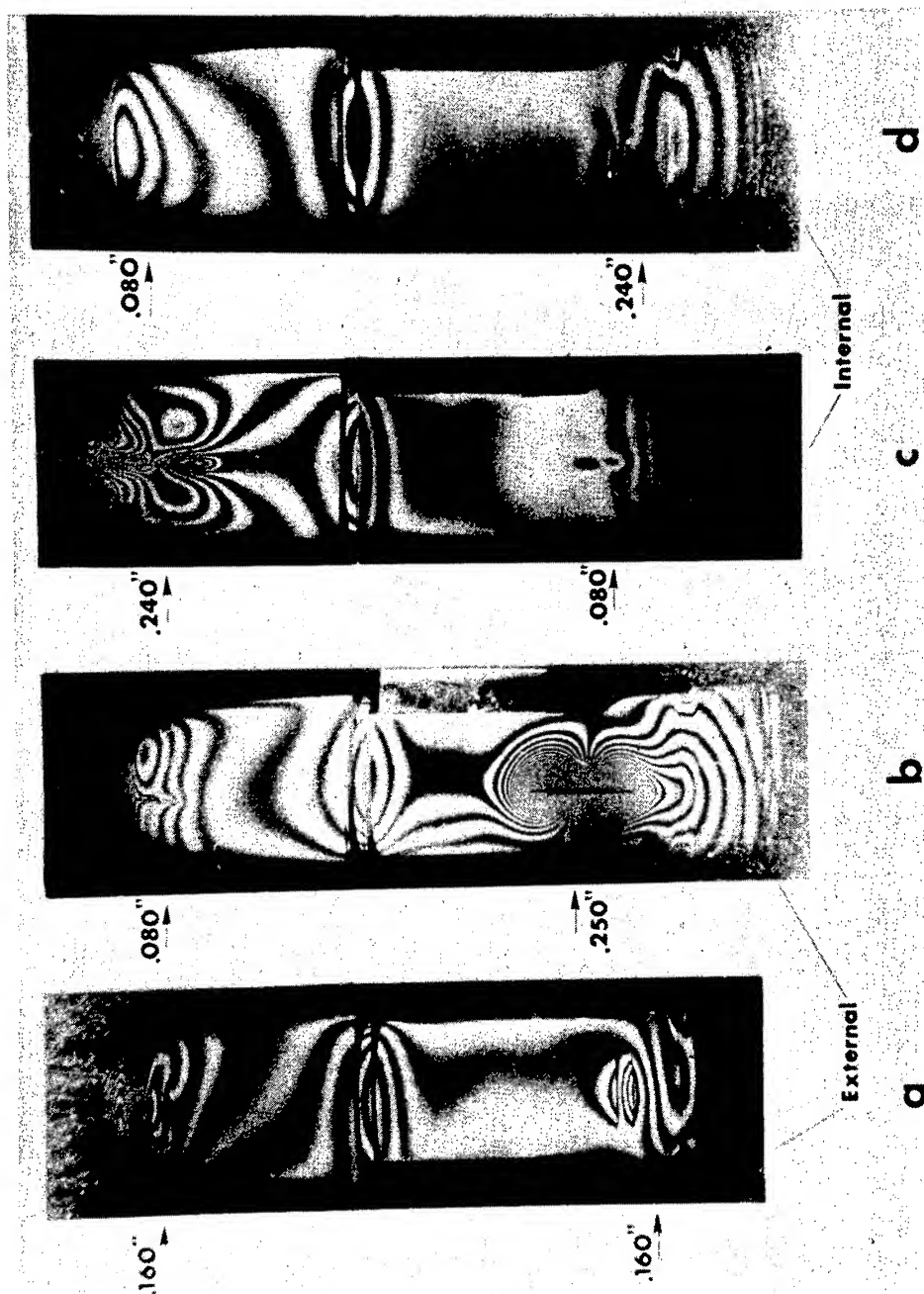


Figure 6 Artificial Defects

*CADWALLENDER, KRAMER, JANKOWSKI
& KISATSKY

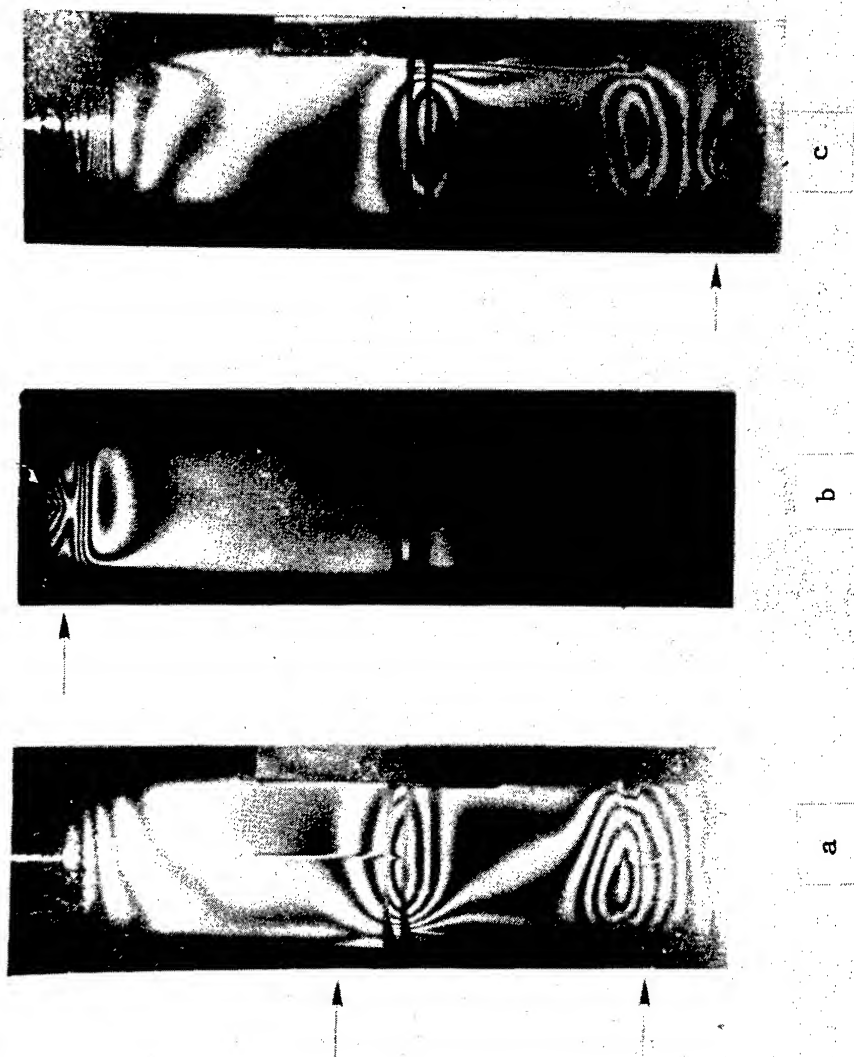


Figure 7 Natural Defects

CADWALLENDER, KRAMER, JANKOWSKI and
KISATSKY

of the keyway signature, which could be avoided by inspecting before
the keyway was cut.

BIBLIOGRAPHY:

1. Barbarisi, Modesto J., and Robert A. Barusefski, Double Exposure Holographic Examination of Projectile 105mm HEP-T-M393A2 For Flaws and Cracks, Feltman Research Laboratories, 1976.
2. Leendertz, J. A., J. Phys. E 3, 214-18 (1970).
3. Archbold, E., J. M. Burch, and A. E. Ennos, Optica Acta 17 (12), 883-898 (1970).
4. Hung, Y. Y., and J. O. Hovanesian, Exper. Mech. 12 (10), 454-460 (1972).
5. Hung, Y. Y., and A. J. Durelli, Simultaneous Determination of Three Strain Components in Speckle Interferometry Using a Multiple Image Shearing Camera, Final report on O. U. Project 32110-18, Grant # EN677-07974, Oakland University, 1978.
6. Erf, R. K., ed., Speckle Metrology, Academic Press, New York 1978.
7. Hung, Y. Y., and C. Y. Liang, Appl. Optics 18, 1046-1051 (1979).
8. Ditchburn, R. W., Light, 3rd ed., Academic Press, New York, 1976, pp. 55-57.

*CANONICO, LITTLE, JAHRLING,
& STEPHEN

MECHANISM OF ACTION OF RIBAVIRIN: AN
ANTIVIRAL DRUG OF MILITARY IMPORTANCE (U)

*PETER G. CANONICO, PhD, JAMES S. LITTLE, CPT, PhD,
PETER B. JAHRLING, PhD, EDWARD L. STEPHEN, MAJ, VC
U.S. ARMY MEDICAL RESEARCH INSTITUTE OF INFECTIOUS DISEASES
FORT DETRICK, FREDERICK, MARYLAND 21701

Ribavirin (1- β -D-ribofuranosyl-1,2,4-triazole-3-carboxamide) is a nucleoside analogue having broad spectrum antiviral activity against both DNA and RNA viruses (18). A variety of specific effects on host cell metabolism have been attributed to ribavirin or its metabolites. For example, ribavirin is reported to be a strong inhibitor of thymidine phosphorylation (6) and its 5'-monophosphate derivative (RMP) is a potent competitive inhibitor of inosine-5'-phosphate dehydrogenase (19). Ribavirin is also reported to decrease DNA, RNA and protein synthesis and reduce the size of the cellular guanosine-5'-triphosphate pool (5,12).

Numerous other reports, however, contradict many of the alleged cellular effects of ribavirin (2,14,15,17). As a result, the pharmacological mechanism of action of ribavirin remains obscure. It is not yet clear whether this compound is specifically antiviral or whether it inhibits virus replication as a result of its effects on host cellular metabolism.

The study reported here attempts to clarify the mode and specificity of action of ribavirin. We have examined its effects on cellular metabolism and on the replication of Venezuelan equine encephalomyelitis virus (VEE) grown in BHK-21 cells.

MATERIALS AND METHODS

Virus Stock and Plaque Assay: The live attenuated VEE vaccine, strain TC-83, was obtained in the lyophilized state from Merrill-National Laboratories (lot 4, run 2). It was reconstituted with 1.2 ml

*CANONICO, LITTLE, JAHRLING,
& STEPHEN

of sterile water, and passaged once in primary duck embryo cell cultures (DEC), concentrated, and purified by rate zonal centrifugation in 10 to 30% sucrose gradients, as described previously (1). Infectious virus was titrated by counting plaque forming units (pfu) in DEC monolayers grown in 10-cm² plastic plates, and maintained in a humidified atmosphere with 5% CO₂ under medium containing 1% agarose, as described previously (9).

Cell Line and Infection: Baby hamster kidney cells (BHK-21, clone 13) were obtained from the American Type Culture Collection, and used at passage levels varying between 55 and 70. To infect cells, concentrated TC-83 virus was diluted in Hanks' balanced salt solution (HBSS) to achieve a multiplicity of inoculum of 2 to 5 pfu per cell. Volumes of 0.2 ml and 10 ml were adsorbed for 1 hr at 36C to cell monolayers grown in 6-well plates or roller bottles, respectively. Following adsorption, the inoculum virus was removed by aspiration and replaced with various maintenance media as detailed below.

Incorporation of Labeled Precursors: BHK-21 cells were grown in BHK-21 medium (Flow Labs, Hamden, CT) with 10% fetal calf serum (FCS) to 80 to 90% confluency in 4-well plastic tissue culture plates. Immediately following infection, both infected and control cultures were treated with varying concentrations of ribavirin for 5 h at 37C and examined for their ability to incorporate labeled precursors into TCA-soluble and -insoluble pools.

Labeling of RNA and protein was accomplished by incubating cell cultures in serum-free medium containing 1 μ Ci/ml of [³H]uridine or [³H]leucine, respectively, for 30 min. Cultures were then washed 3 times with ice-cold HBSS and the radioactive content of TCA-soluble and -insoluble pools determined by scintillation spectrometry as described by Minor and Dimmock (11).

RNA Synthesis in Permeable Cells: BHK-21 cells were made permeable by treatment with lysolecithin at 4C. This procedure as well as the assay for [³H]uridine 5'-triphosphate incorporation into acid-insoluble products of permeable cells followed previously published methods (3,4).

Isolation of RNA: For the preparation of RNA, roller bottle cultures of infected and control cells were incubated in the presence of varying concentrations of ribavirin in BHK-21 media containing 2% fetal calf serum and 10 μ Ci/ml of tritiated uridine or guanosine. After 5 h, the cells were harvested, washed free of medium, resuspended at 4C in 10 mM Tris, 10 mM NaCl and 1.5 mM MgCl₂, pH 7.3 (TNM buffer) and disrupted by several freeze-thaw cycles. Cellular homogenates were

*CANONICO, LITTLE, JAHRLING,
& STEPHEN

centrifuged (1400 g for 5 min) and the nuclear pellet washed with TNM containing 1% Nonidet P-40 and 0.5% deoxycholate. Supernatants were combined and adjusted to final concentrations of 10 mM EDTA, 1% sodium dodecylsulfate (SDS) and 0.4 N sodium acetate (pH 5.2) then extracted twice with a mixture of 50% phenol, 49% chloroform and 1% isoamyl alcohol. The resulting organic phase and cake were re-extracted first with equal volumes of 0.1 M Tris (pH 9.0) in 0.5% SDS, then with 0.1 M Tris (pH 9.0). The alkaline extracts were combined with previous aqueous extracts and the RNA precipitated overnight at -20°C with 2 volumes of ethanol. The precipitate was washed twice with ethanol and dried in vacuo.

For the mRNA isolation, RNA was dissolved in binding buffer consisting of 10 mM Tris (pH 7.4), 0.5 M NaCl and 0.02% SDS and applied to 0.5 g of oligo-dT cellulose in a disposable column, then washed with 10 ml of binding buffer. Messenger RNA was eluted with 0.05% SDS in 10 mM Tris (pH 7.4), precipitated with 2 volumes of ethanol, recovered by centrifugation at 100,000 g for 1 h and dried under vacuum.

In some experiments, actinomycin D (1 µg/ml) and [³H]uridine were added to cell cultures 3.5 and 4 h, respectively, after addition of ribavirin. RNA was isolated after a 2-h incubation.

Polyacrylamide Gel Electrophoresis (PAGE): One hundred-cm 2.5% bis-acrylamide cross-linked gels were prepared as previously reported (1). The gels were prerun at 5 mA/tube and electrophoresed for 2 to 2.5 h. The RNA sample was suspended in 120 mM Tris, 60 mM sodium acetate, 3 mM EDTA (pH 7.4) plus 10% glycerol and 0.1% bromophenol blue. Following electrophoresis, gels were sliced into 1-mm fractions and incubated for 18 h at 37°C with 3% Protosol in 10 ml of Econofluor (New England Nuclear) in tightly capped vials, then counted for radioactivity.

Analysis of 5'-Ends of mRNA: [³H]Guanosine-labeled mRNA was dissolved in 0.05 M sodium acetate buffer (pH 4.5) and incubated for 15 h at 37°C with 2 to 5 units of ribonuclease T₂. The resulting hydrolysate was subjected to DEAE-cellulose chromatography as described by Groner and Hurwitz (8).

Cell-Free Protein Synthesis: A commercial translation assay provided by New England Nuclear, Boston, MA, was used. The assay employed reticulocyte lysate and measured incorporation of [³H]leucine.

Reagents: RNase T₂ was obtained from Sankyo Co., Tokyo, Japan. Oligo-(dT) cellulose type T-3 was bought from Collaborative Research, Waltham, MA. Reagents for casting of acrylamide gels were purchased

*CANONICO, LITTLE, JAHRLING,
& STEPHEN

from Bio-Rad, Richmond, CA. [5-³H]Uridine, [5-³H]uridine 5'-triphosphate, [8-³H]guanosine and [3,4,5-³H]leucine were purchased from New England Nuclear. Ribavirin and its mono- (RMP), di- (RDP), and tri- (RTP) phosphorylated derivatives were a gift of ICN Pharmaceuticals, Irvine, CA. Cap standards were obtained from P. L. Biochemicals, Milwaukee, WI. All other biochemicals were purchased from Sigma, St. Louis, MO.

RESULTS

Virus Replication: Replication of VEE in BHK-21 cells occurs rapidly and results in a 3-log increase in virions within 5 h after infection (Table 1). This increase is inhibited by ribavirin at concentrations as low as 10 µg/ml by more than 99% when compared to non-treated infected cultures. Ribavirin, however, does not completely inhibit VEE virus replication. Rather it appears to reduce the rate of virus production as evidenced by the increase in virus titers following longer-term incubation of ribavirin treated infected cells.

Table 1. Effect of Ribavirin on VEE Virus Replication in BHK-21 Cells
Cells were infected with 2 pfu per cell at 37C for 1 h then incubated in BHK-21 medium with 10% FCS containing appropriate concentrations of ribavirin. Titers represent pfu/ml of supernatant culture fluid expressed as log of the reciprocal of the dilution at the endpoint of titration.

Ribavirin (µg/ml)	Log ₁₀ PFU/ml			
	Hours after virus adsorption			
	0	3	5	17
0	4.4	4.4	7.2	8.6
10	4.6	4.5	4.8	5.6
25	4.6	4.3	5.0	5.4
50	4.7	4.5	5.2	5.3
100	4.6	4.4	4.8	5.4

RNA Synthesis: The effect of ribavirin on uridine uptake and incorporation into acid-soluble material was assessed in control and virus-infected cells (Figure 1). Ribavirin inhibits uridine incorporation by more than 80% at a dose of 8 µg/ml. However, ribavirin also causes a parallel decrease in the uptake of uridine into the soluble cellular pool. Hence, the inhibition of RNA synthesis may be an anti-

*CANONICO, LITTLE, JAHRLING,
& STEPHEN

fact resulting from a decrease in the specific activity of [^3H]uridine in the soluble cellular pool of ribavirin-treated cells. RNA synthesis

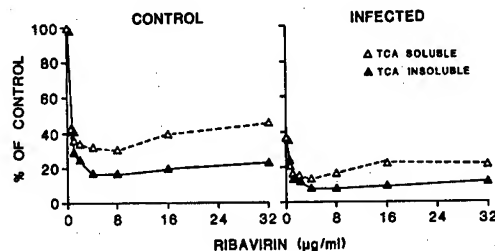


Figure 1. Effect of Ribavirin on Uptake and Incorporation of [^3H]Uridine in Control and Infected BHK-21 cells. Results are expressed as a percentage of the uptake or incorporation of [^3H]uridine found for uninfected, untreated (control) cells. Each point represents the mean value obtained from three replicate measurements.

was also assessed in infected cells made permeable to low molecular weight charged molecules by pretreatment with lysolecithin. These cells incorporated [^3H]UTP into TCA-insoluble products at a linear rate for at least 15 min. The amount of [^3H]UTP incorporation, in the presence of actinomycin D at 1 µg/ml, was not altered by ribavirin or its phosphorylated derivatives (Figure 2). These data suggest that neither ribavirin nor its phosphorylated metabolites inhibit the synthesis of mRNA in virus-infected cells.

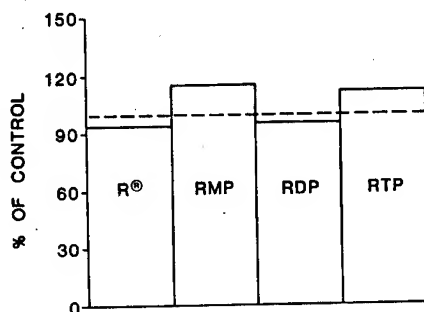


Figure 2. Effect of Ribavirin and Phosphorylated Derivatives on [^3H]UTP Incorporation in Permeable VEE-infected BHK-21 Cells. Cells were made permeable 5 h after infection for [^3H]UTP incorporation. Permeable cells were incubated for 12 min in the presence of 1 µg/ml of actinomycin D and 100 µg/ml of phosphate derivatives. Results are expressed as a percentage of the incorporation found in the absence of drug.

*CANONICO, LITTLE, JAHRLING,
& STEPHEN

The effects of ribavirin treatment on synthesis of specific mRNA was also studied. In the first series of experiments, RNA was labeled with [^3H]uridine for the first 5 h following virus adsorption in the presence of 0–200 $\mu\text{g/ml}$ of ribavirin. PAGE subfractionation of oligo-(dT) cellulose binding RNA revealed a viral specific 42S mRNA at a relative migration of 0.1 and accounted for about 10 to 11% of the total mRNA isolated (Figure 3). Treatment of infected and control cultures with up to 300 $\mu\text{g/ml}$ of ribavirin did not alter the quantity and size distribution of the recovered mRNA.

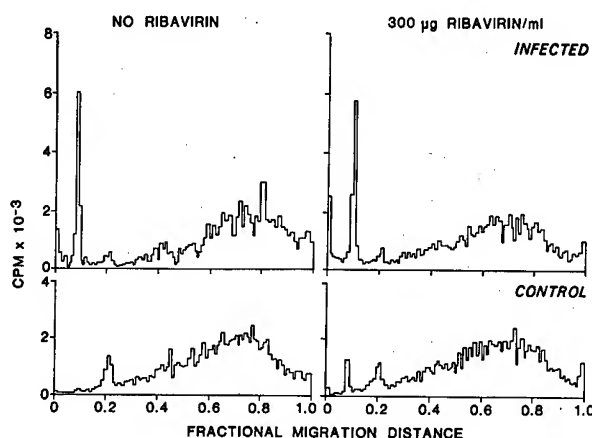


Figure 3. Polyacrylamide Gel Electrophoresis of mRNA. Infected and control cells were labeled with [^3H]uridine for 5 h; then mRNA was isolated by binding to oligo-(dT) cellulose as described in Materials and Methods.

In other experiments, cells were treated with 1 $\mu\text{g/ml}$ of actinomycin D 3.5 h after infection. Thirty minutes later, [^3H]uridine was added for 2 h, labeled with [^3H]uridine at hour 4 to 6. Electrophoretic analysis of mRNA in these cells showed two mRNA peaks representing 42S and 26S species. Treatment of infected cells with 100 $\mu\text{g/ml}$ of ribavirin initiated 4 h prior to labeling did not later production of either mRNA species (Figure 4).

Effects on Protein Synthesis: Ribavirin at concentrations up to 32 $\mu\text{g/ml}$, inhibited protein synthesis by 50 to 60%, as measured by the incorporation of [^3H]leucine into acid-soluble products of control and infected cells. Furthermore, this reduction in leucine incorporation occurred in the presence of nearly constant levels in the soluble cellular pool of [^3H]leucine (Figure 5).

The capacity of mRNA from ribavirin-treated and untreated virus-

*CANONICO, LITTLE, JAHRLING,
& STEPHEN

infected cells to direct the synthesis of proteins in an in vitro cell-free translation system was evaluated in order to determine the mechanism for the inhibition of protein synthesis. Messenger RNA from

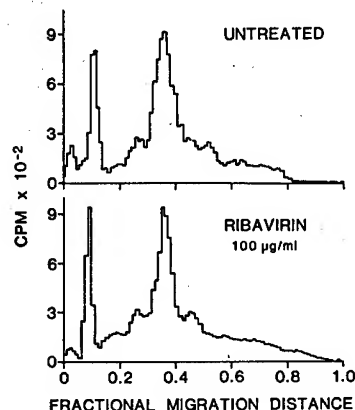


Figure 4. Polyacrylamide Gel Electrophoresis of RNA. Infected cells were pulse-labeled with [^3H]uridine for 2 h in the presence of actinomycin D (1 $\mu\text{g/ml}$) as described in Materials and Methods.

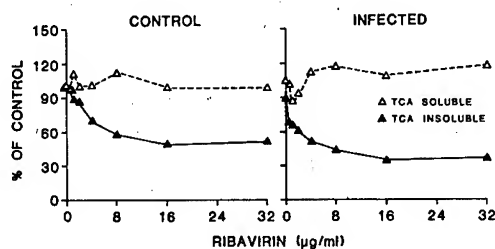


Figure 5. Effect of Ribavirin on Uptake and Incorporation of [^3H]Leucine in Control and Infected BHK-2 Cells. Results are expressed as a percentage of the uptake or incorporation of [^3H]leucine found for untreated, uninfected (control) cells. Each point represents the mean value obtained from three replicate experiments.

infected cells treated with 100 $\mu\text{g/ml}$ of ribavirin for 5 h was no more than 30% as effective as mRNA from untreated infected cells in its ability to direct the incorporation of labeled leucine into acid insoluble material (Figure 6).

Effect of Ribavirin on mRNA Cap Structure: Resulting chromatographs of [^3H]guanosine-labeled mRNA digests are shown in Figure 7. A radioactive peak corresponding to the elution profile of a cap standard

*CANONICO, LITTLE, JAHRLING,
& STEPHEN

was found in all chromatographs of mRNA digests from both control and infected cells. The magnitude of this peak decreased 3- to 10-fold in mRNA preparations from cells treated with ribavirin at concentrations of 50 to 300 $\mu\text{g/ml}$.

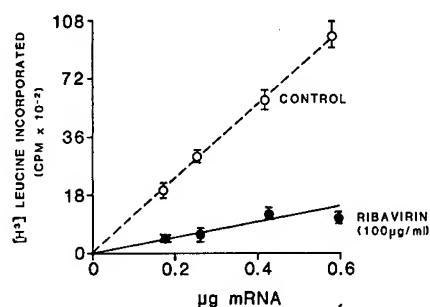


Figure 6. In Vitro Translation of mRNA in a Reticulocyte System. Incorporation of [^3H]leucine into TCA-insoluble products was measured using oligo-(dT) cellulose binding RNA from infected cells treated for 5 h with or without ribavirin.

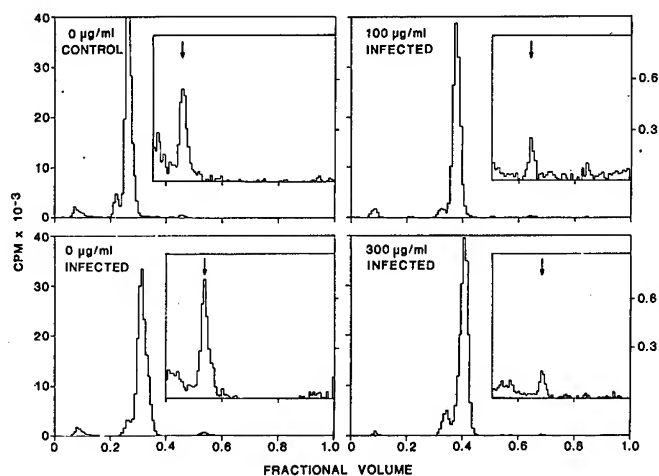


Figure 7. DEAE-Cellulose Chromatography of mRNA Hydrolysates. [^3H]Guanosine-labeled nucleotides released by RNase T₂ digestion of oligo-(dT) cellulose binding RNA. The insets in each panel represent a 1000-fold expansion of the ordinate of the corresponding chromatographs. The elution peak of a cap standard is indicated by an arrow.

DISCUSSION

Uridine incorporation has been used to assess the effect of ribavirin on RNA synthesis (2,16). Such studies have led to the proposal that ribavirin inhibits RNA synthesis. Our current finding, that the uptake of uridine by BHK-21 cells is inhibited by ribavirin, raised the possibility that the apparent inhibition of RNA synthesis by ribavirin is an artifact resulting from a decrease in the specific activity of isotopic labeling. The experiment with permeable cells, in fact, demonstrates that ribavirin does not affect actinomycin D-insensitive RNA synthesis in BHK-21 cells. Furthermore, the quantity of mRNA isolated by oligo-(dT) cellulose binding showed that ribavirin has little if any effect on the total amount of mRNA in either control or virus-infected cells.

The inhibition of protein synthesis in both control and infected cells exposed to varying concentrations of ribavirin cannot be explained by reduced levels of mRNA in these cells. The inefficiency in translation of mRNA from ribavirin-treated cells suggests that treatment with ribavirin results in synthesis of altered mRNA.

Recently, in vitro studies by Goswami et al. (7) showed that ribavirin triphosphate is a potent competitive inhibitor of the capping guanylation of viral mRNA. This posttranscriptional modification results in a 7-methylguanosine residue linked from its 5' position via a triphosphate bridge to a 2'-O-methylribonucleotide of the 5'-terminal of a large number of viral and eukaryotic mRNA. The 5'-terminal 7-methylguanosine in mRNA is required for efficient translation (13). The present data show that ribavirin also inhibits the formation of the 5'-guanosine triphosphate cap on mRNA from normal and virus-infected BHK-21 cells. Interference with the proper formation of the 5'-cap of mRNA by ribavirin could lead to accumulation of mRNA in cells which are, as observed, less efficient in protein synthesis.

The cap structure analysis was performed on digests of mRNA labeled with guanosine for 5 h following virus adsorption and addition of varying concentrations of ribavirin. This was done in order to obtain the largest representation of mRNA species which may have contributed to the impairment of protein synthesis in ribavirin-treated infected cells. Under these conditions about 90% of the radiolabeled oligo-(dT) binding RNA from infected cells is of host cell origin. Hence, host cellular mRNA must be largely responsible for the 3- to 10-fold reduction in cap formation of virus-infected cells. It is clear that ribavirin's effect on cap formation is nonspecific and leads to inhibition of both cellular and viral protein synthesis. Consistent with previous observations, ribavirin can be expected,

*CANONICO, LITTLE, JAHRLING,
& STEPHEN

therefore, to interfere with virus as well as cellular growth (16).

Although Goswami *et al.* (7) proposed that inhibition of cap formation may account for ribavirin's antiviral potency against DNA and RNA viruses, it is unclear to what extent other mechanisms may play a role. It is apparent that ribavirin exerts a myriad of effects on cellular metabolism and it is conceivable that its antiviral effects may be, in fact, expressed through an interaction of multiple mechanisms.

1. Bishop, D. H. L., J. R. Claybrook, and S. Spiegelman. 1967. Electrophoretic separation of viral nucleic acids on polyacrylamide gels. *J. Mol. Biol.* 26:373-387.
2. Browne, M. J. 1979. Mechanism and specificity of action of ribavirin. *Antimicrob. Agents Chemother.* 15:747-753.
3. Castellot, J. J., Jr., M. R. Miller, and A. B. Pardee. 1978. Animal cells reversibly permeable to small molecules. *Proc. Natl. Acad. Sci. USA* 75:351-355.
4. Castellot, J. J., Jr., M. R. Miller, and A. B. Pardee. 1978. A general method for permeabilizing animal cells. *J. Cell Biol.* 79:252a.
5. De Clercq, E., M. Luczak, J. C. Reepmeyer, K. L. Kirk, and L. A. Cohen. 1975. Fluoroimidazoles as antiviral agents and inhibitors of polynucleotide biosynthesis. *Life Sci.* 17:187-194.
6. Drach, J. C., M. A. Thomas, and C. Shipman, Jr. 1978. Ribavirin inhibition of thymidine phosphorylation in KB cells. Abstracts, Annual Meeting, American Society for Microbiology, 1978, p. 7.
7. Goswami, B. B., E. Borek, O. K. Sharma, J. Fujitaki, and R. A. Smith. 1979. The broad spectrum antiviral agent ribavirin inhibits capping of mRNA. *Biochem. Biophys. Res. Commun.* 89:830-836.
8. Groner, Y., and J. Hurwitz. 1975. Synthesis of RNA containing a methylated blocked 5' terminus by HeLa nuclear homogenates. *Proc. Natl. Acad. Sci. USA* 72:2930-2934.
9. Jahrling, P. B., E. Dendy, and G. A. Eddy. 1974. Correlates to increased lethality of attenuated Venezuelan encephalitis virus vaccine for immunosuppressed hamsters. *Infect. Immun.* 9:924-930.
10. Jahrling, P. B., and L. Gorelkin. 1975. Selective clearance of a benign clone of Venezuelan equine encephalitis virus from hamster plasma by hepatic reticuloendothelial cells. *J. Infect. Dis.* 132:667-676.
11. Minor, F. D., and N. J. Dimmock. 1977. Selective inhibition of influenza virus protein synthesis by inhibitors of DNA function. *Virology* 78:393-406.
12. Muller, W. E. B., A. Maidhof, H. Taschner, and R. K. Zahn. 1977. Virazole (1- β -D-ribofuranosyl-1,2,4-triazole-3-carboxamide), a cytostatic agent. *Biochem. Pharmacol.* 26:1071-1075.

*CANONICO, LITTLE, JAHRLING,
& STEPHEN

13. Muthurishnan, S., B. Moss, J. A. Cooper, and E. S. Maxwell. 1978. Influence of 5'-terminal cap structure on the initiation of translation of vaccinia virus mRNA. *J. Biol. Chem.* 253:1710-1715.
14. Oxford, J. S. 1975. Effects of 1- β -D-ribofuranosyl-1,2,4-triazole-3-carboxamide on influenza virus replication and polypeptide synthesis. *J. Antimicrob. Chemother.* 1(Suppl.):71-76.
15. Oxford, J. S. 1975. Inhibition of the replication of influenza A and B viruses by a nucleoside analogue (ribavirin). *J. Gen. Virol.* 28:409-414.
16. Sarver, N., and V. Stollar. 1978. Virazole prevents production of Sindbis virus and virus-induced cytopathic effect in Aedes albopictus cells. *Virology* 91:267-282.
17. Scholtissek, C. 1976. Inhibition of influenza RNA synthesis by Virazole (ribavirin). *Arch. Virol.* 50:349-352.
18. Sidwell, R. W., J. H. Huffman, G. P. Khare, L. B. Allen, J. T. Witkowski, and R. K. Robins. 1972. Broad-spectrum antiviral activity of Virazole: 1- β -D-ribofuranosyl-1,2,4-triazole-3-carboxamide. *Science* 177:705-706.
19. Streeter, D. G., J. T. Witkowski, G. P. Khare, R. W. Sidwell, R. J. Bauer, R. K. Robins, and L. N. Simion. 1973. Mechanism of action of 1- β -D-ribofuranosyl-1,2,4-triazole-3-carboxamide (Virazole), a new broad spectrum antiviral agent. *Proc. Natl. Acad. Sci. USA* 70:1174-1178.

CHARLAND

COMPUTER GRAPHICS FOR THE ARMY (U)

JOHN J. CHARLAND, CPT, EN
DEPARTMENT OF GEOGRAPHY AND COMPUTER SCIENCE
UNITED STATES MILITARY ACADEMY
WEST POINT, NEW YORK 10996

I. INTRODUCTION

General

Computer Graphics for the Army, as described in this paper, are the products of a trilateral cooperative research project involving the U.S. Military Academy, West Point, New York, the Defense Mapping Agency (DMA), Washington, D.C., and the U.S. Army Engineer Topographic Laboratories (ETL), Fort Belvoir, Virginia. Many other such research efforts are underway throughout the Department of Defense. The intent of this paper is to focus on the work done at West Point during the past 2-1/2 years. This project is referred to as the DMA/ETL Research Project.

The West Point Computer Graphics Laboratory (CGL)

This facility, located in the Department of Geography and Computer Science, has been in full operation for the past two academic years. It provides an excellent "state of the art" environment for individual cadet and faculty projects as well as for funded research efforts in computer graphics. The hardware configuration combines the power of the Academy's main frame computer (UNIVAC-1100/12) with the responsiveness of a minicomputer (PDP-11/40) and the dedication of a number of different microprocessors (AM-100, LSI-11, IMSAI-8080 and others). The PDP-11/40 is currently being replaced by a VAX-11/780 minicomputer. The portion of the laboratory most directly related to the work on this project is shown in figure 1.

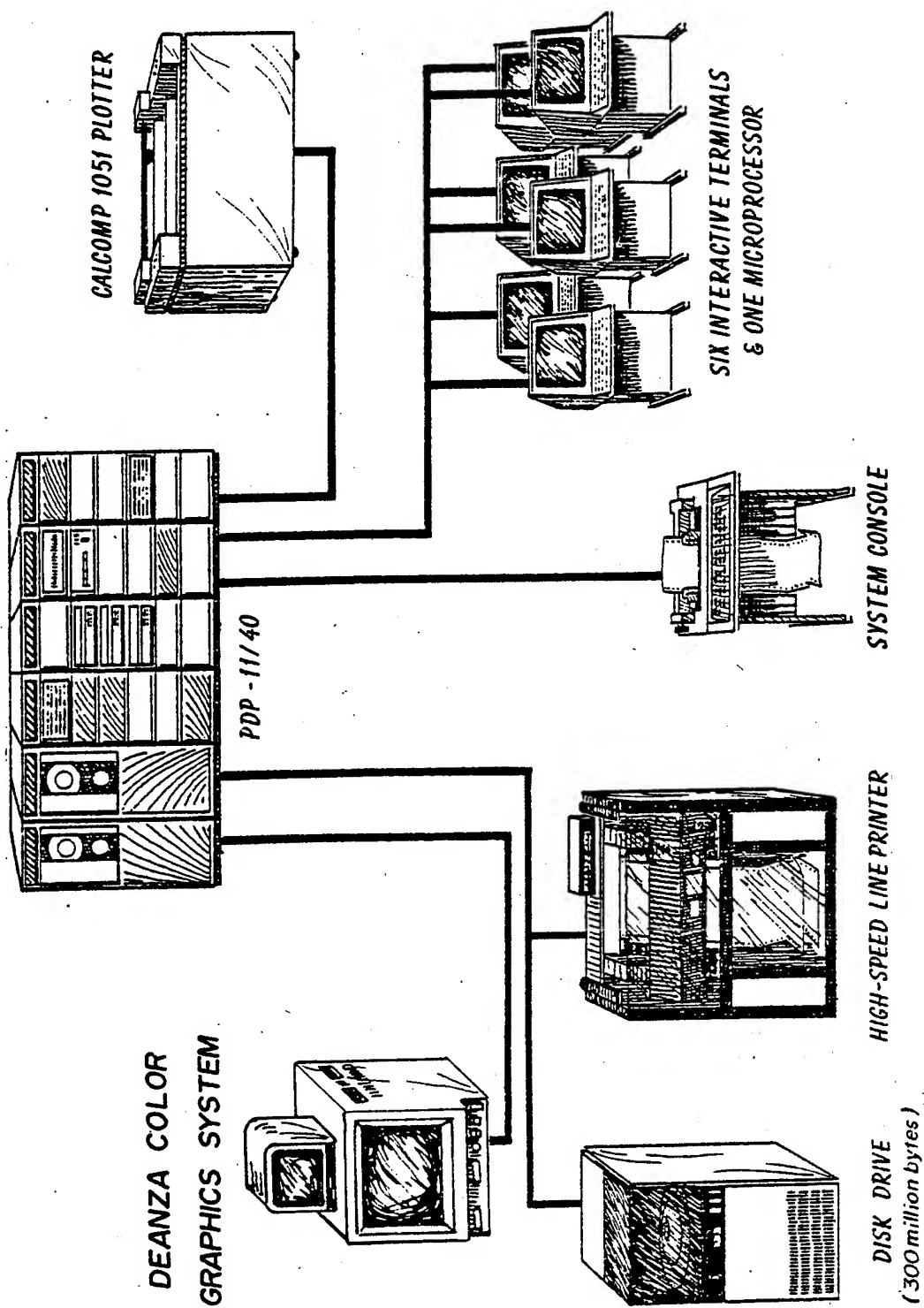


FIGURE 1. Computer Graphics Laboratory Equipment Supporting DMA/ETL Research Project.

CHARLAND

II. THE DMA/ETL RESEARCH PROJECT

Objectives

1) Receive experimental graphics software packages from the ETL and make all modifications to bring these programs to a totally operational status at West Point.

2) Receive a DMA special data base of West Point and vicinity and transform it to a disk resident file in the CGL which can be efficiently accessed by the ETL software.

3) Link the software (1) and the data base (2) to develop computer-generated views and overlays of the West Point Military Reservation. Included within the area of coverage is Camp Buckner, the cadet field training area located approximately 10 miles west of the U.S. Military Academy.

4) Conduct an accuracy study of the West Point digital data base to include a ground truth survey of a portion of the digitized area. The goal of this study is to determine the minimum essential data accuracy for various Army applications.

5) Incorporate computer-generated graphics into the cadet field training program during the summer months and into the academic curriculum as appropriate.

6) Evaluate the military utility of these graphics and report on all findings.

Status

Substantial progress has been achieved in the generation of four basic graphic products. These include the line of sight profile, line perspective view, line oblique view and shaded perspective view. The ability to generate these graphics is not a new concept. The significance of the research at West Point is that the generation of these graphics has been tailored for Army needs. The next chapter will provide a look at each of these four packages with a focus on the final product, the user's prompts and on major software modifications.

Progress has also been accomplished on the accuracy study and on the objective to implement this technology into the cadet field training program. The results of this work are described in Chapters IV and V respectively.

CHARLAND

III. APPLICATIONS SOFTWARE

General

The software packages used in support of the DMA/ETL research project were developed in the Automated Cartography Branch, U.S. Army Engineer Topographic Laboratories. This branch is headed by Mr. Howard Carr. The developer of the basic concepts and programs was Mr. James Jancaitis.¹

Line Of Sight Profiles

Although clearly the simplest of the four programs, the ability to generate a profile between any two points, in less than two minutes, is a valuable tool for the soldier. In fact hand generation of these profiles, which could take 20-30 minutes, is often necessary.

As seen by the prompts in figure 2, the user input parameters are minimal. The resulting product (fig. 3) is a cross-sectional view of the intervening terrain. The accuracy and speed of this plot varies as a function of the number of points sampled.

Changes to this software included modifications of all interactive prompts, overlaying the task to permit either TEKTRONIX screen (CRT) or CALCOMP plotter output and the implementation of SUBROUTINE CARTO which opens the user-specified unformatted random access data files. Upon receipt of a new data base, the user need only add the name and characteristics of that data base to CARTO, and the remaining software can access it immediately.

Enter '1' for TEKTRONIX output, or
'2' for CALCOMP output

1

Enter '1' for West Point,
'2' for Fulda Gap, or
'3' for Cache data base.

1

Enter the left side coordinates.
Example: NB50003000

UA76417576

Enter the right side coordinates.

UA77637782

Enter height above ground at
left end and right end (meters).
Example: 2.0,2.0

2.0,2.0

Enter # pts along LOS - INTEGER

100

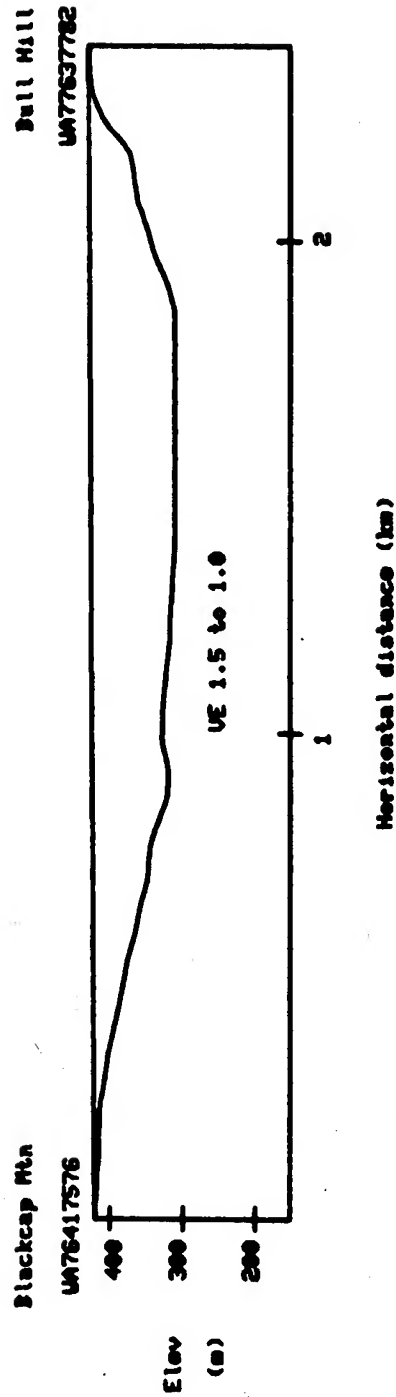
Enter vertical scaling factor

1.5

FIGURE 2. Prompts and Responses for Line of Sight Profile at Figure 3.

LINE OF SIGHT PROFILE

VISIBLE



NOTE: Plot time 1 min 10 sec

FIGURE 3. Line of Sight Profile.

CHARLAND

Line Perspective Views

The following (fig. 4) is an illustration of the prompts and responses to produce a line perspective view. In approximately six minutes a three-dimensional graphic, such as the example shown in figure 5, is generated.

In addition to modification of the input prompts and inclusion of SUBROUTINE CARTO, a new subroutine was developed to facilitate efficient generation of perspective views. This subroutine, called PWINDO, accesses elevation data from disk conforming to a pie-shaped subarea and stores this data in core. If the area being viewed is too large to fit in core at one time, this routine will read what it can and then trigger successive iterations until the entire perspective view is completed. In conjunction with PWINDO, SUBROUTINE ALTP was developed to extract the correct data values from the core buffer and compute the required elevations.

Change plot size? Any response other than YES causes the final plot dimensions to be 14" wide and 10" high.

NO

Change viewing parameters? (YES or NO)

YES

Enter the INTEGER # of radials (75 max).
Example: 75

75

Enter the INTEGER # of points per radial (199 max).
Example: 100

100

Enter how far you can see (Km).
Example: 3.5

6.2

Enter the vertical exaggeration.
(the example below implies 2:1)
Example: 2.0

1.5

Enter '1' for West Point(1),
'2' for Fulda Gap,
'3' for Cache,
'4' for West Point(2)
'5' for West Point(3), or
'6' for West Point(4).

5

Enter square ID and 8-digit coordinates of the southwest corner of the viewing window (oblique view) or the viewers position (persp. view).
Example: NB50003000

UA83008000

Input azimuth (deg) and height (ft).

226.,500.

FIGURE 4. Prompts and Responses for Line Perspective View at Figure 5.

Perspective View of the Artillery Impact Area - West Point -----

Viewer's location: WA83008000
Viewing azimuth: 226 degrees
Viewing depth: 6.2 km
Vertical exaggeration: 1.5 to 1.0
Viewer's elevation: 500 feet
Plot time: 6min 10sec

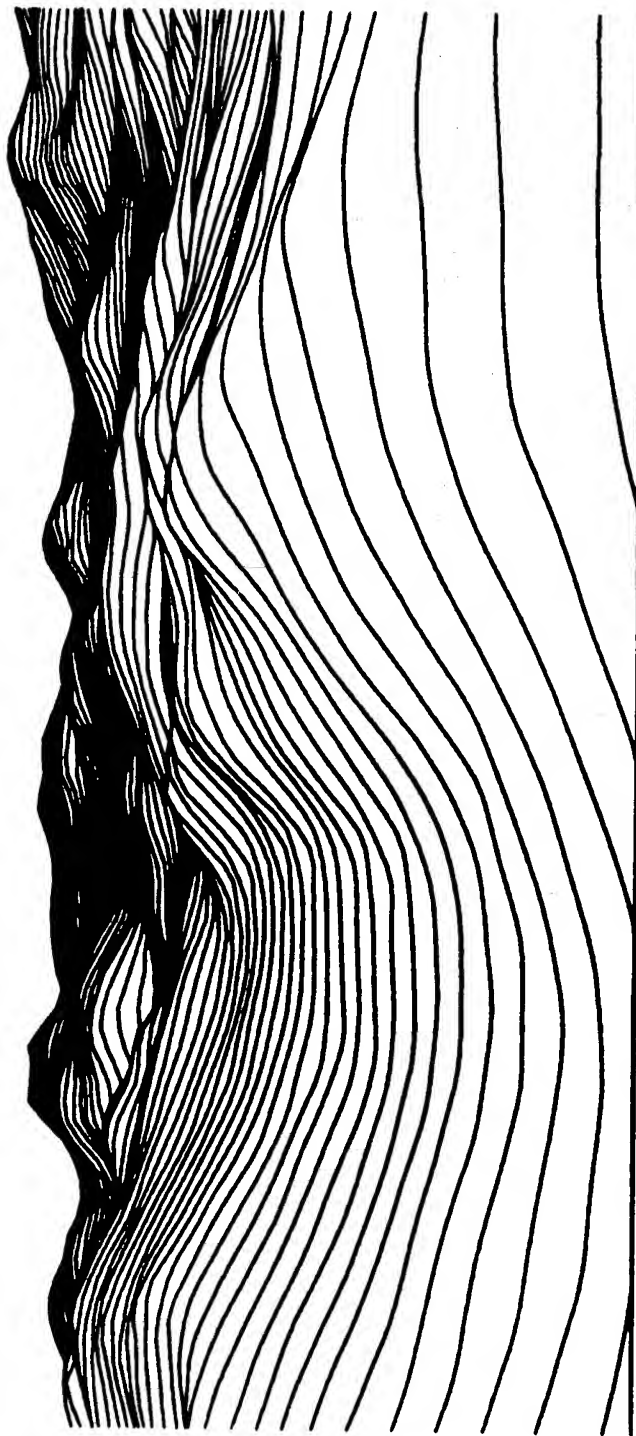


FIGURE 5. Line Perspective View.

CHARLAND

Line Oblique Views

Experimentation with this form of terrain representation during the 1979 Cadet Field Training Program indicated widespread potential military applications, especially for large areas. Refer to figure 6 for the sample prompts and figure 7 for the resulting sample graphic.

Modifications of this software are similar to those required for the line perspective case. The program structure was first overlaid to allow for greater core data arrays. The interactive prompts were changed. SUBROUTINE CARTO was implemented, and the program was configured to generate either TEKTRONIX or CALCOMP output. Substantial effort was also devoted to improving the internal documentation and efficiency of the source code.

This program will generate oblique views of West Point and Vicinity, Fulda Gap or Cache, Oklahoma. Enter GO to continue or STOP to terminate. Upon completion of plot, hit RETURN to return to this prompt.

GO

Enter *1* for West Point(1),
 2 for Fulda Gap,
 3 for Cache,
 4 for West Point(2)
 5 for West Point(3), or
 6 for West Point(4).

5

Enter square ID and 8-digit coordinates of the
southwest corner of the viewing window (oblique view)
or the viewers position (perspective view)
Example: NB50003000

UAB4008000

Enter width and depth of area being viewed (km).
Example: 5.0,5.0

5.,5.

Enter # of profiles to be plotted (INTEGER 199 max)
Example: 175

100

Enter the vertical exaggeration.
(the example below implies 2:1)
Example: 2.0

1.5

Enter the aspect angle and viewing azimuth (deg)

40.,226.

FIGURE 6. Prompts and Responses for Line Oblique View at Figure 7.

Oblique View - Site of the U.S. Military Academy -----

Viewing azimuth: 226 degrees
Vertical exaggeration: 1.5 to 1.0
Plot time: 5min 45sec

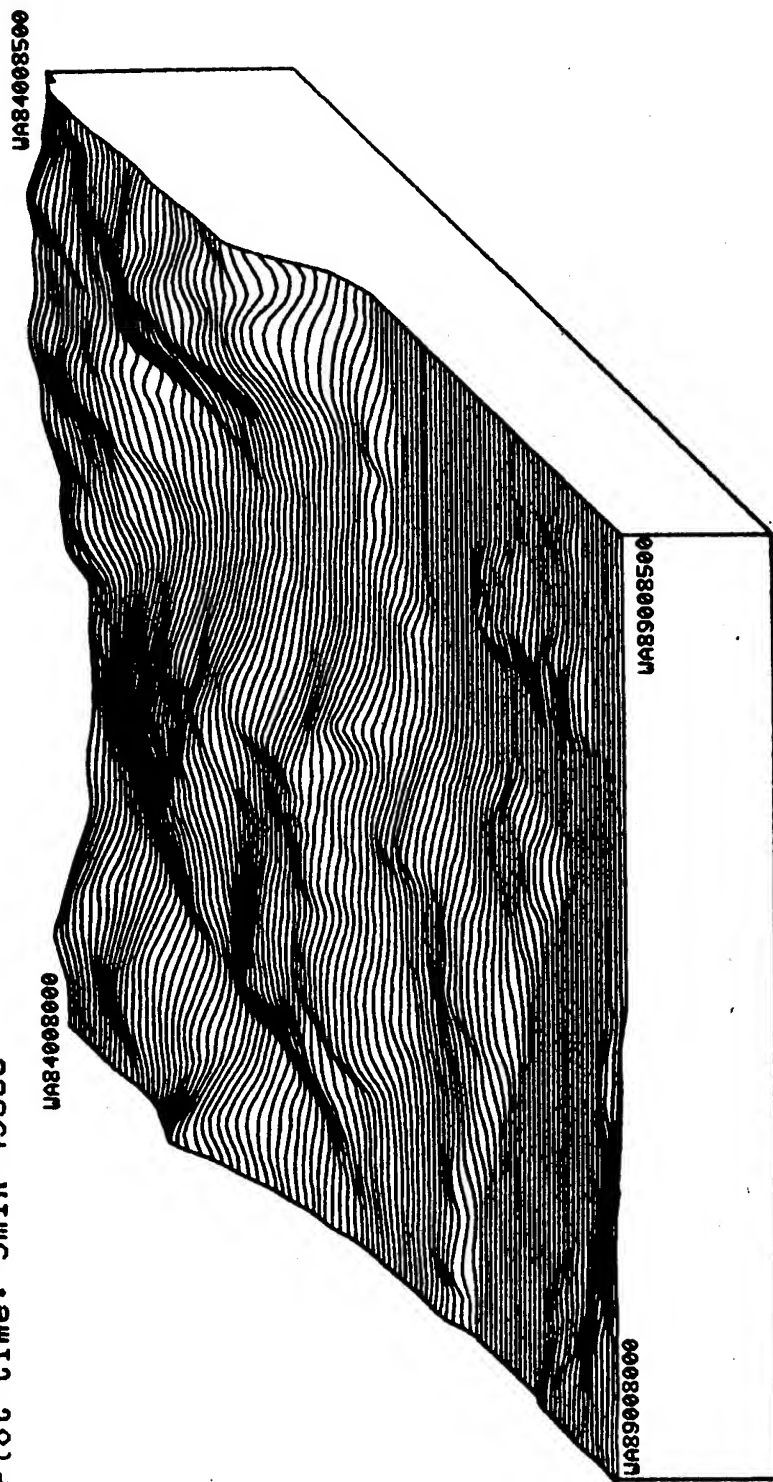


FIGURE 7. Line Oblique View.

Shaded Perspective View

This software package represents the first major accomplishment involving color graphics within the CGL. The preliminary successes are very promising. Originally, the shaded perspective software was written at the ETL by Mr. Cyrus Taylor² and made available to West Point in August 1979. Its output was a black-and-white image produced on a VERSATEC dot matrix plotter. Modifications at West Point included code simplifications and internal documentation, task overlaying, the inclusion of SUBROUTINES CARTO and PWINDO, the development of the prompts illustrated in figure 8 and the addition of synthetic color to generate the graphic shown in figure 9. Current efforts are underway at both the ETL and West Point to further simplify the production of these images. The goal is to retain the current detail while reducing the image generation time to be compatible with the line perspective software. Additionally, with the assistance of Mr. Robert Getz, the department illustrator, and Cadet Joseph Hafeman, who is conducting graded research in computer graphics, a series of color tables are being developed to increase the realism of the synthetic color process.

Enter '1' for West Point(1), '2' for Fulda Gap, '3' for Cache, '4' for West Point(2), '5' for West Point(3), or '6' for West Point(4).	Enter how far you can see (km). Example: 6.2 6.2
S	Enter # radials, # points per radial and # pixels per column (INTEGERS). Example: 512,150,480 512,200,480
Enter square ID and 8-digit coordinates of the southwest corner of the viewing window (oblique view) or the viewers position (perspective view). Example: NB50003000	Enter the vertical exaggeration. (the example below implies 2:1). Example: 2.0 1.5
UA83008000	
Enter viewing azimuth (degrees) and height above ground (feet). Example: 226.0,1000.0 226.,500.	Enter the vertical and horizontal sun angles (degrees). Example: 45.,90. 45.,315.

FIGURE 8. Prompts and Responses for
the Shaded Perspective
View at Figure 9.

CHARLAND



FIGURE 9. Shaded Perspective View.

CHARLAND

IV. DATA BASES

Acquisition

Data bases for this research effort are provided by the DMA. All current applications have utilized DMA special data of Fulda Gap, Germany, and West Point, New York. The data have been reprocessed into polynomial coefficients by the DMA Aerospace Center (DMAAC) and delivered to West Point encoded in 8-bit ASCII format. This system has proven to be quite convenient when transferring data from a 36-bit main frame computer to a 16-bit minicomputer. Additionally, the polynomial coefficients appear to afford an advantageous compaction benefit plus a rather accurate means of computing intermediate elevations. Efforts are underway to experiment with DMA source tapes directly. This may eliminate the requirement to reprocess. In conjunction with these tests is the overall program to study data base accuracy, whether the data is represented by polynomial coefficients or strictly as nodal elevations.

Accuracy

Two major questions exist regarding digital data when one considers computer graphics for the Army. The first is, how well do data bases of various intervals and characteristics represent the terrain in question and second, what is the minimum accuracy required for the particular application in question? The accumulation of statistics to answer both questions is being presently undertaken at West Point. In cooperation with the DMAAC, the West Point data base has been reprocessed into eight successively thinner polynomial representations. Computed elevations are being compared to surveyed elevations to observe accuracy degradation as a function of thinning when polynomials are used. Elevations for the same locations will be computed from the source data base and compared as well. Additionally, graphics of the area will be generated utilizing each of the data bases, and the resulting products will be compared with the actual terrain. This effort is expected to be completed by June 1981. The table on the following page (fig. 10) is a sample of the information that has been gathered thus far.

CHARLAND

UTM COORDINATES	SURVEY	ELEVATIONS (FT)		DMA DATA BASE(1) (12.5m / NFF-4)	DMA DATA BASE(2) (25.0m / NFF-4)
		INTERPOLATION 1:24000 MAP			
UAS038279	575.40	570.00	578.00	578.70	578.70
UAS178286	554.00	550.00	548.70	547.40	547.40
UAS228291	538.40	530.00	537.70	537.30	537.30
UAS348290	607.10	600.00	604.00	604.00	604.00
UAS458273	647.10	630.00	631.10	631.10	631.10
UAS488268	666.00	660.00	664.20	663.20	663.20
UAS538260	672.00	680.00	689.00	689.00	689.10
UAS5578254	681.70	690.00	699.00	699.40	699.40
UAS668248	732.50	720.00	726.70	727.40	727.40
UAS668245	743.70	740.00	749.10	744.00	744.00
UAS658240	769.10	770.00	767.10	769.60	769.60
UAS648240	772.70	770.00	769.40	771.90	771.90
UAS698232	977.10	970.00	967.50	970.40	970.40
UAS158230	984.70	970.00	969.40	969.00	969.00
UAS188225	987.50	990.00	978.20	973.10	973.10
UAS208220	981.30	990.00	978.70	978.00	978.00
UAS198217	986.70	970.00	953.30	951.70	951.70
UAS148213	959.50	960.00	963.40	962.70	962.70
UAS138210	970.90	970.00	969.70	969.70	969.70
UAS098206	977.70	970.00	977.40	967.20	967.20
UAS058201	994.10	990.00	994.40	984.20	984.20
UAS038195	1002.20	1010.00	982.30	971.80	971.80
UAS018191	978.60	970.00	948.60	943.80	943.80
UAS028188	957.70	940.00	916.40	915.90	915.90
UAS038184	910.60	900.00	898.00	898.30	898.30
UAS088186	908.20	890.00	889.40	882.80	882.80
UAS098181	881.50	870.00	864.40	861.80	861.80
UAS118179	862.10	850.00	839.40	833.40	833.40
UAS088180	832.40	820.00	812.00	809.90	809.90
UAS028200	798.60	780.00	782.40	778.00	778.00
UAS708206	719.60	720.00	722.40	718.30	718.30
UAS538222	734.10	730.00	736.50	737.80	737.80
UAS788228	739.20	730.00	725.90	730.20	730.20
UAS608230	737.70	730.00	722.40	724.50	724.50

FIGURE 10. Quantitative Comparison of Terrain Elevations from Different Sources.

V. FIELD APPLICATIONS

General

During the summer of 1979 the class of cadets having just completed their freshman year spent approximately seven weeks in field training at Camp Buckner. During the last two weeks of the training program, computer-generated terrain graphics were incorporated into portions of the field training on a trial basis. These graphics were provided to the Artillery, Engineer and Infantry instruction committees.

Findings

Although the duration of this application phase was limited, a number of significant facts were determined.

- 1) The users of this technology must be educated on its application and potential before they can apply it properly. Merely showing examples of sample graphics does not sufficiently enable the users to intelligently request the exact graphics they need.
- 2) The data base will not provide the minute detail of actual slopes. This detail is not available on the source maps.
- 3) There is substantial need for graphics which are well labeled and which include cultural features.
- 4) The graphics are excellent tools which can be used to illustrate what is being portrayed on a 2-D topographic map. They leave a picture in one's mind which topographic map sheets do not often do. They are valuable aids for planning operations, and their potential utility in the teaching mode is limitless.
- 5) Oblique views are applicable to areas that are 4km square or larger. For areas of this size, they represent the terrain accurately; in fact, this representation proved to be a valuable asset to the Artillery training in particular.

VI. SUMMARY

Applications of computer graphics at Camp Buckner, utilizing the graphics packages discussed, will be conducted once again this summer. Emphasis will be placed on utilization of the graphics to stress key training objectives. Cadet Scott Keller is conducting a graded research project to support this effort.

CHARLAND

Emphasis has already been placed on automatically labeling and overlaying all the computer-generated graphics. Actually, this problem has been partially solved but not yet implemented.

Contour plots with overlays, both raster and vector, and radar masking diagrams will be implemented in the near future.

As mentioned in Chapter IV, the data base accuracy study will continue for another year. Both DMA Standard and Special data bases with nodal spacing conforming to either the UTM or Geographic coordinate systems will be employed.

Color perspectives with a focus on near-real-time image generation will be stressed. The initial response to the color perspective views has been encouraging.

In conclusion, a number of computer graphics packages have been presented which are tailored for Army needs. The initial response to these products at West Point has been resoundingly positive. The tasks that remain are refinement, education, application and further refinement. If this approach is followed, computer graphics will play a significant role in the Army of the future.

VII. ACKNOWLEDGEMENT

The patience, generosity and continuous support rendered by both the DMA and the ETL is gratefully acknowledged.

A special word of thanks is due to Mr. James Jancaitis (ETL), Mr. Cyrus Taylor (ETL) and to Mr. Russell Gustin (DMAAC) for their personal contributions of time and effort.

Finally, Mrs. Jane R. Tosolini is to be thanked for reviewing and typing this manuscript.

VIII. REFERENCES

¹Jancaitis, J. R., "Modeling and Contouring Irregular Surfaces Subject to Constraints," Final Technical Report No. ETL-CL-74-19 for U. S. Army Engineer Topographic Laboratories, Fort Belvoir, Virginia, on contract DAAK02-73-C-0213, January 1975, 171 pages.

²Taylor, C. C., "Computer Generation of Shaded Relief Images for Cartographic Applications," Final Technical Report for U. S. Army Engineer Topographic Laboratories, Fort Belvoir, Virginia, July 1979, 223 pages.

CHEN

MATERIALS DETERIORATION IN TROPIC VERSUS CONUS SITES

FREDDY CHEN, Ph.D.
US ARMY TROPIC TEST CENTER
APO Miami 34004

The US Army has had considerable involvement in the humid tropics since before World War II. These involvements have revealed many unexpected materiel problems. Warm temperatures, high rainfall and high humidity interact to produce an environment which adversely affects the performance of materiel. The US Army Tropic Test Center (USATTC), located in the Republic of Panama (latitude 9°N, longitude 80°W), conducts materiel tests and environmental research to increase the effectiveness of systems designed to operate in humid tropic areas.

The continued availability of test facilities in Panama is questionable after the year 2000 because of changing international political situations. In addition, increasingly sophisticated equipment, increases in materiel system inventory, and bulk of Army equipment make it difficult to test in areas remote from the Continental United States (CONUS). Recognizing these real and potential problems, the Army Scientific Advisory Panel (now the Army Science Board) recommended in 1976 that a program of correlative tests be initiated between Panama sites and selected CONUS sites. The concept of using CONUS sites to predict materiel performance in the tropics may be a necessity in the near future.

To determine if this concept is feasible, this research takes an exploratory first look at material performance at a basic level. A number of single environmental factors such as temperature, relative humidity, and rainfall are being measured for their effects on several basic materials such as latex and steel. The approach compares basic degradation curves from material samples exposed at

CHEN

CONUS sites to deterioration rates and mechanisms found in the tropics of Panama. At the end of this study, correlations between single and multiple environmental factors and degradation rates will be made. This research then takes a basic look at material degradation. There is no attempt at this exploratory stage to predict materiel system performance in the tropics by analyzing data obtained in CONUS, although this project is the first step in that direction. Subsequent research will help to achieve that ultimate goal.

At present, USATTC is studying six areas in CONUS that have some environmental characteristics similar to those found in Panama. Exposure sites have been established at locations in CONUS shown in figure 1. Figure 2 shows the location of the Panama exposure sites; figure 3 identifies analog parameters for CONUS and tropic sites.

Several basic materials and several standard Army materiel items are being exposed as shown in figure 4. These basic materials were exposed during previous tests.(1-6) The knowledge obtained from these tests will be used to compare the severity of the environment to the deterioration of materials and materiel exposed in this study. The same exposure design and analytical procedures will be used for all sites. Since data for all sites have not been collected, the results at this time are not complete. However, some preliminary degradation trends from early exposure data show that the basic concept of using CONUS data to predict tropic results may be feasible. One preliminary result from the study is the percent corrosion weight loss at different sites over a period of time (figure 5). The two coastal sites, Key West and Fort Sherman Coastal, exhibited the highest rate of corrosion. Common deteriorating factors were high atmospheric salt levels, high humidity, and high temperatures. As expected, the Quinault site, with low atmospheric salt, high humidity, and low temperatures had the lowest rate of deterioration. As shown in figure 5, high humidity alone does not accelerate corrosion.

Another early result at this stage of the study is the change in tensile strength for latex and POL tank fabrics (figures 6 and 7). Because latex is sensitive to ultraviolet (UV) radiation, the tensile strength for latex drops rapidly at all sites that have intense solar radiation, but not as rapidly in forest sites. Because the nylon fibers in the POL tank fabrics are not exposed but are contained between layers of PVC and nitrile-neoprene, the tensile strength of POL tank fabrics did not change during any exposure testing. UV radiation cannot penetrate the PVC layers to deteriorate the nylon.

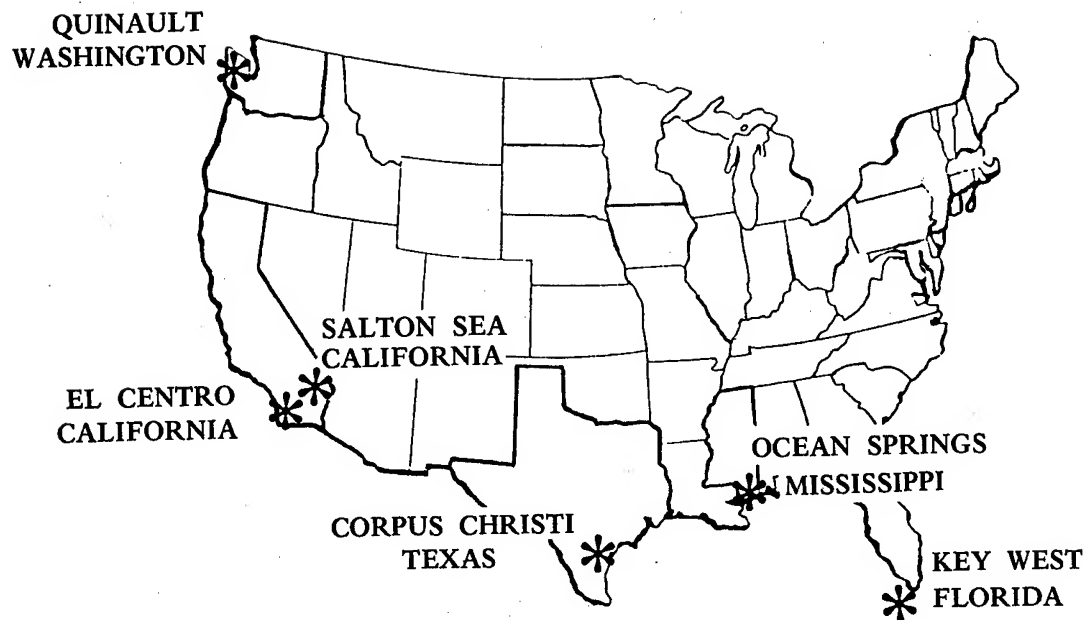


Figure 1. Location of CONUS Exposure Sites.

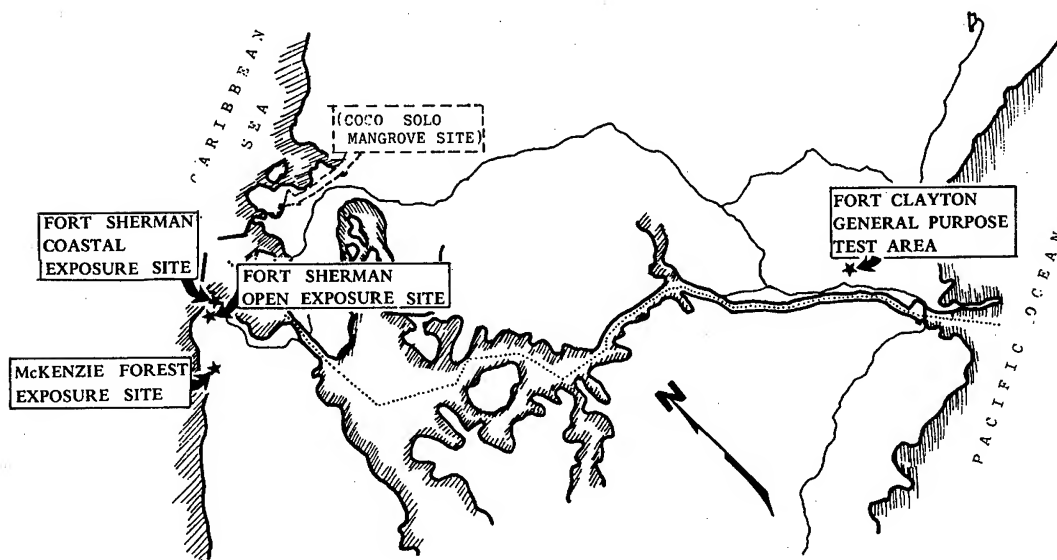


Figure 2. Location of Panama Exposure Sites.

CHEN

<u>CONUS SITES</u>	<u>ANALOG ENVIRONMENTAL PARAMETERS</u>	<u>PANAMA SITE</u>
QUINAULT, WA	HIGH RAINFALL, HUMIDITY AND ACTIVITY	BATTERY McKENZIE FOREST SITE
SALTON SEA, CA	HIGH AMBIENT TEMPERATURE, SOLAR RADIATION AND HUMIDITY	FORT SHERMAN OPEN EXPO- SURE SITE AND FORT CLAYTON GENERAL PURPOSE TEST AREA
EL CENTRO, CA	HIGH SOLAR RADIATION AND AMBIENT TEMPERATURE	FORT SHERMAN OPEN EXPO- SURE SITE
CORPUS CHRISTI, TX	HIGH ATMOSPHERIC SALT, HIGH SOLAR RADIATION	FORT SHERMAN COASTAL EXPOSURE SITE
OCEAN SPRINGS, MS	SUBTROPICAL MARINE CLIMATE, HIGH SUMMER HEAT, HUMIDITY AND RAINFALL	PREVIOUS MANGROVE SITE RESULTS
KEY WEST, FL	TROPICAL MARINE CLIMATE DURING CERTAIN MONTHS	FORT SHERMAN COASTAL EXPO- SURE SITE

Figure 3. Analogy Between CONUS and Panama Exposure Sites.

TEST ITEMS

Low Carbon Steel	Jungle Fatigues (Strips)
Cotton	Petroleum, Oil, Lubricant (POL) Tank Fabrics
Latex	Electronic Components
Nylon	Jungle Boots
Mylar	Assorted Glues
Cellulose Acetate	

Figure 4. List of Test Items.

CHEN

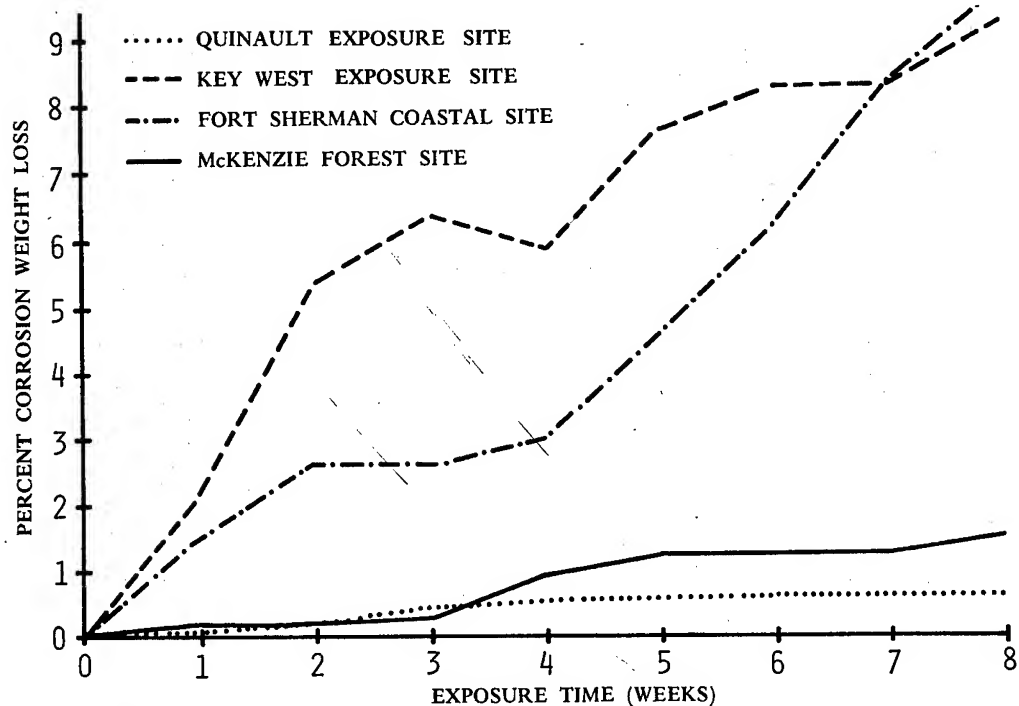


Figure 5. Percent Corrosion Weight Loss at Selected Exposure Sites.

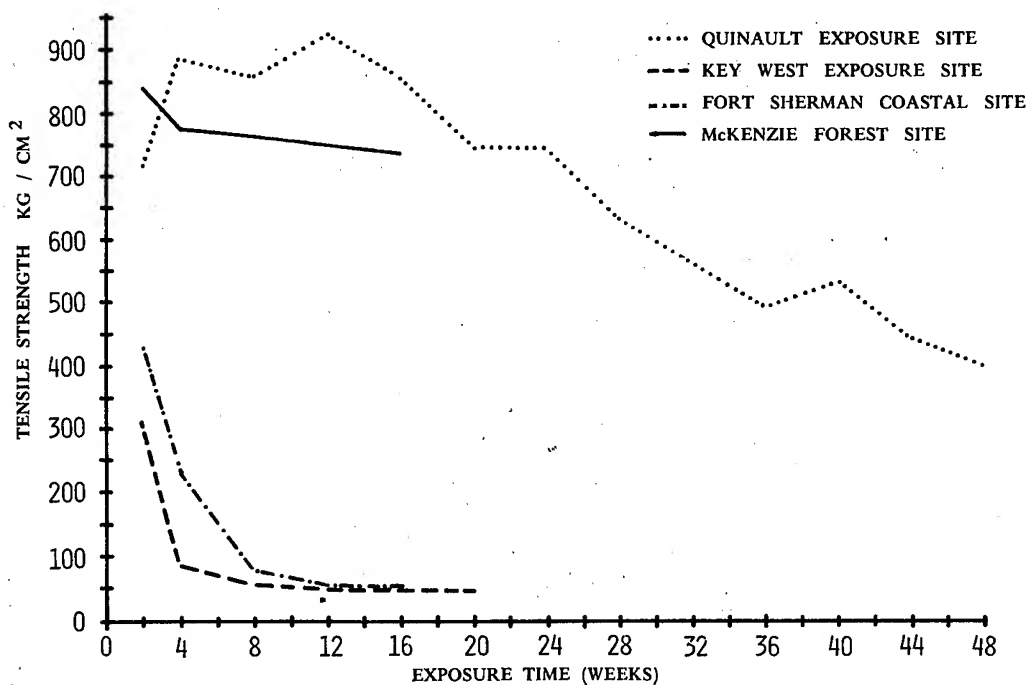


Figure 6. Change in Tensile Strength for Latex at Selected Exposure Sites.

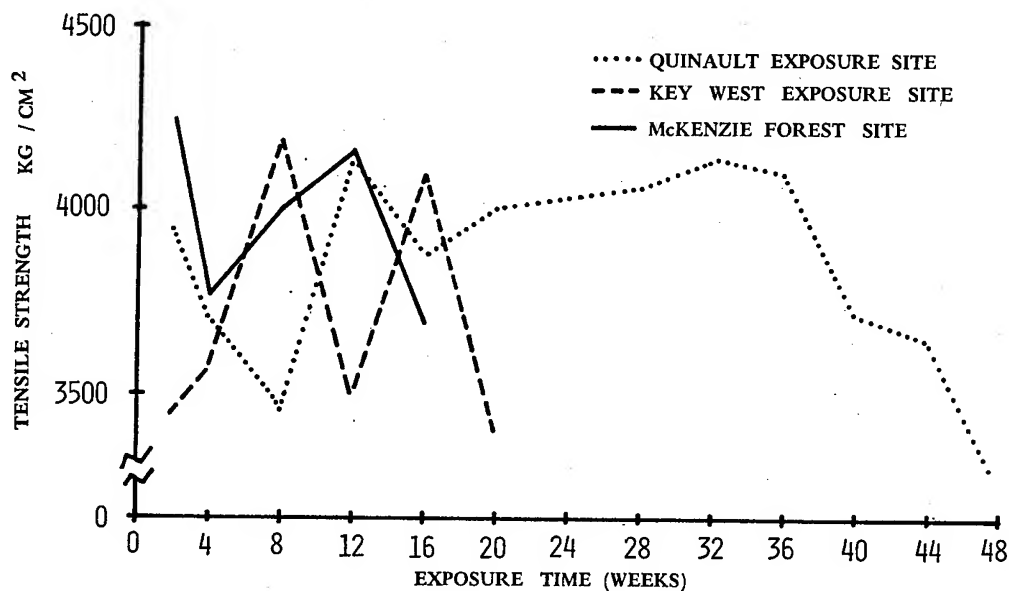


Figure 7. Change in Tensile Strength for POL Tank Fabrics at Selected Exposure Sites.

Environmental degradation occurs most readily on the surface of the POL tank fabric. Therefore, a scanning electron microscope was used to determine the various results in surface deterioration. Figure 8 shows severe deterioration of POL tank fabric exposed for 2 weeks at Key West, a coastal site. Some sections of this fabric had deep cracks. The same result of cracking occurred, but not severely, on fabrics exposed at McKenzie Forest in Panama (figure 9). The McKenzie Forest sample also contained fungal activity with a collection of debris and salts. The deterioration process was different for fabrics exposed at Quinault; the fabric did not crack but curled. Figure 10 shows a POL tank fabric that had been exposed at Quinault for 7 months.

One main difference between exposure at Key West and its counterpart in Panama--Fort Sherman Coastal--was fungal activity. Cellulose acetate samples exposed for 2 weeks in Key West did not show evidence of fungal attack, but did exhibit surface deterioration (figure 11). However, samples exposed for 2 weeks at the Fort Sherman Coastal site were covered with fungal mycelia, debris and salts (figure 12).

Jungle fatigue strips also were used as exposure samples (figures 13 and 14), undergoing exposure for 2 weeks at the Fort Sherman Coastal Site. The fatigue strips contained a fungus

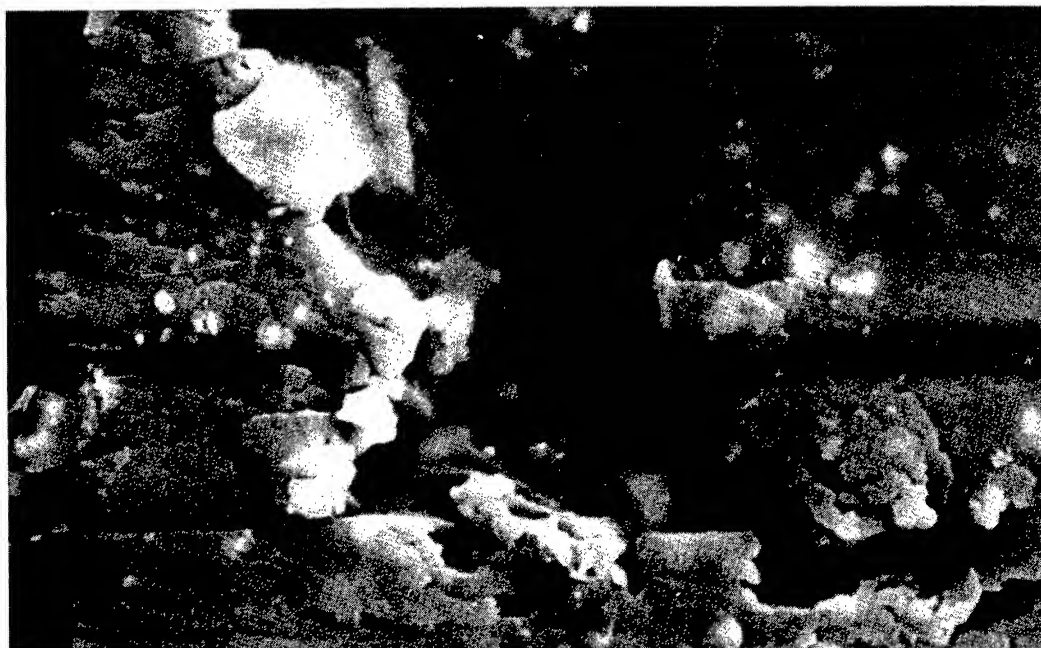


Figure 8. Photomicrograph of Deterioration to Surface of POL Tank Fabric Exposed at Key West for 2 Weeks, 560X.

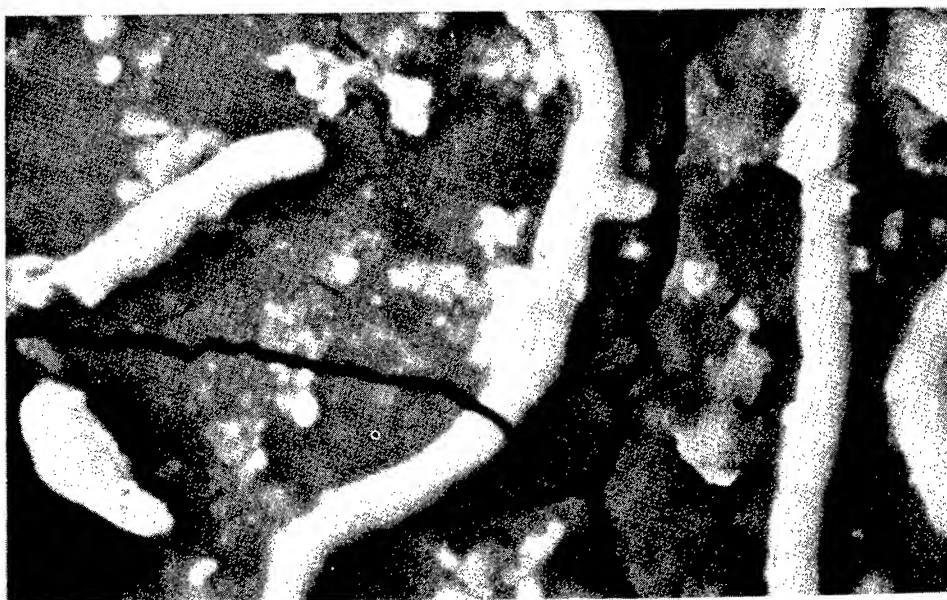


Figure 9. Photomicrograph of Deterioration to Surface of POL Tank Fabric Exposed at McKenzie Forest for 2 Weeks, 1200X.



Figure 10. Photomicrograph of Deterioration to Surface of POL Tank Fabric Exposed at Quinault for 7 Months, 1000X.

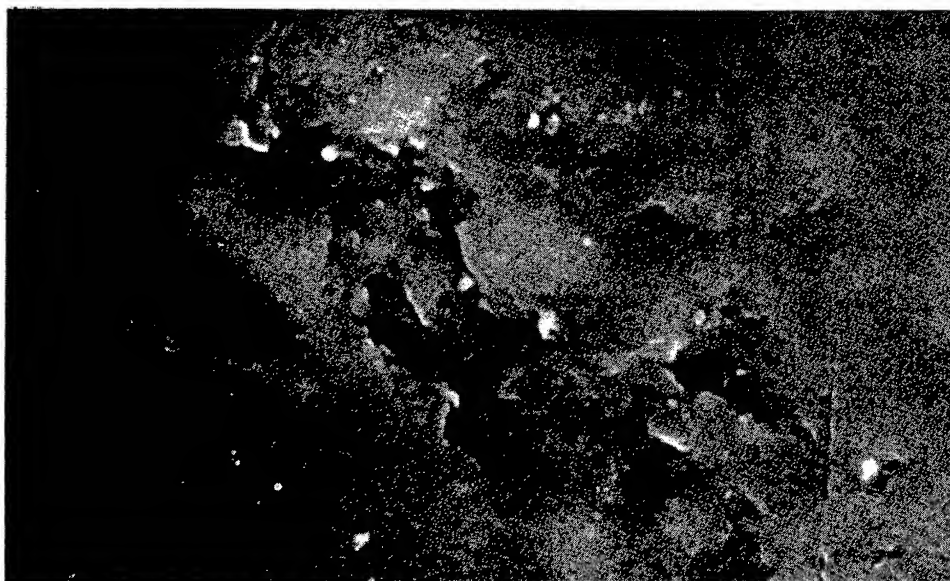


Figure 11. Photomicrograph of Deterioration to Surface of Cellulose Acetate Exposed at Key West for 2 Weeks, 1080X.

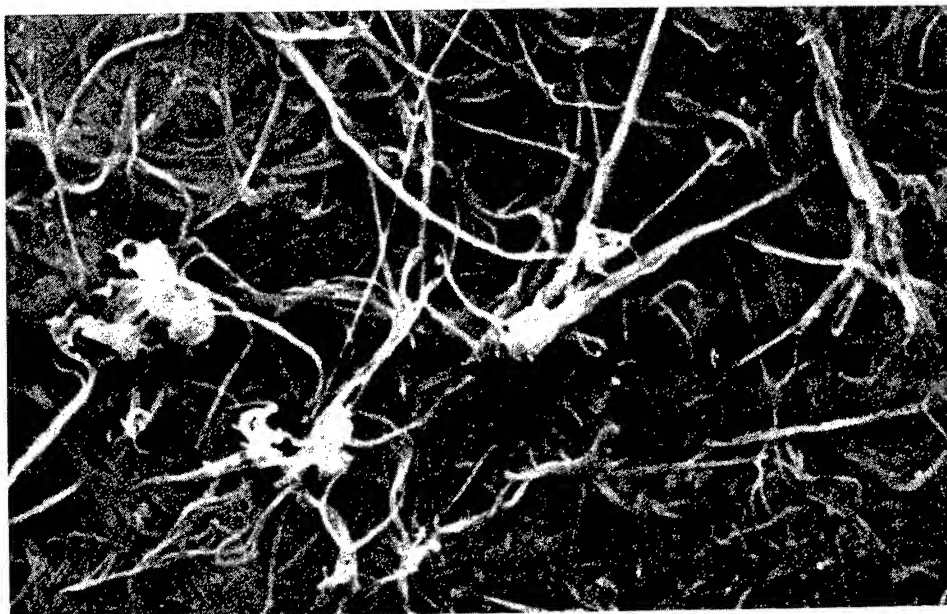


Figure 12. Photomicrograph of Deterioration to Surface of Cellulose Acetate Exposed at Fort Sherman Coastal Site for 2 Weeks, 520X.

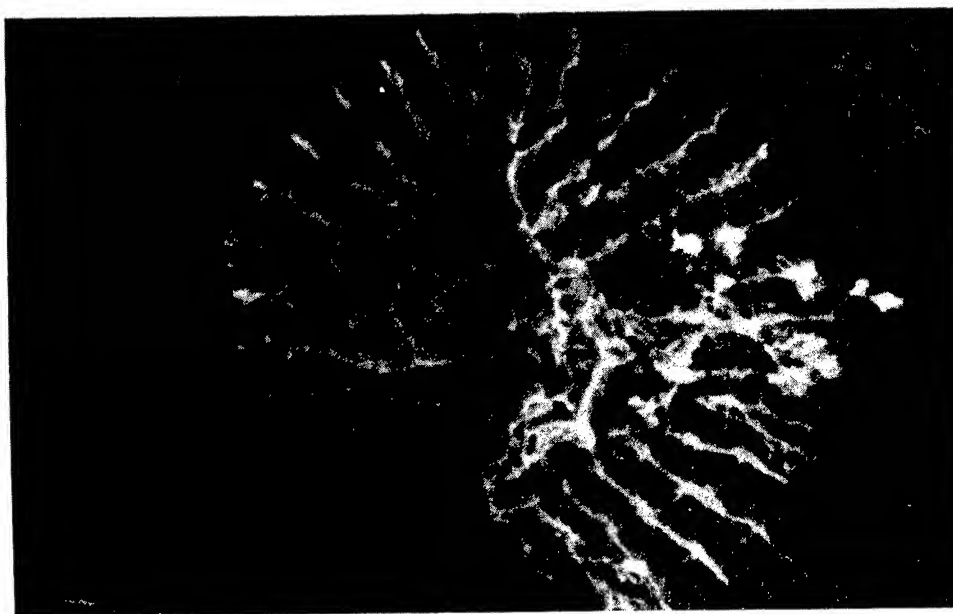


Figure 13. Photomicrograph of Fungi on Surface of Jungle Fatigue Strip Exposed at Fort Sherman Coastal Site for 2 Weeks, 160X.

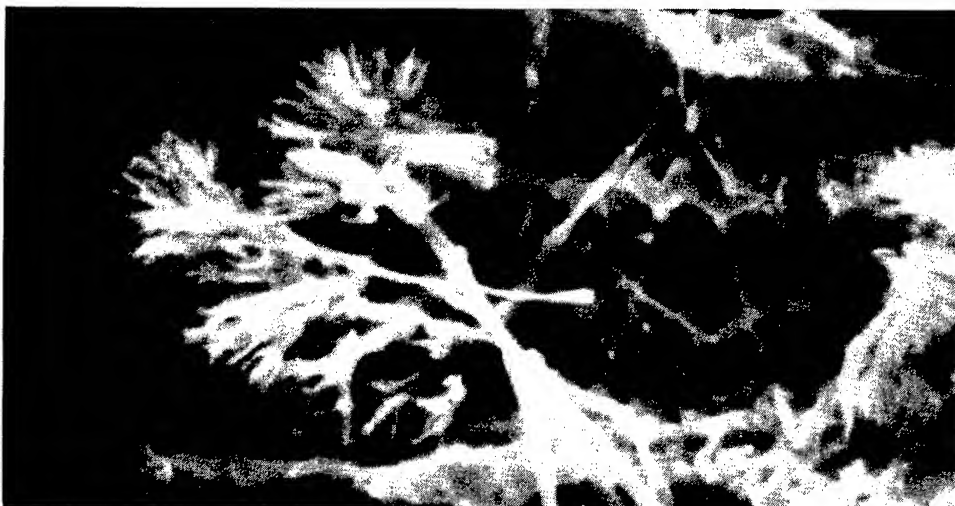


Figure 14. Photomicrograph of Fungi on Surface of Jungle Fatigue Strip Exposed at Fort Sherman Coastal Site for 2 Weeks, 650X.

tentatively identified as belonging to the triconderma species. Other unknown fungal species attacked cotton fibers (figure 15) exposed for 20 weeks at the Fort Sherman Coastal Site.

Fungal attack occurred either by a suction process as shown in figure 16, or by surface penetration as shown in figure 17. Figure 16 shows the deterioration of latex after being exposed for 4 months in Quinault. Figure 17 shows the deterioration of mylar after being exposed for 7 weeks at McKenzie Forest. Salt also can penetrate surfaces (figures 18 and 19) as shown on the mylar samples exposed at the Fort Sherman Open Exposure Site for 2 weeks (figure 18). The cellulose acetate sample (figure 19) exposed for 12 weeks at Key West showed severe surface salt penetration.

Another cause of surface deterioration is stress relaxation. A good example is shown in figure 20. The latex sample was exposed at the Quinault site for 7 months. After 7 months, a partial coalescence of surface particles had occurred. Stress relaxation from surface coalescence caused the surface fibers to pull apart. Surface deterioration at this site was so slow that the process was observed and analyzed easily. At sites with surface deterioration occurring rapidly, it was difficult to capture and analyze the deterioration process. High solar radiation levels found at the Fort Sherman Coastal Exposure Site caused surface deterioration to occur rapidly. Severe surface destruction occurred on latex samples exposed at this site for 2 weeks (figure 21).

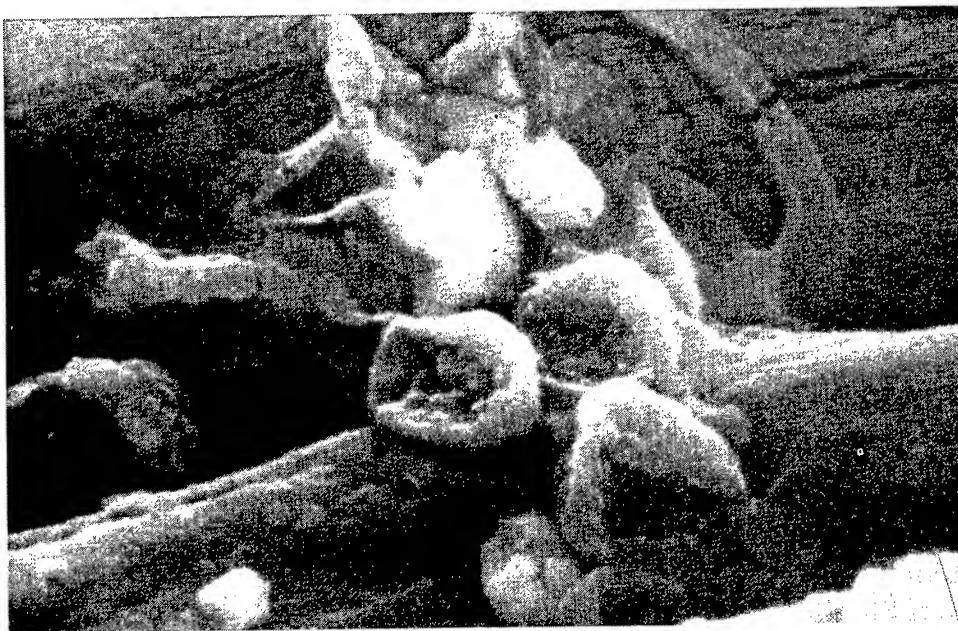


Figure 15. Photomicrograph of an Unknown Fungi on Surface of Cotton Exposed at Fort Sherman Coastal Site for 20 Weeks, 2750X.



Figure 16. Photomicrograph of Fungi on Surface of Latex Exposed at Quinault for 4 Months, 1000X.

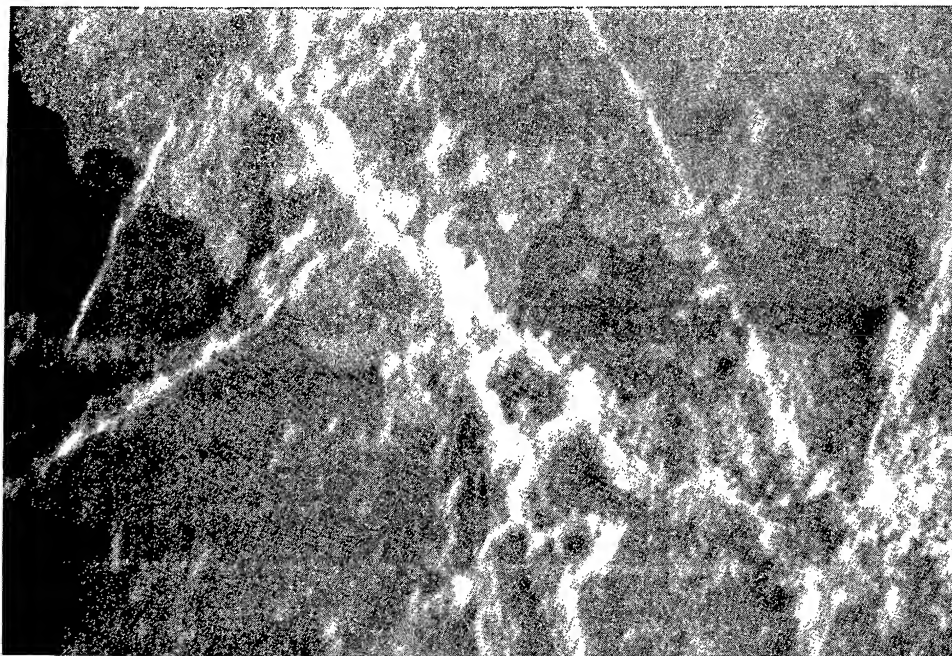


Figure 17. Photomicrograph of Fungi on Surface of Mylar Exposed at McKenzie Forest for 7 Weeks, 665X.

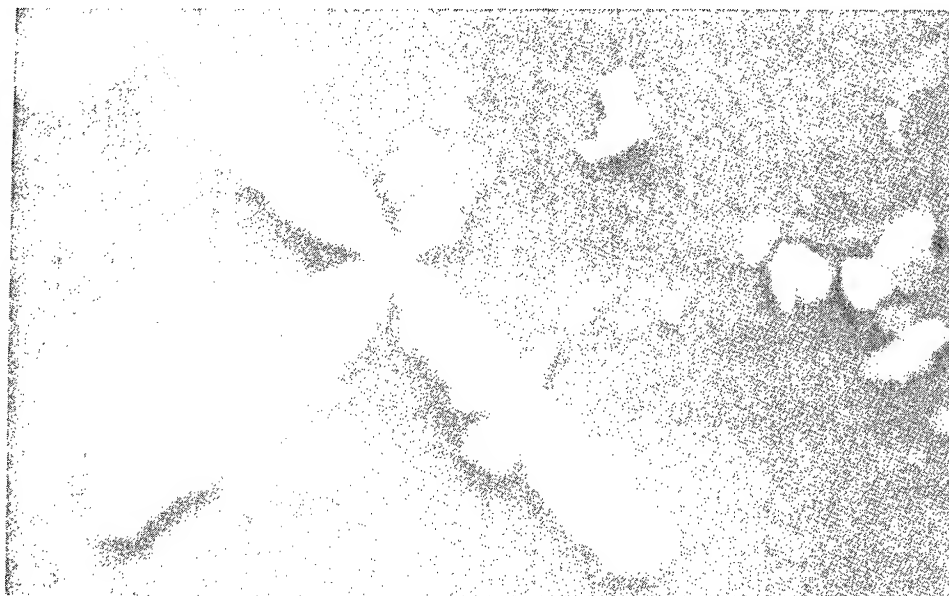


Figure 18. Photomicrograph of Salt Inside Surface of Mylar Exposed at Fort Sherman Open Site for 2 Weeks, 1800X.

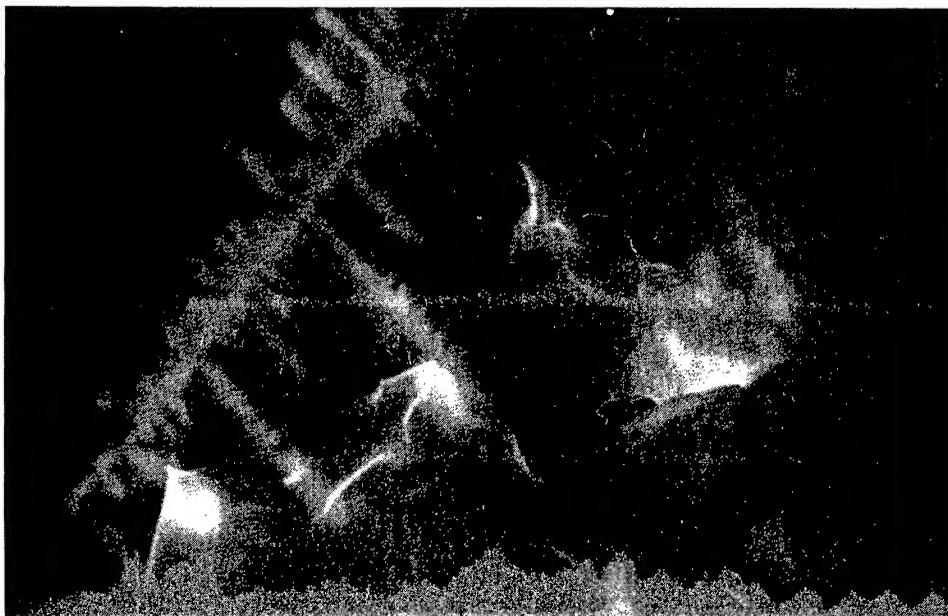


Figure 19. Photomicrograph of Salt Inside the Surface of Cellulose Acetate Exposed at Key West for 12 Weeks, 1560X.

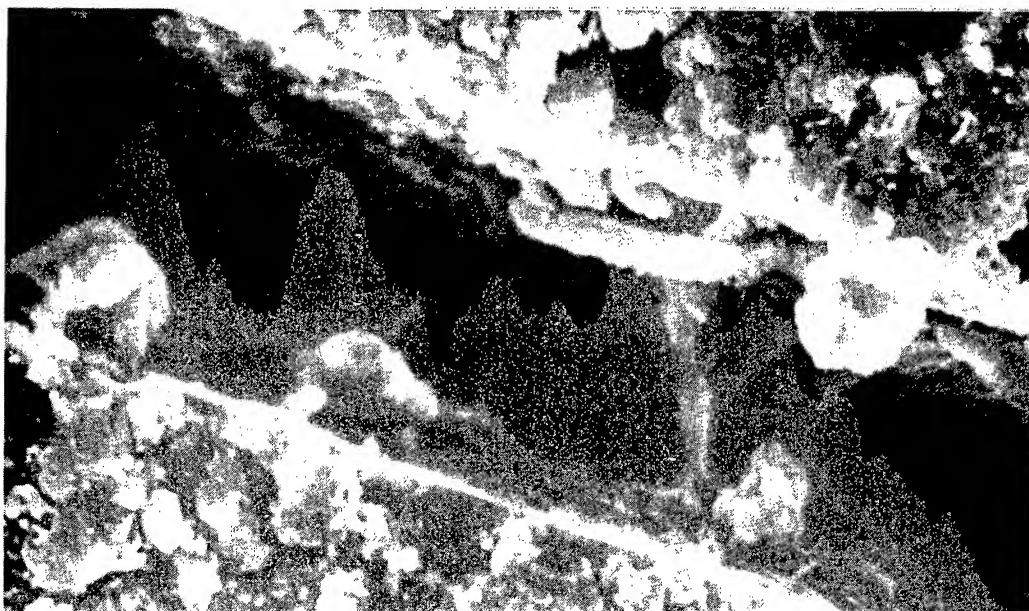


Figure 20. Photomicrograph of Surface Deterioration to Latex Exposed at Quinault for 7 Months, 1000X.

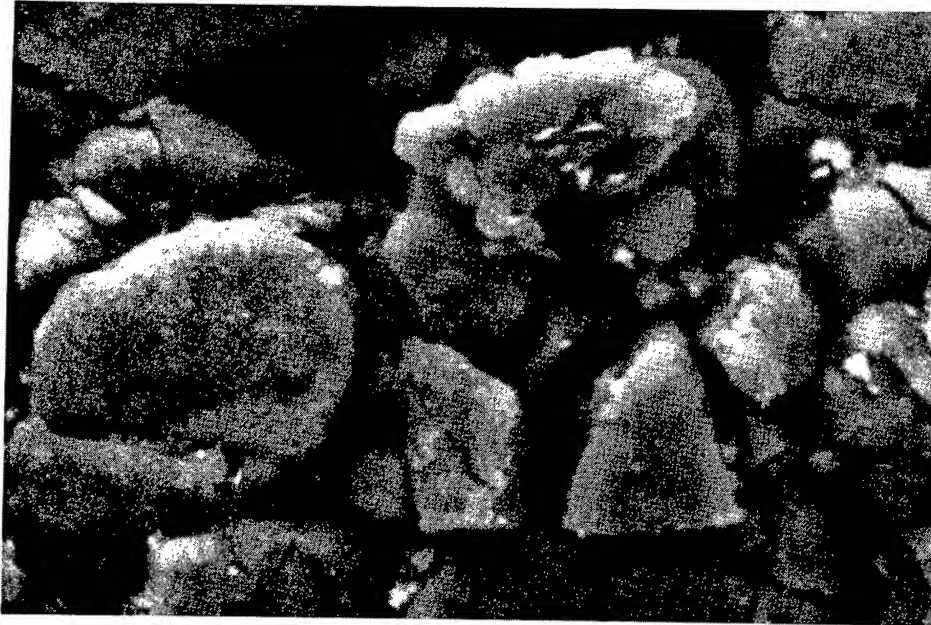


Figure 21. Photomicrograph of Surface Deterioration to Latex
Exposed at Ft Sherman Coastal Site for 2 Weeks,
378X.

On occasion, unknown substances can be seen on exposed items. These substances, presumably of a biological nature, were found on POL tank fabrics exposed at the Fort Sherman Coastal Exposure Site for 2 weeks (figure 22). Phenomena of this nature are rarely encountered in samples exposed at CONUS Sites.

In conclusion, we are finding that some basic materials deteriorate at CONUS sites at rates similar to the deterioration rates found at sites in the tropics, although the deterioration mechanisms may be different. Future studies will index the severity of different mechanisms, develop a predictive model for material deterioration, and attempt to determine a valid procedure to predict materiel performance in the tropics using data obtained in CONUS.

REFERENCES:

1. Dobbins, D. A., and Downs, G. F. Laboratory Versus Field Tests: A Limited Survey of Materials and Deterioration Studies. Canal Zone: US Army Tropic Test Center, TECOM Project No. 9-CO-009-000-021, July 1973.



Figure 22. Photomicrograph of Unknown Substance on Surface of POL Tank Fabric Surface Exposed at Fort Sherman Coastal Site for 2 Weeks, 3850X.

2. Downs, George F., and Lawson, W. F. Determination of Optimum Tropic Storage and Exposure Sites Report I: Survey of Programs on Tropic Materials Research. Canal Zone: US Army Tropic Test Center, TECOM Project No. 9-CO-009-000-006, AD A005 016, April 1973.

3. Downs, George F., and Gorak, Robert J. Methodology Investigation: Exposure/Performance Tests of Selected Materiel Items. Canal Zone: US Army Tropic Test Center, TECOM Project No. 7-CO-RD5-TT1-016, January 1979.

4. Portig, W. H., Bryan, J. C., and Dobbins, D. A. Determination of Optimum Tropic Storage and Exposure Sites. Phase II: Patterns and Predictions of Tropic Materials Deterioration. Canal Zone: US Army Tropic Test Center, TECOM Project No. 9-CO-009-000-005, AD A005 018, May 1974.

5. Sprouse, J. F., Neptune, M. D., and Bryan, J. C. Determination of Optimum Tropic Storage and Exposure Sites, Report II, Empirical Data. Canal Zone: US Army Tropic Test Center, TECOM Project No. 9-CO-009-000-006, AD A005 017, March 1974.

6. US Army Tropic Test Center. Materiel Testing in the Tropics. TECOM Project No. 9-CO-150-000-099, Fort Clayton, Canal Zone, April 1979.

*CHEN and SEEMULLER

DETECTION OF SIGNAL SIGNATURES
OF CARTOGRAPHIC FEATURES

*PI-FUAY CHEN, DSC
WILLIAM W. SEEMULLER, PHD
U.S. ARMY ENGINEER TOPOGRAPHIC LABORATORIES
FORT BELVOIR, VA 22060

Currently photo interpretation and terrain image identification for military applications is performed manually. This work is time consuming and costly. The work described below is a first step to aiding or semi-automating some of these labor intensive tasks.

A semi-automated technique for extracting a selected set of cartographic features such as, road intersections, straight line roads, and rectangular objects from aerial photographs was recently developed at the U.S. Army Engineer Topographic Laboratories (USAETL) using the Walsh transform. The discrete function (Walsh) transform was chosen because of its simplicity (Walsh functions are only two-valued) resulting in simple implementation, and because Walsh functions conform to the selected set of the cartographic features. Since the Walsh transform coefficients were produced by using Walsh functions having alternate magnitudes (either +1 or -1) at different sequences, the Walsh transform coefficients are also decomposed spectral components of the signal signature of the input aerial photographic images.

The technique was investigated in two ways as follows:
(1) Using a 32-by 32-element solid state sensor array to convert aerial imagery into an electronic signal which was processed in a minicomputer to yield Walsh transforms of the image [1]. (2) A prototype image spectrum analyzer (PISA) was developed which utilizes a large size plasma discharge device (8.5-by 8.5-inch illuminating area with 512 electrodes each in both x and y directions) to generate two-dimensional Walsh function patterns, and produce 512 by 512 Walsh coefficients in 14 seconds [2]. The PISA produced successful results

*CHEN and SEEMULLER

for a selected set of targets representing man-made cartographic features of the type stated above. The sensor array-minicomputer system provides a variable image threshold which results in better control of the input images. The cartographic features as described with background scenes and noise were extracted successfully from aerial imagery.

The sensor array-minicomputer system described in [1] was further expanded to incorporate a classification scheme to become a semi-automated cartographic feature extraction and recognition system. This paper describes this experimental system which was implemented with a solid state sensor array as an opto-electronic converter, a minicomputer as a signal processor to perform the functions of feature extraction and recognition, and a computer-controlled translational stage as the imagery holder. Successful extraction and recognition results for the selected set of cartographic features using this experimental system are presented. An alternate method for detecting the decomposed signal signatures representing cartographic features using analog signal processors is briefly described, and conclusions are given.

SYSTEM CONFIGURATION

A system that will produce signal signatures from the grey-shade distribution of a photo transparency in a short time and with recognizable resolution was developed. The block diagram of such a system is shown in Figure 1.

A 9- by 9-inch aerial transparency is illuminated by a white light source, and a section of the image is projected on a Reticon 32- by 32-element solid state array with a lens. The array converts the optical energy of the image into a video signal. The array timing and video signals, after being conditioned and digitized by the computer interface are sliced by the Hewlett-Packard (HP) 2100 minicomputer into two values, "on" and "off." The threshold value of the slicing is variable, which provides a very convenient means for isolating signals representing the selected feature image from the unwanted background noise. The "on" value of the video is arbitrarily set to "100" and "off" to "0," and the quantized image is printed by a line printer as a two-dimensional binary array of 32 by 32 pixels that represent the spatial signal signature of the selected topographic features. The sliced signal is transformed into a 32 by 32 Walsh matrix with a conventional Walsh transform algorithm in the computer. This algorithm implements the two-dimensional discrete Walsh transform [3],

*CHEN and SEEMULLER

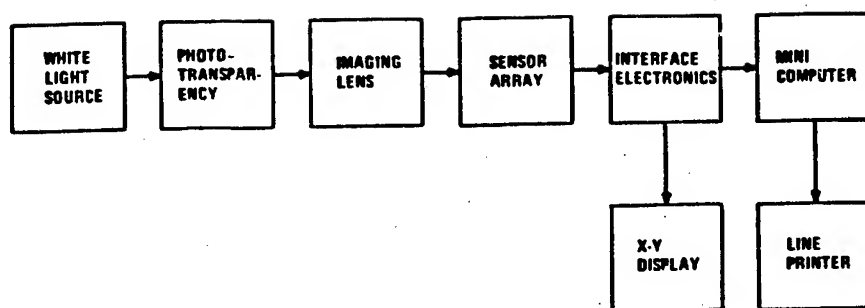


Figure 1. System Block Diagram

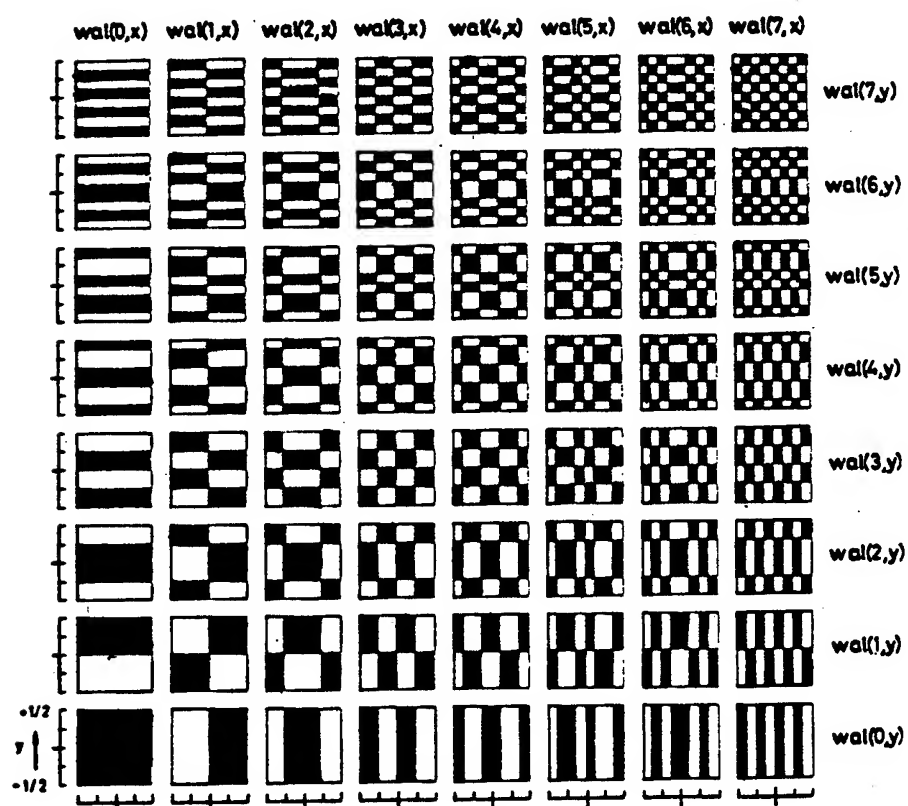


Figure 2. First 8-by 8-Order, Two-Dimensional Walsh Functions

$$A(i,j) = \frac{1}{1024} \sum_{x=1}^{32} \sum_{y=1}^{32} f(x,y) \text{Wal}(i,x) \text{Wal}(j,y)$$

where $f(x,y)$ is the image binary array, $\text{Wal}(i,x) \text{Wal}(j,y)$ is the two-dimensional Walsh function of order i and j , and x,y,i , and j take values from 1 through 32. By sequentially changing the order of the Walsh function, the complete set (32 by 32) of the Walsh transform coefficients was obtained. The Walsh functions used are permanently stored in the minicomputer. Figure 2 shows the first 8 by 8 order, two-dimensional Walsh functions in the x and y ranges of $-\frac{1}{2}$ to $+\frac{1}{2}$. The black areas indicate +1 in magnitude, and white -1.

Since the Walsh transform coefficients are produced by using Walsh functions having spatially alternating magnitudes (from +1 to -1) at different sequences, the Walsh transform coefficients represent the decomposed spectral components of the signal signature of the input signal. These spectral components were divided by a convenient constant, in this case 1,024, which is the number of pixels in a frame for normalization purposes. The entire normalized set of the spectral components was printed out by the line printer.

A detection scheme was implemented based on the uniqueness of the Walsh transform of each feature under consideration. At first a reference signal signature was established for each cartographic feature of the entire selected set. The test imagery after being transformed into the Walsh domain was then compared to each reference signal signature sequentially, and classification was made. Since cartographic features may appear in a variety of locations in the window of inspection (for this case, the active surface of the solid state array), and because Walsh transforms are neither translationally nor rotationally invariant, two or more reference signal signatures are required for each class of cartographic feature to avoid misclassification. With this modification, four classes out of the entire seven cartographic feature classes selected were recognized without error regardless of their location with respect to the window. The rest of the features were also classified correctly in the majority of locations. However, misclassification occurred when these feature classes were located very close to the corners of the window. Both the magnitude of a single Walsh transform coefficient (or the sum of a row or column of the transform coefficients), and the ratio of each significant coefficient to $A(1,1)$ or $A(2,1)$ or $A(3,1)$ were used as reference signal signatures for classification. At the end of each classification, the translational stage was automatically moved a predetermined number of steps in the x and y directions, and the new

segment of the test image was projected on the surface of the array. The same procedure described above was repeated.

EXPERIMENTAL RESULTS

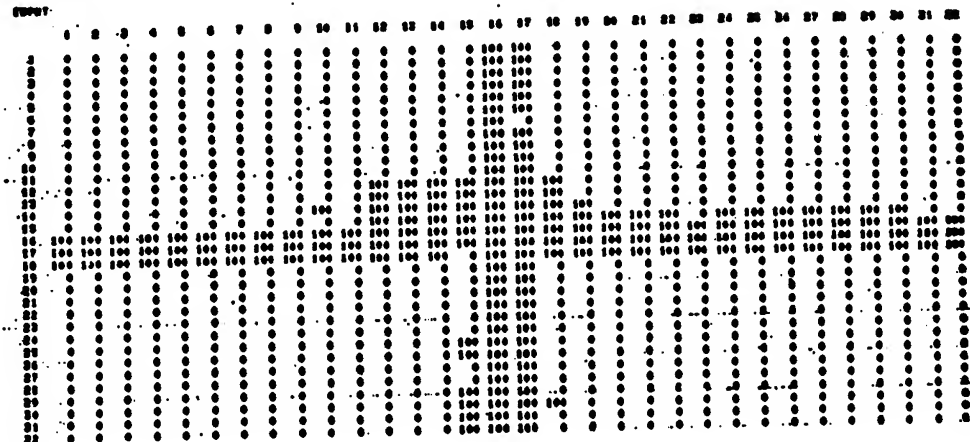
A selected set of images containing man-made cartographic features such as, road intersections, straight line roads, and rectangular objects from an aerial photo transparency and a few mask patterns were used as input test patterns for the system. The spatial signal signatures, the associated Walsh transforms (decomposed spectral signal signatures) and the classification results are shown for each of the test images. Figures 3 through 6 indicate the results for a road intersection, a horizontal line road, a vertical line road, and a rectangular object. These cartographic features were placed at various positions with respect to the window of inspection. They were detected and classified correctly regardless of their location with respect to the window. The results for these different positions are not shown because of the limited paper size. Figure 7 shows the detection results for a diagonally oriented road intersection. It is found that the correct classification was obtained for a majority of feature locations with respect to the window. However, it was misclassified as a diagonally oriented line road only when the center of the diagonally oriented road intersection was positioned against four corners of the window (not shown). This is because the energy contributed by one branch of the diagonally oriented road intersection is much stronger than that of the other branch. Figures 8 and 9 are the results of the classification for the diagonally oriented line roads having 45- and 135-degree angles with respect to the x-axis of the window. They are recognized correctly in a majority of locations. It was noted that these roads were not recognized when they moved towards the corners of the window (not shown). A few other aerial photo-transparencies containing relatively complicated scenes were also tried. Most of them were recognized correctly, while some were misclassified, or were not recognized. The results are not shown, in the interest of brevity. The overall results indicate that the Walsh transform processing technique is quite successful for detecting well-defined linear man-made cartographic features. Nearly 90 percent recognition accuracy was obtained for a set of selected cartographic features of the classes described. A rotational dimension may be incorporated in the future to refine the method for detecting the above cartographic features at various angles with respect to the axes of the window.

This system or feature extractor will be integrated in parallel with other feature extractors which are to be developed in the future

*CHEN and SEEMULLER

MAY 16 1979 8:42

REPORT



MAY 16 1979 8:44

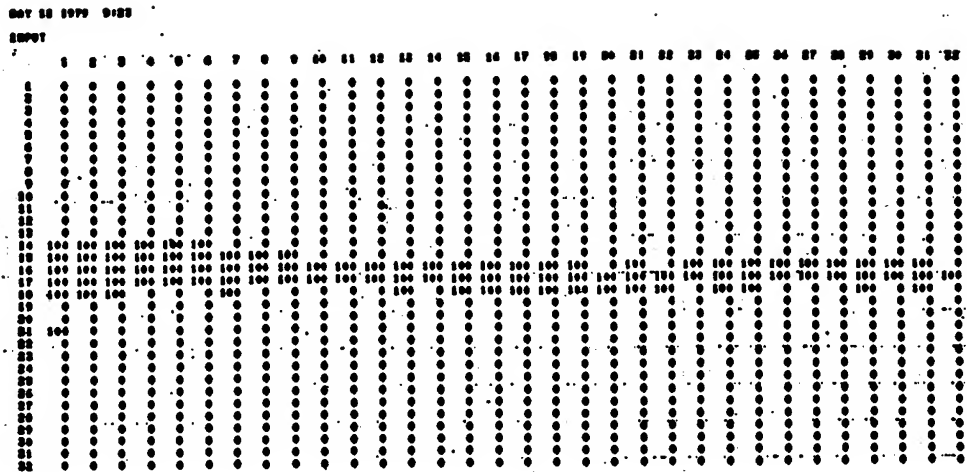
TRANSFORM

	1	2	3	4	5	6	7	8	9	10	11	12	13	14	15	16
1	18	0	-8	-1	7	0	-7	0	5	0	-5	0	6	0	-6	0
2	0	0	-1	0	0	0	0	0	-1	0	0	1	0	0	0	0
3	-11	0	0	0	0	0	0	0	2	1	-1	-1	1	0	0	-1
4	-1	0	3	1	-1	0	2	0	0	0	0	0	0	0	1	0
5	11	0	0	0	0	0	0	0	0	0	0	0	0	0	0	0
6	0	0	-1	0	0	0	0	0	0	0	0	0	0	0	0	0
7	-10	0	0	0	0	0	0	0	1	0	-1	0	1	0	0	0
8	0	0	1	0	0	0	1	0	0	0	0	0	0	0	0	0
9	8	-1	1	0	-1	0	1	0	0	1	0	0	0	0	0	0
10	-3	-1	1	0	0	0	0	0	0	0	0	0	0	0	0	0
11	-8	2	-1	0	1	0	-1	0	0	0	0	0	0	0	0	0
12	2	1	0	0	0	0	0	0	-1	0	0	0	0	0	0	0
13	9	-1	1	0	-1	0	0	0	-1	0	0	0	0	0	0	0
14	-1	0	0	0	0	0	0	0	0	0	0	0	0	0	0	0
15	-9	0	0	0	0	0	0	0	0	0	0	0	0	0	0	0
16	2	0	0	0	0	0	0	0	0	0	0	0	0	0	0	0

ROAD INTERSECTION

Figure 3. Spatial Signal Signature, Walsh Transform, and Classification Result for Road Intersection.

* CHEN and SEEMULLER



MAY 15 1979 9:23

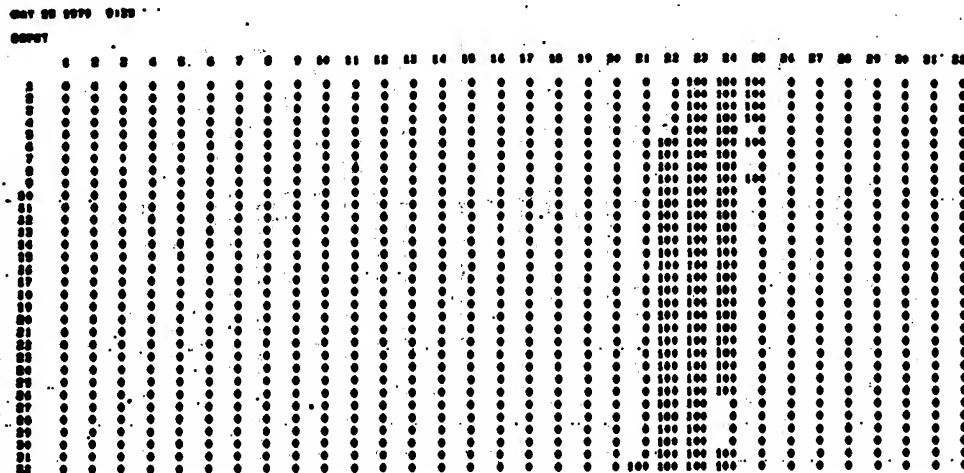
TRANSFORM

	1	2	3	4	5	6	7	8	9	10	11	12	13	14	15	16
1	9	1	1	1	0	0	0	0	0	0	0	0	0	0	0	0
2	0	1	1	0	0	0	0	0	0	0	0	0	0	0	0	0
3	-9	-1	-1	-1	0	0	0	0	0	0	0	0	0	0	0	0
4	0	-1	-1	0	0	0	0	0	0	0	0	0	0	0	0	0
5	8	1	0	1	0	0	0	0	0	0	0	0	0	0	0	0
6	0	2	1	0	0	0	0	0	0	0	0	0	0	0	0	0
7	-8	-1	0	-1	0	0	0	0	0	0	0	0	0	0	0	0
8	0	-2	-1	0	0	0	0	0	0	0	0	0	0	0	0	0
9	7	0	0	0	0	0	0	0	0	0	0	0	0	0	0	0
10	-1	0	0	0	0	0	0	0	0	0	0	0	0	0	0	0
11	-7	0	0	0	0	0	0	0	0	0	0	0	0	0	0	0
12	1	0	0	0	0	0	0	0	0	0	0	0	0	0	0	0
13	8	0	0	0	0	0	0	0	0	0	0	0	0	0	0	0
14	-1	0	0	0	-1	0	0	0	0	0	0	0	0	0	0	0
15	-8	0	0	0	0	0	0	0	0	0	0	0	0	0	0	0
16	1	0	0	0	1	0	0	0	0	0	0	0	0	0	0	0

HORIZONTAL LINE ROAD

Figure 4. Spatial Signal Signature, Walsh Transform, and Classification Result for Horizontal Line Road.

*CHEN and SEEMULLER



MAY 15 1979 9:36

TRANSFORM

	1	2	3	4	5	6	7	8	9	10	11	12	13	14	15	16
1	9	-9	-8	8	-9	9	8	-8	3	-3	-2	2	-3	3	2	-2
2	0	0	0	0	0	0	0	0	1	-1	0	0	-1	1	0	0
3	0	0	1	-1	0	0	-1	1	0	0	0	0	0	0	0	0
4	0	0	0	0	0	0	0	0	1	-1	0	0	-1	1	0	0
5	0	0	0	0	0	0	0	0	0	0	0	0	0	0	0	0
6	0	0	0	0	0	0	0	0	0	0	0	0	0	0	0	0
7	0	0	0	0	0	0	0	0	0	0	0	0	0	0	0	0
8	0	0	0	0	0	0	0	0	0	0	0	0	0	0	0	0
9	0	0	0	0	0	0	0	0	0	0	0	0	0	0	0	0
10	0	0	0	0	0	0	0	0	0	0	0	0	0	0	0	0
11	0	0	0	0	0	0	0	0	0	0	0	0	0	0	0	0
12	0	0	0	0	0	0	0	0	0	0	0	0	0	0	0	0
13	0	0	0	0	0	0	0	0	0	0	0	0	0	0	0	0
14	0	0	0	0	0	0	0	0	0	0	0	0	0	0	0	0
15	0	0	0	0	0	0	0	0	0	0	0	0	0	0	0	0
16	0	0	0	0	0	0	0	0	0	0	0	0	0	0	0	0

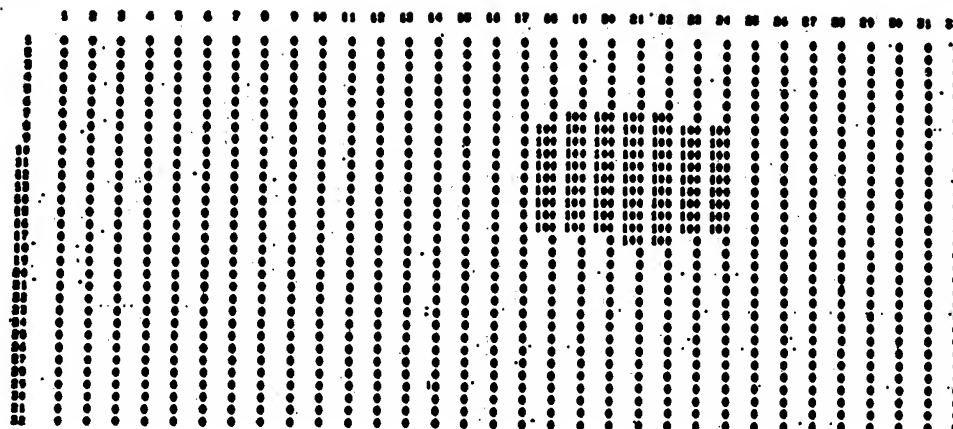
VERTICAL LINE ROAD

Figure 5. Spatial Signal Signature, Walsh Transform, and Classification Result for Vertical Line Road.

*CHEN and SEEMULLER

MAY 05 1979 20: 4

INPUT



MAY 15 1979 10: 4

TRANSFORM

	1	2	3	4	5	6	7	8	9	10	11	12	13	14	15	16
1	6	-6	-6	6	-1	1	1	-1	-1	1	1	-1	0	0	0	0
2	6	-6	-6	6	0	0	0	0	-1	1	1	-1	-1	1	1	-1
3	-4	4	4	-4	0	0	0	0	0	0	0	0	0	0	0	0
4	-4	4	4	-4	0	0	0	0	0	0	0	0	0	0	0	0
5	0	0	0	0	0	0	0	0	0	0	0	0	0	0	0	0
6	-1	1	1	-1	0	0	0	0	0	0	0	0	0	0	0	0
7	-1	1	1	-1	0	0	0	0	0	0	0	0	0	0	0	0
8	0	0	0	0	0	0	0	0	0	0	0	0	0	0	0	0
9	1	-1	-1	1	0	0	0	0	0	0	0	0	0	0	0	0
10	0	0	0	0	0	0	0	0	0	0	0	0	0	0	0	0
11	0	0	0	0	0	0	0	0	0	0	0	0	0	0	0	0
12	1	-1	-1	1	0	0	0	0	0	0	0	0	0	0	0	0
13	0	0	0	0	0	0	0	0	0	0	0	0	0	0	0	0
14	-1	1	1	-1	0	0	0	0	0	0	0	0	0	0	0	0
15	-1	1	1	-1	0	0	0	0	0	0	0	0	0	0	0	0
16	0	0	0	0	0	0	0	0	0	0	0	0	0	0	0	0

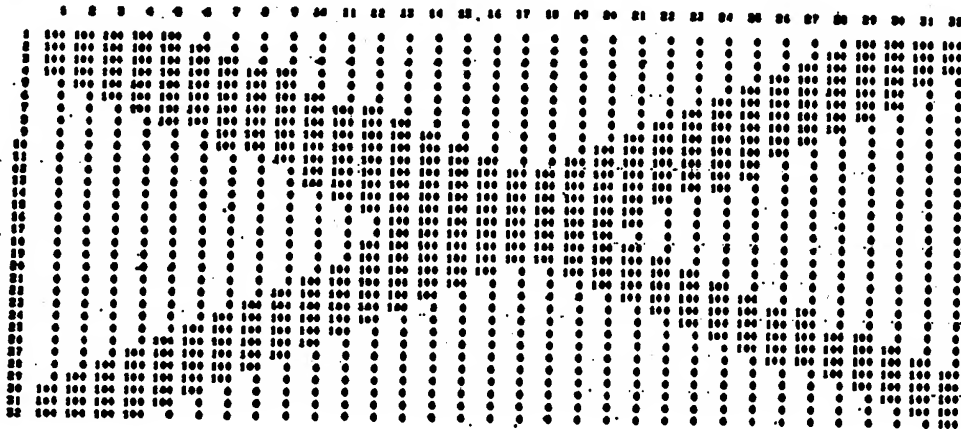
RECTANGULAR OBJECT

Figure 6. Spatial Signal Signature, Walsh Transform, and Classification Result for Rectangular Object.

*CHEN and SEEMULLER

MAY 15 1979 00:12

INPUT



MAY 15 1979 10:31

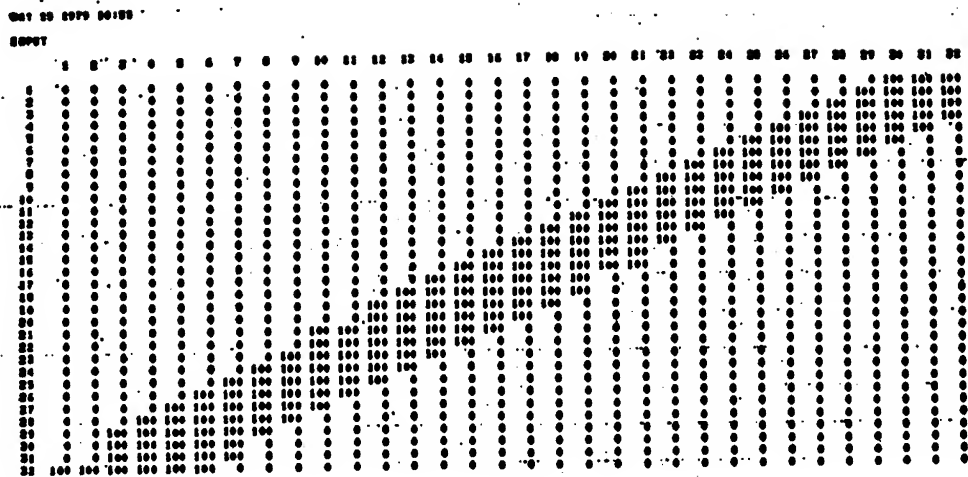
TRANSFORM

	1	2	3	4	5	6	7	8	9	10	11	12	13	14	15	16
1	37	2	-1	-1	-3	0	0	-1	-2	0	0	0	-2	0	0	0
2	5	0	-1	0	-1	0	0	0	0	0	0	0	0	0	0	0
3	0	2	27	1	0	-4	4	0	0	0	-8	0	0	0	0	0
4	0	0	2	0	-2	0	0	1	0	0	-1	1	0	0	0	0
5	-4	0	0	4	17	0	0	0	-2	0	0	-2	8	0	0	0
6	0	-1	3	-1	0	-1	0	0	0	1	-1	1	0	0	0	0
7	0	1	3	0	0	2	9	0	1	-2	2	0	0	0	2	0
8	1	0	1	0	2	0	-1	-1	0	2	0	0	0	0	0	0
9	-2	0	0	-1	-2	0	-1	2	3	0	0	1	-1	0	0	0
10	0	0	0	0	0	0	1	-3	-1	-1	1	0	0	0	0	0
11	0	0	-7	0	0	1	2	0	0	0	1	0	0	0	0	0
12	0	0	0	0	1	-2	0	0	0	-2	0	0	1	1	0	0
13	-3	0	0	1	8	0	0	0	-1	0	-1	-1	1	0	0	0
14	0	0	1	0	1	0	0	0	0	0	-1	-1	0	1	0	0
15	0	0	2	0	0	0	2	0	0	0	0	0	0	0	-1	0
16	0	0	0	0	0	0	0	0	0	0	0	0	-1	0	0	2

DIAGONALLY ORIENTED ROAD INTERSECTION

Figure 7. Spatial Signal Signature, Walsh Transform, and Classification Result for Diagonally Oriented Road Intersection.

*CHEN and SEEMULLER



MAY 15 1979 10:56

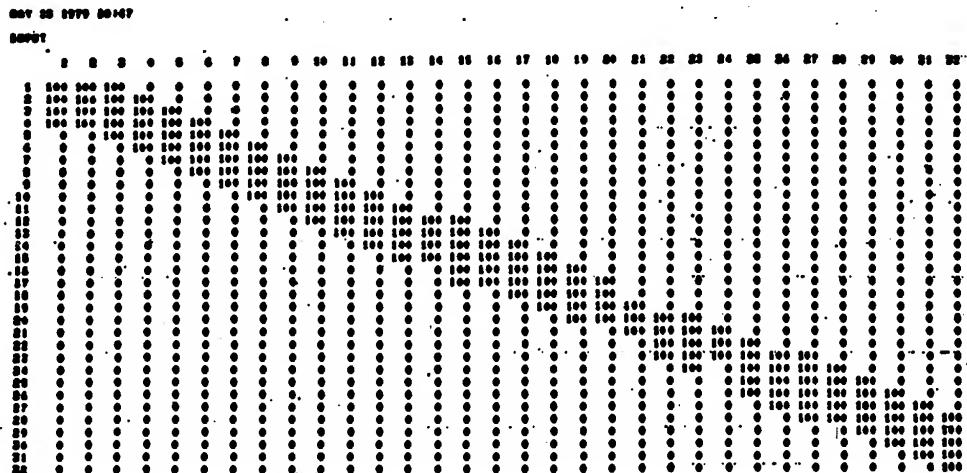
TRANSFORM

	1	2	3	4	5	6	7	8	9	10	11	12	13	14	15	16
1	18	0	-2	0	-1	-1	-2	-1	0	0	0	0	0	0	-1	0
2	0	-16	2	0	0	3	2	0	0	2	0	0	0	2	0	0
3	-1	1	14	0	-3	-3	2	0	0	0	-3	0	-1	0	1	0
4	0	-1	0	-12	4	0	0	0	0	0	0	4	1	0	0	0
5	0	0	0	3	9	-1	-2	-1	-1	0	-1	-1	4	-1	-1	0
6	0	2	-2	-2	0	-7	2	0	0	2	2	1	0	0	1	0
7	0	1	3	0	-1	0	5	-2	-1	-2	1	0	0	0	0	0
8	0	-1	0	0	0	-1	0	-3	2	0	0	0	0	0	0	0
9	0	0	0	0	0	0	0	1	2	0	0	0	0	0	0	0
10	0	1	0	0	0	1	-1	-1	1	-2	0	0	0	0	0	0
11	0	0	-2	0	0	1	1	0	0	0	1	0	0	0	0	0
12	0	0	0	3	-1	0	0	0	0	0	0	-1	-1	0	1	0
13	0	0	0	1	3	0	-1	0	0	0	0	-1	0	1	0	0
14	0	1	-1	0	0	-2	0	0	0	0	0	0	0	0	-1	0
15	0	0	2	0	0	0	1	0	0	0	0	0	0	0	0	2
16	0	0	0	0	0	0	0	0	0	0	0	0	0	0	-1	0

DIAGONALLY ORIENTED LINE ROAD, 45 DEGREES

Figure 8. Spatial Signal Signature, Walsh Transform, and Classification Result for Diagonally Oriented Line Road (45 Degrees).

*CHEN and SEEMULLER



MAY 15 1979 10:47

TRANSFORM

	1	2	3	4	5	6	7	8	9	10	11	12	13	14	15	16
1	14	0	0	0	0	0	0	0	0	0	0	0	0	0	0	0
2	1	13	-1	2	0	-1	0	0	0	-1	0	0	0	-1	0	0
3	-1	0	12	0	0	-1	2	0	-1	0	-1	0	0	0	1	0
4	0	0	1	10	-2	2	0	1	0	0	0	-2	-1	1	1	0
5	-1	0	-3	3	9	0	0	0	0	0	1	-1	3	0	0	0
6	1	-2	2	-1	1	8	0	1	0	0	-1	2	1	2	0	1
7	-1	1	1	0	-2	2	6	0	1	-1	1	0	0	0	1	0
8	0	0	0	0	1	0	1	5	-2	2	0	0	0	0	0	0
9	0	0	0	0	-1	0	-3	3	3	1	0	0	0	0	0	0
10	0	-1	0	1	0	-2	2	-1	1	2	0	0	0	-1	0	0
11	-1	1	-3	0	-1	1	1	0	0	0	2	0	0	0	0	0
12	0	0	0	-4	1	0	0	0	0	0	0	1	0	0	0	0
13	0	0	-1	1	3	0	0	0	0	-1	0	0	1	0	0	0
14	0	-2	0	0	0	2	0	1	-1	0	0	0	0	0	0	0
15	0	0	1	0	-1	0	1	0	0	0	1	0	0	0	0	-1
16	0	0	0	0	0	0	0	0	0	0	0	0	0	0	-1	0

DIAGONALLY ORIENTED LINE ROAD, 135 DEGREES

Figure 9. Spatial Signal Signature, Walsh Transform, and Classification Result for Diagonally Oriented Line Road (135 Degrees).

to become a total automated feature extraction system.

AN ALTERNATE DETECTION SCHEME

In this section, an alternate scheme for detecting the decomposed spectral components (or Walsh transform coefficients) using analog processors is described. In the scheme, two cascaded, 32-stage programmable, binary-analog correlators [4] are used as shown in Figure 10. In the previous section it was shown that the significant spectral components in most cases appear in the first 8 by 8 lower order Walsh transform coefficients. Thus, two cascaded, 32-stage, binary-analog correlators should be sufficient to process the important coefficients to yield recognizable results. The Walsh transform coefficients are connected to the input of the analog delay line, and the binary patterns that represent reference signal signatures will be connected to the input of the static shift register. Each stage of the analog delay line has a pair of taps. These taps have switches in series with them that are controlled by the true and complement outputs of the static digital shift register. By loading a binary word to it, the static shift register will select the taps, which are connected to two output lines, thus proving the ability to do correlation. By sweeping the known binary words at a megahertz rate, the Walsh coefficients representing a particular type of feature will be quickly detected in the output of the operational amplifier.

The system described in the previous sections can be replaced by using this suggested scheme together with a solid state array, a hardware Walsh function generator, and some minor interface and display electronics. Although the analog method is relatively compact, it is much less flexible than the digital method described earlier.

CONCLUSIONS

1. The signal signature of the spectrally decomposed cartographic features is much simpler in distribution than the spatial signal signature of the same cartographic feature for all selected cases.
2. In most cases, the significant spectral components are distributed among few lower order Walsh transform coefficients. Further, each transform pattern is unique in itself, and it can be easily distinguished from the rest.
3. One or more reference signal signatures were required for each class of the selected set of cartographic features since they may

*CHEN and SEEMULLER

appear in a variety of locations with respect to the window of inspection.

4. Four classes out of the entire seven cartographic feature classes selected were detected and recognized without error regardless of their locations with respect to the window. The rest of the feature classes were also classified correctly in a majority of locations. However, misclassifications occurred when these features were positioned very close to the corners of the window. Nearly 90 percent recognition accuracy was obtained for the selected set of the cartographic features.

5. The feature extraction scheme presented can also be implemented by using a group of analog signal processors together with the appropriate interfaces.

6. Image rotation may be incorporated in the future to refine the scheme for detecting these cartographic features at a variety of angles with respect to the axes of the window.

REFERENCES

- (1) P. F. Chen and W. W. Seemuller, "Signal Signatures of Topographic Features Using Analog Technology," USAETL Research Note No. ETL-0185, May 1979.
- (2) P. F. Chen, F. W. Rohde, and W. W. Seemuller, "Prototype Image Spectrum Analyzer (PISA) for Cartographic Feature Extraction," USAETL Research Note No. ETL-0204, Oct 1979.
- (3) H. F. Harmuth, "Sequency Theory, Foundation and Application," New York, Academic Press, Inc., 1977, pp 55-56.
- (4) V. Strasilla, "A Programmable Binary-Analog Correlator," Reticon Corporation, Sunnyvale, CA, Technical Note No. 106.

OPTICAL CORRELATION SEEKER (U)

CHARLES R. CHRISTENSEN, Dr.* and RICHARD L. HARTMAN, Dr.
RESEARCH DIRECTORATE, US ARMY MISSILE LABORATORY
US ARMY MISSILE COMMAND
REDSTONE ARSENAL, ALABAMA 35809

INTRODUCTION

A "super-smart weapon" which outperforms our smart weapons just going into the field, yet is much cheaper than those current systems? It sounds like the answer to the Army's prayer for a method to cope with a dramatically increasing threat. We think we have demonstrated the key ingredients of such a system, through the marriage of a long-term fundamental effort at the Missile Command, significant industrial developments, and recognition of how this developing technology can pay off for the Army.

Through the application of some recent existing developments in optical data processing, we can now propose to build a seeker which recognizes a tank by its image, homes on it, and destroys it. The seeker autonomously detects and locks on the target, provides guidance signals, reacquires if the target is lost, and re-targets if necessary. The sensor will fit in a submissile, weigh under a pound, consume less than a watt of power, and possibly even cost under \$100!

In this paper we will discuss the concept and its applications to set the stage for our interest. The bulk of the paper following will dwell on the technological advances we have made which make this concept feasible.

CONCEPT

The sections below will show how we have built an optical computer which can:

- o Autonomously acquire a target.
- o Provide guidance signals.
- o Discriminate.
- o Operate against a variety of predetermined targets.
- o Reacquire a temporary obscured target.

We will also show a significant development which will allow us to do this in a small inexpensive package.

Figure 1 demonstrates the operation of our laboratory computer. The image of the tank model is the desired target. The optical computer located this target in the input scene, and showed its location in the correlator output plane.

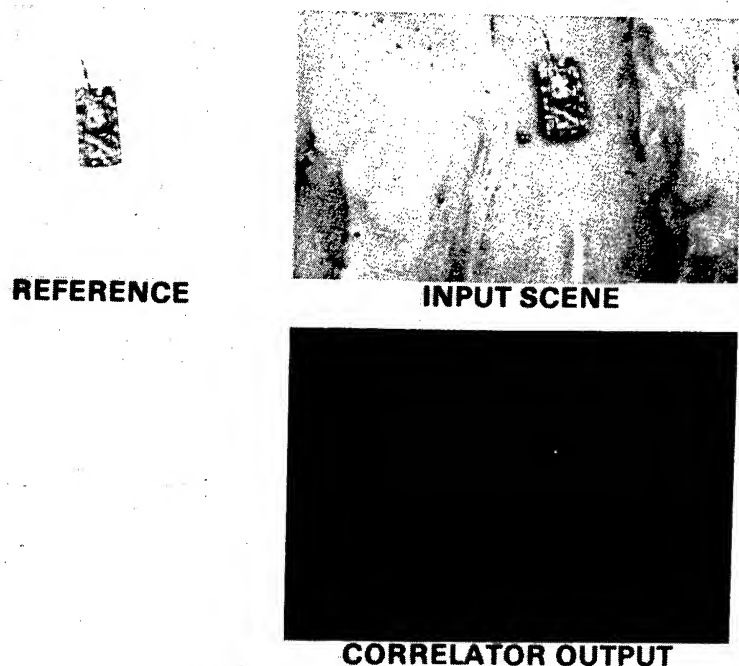


Figure 1. Demonstration of Optical Correlation

The optical computer could be used with any imaging sensor, such as radar, mm, or IR. But it has its greatest potential in a direct visible role, and we believe there are important applications in this role.

The conceptual seeker takes the form of Figure 2.

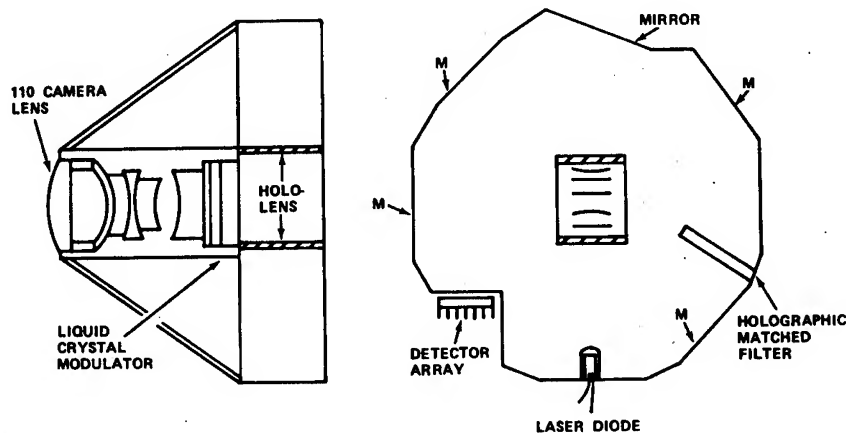


Figure 2. The Optical Correlator Seeker in a Visible Mode

This sensor is designed to correlate to a target from the top, as in Figure 3. It will recognize the target at any orientation, and operate over a wide span of distances to the target. It can recognize and discriminate between targets to about the same degree as a human can.

Unlike many other "top attack" sensors, the optical correlator does not need to search the field of view, or search the scene against the reference. This allows it the time to select targets of lesser value, or to pull a fly-out maneuver to look for targets, as in Figure 4.

The system could also perform some damage assessment, and retarget if possible, as in Figure 5. The high resolution allows us to detect smoke, flames, or debris flying off.

One application of our concept would be a guided mortar, such as GAMP. The guided mortar provides the infantry company with

tank killing firepower. The target probably will be acquired with the human eye, so the visible operation of the optical seeker should be acceptable. The optical computer can be configured to fit within an 81 mm package, and if cheap enough, could be widely distributed.

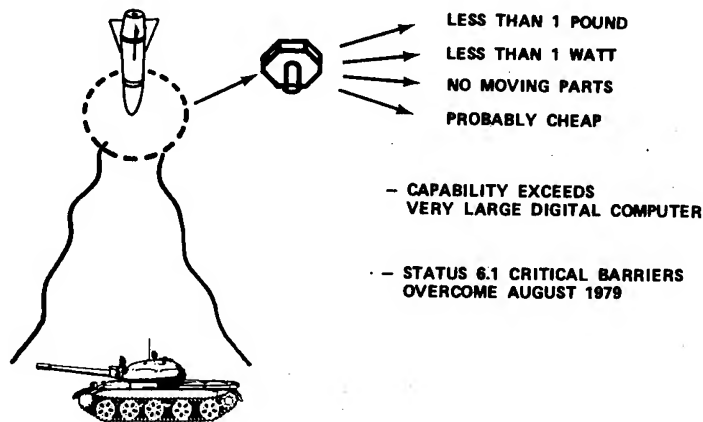


Figure 3. The Simplest Optical Correlator Seeker Works on a Top View

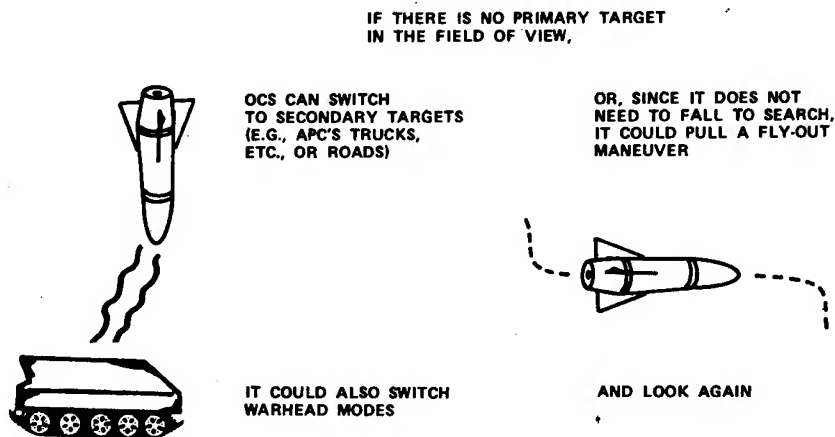


Figure 4. Alternate Targeting Mode

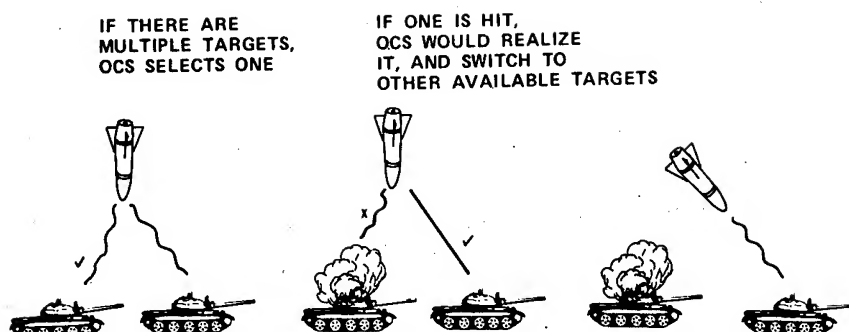


Figure 5. Damage Assessment/Detargeting

A top attack anti-tank missile is another role. Concepts (FFAST, Tank Breaker) using top attack are now popular, because of the vulnerability of the tank on top. In this concept a shoulder fired missile would pull a preprogrammed maneuver to fly a lofted trajectory, and then home on the top of the target.

The ASSAULT BREAKER concept, or Corps Support Weapon System, proposes to disperse submunitions over an area rich in targets. Coupled with long range target acquisition, this system would interdict fighting material on its way to the front.

In this role the exceptional computing power of the optical computer comes into its forte. This system automatically acquires and locks onto target. It can discriminate between targets of interest. It can search a stored reference target array, and select targets of highest value. It could go after tanks, trucks, buildings, roads, bridges, or whatever is deemed of value.

We optimistically expect that a given missile platform could carry more submunitions using this technology, yet at a greatly reduced cost. The higher versatility effectiveness of the optical system means it would be so effective that it would be worth having, even if it didn't work in fog. Inclusion of a few flares in the payload would provide for night-time operation. In Europe, morning fog can be quite prevalent, and last long enough for tactical use; but an interdiction role may allow early use of the weapon system or waiting a few hours for the right conditions.

COHERENT OPTICAL CORRELATION

Cross-correlation is a very effective method for recognizing images. The advantages of using optical processing for cross-correlation are due to the large information handling capacity of optical systems. A modest system can process scenes having over 10^7 resolution elements. Such a system handles two-dimensional data isotropically and in parallel with the processing time determined by the time required for data input and output. The large capacity of optical storage media can be used to provide rapid access to a large number of reference images.

The cross-correlation function is defined as

$$R_{fg}(\eta, \xi) = \int_0^\infty \int_0^\infty f(x, y) g(x - \eta, y - \xi) dx dy. \quad (1)$$

In this equation, $f(x, y)$ describes a signal image (the real-time scene), and $g(x, y)$ describes a reference (the desired target). $R_{fg}(\eta, \xi)$ then describes how well the two match, and the location of a target in the scene.

This cross-correlation can be calculated through the use of Fourier transforms,

$$R_{fg}(\eta, \xi) = \int_{-\infty}^{\infty} \int_{-\infty}^{\infty} F(p, q) G^*(p, q) \exp \left[-i(p\eta + q\xi) \right] dp dq \quad (2)$$

where the Fourier transform of $f(x, y)$ is defined as

$$F(p, q) = \mathcal{F}[f(x, y)] = \iint f(x, y) \exp \left[-i(px + qy) \right] dx dy, \quad (3)$$

and G^* is the complex conjugate of the Fourier transform of $g(x, y)$.

To implement (2) using optical techniques, an optical system such as the one shown in Figure 6 is used. The reference scene $g(x, y)$ is placed in the front focal plane of the lens L_1 and illuminated by coherent light; the Fourier transform $G(p, q)$ appears in the back focal plane. As can be seen in Figure 6, a reference beam is used to holographically record G , i.e., the amplitude and phase of G are recorded. The input can now be changed to $f(x, y)$

as shown in Figure 6(b). The hologram in the back focal plane of $L1$ diffracts the product of Fourier transforms FG^* along the optical axis of $L2$. The lens $L2$ forms the inverse Fourier transform, i.e., $R(\eta, \xi)$ in its back focal plane.

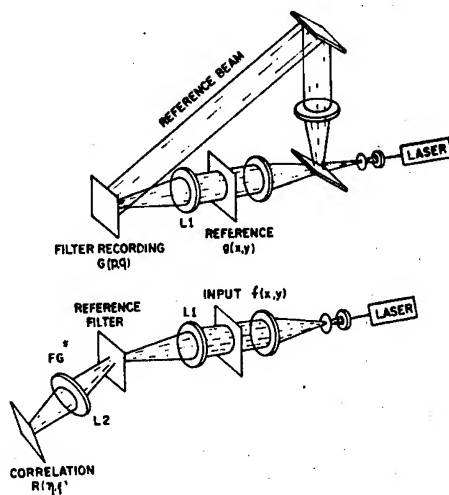


Figure 6. The Optical Correlator

This process was demonstrated above in Figure 1. The image of a tank model was used to form the reference filter as illustrated in Figure 1(a). This reference filter was matched against the input scene containing the tank as shown in Figure 1(b). The correlator input, a spot of light in a dark background, is shown in Figure 1 at the same scale as the input scene. The presence of the correlation spot identifies that the tank in the input scene is the same as the reference and the location of the spot designates the location of the tank in the scene. The small size of the correlation spot indicates the precision with which the tank can be located. A measure of this precision, the half-width at half-height of a trace through the correlation, was $1/12$ of the tank width in this example; and the signal/noise limited accuracy was $1/50$ of the tank width.

The laboratory correlator used in these experiments has been described previously (1). A major breakthrough a few years ago

was the development of real-time data input through use of a liquid crystal light valve (2,3). MICOM participated in the funding of this development. The light source is a He-Ne laser operating at 633 nm or a GaAlAs diode injection laser operating at 820 nm. Reference filters are recorded on photographic plates with a He-Ne laser. When correlating with a diode laser source, a scale change of the input image is required to compensate for the change in wavelength from that used in filter recording.

Composite Filter

Earlier attempts at correlation guidance were sensitive to angular orientation. Filter multiplexing was tried as a way to solve this problem (4-5). Several reference filters, each of a different perspective of the vehicle, were recorded at the same spatial location in the Fourier transform plane. The exposure time of each of the N multiplexed filters was T/N , where T is the exposure time for a single reference filter. Since only vehicle recognition and location is required, the correlation functions of the superimposed filters coincide in the output plane.

Figure 7 shows a polar plot of the relative correlation peak amplitude for an eight-fold multiplexed filter. Images of the vehicle are displayed around the polar plot in Figure 7 to aid in visualization. Arrows on the graph indicate the orientation used in recording the eight superimposed filters. The single reference filter produced a correlation peak whose amplitude remained above 40% of its maximum over a 50° angular change. The eight-fold multiplexed filter demonstrated similar performance over 360° . This technique has solved the angular orientation problem.

A four-fold multiplexed filter demonstrated similar performance but the correlation peak dipped below 40% of the maximum value at two orientations. The choice of different recording positions and adjustment of individual filter exposure levels could make the angular response curve much more uniform.

A similar experiment successfully compensated for angle-of-view change in elevation. The technique of multiplexing is expected to work equally well for change of scale to operate over a variety of ranges to the target.

Discrimination

Does multiplexing destroy the filter's capacity to

discriminate between various objects? A simple test was performed to compare the ability of the filter to discriminate against a different model. The results of this test are shown in Figure 8, where a single TV line through the correlation peak is displayed for the case when the input image was Model A and when the image was Model B. Model B was used to construct the filters.

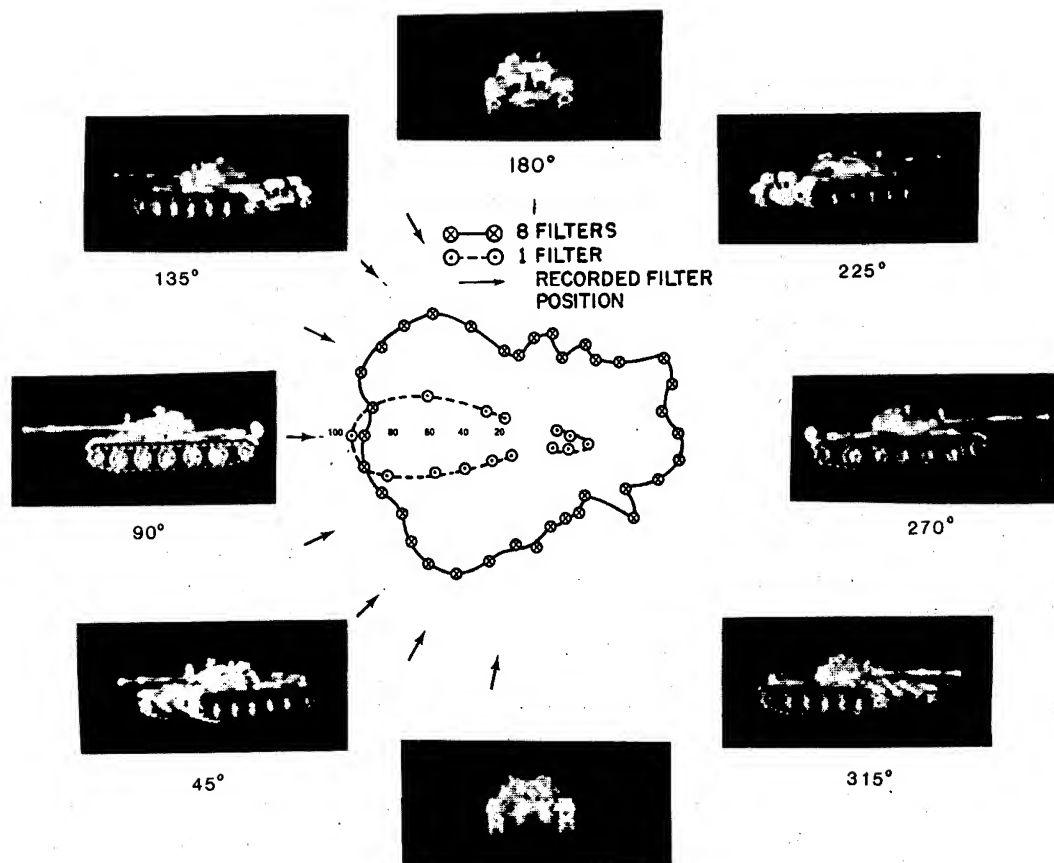


Figure 7. Correlation at any Aspect Angle with Multiplex Filter

The maximum peak amplitude for the eight-fold multiplex filter was unexpectedly high: one-fourth the amplitude obtained when using a single filter. Linear recording theory predicts that the correlation peak should drop to $1/N^2$ of that of a single filter for single filter contributions, or to $1/N$ of that of a single filter for simultaneous filter contributions (N is the number of superimposed

filters). The abnormally large correlation peak amplitude may be the result of nonlinear recording and in-phase amplitude addition of the correlation peaks from individual filters.

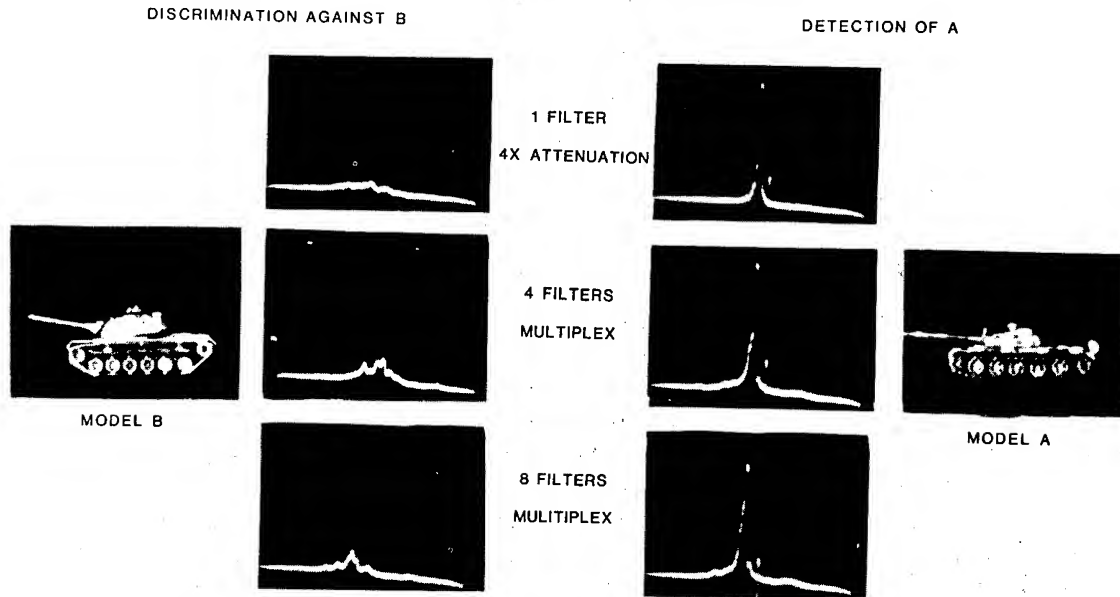


Figure 8. Target Discrimination with the Optical Correlator

Our explanation of the origin of the angular insensitivity of the multiplexed filter is purely speculative. The theory of two-dimensional moment invariants (6) may provide an explanation and might be used for the digital generation of this type of filter.

Multichannel Correlator

An input image can be correlated against a number of reference filters within one optical system (7). This can be used to obtain a correlation over a wide range of image angle or size, or it can be used to search for a number of different objects within the input scene. A filter array can be addressed by a holographic lens (8,9) or by multiple light sources (10). The use of a light source array to address a corresponding reference filter array is illustrated in Figure 9.

This allows each filter to be sequentially addressed, requiring no more light power or detector sensitivity than a single channel correlator. A search through a hierarchy of targets, e.g., tanks, armored personnel carriers, trucks, etc., can also be performed. A two-channel correlator has demonstrated continuous vehicle tracking (4).

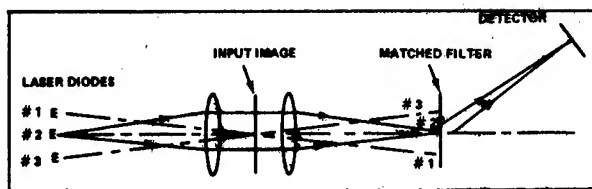


Figure 9. Multichannel Optical Correlator

Diode Laser Sources

One of the major barriers to fielded application of optical computers is the use of large, non-rugged gas lasers for the light source. We have solved this problem by designing and demonstrating a correlator which works with room temperature cw diode injection lasers. These lasers typically have an output power of 10 mW at 820 nm wavelength and require approximately 200 ma at 2.5V or 0.5W of input power. The microscopic size and low power consumption of these lasers make them suitable as light sources in a multichannel correlator. A correlator with up to a 5 X 5 element source array addressing a corresponding reference filter array is feasible (10). Suitable diode laser arrays are available from manufacturers. The IR wavelength and limited coherence of currently available diode lasers make them direct-holographic-recording impossible. However, we have developed an indirect technique for making filters for use in a diode laser correlator.

The light source temporal and spatial coherence requirements for coherent optical correlation have been analyzed previously (11,4). Relatively low source coherence is required for low resolution input imagery.

The maximum spectral width, $\Delta\lambda_m$, that will have a negligible effect on the correlation is

$$\Delta\lambda_m = \frac{\lambda_0}{N}, \quad (4)$$

where λ_0 is the light source wavelength and N is the number of resolvable points across the image input to the correlator. For correlation on an entire TV screen input using a diode laser with $\lambda_0 = 820$ nm, the maximum spectral bandwidth is 820 nm/512 or 1.6 nm. In practice the temporal coherence requirements are much less than this due to lower input image resolution and due to the lower spatial

frequency distribution recorded on the filter.

A change, S , in input scale is equivalent to a wavelength change

$$S = \frac{\Delta\lambda}{\lambda} \quad (5)$$

therefore, the measured scale change tolerances can be used to determine the spectral width tolerances for the correlator light source. Our earlier work indicated a $\pm 8\%$ scale change tolerance for vehicle recognition (4,8), so the light source bandwidth can be $0.16 \lambda_0$ or 130 nm. Diode laser spectral bandwidths are 2 nm or less.

The spatial coherence or source size requirements can be determined by measuring the tolerance of the correlation to lateral filter displacement. A filter displacement is equivalent to a source displacement scaled by the ratio of the transform lens and collimating lens focal lengths. In previous experiments (4) using a coherent helium-neon laser source, a $\pm 12 \mu\text{m}$ filter displacement resulted in no more than a 3 dB decrease in correlation amplitude, indicating that a $24 \mu\text{m}$ diameter source would be acceptable. An advantage of using a less spatially coherent source is that the matched filter alignment requirements are reduced (11,12). Matched filter correlation using a large spatially noncoherent source has been demonstrated (13).

These considerations indicate that even light emitting diodes, with 30 nm spectral width and $200 \mu\text{m}$ diameter emitting area, have adequate temporal and spatial coherence for optical matched filter correlation. Light emitting diodes will be evaluated in future work.

A comparison between coherent optical matched filter correlation using a helium-neon laser and a diode laser is shown in Figure 10. The photograph of the automobile was used to make a reference filter. This picture was autocorrelated using a helium-neon and diode laser source with approximately 10 mW output power. Traces through the correlation spots obtained with the two sources are shown. The correlation linewidths are the same, as is expected from the preceding discussion of coherence requirements. This filter was able to track the vehicle as it moved across the scene, to better than 1/20th the vehicle size.

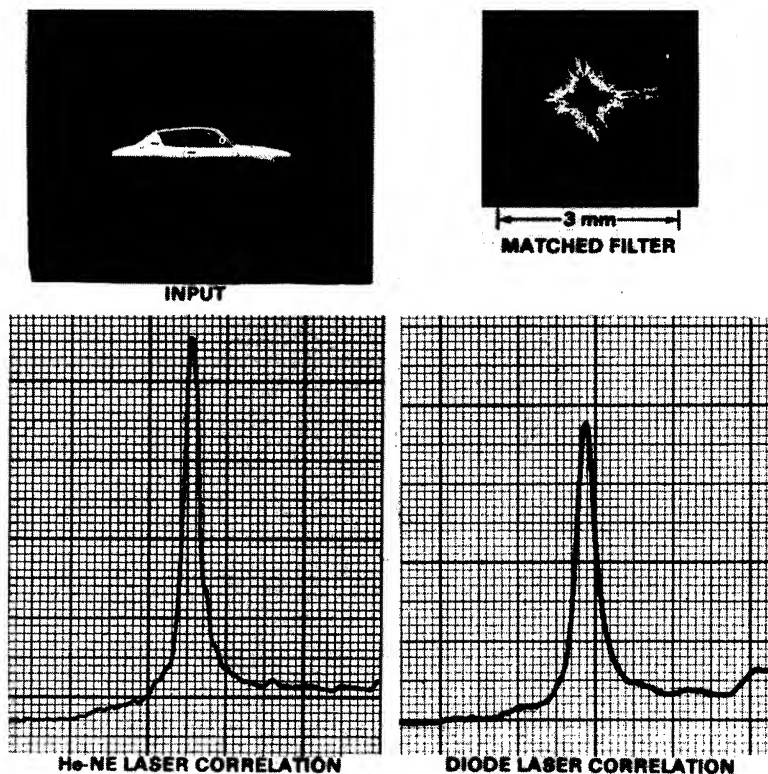


Figure 10. Performance of the Diode Laser Correlator

Packaging of a correlator in a configuration that can be fitted in a small missile was also considered. Two miniature correlators were designed, one a cylindrical package with the image input at the center and the other rectangular with the input at one end.

Figure 2 showed a correlator folded into a 100 mm diameter cylindrical package. The input device is an optically addressed liquid crystal light valve. The correlator output is detected by a solid state CCD detector array.

Figure 11 shows a correlator design contained within a transparent solid. This monolithic construction increases mechanical rigidity and ruggedness and eliminates the possibility of optical surface contamination. If an electronic input coherent light modulator (14) is used, imaging lens L_2 would be eliminated. This correlator is compact enough to fit within an 81 mm mortar projectile.

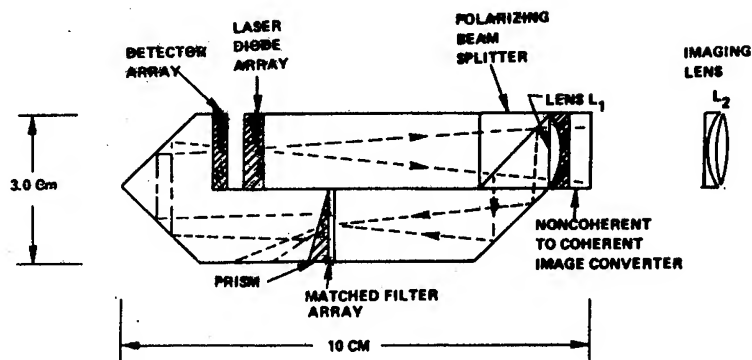


Figure 11. A Monolithic Optical Correlator

CONCLUSIONS

The developments in the field of optical data processing over the past few years make this a technology ripe for exploitation by the Army. The work described in this paper has demonstrated a way of making optical computers practical for missile applications. There will be spin-off to other areas, including navigation and helicopter hover control. As we develop more sophisticated multichannel, multiplex devices, we expect to demonstrate fire and forget guidance for direct fire missiles.

ACKNOWLEDGEMENTS

Dr. B. D. Guenther, now of ARO, and Mr. J. Upatnieks, ERIM, made major contributions to this effort while working in the MICOM laboratory. Mr. D. L. Fuqua, Mr. R. D. McKenzie, Jr., and Dr. J. G. Duthie also made valuable contributions.

REFERENCES

1. J. G. Duthie, J. Upatnieks, C. R. Christensen, and R. D. McKenzie, Jr., "Real-time Optical Correlation with Solid State Sources", Proceedings SPIE, Vol. 232 (1980).
2. J. Grinberg, A. J. Jacobson, W. Bleha, L. Miller, L. Graas, D. Boswell, and G. Meyer, Opt. Eng. 14, 217-225 (1975).
3. W. P. Bleha, L. T. Lipton, E. Weiner-Avneer, J. Grinberg, P. G. Reif, D. Casasent, H. B. Brown, and B. V. Markevitch, Opt. Eng. 17, 371-384 (1978).
4. B. D. Guenther, C. R. Christensen, and Juris Upatnieks, IEEE J. Quant. Elec. QE-15, 1348-1362 (1979).
5. C. F. Hester and D. Casasent, Proceedings SPIE, Vol. 201, 77-82 (1979).
6. M. K. Hu, IRE Trans. Inform. Theory IT-8, 179-187 (1962).
7. W. T. Maloney, Appl. Opt. 10, 2127-2131 (1971).
8. K. G. Leib, R. A. Bondurant, S. Hsiao, R. Wohler, and R. Herold, Appl. Opt. 17, 2892-2899 (1978).
9. J. D. Armitage and A. W. Lohmann, Appl. Opt. 4, 461-467 (1965); see also A. Vander Lugt and E. N. Leith, Annals New York Acad. Sci. 157, 99-110 (1969).
10. J. Upatnieks, B. D. Guenther, and C. R. Christensen, "Real-time Correlation for Missile Terminal Guidance", US Army Missile Research and Development Command Technical Report H-78-5 (1978).
11. A. W. Lohmann, Appl. Opt. 7, 561-563 (1968).
12. O. I. Potaturkin, Appl. Opt. 18, 4203-4205 (1979).
13. A. W. Lohmann and H. W. Werlich, Appl. Opt. 10, 670-672 (1971).
14. J. Grinberg, W. P. Bleha, P. O. Braatz, K. Chow, D. H. Close, A. D. Jacobson, M. J. Little, N. Massetti, R. J. Murphy, J. G. Nash, and M. Waldner, Proceedings SPIE 128, 253-266 (1977).

COLEMAN

THE ADSORPTION AND ELECTROOXIDATION OF SIMPLE HYDROCARBONS
FOR DIRECT OXIDATION HYDROCARBON-AIR FUEL CELLS (U)

AMOS J. COLEMAN, MR.
US ARMY MOBILITY EQUIPMENT RESEARCH AND DEVELOPMENT COMMAND
FORT BELVOIR, VIRGINIA 22060

INTRODUCTION

The development of new and more sophisticated tactical weapon systems mandates that reliable electrical power sources are also available. The ideal tactical power source should be silent, lightweight and mobile. A fuel cell system would meet these requirements. Hydrogen-air fuel cells are now being considered for deployment for the near future. In order to obtain hydrogen rich mixtures for fuels, these fuel cell systems must be equipped with one of the following: hydrogen storage devices, thermal crackers, steam reformers, or partial oxidizers. A direct oxidation hydrocarbon-air fuel cell would be more attractive, since it would eliminate the above items and result in a lighter, less complex system. A fuel cell system, which could operate interchangeably on a variety of fuels, would be an added benefit. This report describes the research effort at MERADCOM to develop such a system. The overall objective is to provide the basic information required for the development of a direct oxidation hydrocarbon-air fuel cell.

A fuel cell is an electrochemical system which converts the free energy of a chemical reaction between a fuel and an oxidant directly to electrical energy. The electrochemical path of a saturated hydrocarbon in a fuel cell may be summarized as shown in Figure 1. A hydrocarbon is adsorbed on the anode to form an adsorbate by a reaction as shown in either 1-a or 1-b. The adsorbate is subsequently oxidized according to reaction 2 to yield carbon dioxide, hydrogen ions and free electrons. These electrons can flow through an external circuit to the cathode where they react with oxygen as

shown in reaction 3. If no side reactions occur, the overall electrooxidation process is as shown by reaction 4. However, important problems have persisted in developing efficient catalysts for these reactions. Even on platinum, one of the best catalysts available, the rate of fuel oxidation has been less than that possible under mass transfer control. It was the specific objective of this research to make a mechanistic study of the anode reaction in hopes of finding the key to improving the reaction kinetics.

PROBABLE REACTION PATH FOR HYDROCARBON OXIDATION

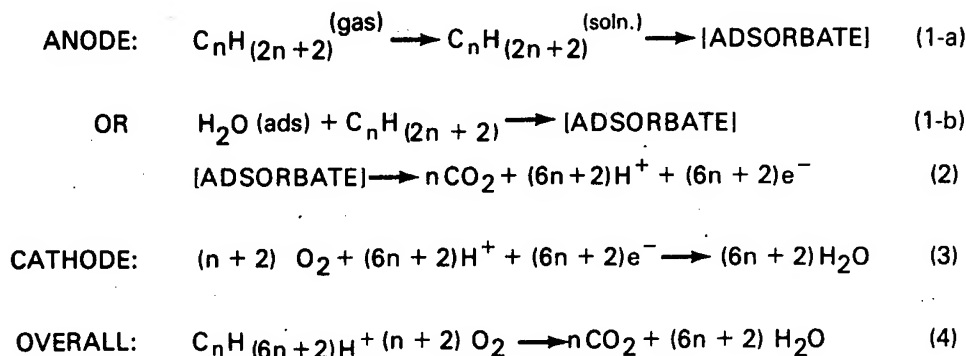


Figure 1. Probable reaction path for the electrooxidation of a saturated hydrocarbon.

Earlier studies(1,2,3,4) have shown that hydrocarbons adsorb and form carbonaceous species on platinum electrodes at potentials greater than 0.1 V vs Reversible Hydrogen Electrode (RHE). Brummer^(5,6) has shown that these species can be classified in three general types which he labeled as CH- α , CH- β and O-type. He discounted the CH- β specie as an active participant in the overall oxidation or reduction. This left the CH- α and O-type for consideration. The role of these species in the overall oxidation reaction has been discussed by Brummer⁽⁸⁾. The observation by Adams and Barger⁽⁹⁾ that higher rates of propane oxidation were attained in trifluoromethanesulfonic acid opens the possibility that these species are influenced by the electrolyte. Therefore, this investigation was undertaken to compare the amounts of these adsorbates in two electrolytes. Since the electrode is an important component in a fuel cell, two electrode structures were also compared.

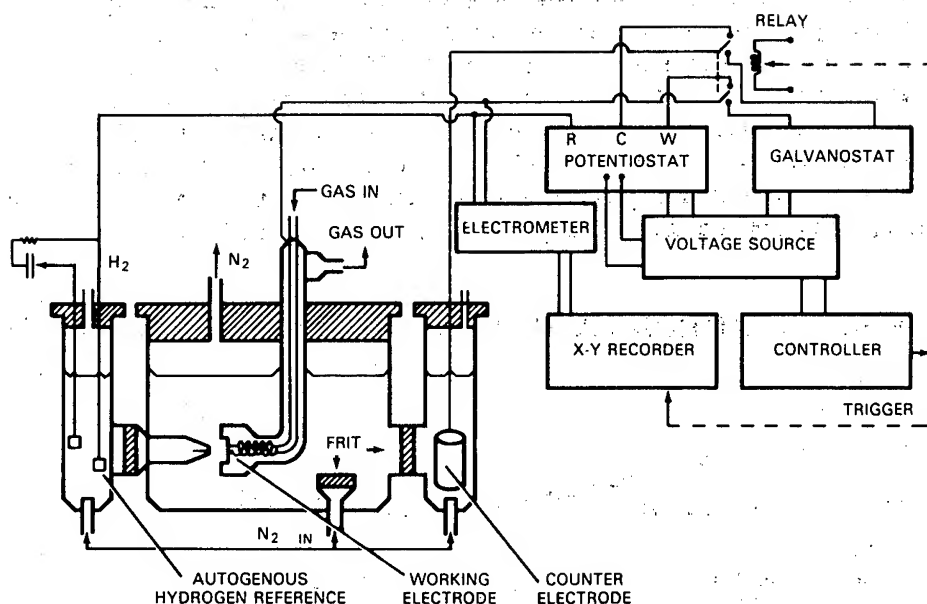


Figure 2. The electrochemical cell and controls.

EXPERIMENTAL

Apparatus and Materials. The electrochemical cell and control circuitry are shown in Figure 2. The cell was a conventional three compartment half-cell normally used in electrochemical investigations. Each compartment is continuously flushed with humidified nitrogen to expel oxygen from the electrolyte. The counter electrode was a high surface area platinized platinum screen. The reference electrode was the autogenous hydrogen electrode described by Giner⁽⁷⁾ and was 10 mv cathodic to the reversible hydrogen electrode. Two types of Teflon-bonded gas diffusion fuel cell electrodes were used as the working electrodes. One contained 4 mg/cm² of platinum-black as the catalyst while the other used carbon-supported platinum with a loading of 0.62 mg Pt/cm² as the catalyst. A circular section of the electrodes was mounted in a Teflon holder which also served as the gas supply.

The electrolytes were phosphoric acid and trifluoromethanesulfonic acid (TFMSA). The phosphoric acid was treated with hydrogen peroxide and solutions of the desired compositions were made by adding distilled water. The TFMSA was distilled and the

fraction between 160 - 161°C was retained for dilution. The solutions were pre-electrolyzed prior to use with a high surface area platinized platinum electrode which was potentiostated at 0.4 V vs RHE for 16 hours.

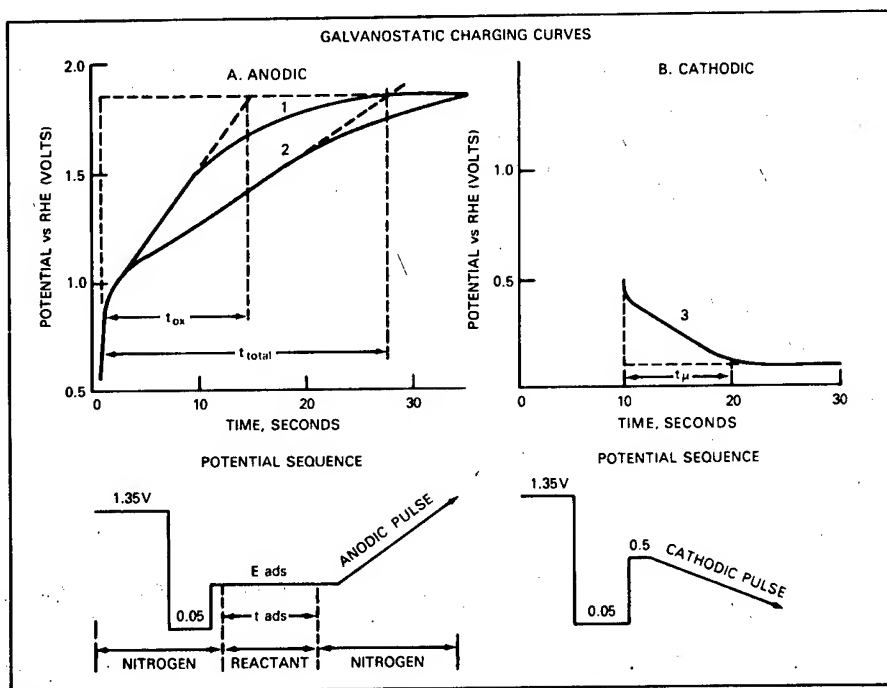


Figure 3. Potential sequences and resulting charging curves.

Experimental Procedures. The experimental procedure is similar to the galvanostatic method devised by Brummer, Ford and Turner. It consists of using a sequence of potentiostatic and galvanostatic pulses to measure surface coverages and amounts of reactants adsorbed. The potential sequences and resulting curves are diagrammed in Figure 3. The electrode is held at a potential where any impurity or previously adsorbed material is oxidized, usually 1.35 V vs RHE, and followed by a potentiostatic pulse to 0.5 V vs RHE to reduce the oxide film and leave a clean surface for adsorption. The electrode is then raised to the potential of interest (E_a) and the reactant allowed to adsorb for a specified time. After removing the excess reactant, an anodic galvanostatic pulse is applied to oxidize the adsorbate. The time required to anodically oxidize the electrode and adsorbate (t_{TOTAL}) can be followed by recording the potential vs time (trace 2, Figure 3).

COLEMAN

When no reactant is present, only the electrode is oxidized and a background curve is obtained (trace 1). Using these curves, the time required to oxidize the adsorbate (t_A) can be computed from

$$t_A = t_{\text{TOTAL}} - t_{\text{ox}}$$

Since the applied current (i) is known, the amount of adsorbate can be computed in terms of the oxidizable charge (Q_A) required to remove the adsorbate.

$$Q_A = i \times t_A$$

A similar sequence of potentials is used with a cathodic pulse to obtain a curve as shown by trace 3. This curve follows the adsorption of hydrogen atoms on the platinum electrode. From the adsorption time (t_H), the charge for depositing hydrogen atoms (Q_H) can be computed. The surface area of the electrode was computed by assuming a monolayer of hydrogen corresponds to 210 $\mu\text{coul}/\text{cm}^2$. Unless otherwise stated, all measurements are referred to this area. The fraction of surface covered by the hydrocarbon material is also measured using a cathodic galvanostatic pulse. The ratio of t_H obtained after adsorption to t_H obtained from a clean electrode under helium gives the fraction of surface occupied by hydrocarbon atoms (θ_H). The fraction covered by the hydrocarbon is $(1 - \theta_H)$. The general background for this method has been discussed earlier.⁽²⁾

Current-voltage curves were measured by potentiostating the electrode at the adsorption potential with the reactant flowing through the gas cavity until steady-state was reached, usually about 10 minutes, and the current recorded. Background curves were measured over the same potential range and subtracted from the current data.

RESULTS AND DISCUSSION

The efficiency of a hydrocarbon-air fuel cell is highly dependent on the adsorption characteristics and oxidation kinetics of the organic molecule used for fuel. Several investigators have examined the oxidation of organic molecules under electrochemical conditions.^(2,3,4) Of general interest is propane because of its availability and relatively low cost. Earlier studies with propane adsorbed on solid electrodes have shown that the mechanism involves the dissociation of the molecule into a number of fragments which

immediately adsorb on the electrode surface. The evidence indicates that the adsorbate is composed of several carbonaceous species in various states of oxidation. The nature of these species and their possible roles in the overall reaction scheme has been discussed previously. (6,8) There is the likelihood that the most highly oxygenated specie is the most preferred in terms of ease of subsequent oxidation to carbon dioxide. Therefore, it is desirable to determine if the concentration of this specie is affected by the electrolyte medium and the electrode structure.

Several experiments were performed to measure the extent of adsorption of propane and methane on platinum electrodes from phosphoric acid and trifluoromethanesulfonic acid electrolytes. Galvanostatic charging curves were used to estimate the amount of adsorbate formed as a function of potential at steady-state coverage on platinum-black and carbon-supported platinum fuel cell electrodes. The amount of adsorbate was measured in terms of the amount of charge per square centimeter required to oxidize the residue. Rates of oxidation, where feasible, were also measured for each electrode-electrolyte system. A number of preliminary experiments were performed for each electrode-electrolyte system, where the adsorption time was varied and the amount of residue measured, to determine when steady-state was reached. The time of maximum adsorption was a function of potential up to about 5 minutes, but in all cases, it was attained after 10 minutes. All additional steady-state experiments were carried out for this time.

Two types of residues were observed, one cathodically desorbable and another which could only be removed by strong oxidation. The cathodically desorbable residue has been labeled as the CH- α and is probably in a highly reduced state. The cathodically non-desorbable residue is considered to be a combination of the previously mentioned CH- β and O-type species.

Adsorption of Propane. The total amount of residues adsorbed from the steady-state adsorption of propane as a function of potential is shown in Figure 4. Maximum adsorption is observed from 14.7 M H_3PO_4 onto platinum-black electrodes. Comparing electrolytes of equal acid strength, i.e., 5.6 M H_3PO_4 and 5.6 M $\text{CF}_3\text{SO}_3\text{H}$, more adsorption occurs on the platinum-black with $\text{CF}_3\text{SO}_3\text{H}$ as electrolyte. At the more cathodic potentials, beyond 0.3 V, more propane is adsorbed on the carbon-supported platinum electrode than on the platinum-black electrode from H_3PO_4 , although it is slightly less than that adsorbed onto platinum-black from $\text{CF}_3\text{SO}_3\text{H}$. Measurements of the surface coverage of the total adsorbate were not possible

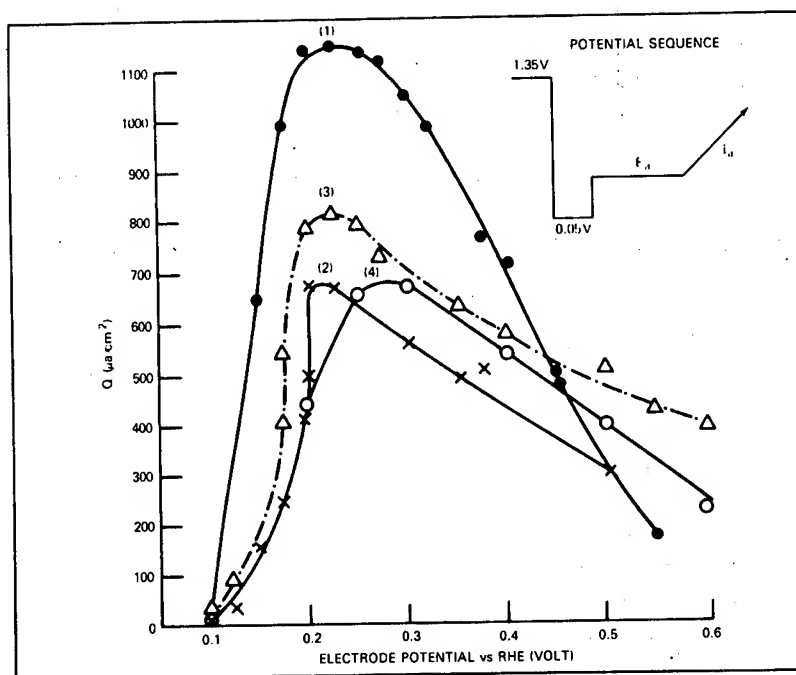


Figure 4. Total propane adsorbate vs potential;
 (1) Pt-blk - 14.7 M H_3PO_4 , (2) Pt-blk - 5.6 M H_3PO_4 ,
 (3) Pt-blk - 5.6 M $\text{CF}_3\text{SO}_3\text{H}$, (4) Pt-C - 5.6 M H_3PO_4 .

since the $\text{CH}-\alpha$ species are rapidly desorbed following application of the cathodic galvanostatic pulse. This is not the case with the cathodically non-desorbable species and the amounts adsorbed along with the surface coverage were measured for these species. These data are shown in Figures 5 and 6. Examination of these plots show that generally there is increased adsorption from the $\text{CF}_3\text{SO}_3\text{H}$ and onto the carbon-supported platinum electrodes. There is also an increase in the accumulation of the cathodically non-desorbable residue. The maximum coverage is observed for platinum-black from $\text{CF}_3\text{SO}_3\text{H}$ with approximately 50% of the surface covered between 0.4 and 0.6 V. The carbon-supported electrodes required approximately the same amount of charge to oxidize the residues, but they had much less coverage. The anodic and cathodic data were further used to characterize this residue. From the ratio of Q_A to $(1 - \theta_H)$ (210×10^{-6}) the number of electrons, $[e]$, per occupied site of platinum required to oxidize the residue to CO_2 was estimated. These data are summarized as a function of potential for each electrode-electrolyte system in Table 1. The values for the phosphoric acid/

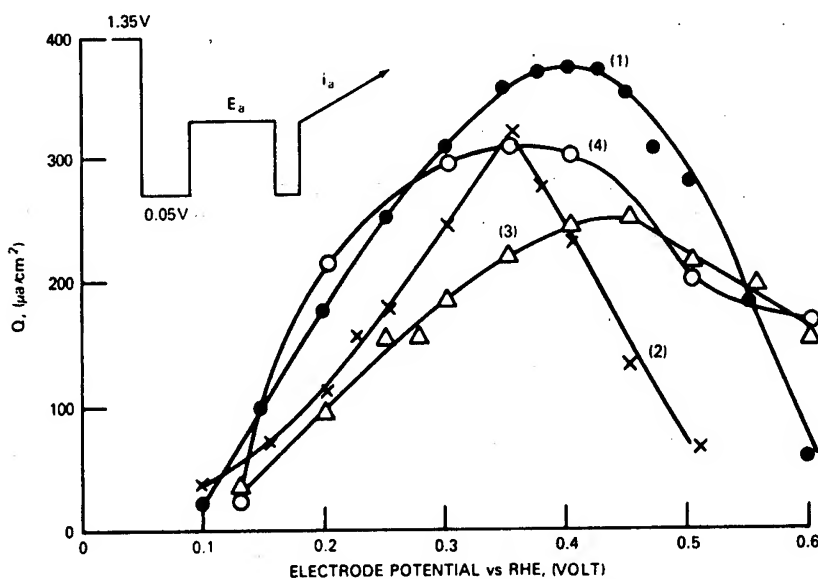


Figure 5. Cathodically non-desorbable propane adsorbates vs potential; (1) Pt-blk - 14.7 M H_3PO_4 , (2) Pt-blk - 5.6 M H_3PO_4 , (3) Pt-blk - 5.6 M $\text{CF}_3\text{SO}_3\text{H}$, (4) Pt-C - 5.6 M H_3PO_4 .

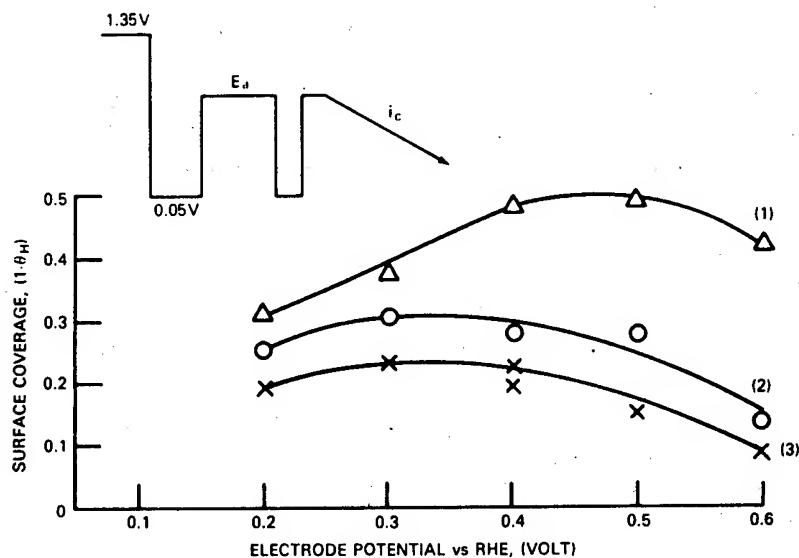


Figure 6. Surface coverage of cathodically non-desorbable propane adsorbates vs potential; (1) Pt-blk - 5.6 M $\text{CF}_3\text{SO}_3\text{H}$, (2) Pt-C - 5.6 M H_3PO_4 , (3) Pt-C - 5.6 M $\text{CF}_3\text{SO}_3\text{H}$.

Table 1. Average Number of Electrons Per Occupied Site of Platinum for Non-Desorbable Adsorbates of Propane and Methane						
		Average Number of Electrons/Site				
Adsorbent	Electrode Potential (Volt)	14.7 M H ₃ PO ₄ Pt-blk	5.6 M H ₃ PO ₄ Pt-blk	5.6 M CF ₃ SO ₃ H Pt-blk	5.6 M H ₃ PO ₄ Pt-C	5.6 M CF ₃ SO ₃ H Pt-C
C ₃ H ₈	0.2	2.3	2.0	1.5	6.7	2.1
	0.3	3.0	3.7	2.2	6.6	3.6
	0.4	3.5	3.7	2.3	6.6	5.3
	0.5	2.8	6.0	1.9	3.7	6.5
CH ₄	0.2	2.5		2.2		
	0.3	3.3		1.7		
	0.4	2.8		2.1		
	0.5	2.7		2.5		

platinum-black system range from 2-4 while the values for the tri-fluoromethanesulfonic acid/platinum-black system averaged about 2 at all potentials. The low values of $[e]$ suggest a highly oxidized specie; for example, a value of 2 would indicate a CO specie. The higher values observed for carbon-supported platinum in both electrolytes infers that the residue contains species which are in a more reduced state. It is also possible that these electrodes contain a mixture of adsorbates with different oxidation states. Although not clearly definitive, the evidence indicates that both the electrode and electrolyte affects the adsorption characteristics of propane.

Adsorption of Methane. Methane adsorbs to a lesser extent than propane in all cases. The adsorption and fractional coverage as a function of electrode potential are summarized in Figures 7 and 8 respectively. No cathodically desorbable residues were detected from the adsorption of methane. Several similarities between the non-cathodically desorbable residues from the adsorption of propane and the residues from methane are noted. The amounts of surface residues and coverage varies with the electrode potential and is greater in CF₃SO₃H than in H₃PO₄. The amounts adsorbed on the carbon-supported platinum is greater than on platinum-black. The average number of electrons is also 2-3 per platinum site. This observation indicates that the molecular species comprising the residue could be the same as the cathodically non-desorbable adsorbate formed from propane.

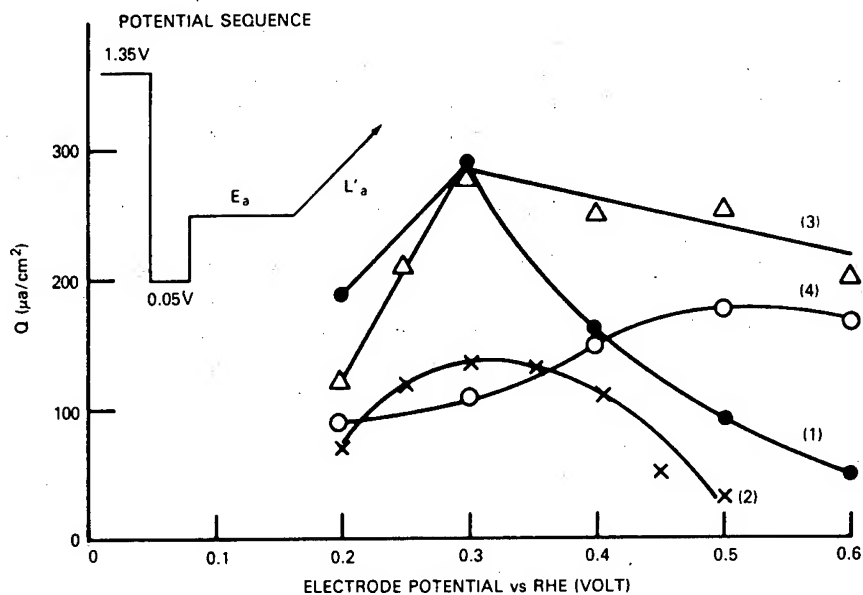


Figure 7. Methane adsorbate vs potential; (1) Pt-blk - 14.7 M H_3PO_4 , (2) Pt-blk - 5.6 M H_3PO_4 , (3) Pt-blk - 5.6 M $\text{CF}_3\text{SO}_3\text{H}$, (4) Pt-C - 5.6 M H_3PO_4 .

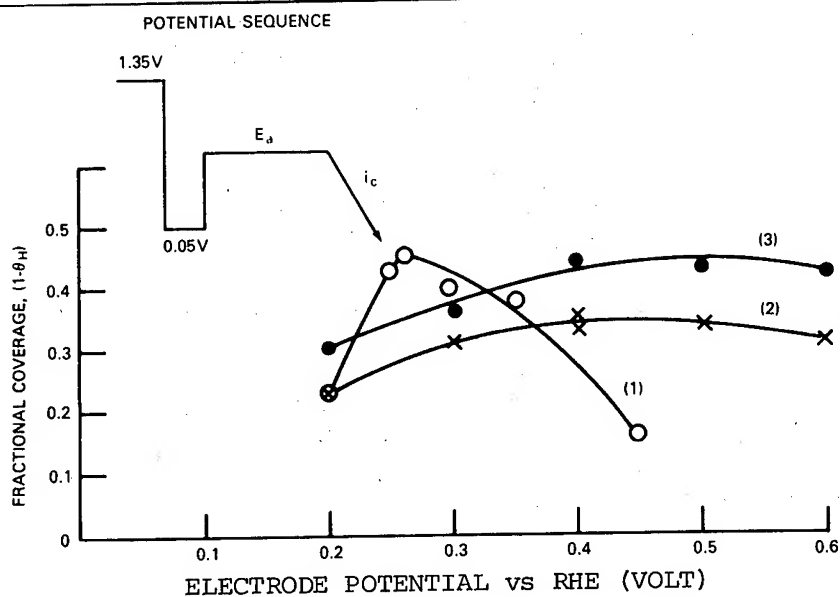


Figure 8. Fraction coverage of methane adsorbate vs potential; (1) Pt-blk - 14.7 M H_3PO_4 , (2) Pt-C - 5.6 M H_3PO_4 , (3) Pt-C - 5.6 M $\text{CF}_3\text{SO}_3\text{H}$.

Rates of Oxidation. Figure 9 shows the steady-state potential-current density plots of the two electrode structures with propane and methane in H_3PO_4 and $\text{CF}_3\text{SO}_3\text{H}$. The electrooxidation rate is greater in $\text{CF}_3\text{SO}_3\text{H}$ than in H_3PO_4 for the same electrode structure while the platinum-black electrode has a greater oxidation rate than carbon-supported platinum in the same electrolyte. The limiting current density for propane in 5.6 M $\text{CF}_3\text{SO}_3\text{H}$ on carbon-supported platinum is $15 \mu\text{A}/\text{cm}^2$ while the value on platinum-black is $27 \mu\text{A}/\text{cm}^2$. Only $3 \mu\text{A}/\text{cm}^2$ was observed for platinum-black in 14.7 M H_3PO_4 . This represents a substantial increase when it is considered that the temperature was 25°C in the former case and 80°C in the latter.

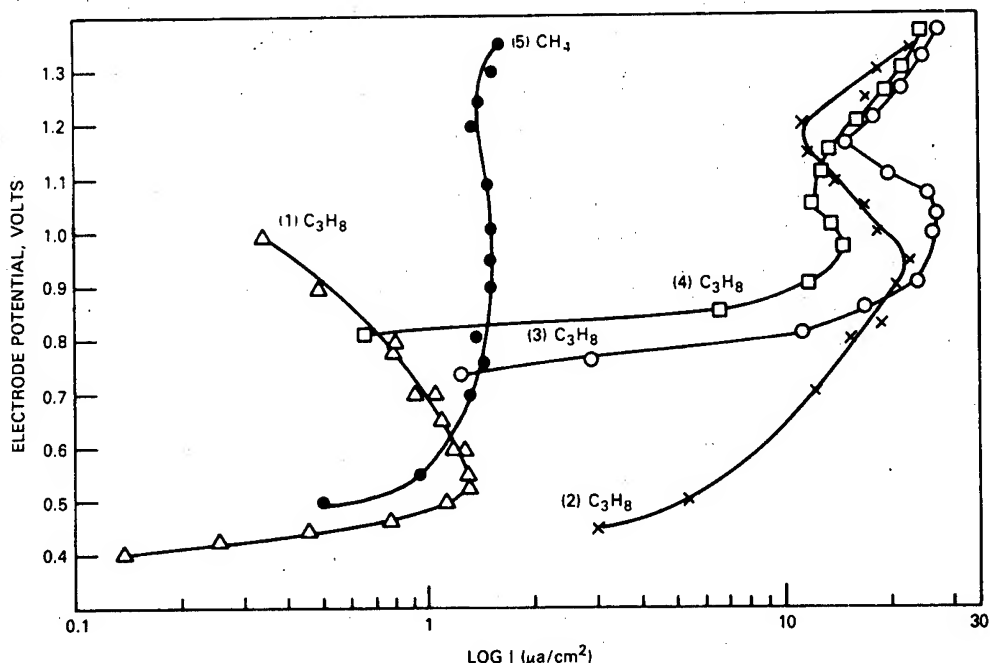


Figure 9. Potential-current density curves for steady-state electrooxidation of methane and propane; (1) Pt-blk - 14.7 M H_3PO_4 , (2) Pt-C - 5.6 M H_3PO_4 , (3) Pt-blk - 5.6 M $\text{CF}_3\text{SO}_3\text{H}$, (4) Pt-C - 5.6 M $\text{CF}_3\text{SO}_3\text{H}$, (5) Pt-blk - 5.6 M $\text{CF}_3\text{SO}_3\text{H}$.

SUMMARY AND CONCLUSION

The findings from this investigation are summarized as follows:

(1) Hydrocarbons are adsorbed on practical fuel cell electrodes in a similar manner as on solid electrodes. The amount adsorbed at steady-state is potential dependent.

(2) Propane produces two types of adsorbates, one which is cathodically desorbable. Methane residues contained only one molecular specie, which is similar to the O-type from propane.

(3) Increased adsorption was observed in trifluoromethanesulfonic acid than in H_3PO_4 . Higher oxidation rates were also obtained in the former electrolyte.

(4) Increased adsorption was measured on the carbon-supported platinum electrodes although the adsorbates on these electrodes were in a more reduced state than those on platinum-black.

It is concluded that the rate of electrochemical oxidation of simple hydrocarbon molecules is highly dependent on electrolyte environment as well as the catalyst structure. By developing specific catalysts and electrolytes, highly reactive intermediates could be produced which oxidize at rates fast enough to make a hydrocarbon-air fuel cell practical.

COLEMAN

REFERENCES

1. S.B. Brummer, J.I. Ford and M.J. Turner, J. Phys. Chem. 69 3424 (1965)
2. M.W. Breiter, Electrochem. Acta. 8 447, 457 (1963)
3. H.J. Barger and M.L. Savitz, J. Electrochem. Soc. 117 686 (1968)
4. L.W. Niedrach, IBID, 111 1309 (1964)
5. S.B. Brummer and M.J. Turner, J. Phys. Chem. 71 2825 (1967)
6. S.B. Brummer and M.J. Turner, IBID, 71 3494 (1967)
7. J. Giner, J. Electrochem. Soc. 111 376 (1964)
8. S.B. Brummer, Fuel Cell Systems II, Advances in Chemistry Series No. 90, American Chemical Society, Washington, D.C., 1969, pp 223-30
9. A.A. Adams and H.J. Barger, J. Electrochem. Soc, 121 987 (1974)

COLLETT

SPATIAL COHERENCE AND INTENSITY PROPERTIES OF
QUASIHOMOGENEOUS OPTICAL SOURCES (U)

EDWARD COLLETT, Ph.D.
US ARMY ELECTRONIC RESEARCH AND DEVELOPMENT COMMAND
FORT MONMOUTH, NEW JERSEY 07703

(U) Until 1960 there existed only incoherent sources in the form of arc lamps and discharge lamps. The most striking characteristic of these optical sources is that in addition to being incoherent, they radiate omnidirectionally. In 1960 a new type of light source, now known as the laser, appeared. Remarkably, this new optical radiation source had properties which are distinctly opposite to those of incoherent sources. These properties are intense brightness, monochromaticity, total coherence and very narrow directionality or unidirectionality of the laser radiation. Thus, there now existed two different optical sources with distinctly opposite properties.

(U) One might have thought that the question would have been asked, "What is the nature of the optical sources and their corresponding fields which are between these two extremes?" Only during the past several years has a new type of optical source whose properties are between these extremes been characterized. This new type of optical source has been named the "quasihomogeneous optical source"^{1,2}.

(U) As mentioned above, one of the most striking properties of the laser is its directionality. From the beginning, the directional property of the laser was associated with its being completely coherent. In fact, this directionality was believed to be due totally to its coherence. The logic here was that incoherent radiation led to omnidirectional radiation, while completely coherent radiation led to unidirectional radiation. This logic implied that light, which is partially coherent, will generate fields or beams with a greater divergence than the laser but less than incoherent sources. This is represented in Fig. 1.

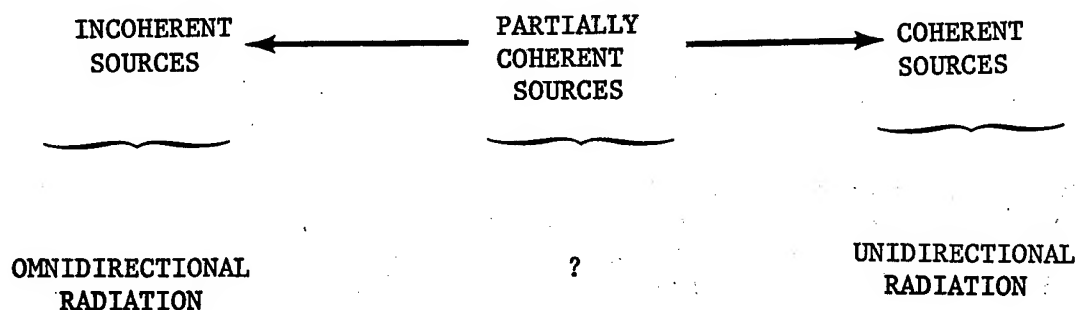


Fig.1. Coherence properties of optical sources. The question mark under the partially coherent sources represents the unknown nature of these sources.

(U) Recently, theoretical and experimental investigations have shown that partially coherent sources can be as directional as a laser beam.^{3,4} This is due to the fact that an optical source must be simultaneously characterized by its degree of coherence and its intensity distribution across the optical surface. This theoretical prediction has been confirmed experimentally.^{5,6}

(U) In this paper the theoretical development of the quasihomogeneous optical source concept is reviewed along with some of the experimental results. No attempt will be made to present a detailed derivation of the fundamental equations as they have been fully developed in the open literature and can be found in the cited references.¹⁻⁶

Mathematical Formulation of Optical Coherence

(U) The optical field in free space can be characterized by the scalar wave equation

$$\nabla^2 V(\mathbf{r}, t) = \frac{1}{c^2} \frac{\partial^2 V(\mathbf{r}, t)}{\partial t^2} \quad (1)$$

where $V(\mathbf{r}, t)$ is the instantaneous field amplitude, c is the speed of light in a vacuum and ∇^2 is the three dimensional Laplacian operator.

COLLETT

In accordance with Wolf's formulation, it is possible to introduce another quantity, known as the mutual coherence function, defined as⁷

$$\Gamma(\underline{r}_1, \underline{r}_2; \tau) = \langle V(\underline{r}_1, t + \tau) V^*(\underline{r}_2, t) \rangle \quad (2)$$

where the angle brackets represent a time average of the optical field, \underline{r}_1 and \underline{r}_2 are two different points in the optical field in space and τ is an increment of time. Wolf has shown that the mutual coherence function, Eq.(2) also satisfies the wave equation. Thus, the coherence properties of the optical field propagate along with the amplitude. It is possible to take the Fourier transform of the mutual coherence function $\Gamma(\underline{r}_1, \underline{r}_2; \tau)$ to form

$$W(\underline{r}_1, \underline{r}_2; \omega) = \frac{1}{2\pi} \int_{-\infty}^{\infty} \Gamma(\underline{r}_1, \underline{r}_2; \tau) e^{i\omega\tau} d\tau \quad (3)$$

The quantity $W(\underline{r}_1, \underline{r}_2; \omega)$ is known as the cross-spectral density and characterizes the correlations of the optical field at the frequency, ω , at two points in space, $P(\underline{r}_1)$ and $P(\underline{r}_2)$. The mutual degree of coherence, $\mu(\underline{r}_1, \underline{r}_2; \omega)$, can be defined in terms of the cross-spectral density $W(\underline{r}_1, \underline{r}_2; \omega)$

$$\mu(\underline{r}_1, \underline{r}_2; \omega) = \frac{W(\underline{r}_1, \underline{r}_2; \omega)}{\sqrt{I(\underline{r}_1, \omega) I(\underline{r}_2, \omega)}} \quad (4)$$

where $I(\underline{r}, \omega) = W(\underline{r}, \underline{r}; \omega)$ represents the average optical intensity at frequency ω , at the point $P(\underline{r})$. It can be shown that $\mu(\underline{r}_1, \underline{r}_2; \omega)$ is normalized so that for all values of \underline{r}_1 , \underline{r}_2 and ω ,

$$0 \leq |\mu(\underline{r}_1, \underline{r}_2; \omega)| \leq 1 \quad (5)$$

The quantity $\mu(\underline{r}_1, \underline{r}_2; \omega)$, defined by Eq.(4), is called the complex degree of spatial coherence of the light fluctuations at frequency ω at the points $P(\underline{r}_1)$ and $P(\underline{r}_2)$. The limiting values of unity and zero in Eq.(5) indicate that the light fluctuations at the points $P(\underline{r}_1)$ and $P(\underline{r}_2)$ are completely correlated or uncorrelated, respectively. If $|\mu(\underline{r}_1, \underline{r}_2; \omega)| = 1$ then the optical field is said to be spatially coherent. On the other hand if the value of $|\mu(\underline{r}_1, \underline{r}_2; \omega)| = 0$

then the optical field is said to be completely spatially incoherent. These limiting cases should be regarded only as convenient mathematical idealizations rather than real physical conditions actually observed in nature. No practical optical field can be spatially incoherent in the sense defined above.

(U) By suppressing the time factor in Eq. (2) one can show that the cross-spectral density function, $W(\underline{r}_1, \underline{r}_2)$, obeys the Helmholtz equation

$$\nabla_i^2 W(\underline{r}_1, \underline{r}_2) + K^2 W(\underline{r}_1, \underline{r}_2) = 0 \quad (6)$$

where the index i on the Laplacian operator indicates differentiation with respect to either variable \underline{r}_1 or \underline{r}_2 . By using standard mathematical techniques for solving the Helmholtz equation, the cross-spectral density function in the optical far-field can be related to its values at all pairs of points in the source plane. More specifically, the far-field solution of Eq. (6) takes the form

$$W(\underline{r}_1, \underline{r}_2) = \left(\frac{2\pi K}{R}\right)^2 \cos^2 \theta \tilde{W}^{(0)}(K \underline{s}_1, -K \underline{s}_1) \quad (7)$$

where $\tilde{W}^{(0)}(\underline{k}_1, \underline{k}_2)$ is the spatial Fourier transform of the cross-spectral density in the source plane

$$\tilde{W}^{(0)}(\underline{k}_1, \underline{k}_2) = \frac{1}{(2\pi)^4} \int_{-\infty}^{\infty} \int_{-\infty}^{\infty} \int_{-\infty}^{\infty} W^{(0)}(\underline{r}_1, \underline{r}_2) e^{-i(\underline{k}_1 \cdot \underline{r}_1 + \underline{k}_2 \cdot \underline{r}_2)} d^2 \underline{r}_1 d^2 \underline{r}_2 \quad (8)$$

The vector \underline{s}_1 is the projection of the unit vector \underline{s} in the plane of the source and θ is the angle between \underline{s} and the normal to the source plane. As has been pointed out above the cross-spectral density is useful for defining the mutual degree of coherence, Eq. (4). In addition, one can also show that the radiant intensity of physical optics, $J(\underline{s})$, is directly proportional to the diagonal element of the cross-spectral density, namely,

$$J(\underline{s}) = \lim_{R \rightarrow \infty} R^2 W(R \underline{s}, R \underline{s}) \quad (9)$$

where \underline{s} is the unit vector in the direction of observation. With this definition, Eq.(7) becomes

$$J(\underline{s}) = (2\pi K)^2 \cos^2 \theta \tilde{W}^{(0)}(K\underline{s}_\perp, -K\underline{s}_\perp) \quad (10)$$

In order to analytically determine $J(\underline{s})$ the Fourier transform of the cross-spectral density on the optical surface, $\tilde{W}^{(0)}(K\underline{s}_\perp, -K\underline{s}_\perp)$ must be known. In order to do this we substitute Eq.(4) into Eq.(8) and we find

$$\tilde{W}^{(0)}(\underline{k}_1, \underline{k}_2) = \frac{1}{(2\pi)^4} \iiint_{-\infty}^{\infty} d^2\underline{r}_1 d^2\underline{r}_2 e^{-i(\underline{k}_1 \cdot \underline{r}_1 + \underline{k}_2 \cdot \underline{r}_2)} \mu(\underline{r}_1, \underline{r}_2) \sqrt{I(\underline{r}_1) I(\underline{r}_2)} \quad (11)$$

Unfortunately, Eq.(11) cannot be evaluated unless the term $\mu(\underline{r}_1, \underline{r}_2) \times \sqrt{I(\underline{r}_1) \cdot I(\underline{r}_2)}$ can be simplified in a manner which conforms to physical reality. For many years the inability to reduce this factor prevented further progress in the development of partially coherent sources.

(U) This impasse was overcome by Wolf and Carter in the following way.¹ The expression for the cross-spectral density

$$W(\underline{r}_1, \underline{r}_2) = \mu(\underline{r}_1, \underline{r}_2) \sqrt{I(\underline{r}_1) \cdot I(\underline{r}_2)} \quad (12)$$

can be cast into a form which agrees with physical reality by noting that most optical sources are statistically homogeneous. This behavior can be expressed by writing

$$\mu(\underline{r}_1, \underline{r}_2) = g(\underline{r}_1 - \underline{r}_2) \quad (13)$$

The treatment of the next factor, $\sqrt{I(\underline{r}_1) \cdot I(\underline{r}_2)}$ is more subtle and difficult and requires a considerable amount of insight. Investigation of optical sources shows the optical intensity, $I(\underline{r})$, changes very slowly with position across the source and is sensibly constant over regions whose linear dimensions are of the order of the correlation distance of the light source. Under these conditions, the intensity varies very slowly across the source and so we can express this behavior by

$$\sqrt{I(r_1) \cdot I(r_2)} \simeq I\left[\frac{1}{2}(r_1 + r_2)\right] \quad (14)$$

Thus, a source which is statistically homogeneous, Eq.(13), and whose intensity varies slowly across the source, Eq.(14), allows one to write

$$W(r_1, r_2) \simeq g(r_1 - r_2) I\left[\frac{1}{2}(r_1 + r_2)\right] \quad (15)$$

An optical source which behaves in accordance with the previous description and satisfies Eq.(15) is said to be quasihomogenous. From Eq.(15) the Fourier transform of the cross-spectral density can be shown to be

$$\tilde{W}(k_1, k_2) = \tilde{I}(k_1 + k_2) \tilde{g}\left[\frac{1}{2}(k_1 - k_2)\right] \quad (15')$$

Evaluation of Eq.(11) on the surface of the optical source we see that the total contribution to the optical far-field radiant intensity, $J(\underline{s})$, is then

$$J(\underline{s}) = (2\pi k^2) \tilde{I}^{(0)} \tilde{g}^{(0)}(k \underline{s}_\perp) \cos^2 \theta \quad (16)$$

Therefore, we have reached the important result that the radiant intensity, $J(\underline{s})$, depends both on the intensity distribution over the source, $\tilde{I}^{(0)}$, and the mutual degree of coherence, $\tilde{g}^{(0)}$. From Eq.(16) we see that we need only know the Fourier transform of the intensity distribution over optical source and the Fourier transform of the correlation function in order to determine the far-field radiant intensity, $J(\underline{s})$.

Far-Field Radiant Intensity for a Gaussian Intensity and Coherence Source

(U) We will now consider an optical source whose intensity distribution and degree of spatial coherence are both gaussian and which can be represented in the form

$$I(r) = A \exp(-r^2/2\sigma_I^2) \quad (17a)$$

$$g(r) = \exp(-r^2/2\sigma_g^2) \quad (17b)$$

Taking the Fourier transform of Eqs.(17a) and (17b) and substituting these transforms into Eq.(16) we find the radiant intensity in terms of its angular spectrum to be

$$J(\theta) = J(0) \cos^2 \theta \exp(-\sin^2 \theta / 2 \Delta^2) \quad (18)$$

where θ is the polar angle of observation as measured from the z axis, and

$$\Delta^2 = \frac{1}{(K\sigma_g)^2} + \frac{1}{(2K\sigma_I)^2} \quad (19a)$$

and

$$J(0) = (\sigma_I^2 / \Delta) A \quad (19b)$$

The angular half-width of the optical field can be found by setting the argument in exponent of Eq.(18) to -2 (the half power point), and we find that

$$\theta = \sin^{-1} \left[2 \sqrt{\frac{1}{(K\sigma_g)^2} + \frac{1}{(2K\sigma_I)^2}} \right] \quad (20)$$

From Eq.(20) we see that the angular intensity distribution is a function of the mean intensity width, σ_I , and the correlation width, σ_g , across the optical source. Let us now consider some special cases.

Laser

For a laser, $\sigma_g \rightarrow \infty$, and we have

$$\Delta_L = 1 / (2K\sigma_L) = \lambda / 4\pi\sigma_L \quad (21a)$$

and

$$\theta_L = \sin^{-1} \left[\frac{\lambda}{2\pi\sigma_L} \right] \quad (21b)$$

For a typical HeNe laser, $\lambda = 6.328 \times 10^{-7} \text{m}$ and $\sigma_L = 5 \times 10^{-4} \text{m}$,

Substituting these values into Eq.(21b) the angular half-width in the far field is

$$\theta_L \approx 11.5 \text{ mrad} \quad (22)$$

This result shows that we may approximate θ_L by

$$\theta_L \approx \lambda / \sigma_L \quad (23)$$

Incoherent Source

In this case, $\sigma_I \rightarrow \infty$, and $\sigma_g \rightarrow 0$ so

$$\Delta_{INC} = \frac{1}{K \sigma_g} \quad (24a)$$

and

$$\theta_{INC} = \sin^{-1} \left[\frac{\lambda}{2\pi \sigma_g} \right] \quad (24b)$$

We note that $\lambda \sim 10(-7)\text{m}$, $\sigma_g \rightarrow 0$ and therefore θ_{INC} will become large as $\sigma_g \rightarrow 0$ in agreement with the well known behavior of incoherent sources.

Partially Coherent Sources

Partially coherent sources are defined to be optical sources whose degree of coherence is greater than 0 but less than 1. We now show that it is possible to construct a source which is as directional as a laser but which is partially coherent. To see this we know from Eq. (21b) that

$$\theta_L = \sin^{-1} \left[\frac{\lambda}{2\pi \sigma_L} \right] \quad (25)$$

Equating Eq.(20) for the laser and the quasihomogenous source, the requirement to have the same beam divergence is

$$\frac{1}{\sigma_Q^2} + \frac{1}{4\sigma_Q^2} = \frac{1}{4\sigma_L^2} \quad (26)$$

COLLETT

Thus, if σ_L of the laser is taken to be equal to $1/4$ we then have

$$\frac{1}{\sigma_Q^2} + \frac{1}{4\sigma_Q^2} = 1 \quad (26')$$

If, we now choose $\sigma_{gQ} = \sqrt{2}$ then σ_Q must be equal to $1/\sqrt{2}$. This trade-off behavior is shown in Fig.2, below. The top figure is that of a laser while the following figures illustrate the variation in the mean width of the intensity and coherence to obtain the same angular divergence.

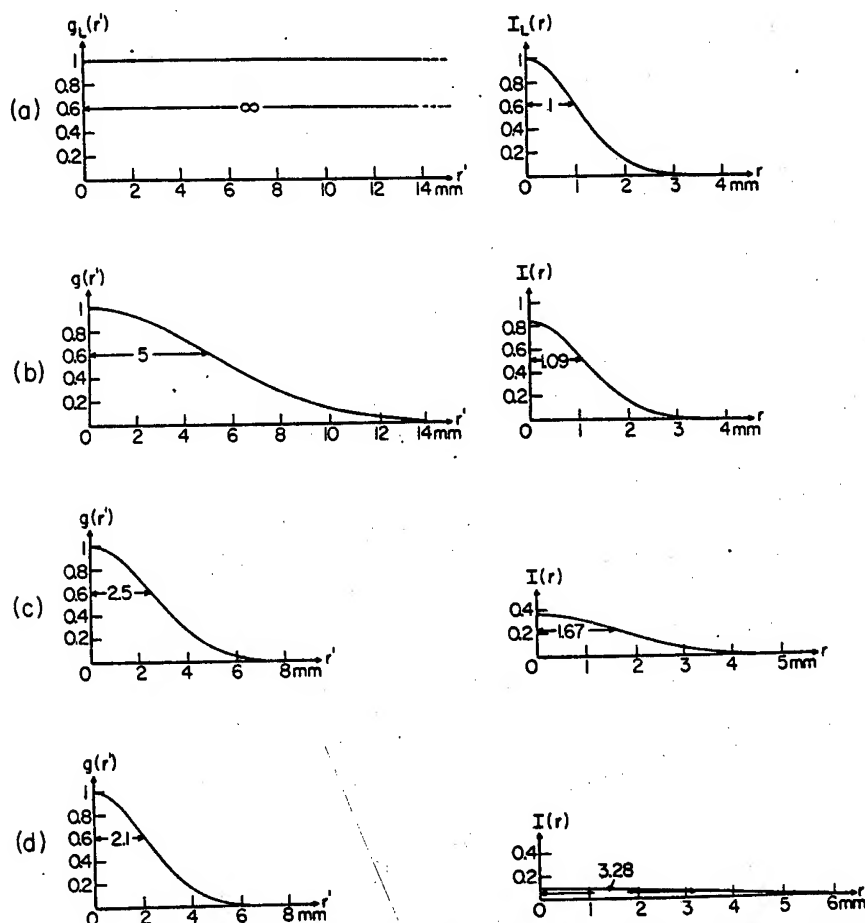


Fig. 2. Illustrating the coherence and the intensity distributions across three partially coherent sources [(b), (c), (d)] which produce fields whose far-zone intensity distributions are the same as that generated by a coherent laser source [(a)]. The parameters characterizing the four sources are:

(a) $\sigma_g = \infty$, $\sigma_I = \delta_L = 1$ mm, $A = 1$ (arbitrary units) (b) $\sigma_g = 5$ mm, $\sigma_I = 1.09$ mm, $A = 0.84$

(c) $\sigma_g = 2.5$ mm, $\sigma_I = 1.67$ mm, $A = 0.36$ (d) $\sigma_g = 2.1$ mm, $\sigma_I = 3.28$ mm, $A = 0.09$.

The normalized radiant intensity generated by all these sources is $J(\theta)/J(0) = \cos^2 \theta \exp\{-2(k\delta_L)^2 \sin^2 \theta\}$, ($\delta_L = 1$ mm).

Quasihomogeneous Source Experiments

(U) In order to test the validity of the theoretical conclusions presented in the previous sections, a series of laboratory measurements were made in the far-field of a quasihomogeneous optical source. At this time there are no primary quasihomogeneous sources, that is, sources which radiate directly in the quasihomogeneous mode. However, it is possible to construct a secondary source which behaves quasihomogeneously, i.e., is statistically homogeneous and whose intensity varies slowly over the source. In order to obtain the statistical homogeneity a gaussian phase screen was constructed. A laser has a natural gaussian intensity and this was used as a primary source. The quasihomogeneous source was created by expanding and collimating the laser into a 25mm beam diameter. This beam was then passed through the phase plate which was rotating at ten Hertz. The mean width of the intensity of the emerging beam is then 5.82mm. The coherence width of the phase plate was measured indirectly. However, by means of indirect measurements made on two phase plates used in the experiments values of $\sigma_g = 8.8 \mu\text{m}$ and $85.4 \mu\text{m}$ were found. The experimental setup is shown in Fig.3. The fact should be emphasized that the use of the laser as a primary source was to obtain a natural gaussian intensity distribution; by passing the laser beam through the rotating phase plate the coherence of the laser beam was reduced thereby making a quasihomogeneous beam.

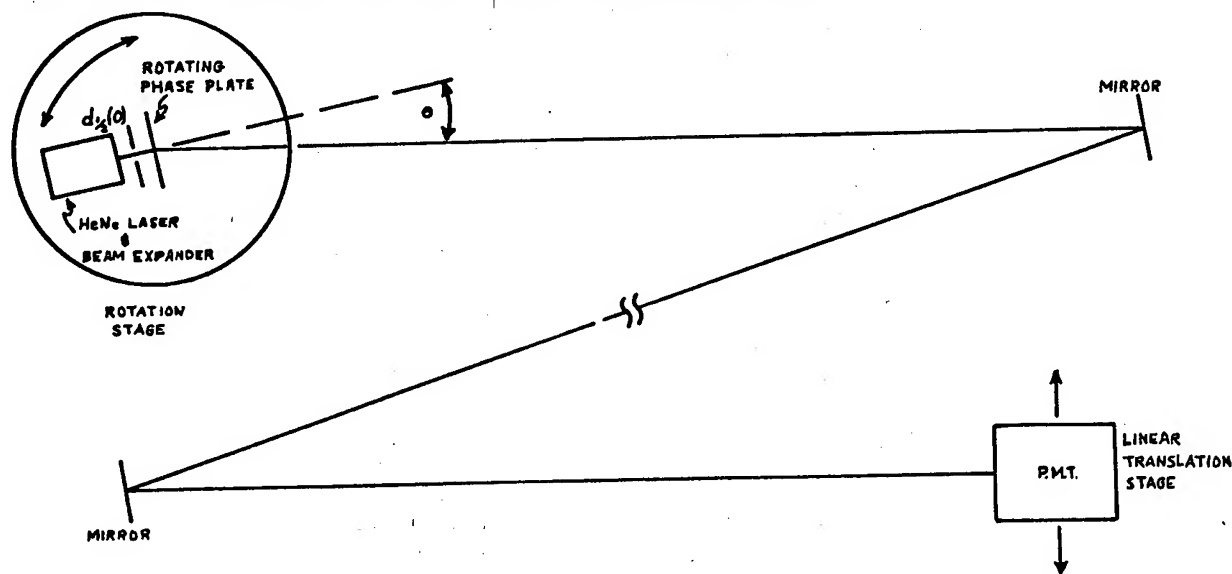


Fig. 3. Experimental arrangement to determine the far-field properties of a quasihomogeneous optical source. The total path length between the rotating phase plate and the PMT was varied by placing additional mirrors in the optical path. With as many as eight mirrors the total path was 12.5m. The rotational stage was made in order to align the quasihomogeneous source with the scanning PMT.

(U) In terms of carrying out a series of measurements a convenient quantity to measure is the beamwidth, $d_{1/2}(z)$, as a function of the path-length, z . The expression which shows this relation is given by

$$d_{1/2}(z) = z \sqrt{\ln 2} \sqrt{\left(z \sigma_g^2 + \frac{z z^2}{K^2 \sigma_g^2} \right)} \quad (27)$$

With the values of σ_g and σ_I given above, the beam width as function of z was measured and the results are shown in Fig. 4. The solid lines represent the theoretical values expressed by Eq.(27). and the dots are the measured values. The agreement is seen to be very good.

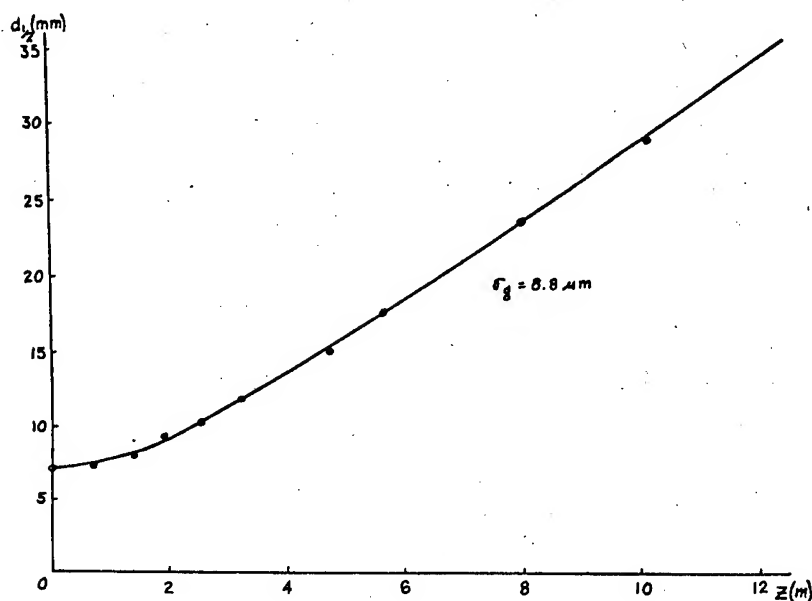


Fig. 4. Experimental confirmation of the quasihomogeneous source far-field behavior. The solid line represents the theoretical value of $d_{1/2}(z)$ and the solid circles the measured values.

Military Applications

(U) It is worthwhile to devote a short section to the possible role of quasihomogeneous optical sources in military systems.

(U) At present there are four known distinct properties of light. These are 1) the intensity, 2) the wavelength, 3) the polarization and 4) the coherence. The intensity property of light has been used by the military since antiquity. With the advent of spectrally pure lasers the wavelength property also came into use. As for the polarization property it is only now being applied in a prototype Army system. The coherency property has never been used but this may change. With the development of the current line of research new methods have been developed to control and generate coherence. Thus, new applications to an unused domain of light are now possible.

(U) To give some examples and possible applications it should now be possible to transmit signals and messages by coherency coding, that is, modulate the laser with a phase plate and then coherently demodulate the received signal. This should find direct use in laser designators and transmission over fiber optics links. Another application is in image improvement by the reduction of laser speckle. By reducing the coherency of the laser beam experiments have shown a dramatic improvement in the image quality. Another application is to the development of laser warning receivers where the variability of coherence adds a new dimension to the detection criteria. Finally, quasihomogeneous sources may find possible application in the manufacture of integrated circuits where the use of this new type of source can reduce and control diffraction effects in the making of photolithographic masks.

(U) Thus, for the military, the development of quasihomogeneous optical sources and the techniques which are now being developed to generate and control the optical field may open the optical coherency domain as a new area of military exploitation.

Summary

(U) In this paper we have introduced the concept of a new type of optical source whose properties are between incoherent optical sources and coherent laser sources. The conditions were established for a source to be quasihomogeneous. In doing this the far-field radiant intensity, $J(s)$, was shown to be directly dependent on both the intensity distribution and the degree of coherence across the optical source.

(U) This last result led to the following realization. For a

COLLETT

quasihomogeneous optical source with a gaussian intensity and coherence function it is possible to generate beams as directional as a laser. This can be done even though the degree of coherence is reduced. However, the mean intensity width of the beam must then be increased in a prescribed manner. This, fortunately, is not difficult to do and the expected behavior has been confirmed experimentally.

(U) Finally, several military applications of the use of quasihomogeneous optical sources was presented. As a result of this present line of research it may now be possible to open up a new area of optics for military exploitation.

References

1. W.H. Carter and E. Wolf, "Coherence and radiometry with quasihomogeneous planar sources", J. Opt. Soc. Am. 67, 785-796(1977).
2. E. Wolf, "The radiant intensity from planar sources of any state of coherence", J. Opt. Soc. Am. 68, 1597-1605(1978).
3. E. Collett and E. Wolf, "Is complete spatial coherence necessary for the generation of highly directional light beams?" Opt. Lett. 2, 27-29(1978).
4. E. Wolf and E. Collett, "Partially coherent sources which produce the same far-field intensity distribution as a laser", Opt. Commun. 25, 293-296(1978).
5. F. Gori and C. Palma, "Partially coherent sources which give rise to highly directional beams", Opt Commun. 27, 185-188(1978)
6. J.D. Farina, L.M. Narducci and E. Collett, "Generation of highly directional beams from quasihomogeneous optical sources", accepted for publication in Opt. Commun.
7. M. Born and E. Wolf, Principles of Optics, 5th ed. (Pergamon, Oxford, 1975).

CROWSON

POWDER METALLURGY STEEL FORGINGS
FOR SMALL ARM APPLICATIONS (U)

ANDREW CROWSON, PhD.
FIRE CONTROL AND SMALL CALIBER WEAPON SYSTEMS LABORATORY
U.S. ARMY ARMAMENT RESEARCH AND DEVELOPMENT COMMAND
DOVER, NEW JERSEY 07801

INTRODUCTION

Powder metallurgy (P/M) steel forging is a relatively new fabrication process. Although experimental activities date back to the early 1960's, it was not until the early 1970's that the process was fully developed as a viable manufacturing technique (ref 1-3). The process combines the advantages of fabricating net or near-net shape parts using conventional P/M processing and of property enhancement achieved by subsequent forging.

The basic process involves the following steps:

Powder → Preform → Sinter → Forge → Finish

First a mixture of prealloyed steel and graphite powder is compacted into a predetermined shape called a preform. The preform density is usually in the range of 80 to 88 percent of the theoretical density (7.87 g/cm^3). The preform is next heated under controlled conditions in a sintering step. This step reduces the undesirable inhomogeneties present in the starting powder, alloys the steel and graphite powders, and increases the strength of the preform. Following sintering, the forging operation is used to fully densify the preform. This is subsequently followed by a minimal number of finishing operations to obtain the final part.

The successful application of the P/M forging process to ordnance components offers substantial economic benefits. Primary cost advantages over the conventional processes lie in more efficient material utilization, simpler forging operations, and reduced finishing

CROWSON

operations. With the P/M forging process a one step forming operation is used instead of the multiple operations required in conventional forging. Thus, scrap losses are reduced since the normal fullering, edging, blocking and flash removal operations of conventional forging are eliminated. Through the use of closed confined P/M forging dies closer tolerance parts are produced than with conventional forging. This reduces and, in some cases, eliminates the machining and surface finishing operations normally required to produce a part to dimensional tolerances. Consequently, by substituting P/M forging for conventional forging costs in the production of many load-bearing components can be reduced by 25-50 percent (ref 4-5).

PROCEDURE

The following procedure was used in forming the P/M forged parts which provided the mechanical and physical property data reported in this paper.

Prealloyed 4600 powder was mixed with flake graphite to obtain a 0.4 percent carbon content (4640 steel). The basic composition of the powder along with the AISI specification for 4600 wrought material is given in Table 1. The powder mixture was compacted into 8.90 cm x

Table 1. Chemical Analysis of 4600 Prealloyed Powder

<u>Element</u>	<u>AISI Specification (%)</u>	<u>4600 Powder (%)</u>
Carbon	---	---
Nickel	1.65-2.00	1.77
Molybdenum	0.2 -0.3	0.48
Manganese	0.6 -0.8	0.23
Copper	---	0.05
Chromium	---	0.05
Phosphorus	0.04 max	<0.01
Sulfur	0.04 max	0.02
Silicon	0.02-0.34	0.07
Oxygen	---	0.152

1.90 cm x 2.54 cm rectangular bars to 80 percent of theoretical density. Compaction was conducted using a closed confined die supported by springs. This enabled the compaction operation to simulate a double acting press, thereby producing compacts with uniform density profiles. The preforms were sintered in a 95 hydrogen-5 methane atmosphere for 40 minutes at

1200°C. Forging of the sintered preforms were carried out in a preheated confined forging die. Forging pressures were adjusted to achieve full densification. The forgings were subsequently austenitized for $\frac{1}{2}$ hour at 843°C and tempered for one hour at 621°C to achieve a hardness of Rockwell C 30-33.

P/M FORGED PROPERTIES

Typical microstructures of heat treated 4640 P/M steel forgings are shown in Figure 1. In the unetched condition, Figure 1a, the microstructure was relatively clean throughout with no residual porosity or inclusions. The etched microstructure, Figure 1b, is characterized as finely tempered martensite and shows no evidence of prior particle boundaries.

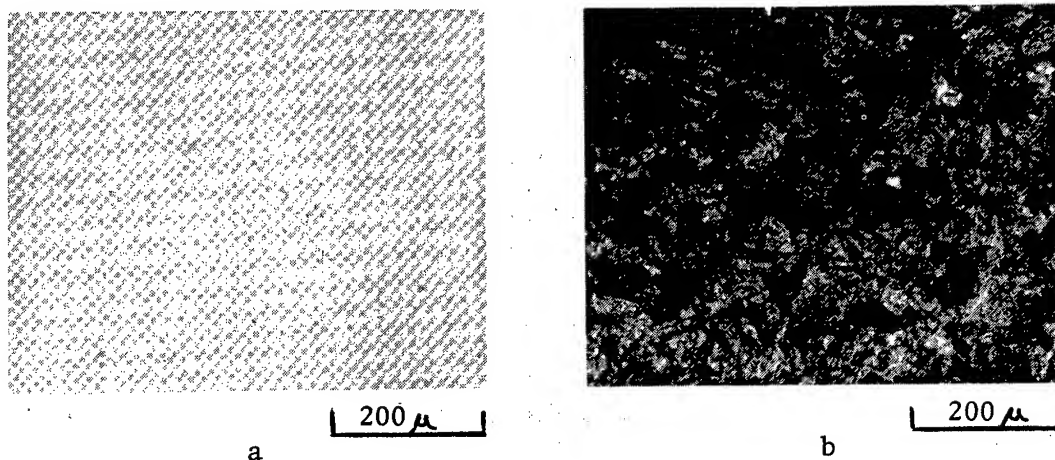


Figure 1. Unetched (a) and etched (b) microstructures of 4640 P/M steel forgings

The ultimate tensile and yield strengths of forged samples for different densities are shown in Figure 2. These properties were determined using standard R2 tensile bars (ASTM A370-E8). Ultimate tensile strengths and yield strengths were comparable to wrought 4640 material providing densities of 98 percent or higher were obtained. The excellent properties were achieved in the transverse as well as the longitudinal direction; thus, exhibiting the uniformity and fineness of the grain structure of the P/M forgings.

Elongation and reduction of area values for P/M forgings are shown in Figure 3. A very strong dependence on the final forged density is evident. As shown in Figure 4, these properties are also

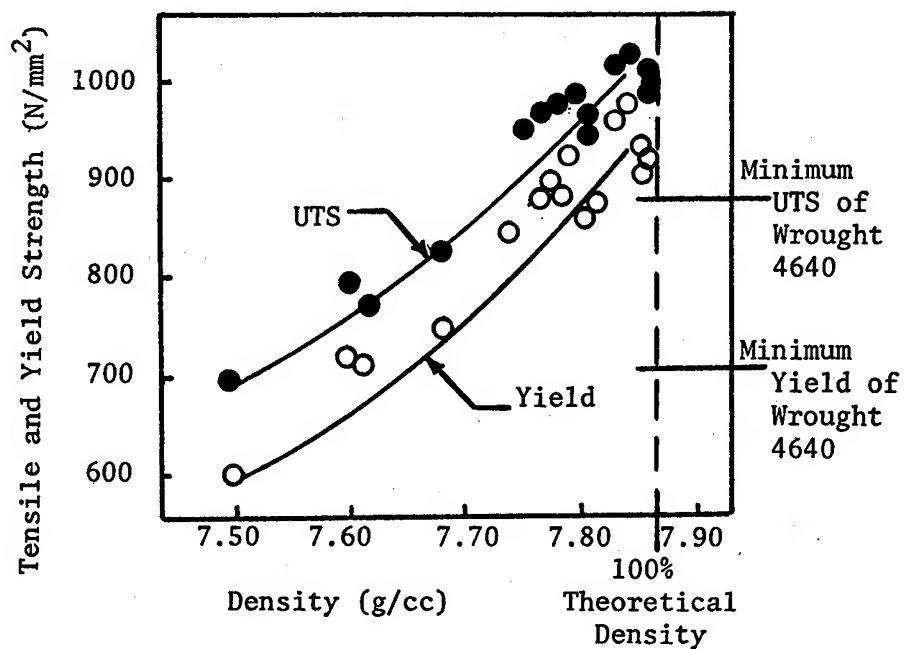


Figure 2. Tensile and yield strength vs. density of P/M steel forgings

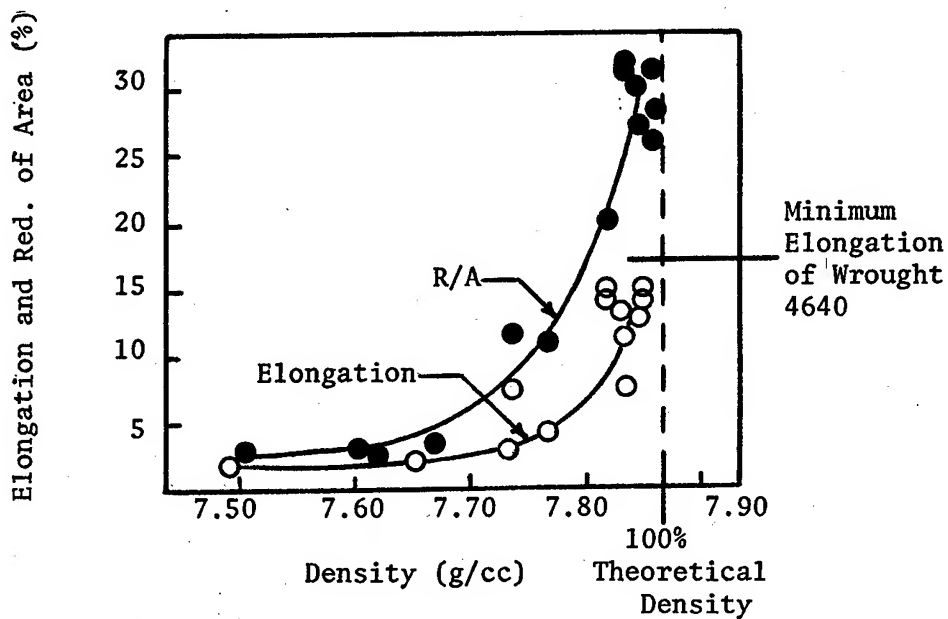


Figure 3. Reduction of area and elongation vs. density of P/M forgings.

very sensitive to oxygen content. To obtain ductilities equivalent to wrought materials requires a density of at least 99.5 percent of theoretical or better and an oxygen content below 300 ppm.

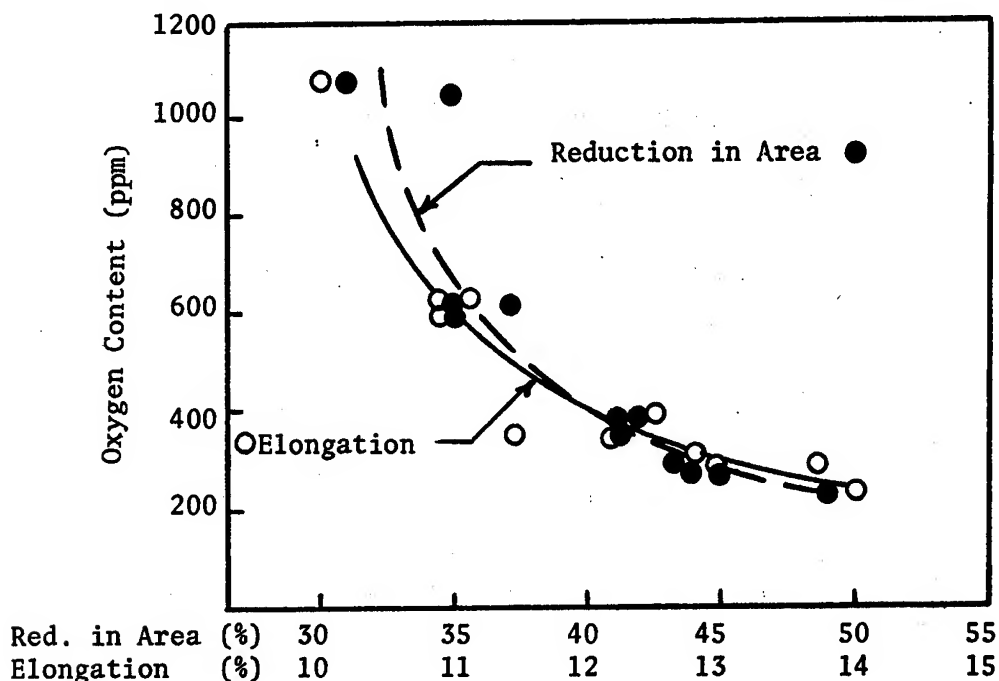


Figure 4. Reduction in area and elongation of P/M steel forgings as a function of oxygen content.

The response of P/M forgings to various heat treatments is shown in Figure 5. For comparison typical tensile properties of wrought 4640 (AMS specification 6317B) are shown. Tensile and yield strengths of the P/M forgings are shown to be comparable to the wrought material. Of greater significance, however, the elongation and reduction in area values are shown to be comparable to the wrought 4640 material throughout the hardness range investigated.

The impact strength (Figure 6) is, as expected, strongly dependent on the forged density. As theoretical density is approached, a dramatic increase in impact strength is obtained. Impact strength values were also found to be strongly dependent on the oxygen content (Figure 7). The presence of inhomogeneties either as oxide inclusions or as residual porosity can have a very detrimental effect on the impact properties.

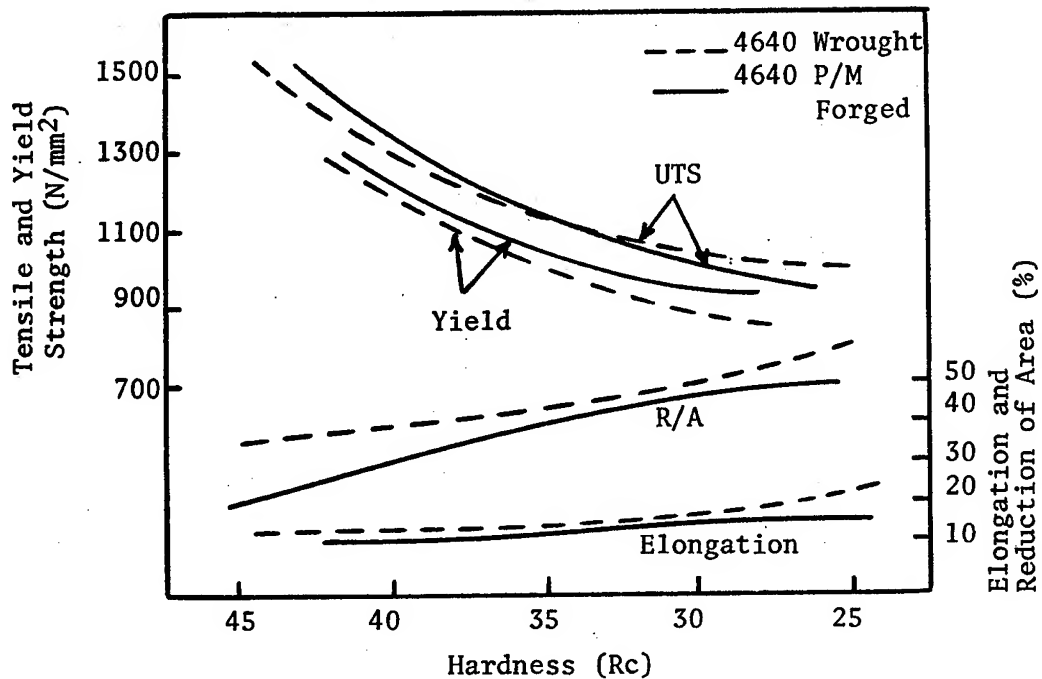


Figure 5. Response of 4640 P/M forgings to heat treatment

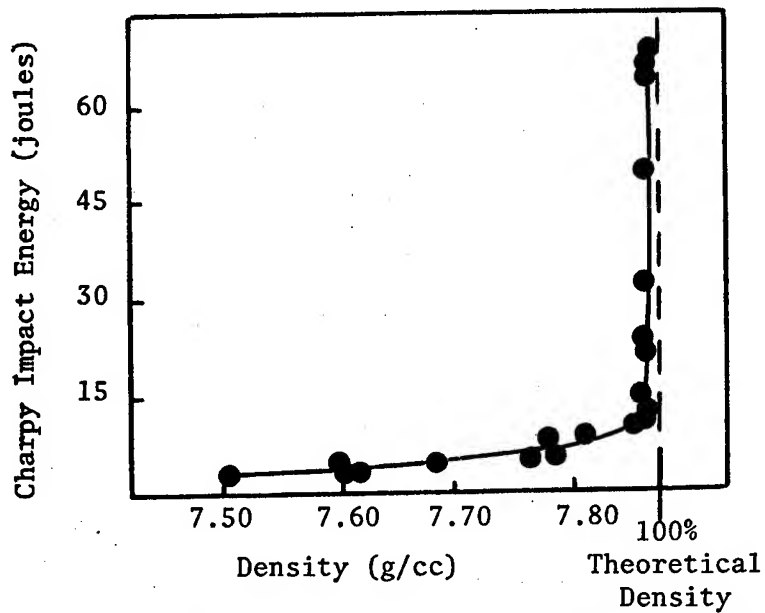


Figure 6. Charpy V-notch impact strength of P/M steel forgings as a function of density.

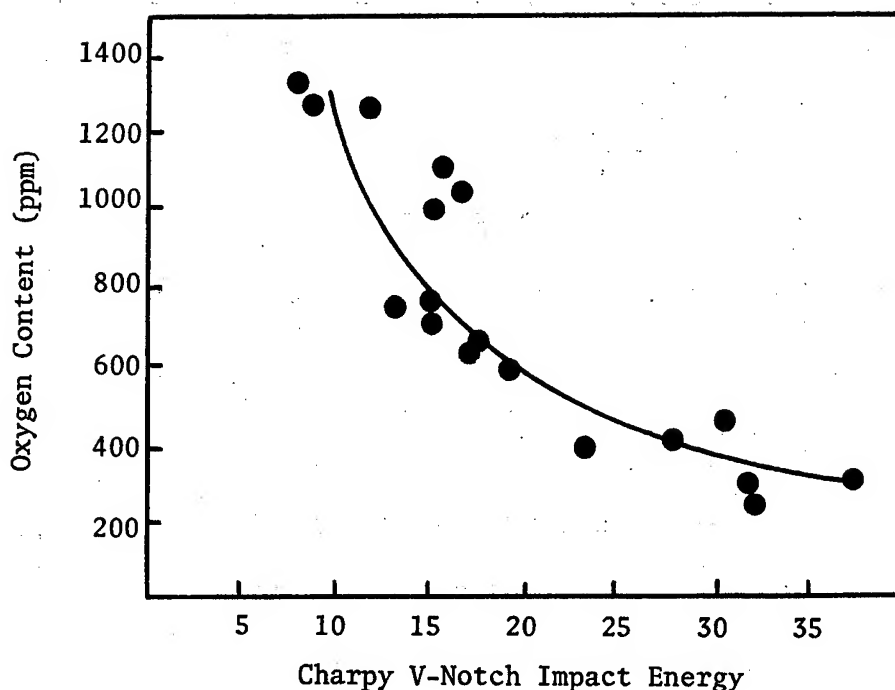


Figure 7. Impact energy of P/M steel forgings as a function of oxygen content

The results of the forging study have shown that P/M steel forgings can be competitive with wrought materials from a property standpoint. Mechanical property levels were reproducible and could be achieved routinely under proper processing conditions. Properties in the longitudinal direction were comparable to the wrought material whereas in the transverse direction they were found to be superior.

SMALL ARM APPLICATIONS

The applicability of the P/M forging process to an actual high-performance weapon component was demonstrated with the accelerator for the .50 caliber M85 machine gun (ref. 6). The actual part is shown in Figure 8. The geometry of the accelerator was sufficiently complex to demonstrate the ability of the P/M process to precision forge a complex configuration with a minimum of secondary machining operations. A comparison between the operations involved in the conventional process and the P/M forging process to fabricate the accelerator is shown in Figure 9. The conventional method involves progressively working through a series of dies which plastically form the metal into the desired shape. Excess stock, which is necessary

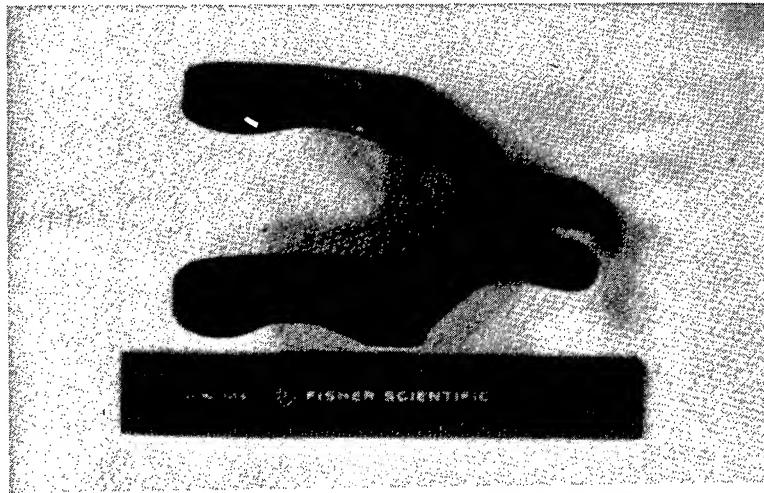


Figure 8. Accelerator for .50 caliber M85 machine gun

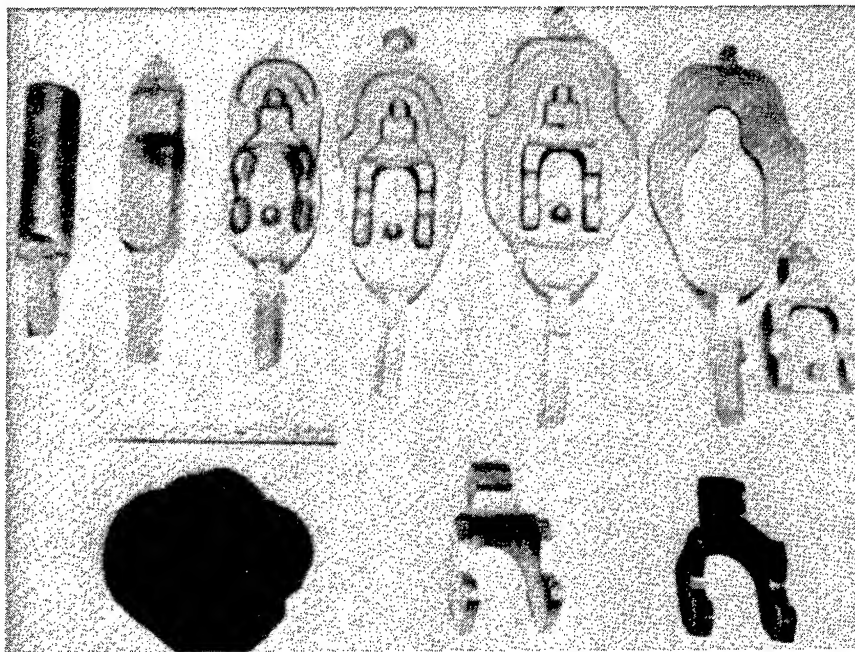


Figure 9. Pictorial comparison of conventional forging and P/M forging processes for producing forged accelerator

in order to completely fill the die, remains in the form of flash and must be trimmed. The final forging requires considerable machining before the desired part is obtained. In contrast, the P/M forging process utilizes a single flashless forging step and thereby reduces the number of machining steps necessary to obtain the final part. The areas requiring additional machining operations are indicated in Figure 10 by heavy lines. All other areas are forged to finish size.

A cost breakdown on the two processes for the fabrication of the M85 accelerator is shown in Table 2. The die costs for the P/M forging process are not included in this estimate. Amortization of the die costs would require a production run of approximately 1000 accelerators. However, once the die costs are amortized, a cost reduction of approximately 50 percent is projected.

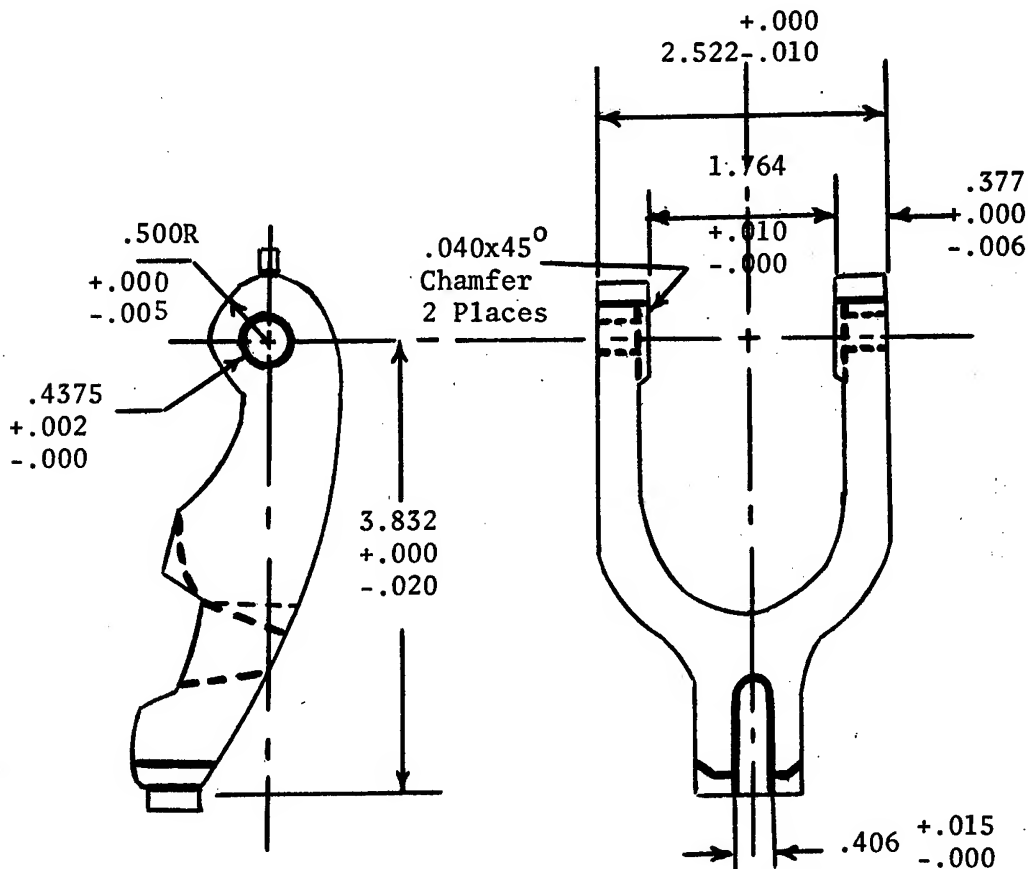


Figure 10. The as-forged accelerator with the post-forge machining operations indicated by heavy lines.

Table 2. *Cost breakdown - conventional forging vs. P/M forging
accelerator for .50 cal M85 machine gun

Conventional Process				P/M Forging Process		
Operation	Standard Hrs/Pc	\$/Pc	Setup Hours	Operation	Standard Hrs/Pc	Setup Hours
Heat & Forge	.0670	2.35	3.0	Compact	.0200	0.70 4.0
Trim	.0083	0.29	1.0	Sinter	.0025	0.09 -
Coin	.0083	0.29	1.0	Forge	.0200	0.70 3.0
Heat Treat*	.1600	5.60	-	Heat Treat	.0800	2.80 -
Sandblast	.0300	1.05	-	Sandblast	.0300	1.05 -
Machine	.8012	28.04	60.3	Machine	.2699	9.45 16.6
Finish	.1882	6.59	1.1	Finish	.1882	6.59 1.1
Material	-	1.50	-	Material	-	0.26 -

Totals Standard				Totals Standard		
Hours 1.2630	\$45.71	66.4		Hours .6106	\$21.64	24.7

*Cost of heat treat is proportional to weight of unmachined part.

The belt retaining pawl shown in Figure 11 is an example of another part found in the M85 machine gun that could be fabricated by P/M forging. Currently, this part is machined from wrought bar stock. The P/M forging process could produce this part net except for the final cross hole. This would result in a substantial cost savings. A summary of other possible parts in the M85 machine gun which could be cost effectively produced by P/M forging is listed in Table 3.

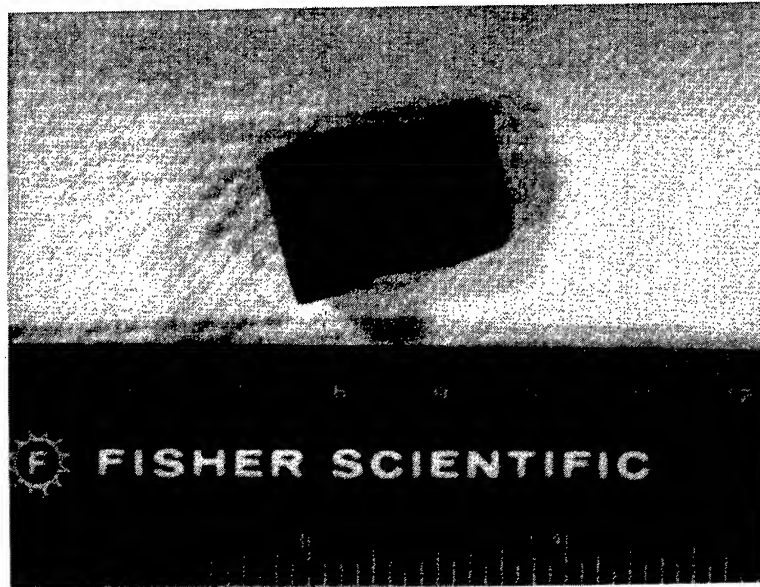


Figure 11. Belt retaining pawl for .50 caliber M85 machine gun

The .50 caliber M2 machine gun, likewise, has a variety of parts that can be fabricated by P/M forging. A partial listing is given in Table 4. As with the M85, the accelerator in the M2 is a prime candidate. The M2 accelerator is shown in Figure 12. A cost savings of approximately 50 percent could be realistically projected for this part, considering its similarity to the M85 accelerator. Other parts such as the alternate feed bolt, aligning pawl, and extractor have geometries similar to the accelerator and can be P/M forged with a minimum of secondary machining operations.

The 7.62mm M60 machine gun parts that could be fabricated by P/M forging are listed in Table 5. The sear, Figure 13, is an ideal part. Its configuration is such that it could be made to net shape requiring no further machining or, if desired with only a minimal amount of machining at the corners. This would be far more cost effective than the current method of machining from wrought bar stock. The barrel extension clamp (Figure 14) used in the M60 machine gun is likewise

CROWSON

Table 3. .50 caliber M85 machine gun parts having P/M forging fabrication potential

<u>Part No.</u>	<u>Nomeclature</u>
7790977	Accelerator
7790978	Housing, Accelerator
7790985	Block, Barrel Latch
7709087	Latch, Barrel
7791278	Interlock, Barrel Extension
7791378	Retainer, Cartridge Case
7792923	Block
7793074	Selector, Rate
7793076	Cylinder, Time Delay
7793083	Cam, Latch
7793132	Detent, Cover
7793157	Trigger
7793193	Extractor, Small Arms Cartridge
7793220	Disconnecter
7793222	Pawl, Cartridge Stop
7793225	Housing, Return Feed
7793230	Latch, Cover
7793232	Ramp, Guide Cartridge
7793244	Pawl, Cartridge Guide
8448210	Latch, Back Plate
8448226	Pawl, Belt Retaining
8448227	Slide, Belt Feed

Table 4. .50 caliber M2 machine gun parts having P/M forging fabrication potential

<u>Part No.</u>	<u>Nomeclature</u>
5351220	Slide, Sear
5504059	Bracket, Belt Holding Pawl
5504060	Latch, Bolt
5504061	Bracket, Bolt Latch
5504065	Extractor
5504070	Bracket, Top Plate
6008913	Pawl, Feed Belt
6008928	Latch, Cover
6008975	Pawl, Aligning Cartridge
6528256	Bolt, Alternate Feed
7161302	Breech Lock
7313081	Pawl, Belt Holding

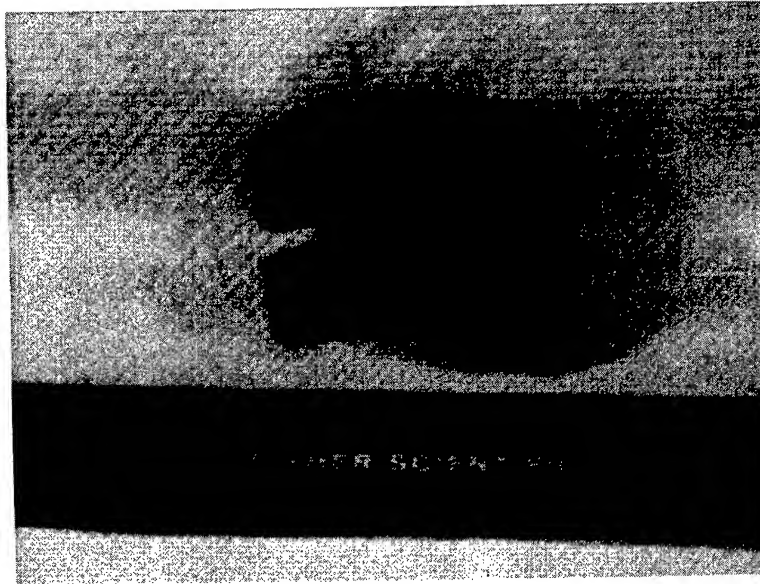


Figure 12. Accelerator for .50 caliber M2 machine gun

Table 5. 7.62mm M60 machine gun parts having P/M forging fabrication potential

<u>Part No.</u>	<u>Nomeclature</u>
7269083	Plunger, Extractor
7269088	Actuator, Cam
7269116	Guide, Cartridge Front
7269117	Guide, Cartridge Rear
7269136	Latch, Cover
7269147	Handle, Lever
7269201	Stop, Guide
7269209	Sear
7269284	Base, Rear Sight
7269285	Knob, Windage
7269288	Cap, Leaf Frame
7269291	Knob, Elevation
7269319	Hinge, Shoulder Rest
7269332	Pawl, Cartridge Retainer
7790907	Extractor
7791525	Plug, Bolt
7792093	Plug, Gas Cylinder
7793010	Pivot, Bipod

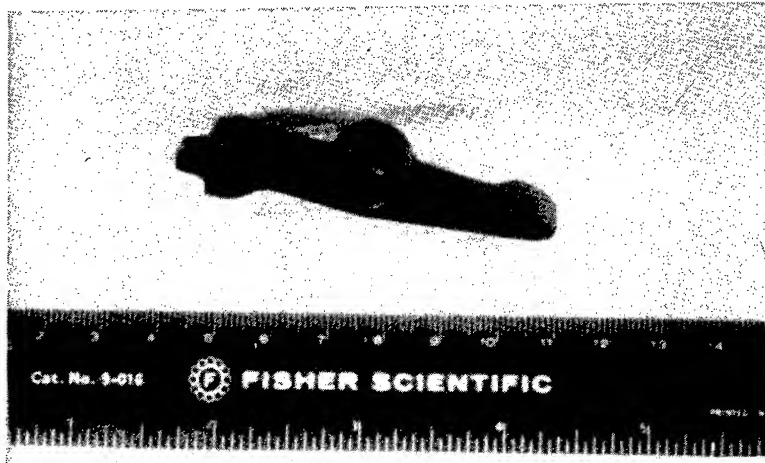


Figure 13. Sear for 7.62mm M60 machine gun

a prime candidate. It can also be made to net shape except for the drilled and tapped hole on the side. Such complexities as exhibited by these examples can be easily formulated in the parts by P/M forging; thus, eliminating many of the costly machining operations presently used.

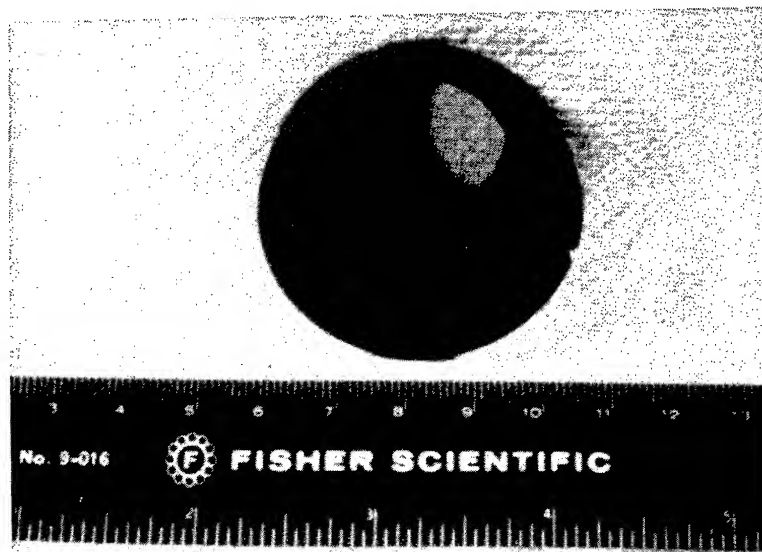


Figure 14. Barrel extension clamp for 7.62mm M60 machine gun

CONCLUSIONS

The applicability of the P/M forging process to fabricate high performance weapon components was demonstrated. Property levels were shown to be comparable to the same parts machined or forged from wrought bar stock. Major cost advantages were realized through more efficient material utilization and a reduction of machining operations. The cost effectiveness of the process, however, was not fully realized until amortization of the P/M compacting and forging dies was achieved. This usually necessitated an initial production run from 1,000 to 3,000 parts depending on the complexity of the part to be fabricated. Once this has been accomplished, a variety of parts from the M2, M60 and M85 machine guns can be fabricated with cost reductions ranging up to 50 percent.

REFERENCES

1. "Forging of P/M Preforms", Modern Developments in Powder Metallurgy, (Ed. H.H. Hausner), Plenum Press, NY, 1971, Vol. 4, pp 369-523.
2. R. F. Halter, "Recent Advances in the Hot Forming of P/M Preforms", Modern Developments in Powder Metallurgy, (Ed. H.H. Hausner), Plenum Press, NY, 1973, Vol. 7, pp. 137-152.
3. R. Gold, "Production P/M Hot Forming is Here", Precision Metal, Vol. 33, No. 11, 1975, pp. 23-26.
4. Gustafen, D. A., "HD:P/M = High Density Parts via P/M Techniques", Metal Progress, April 1972, pp. 49-58.
5. Lally, F.T. and Toth, I.J., "Forged Metal Powder Gears", Technical Report No. 11960, US Army Tank Automotive Command, Warren, MI, September 1974.
6. F. T. Lally, I. J. Toth and J. DiBenedetto, "Forged Metal Powder Products", SWERR-TR-72-51, Rock Island Arsenal, Rock Island, IL, August 1972.

DANIELS, WRIGHT, KNAPIK, VOGEL, FRIMAN & BEISEL

THE EFFECT OF EXPERIMENTALLY INDUCED VIRAL INFECTION
ON PHYSICAL PERFORMANCE CAPACITY

*WILLIAM L. DANIELS, CPT, MS, Ph.D., JAMES E. WRIGHT, CPT, MS, Ph.D.
JOSEPH J. KNAPIK, SP6, M.S., JAMES A. VOGEL, Ph.D.
GORAN FRIMAN, M.D. and WILLIAM R. BEISEL, M.D.

US ARMY RESEARCH INSTITUTE OF
ENVIRONMENTAL MEDICINE

NATICK, MA 01760

US ARMY MEDICAL RESEARCH INSTITUTE OF
INFECTIOUS DISEASES
FORT DETRICK, MARYLAND 21701

I. Introduction

The purpose of this study was to investigate the effect of a viral infection upon the individual soldier's performance capabilities. Sandfly fever was induced for this study, not because of any threat which sandfly fever may potentially carry, but because it is an appropriate disease model for a viral infection. Sandfly fever, known medically as Phlebotomus or Papatasi fever, is a self-limiting febrile illness which is transmitted by biting insects of the genus Phlebotomus. Although this illness is not serious clinically, it does have a tendency toward explosive outbreaks in large groups of susceptible individuals after short periods of exposure and thus has some potential for hazard to military operations in certain parts of the world. However, the reason for its use in this study is that it is a well understood, limited, viral illness which is suitable for study as a model infection.

The disease is characterized by the sudden onset of flu-like symptoms. These include headache, generalized malaise, photophobia and aching in the muscles and joints. The most common clinical feature is leukopenia, which is a decrease in the white blood cell count. Anorexia, nausea and vomiting may also be associated with ill defined abdominal distress. The disease has a very predictable clinical course with no sequelae or complications (1).

The purpose of this study was to evaluate the ability of soldiers to perform physical exercise during the febrile and early convalescent periods of an acute infectious disease. The effect of the disease on measurements used to assess an individual's level of physical conditioning were also determined.

II. Methodology

For this study, 9 subjects (7 experimentals, 2 controls) volunteered to undergo a series of tests before, during and after an experimentally induced episode of sandfly fever. The 2 control subjects were sham-inoculated with isotonic saline. The 7 experimental subjects were inoculated with plasma containing the sandfly fever virus. This plasma had been obtained, on the first day of illness, from a previous human volunteer. The overall experimental schedule for the study is outlined in Table 1.

Test subjects were divided into two groups for initial testing. While one group performed the aerobic test procedures, the second group performed the muscle strength tests. The morning of days -4 and -2 served as an introductory period for the test subjects. During this time, they were familiarized with the tests that they were to undergo.

On the afternoon of days -4 and -2 subjects began testing. The aerobic portion consisted of three types of procedures:

- 1) resting measurements
- 2) submaximal walking
- 3) maximal oxygen uptake ($\dot{V}O_{2\max}$) test

1. Resting measurements

At the beginning of each aerobic exercise session, subjects underwent resting measurements of heart rate (12 lead ECG), blood pressure and rectal temperature. In addition, all subjects performed a pulmonary function test. Weight and skin fold measures were taken for estimation of % body fat.

2. Submaximal walking

After the resting measurements, subjects began walking on a motor-driven treadmill at a speed of 3 mph and 0% grade. Every 3 minutes the grade was increased by 3% up to a maximum work load of 15% grade. During the last minute at each work load, heart rate,

Table 1: Experimental Schedule

<u>Day of Week</u>	<u>Study Day</u>	<u>Testing Procedure</u>		<u>Strength</u>
		<u>Aerobic</u>		
Friday	-7	Screening Physical		-
Monday	-4	AM Introduction of Procedures to Group A PM Sub-max Walking Group A		Group B Static & Dynamic
Tuesday	-3	Running $\dot{V}O_2$ max on Group A		Group B Hand-grip
Wednesday	-2	AM Introduction of Procedure to Group B PM Sub-max Walking Group B		Group A Static & Dynamic
Thursday	-1	Running $\dot{V}O_2$ max on Group B		Group A Hand-grip
Friday	0	Inoculation with Plasma or Saline 0800 hours		-
Sunday	2	Hospitalization 1200 hours		-
Monday	3	PM Sub-max Walking for Febrile S's		AM Static Dynamic & Handgrip on Febrile S's
Tuesday	4	PM Sub-max Walking for Remaining S's		AM Static Dynamic & Handgrip on Remaining S's
Thursday	6	AM Sub-max Walking for S's Febrile on Day 3. PM $\dot{V}O_2$ max run		AM Static Dynamic Hand-grip on S's Day 3
Friday	7	AM Sub-max Walking on Remaining S's PM $\dot{V}O_2$ max run		AM Static Dynamic & Handgrip on Remaining S's
Hospital Discharge 1600 hours				

blood pressure, RPE, rectal temperature and oxygen consumption were measured. Rating of perceived exertion (RPE) is a measure of perception of effort and is a valid predictor for the point at which an individual will discontinue work (2).

3. Maximal oxygen uptake ($\dot{V}O_{2\max}$) test

During the pre- and post-fever exercise session, the subject performed a $\dot{V}O_{2\max}$ determination. Initially, all subjects began running on the treadmill at a speed of 6 mph and 0% grade for 6 minutes. Following a 5-10 minute rest period, two to four additional runs were performed, each interrupted by a rest period. Work load was increased by adjusting speed and/or grade. During the last minute of each work load expired air was collected and analyzed. A plateau in oxygen consumption was defined as $\dot{V}O_{2\max}$.

Muscle strength capacities were assessed by both static and dynamic strength and endurance tests.

Maximal static strength

Maximal static strength of three muscle groups were measured by a device designed in this lab (3). The muscle groups tested were: upper torso, trunk extensors and legs. Two 3-4 second maximal isometric contractions were performed for each muscle group with a one minute rest between contractions. Forces were registered on electronic force transducers (BLD Model C2M1) and through digital transducer indicators (BLH Model 450A) were input displayed and recorded in a DECLAB 11/03 minicomputer which analyzed the force curves at 0.01/sec intervals.

Strength of the upper torso group was assessed with the subject securely fastened in a sitting position with a lap belt. The upper arms were positioned parallel to the floor with the elbows at a 90° angle. The hands grasped an overhead bar that is attached by a cable to the force transducer.

Strength of the leg extensors was assessed with the subject seated as above with the knees bent at 90°, the arch of the feet pushing against a bar attached by a cable to the transducer.

Strength of the trunk extensors was assessed with the subject in a standing position with the shoulders strapped to a bar which was connected to a transducer. The subject flexed back against the shoulder harness while driving the pelvic girdle against a stabilizing plate.

Isometric grip strength was measured with a handgrip ergometer which was adjusted for each subject so as to allow maximal grip output. Subjects exerted maximal grip strength for 3-5 seconds which was transferred through a turn-buckle to a force transducer and into the DECLAB 11/03 minicomputer. Static handgrip strength endurance time at 40% maximal force was assessed using the same apparatus.

Dynamic muscle strength

Maximal dynamic strength and power of the elbow-flexors and knee extensors was assessed utilizing isokinetic measuring equipment (Cybex Div., Lumex Corp., Bayshore, NY). For both the arm and leg measurements, the subject was seated and fastened by arm, leg and shoulder restraints into a heavy well-padded wooden chair which was in turn securely coupled to the isokinetic torque unit (Cybex II dynamometer). A separate apparatus was used to measure arm and leg capacities. Force exerted by the subject, measured as torque, was transferred from the dynamometer via an amplifier to a paper recorder and work integrator. Muscle strength was assessed with two individual maximal contractions for each muscle group at each of two contractile velocities, 36 and 180 degrees per second.

III. Results

The effect of virus inoculation on the test subjects is clearly illustrated in Figure 1. Rectal temperatures (T_{re}) began to increase 48 hrs after inoculation in the experimental subjects and reached their peak values within 72-96 hours after inoculation. No significant changes occurred in the T_{re} of the two controls. Experimental subjects developed the characteristic clinical findings and symptomatology for sandfly fever (Figure 2).

During the fever state, 3 subjects were unable to complete the submaximal treadmill walk.

Subject #4302 - felt dizzy at the end of 9% workload and the treadmill was stopped.

Subject #4307 - complained of shortness of breath, headache, and dizziness; treadmill stopped after 30 seconds at 12% grade.

Subject #4308 - stated that he could not complete test and stopped after 1.5 minutes at 9% grade.

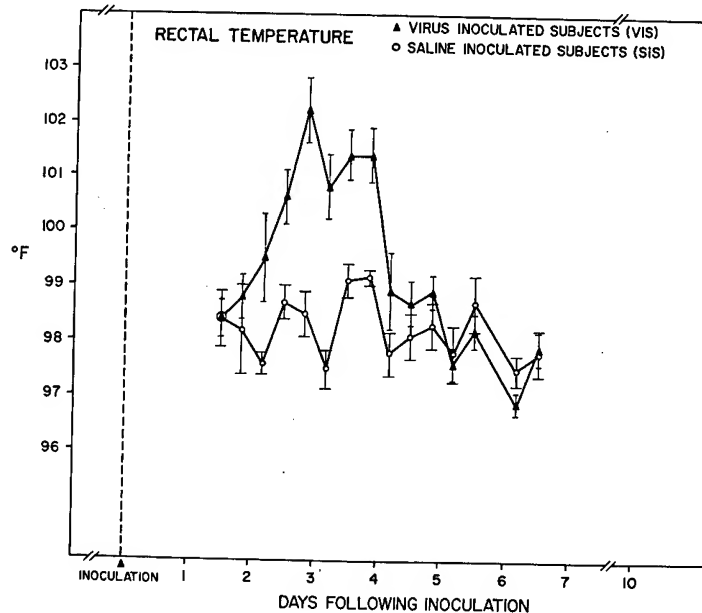


Figure 1. Effect of Sandfly Fever virus on rectal temperature.

During fever, the T_{re} was higher at all submaximal workloads as well as at rest. However, the rate at which T_{re} increased with exercise was not altered by the fever (Figure 3). Resting heart rate was also significantly elevated during fever. Exercise heart rates were also higher during fever than in either the pre or post fever state but the only significant difference was between the fever and post fever state at 0% grade (Figure 3).

The energy cost of walking was unaffected by the viral infection. Values obtained for oxygen consumption are listed in Table 2. Any differences between the values are within the limits of the measurement system or variations normally seen between subjects on repeated testing.

There were shifts in other parameters during fever that did indicate some effect due to viral infection. Perceived exertion (RPE)

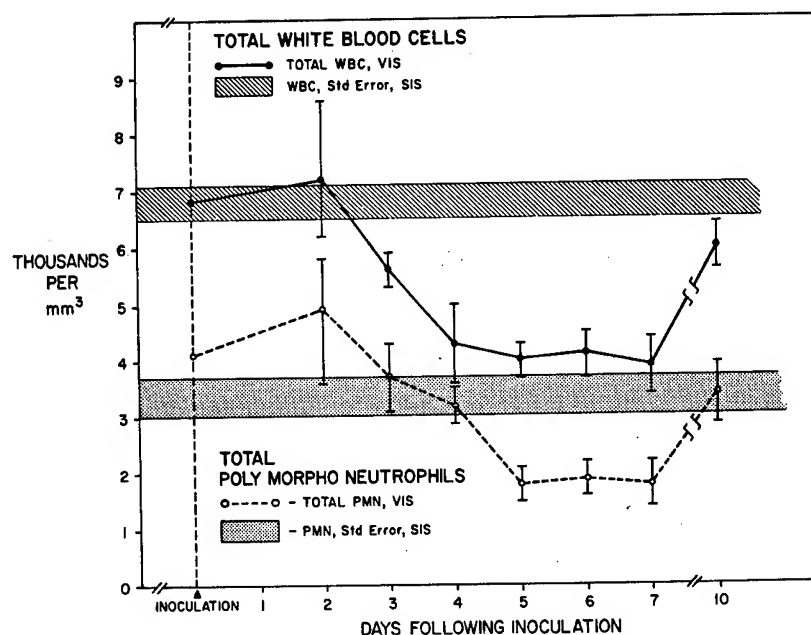


Figure 2. Effect of Sandfly Fever on total white cell count and polymorphoneutrophils.

(Borg's Scale) was significantly higher than the pre-inoculation values at 0% and 6% grade during the fever. Controls showed no change in RPE (Figure 4).

An increase in the ventilatory equivalent was also seen at the higher workloads in the experimental subjects (Figure 4). However, the control subjects also showed an increase in VEQ at higher workloads during the fever and post fever testing. Therefore, this increase could be due to some factor other than a direct effect of the virus.

In addition to the effects on submaximal walking performance, viral infection also caused a significant decrement on muscle strength measures. Mean strength capacities were reduced from 2 to 28% during fever. Values showed some signs of recovery during early convalescence but for the most part, they were still reduced. The control subjects were not affected in the same manner. The results of the muscle strength testing are summarized in Figure 5.

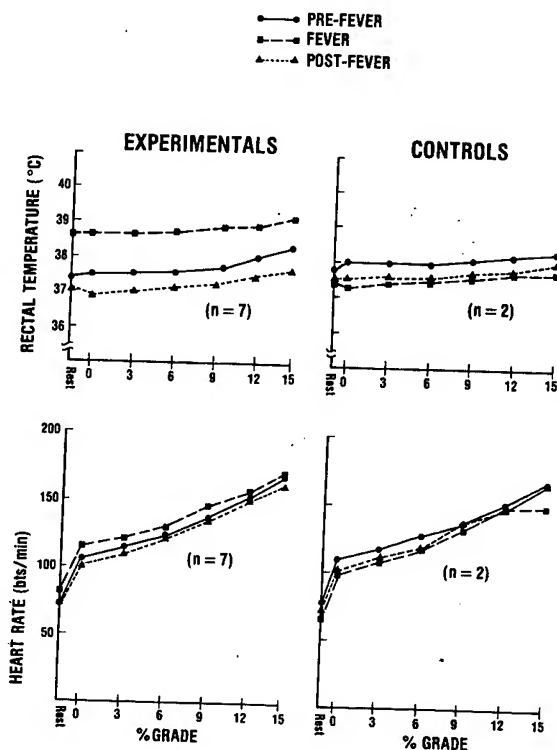


Figure 3. Comparisons of heart rate and rectal temperature during exercise.

All isometric tests were markedly decreased during fever. The decreases in upper torso, handgrip and leg isometric strength were all statistically significant ($p < 0.05$). Although the overall effect of fever on back extensors and handgrip endurance was a decrease (15 and 28.6%, respectively), the effect was much more variable than in the other isometric measures and the decreases were not statistically significant. Dynamic strength was decreased only in the legs and this decrease was statistically significant only at the slow speed.

The final test results to be reported here are those obtained during the two maximal oxygen consumption determinations that the subjects performed. The results are summarized in Figure 6, which

Table 2. Oxygen consumption (ml/kg.min) while walking at increasing grade before, during and after fever.

	<u>Pre- Inoculation</u>	<u>Fever</u>	<u>Conva- lescence</u>
		3 mph 0%	
Experimentals (n = 6)	15.35	15.77	14.97
Controls (n = 2)	16.15	14.55	15.25
		3 mph 3%	
Experimentals	18.70	18.42	18.13
Controls	18.80	17.70	18.25
		3 mph 6%	
Experimentals	21.52	21.40	21.35
Controls	22.05	20.35	21.05
		3 mph 9%	
Experimentals	25.15	26.06	25.85
Controls	24.95	24.65	25.75
		3 mph 12%	
Experimentals	29.97	30.52(n=4)	29.32
Controls	30.45	29.30	30.25
		3 mph 15%	
Experimentals	35.15	33.70(n=4)	33.68
Controls	34.75	28.80(n=1)	34.40

illustrates that in all the parameters measured the response of the experimental subjects during early convalescence was lower than that of the controls. Generally the responses of the controls and experimentals were similar when compared to pre-fever values. Experimentals had slightly larger decreases in $\dot{V}O_{2\max}$ and HR_{\max} . Ventilation increased more in controls than the experimentals. The major difference between controls and experimentals was the grade at which they were working when they achieved maximum effort.

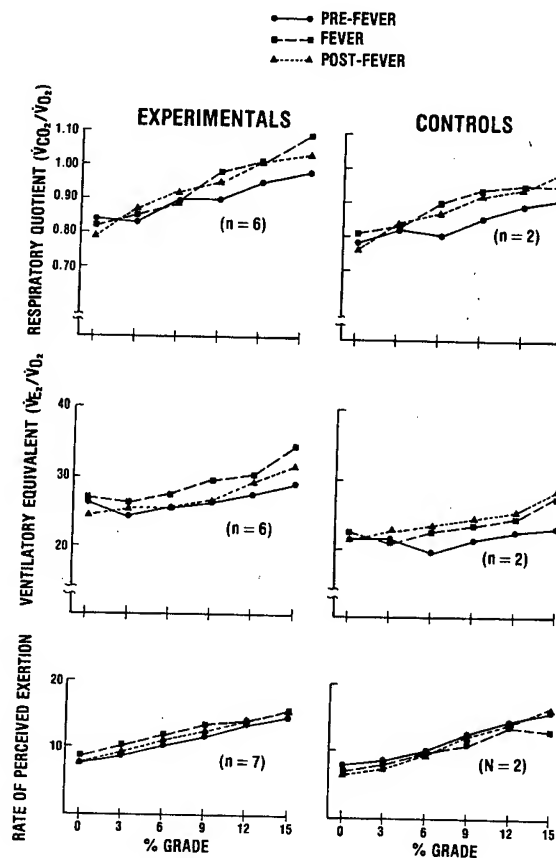


Figure 4. Comparison of respiratory quotient, ventilatory equivalent, and perceived exertion during exercise.

IV. Discussion

The results of this study indicate that in respect to physical performance, an acute viral infection shows the most detrimental effects on measures of muscle strength. These were especially apparent during the fever state. Although strength measures were still reduced during early convalescence, the reductions were not statistically significant. It is interesting to note that maximal isometric strength contractions appeared to be more affected than dynamic strength.

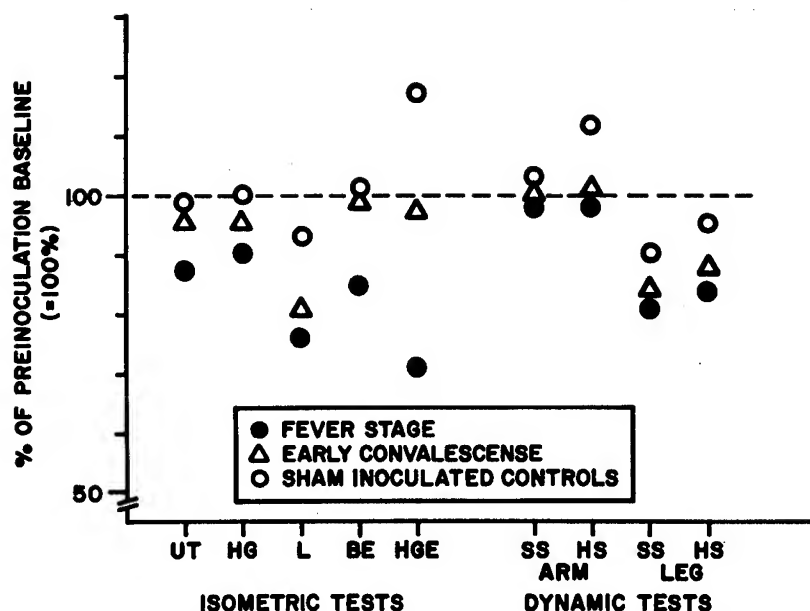


Figure 5. Comparison of muscle performance tests during Sandfly Fever Study.

The results obtained in this study agree very nicely with previous studies (4) which indicate that infectious disease has a detrimental effect on isometric muscle strength. The exact mechanism by which this occurs is not known. Muscle biopsies which were taken in this study indicate that a certain amount of protein breakdown occurs during viral infection. However, effects of virus upon the central and peripheral nervous system and upon the neuromuscular junction cannot be ruled out. The fact that isometric strength is affected more than dynamic strength may indicate that the viral infection interferes with the recruitment of muscle fibers during maximal contractions rather than having a direct effect on the muscle cells.

The submaximal walking data showed very few physiological differences between the various stages. Heart rate was elevated during the fever but this was only significant at the lower levels of exercise. This seems to indicate that the sympathetic drive which was present at rest during fever did not have an additive effect upon

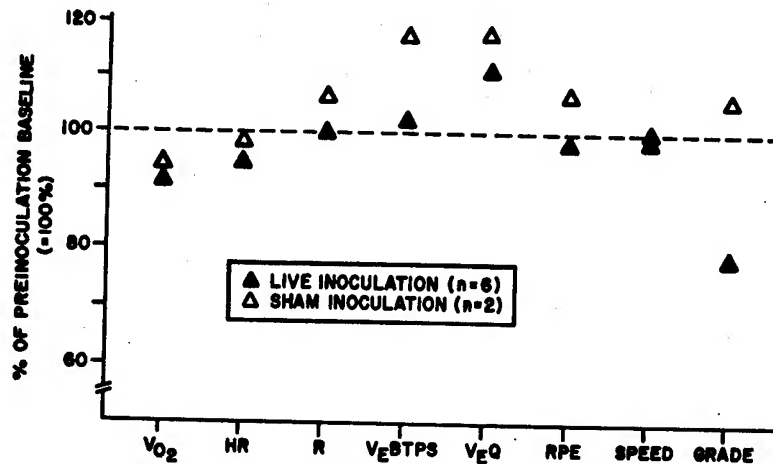


Figure 6. Data collected at $\dot{V}O_{2\text{max}}$ prior to fever compared to early convalescence.

the sympathetic response to exercise at the higher workloads. It is also important to note that the rate of temperature increase during exercise was not altered during the fever state even though the T_{re} were almost 1°C higher during the fever stage. Elevated temperature also did not affect oxygen consumption. The most apparent effect of the virus on submaximal walking was the inability of three subjects to complete the task. However, there was no parameter that we measured which predicted this. The most striking relationship occurred between the subject's performance and his own rating of 4 specified symptoms (headache, myalgia, nausea and chills). The greater the sum of these symptoms; i.e., the sicker the individual felt; the worse his performance. Therefore, the virus appears to have a very marked effect upon the ability and/or the willingness of various individuals to perform work, more so than an actual decrement in capacity.

Finally, in terms of aerobic capacity ($\dot{V}O_2\text{max}$), both the experimental and control subjects responded with a decrease in $\dot{V}O_2\text{max}$. It therefore appears that some other factor, other than the virus, was responsible. It is well known that bedrest or inactivity can cause significant decreases in aerobic capacity (5). This may have been a contributing factor in the decrease seen here. Another factor that may have influenced aerobic capacity was a loss of blood volume by the subjects. During this study a number of blood samples were obtained over the two week period in order to perform various laboratory and clinical tests. Although the amount taken at any one time was not large, the cumulative total was over 1.5 units of blood. It has also been demonstrated that if this amount of blood is removed at any single time, there will be a decrease in aerobic power (6). Therefore, it seems logical that this may also be a contributing factor to the decrease. There was one result, however, which also indicates that the virus is not without affect. Experimental subjects showed a marked decrease in the grade at which they achieved their maximum effort after the fever. This was in marked contrast to what was seen for the control subjects. This seems to indicate that the virus has some effect but just exactly what the mechanism involved would be, is not known.

In conclusion, the results of this study demonstrated quite clearly that an acute viral infection can have detrimental effects upon the individual's physical performance. Muscle strength and ability to perform submaximal work were clearly affected during the fever stage. Muscle strength and maximal aerobic power were still reduced in early convalescence although factors other than the infection may be responsible for the decrease in aerobic power. The effect of analgesic and anti-pyretic agents upon the symptoms of this viral infection were not looked at in this study. How the alleviation of symptoms would affect performance and muscle strength can only be determined by future study. However, commanders can expect that individuals suffering from acute viral infections will be unable to perform up to their potential capacity, not only during the infection, but also for at least a few days following the infection.

References

1. Bellanti, J.A., R.I. Krasner, P.J. Bartelloni, M.C. Young and W.R. Beisel. Sanfly fever: Sequential Changes in Neutrophil Biochemical and Bactericidal Functions. J. of Immunol. 108: 142-151, 1972.
2. Borg, G. and B.J. Noble. Perceived Exertion. In: Exercise and Sports Sciences Reviews, J.H. Wilmore (ed.). New York, Academic Press. pp. 131-153, 1974.
3. Knapik, J.J., D.M. Kowal, P. Riley, J.E. Wright and M. Sacco. Development and Description of a Device for Static Measurement in Armed Forces Examination and Entrance Station. USARIEM Technical Report T-2/79, 1979.
4. Friman, G. Effect of Acute Infectious Disease on Human Isometric Muscle Endurance. Upsala J. Med. Sci. 83:105-108, 1978.
5. Friman, G. Effect of Clinical Bed Rest for Seven Days on Physical Performance. Acta Med. Scand. 205:389-393, 1979.
6. Ekblom, B., A.N. Goldborg and B. Gullbring. Response to exercise after blood loss and reinfusion. J. Appl. Physiol. 33(2):175-180, 1972.

DEAN

EVALUATION OF ICE-COVERED WATER CROSSINGS

ARNOLD M. DEAN, JR.

U.S. Army Cold Regions Research and Engineering Laboratory
Hanover, New Hampshire 03755

Introduction

When mobility in northern regions is being considered, the need for a means to assess ice-covered water crossings becomes evident. There are two major aspects to this problem: determination of the crossing profile (from which one obtains ice thickness, support characteristics, and crack locations), and determination of the bearing capacity of the crossing. This paper discusses instrumentation developed through the U.S. Army Cold Regions Research and Engineering Laboratory to remotely measure the ice thickness and its relationship to the water body, the banks, and other ice forms. It further references applicable work done on the bearing capacity of ice sheets, and comments on the problems associated with the determination of ice strength.

Description of Instrumentation

The instrumentation used is a commercially available broad-band impulse radar system, which has been modified specifically for the remote sensing of ice thickness. The components of the system are shown in Figures 1 and 2.

The selection of the antenna (Fig. 1) determines the operating frequencies of the system. The center frequencies of the antenna range from about 100 MHz to 600 MHz, with about a 200-MHz bandwidth, and the peak radiated power varies from 2 W to 15 W. The radio frequency (RF) transmit and receive (T/R) functions are entirely within the antenna. By a sampling technique the RF is shifted down to audio

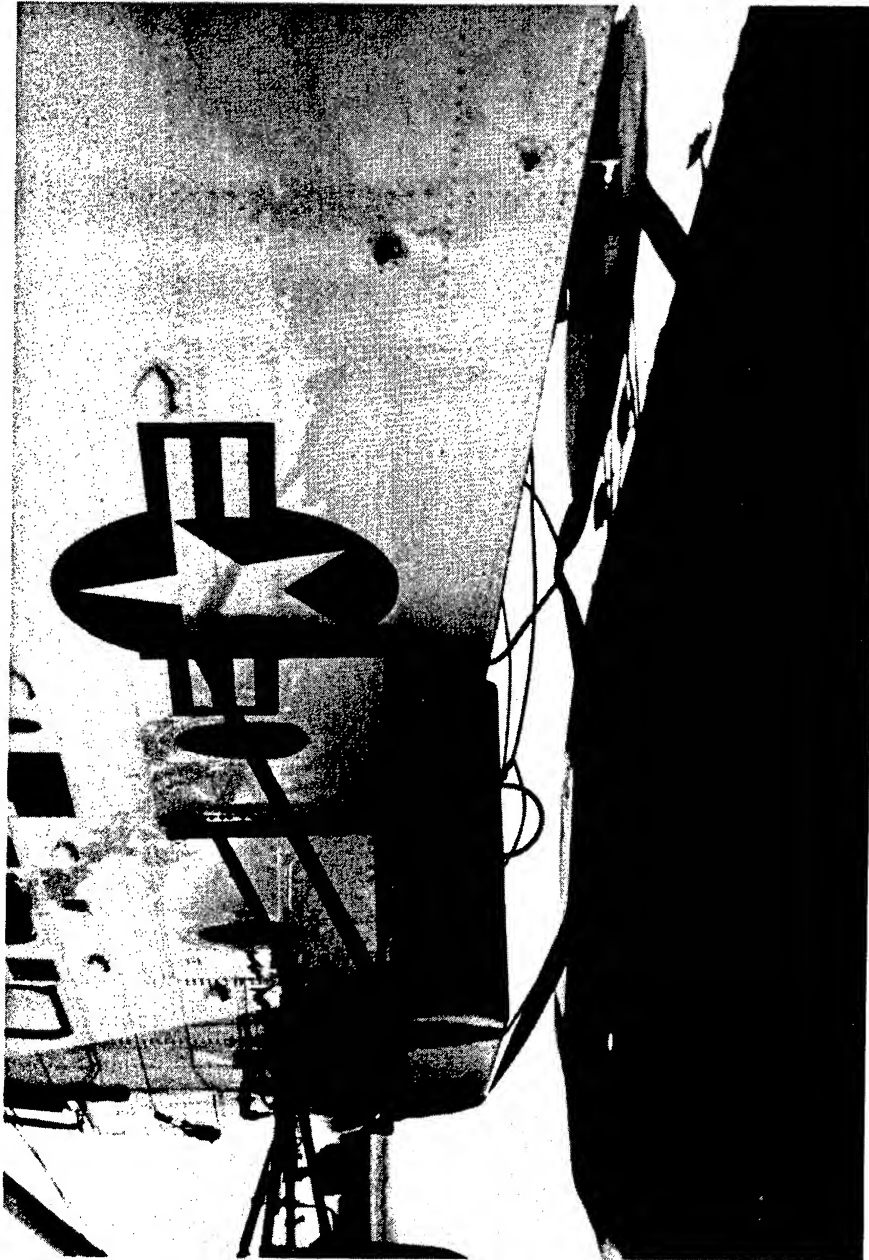


Figure 1. Radar ice-profiling antenna attached to USCG SAR helicopter for airborne operation.

DEAN

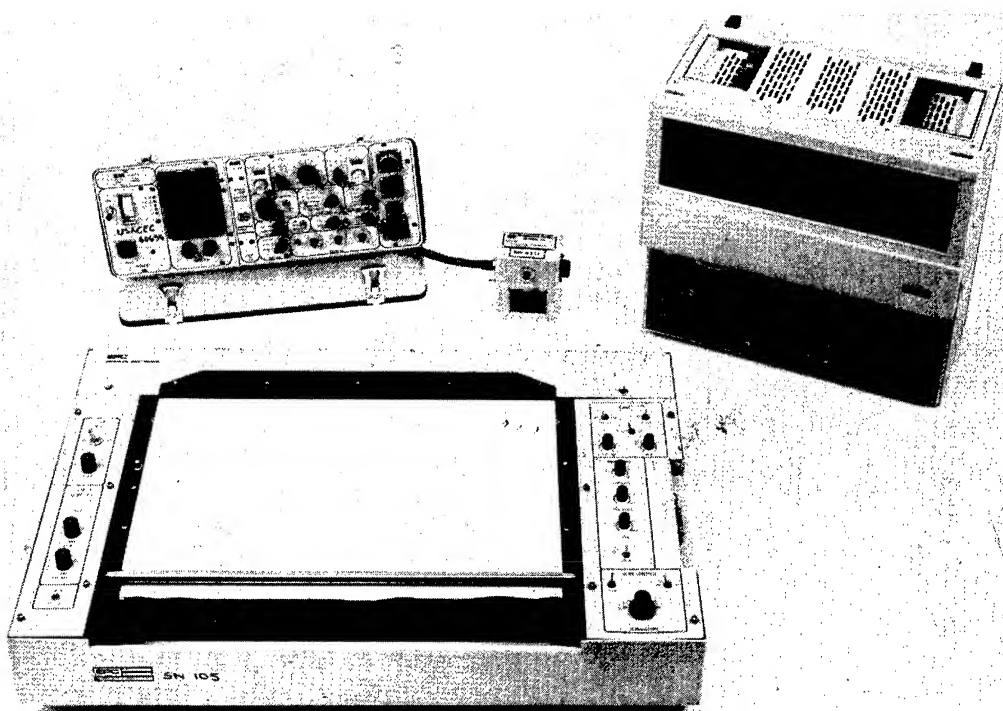


Figure 2. Components of the ice-profiling radar system (left rear control unit; right rear, analog tape recorder; foreground, graphic display unit).

DEAN

frequencies (AF) of 0-50 kHz to communicate with the control unit (upper left, Fig. 2) and to be compatible with the analog recorder (upper right, Fig. 2). The antenna is a center-fed, resistively loaded bow tie design.

The control unit provides control, timing, power and data manipulation. The unit allows the operator to control sample rates, recording rates, time gain, and data manipulation parameters, and to monitor the signal analog at various points throughout the system. Data manipulation is effected through an 8-bit microprocessor which implements a real-time digital filter. The characteristics of the filter are externally programmable. The microprocessor provides a precise band-pass/reject function which aids noise rejection and signal enhancement. Further, a non-biasing filter prevents harmonic interference.

The analog tape recorder and the graphic unit (foreground, Fig. 2) are commercially available and standard storage and display units, respectively. The radar system transmits a broad band of energy into the medium being surveyed, and waits with an equally broad-windowed receiver for the returning signals. The signals are reflections from interfaces where the dielectric constant changes. A typical return signal on the CRT monitor (Fig. 3, left) has its counterpart on the graphic display printout (Fig. 3, right). Reflections cause signal excursions from the center region, which are depicted as sets of dark bands on the graphic. As the antenna is moved across a river section, for instance, the ice/water interface and the water/earth interface are detected and displayed as bands whose positions vary with the ice thickness and the channel configuration, respectively. The physical characteristics of the units which compose the radar system are listed in Table 1.

Table 1. Physical characteristics of the CRREL impulse radar system.

	Weight kg (lb)	Dimensions hxwxl, cm (~ in.)
Control unit	11 (24)	18x44x39 (7x28x16)
Graphic recorder	27 (60)	12x82x53 (5x33x21)
Tape recorder	28 (62)	41x48x24 (16x19x10)
Antenna, T/R	36 (80)	34x97x94 (14x38x37)
Airborne antenna, T or R	7.5 (16.5)	27x54x90 (11x22x35)

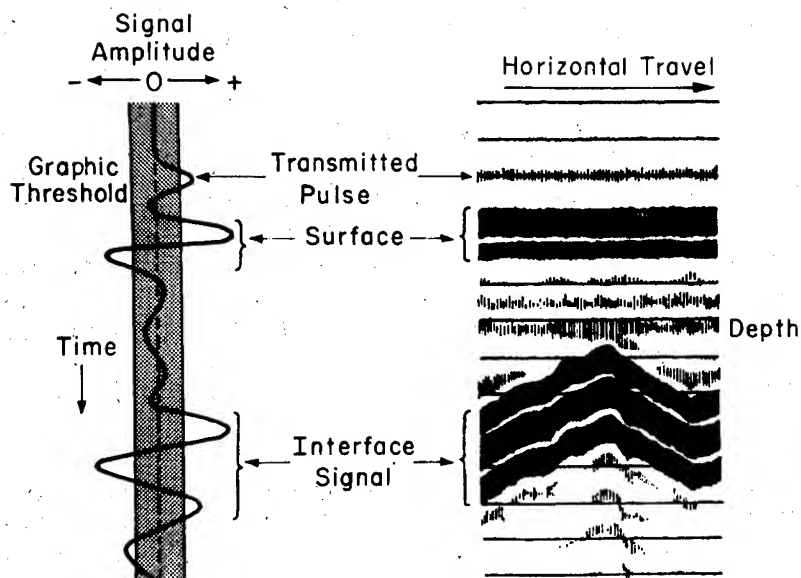


Figure 3. Ice-profiling radar system, received signal and graphic analogy.

Applications -- General

The CRREL prototype system has enjoyed a variety of applications in the last 5 years. These include both surface and air deployment. The unit has been pulled behind vehicles to measure sheet ice thickness, and flown in helicopters to measure brash and frazil accumulations, ice jams and ice runs. It has been used to profile lake bottoms and river bottoms in highly air-entrained water, and to evaluate ice bridge construction.

The airborne configuration of the system is shown in Figure 4. The helicopter positions the antenna some 4 m off the ice. When data are collected, the control unit and the tape recorder are taken to the graphic display device on the ground and a printout is made. Interpretation is made from the printout.

Figure 5 shows a transverse profile of ice accumulation due to ship traffic in the St. Marys River near Sault Ste Marie, Michigan. These data were taken in the airborne configuration and illustrate the capability of the system to be used in the airborne mode and still

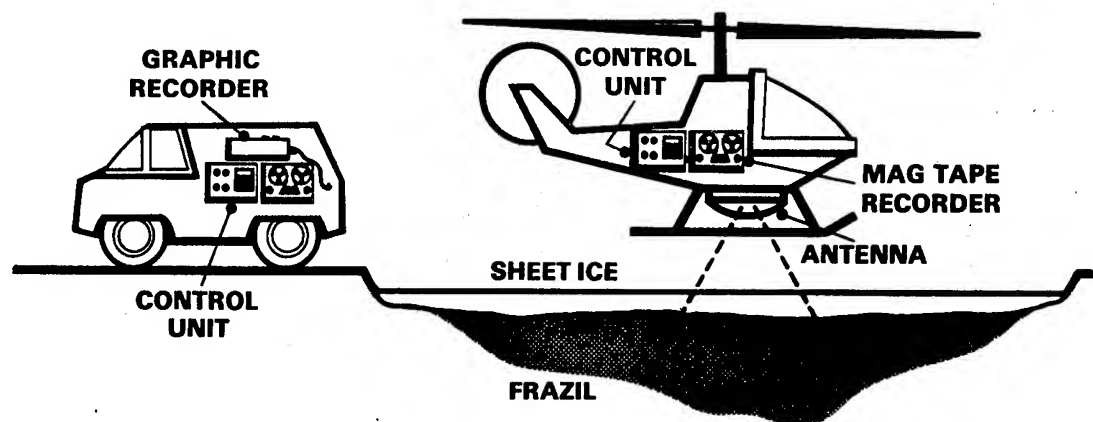


Figure 4. Airborne configuration of the ice-profiling radar system.

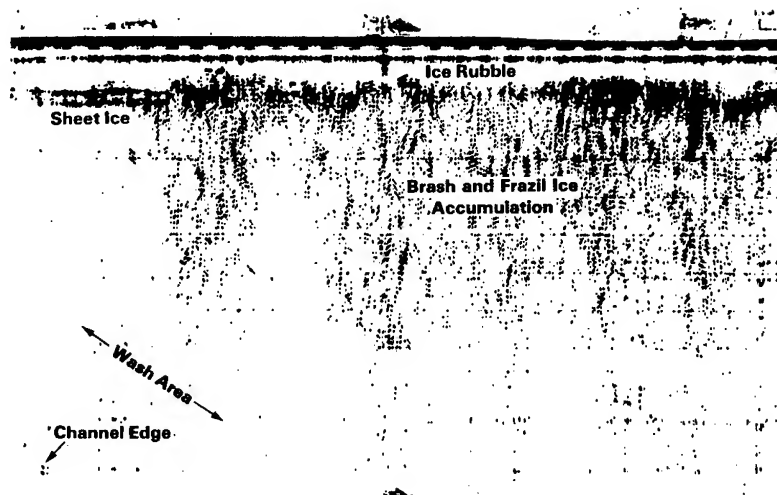


Figure 5. Graphic record of processed data representing a cross section of ice accumulation due to ship traffic in the St. Marys River.

DEAN

penetrate some 3 to 5 m of 50% water and ice mixture, which is responsible for significant scattering of the transmitted signal. Figure 6 illustrates the interpretation of the data in Figure 5, and the identification of a significant factor in the accumulation of the ice, i.e. the channel edge/wash interaction which bounds the accumulation.

Application -- Ice Bridges

During the 1979 Operation Jack Frost near Fairbanks, Alaska, CRREL was asked to aid in evaluating ice bridge construction across the Tanana River. Engineer units responsible for the work were plagued with warm weather and a braided stream and had lost several pieces of equipment through the ice. At the Tanana crossings the water velocities were high and the channel variable, and the bridging was quite extensive because of the braids of the stream. The radar unit was used to obtain a continuous profile of the ice thickness on the bridges and the channel configurations. One such traverse profile of a channel crossing is shown in Figure 7. Since the sheet (bridge) thickness, the channel, the water, and frazil accumulations can be identified, a complete evaluation of the crossing can be made. A picture of this ice bridge is shown in Figure 8. Another point of interest concerns a profile taken transverse to the bridge itself, i.e. longitudinal to the channel. A significant reduction in the sheet ice thickness was found under the snow dikes on each side of the ice bridge (caused by the insulating effect of the snow bank). Such a thickness variation affects the bearing capacity of the ice bridge. Hence, as soon as bridge construction is completed the snow banks should be removed.

Advantages

The broadbanded characteristic has a specific advantage in ice/water mixtures over carrier or single-frequency radar systems. The higher frequencies in the band provide the resolution, while the lower frequencies provide the penetration into and through the water. Conventional single-frequency systems cannot have both of these characteristics.

The system is commercially available, packaged, field-worthy, and reasonably portable. The unit is not a modified laboratory unit which can be taken to the field, but a system designed for field use, and proven in the discussed applications. It can use a variety of AC or DC power sources. The implementation of the system microprocessor makes the data manipulation very flexible.

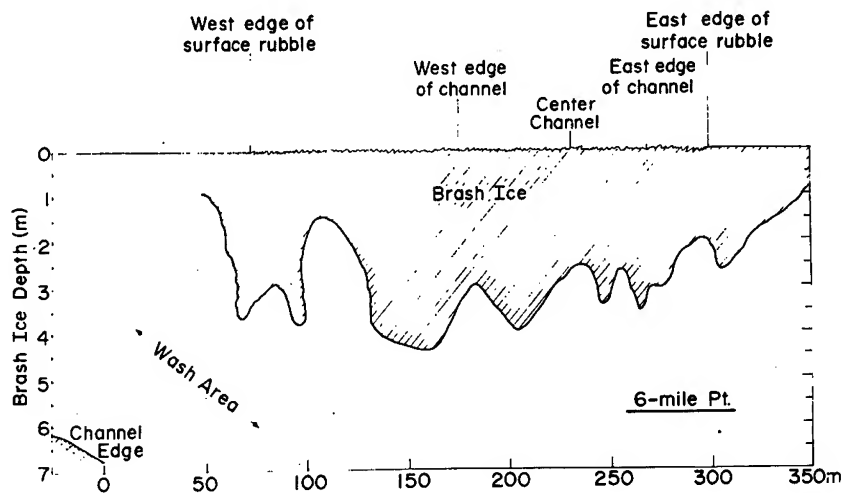


Figure 6. Sketch of the previous figure illustrating the interpretation technique.

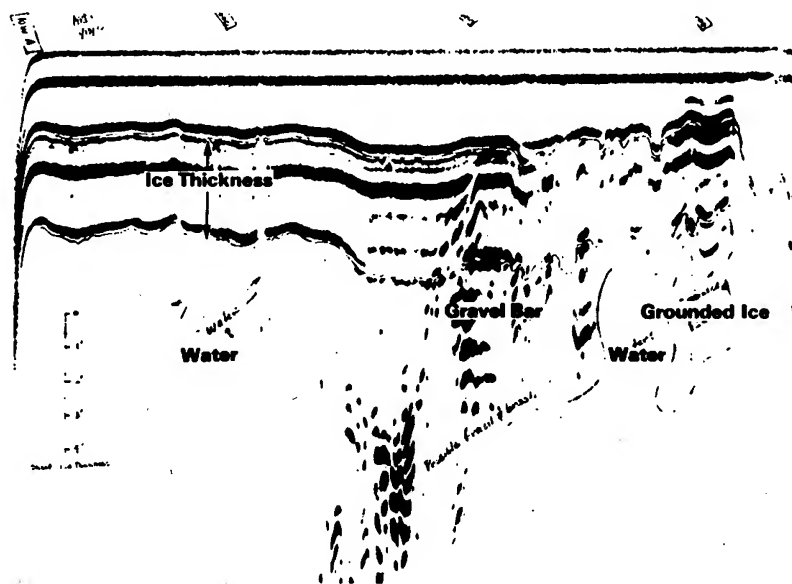


Figure 7. Graphic record of unprocessed data representing a longitudinal profile of an ice bridge across a channel of the Tanana River, January 1979.



Figure 8. The ice bridge whose profile is shown in Figure 7.

Disadvantages

The major disadvantage of the system is the difficulty of interpretation. Because of this, the system is still only a research tool. For massive data processing, or for real-time data interpretation, the graphic display must be replaced, since it takes at least 16 times longer to generate the print-out as it does to acquire the data.

Since the system is broad-banded, the transmitted energy from the antenna cannot be focused as in carrier-frequency radar without an elaborate antenna array and electronics package. This requires low survey flights and an integration over an antenna footprint some 3 to 5 m in diameter for the lower frequency bands in an airborne configuration.

Although theoretically it is possible to use two antennas to make the measurement insensitive to a varying dielectric constant in the medium, this is not practical in the field with the existing equipment. Therefore, periodic ground truth data are required to assure the consistency of the dielectric constant.

DEAN

Bearing Capacity of Ice Sheets

Below 0°C the bearing capacity of an ice sheet is dependent principally upon thickness, and less so upon ice type and temperature. Below -10°C the bearing capacity may be estimated as a function of thickness. The equation

$$h = 10\sqrt{P},$$

where h is ice thickness in centimeters and P is the applied load in metric tons, is a practical field relationship and gives a reasonable safety margin for single moving loads. This relationship does not apply to the bearing capacity of an ice sheet over an extended time. A number of parameter variations are tabulated in current Army publications. A more refined evaluation requires a knowledge of the ice properties and/or field testing. Selected references are given which treat these refinements.

If continued operation on the ice is considered or if ice temperatures are warm CRREL should be contacted.

DEAN

Selected References

1. Dean, A.M., Jr. (1977) Remote Sensing of Accumulated Frazil and Brash Ice in the St. Lawrence River, CRREL Report 77-8.
2. Kerr, A.D., (1975) The Bearing Capacity of Floating Ice Plates Subjected to Static or Quasi-static Loads, CRREL RR 333.
3. Kerr, A.D. (1976) The Bearing Capacity of Floating Ice Plates Subjected to Static or Quasi-Static Loads, Journal of Glaciology, Vol. 17, No. 76.
4. Kerr, A.D. (1980) Third Quarterly Report on CRREL Contract DACA 89-79-C-0002.
5. Korunov, M.M. (1939) Raschet Ledyanykh Pereprav, Avtobronetankovyi Zhurnal, No. 8.
6. Korunov, M.M. (1956) Load-Carrying Capacity of Ice for Timber Transport, Lesnaia Promyshlennost, Vol. 11. Translation published by NRC Canada as Report TT-863, 1960.
7. Lysukhin, I.F. (1968) Inzhenernoe Obespiechenie Forsirovaniya Rek, Veinennoe Izdatel'stvo Ministerstva Oborony SSSR, Moscow.
8. Nevel, D.E. (1977) Safe Ice Loads Computed with a Pocket Calculator, U.S. Army Cold Regions Research and Engineering Laboratory, CRREL Technical Note (unpublished).
9. Panfilov, D.F. (1961) Analysis of a Floating Ice Cover Subjected to Loads of Long Duration (text in Russian). Izvestia Vuzov, Stroitel'stvo i Arkhitektura, no. 6.
10. Department of the Army (1973) Float and Ski Operations for Army Aircraft, Field Manual 1-106.
11. Department of the Army (1962) Arctic Construction, Technical Manual 5-349.

DEHN

THE PARTICLE DYNAMICS OF PENETRATION

JAMES DEHN, DR.

ARRADCOM, BALLISTIC RESEARCH LABORATORY
ABERDEEN PROVING GROUND, MD. 21005

Mathematical modeling of the target penetration process is an old field and the great variety of models we now have reflects this fact. At one end of the model spectrum we have simple empirical interpolation formulas which can serve as convenient summaries of what we know already, though they cannot further our understanding. At the other extreme we have very complicated continuum models which include all the science we think is appropriate and offer the possibility of prediction without further experimentation. However, such advanced models have a number of shortcomings at present. On the one hand, many of the material properties needed to implement them have not been measured, while on the other, the numerical methods used in solving the equations involved are not yet sufficiently advanced to provide either rapid or routine calculational tools. Consequently, they have not yet improved our understanding of penetration very much, at least in the ordnance range. Between these two extremes there are a number of intermediate approaches which are based on simplified physical laws and so offer the possibility of improved understanding together with a calculational tool which can be routine, rapid and reliable.

The oldest type of simplified physical model in use consists of replacing the projectile by a mass point and the target by a force field. If the striking mass, m_0 , is constant in time, then the equation

$$m_0 \ddot{v} = F = -(a + b_1 v + b_2 v^2) \quad (1)$$

can be used to describe certain types of rectilinear motion. Here a ,

b_1 and b_2 are constants so the force, F , is a quadratic form in the velocity, v . Euler and Robins in 1742 applied this equation to target penetration with $b_1 = b_2 = 0$. In 1830 Poncelet did the same with only $b_1 = 0$, while Résal continued this tradition in 1895 by applying the solution with only $a = 0$. Today we know that both the velocity, $v = \dot{s}$, and the displacement, s , can be found explicitly as closed form functions of time by standard integrations with none of the constants zero.

In applications of equation (1) to penetration problems, the force is taken antiparallel to the velocity and the "normal" case of zero obliquity impact is discussed. Thus equation (1) is limited to one-dimensional motion, since there is no force component to make the mass deviate from a straight line. This is a severe limitation since curvilinear motion, including ricochet, is known to occur. Even for rectilinear motion the force in equation (1) cannot describe embedment of the projectile in the target unless $a = 0$. If $a \neq 0$, then F can never vanish and the mass can come to rest only momentarily instead of permanently as occurs in the case of embedment.

The constant a in equation (1) has been interpreted as the force needed to detach a certain amount of target material and move it out of the way of the projectile as a single plug or in some other manner. Since a projectile of larger cross-sectional area, A , must move more target material, this force is usually taken to be proportional to A . Similarly, since a thicker target plate will require the removal of more material for a given A , we might also take this force proportional to the target thickness, T . Thus, the product, AT , becomes a lower bound on the volume of target material which is removed during a complete perforation. If the projectile striking speed, v_0 , is increased, then in general more momentum will be transferred to the material which is removed, so it is also reasonable to assume a dependence of this force on v_0 as well. In this paper we will use the simple assumption that

$$a = a_0 T + a_1 v_0 \quad (2)$$

where a_0 and a_1 depend on the properties of the target and projectile as well as the projectile shape.

Another interpretation for part of this force is the frictional resistance offered by the target which depends on the area of contact rather than the cross-sectional area. It also depends on the pressure in the simplest approximation and so also depends on v_0 .

The term $b_1 v$ in equation (1) can be called a viscous force. This does not imply the presence of the liquid state. The terminology, "viscosity of solids" is well established and only implies a proportionality between shear stress and time rate of strain. The viscosities of various solids have been measured up to explosive rates of motion and a discussion of these experiments has been given by Walters¹. This force also will depend on the geometry of the projectile. For a sphere moving through a viscous liquid, for example, Stokes' law gives us a force which depends on the radius of the sphere as well as the speed.

The term $b_2 v^2$ in equation (1) can be called a drag force. Again this does not imply the presence of a liquid. Drag forces in solids are not well studied, but they should also depend on the cross-sectional area of the projectile. In an isotropic fluid such as still air, the components of the drag force are $b_2 v_x^2$ and $b_2 v_z^2$ for the two coordinates x and z with $v^2 = \dot{x}^2 + \dot{z}^2$. In an anisotropic medium we might use $b_{2x} \neq b_{2z}$ or the components of the speed instead of the speed, or both. Since penetration problems of interest are very anisotropic because of the presence of air-metal interfaces which make the resistance parallel or perpendicular to such interfaces quite different, we propose the form $b_{2s} \dot{s}^2$ with $s = x, y, z$ in general.

Several of the forces described above involve areas which can depend on the depth of penetration. For example, for a projectile with a curved nose the cross-sectional area will increase as it penetrates more deeply, while for a long rod the contact area will increase with penetration depth. Such behavior will not generally be simply proportional to s . If the trajectory is curved the situation may change in time and when a projectile enters its final breakout phase before exiting the target in a ricochet or perforation, the various forces being described may decrease as the penetration progresses. In any case the amount of target material moved out of the way in time t depends on s , the current length of the trajectory. For simplicity we will assume a form cs with $s = x, y, z$ and c constant.

This line of reasoning suggests that we consider component equations of motion of the form

$$m_0 \ddot{s} + F_s = m_0 \ddot{s} + a_s + b_{1s} \dot{s} + b_{2s} \dot{s}^2 + c_s s = 0 \quad (3)$$

where $s = x, y, z$ in a rectangular coordinate system with origin at the point of impact. For a plate target let us take the z axis pointing along the line of flight of a projectile which impacts at

zero obliquity and choose the x axis so that an oblique striking velocity vector lies in the x,z plane. Then the y coordinate is ignorable for such a target which is "effectively infinite" in the x,y plane. Analysis shows² that we can neglect the $b_2 s^2$ term in equation (3) and still describe ricochet, embedment and perforation. However, we cannot do this if we neglect the $c_s s$ term. This is fortunate since we can find an exact solution for equation (3) if we neglect $b_2 s^2$. Such a solution should be appropriate for lower speeds like those of ordnance interest and can be amended if we wish to include hypervelocity impacts. Without the $b_2 s^2$ term the solution is

$$s = A_{1s}^+ e^{\gamma_s^+ t} + A_{1s}^- e^{\gamma_s^- t} + \Delta_s \quad (4)$$

where $A_{1s}^\pm = (v_{os} + \Delta_s \gamma_s^\pm) / (\gamma_s^+ - \gamma_s^-)$ for initial conditions $s = 0$ and $\dot{s} = v_{os}$ at $t = 0$. Here $v_{os} = v \sin \theta$ and $v_{oz} = v \cos \theta$ where θ is the striking obliquity measured counterclockwise from the negative z axis to v_o . In addition $\gamma_s^\pm = -\alpha_s \pm \sqrt{\alpha_s^2 - c/m_o}$ where $\alpha_s = b_{1s}/(2m_o)$, and $\gamma_s^- < \gamma_s^+ < 0$ if s and \dot{s} always remain finite. The degenerate case of $\alpha_s^2 = c/m_o$ has a special solution². Positive c_s and real γ_s^\pm requires $0 < c_s < m_o \alpha_s^2$.

The constants Δ_s in equation (4) are position components of a stable node and have the form

$$\Delta_s = -a_s/c_s = -(a_{os} T + a_{1s} v_{os})/c_s \quad (5)$$

when we use equation (2) in component form. Here $T = T$ while $T = T \tan \theta_o$. If we include the $b_2 s^2$ term we can write approximate solutions by using standard perturbation theory or we can construct closed forms which reduce to the known solutions when $b_2 \rightarrow 0$ or $c \rightarrow 0$. We will not discuss such matters here. Instead, let us consider the force components at the ricochet limit velocity, v_{ozRL} , and at the perforation limit velocity, v_{ozPL} . At the ricochet limit $v_{oz} = v_{ozRL}$ and $F_z = \dot{z} \rightarrow 0$ as $t \rightarrow \infty$, so (even if we retain the drag force)

$$F_z \rightarrow 0 = -[a_{oz} T + a_{1z} v_{ozRL}] \quad (6)$$

and at the perforation limit, $v_{oz} = v_{ozPL}$, $z \rightarrow T$ and $F_z = \dot{z} \rightarrow 0$ as $t \rightarrow \infty$, so

$$F_z \rightarrow 0 = -[a_{oz} T + a_{1z} v_{ozPL} + c_z T]. \quad (7)$$

From equations (6) and (7) we can find a_{oz}/c_z and a_{1z}/c_z in terms of v_{ozRL} , v_{ozPL} and T . If we use these values² in equation (5), we obtain

$$\Delta_z = T(v_{oz} - v_{ozRL})/(v_{ozPL} - v_{ozRL}). \quad (8)$$

DEHN

If $v_{oz} < v_{ozRL}$, then $\Delta_z < 0$ and ricochet will occur.

If $v_{oz} > v_{ozPL}$, then $\Delta_z > T$ and perforation will occur.

If $0 < \Delta_z < T$, then embedment will occur. Thus Δ_z , the z-component of the final position, is a convenient index for predicting the eventual outcome. A similar procedure for the x-component of the force gives

$$\Delta_x = [(x_{AL} v_{oxPL} - x_{PL} v_{oxRL}) + (x_{PL} - x_{RL}) v_{ox}] / (v_{oxPL} - v_{oxRL}). \quad (9)$$

For the z-component we had the ricochet limit position $z_{RL} = 0$ and the perforation limit position $z_{PL} = T$. Similarly, x_{RL} and x_{PL} are the x-components of these limit positions and Δ_x is the x-component of the final position towards which the motion tends. Since all of these limit positions and velocities are measurable quantities, then a_{os}/c_s , a_{ls}/c_s and so a_s/c_s (or Δ_s) for $s = x, y$ can be determined experimentally.

As mentioned above, the b_{1s} parameters can be estimated from viscosity experiments. For a sphere we can take advantage of the fact that Stokes' law is proportional to the speed and write $b_{1s} \dot{s} \sim R \mu \dot{s}$ where R is the radius and μ is the dynamic (density-dependent) viscosity as discussed by Walters¹. For other shapes we might expect somewhat different forms. If we neglect the b_{2s} parameters we are ready to calculate trajectories, exit speeds and exit angles for a variety of conditions.

Figures 1a and 1b show the exit speed and exit angle of a one gram steel sphere which strikes a 9.53 mm thick aluminum plate at $\theta_0 = 45^\circ$ over a range of v_0 which covers the ricochet, embedment and perforation regions. The data points were obtained by Backman and Finnegan³, while the solid lines were calculated by using the time derivatives of the components in equation (4) with the parameters indicated in the Figures. The exit speed is $v = \sqrt{\dot{x}^2 + \dot{z}^2}$ while the exit angle, $\theta = \arctan(\dot{x}/\dot{z})$, is measured from the z axis in the counterclockwise direction. For perforation, $\theta < 90^\circ$, while for ricochet $\theta > 90^\circ$. Similar calculations for other striking obliquities from 0 to 60 degrees using the same parameters also show general agreement with experiment. Comparisons for other materials and other target and projectile geometries are in progress. If we retain the $b_{2s} \dot{s}^2$ term in equation (3), the agreement with experiment can be improved.

Now let us extend our linear model to an eroding penetrator. For a constant mass penetrator energy is dissipated through the

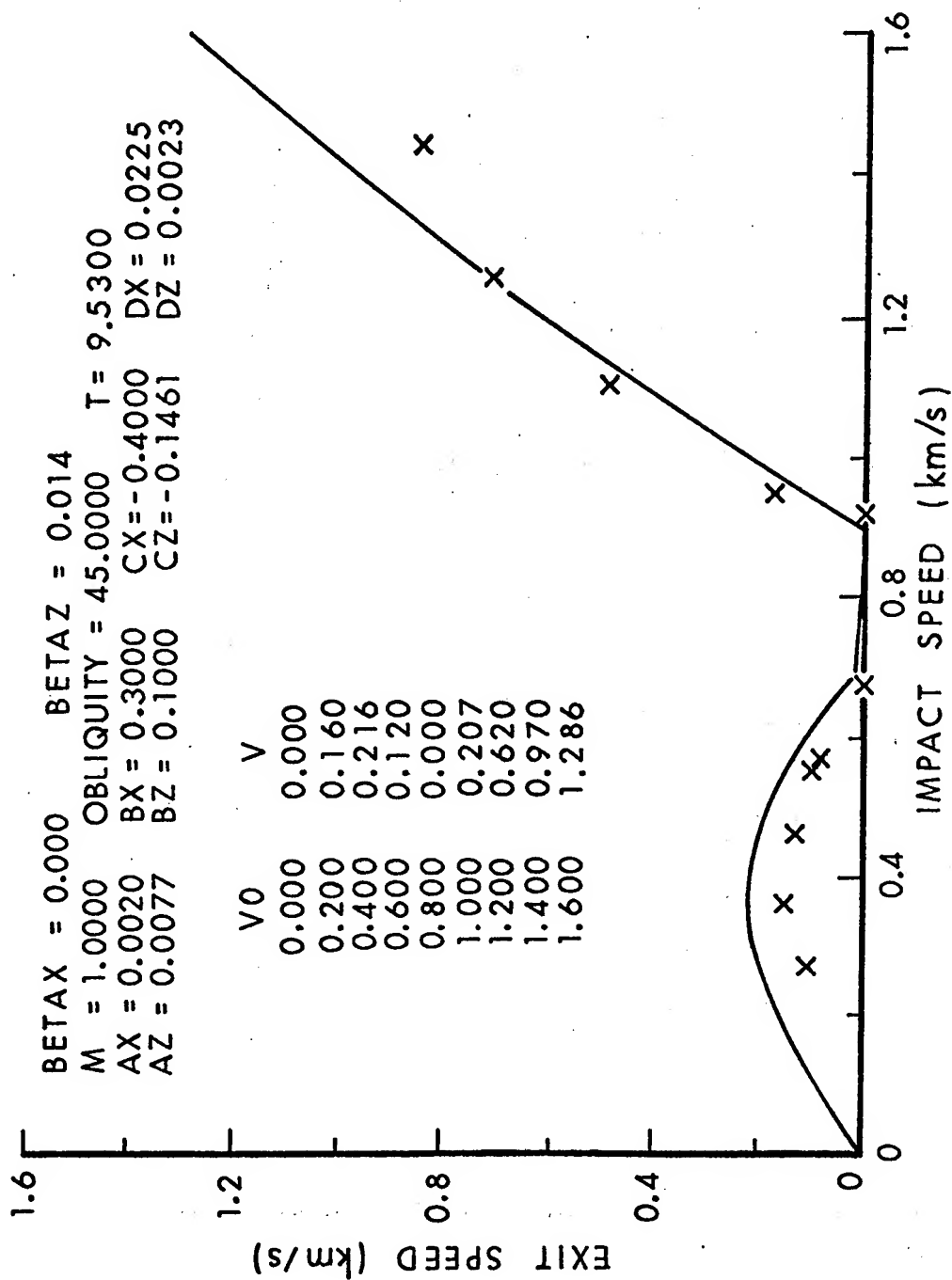


Figure 1a. Measured and calculated exit speeds for steel spheres vs aluminum plates at 45° obliquity.

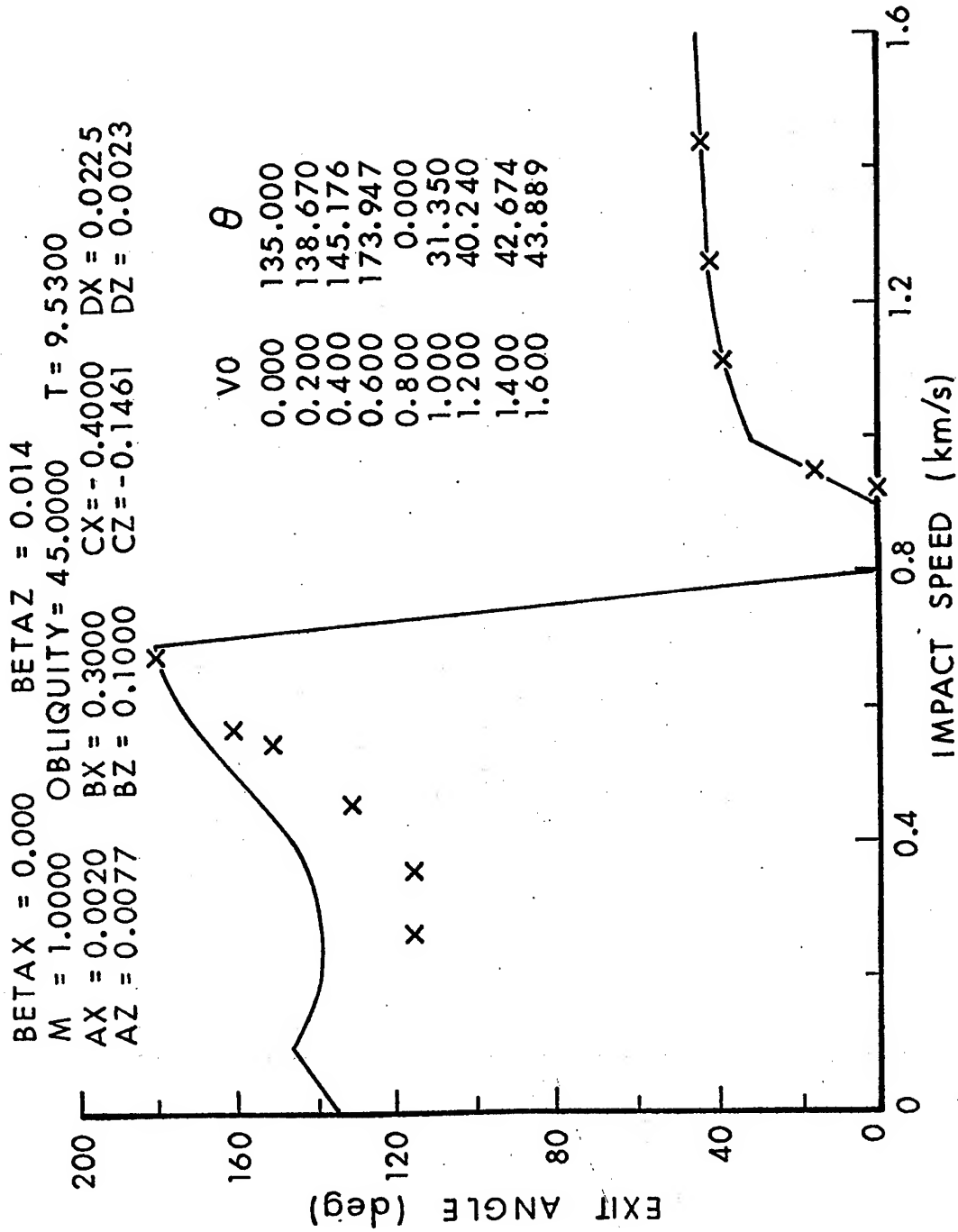


Figure 1b. Measured and calculated exit angles for steel spheres vs aluminum plates at 45° obliquity.

viscous term and shows up as a decrease in velocity. If $\dot{m} \neq 0$, energy can also be dissipated by a decrease in mass. Since the only dissipative term we have in our force field is the viscous term, we might consider amending this term to reflect this additional means of dissipating energy. If we modify this term to be $(b_{1s} - \epsilon_s \dot{m})s$ where ϵ_s is a positive, dimensionless constant, we have a form which reduces to our previous form when $\dot{m} = 0$. If $\dot{m} < 0$ and mass is lost, then this term is larger, and if $\dot{m} > 0$ it is smaller. Cases of $\dot{m} > 0$ could include precipitation of various kinds, while cases of $\dot{m} < 0$ could include re-entry shield ablation, penetrator erosion and a variety of other phenomena. Our equation, neglecting drag, becomes

$$ms'' + \dot{m}s' + a_s + (b_{1s} - \epsilon_s \dot{m})s + c_s s = 0 \quad (10)$$

which reduces to equation (3) for $\dot{m} = b_{2s} = 0$. If we make an arbitrary transformation of the independent variable, time, to a new independent variable, ϕ , we find

$$Ms'' + B_s s' + a_s + c_s s = 0 \quad (11)$$

where a prime means $d/d\phi$ and

$$M = m\dot{\phi}^2 \quad (12)$$

while

$$B_s = [m\dot{\phi}' + b_{1s} + (1-\epsilon_s)\dot{m}]\dot{\phi}. \quad (13)$$

Since we are free to choose $\phi(t)$, let us choose it so M and B_s in equations (12) and (13) are constants. Then $\dot{m} = -2m\dot{\phi}'$ from equation (12) so we can eliminate $m\dot{\phi}'$ from equation (13) and obtain $B_s = [b_{1s} + (.5-\epsilon_s)\dot{m}]\dot{\phi} = [b_{1s} + (.5-\epsilon_s)\dot{m}_0]\dot{\phi}_0$ since B_s is constant. In order that $B_{1s} \rightarrow b_{1s}$ in the constant mass case, $\dot{m} = \dot{m}_0 = 0$, we must have $B_{1s} \rightarrow b_{1s}\dot{\phi}_0 = b_{1s}$ or $\dot{\phi}_0 = 1$. Thus $M = m\dot{\phi}^2 = m_0\dot{\phi}_0^2 = m_0$. For this reason we will call this choice of ϕ a constant mass transformation. If we eliminate m and \dot{m} from equation (13) in favor of $\dot{\phi}'$ and $\dot{\phi}^2$ we can integrate with respect to ϕ to obtain $\dot{\phi}$ and then with respect to t to obtain

$$(b_{1s}/B_s)\phi + D_s(1-b_{1s}/B_s)(1 - e^{-\phi/D_s}) = t \quad (14)$$

as the transformation which makes M and B_s constant. Here $D_s = m_0(2\epsilon_s - 1)/B_s$. If we use $\dot{\phi}$ in equation (12), we find

$$m = m_0 [(1-b_{1s}/B_s)e^{-\phi/D_s} + b_{1s}/B_s]^2 \quad (15)$$

and the solution of equation (11) is

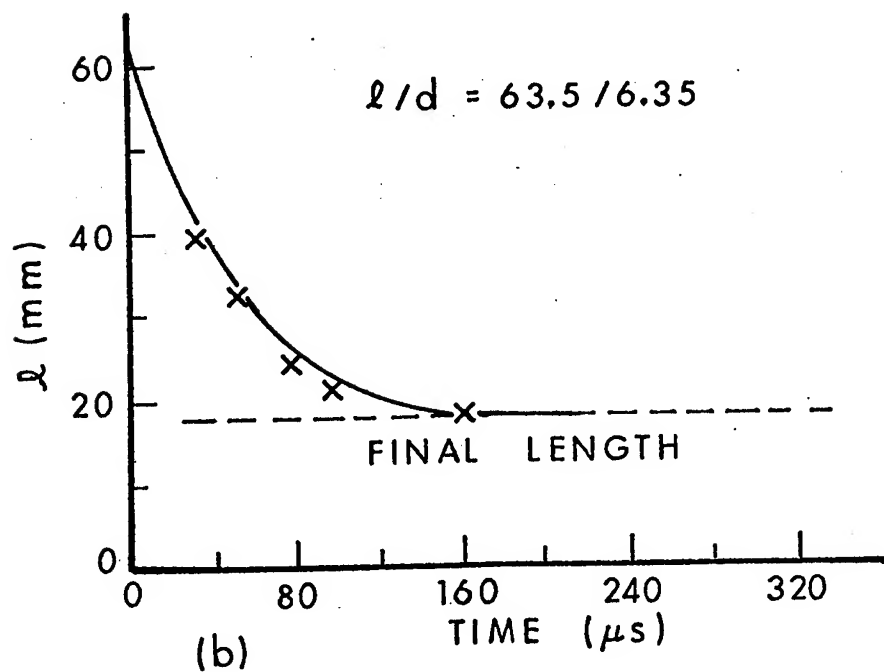
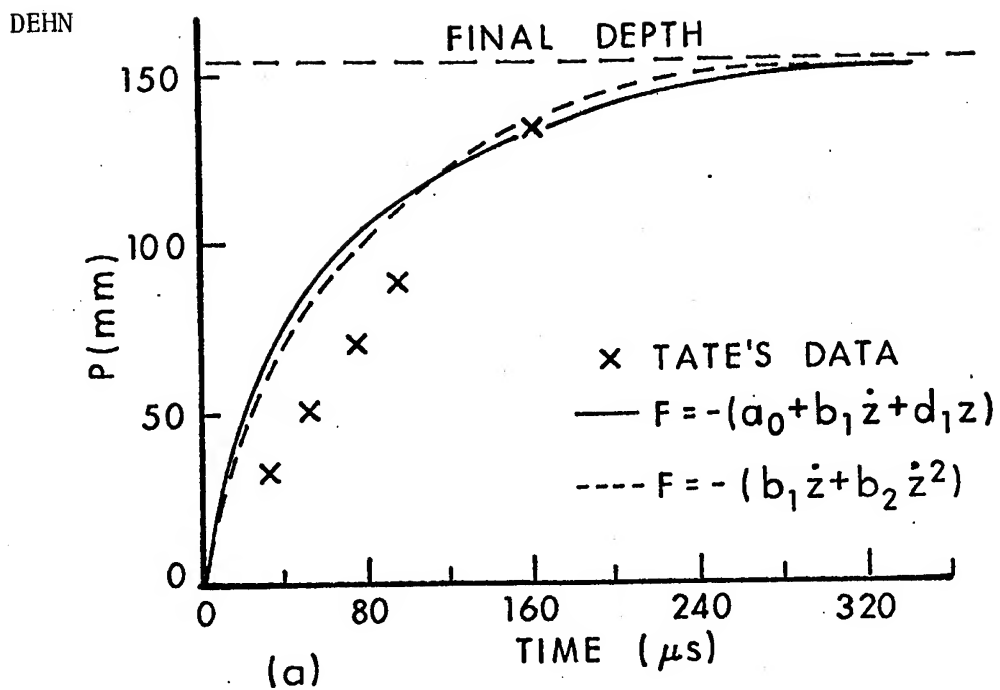


Figure 2. Dural rod penetrating polyethylene: measured and calculated values.

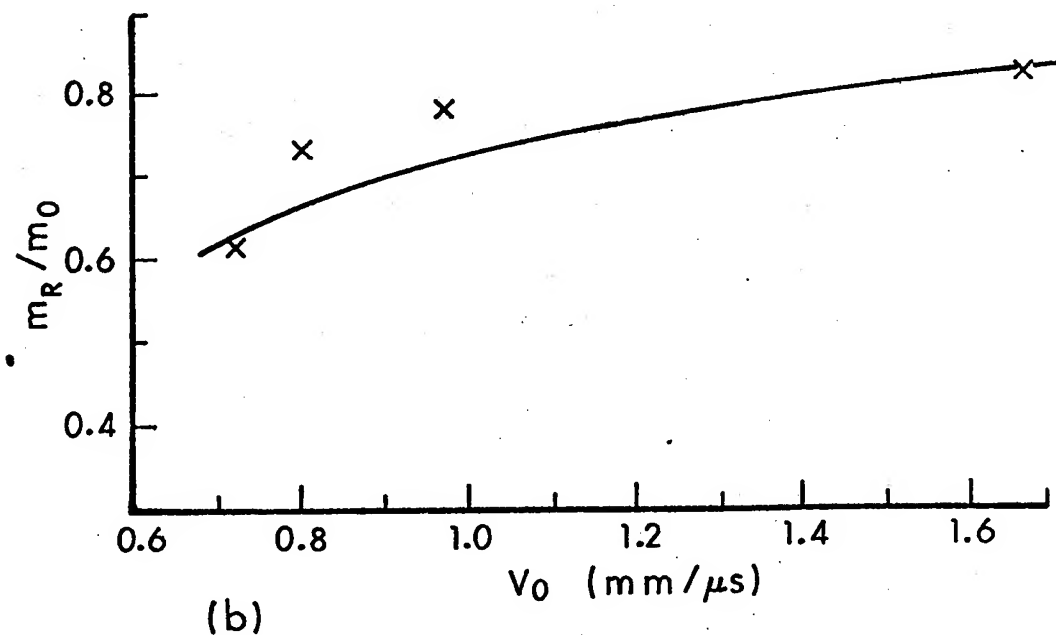
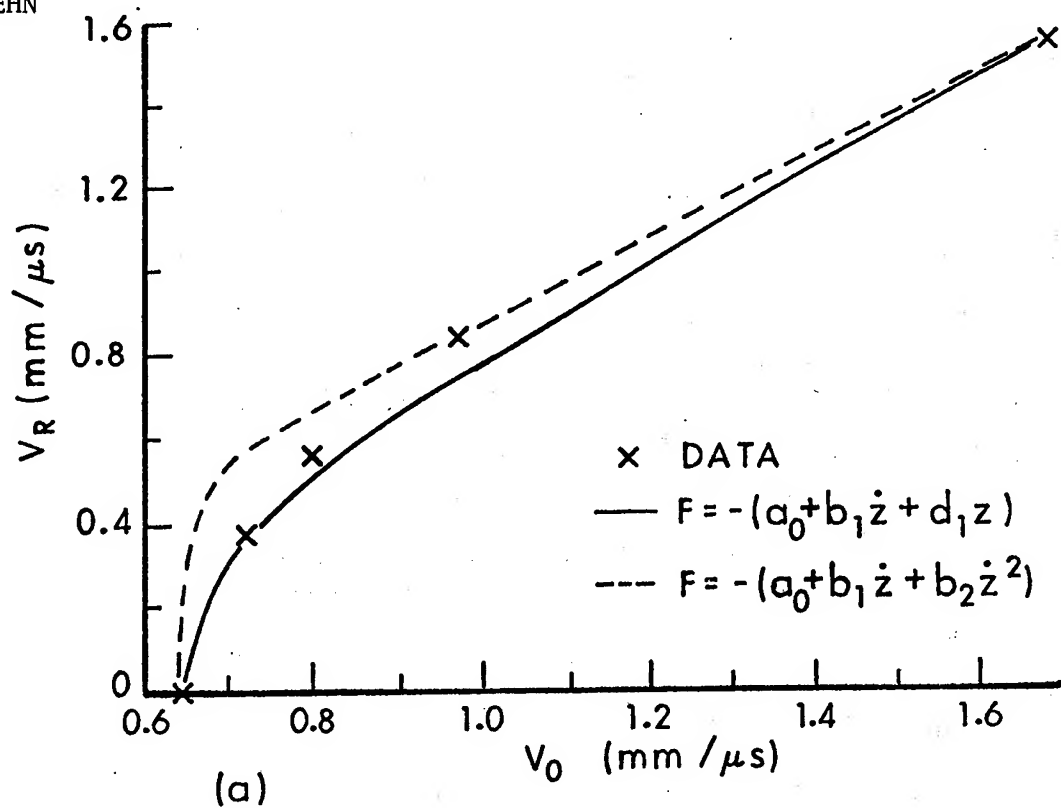


Figure 3. Residual speed and mass versus striking speed for a long steel rod penetrating a steel plate: measured and calculated values.

$$s = A_{2s}^+ e^{\lambda_s^+ \phi} + A_{2s}^- e^{\lambda_s^- \phi} + \Delta_s \quad (16)$$

with the same mode Δ as equation (4). Here A_{1s}^+ and λ_s^+ are analogous to A_{1s}^+ and γ_s^+ above.

If we analyze the case $\dot{m} < 0$, we find² that for $\epsilon_s > .5$ and $b_{1s} > 0$, m will not vanish, although it may become very small if $b_{1s}/B_s \ll 1$. For $\epsilon_s < .5$ m will always vanish in a semi-infinite target. Since penetrators do not always vanish in a semi-infinite target, we see why $\epsilon_s = 0$ in equation (10) (a particular case of $\epsilon_s < .5$) is not a general enough case to apply to penetration.

We have applied the particular solution represented by equations (14), (15), and (16) to a variety of problems. A special case of a frictionless harmonic oscillator with variable mass is a liquid-filled vessel of constant horizontal cross-section with a hole in the bottom through which it loses its contents as it oscillates on a spring in the earth's gravitational field. Here we will merely mention the result² that the motion and its variable periodicity can be described over many cycles from full to nearly empty vessel with an accuracy of better than 5%. Our main interest here is to apply this solution to an eroding penetrator.

Figures 2a and 2b give the depth of penetration, $P = z + \ell/2$, of the tip of a dural rod of initial length $\ell_0 = 63.5$ mm and constant diameter $d = 6.35$ mm and the variable length $\ell = m/[\pi \rho d^2/4]$ versus time in a semi-infinite polyethylene target. The data was obtained by Tate⁴ while the calculations employed equations (14), (15) and (16). An alternate force calculation compatible with equations (14) and (15) gave the dashed curve.

Figures 3a and 3b give the exit speed and the fractional mass remaining after perforation of a 6.35 mm thick steel plate by a 7.78 gm steel rod ($\ell_0/d = 50$ mm/5 mm) striking end on at zero obliquity and various speeds, v_0 . The data were obtained by Herr and Grabarek⁵ while equations (14), (15) and (16) were used for the calculation. An alternate force calculation compatible with equations (14) and (15) gave the dashed curve. For simplicity the initial erosion rate was taken to be independent of v_0 , although better agreement could have been obtained by assuming that m_0 is a function of v_0 . Since \dot{m} declines only slightly during the brief times required for perforation over the measured range of v_0 , we have a simple explanation for the observed fact that the length of rod remaining increases as v_0 increases (for a fixed target thickness). At higher v_0 the projectile spends less time

in the target so that less erosion takes place (since the rate is approximately constant). Other types of behavior are also allowed by the model².

In this paper we have discussed a model which describes the particle dynamics of penetration in a manner which can improve our understanding and provide us with a routine, rapid and reasonably reliable method of calculation. Once a library of experimental results has been established we should be able to interpolate and extrapolate with considerable confidence. The model describes the main features of oblique penetration, namely exit speed, angle and mass, over the entire region of interest, including ricochet embedment and perforation. Applications to multiple plate targets and other geometries should also be possible. In addition, other features of interest such as projectile breakup² can be linked with this model.

REFERENCES

1. W.P. Walters, "Influence of Material Viscosity on the Theory of Shaped-Charge Jet Formation," ARBRL-MR-02941, August 1979.
2. J. Dehn, "The Particle Dynamics of Target Penetration," ARBRL-TR-02188, September 1979.
3. M.E. Backman and S.A. Finnegan, "Dynamics of the Oblique Impact and Ricochet of Nondeforming Spheres Against Thin Plates," NWC TP 5844, September, 1976.
4. A. Tate, "A Theory for the Deceleration of Long Rods after Impact", J. Mech. Phys. Solids 15, 387 (1967).
5. L. Herr and C. Grabarek, "Ballistic Performance and Beyond Armor Data for Rods Impacting Steel Armor Plates," BRL MR 2575, January 1976.

*DEVINE & BRODMAN

THE EFFECT OF CHEMICAL INTERACTIONS ON THE
SMALL ARMS DETERRING PROCESS (U)

*MR. MICHAEL P. DEVINE
MR. BRUCE W. BRODMAN
US ARMY ARMAMENT RESEARCH AND DEVELOPMENT COMMAND
DOVER, NEW JERSEY 07801

INTRODUCTION

Nitrocellulose (NC) based small arms propellants utilize a material called a deterrent in order to moderate their burning rates early in the ballistic cycle when the surface area of the propellant is at maximum. In spherical-type propellant, di-n-butyl phthalate (DBP, a deterrent) is diffused into a portion of the propellant grain. The concentration profile of DBP in ball propellant was established by autoradiographic techniques (1). This work indicated that the concentration of DBP was level throughout its depth of penetration with an abrupt drop-off at the boundary. Examination of sectioned grains under a microscope revealed the presence of a visually distinct concentric region around the periphery of the grain (1). Measurement of the depth of this region and comparison with autoradiographic data indicated that it corresponded exactly to the visually observed deterred layer of the grain (1). A series of subsequent studies established that hydrogen bonding occurs between a variety of deterrent materials (2) and unesterified hydroxyl groups in nitrocellulose. Specifically, the carbonyl groups of DBP hydrogen bond to the unesterified hydroxyl groups in nitrocellulose.

The depth of deterrent penetration into the nitrocellulose grain is an important parameter in charge design since it controls the gas generation schedule. This study describes a novel method for altering this depth for a given molar concentration of deterrent material, utilizing the information gained in the previous studies (1-4).

EXPERIMENTAL

NC spheres used in this study were undeterred WC 870 ball propellant made by Badger Army Ammunition Plant. The moisture-free composition of the NC spheres was 1.22% diphenylamine, 0.49% EA, 0.64% DNT, 0.31% DBP (both DNT and DBP are present as contaminants), 9.40% NG, and 87.94% NC (13.15%N) determined by difference from a solvent extractable fraction. The spheres ranged in size from 0.034 to 0.27 in. (.086-.688 cm). The methyl benzoate was purchased from Aldrich Chemical Co., and the ethyl, propyl and butyl benzoate were acquired from Eastman Organic Chemicals.

Scaled-Down Detering Process

Two hundred grams of WC 870 propellant, 500 ml water and 1.3 grams Swifts Colloid #1 (Swift and Co.) were placed in a 2-liter, three-neck flask equipped with a stirring blade and a condenser. During the detering process the flask was placed in a constant-temperature water bath and maintained at $76^{\circ} \pm 0.5^{\circ}\text{C}$ for six hours with constant stirring.

A separate emulsion of each benzoate was prepared by dissolving 0.1g of Swifts #1 Colloid in 50 ml water and adding the weight of benzoate shown in Table I. This emulsion was maintained at 76°C prior to addition to the flask. The amount of deterrent suspension added to the flask is given in Table I. After addition of the deterrent emulsion, the flask was maintained at $76^{\circ} \pm 0.5^{\circ}\text{C}$ for six hours with constant stirring. These conditions have been shown to result in the quantitative transfer of deterrent to the propellant grains.

At the end of the six hour period the liquid was poured off and the propellant washed with 1 liter of water. After washing, the deterred propellant was allowed to air dry overnight at ambient temperature.

Microtoming

Thirty individual grains of the deterred propellant from each run were mounted on 1/8 in. ceramic rods with Titebond Glue (Franklin Glue Co.) and microtomed into sections about 22μ thick. The sections were then mounted on microscope slides with Permount (Fisher Scientific Co.).

Measuring

The mounted grain segments were examined using a Unitron TMS-1566 measuring microscope equipped with a 10X eyepiece and 10X objective lens. The maximum error in measuring the depth of penetration was $\pm 5\mu$. The relative depth of penetration for each deterrent was determined by measuring the diameter and depth of penetration of the grains. In some cases the grains were oblong so the major and minor axes were measured and the diameter taken as the average.

Table I. Benzoate and Benzoate Emulsion Weights.

<u>Compound</u>	<u>Weight (grams)</u>	<u>Weight Emulsion (grams)</u>
Methyl benzoate	5.87	9.78
Ethyl benzoate	6.47	10.79
n-Propyl benzoate	7.08	11.48
n-Butyl benzoate	7.68	12.80

Discussion

The purpose of this study was to measure the depth of penetration of a homologous series of benzoic acid esters when diffused into a spherical nitroglycerine containing nitrocellulose propellant grain. Past work involving di-n-butyl phthalate has established that the concentration is level through the deterred region (1) and that hydrogen bonding occurred between the ester carbonyl group and unesterified hydroxyl group in nitrocellulose (2).

A subsequent study indicated that the observed concentration profile could best be explained by a diffusion with interaction mechanism (3). In such a case, deterrent molecules would move into the nitrocellulose matrix until steric and electrostatic factors allowed an interaction to occur with unesterified hydroxyl groups in the nitrocellulose. Subsequent deterrent molecules would then be forced to move deeper into the grain in order to interact with these hydroxyl groups.

The benzoic acid esters are of potential interest as deterrent materials and for this reason were the subject of an investigation involving their hydrogen bonding properties when present in a nitrocellulose matrix. This study established that hydrogen bonding occurred between the benzoic acid ester carbonyl group and unesterified hydroxyl groups in nitrocellulose (4)

and developed a relationship between Tafts σ^* value and the magnitude of the shift in the hydroxyl stretching frequency in the infrared (4).

Methyl, ethyl, n-propyl and n-butyl benzoate, at equivalent molar concentration, were diffused into ball propellant utilizing a scaled-down manufacturing technique. The resulting deterred propellant was microtomed, and both the diameter of the grain and the diameter of the undeterred region were measured. From this data the radius of the grain (R_o) and the radius of the undeterred region (R_i) were obtained.

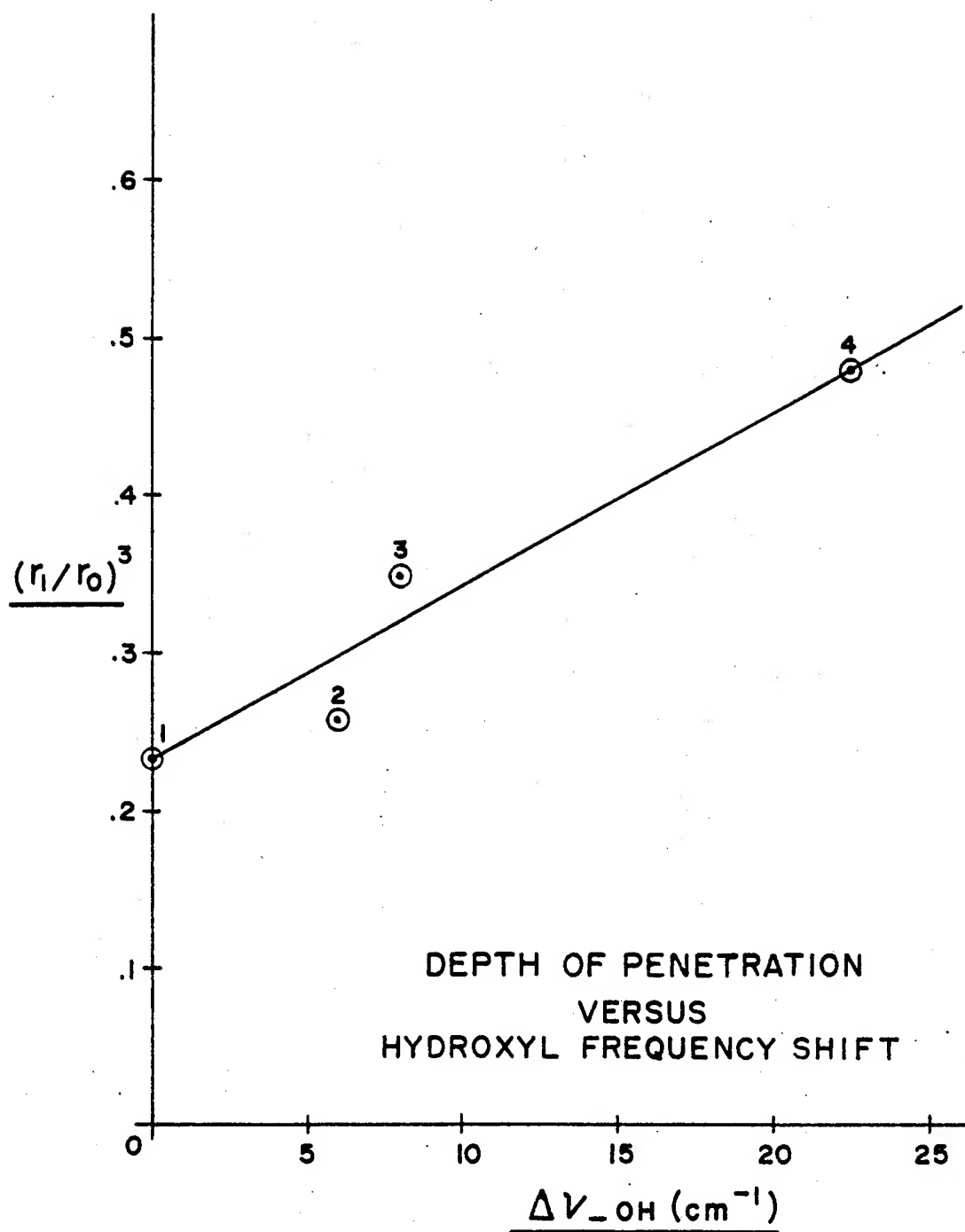
In order to minimize the effect of particle size variation, the depth of penetration is expressed as $\left(\frac{R_i}{R_o}\right)^3$. This data for each benzoic acid ester is shown in Table II. It can be seen that the methyl ester gave the lowest value for $\left(\frac{R_i}{R_o}\right)^3$ indicating the deepest penetration into the grain. Fig. 1 shows a correlation between $\left(\frac{R_i}{R_o}\right)^3$ and the shifted hydroxyl stretching frequency data previously reported. There appears to be a linear relationship between depth of penetration and observed shift in the hydroxyl stretching frequency.

Further examination of the Taft σ^* (indication of the electron donating effect of the various groups) listed in Table II shows that the molecule containing the group with the least electron donating effect, the methyl group, penetrated deepest into the grain. As the Taft constants increase in magnitude, the electron donating effect of the group increases and more negative charge would be present on the carbonyl oxygen as shown below:

Table II. Taft Constants and Depth of Penetration Expressions.

<u>Compound</u>	<u>σ^*</u>	<u>$\left(\frac{R_i}{R_o}\right)^3$</u>
methyl benzoate	0.00	0.235
ethyl benzoate	-0.10	0.255
n-propyl benzoate	-0.12	0.350
n-butyl benzoate	-0.13	0.480

Thus, the methyl ester would have the least negative character while the butyl ester would have the most. It appears that as a molecule is diffused into the nitrocellulose matrix, the likelihood



of an interaction with a free hydroxyl group is enhanced by increased negative charge on the carbonyl oxygen. This explains why the methyl ester penetrated deepest into the grain while the butyl ester penetrated least. Thus it appears that the depth of penetration of a deterrent can be regulated, for a given molar concentration, by the negative charge present on the carbonyl oxygen which in turn determines the likelihood of a hydrogen bond being formed. This finding could serve as a basis for evaluating potential deterrent materials as well as serving as a novel means for regulation of the propellant gas generation schedule.

REFERENCES

1. B. W. Brodman, M. P. Devine, R. W. Finch, and M. S. Mac Claren, J. Appl. Polym. Sci., 18, 3739 (1974).
2. B. W. Brodman, M. P. Devine, and M. T. Gurbarg, J. Appl. Polym. Sci., 18, 943 (1974).
3. B. W. Brodman, J. A. Sipia, Jr., and S. Schwartz, J. Appl. Polym. Sci., 19, 1905 (1975).
4. B. W. Brodman, M. P. Devine, and M. T. Gurbarg, J. Appl. Polym. Sci., 19, 2913 (1975).

MILLIMETER-WAVE SELF MIXING OSCILLATORS

SAMUEL DIXON, Mr.
HAROLD JACOBS, PhD.

USA Electronics Technology and Devices Laboratory (ERADCOM)
Fort Monmouth, New Jersey 07703

INTRODUCTION

The self-mixing oscillator has been of considerable interest in recent years (1)-(3) because it embodies simplifications for the circuitry of electronic systems. Schottky barrier and other rectifier diodes suffer from the disadvantage of fragility and low burn-out power limit. Bulk effect self-oscillating mixers using the non-linearity of transferred electron (GUNN) devices offer competitive sensitivities and the attractive feature of high power handling capability.

Conventional mixers, ususally consist of a mixer diode of the rectifier type and a separate local oscillator. In the self-oscillating mixer, the mixer diode is eliminated, the Gunn diode (or BARITT diode) serving both as a local oscillator, and because nonlinearities are always present in an oscillator, as a mixing element. With the Gunn diode oscillator serving both these functions, the integrated receiver front-end design using the dielectric image guide approach becomes extremely compact and simplified. In the latter arrangement, the signal is fed directly into the oscillator and a suitable IF probe removes the IF signal power for use in subsequent amplifier stages. What makes self-oscillating mixing different intrinsically from the conventional mixing process with a passive device (such as the Schottky junction diode) is that self-mixing occurs with conversion gain (rather than loss) similar to parametric amplification (1), (3).

One of the objectives of this work was the design of self-oscillating mixers with considerable simplification, with the attendant

reductions in cost. In the quest for lower cost, the dielectric waveguide (or image-line) technology was applied using a Gunn diode, in a simply constructed cavity, in a self-excited oscillator-mixer mode of operation. Both GaAs and InP Gunn diodes were imbedded in an aperture which was cut in a high resistivity aluminum oxide dielectric waveguide. The significance of the dielectric waveguide technology is that active devices, as well as passive components, can be developed and integrated into circuit modules to construct functional subsystems.

DEVICE DESIGN

The metal waveguide self-mixing oscillator utilizing a coax-waveguide hybrid circuit is shown in Fig. 1. The packaged diode is imbedded in a copper heat sink at the end of a coaxial line section. A large section of the outer conductor is removed with the removed section facing the waveguide opening to form a broad-band coaxial-to-waveguide transition. A wide-band choke terminates the opposite end of the line. The dc bias to the Gunn diode and extraction of the IF signal is also provided at this end. The dielectric waveguide oscillator cavity design is based on an image-line concept first formulated by Marcatili (4) and modified for millimeter-waves (5), (6). The fundamental electromagnetic wave propagating in a dielectric waveguide is the E_{11} mode, a hybrid mode which propagates when correctly launched. Theory indicates that the dielectric waveguide for proper operation should be on the order of one wavelength in the medium in width, and less than one-half wavelength in height. At 60 GHz, cross-sectional dimensions of the dielectric guides were oversized, i.e., slightly greater than 1 millimeter in height and about 2 millimeters in width. Experiments indicated that in this oversized condition, the E_{11} mode dominated. The resonant length of the dielectric section in back of the diode chosen for optimum power, was approximately $(2n+1)\lambda/2$ in length.

A simplified schematic of the self-oscillating mixer (Fig. 2) shows the manner of coupling to the metal waveguide; note that one end of the resonant cavity is tapered. The dielectric image guide taper can effect a low loss match to the metal waveguide by sliding the tapered end into the metal waveguide for maximum power transfer. This matching condition also yielded optimum IF output when the RF input signal was introduced. Fig. 3 gives a more detailed cut-away view of the device investigated; the IF exits out of the top of the dielectric guide with a metal disc being used as a matching element from the Gunn diode to the dielectric waveguide. Fig. 4 shows an exploded view of a 60 GHz dielectric waveguide self-oscillating mixer which utilizes a tuneable short to optimize performance; Fig. 5

shows the same unit ready for operation.

Referring to Fig. 4, the metal housing was designed for minimum radiation leakage with dimensions that were oversized with respect to WR-15 waveguide. The Gunn diode is mounted flush with the bottom of the metal structure. The aluminum oxide dielectric waveguide with tapered front end was bonded to the metal housing in such a way that the Gunn diode tip protruded up into the dielectric. A 0.045" hole in the dielectric waveguide allowed the IF and bias voltage post to come down and make a pressure contact with the top of the Gunn diode. This method of applying the bias voltage made it possible to mount a tuning short behind the dielectric guide.

EXPERIMENTAL RESULTS

Fig. 6 shows the output power and frequency characteristics of an InP diode in a waveguide cavity as a function of the bias voltage. Note that the frequency can be tuned over a range of 280 MHz with a change of bias of 1.2 volts; this change in bias voltage gave a change in output power from 19 to 23 mW. Similar characteristics were obtained with the GaAs Gunn diode in a waveguide cavity except that the peak bias voltage was in the order of 4.5 volts with peak powers of 6.5 mW. These peak output powers are typical of those used in the self-mixing experiments.

In the quest for a much lower cost device, GaAs and InP Gunn diodes were imbedded in an image guide cavity structure and their performance evaluated. This is the first time InP Gunn diodes have been evaluated as self-mixing oscillators either in metal waveguides or image line configurations. Figure 7 shows the output power and frequency characteristics of a GaAs diode as a function of the bias voltage. Figure 8 shows the same information using an InP diode. It should be noted that the bias voltage on the InP diode required for oscillation occurs at a higher value than that of the GaAs diode. The output powers are typical of those used in the self-mixing experiments. Figure 9 shows a block diagram of the RF circuit used in evaluating the two types of self-mixing Gunn oscillators. A backward wave oscillator in a mechanically tuneable mode was used as the signal source. The single frequency output from this source was stable within +0.001% with non-harmonic spurious signals recorded 40 dB down. This very stable signal was tuned 60 MHz above or below the Gunn oscillator frequency to produce the IF frequency.

The difference signal at 60 MHz was displayed on the face of a spectrum analyzer oscilloscope. By increasing the attenuation in

the signal channel, the IF energy could be made to decrease and disappear into the noise level of the spectrum analyzer. The attenuation was then decreased until the detected IF power was 3 dB above the noise level. At this point, the signal level was equal to the noise level and this IF power was defined as the minimum detectable signal power measured in decibels referred to 1 mW. The oscillating diode was tuned by the bias voltage just above the threshold field and also by the RF circuit to achieve the desired operating point. Care was taken to insure that no spurious oscillation or bias circuit instabilities were present.

The amplitude of the IF power in dBm was compared with measured values of input signal power for conversion gain or loss measurements. Figure 10 shows the IF output power as a function of signal power input for a GaAs Gunn diode. Figure 11 shows the same information for a InP Gunn diode. On both figures the last data point at the lowest power level indicates the noise reference level. The minimum detectable signal is defined as 3 dB higher and is shown in the next higher point of the figure. Note that the GaAs and InP Gunn diodes have a minimum detectable signal in the order of -77 and of -81 dBm respectively. This minimum detectable power is the principle parameter for determining the sensitivity of a self-mixing oscillator. It indicates how weak a signal the device can detect. Figure 12 shows the conversion gain measured on the GaAs Gunn oscillator. Figure 13 shows the same information for an InP Gunn self-mixing device; note that the conversion gain increases as the signal-input power decreases. The conversion efficiency as a function of bias voltage, with the signal held constant, is shown in Figure 14; the conversion gain peaks at a bias voltage just above the threshold voltage for oscillation. This behavior is consistent with information reported previously by investigators at lower frequencies using GaAs Gunn diodes in waveguide cavities.

DISCUSSION OF RESULTS

In terms of sensitivity, the data indicates that the InP self-mixing oscillator's performance is better than that of the GaAs device. This seems to verify the fact that InP is a superior material in several respects. It has a current peak-to-valley ratio of 3.5 as opposed to 2.5 for GaAs (7); this, in theory, will provide higher oscillator conversion efficiencies. In addition, the peak-to-valley ratio degrades less rapidly with temperature operation (7). The peak conversion gain was found to be approximately 10 dB for the InP device and 5 dB for the GaAs self-mixing device. Similar gain characteristics has been reported by several investigators for gallium arsenide when the diode is operated at voltages just above

*DIXON & JACOBS

threshold (1), (3). We conclude that InP diodes have higher conversion gain and hence lower noise.

An outstanding characteristic of the self-mixing oscillator is that the sensitivity or conversion gain increases as the signal level decreases. This characteristic has also been reported in the literature by investigators working at 34 GHz (1).

The principal design thrust for this program was the quest for a low weight, low cost device with simple construction. The dielectric image line approach has been shown to be well suited to accomplishing these objectives. The high sensitivities of -77 dBm for GaAs and -81 dBm for InP self-mixing oscillators makes these devices very attractive for the mixer function in certain applications.

CONCLUSION

It has been shown that, using GaAs and InP diodes imbedded in dielectric waveguide in simplified design principals given here, self-mixing Gunn oscillators of different operating voltages and frequencies can be successfully designed. Experimental data indicates that the sensitivity of these devices are in the order of -80 dBm which would make them competitive with other conventional mixers. However, these devices have the advantage of having simplified construction with a high signal power burnout level coupled with very low unit cost. These characteristics make the self-mixing oscillator a viable device in low cost receivers, expendable EW sensors, and short range terminal guidance. In addition, the InP self-mixing device has great potential in the higher millimeter-wave frequency region (above 100 GHz) due to its higher effective transit velocity and fast intervalley scattering.

ACKNOWLEDGEMENTS

The authors wish to express their gratitude to Mr. M.M. Chrepta, CORADCOM, for his efforts and discussions on the initiation of this program.

REFERENCES

1. M. J. Lazarus, S. Novak, and E. D. Bullimore, "A Sensitive Millimeter-wave Self-oscillating Gunn Diode Mixer," Proc IEEE, Vol. 59, No. 5, pp. 812-814 (May 1971).
2. M. R. Inggs, "Self-oscillating Mixer Cuts Antenna Test Costs," Microwaves, Vol. 17, No. 4, pp. 100-102 (April 1978).
3. M. Kotani and S. Mitsui, "Self-mixing Effect of Gunn Oscillator," Electronics and Communication in Japan, Vol. 55-B, No. 12, pp. 60-67, (1972).
4. E. A. J. Marcatili, "Dielectric Rectangular Waveguide and Directional Coupler for Integrated Optics," Bell System Tech. Journal, Vol. 48, pp. 2071-2102 (Sept. 1969).
5. H. Jacobs, G. Novick, C. M. LoCascio, and M. M. Chrepta, "Measurement of Guide Wavelengths in Dielectric Rectangular Waveguide," IEEE Trans. on Microwave Theory and Techniques, Vol. MTT-24, pp. 815-821 (Nov. 1976).
6. K. Klohn, J. Armata, M. M. Chrepta, "Transverse Propagation Constants In Dielectric Waveguides," USAECOM, Fort Monmouth, NJ Tech. Rpt. 4242 (Aug. 1974).
7. R. J. Hamilton, Jr., R. D. Fairman, S. I. Lang, M. Omori, and F. B. Fank, "InP Gunn Effect Devices for Millimeter-wave Amplifiers and Oscillators," IEEE Trans. on Microwave Theory and Techniques, Vol. MTT-24, No. 11 (Nov. 1976).

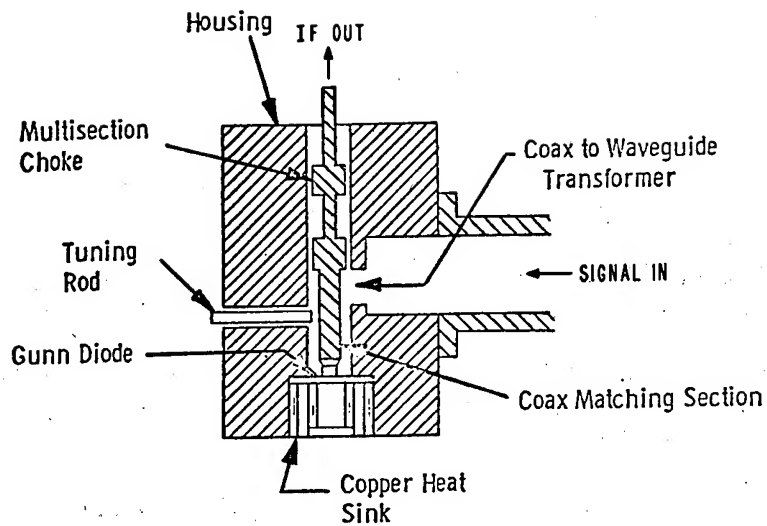


Fig. 1 Cutaway view of waveguide self-oscillating mixer.

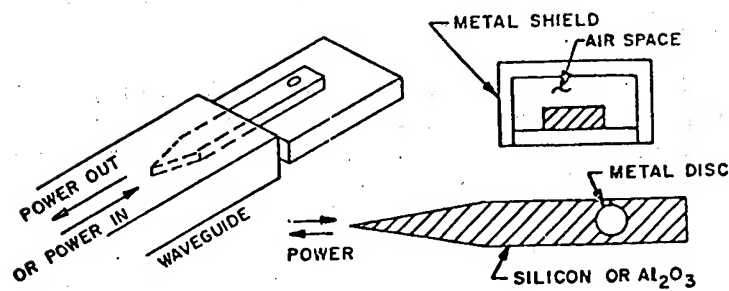


Fig. 2 Image guide mixer coupling to waveguide.

* DIXON & JACOBS

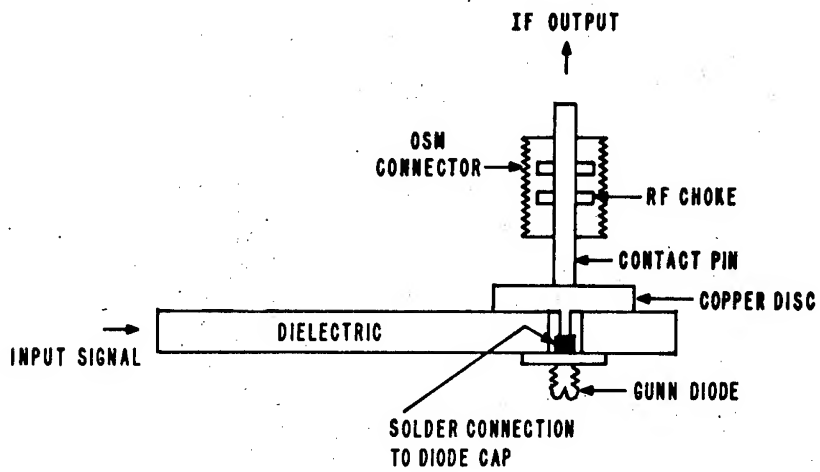


Fig. 3 Cutaway view of image guide self-oscillating mixer.

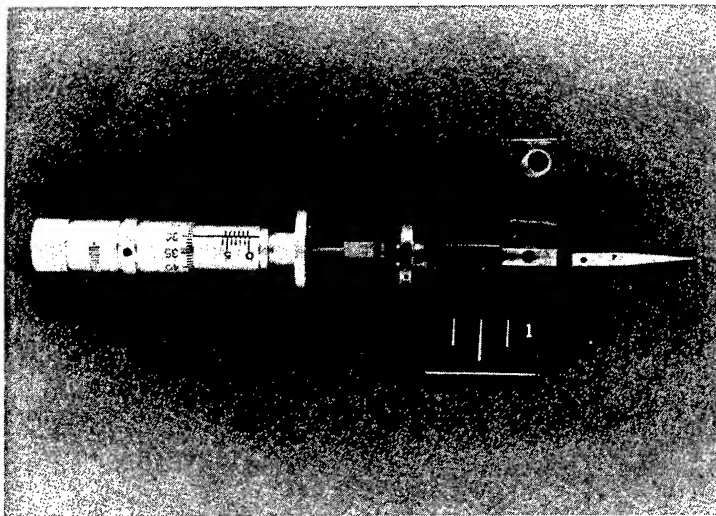


Fig. 4 Exploded view of image guide self-oscillating mixer.

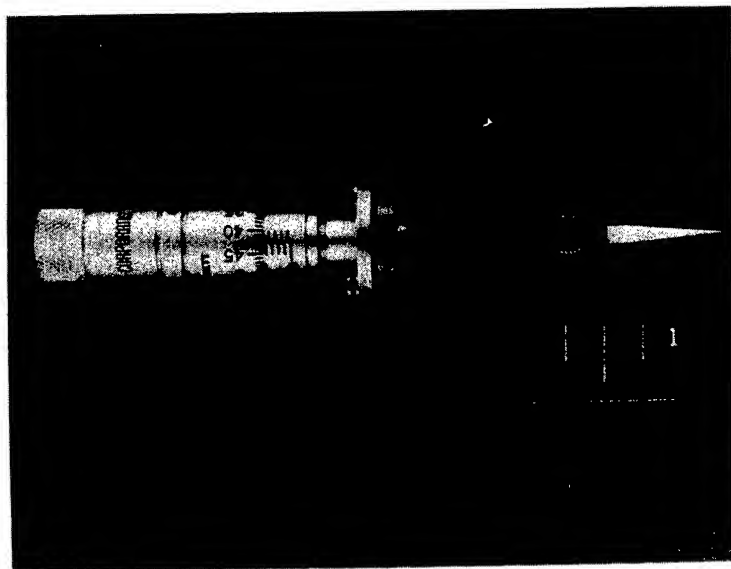


Fig. 5 Assembled image guide self-oscillating mixer.

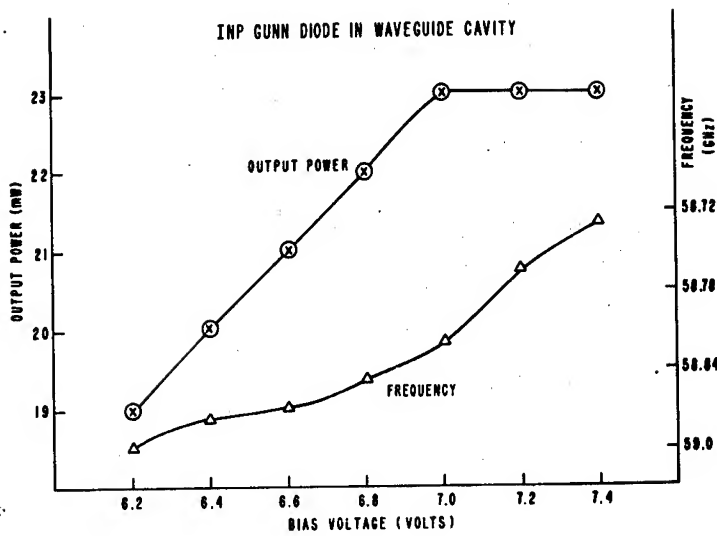


Fig. 6 Characteristics of InP waveguide cavity oscillator.

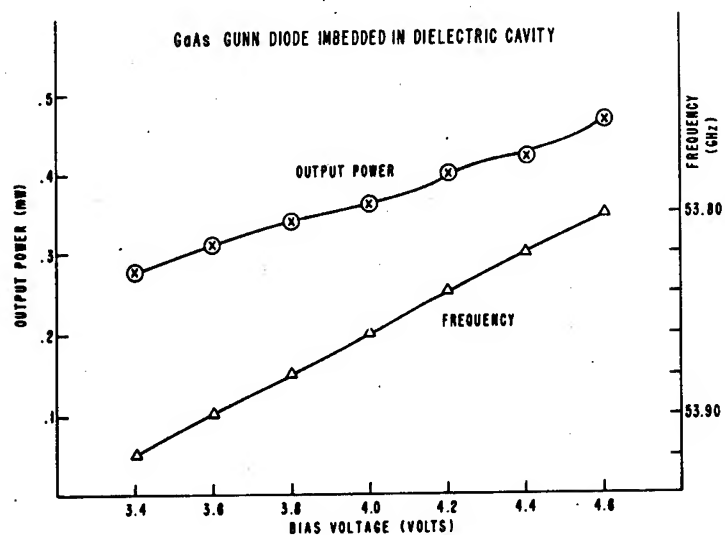


Fig. 7 Characteristics of GaAs image guide oscillator.

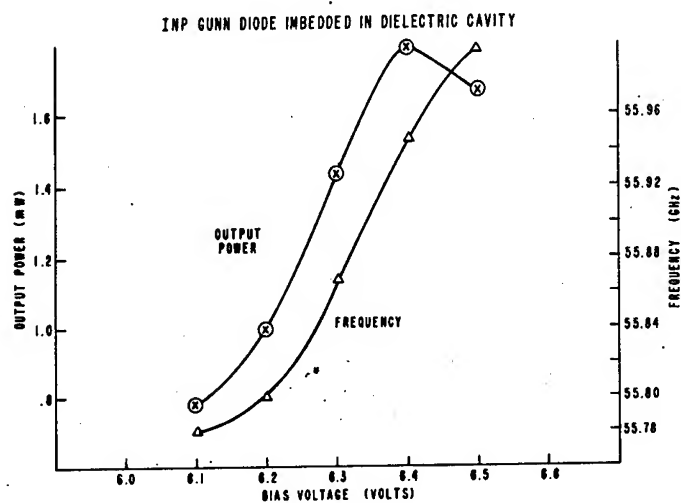


Fig. 8 Characteristics of InP image guide oscillator.

BLOCK DIAGRAM OF MILLIMETER-WAVE SYSTEM USED IN MEASUREMENTS OF
MINIMUM DETECTABLE SIGNAL

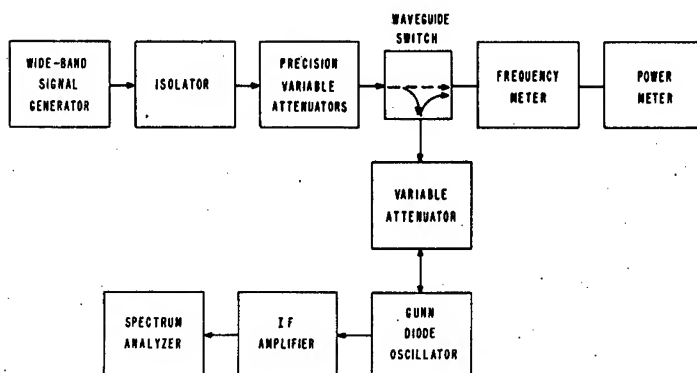


Fig. 9 Block diagram of measurement system for minimum detectable signal.

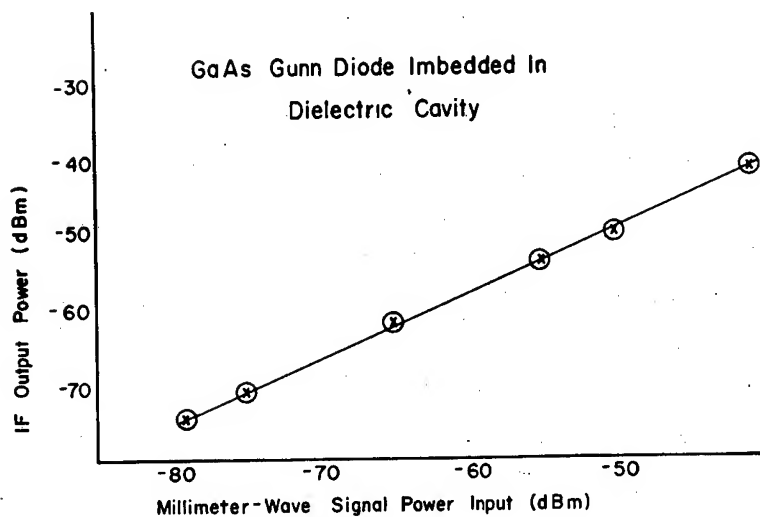


Fig. 10 IF output versus signal power for GaAs diode in image guide.

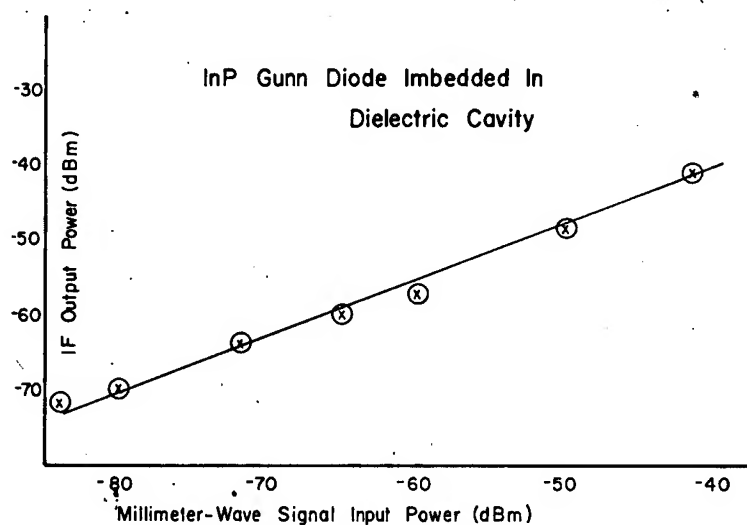


Fig. 11 IF output versus signal power for InP diode in image guide.

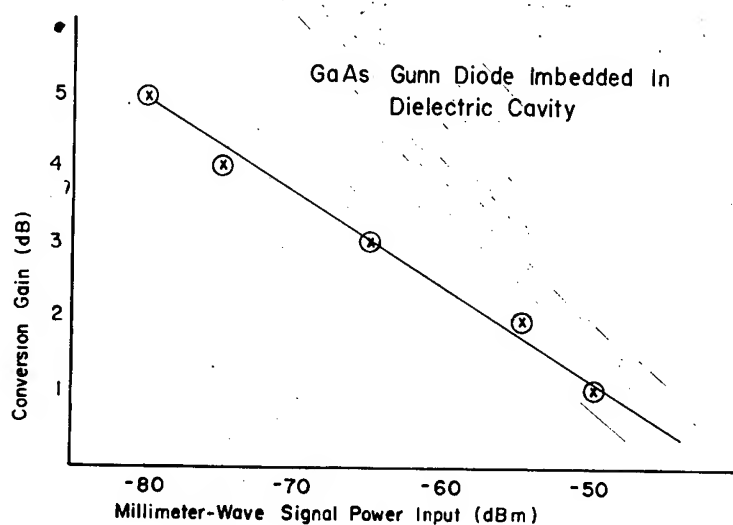


Fig. 12 Conversion gain versus signal power for GaAs diode in image guide.

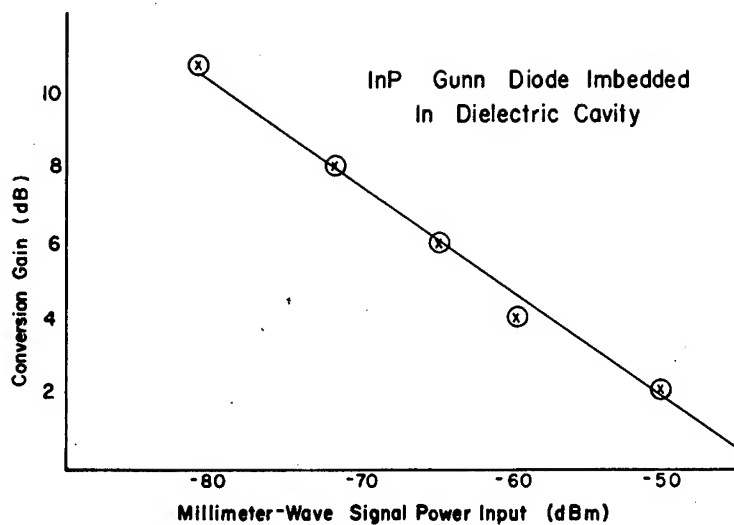


Fig. 13 Conversion gain versus signal power for InP diode in image guide.

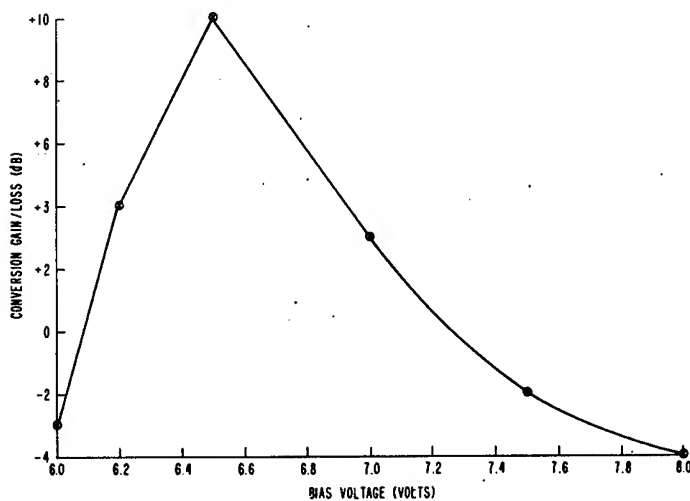


Fig. 14 Conversion gain versus bias voltage for InP diode in image guide.

*DOCTOR, BROWN and SLEEMAN

THE STABILITY OF BENACTYZINE.HCl UNDER SIMULATED
STORAGE AND PACKING CONDITIONS

*BHUPENDRA P. DOCTOR, Ph.D
NESBITT D. BROWN, MS, H. KENNETH SLEEMAN, Ph.D
WALTER REED ARMY INSTITUTE OF RESEARCH
WASHINGTON, D. C. 20012

Nerve agent antidote formulations, unlike most pharmaceutical formulations, have a unique requirement in that the potency of the active ingredients must remain stable upon prolonged storage under widely variable conditions. Previous studies in this laboratory and by the US Army Biomedical Laboratory showed that temperature was a major contributing factor to the instability of TAB (first letters of the active ingredients, Trimedoxime or TMB-4, Atropine Sulfate and Benactyzine.HCl with preservatives Methylparaben and Propylparaben). In addition to fulfilling the biomedical requirements of the nerve agent antidote, the logistical cost of packaging, storage and replacement of the antidote must be established.

The purpose of the present study was to assess the stability of Benactyzine and other active components of TAB under various conditions of packaging and storage in order to establish shelf-life and to determine the mechanism of degradation. The specific objectives were (a) to determine the effect of temperature on Benactyzine.HCl when packaged in glass ampules or cartridges with and without pH adjusted to 2.7, (b) to determine the effects of a plasticizer (1) on the rate of degradation of Benactyzine.HCl, (c) to determine whether the degradation products of TAB components influenced the rate of degradation of Benactyzine.HCl, and (d) to study effects of added propylene glycol as a stabilizer of Benactyzine.HCl.

Materials and Methods:

Eight different formulations of Benactyzine.HCl or TAB were

*DOCTOR, BROWN and SLEEMAN

prepared and packaged by Survival Technology, Inc. and were refrigerated at 5°C until used in the study. These formulations were distributed into 26 different groups as described in Table 1.

Three randomly selected samples were analyzed from each group (i.e. I at 5°C, II at 25°C, III at 54°C and etc) biweekly for 6 months, except groups XIII and XX which were analyzed monthly after the initial analysis. The concentration of Benactyzine.HCl and the TAB components, with the exception of Atropine Sulfate, was determined by high performance liquid chromatography (2,3). Atropine and the plasticizer were determined by gas chromatography (4). Ten samples from each of the eight original formulations were analyzed prior to starting the study for the purpose of establishing baseline concentrations of the components. The pH of each group was measured monthly.

Reference standards were prepared from chromatographically pure compounds. Regression and location parameters estimates were defined at 95 percent confidence levels, using an assumed t distribution for these parameter estimates. Comparisons were made between groups consistent with the objectives of the study.

Results:

The concentrations of Benactyzine.HCl and other TAB components when applicable were determined in 8 different formulations or packagings that were stored at three different temperatures, 5°, 25° and 54°C (24 groups). In addition 2 groups (XIII and XX) were stored at 54°C for two weeks and then for 6 months at 5°C to study the effects of any breakdown products on the stability of Benactyzine.HCl. The concentrations (Mg/2ml) of Benactyzine.HCl in these samples stored for a period of 27 weeks are listed in Table 2.

The groups (I, IV, VII, X, XIV, XVII, XXI, XXIV) stored at 5°C for the entire study showed no significant change in Benactyzine.HCl content, therefore will not be discussed further in this report. In the groups (II, V, VIII, XI, XV, XVIII, XXII, XXIV), stored at 25°C for the entire study, some degradation of Benactyzine.HCl was noted and will be discussed with the appropriate group(s). All the groups (III, VI, IX, XII, XVI, XIX, XXIII, XXVI) stored at 54°C for the entire study showed Benactyzine.HCl degradation and will provide the primary basis for the comparison of different treatments.

Effect of pH adjustment on Benactyzine.HCl stability:

Benactyzine.HCl packaged in glass vials (Groups I through VI) with no pH adjustment (original pH 4.3) and with pH adjusted to 2.7 with HCl showed the pH adjusted formulation to be more stable (Figure 1). The time required for Benactyzine.HCl to degrade to 50 percent of initial concentration, when pH was either adjusted to 2.7 or not adjusted was, at 25°C, 10 years and 3.1 years where as at 54°C it was 4.1 months and 3.6 months respectively. The pH change at 54°C during the 6 month period was -0.5 units for the non-adjusted and -0.3 units for the pH 2.7 adjusted formulation. The mechanism of degradation was different as shown by mixed kinetics for the non-adjusted pH and zero order kinetics for the pH 2.7 adjusted formulations.

Effects of packaging material on the stability of Benactyzine.HCl:

Benactyzine.HCl packaged in glass vials or cartridges with no pH adjustment (groups I, II, III and XXIV, XXV, XXVI) showed a considerable difference in the rate of degradation (Figure 2). The time for Benactyzine.HCl to degrade to 50 percent of its initial value was, at 25°C, 3.1 years in glass vials and 2.3 years in cartridges and at 54°C, 3.6 months in glass vials and 2.1 months in cartridges. Both formulations showed mixed order kinetics. The degradation of Benactyzine.HCl in cartridges was initially very rapid (first 6 to 8 weeks), which possibly reflects an initial adsorption and saturation of the rubber septums in the cartridges. The pH change was -0.5 and -0.75 pH units for the glass vials and cartridges, respectively.

Similarly, Benactyzine.HCl with the pH adjusted to 2.7 (group IV, V, VI and XIV, XV, XVI) was more stable in glass vials than in cartridges (Figure 3). The time for Benactyzine.HCl to reach 50 per percent of its initial value was over 10 years at 25°C, but at 54°C it was 4.1 and 3.4 months in glass vials and cartridges, respectively. The degradation in each instance followed zero order kinects. The pH change was -0.3 units in glass but there was essentially no pH change (less than 0.1 units) in the cartridges.

Effect of added plasticizer on the stability of Benactyzine.HCl:

The addition of plasticizer (20ug/ml) had no effect on the stability of Benactyzine.HCl (groups I, II, III and VII, VIII, IX) (Figure 4).

Effect of added propylene glycol on the stability of Benactyzine.HCl:

The addition of propylene glycol (40%) had a stabilizing

*DOCTOR, BROWN and SLEEMAN

effect on Benactyzine.HCl. When groups XIV, XV, XVI were compared to groups XXI, XXII, XXIII (cartridges at pH 2.7) the presence of propylene glycol increased the time required for Benactyzine.HCl to degrade to 50 percent of its initial concentration. At 25°C (Figure 5), propylene glycol extended the calculated shelf-life from 7.4 years to over 10 years and at 54°C, from 3.2 to 4.9 months. No significant pH change was noted among these groups. Plasticizer extracted from the septums was present in the groups (XXI to XXIV) which contained propylene glycol.

Effect of packaging material on the stability of the TAB components:

(a) The stability of Benactyzine.HCl at pH 2.7 in glass vials was greater than in cartridges. The time for a 50 percent decrease in Benactyzine.HCl concentrations at 25°C (groups XI and XVIII) was over ten years in either glass vials or cartridges but at 54°C it was 6.3 in glass vials and 4.3 months in cartridges respectively (Figure 6). There was no significant change in pH with either packaging.

(b) Atropine Sulfate was stable in all groups at all studied temperatures.

(c) Trimedoxime (TMB-4) stability was not affected by packaging in glass vials or cartridges and no significant differences in concentrations were found when groups X, XI, XVII, and XVIII were compared. However, the highest temperature, 54°C, did produce a significant ($p < .01$) degradation when groups X or XI vs XII and XVII or XVIII vs XIX were compared.

(d) Methyl paraben degradation was more rapid in cartridges than in glass vials (Table 3). The time required for Methylparaben to degrade to 50 percent of its original concentration was, at 25°C, over 10 years in glass vials (group XI) and 3.5 years in cartridges (group XVIII), at 54°C, 7.3 months in glass vials and 6.1 months in cartridges (groups XII and XIX) respectively (Figure 7).

(e) Propylparaben concentration was decreased in cartridges (groups XVIII, XIX) more than in glass vials (groups XI, XII). The time required for Propylparaben to decrease to 50 percent of its initial concentration was, at 25°C, over 10 years in glass vials but only 6.9 months in cartridges. At 54°C the time was 8.3 months in glass vials compared to 2.3 months in cartridges (Figure 8).

Effects of degradation products and packaging on the stability of TAB components:

The degradation products formed storing the TAB formulation at 54°C for two weeks in either glass vials or cartridges (groups XIII and XX) had no appreciable effect on the stability of the active components of TAB when subsequently stored at 5°C. There

*DOCTOR, BROWN and SLEEMAN

was a slight initial decrease in Benactyzine.HCl concentration during the 2 weeks storage at 54°C which then remained constant for the duration of the study. The only other changes noted was a slight initial decrease in methylparaben and Propylparaben concentrations in group XX (cartridge) which then remained constant for the duration of the study. No change in pH was noted.

Comparison of the stability of Benactyzine.HCl when formulated alone and with the TAB formulation:

Benzactyzine.HCl was slightly more stable in TAB than when packaged alone. This was found in both glass vials and cartridges. The time at 54°C for Benactyzine.HCl concentration to reach 50 percent of the initial concentration was 3.96 months alone and 5.92 months in TAB (group VI and XII), when packaged in glass, and 3.23 months and 3.54 months, respectively, when packaged in cartridges (groups XVI and XIX). No significant change in pH was noted.

Discussion and Conclusions:

The logistical costs of formulation, packaging, storage and replacement of a medical item are determined frequently by the stability of one of the constituents. The shelf-life of the nerve agent antidote TAB was found to be dependent on the stability of one of the active ingredients, Benactyzine.HCl. Whereas Benactyzine.HCl was stable at 5°C, at temperatures above 25°C it undergoes a rapid and continuous breakdown. This study shows, that in addition to temperature, other factors such as pH, packaging and some additives also effect the rate of Benactyzine.HCl breakdown and hence have a bearing on the shelf-life of formulations containing Benactyzine.HCl.

The stability of Benactyzine.HCl was improved by adjusting the formulation to pH 2.7 with HCl. When the pH adjusted and pH non-adjusted formulations, in glass vials were compared, the stability of Benactyzine.HCl was significantly ($p < .02$) improved at 54°C in the pH adjusted specimen. The time required for Benactyzine.HCl to degrade to 50 percent of the initial value was extended also at both 25°C and 54°C (Figure 1) in the pH 2.7 adjusted formulations.

Generally, the stability of Benactyzine.HCl stored in glass vials was better than when stored in cartridges. This was true whether the pH was adjusted to 2.7 or was not adjusted. In the Benactyzine.HCl formulations with no pH adjustment there was a significant ($p < .01$) difference between glass vials and cartridges

*DOCTOR, BROWN and SLEEMAN

at 54°C. The time for Benactyzine.HCl to degrade to 50 percent of its initial concentration was 3.1 years in glass and 2.3 years in cartridges at 25°C and at 54°C, 3.6 months in glass and 2.1 months in cartridges (Figure 2) respectively. Formulations of Benactyzine.HCl and TAB at pH 2.7 in glass and cartridges also showed the breakdown of Benactyzine.HCl. It was more rapid in cartridges. This was also true for the parabens (Figures 7 and 8). The results would suggest a positive role for the rubber septums in the decrease of Benactyzine.HCl and the parabens.

The adverse effect on stability found with the cartridges could result from (a) the surface effect of the rubber septum, (b) the adsorption into or by the rubber septum, and (c) the plasticizer (tributoxy ethylphosphate) which leeches from the rubber septum. The addition of the plasticizer to the Benactyzine.HCl formulation did not effect the degradation rate of Benactyzine.HCl. However, because of the limited solubility of the plasticizer in water, only 20ug/ml was added. This amount of plasticizer may be insufficient to affect the degradation of Benactyzine.HCl or may have been rapidly destroyed. Plasticizer was detected in all formulations packaged in cartridge and the amount increased with increasing temperature. The groups XXI, XXII, and XIII which contained propylene glycol, showed high levels of plasticizer. Any effects produced by the plasticizer could not be fully evaluated due to other variables involved. Some type catalytic role was indicated for the plasticizer, since all formulations in cartridges or with added plasticizer, gave zero order kinetics. This is in contrast with samples which contained no plasticizer and gave mixed order kinetics. The contributions made by the rubber septums to the decrease in Benactyzine.HCl can not be evaluated, however, Benactyzine.HCl and the parabens are known to be adsorbed on or into the septum.

The addition of propylene glycol (40 percent) to the Benactyzine.HCl formulation improved the stability of Benactyzine.HCl at 25° and 54°C. At 25°C (groups XV and XXII), propylene glycol extended the time required to reach 50 percent of the initial concentration of Benactyzine.HCl from 7.4 years to over 10 years and at 54°C (groups XV and XXIII), from 3.2 to 4.9 months (Figure 5). The use of propylene glycol would require further study if added to other compounds or combination of compounds.

Benactyzine.HCl was more stable when combined in the TAB formulation than when formulated alone. This was true when packaged either in glass vials or in cartridges. The differences (Figure 6) were not significant at 25°C but at 54°C highly significant ($p < .02$)

*DOCTOR, BROWN and SLEEMAN

differences were found.

The formulations adjusted to pH 2.7 with HCl showed no significant change in pH during the study. The slight decrease in pH of 0.5 to 0.7 units found in the unadjusted formulations probably reflect the formation of Benzoic acid, a breakdown product of Benactyzine.

This study established several facts about the stability of Benactyzine under the studied storage and packaging conditions: (a) Benactyzine.HCl alone or in TAB is stable for over 10 years at 5°C. (b) Benactyzine.HCl is stable for over 10 years at 25°C when stored in glass at pH 2.7. (c) Benactyzine.HCl or TAB is more stable packaged in glass than in cartridges. (d) The rubber septums and/or plasticizer have an adverse effect on the stability of Benactyzine.HCl and the parabens. There is evidence of a surface and/or catalytic effect. (e) Propylene glycol improves the stability of Benactyzine.HCl. (f) Other ingredients of TAB formulations, Atropine and TMB₄ are stable at normal storage temperatures for approximately 10 years when pH is adjusted to 2.7 and packaged in glass container. The stability of Benactyzine.HCl or TAB would be maximal when packaged in glass at pH 2.7 and stored at 5°C. However, for practical purposes, these formulations stored at a controlled room temperature ($22 \pm 5^\circ\text{C}$) appear to be stable for about 10 years.

Acknowledgment

We wish to thank Gale D. Demaree, COL, MSC for his advice and encouragement and to James E. Brown, CPT, MSC, R. Richard Gray, SSG Piyush K. Gandhi, and SP4 Gregory Schoo for their excellent assistance in performing some of these investigations.

Table 1

The Experimental Design for Stability Studies

<u>Groups</u>	<u>Compounds*</u>	<u>Packaging</u>	<u>Expt. Conditions</u>
I,II,III	Benactyzine.HCl	Glass Vial	5°, 25°, 54°C No pH adjustment
IV,V,VI	Benactyzine.HCl	Glass Vial	5°, 25°, 54°C pH 2.7
VII,VIII,IX	Benactyzine.HCl plasticizer	Glass Vial	5°, 25°, 54°C No pH adjustment
X,XI,XII	TAB	Glass Vial	5°, 25°, 54°C pH 2.7
XIII	TAB	Glass Vial	54°C for 2 wks and 5°C for 5 mo.
XIV,XV,XVI	Benactyzine.HCl	Cartridges**	5°, 25°, 54°C pH 2.7
XVII,XVIII,XIX	TAB	Cartridge	5°, 25°, 54°C pH 2.7
XX	TAB	Cartridge	54°C for 2 wks and 5°C for 5 mo.
XXI,XXII,XXIII	Benactyzine.HCl propylene glycol	Cartridge	5°, 25°, 54°C pH 2.7
XXIV,XXV,XXVI	Benactyzine.HCl	Cartridge	5°, 25°, 54°C no pH adjustment

*The concentration and volume of formulations were kept identical to original TAB formulation.

**Cartridge contained a glass tube with a rubber plunger at one and a rubber septum and needle at the other end.

*DOCTOR, BROWN and SLEEMAN

Table 2

Benactyzine.HCl Concentration (mg/2ml) With Time (Days)

<u>Group</u>	<u>Time (Days)</u>						
	0	28	56	84	112	161	189
I	5.25	5.38	5.26	5.15	5.19	5.25	5.09
II		5.30	5.28	5.05	5.16	4.98	4.81
II		4.16	3.38	2.64	2.25	1.74	1.36
IV	5.40	5.26	5.22	5.36	5.46	5.36	5.11
V		5.44	5.31	5.30	5.20	5.36	5.25
VI		4.67	3.85	3.26	2.90	1.90	1.60
VII	5.25	5.23	5.20	5.20	5.25	5.10	5.12
VIII		5.36	5.14	5.16	5.04	4.91	4.98
IX		4.00	3.22	2.78	2.18	1.64	1.40
X	4.47	4.38	4.37	4.42	4.02	4.35	4.40
XI		4.24	4.17	4.27	4.08	4.44	4.18
XII		3.87	3.55	3.10	2.97	2.57	2.37
XIII		4.25	4.14	4.05	4.18	4.27	4.29
XIV	5.43	5.44	5.31	5.32	5.30	5.44	5.43
XV		5.40	5.32	5.17	5.40	5.23	5.28
XVI		4.30	3.39	2.86	2.10	1.56	1.30
XVII	4.42	4.13	4.50	4.18	4.15	4.37	4.39
XVIII		4.33	4.13	4.40	4.13	4.35	4.34
XIX		3.60	2.97	2.71	2.07	1.85	1.71
XX		4.21	4.14	4.09	4.09	4.22	4.22
XXI	4.80	4.88	4.75	4.92	4.81	4.68	4.78
XXII		4.82	4.78	4.78	4.64	4.80	4.73
XXIII		4.20	3.66	3.28	2.75	2.36	2.27
XXIV	5.40	5.38	5.18	5.39	5.30	5.47	5.28
XXV		5.46	5.22	5.22	4.94	4.92	4.90
XXVI		3.66	2.10	1.28	0.96	0.54	0.32

Table 3

Methylparaben Concentration (mg/2ml) With Time (Days)

Group	<u>Time (Days)</u>						
	0	28	56	84	112	161	189
X	1.07	1.06	1.04	1.09	1.04	1.08	1.06
XI		1.06	1.05	1.07	1.06	1.04	1.05
XII		1.03	0.93	0.89	0.80	0.70	0.60
XVII	1.07	1.05	1.09	1.08	1.01	1.07	1.04
XVIII		1.04	1.03	1.03	1.02	1.00	0.99
XIX		0.93	0.81	0.78	0.69	0.62	0.54

Table 4

Propylparaben Concentration (mg/2ml) With Time (Days)

X	.105	.100	.102	.106	.010	.105	.102
XI		.101	.104	.105	.100	.104	.101
XII		.101	.094	.084	.079	.074	.067
XVII	.093	.090	.092	.091	.090	.093	.088
XVIII		.081	.076	.066	.061	.056	.050
XIX		.049	.044	.031	.028	.023	.021

*DOCTOR, BROWN and SLEEMAN

Figure 1

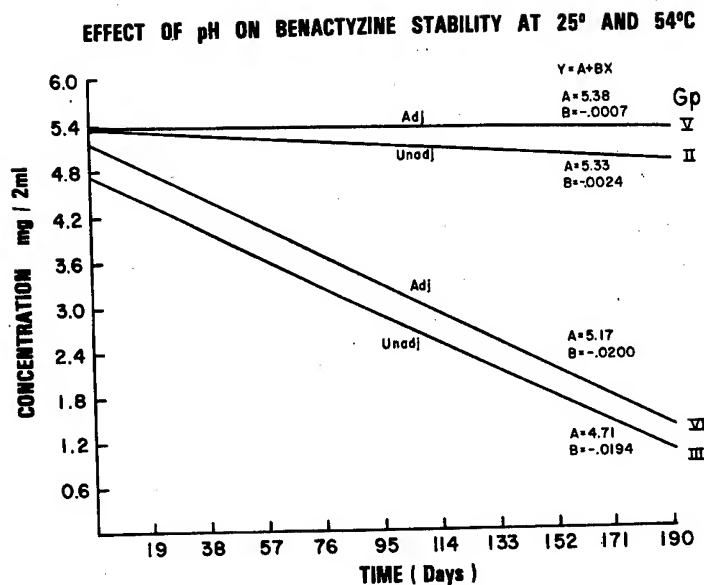


Figure 2

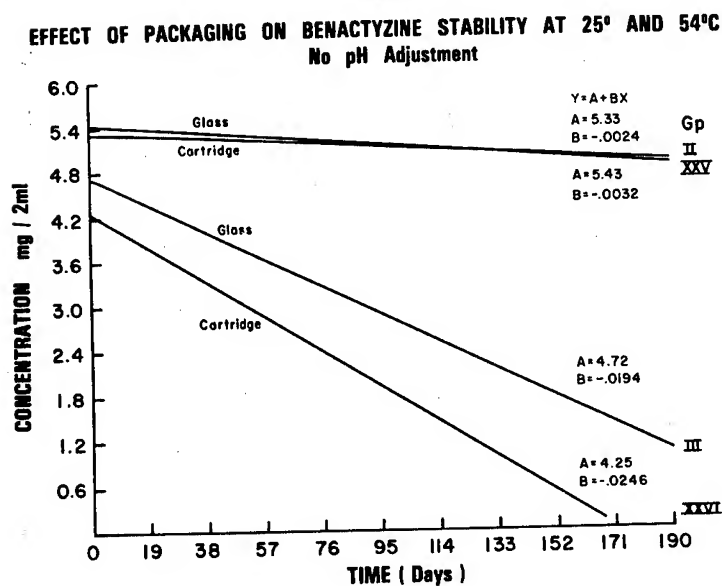


Figure 3

EFFECT OF PACKAGING ON BENACTYZINE STABILITY AT 25° AND 54°C
pH 2.7

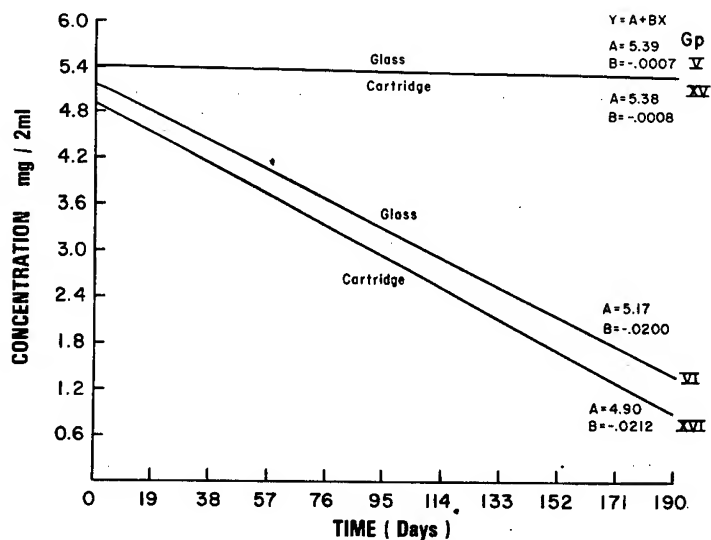
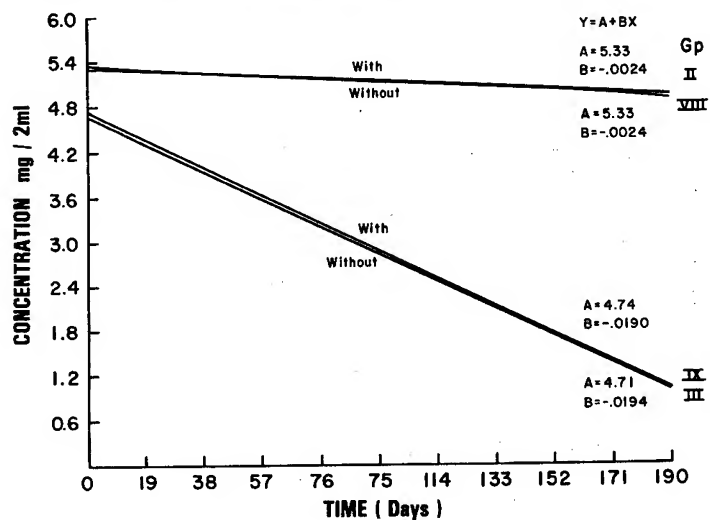


Figure 4

EFFECT OF PLASTICIZER ON BENACTYZINE STABILITY AT 25° AND 54°C



*DOCTOR, BROWN and SLEEMAN

Figure 5
EFFECT OF PROPYLENE GLYCOL ON BENACTYZINE STABILITY AT 25° AND 54°C

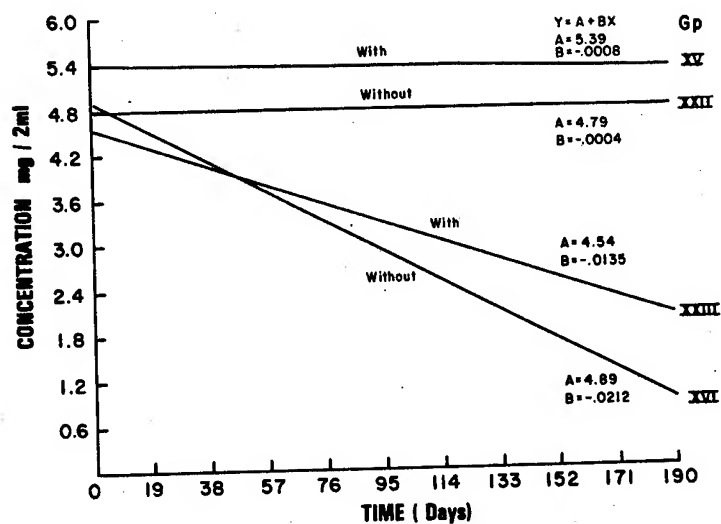


Figure 6
EFFECTS OF PACKAGING ON BENACTYZINE STABILITY IN TAB AT 25° AND 54°C
pH 2.7

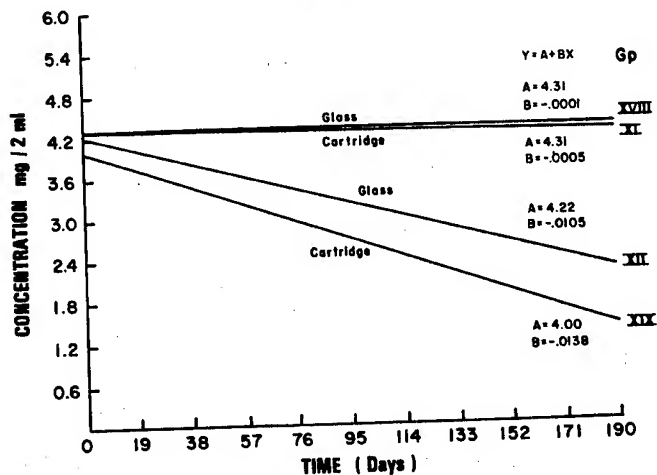


Figure 7

EFFECT OF PACKAGING ON MENTYL PARABEN STABILITY IN TAB AT 25° AND 54°C

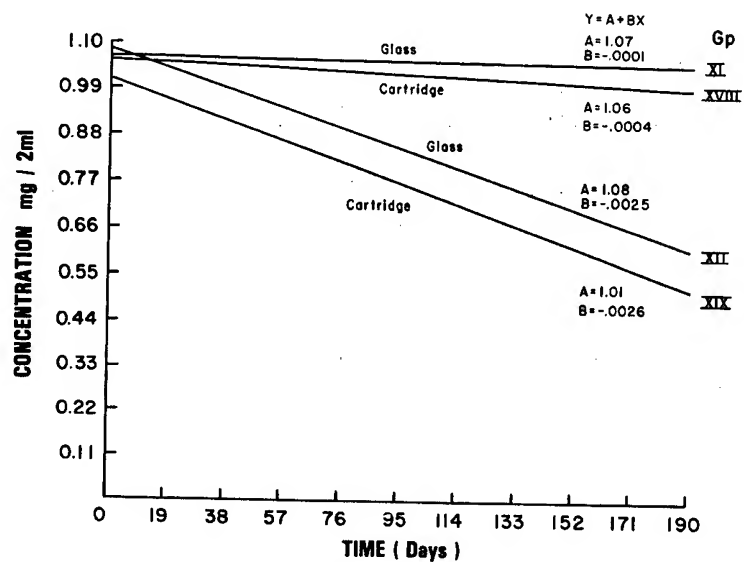
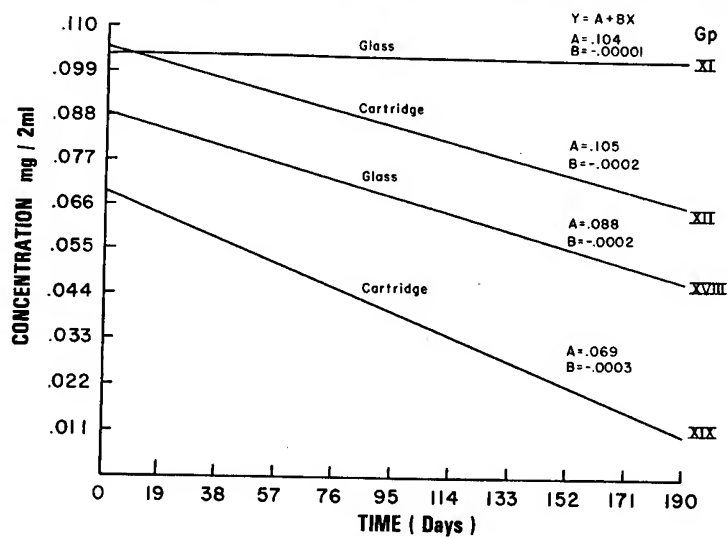


Figure 8

EFFECT OF PACKAGING ON PROPYL PARABEN STABILITY IN TAB AT 25° AND 54°C



References

1. Farshy, D.C.: Tri-butoxyethyl phosphate as a contaminant in B-D Vacutainers. *Applied Microbiology* 27: 300-304, 1974.
2. Brown, N.D. and Sleeman, H.K.: An ultramicro high performance liquid chromatographic method for assaying ion-pair species of benactyzine. *J. Chromatography* 140: 300-303, 1977.
3. Brown, N.D., Hall, L.L., Sleeman, H.K., Doctor, B.P. and Demaree, G.E.: Ion-pair high-performance liquid chromatographs separation of a multicomponent anticholinergic drug formulation. *J. Chromatography* 148: 453-457, 1978
4. The United States Pharmacopeia, 18th Revisions, Bethesda, Md, 1970. p.57.

ADVANCED COMPOSITE APPLICATIONS TO LARGE
CALIBER WEAPONS SYSTEMS (U)

CRAIG D. DOUGLAS*
ROBERT W. LEWIS, ScD
ARMY MATERIALS AND MECHANICS RESEARCH CENTER
WATERTOWN, MA 02172

I. INTRODUCTION

Composite materials are ideal for structural applications where high strength-to-weight and stiffness-to-weight ratios are required. Aircraft, spacecraft, and missiles are typical weight-sensitive structures in which composite materials are utilized.

According to Jones (1) there are three commonly accepted types of composites: (1) Fibrous composites which consist of fibers in a binding matrix, (2) Laminated composites which consist of layers of various materials, and (3) particulate composites which are composed of particles in a binding matrix.

This study deals with composites of the first type--the application of an advanced fibrous composite, graphite/epoxy, to increase the overall performance of the barrel extension used on the 75mm rotating chamber single shot firing fixture. In order to increase accuracy and muzzle velocity, an all-metal barrel extension (Figure 1) had been added to the 75mm gun tube where the muzzle brake had been located. This extension increased the muzzle velocity, but round dispersion was still apparent. This round dispersion was attributed to the initial "droop" of the tube caused by its body forces.

Advanced composites proved to be a good candidate for the solution of this problem. A comparison of specific properties, (Figure 2) where the specific property is defined as that material property divided by the material density, shows that if one takes specimens of steel and graphite-epoxy, both of the same weight, the

DOUGLAS and LEWIS

graphite-epoxy would have up to four times the stiffness and five times the strength.

With this in mind, if much of the outer metal were replaced with a graphite/epoxy composite with its fibers oriented uniaxially along the tube direction, the new tube would (1) be



Figure 1. ALL METAL BARREL EXTENSION

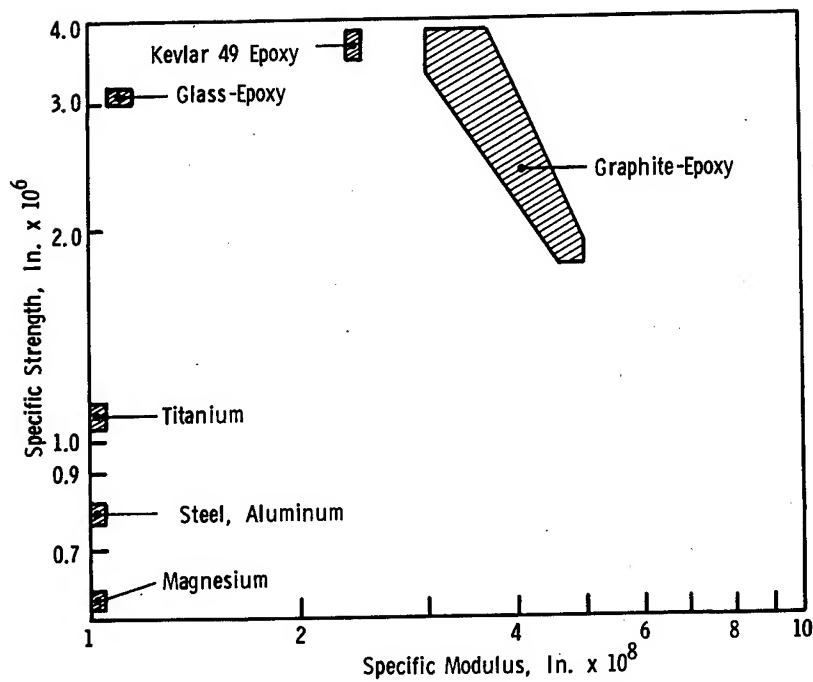


Figure 2. PROPERTY COMPARISON

lighter in weight; (2) the tube would be stiffer in the longitudinal direction, and (3) with the combination of the above, initial "droop" would be less, and the natural frequency of the extension in the longitudinal sense would be higher, thus combating the well known whip phenomenon that large caliber weapons exhibit.

II. DESIGN APPROACH

The basic design approach was to remove the outer metal of the original extension, and then to replace that removed metal with a composite. Once the metal was removed, the original extension would become both an internal liner to protect against erosion, and a permanent mandrel on to which the composite would be applied.

Figure 3 shows the pressure-history experienced by the chamber. A maximum pressure of 55,000 psi is what the chamber of the gun sees, but this is not what the muzzle extension must withstand. The projectile exits at approximately 7-8 milliseconds after charge ignition. This means that the end of the tube is exposed only to atmospheric pressure up to that time. At exit time, the pressure has already decreased to 15,000 psi in the chamber. Also, there is a pressure gradient along the tube such that the muzzle pressure is 80% that of the chamber pressure. The working pressure, then, seen by the extension is roughly 12,000 psi.

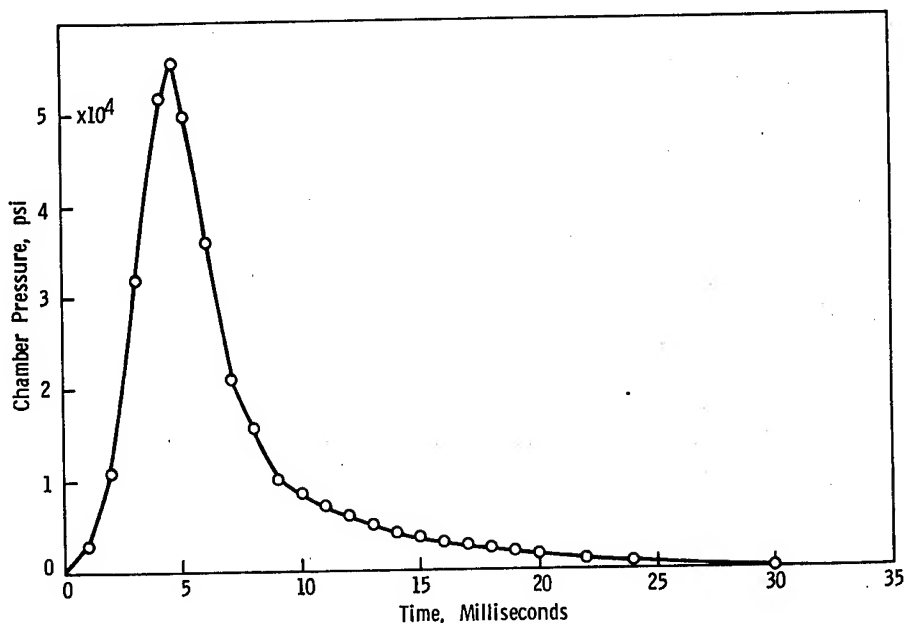


Figure 3. PRESSURE-HISTORY

The internal heat input per round was experimentally determined to be $68 \text{ BTU/ft}^2/\text{round}$ (2). This caused a temperature rise of 27°F per round at the outer wall of the tube.

After examining these operating conditions, both finite element and classical techniques were used to determine exactly how much metal was to be removed and how much composite would be added, in order to increase the overall performance while staying within material property limits.

An orthotropic finite element code ORFE (3) was used to predict the hoop and radial stresses developed during fire. This code is an interactive substructured routine installed on the AMMRC U-1106 computer. For this particular model isoparametric axisymmetric finite elements were used. Figure 4 shows a sample grid used in the analysis. Classical equations were also developed to analyze the isotropic cylinder overwrapped with an orthotropic composite subjected to an internal pressure pulse. This analysis calculated the radial stress (Figure 5) and the hoop stress (Figure 6) as a function of radius.

To verify that the assumption of a static loading case was valid in the pressure-stress relations, it was necessary to determine the radial and hoop-type ring frequencies and compare their period of oscillation to that of the rise time of the pressure pulse. Calculations showed that these periods of oscillation were sufficiently high so that the internal pressure pulse would not excite the system and cause a dynamic loading case.

A thermal analysis was used to determine the axial stress developed during the cure cycle used for the composite, and also to determine the temperature at the metal/composite interface during fire. The mismatch of coefficients of thermal expansion of the metal and the graphite/epoxy was the reason that the thermal study was needed during cure. Steel has a coefficient of thermal expansion that is approximately $6 \mu\text{in/in}/^\circ\text{F}$ while that of the composite is essentially zero (actually, it is slightly negative in the fiber direction).



Figure 4. FINITE-ELEMENT GRID

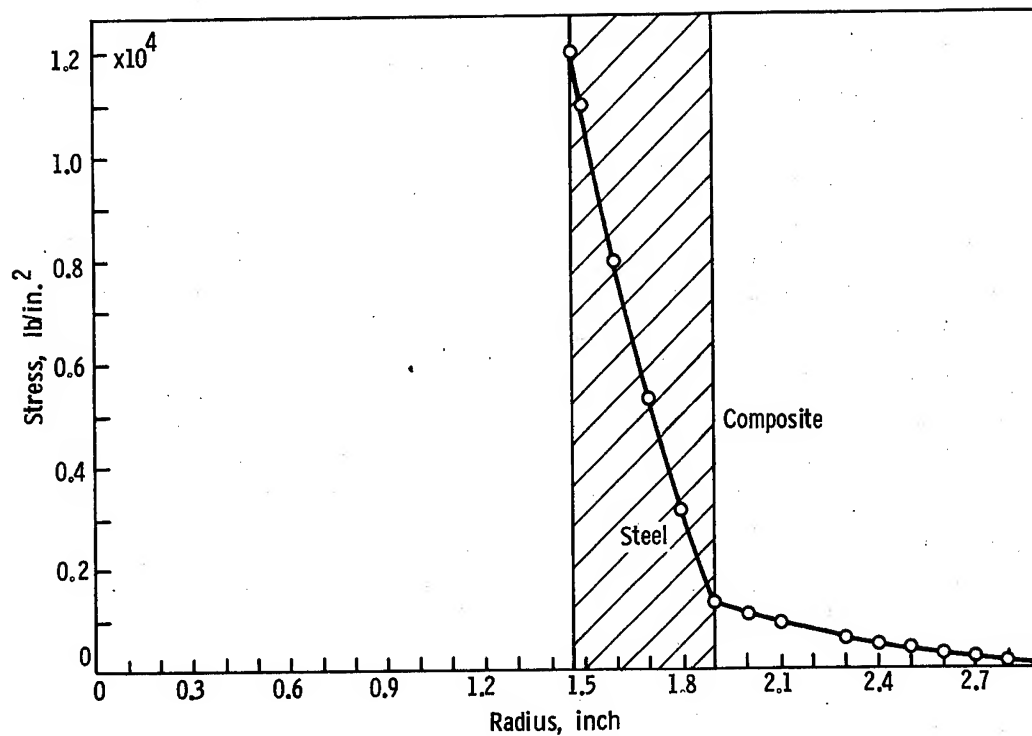


Figure 5. RADIAL STRESS VERSUS RADIUS

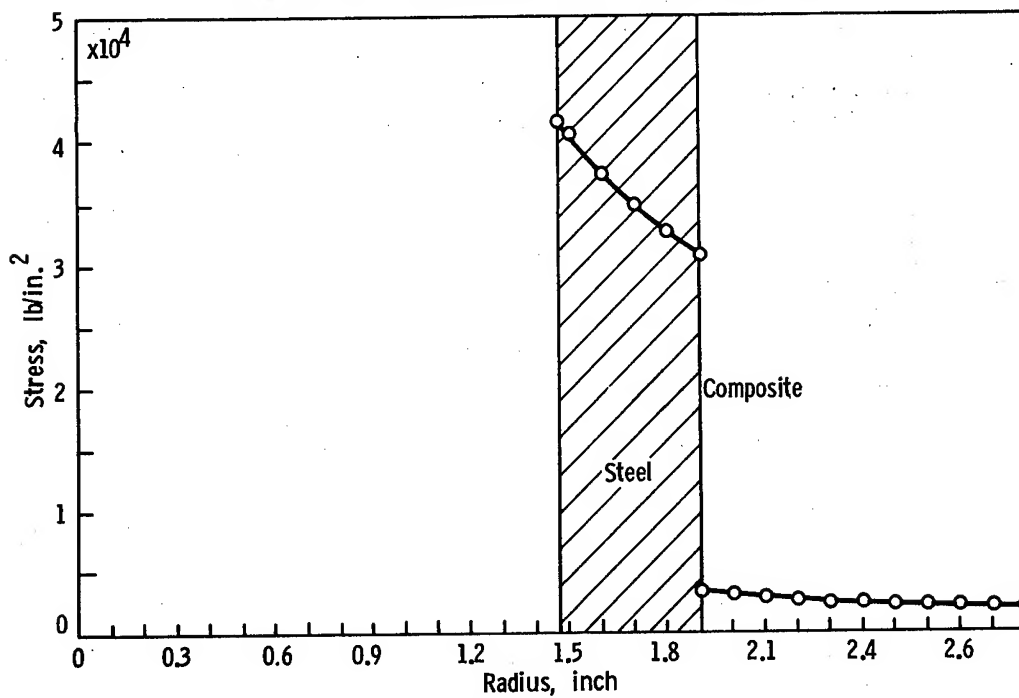


Figure 6. HOOP STRESS VERSUS RADIUS

When the liner/mandrel with the uncured composite (oriented 0° along the tube axis) is placed in the autoclave and raised to 350°F , which is the cure temperature of the composite, the extension is virtually stress free. At 350°F the composite system cures, thereby restraining the internal steel mandrel in its elongated state. When the extension is cooled, it wants to contract by the amount $\alpha\Delta TL$ (where α is the coefficient of thermal expansion and L is the length of the tube). It is constrained from doing so, however, by the cured composite thus introducing a residual stress field. It is this stress field that had to be determined in order to prevent the composite from buckling during cool-down.

Graphite/epoxy systems tend to lose their structural integrity as the operating temperature approaches that of the cure temperature. Hence it is necessary to assure that the operating temperature does not exceed 350°F . Figure 7 shows the predicted peak temperature above ambient as a function of time for a single shot. In this case where the gun was not fired in a repeating mode, the peak interfacial temperature was determined to be 56°F above that of the ambient, well within the operating range of the composite.

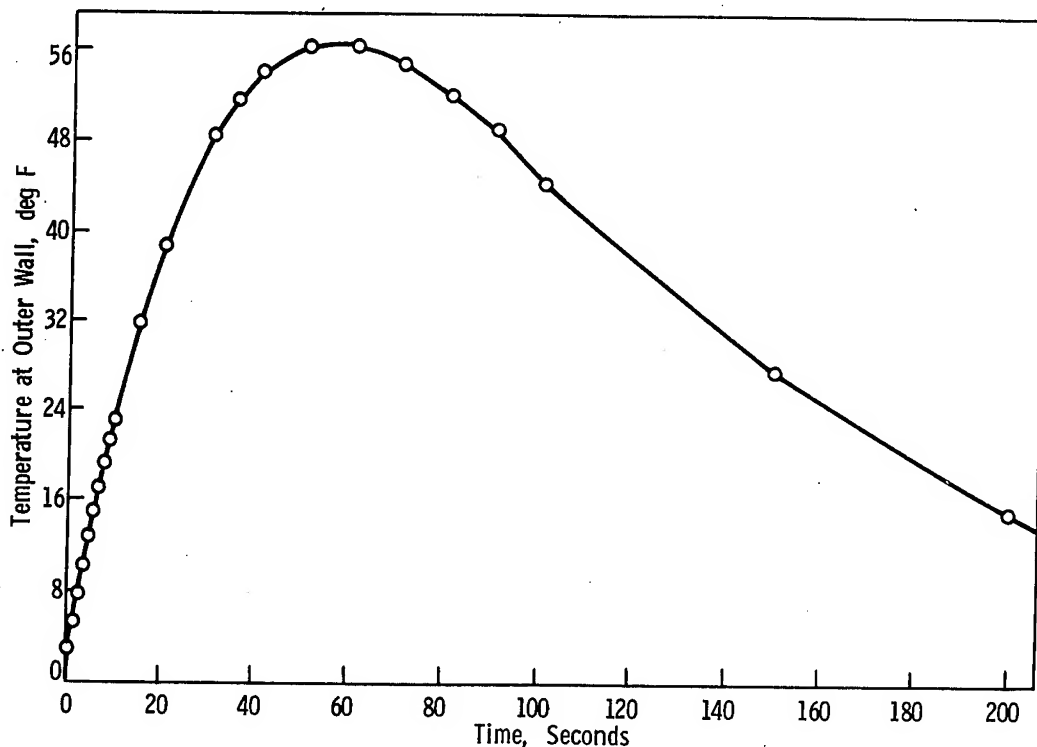


Figure 7. PLOT OF WALL TEMPERATURE VERSUS TIME OF EXIT

III. FABRICATION

Upon converging on a final liner/mandrel design, an original extension was modified as shown in Figures 8 and 9. The surface was then prepared for interfacial instrumentation and composite application.

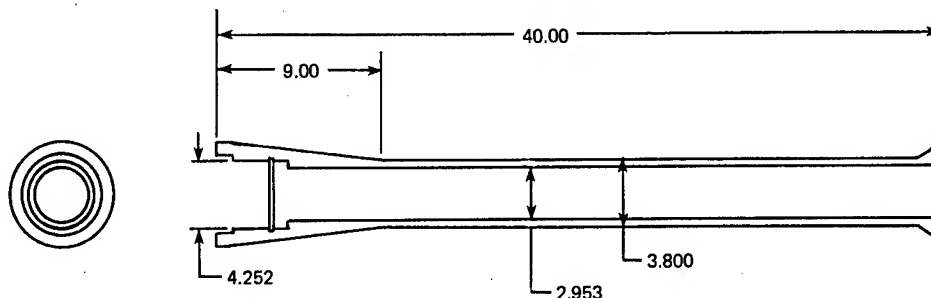


Figure 8. DIMENSIONS OF LINER/MANDREL



Figure 9. LINER/MANDREL READY FOR COMPOSITE APPLICATION

A ten percent solution of hydrochloric acid was used to clean all major dirt and grease left on the part after the machining process. The part was then chucked in a filament winding machine which was used to facilitate part instrumentation and the hand layup of the graphite-epoxy. The filament winding process was not used at this point in the fabrication.

A methanol and subsequent acetone rinse were used to clean the liner/mandrel just prior to instrumenting and composite application. Two strain gages and a thermocouple were applied to the interface. The strain gage orientation was such that longitudinal and hoop stresses could be recorded during fire. The gages and thermocouple were then insulated to prevent the graphite/epoxy from electrically shorting out the gages. The extension was then ready for the first graphite/epoxy application.

DOUGLAS and LEWIS

Because the composite was up to an inch thick toward the breech end, the graphite/epoxy had to be applied in three separate operations, with autoclaving between each application; otherwise too much resin "bleedout" would have occurred during cure, resulting in a "dry" composite part. These multiple fabrication steps allowed the application of intracomposite instrumentation to monitor stresses and temperatures through the wall during fire.

After cleaning and instrumentation a film adhesive was applied, and three inch wide prepreg tape (HMS-3501-6) was layed up unidirectionally along the tube axis. Once the composite was at the desired thickness (.33 in) for the first application, a bleeder ply was applied, then a burlap bleeder ply, and finally a vacuum bag and gland. The extension was then autoclaved according to the recommended cure cycle for the 3501-6 epoxy resin--90 minutes at 120°F, followed by 90 minutes at 350°F. When the autoclave cycle was completed the tube was debagged and cleaned. Two more layers of graphite/epoxy were applied in the same manner.

To provide field durability and protect the graphite/epoxy from the "zippering" effect, or splitting along the fiber axis, that could occur with unidirectional composites, a hoop winding of S2 glass/epoxy was applied using a filament winding machine. The extension was then post-cured at 370°F for three hours. Figure 10 shows the composite extension with its final instrumentation ready for firing tests.



Figure 10. COMPLETED LINER/MANDREL

IV. FIRING TESTS

The firing tests were performed at Ares Corporation, Port Clinton, OH. The gun used was their rotating chamber single shot test fixture (RCSSTF). Figure 11 shows the composite extension mounted on the tube.

The firing procedure used was: (1) Ready the RCSSTF in accordance with pre-firing procedures established for proof test of ammunition. (2) Install the all-metal barrel extension. (3) Verify

DOUGLAS and LEWIS

barrel bore, breech and barrel insert, barrel extension, and chamber alignment with projectile bore gage. (4) Fire warm-up rounds to insure instrumentation is operating properly. (5) Verify barrel extension bore alignment with bore sight to the center of the target. (6) Fire ten rounds of armor piercing, fin stabilized, discarding sabot (APFSDS) ammunition which has been conditioned at 70°F for at least eight hours. (7) Repeat steps two through six utilizing the composite barrel extension.



Figure 11. COMPOSITE EXTENSION READY FOR FIRING

V. RESULTS

Table 1 shows the data taken from the round locations on the target. The average shot location was significantly closer to the center of the target for the composite extension in the vertical direction and approximately the same in the horizontal direction. This suggests that initial barrel droop was indeed less with the composite extension.

Table 1. ROUND DISPERSION RESULTS

• FIRING RANGE = 80 METERS

	METAL EXTENSION		COMPOSITE EXTENSION	
	VERTICAL	HORIZONTAL	VERTICAL	HORIZONTAL
LOCATION	1.448 MRAD	-0.820 MRAD	0.346 MRAD	-0.806 MRAD
VARIANCE	0.131 MRAD	0.198 MRAD	0.072 MRAD	0.370 MRAD

Longitudinal and hoop strain data showed a definite advantage in using the composite extension. From the longitudinal strains recorded during the fire, it was found that the composite extension had a natural frequency that was 22% higher than the metal extension. The damping time (Figure 12) for the composite extension was almost 45% lower than that of the metal extension, where the time to damp, t_D , is that time at which the amplitude of vibration is 0.10 that of the original input.

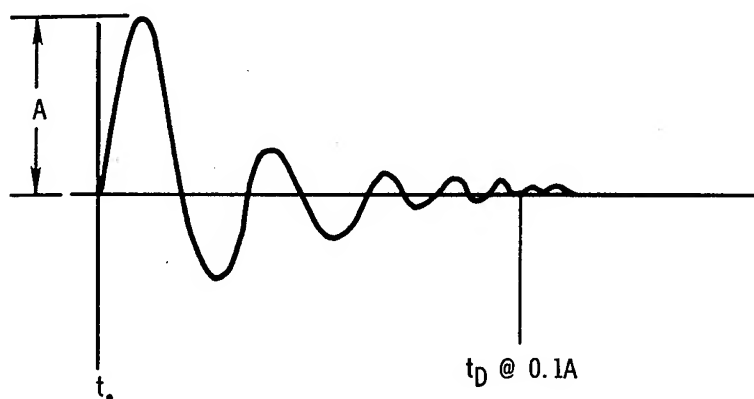
Composite Extension $t_{Davg} = 29$ msecMetal Extension $t_{Davg} = 51$ msec

Figure 12. DAMPING HISTORY

Hoop strain data agreed well with the finite element predictions. It was predicted that the hoop strain during fire would reach a value of $870 \mu\text{in/in}$ and the measured value was $990 \mu\text{in/in}$, an error of only 11% in the estimate.

Thermal data agreed quite well with the predicted value, except for the decay time. The peak temperature predicted was 56°F above ambient, or 106°F, approximately sixty seconds after fire. The actual temperature measured was 112°F at 1.25 minutes after fire. The decay time, however, was almost an order of magnitude greater than the predicted value.

Erosion data taken by standard star gage techniques showed no difference between the two extensions.

Finally, the weights of the composite and metal extension were 82 and 95 pounds respectively. The metal extension was 16% heavier than the composite. Note that the weight of the turned-down barrel was 57 lbs. Thus, 38 pounds of metal were replaced with 25 lbs of graphite/epoxy.

VI. DISCUSSION

The feasibility of using advanced composites in large caliber weapon systems has been demonstrated. The graphite/epoxy barrel extension was found to be more accurate and lighter than the all-metal barrel extension. Barrel whip has been reduced significantly as evidenced by the damping time.

The use of classical and finite element techniques has proven to be an accurate method when used to predict operating quantities such as the dynamic stresses and strains. Experimental data taken during the firing tests were very close to the analytical predictions; however, some error was present. The greatest discrepancy between the predicted and actual values was in the thermal predictions at the metal/composite interface. Although the rise time and peak temperature were very close to the actual, there was almost no correlation in the decay. Classical heat transfer methods predicted an exponential decay that would approach zero within roughly 350 seconds, whereas actually the time required was 1800 sec. The reason for this difference is thought to arise from the calculation of the negative exponent in the decay term of the heat balance equation. This term has as part of it, the internal convective heat transfer coefficient. It is this quantity that was poorly estimated. It is interesting to note, however, that one can actually use the experimentally measured thermal data to modify the solution to the heat balance equation in order to obtain the actual heat transfer coefficient. This could then be used in future studies.

Regarding the hoop strain calculations, the actual strain was only 11% higher than the predicted value. Such a small

difference could be attributed to many things, e.g. a slight difference in material properties with respect to what was used in the calculations, especially, in the transverse direction of the composite overwrap (which was in the hoop direction of the extension).

These hoop data also verified the assumption that the model--isotropic cylinder overwrapped with an orthotropic composite--could assume a static loading case. Had there been any dynamic overshoot (i.e. greater than 25% that of the steady state case) there would have been a much greater difference between actual and predicted values of hoop strain at the interface. From these data it can be concluded that the metal liner could have been made thinner providing that the hoop strain at the interface did not exceed that of the strain-to-failure of the graphite/epoxy in the transverse direction.

Because of the increased stiffness and decreased weight, the natural frequency of the composite extension was higher than that of the metal. In addition, the damping time of the composite was less. This could lead to an increased rate of fire in that the composite will have already stopped "whipping" when the metal extension would still be in motion.

Probably the most significant aspect of the results was the target data. Overall dispersion area for the composite was one third of that for the metal (Figure 13). The standard deviation of the round dispersion in the vertical direction was much less for the composite. This fact is attributed to the quicker response of the barrel as it is straightened from its initial droop when the projectile approaches the muzzle and also to the fact that the initial droop was less because of the lighter weight.

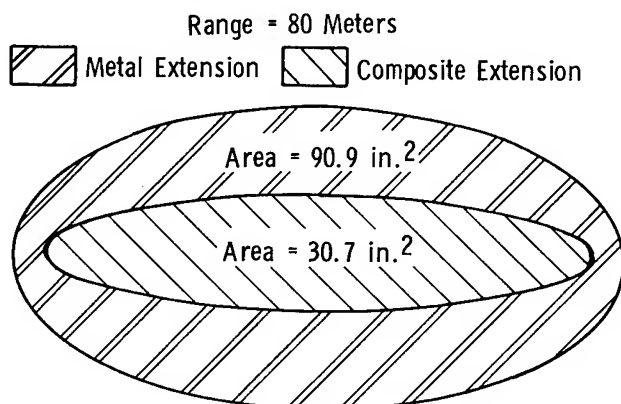


Figure 13. ROUND DISPERSION AREA

One point that must not be overlooked is that the horizontal variance was higher for the composite even though the average horizontal shot locations were very similar for the two extensions. This phenomenon has not been explained. One suggestion is that because the composite extension was mounted and fired after the metal extension, the test stand might have loosened. It is also interesting to note that on the day of the firing of the metal extension there was essentially no wind, whereas on the day that the composite extension was tested the winds were gusting up to 15 mph. Whether this point is significant or not has not been determined.

VII. RECOMMENDATIONS

Although vertical round dispersion was significantly decreased with the current graphite/epoxy system, and the accuracy of the gun increased, further addition of composites would result in still better overall performance.

At the breech end of the tube, where the highest bending stresses occur, is where the composite would be most needed. To implement this, more detailed analyses would be needed, especially with respect to the thermal problems.

Finally, there are other components used in large caliber weapons systems such as suspension components, trails, hydraulic accumulators etc. that would be candidates for the use of composite materials, and further investigation could be beneficial in many aspects such as cost, performance, and weight savings.

VIII. CONCLUSION

An advanced composite barrel extension for a 75mm gun to replace an all-metal extension has been designed, fabricated and tested. Test firings verified the thermal and structural behavior predicted by the computer codes. Round dispersion, muzzle deflections, and "time-to-damp" were markedly decreased, accompanied by a 16% weight savings and an increased natural frequency. The work serves as a base for a complete composite gun barrel to be designed, fabricated and field tested next year.

Weight savings, while modest at 16% in this first design, can be substantial. Taking into consideration the amount of steel that was replaced by graphite/epoxy, 37% weight savings resulted.

DOUGLAS and LEWIS

Other applications where graphite/epoxy has replaced steel have demonstrated weight savings up to 70%. This magnitude of weight savings augurs the development of highly mobile, lightweight vehicles capable of bearing large caliber weapons at a fraction of current systems weight.

IX. REFERENCES

- (1) R. M. Jones, Mechanics of Composite Materials 1975, McGraw-Hill, New York, NY
- (2) F. A. Vassallo and W. R. Brown, "Heat Transfer and Erosion in the Ares 75mm High Velocity Cannon," Vol 2, Calspan Technical Report, VL-5873-D-1, Buffalo, NY, October 7, 1977.
- (3) ORFE Version III, December 19, 1978, Developed by C. F. Freese at AMMRC, Watertown, MA 02172.